Exploring sex differences in the human brain *p. 915*

Inducing gain through loss in lasers *pp. 972 & 975*

Mathematical and mouse models for Ebola *p. 987*

Science

$10
21 NOVEMBER 2014
sciencemag.org

AAAS

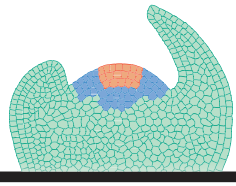


SPECIAL ISSUE

Exploring the skin

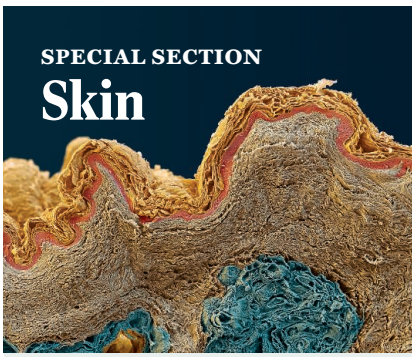
A close-up view of our largest organ *p. 932*

CONTENTS



922
Avoiding damaging mutations during fungal growth

21 NOVEMBER 2014 • VOLUME 346 • ISSUE 6212



INTRODUCTION

932 From bench to bedside

NEWS

934 Shedding light on skin color
By A. Gibbons

REVIEWS

937 Mammalian skin cell biology: At the interface between laboratory and clinic *F. M. Watt*

941 Advances in skin grafting and treatment of cutaneous wounds *B. K. Sun* et al.

945 The melanoma revolution: From UV carcinogenesis to a new era in therapeutics
J. A. Lo and D. E. Fisher

950 The gentle touch receptors of mammalian skin
A. Zimmerman et al.

954 Dialogue between skin microbiota and immunity
Y. Belkaid and J. A. Segre

SEE ALSO

▸ VIDEOS
▸ sciencemag.org/special/skin

ON THE COVER

An extreme close-up of the skin on a human hand. In this issue of *Science*, a special section explores the basic biology of mammalian skin in health and disease. See page 932. *Photo: © Joe McNally*



NEWS

IN BRIEF

898 Roundup of the week's news

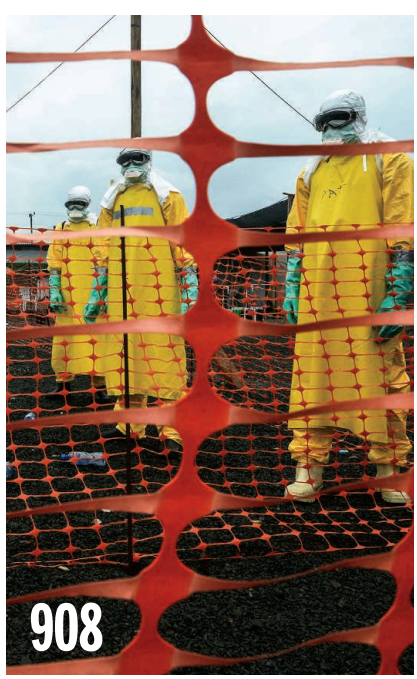
IN DEPTH

900 **PHILAE PROBE MAKES BUMPY TOUCHDOWN ON A COMET**
Elation and disappointment as lander goes into early hibernation, curtailing experiments *By E. Hand*

902 **NEW SUPPORT FOR 'GAY GENE'**
Replication of 1993 study highlights same region on X chromosome, but some still call evidence inconclusive
By K. Servick

903 **CHINA'S PEAK CARBON PLEDGE RAISES POINTED QUESTIONS**
Modelers move to analyze implications of largest emitter's commitment to stabilize emissions by 2030
By D. Malakoff

904 **EXIT OF E.U. SCIENCE ADVISER TRIGGERS FUROR**
New European Commission says it hasn't decided how it will organize its scientific advice *By T. Rabesandratana*



FEATURES

905 **THE MYSTERY OF THE DEAD GALAXIES**
Astronomers thought they knew why all galaxies eventually redden and die. They were wrong *By A. Finkbeiner*

908 **A DOSE OF REALITY**
Does any treatment work against Ebola? Researchers may soon find out, if they can overcome daunting ethical and practical challenges
By J. Cohen and K. Kupferschmidt

911 **Saving lives without new drugs**
By J. Cohen

INSIGHTS

PERSPECTIVES

912 **RETHINKING CHINA'S NEW GREAT WALL**
Massive seawall construction in coastal wetlands threatens biodiversity *By Z. Ma*

915 **HIS BRAIN, HER BRAIN?**
Research exploring sex differences in the human brain must overcome "neurosexist" interpretations *By C. Fine*
▸ PODCAST

916 **TAKING THE MEASURE OF MOLTEN URANIUM OXIDE**
Levitated droplets of uranium oxide reveal a complex structure below and above the melting point *By A. Navrotsky*
▸ REPORT P. 984

918 **CAN EROSION DRIVE TECTONICS?**
Data from the eastern Himalaya challenge the idea that climate-driven erosion can control tectonics
By K. X. Whipple
▸ REPORT P. 978

919 **CHARTING THE LIFE-COURSE EPIDEMIOLOGY OF INFLUENZA**
How does influenza immunity develop over one's lifetime? *By J. Lessler*
▸ REPORT P. 996

921 **TEMPORAL TARGETS OF DRUG ACTION**
A circadian gene expression atlas shows that time of day is relevant to the oscillation of drug targets and the effects of medications *By G. A. FitzGerald*

Published by AAAS

CONTENTS

21 NOVEMBER 2014 • VOLUME 346 • ISSUE 6212



1007
Regulatory regions determine man or mouse



922 **HOW A LONG-LIVED FUNGUS KEEPS MUTATIONS IN CHECK**
Specific mechanisms of somatic growth protect long-lived fungi and plants from deleterious mutations *By D. K. Aanen*

BOOKS *ET AL.*

925 **FERAL**
By G. Monbiot, reviewd by C. Griffiths

926 **LONGITUDE PUNK'D**
H. Finch-Boyer, curator; reviewd by D. Dixon

LETTERS

928 **TROPICAL CROPS: CAUTIOUS OPTIMISM**
By X. Giam et al.

928 **RESPONSE**
By L. R. Carrasco et al.

928 **REWARDING ACADEMIC INNOVATION**
By P. R. Sanberg et al.

929 **OLDER SCIENTISTS GET THEIR DUE**
By K. B. Wray

RESEARCH

IN BRIEF

960 From *Science* and other journals

RESEARCH ARTICLES

CHROMOSOMES

963 Closing the cohesin ring: Structure and function of its Smc3-kleisin interface *T. G. Gligoris* et al.

968 Characterization of a DNA exit gate in the human cohesin ring *P. J. Huis in 't Veld* et al.

REPORTS

OPTICS

972 Single-mode laser by parity-time symmetry breaking *L. Feng* et al.

975 Parity-time–symmetric microring lasers *H. Hodaei* et al.

978 **GEOMORPHOLOGY**
Tectonic control of Yarlung Tsangpo Gorge revealed by a buried canyon in Southern Tibet *P. Wang* et al.
▸ PERSPECTIVE P. 918

981 **EXOPLANET MAGNETISM**
Magnetic moment and plasma environment of HD 209458b as determined from Lyα observations *K. G. Kislyakova* et al.

984 **LIQUID STRUCTURE**
Molten uranium dioxide structure and dynamics *L. B. Skinner* et al.
▸ PERSPECTIVE P. 916

987 **EBOLA MOUSE MODEL**
Host genetic diversity enables Ebola hemorrhagic fever pathogenesis and resistance *A. L. Rasmussen* et al.

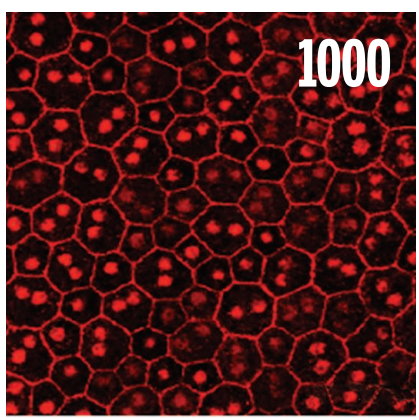
991 **EBOLA EPIDEMIOLOGY**
Strategies for containing Ebola in West Africa *A. Pandey* et al.

996 **INFLUENZA IMMUNOLOGY**
Antibody landscapes after influenza virus infection or vaccination
J. M. Fonville et al.
▸ PERSPECTIVE P. 919

1000 **INFLAMMATION**
Nucleoside reverse transcriptase inhibitors possess intrinsic anti-inflammatory activity
B. J. Fowler et al.

1004 ***HOX* LOCI REGULATION**
Convergent evolution of complex regulatory landscapes and pleiotropy at *Hox* loci *N. Lonfat* et al.

1007 **MOUSE GENOMICS**
Mouse regulatory DNA landscapes reveal global principles of cis-regulatory evolution *J. Vierstra* et al.



DEPARTMENTS

895 **EDITORIAL**
More *Science* in the Classroom
By Marcia McNutt

1026 **WORKING LIFE**
The winding road
By Ranjan Mukherjee

Science Staff 892
New Products 1016
Science Careers 1018

SCIENCE (ISSN 0036-8075) is published weekly on Friday, except the last week in December, by the American Association for the Advancement of Science, 1200 New York Avenue, NW, Washington, DC 20005. Periodicals mail postage (publication No. 484460) paid at Washington, DC, and additional mailing offices. Copyright © 2014 by the American Association for the Advancement of Science. The title SCIENCE is a registered trademark of the AAAS. Domestic individual membership and subscription (51 issues): $153 ($74 allocated to subscription). Domestic institutional subscription (51 issues): $1282; Foreign postage extra: Mexico, Caribbean (surface mail) $55; other countries (air assist delivery) $85. First class, airmail, student, and emeritus rates on request. Canadian rates with GST available upon request, GST #1254 88122. Publications Mail Agreement Number 1069624. **Printed in the U.S.A.**
Change of address: Allow 4 weeks, giving old and new addresses and 8-digit account number. **Postmaster:** Send change of address to AAAS, P.O. Box 96178, Washington, DC 20090–6178. **Single-copy sales:** $10.00 current issue, $15.00 back issue prepaid includes surface postage; bulk rates on request. **Authorization to photocopy** material for internal or personal use under circumstances not falling within the fair use provisions of the Copyright Act is granted by AAAS to libraries and other users registered with the Copyright Clearance Center (CCC) Transactional Reporting Service, provided that $30.00 per article is paid directly to CCC, 222 Rosewood Drive, Danvers, MA 01923. The identification code for *Science* is 0036-8075. *Science* is indexed in the *Reader's Guide to Periodical Literature* and in several specialized indexes.

Published by AAAS

Science
AAAS
1200 New York Avenue, NW, Washington, DC 20005
Bateman House, 82-88 Hills Road, Cambridge, UK CB2 1LQ

Editor-in-Chief Marcia McNutt
Executive Editor Monica M. Bradford **News Editor** Tim Appenzeller
Managing Editor, Research Journals Katrina L. Kelner
Deputy Editors Barbara R. Jasny, Andrew M. Sugden(UK), Valda J. Vinson, Jake S. Yeston

Research and Insights

SR. EDITORS Caroline Ash(UK), Gilbert J. Chin, Lisa D. Chong, Maria Cruz(UK), Julia Fahrenkamp-Uppenbrink(UK), Pamela J. Hines, Stella M. Hurtley(UK), Paula A. Kiberstis, Marc S. Lavine(Canada), Kristen L. Mueller, Ian S. Osborne(UK), Beverly A. Purnell, L. Bryan Ray, Guy Riddihough, H. Jesse Smith, Jelena Stajic, Peter Stern(UK), Phillip D. Szuromi, Brad Wible, Nicholas S. Wigginton, Laura M. Zahn **ASSOCIATE EDITORS** Brent Grocholski, Melissa R. McCartney, Margaret M. Moerchen, Sacha Vignieri **ASSOCIATE BOOK REVIEW EDITOR** Valerie B. Thompson **ASSOCIATE LETTERS EDITOR** Jennifer Sills **CHIEF CONTENT PRODUCTION EDITOR** Cara Tate **SR. CONTENT PRODUCTION EDITORS** Harry Jach, Trista Wagoner **CONTENT PRODUCTION EDITORS** Jeffrey E. Cook, Chris Filiatreau, Cynthia Howe, Lauren Kmec, Barbara P. Ordway **SR. EDITORIAL COORDINATORS** Carolyn Kyle, Beverly Shields **EDITORIAL COORDINATORS** Ramatoulaye Diop, Joi S. Granger, Lisa Johnson, Anita Wynn **PUBLICATIONS ASSISTANTS** Aneera Dobbins, Jeffrey Hearn, Dona Mathieu, Le-Toya Mayne Flood, Shannon McMahon, Scott Miller, Jerry Richardson, Rachel Roberts(UK), Alice Whaley(UK), Brian White **EXECUTIVE ASSISTANT** Anna Bashkirova **ADMINISTRATIVE SUPPORT** Janet Clements(UK), Michael Crabtree(UK, Intern), Lizanne Newton(UK), Maryrose Madrid, John Wood(UK)

News

NEWS MANAGING EDITOR John Travis **INTERNATIONAL EDITOR** Richard Stone **DEPUTY NEWS EDITORS** Daniel Clery(UK), Robert Coontz, Elizabeth Culotta, David Grimm, David Malakoff, Leslie Roberts **CONTRIBUING EDITORS** Martin Enserink(Europe), Mara Hvistendahl (Asia) **SR. CORRESPONDENTS** Jeffrey Mervis, Elizabeth Pennisi **NEWS WRITERS** Adrian Cho, Jon Cohen, Jennifer Couzin-Frankel, Carolyn Gramling, Eric Hand, Jocelyn Kaiser, Kelly Servick, Robert F. Service, Erik Stokstad, Emily Underwood **INTERNS** David Shultz, Jia You **CONTRIBUTING CORRESPONDENTS** Pallava Bagla(South Asia), Michael Balter(Paris), John Bohannon, Ann Gibbons, Sam Kean, Richard A. Kerr, Eli Kintisch, Kai Kupferschmidt(Berlin), Andrew Lawler, Christina Larson(Beijing), Mitch Leslie, Charles C. Mann, Eliot Marshall, Virginia Morell, Dennis Normile(Tokyo), Heather Pringle, Tania Rabesandratana(Brussels), Gretchen Vogel(Berlin), Lizzie Wade(Mexico City) **CAREERS** Jim Austin(Editor), Donisha Adams **COPY EDITORS** Kara Estelle, Nora Kelly, Jennifer Levin **ADMINISTRATIVE SUPPORT** Scherraine Mack

Executive Publisher Alan I. Leshner
Publisher Kent R. Anderson **Chief Digital Media Officer** Rob Covey

BUSINESS OPERATIONS AND ADMINISTRATION DIRECTOR Deborah Rivera-Wienhold **BUSINESS SYSTEMS AND FINANCIAL ANALYSIS DIRECTOR** Randy Yi **MANAGER OF FULFILLMENT SYSTEMS** Neal Hawkins **SYSTEMS ANALYST** Nicole Mehmedovich **ASSISTANT DIRECTOR, BUSINESS OPERATIONS** Eric Knott **MANAGER, BUSINESS OPERATIONS** Jessica Tierney **BUSINESS ANALYSTS** Cory Lipman, Cooper Tilton, Celeste Troxler **FINANCIAL ANALYST** Jeremy Clay **RIGHTS AND PERMISSIONS ASSISTANT DIRECTOR** Emilie David **PERMISSIONS ASSOCIATE** Elizabeth Sandler **RIGHTS, CONTRACTS, AND LICENSING ASSOCIATE** Lili Kiser

MARKETING DIRECTOR Ian King **MARKETING MANAGER** Julianne Wielga **MARKETING ASSOCIATE** Elizabeth Sattler **SR. MARKETING EXECUTIVE** Jennifer Reeves **SR. ART ASSOCIATE, PROJECT MANAGER** Tzeitel Sorrosa **ART ASSOCIATE** Seil Lee **ASSISTANT COMMERCIAL EDITOR** Selby Frame **MARKETING PROJECT MANAGER** Angelissa McArthur **SR. WRITER** Bill Zimmer **PROGRAM DIRECTOR, AAAS MEMBER CENTRAL** Peggy Mihelich **FULFILLMENT SYSTEMS AND OPERATIONS** membership@aaas.org **MANAGER, MEMBER SERVICES** Pat Butler **SPECIALISTS** LaToya Casteel, Javia Flemmings, Latasha Russell **MANAGER, DATA ENTRY** Mickie Napoleoni **DATA ENTRY SPECIALISTS** JJ Regan, Jaimee Wise, Fiona Giblin

DIRECTOR, SITE LICENSING Tom Ryan **DIRECTOR, CORPORATE RELATIONS** Eileen Bernadette Moran **SR. PUBLISHER RELATIONS SPECIALIST** Kiki Forsythe **PUBLISHER RELATIONS MANAGER** Catherine Holland **PUBLISHER RELATIONS, EASTERN REGION** Keith Layson **PUBLISHER RELATIONS, WESTERN REGION** Ryan Rexroth **MANAGER, SITE LICENSE OPERATIONS** Iquo Edim **FULFILLMENT ANALYST** Lana Guz **ASSOCIATE DIRECTOR, MARKETING** Christina Schlecht **MARKETING ASSOCIATES** Thomas Landreth, Minah Kim

DIRECTOR OF WEB TECHNOLOGIES Ahmed Khadr **SR. DEVELOPER** Chris Coleman **DEVELOPERS** Dan Berger, Jimmy Marks **SR. PROJECT MANAGER** Trista Smith **SYSTEMS ENGINEER** Luke Johnson **PRODUCT MANAGER** Walter Jones

CREATIVE DIRECTOR, MULTIMEDIA Martyn Green **DIRECTOR OF ANALYTICS** Enrique Gonzales **SR. WEB PRODUCER** Sarah Crespi **WEB PRODUCER** Alison Crawford **VIDEO PRODUCER** Nguyen Nguyen **SOCIAL MEDIA PRODUCER** Meghna Sachdev

DIRECTOR OF OPERATIONS PRINT AND ONLINE Lizabeth Harman **PRINT PRODUCTION DIRECTOR** Wendy K. Shank **PREFLIGHT MANAGER** Marcus Spiegler **ASSISTANT MANAGER ONLINE** Lisa Stanford **ASSISTANT MANAGER PRINT** Rebecca Doshi **SR SPECIALISTS** Steve Forrester, Jason Hillman, Antoinette Hodal, Tara Kelly, Anthony Rosen **SPECIALISTS** Jacob Hedrick, Nichele Johnston, Lori Murphy, Kimberley Oster

DESIGN DIRECTOR Beth Rakouskas **ASSOCIATE ART DIRECTOR** Laura Creveling **SR. ILLUSTRATORS** Chris Bickel, Katharine Sutliff **ILLUSTRATOR** Valerie Altounian **SR. ART ASSOCIATES** Holly Bishop, Preston Huey **ART ASSOCIATES** Kay Engman, Garvin Grullón, Chrystal Smith **SR. PHOTO EDITOR** William Douthitt **PHOTO EDITOR** Leslie Blizard

DIRECTOR, GLOBAL COLLABORATION, CUSTOM PUBLICATIONS, ADVERTISING Bill Moran **EDITOR, CUSTOM PUBLISHING** Sean Sanders: 202-326-6430 **ASSISTANT EDITOR, CUSTOM PUBLISHING** Tianna Hicklin: 202-326-6463 **ADVERTISING MARKETING MANAGER** Justin Sawyers: 202-326-7061 science_advertising@aaas.org **ADVERTISING MARKETING ASSOCIATE** Javia Flemmings **ADVERTISING SUPPORT MANAGER** Karen Foote: 202-326-6740 **ADVERTISING PRODUCTION OPERATIONS MANAGER** Deborah Tompkins **SR. PRODUCTION SPECIALIST/GRAPHIC DESIGNER** Amy Hardcastle **PRODUCTION SPECIALIST** Yuse Lajiminmuhip **SR. TRAFFIC ASSOCIATE** Christine Hall **SALES COORDINATOR** Shirley Young **ASSOCIATE DIRECTOR, COLLABORATION, CUSTOM PUBLICATIONS/CHINA/TAIWAN/KOREA/SINGAPORE** Ruolei Wu: +86-186 0822 9345, rwu@aaas.org **COLLABORATION/CUSTOM PUBLICATIONS/JAPAN** Adarsh Sandhu + 81532-81-5142 asandhu@aaas.org **EAST COAST/E. CANADA** Laurie Faraday: 508-747-9395, FAX 617-507-8189 **WEST COAST/W. CANADA** Lynne Stickrod: 415-931-9782, FAX 415-520-6940 **MIDWEST** Jeffrey Dembksi: 847-498-4520 x3005, Steven Loerch: 847-498-4520 x3006 **UK EUROPE/ASIA** Roger Goncalves: TEL/FAX +41 43 243 1358 **JAPAN** Katsuyoshi Fukamizu(Tokyo): +81-3-3219-5777 kfukamizu@aaas.org **CHINA/TAIWAN** Ruolei Wu: +186-0082-9345

WORLDWIDE ASSOCIATE DIRECTOR OF SCIENCE CAREERS Tracy Holmes: +44 (0) 1223 326525, FAX +44 (0) 1223 326532 tholmes@science-int.co.uk **CLASSIFIED** advertise@sciencecareers.org **U.S. SALES** Tina Burks: 202-326-6577, Nancy Toema: 202-326-6578 **SALES ADMINISTRATOR** Marci Gallun **EUROPE/ROW SALES** Axel Gesatzki, Sarah Lelarge **SALES ASSISTANT** Kelly Grace **JAPAN** Hiroyuki Mashiki(Kyoto): +81-75-823-1109 hmashiki@aaas.org **CHINA/TAIWAN** Ruolei Wu: +86-186 0082 9345 rwu@aaas.org **MARKETING MANAGER** Allison Pritchard **MARKETING ASSOCIATE** Aimee Aponte

AAAS BOARD OF DIRECTORS RETIRING PRESIDENT, CHAIR Phillip A. Sharp **PRESIDENT** Gerald R. Fink **PRESIDENT-ELECT** Geraldine (Geri) Richmond **TREASURER** David Evans Shaw **CHIEF EXECUTIVE OFFICER** Alan I. Leshner **BOARD** Bonnie L. Bassler, May R. Berenbaum, Carlos J. Bustamante, Claire M. Fraser, Laura H. Greene, Elizabeth Loftus, Raymond Orbach, Inder M. Verma

SUBSCRIPTION SERVICES For change of address, missing issues, new orders and renewals, and payment questions: 866-434-AAAS (2227) or 202-326-6417, FAX 202-842-1065. Mailing addresses: AAAS, P.O. Box 96178, Washington, DC 20090-6178 or AAAS Member Services, 1200 New York Avenue, NW, Washington, DC 20005

INSTITUTIONAL SITE LICENSES 202-326-6755 **REPRINTS:** Author Inquiries 800-635-7181 **COMMERCIAL INQUIRIES** 803-359-4578 **PERMISSIONS** 202-326-6765, permissions@aaas.org **AAAS Member Services** 202-326-6417 or http://membercentral.aaas.org/discounts

Science serves as a forum for discussion of important issues related to the advancement of science by publishing material on which a consensus has been reached as well as including the presentation of minority of conflicting points of view. Accordingly, all articles published in *Science*—including editorials, news and comment, and books reviews—are signed and reflect the individual views of the authors and not official points of view adopted by AAAS or the institutions with which the authors are affiliated.

INFORMATION FOR AUTHORS See pages 680 and 681 of the 7 February 2014 issue or access www.sciencemag.org/about/authors

SENIOR EDITORIAL BOARD
A. Paul Alivisatos, *Lawrence Berkeley Nat'l. Laboratory,* **Ernst Fehr,** *U. of Zürich*
Susan M. Rosenberg, *Baylor College of Medicine,* **Michael S. Turner,** *U. of Chicago*

BOARD OF REVIEWING EDITORS (Statistics board members indicated with **(S)**)
Adriano Aguzzi, *U. Hospital Zürich*
Takuzo Aida, *U. of Tokyo*
Leslie Aiello, *Wenner-Gren Foundation*
Judith Allen, *U. of Edinburgh*
Sonia Altizer, *U. of Georgia*
Virginia Armbrust, *U. of Washington*
Sebastian Amigorena, *Institut Curie*
Kathryn Anderson, *Memorial Sloan-Kettering Cancer Center*
Peter Andolfatto, *Princeton U.*
Meinrat O. Andreae, *Max-Planck Inst. Mainz*
Paola Arlotta, *Harvard U.*
Johan Auwerx, *EPFL*
David Awschalom, *U. of Chicago*
Jordi Bascompte, *Estación Biológica de Doñana CSIC*
Facundo Batista, *London Research Inst.*
Ray H. Baughman, *U. of Texas, Dallas*
David Baum, *U. of Wisconsin*
Kamran Behnia, *ESPCI-ParisTech*
Yasmine Belkaid, *NIAID, NIH*
Philip Benfey, *Duke U.*
Stephen J. Benkovic, *Penn State U.*
Carlo Beenakker, *Leiden U.*
Gabriele Bergers, *U. of California, San Francisco*
Christophe Bernard, *Aix-Marseille U.*
Bradley Bernstein, *Massachusettes General Hospital*
Peer Bork, *EMBL*
Bernard Bourdon, *Ecole Normale Supérieure de Lyon*
Chris Bowler, *École Normale Supérieure*
Ian Boyd, *U. of St. Andrews*
Emily Brodsky, *U. of California, Santa Cruz*
Ron Brookmeyer, *U. of California Los Angeles* **(S)**
Christian Büchel, *U. Hamburg-Eppendorf*
Joseph A. Burns, *Cornell U.*
Gyorgy Buzsaki, *New York U. School of Medicine*
Blanche Capel, *Duke U.*
Mats Carlsson, *U. of Oslo*
David Clapham, *Children's Hospital Boston*
David Clary, *U. of Oxford*
Joel Cohen, *Rockefeller U., Columbia U.*
Jonathan D. Cohen, *Princeton U.*
James Collins, *Boston U.*
Robert Cook-Deegan, *Duke U.*
Alan Cowman, *Walter & Eliza Hall Inst.*
Robert H. Crabtree, *Yale U.*
Roberta Croce, *Vrije Universiteit*
Janet Currie, *Princeton U.*
Jeff L. Dangl, *U. of North Carolina*
Tom Daniel, *U. of Washington*
Frans de Waal, *Emory U.*
Stanislas Dehaene, *Collège de France*
Robert Desimone, *MIT*
Claude Desplan, *New York U.*
Ap Dijksterhuis, *Radboud U. of Nijmegen*
Dennis Discher, *U. of Pennsylvania*
Gerald W. Dorn II, *Washington U. School of Medicine*
Jennifer A. Doudna, *U. of California, Berkeley*
Bruce Dunn, *U. of California, Los Angeles*
Christopher Dye, *WHO*
Todd Ehlers, *U. of Tuebingen*
David Ehrhardt, *Carnegie Inst. of Washington*
Tim Elston, *U. of North Carolina at Chapel Hill*
Gerhard Ertl, *Fritz-Haber-Institut, Berlin*
Barry Everitt, *U. of Cambridge*
Ernst Fehr, *U. of Zurich*
Anne C. Ferguson-Smith, *U. of Cambridge*
Michael Feuer, *The George Washington U.*
Kate Fitzgerald, *U. of Massachusetts*
Peter Fratzl, *Max-Planck Inst.*
Elaine Fuchs, *Rockefeller U.*
Daniel Geschwind, *UCLA*
Andrew Gewirth, *U. of Illinois*
Karl-Heinz Glassmeier, *TU Braunschweig*
Ramon Gonzalez, *Rice U.*
Julia R. Greer, *Caltech*
Elizabeth Grove, *U. of Chicago*
Kip Guy, *St. Jude's Children's Research Hospital*
Taekjip Ha, *U. of Illinois at Urbana-Champaign*
Christian Haass, *Ludwig Maximilians U.*
Steven Hahn, *Fred Hutchinson Cancer Research Center*
Michael Hasselmo, *Boston U.*
Martin Heimann, *Max-Planck Inst. Jena*
Yka Helariutta, *U. of Cambridge*
James A. Hendler, *Rensselaer Polytechnic Inst.*
Janet G. Hering, *Swiss Fed. Inst. of Aquatic Science & Technology*
Michael E. Himmel, *National Renewable Energy Lab.*
Kai-Uwe Hinrichs, *U. of Bremen*
Kei Hirose, *Tokyo Inst. of Technology*
David Hodell, *U. of Cambridge*
David Holden, *Imperial College*
Lora Hooper, *UT Southwestern Medical Ctr. at Dallas*
Raymond Huey, *U. of Washington*
Steven Jacobsen, *U. of California, Los Angeles*
Kai Johnsson, *EPFL Lausanne*
Peter Jonas, *Inst. of Science & Technology (IST) Austria*
Matt Kaeberlein, *U. of Washington*
William Kaelin Jr., *Dana-Farber Cancer Inst.*
Daniel Kahne, *Harvard U.*
Daniel Kammen, *U. of California, Berkeley*
Masashi Kawasaki, *U. of Tokyo*
Joel Kingsolver, *U. of North Carolina at Chapel Hill*
Robert Kingston, *Harvard Medical School*
Eitonne Koechlin, *Ecole Normale Suprieure*
Alexander Kolodkin, *Johns Hopkins U.*
Roberto Kolter, *Harvard Medical School*
Alberto R. Kornblihtt, *U. of Buenos Aires*
Leonid Kruglyak, *UCLA*
Thomas Langer, *U. of Cologne*
Mitchell A. Lazar, *U. of Pennsylvania*
David Lazer, *Harvard U.*
Thomas Lecuit, *IBDM*
Virginia Lee, *U. of Pennsylvania*
Stanley Lemon, *U. of North Carolina at Chapel Hill*
Ottoline Leyser, *Cambridge U.*
Marcia C. Linn, *U. of California, Berkeley*
Jianguo Liu, *Michigan State U.*
Luis Liz-Marzan, *CIC biomaGUNE*
Jonathan Losos, *Harvard U.*
Ke Lu, *Chinese Acad. of Sciences*
Christian Lüscher, *U. of Geneva*
Laura Machesky, *CRUK Beatson Inst. for Cancer Research*
Anne Magurran, *U. of St. Andrews*
Oscar Marin, *CSIC & U. Miguel Hernández*
Charles Marshall, *U. of California, Berkeley*
C. Robertson McClung, *Dartmouth College*
Graham Medley, *U. of Warwick*
Yasushi Miyashita, *U. of Tokyo*
Richard Morris, *U. of Edinburgh*
Alison Motsinger-Reif, *NC State U.* **(S)**
Sean Munro, *MRC Lab. of Molecular Biology*
Thomas Murray, *The Hastings Center*
James Nelson, *Stanford U. School of Med.*
Karen Nelson, *J. Craig Venter Institute*
Daniel Neumark, *U. of California, Berkeley*
Timothy W. Nilsen, *Case Western Reserve U.*
Pär Nordlund, *Karolinska Inst.*
Helga Nowotny, *European Research Advisory Board*
Ben Olken, *MIT*
Joe Orenstein, *U. of California Berkeley & Lawrence Berkeley National Lab*
Harry Orr, *U. of Minnesota*
Andrew Oswald, *U. of Warwick*
Steve Palumbi, *Stanford U.*
Jane Parker, *Max-Planck Inst. of Plant Breeding Research*
Giovanni Parmigiani, *Dana-Farber Cancer Inst.* **(S)**
Donald R. Paul, *U. of Texas, Austin*
John H. J. Petrini, *Memorial Sloan-Kettering Cancer Center*
Joshua Plotkin, *U. of Pennsylvania*
Albert Polman, *FOM Institute AMOLF*
Philippe Poulin, *CNRS*
David Randall, *Colorado State U.*
Colin Renfrew, *U. of Cambridge*
Felix Rey, *Institut Pasteur*
Trevor Robbins, *U. of Cambridge*
Jim Roberts, *Fred Hutchinson Cancer Research Ctr.*
Barbara A. Romanowicz, *U. of California, Berkeley*
Jens Rostrup-Nielsen, *Haldor Topsoe*
Mike Ryan, *U. of Texas, Austin*
Mitinori Saitou, *Kyoto U.*
Shimon Sakaguchi, *Kyoto U.*
Miquel Salmeron, *Lawrence Berkeley National Lab*
Jürgen Sandkühler, *Medical U. of Vienna*
Alexander Schier, *Harvard U.*
Randy Seeley, *U. of Cincinnati*
Vladimir Shalaev, *Purdue U.*
Robert Siliciano, *Johns Hopkins School of Medicine*
Joseph Silk, *Institut d'Astrophysique de Paris*
Denis Simon, *Arizona State U.*
Alison Smith, *John Innes Centre*
Richard Smith, *U. of North Carolina* **(S)**
John Speakman, *U. of Aberdeen*
Allan C. Spradling, *Carnegie Institution of Washington*
Jonathan Sprent, *Garvan Inst. of Medical Research*
Eric Steig, *U. of Washington*
Paula Stephan, *Georgia State U. and National Bureau of Economic Research*
Molly Stevens, *Imperial College London*
V. S. Subrahmanian, *U. of Maryland*
Ira Tabas, *Columbia U.*
Sarah Teichmann, *Cambridge U.*
John Thomas, *North Carolina State U.*
Shubha Tole, *Tata Institute of Fundamental Research*
Christopher Tyler-Smith, *The Wellcome Trust Sanger Inst.*
Herbert Virgin, *Washington U.*
Bert Vogelstein, *Johns Hopkins U.*
Cynthia Volkert, *U. of Göttingen*
Douglas Wallace, *Dalhousie U.*
David Wallach, *Weizmann Inst. of Science*
Ian Walmsley, *U. of Oxford*
David A. Wardle, *Swedish U. of Agric. Sciences*
David Waxman, *Fudan U.*
Jonathan Weissman, *U. of California, San Francisco*
Chris Wikle, *U. of Missouri* **(S)**
Ian A. Wilson, *The Scripps Res. Inst.* **(S)**
Timothy D. Wilson, *U. of Virginia*
Rosemary Wyse, *Johns Hopkins U.*
Jan Zaanen, *Leiden U.*
Kenneth Zaret, *U. of Pennsylvania School of Medicine*
Jonathan Zehr, *U. of California, Santa Cruz*
Len Zon, *Children's Hospital Boston*
Maria Zuber, *MIT*

BOOK REVIEW BOARD
David Bloom, *Harvard U.,* **Samuel Bowring,** *MIT,* **Angela Creager,** *Princeton U.,* **Richard Shweder,** *U. of Chicago,* **Ed Wasserman,** *DuPont*

Published by AAAS

EDITORIAL

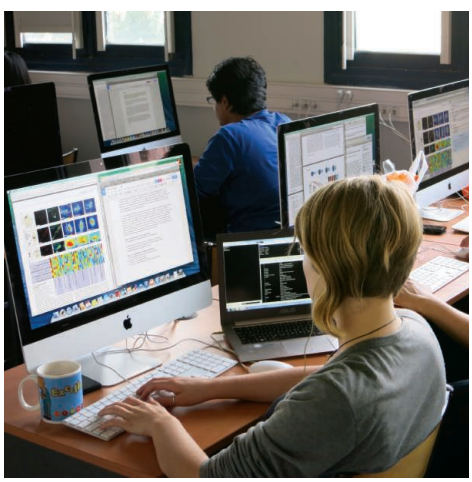
More *Science* in the Classroom



Marcia McNutt
Editor-in-Chief
Science *Journals*

About a year ago, Bruce Alberts and I announced the launch of *Science* in the Classroom (scienceintheclassroom.org), an online resource of annotated research papers published in *Science*, with associated teaching materials designed to help pre-college and college students understand how science moves forward as a structured way of revealing the laws of nature. Since its fledgling beginning last year, the project has expanded its subject diversity and continues to add articles at the rate of two per month. These articles have reached about 3000 users per month. But now it is time to take this project to the next level—and you can help, by annotating new papers and designing creative activities to accompany them.

The project depends on contributors who are graduate students or Ph.D.-level scientists with a solid understanding of the scientific method and a talent for translating specialized terms into language that is accessible to pre-college and college students. Volunteers are asked to contribute about 10 hours to annotate a scientific article. To date, the response from biologists has been strong, but volunteers from other fields, especially physical scientists, would ensure more choice of topics for students and educators in all classrooms. This activity might particularly appeal to scientists interested in exploring a career in education or writing.



...it is time to take this project to the next level—and you can help...

Indeed, *Science* in the Classroom has been used in college-level science writing courses and introductory general science courses. Using existing annotated papers as examples, students analyze, annotate, and review additional *Science* papers for posting to the *Science* in the Classroom library. They benefit by carefully deconstructing how a well-written research paper is composed. Through the annotation process, they broaden their vocabulary, and reviewing a paper sharpens critical-thinking skills. A byline on the *Science* in the Classroom website identifies the student group that annotated a particular paper.

The current collection of articles is an excellent pedagogical tool for understanding the science process: proposing a hypothesis, collecting evidence, testing the hypothesis, analyzing the results, and drawing conclusions. Understanding that science is an organized approach to objectively assessing evidence (whether from experiments, field observations, or models) is a good first step to counteracting the misconception that science is a static collection of facts. However, proper scientific methodology is more than just those steps. Hands-on engagement is an important part of the learning process. Therefore, *Science* in the Classroom is looking for creativity in the activities that complement the articles. For example, in "A Tiny Fungus is Causing Big Problems," the activity that accompanies the *Science* paper allows students to count bats exiting a cave from video footage and then determine the population through the same process used by the researchers (hint: It isn't easy!). In "Replicating Photosynthesis," the authors provided data on cathode materials that that were not included in their research paper. Instead of being lost in a lab notebook, the data are available for students to perform the same calculations that the authors used (including applying the gas law, something every science student learns but rarely uses in context) and generate a data figure similar to those published in *Science*. Well-designed activities effectively connect students to the material they are learning—both the process and the subject matter. I challenge educators to get involved by working with the authors of a *Science* paper to create more of these associated activities.

Student volunteers* grow as science translators while demystifying science for others. As graduate student Stephanie Redmond from the University of California, San Francisco, reflected, "I realized that helping people look at things in a slightly different way can allow them to get it. It doesn't have to be scary. Especially in high school and the early college years, people get turned off to science for no good reason!"

– Marcia McNutt

PHOTO: DUSAN MISEVIC

*Information at scienceeducation@aaas.org.

10.1126/science.aaa1728

Downloaded from www.sciencemag.org on November 22, 2014

Published by AAAS

NEWS

> "I'm feeling a bit tired, did you get all my data? I might take a nap ..."
>
> **Tweet by "Philae Lander" (@Philae2014)** on 14 November.

See page 900 for full story.



A blood star afflicted with the wasting syndrome, near Washington's Whidbey Island in 2013.

IN BRIEF

Sea star killer probably a virus

A wasting disease that has devastated sea stars along the west coast of the United States is likely due to a densovirus, a type of virus that infects crustaceans and insects. Ian Hewson, a microbial oceanographer at Cornell University, sequenced tissue samples and found that the virus was more common in the sick stars than in those that looked healthy. In experiments, viral levels increased as sea stars fell sick, researchers reported this week in a paper in the *Proceedings of the National Academy of Sciences*. The virus also turned up in museum samples dating back to 1942, suggesting that it persists in the environment—and deepening the mystery about why the current outbreak has been so severe. One idea is that an overabundance of sea stars increases the transmission of the virus. Ecologists are already seeing impacts from the sea star die-off, as their prey increase. More than 20 species of sea star have been afflicted.

AROUND THE WORLD

U.S. survey question in peril

WASHINGTON, D.C | A proposal to drop a question about college degrees from the American Community Survey (ACS) would make it much harder for the National Science Foundation (NSF) to track trends in the U.S. scientific workforce. The ACS, which debuted in 2005 as a successor to the long form of the decennial census, surveys 3.5 million households a year. In 2009, the Census Bureau added a question about one's undergraduate major. That saved NSF from fielding a separate survey to help analyze the nation's scientific workforce. But last month, under pressure from Congress to streamline the ACS, the Census Bureau proposed dropping that question and six others. Social scientists hope to persuade the Obama administration to retain the question, which they say provides valuable data not available elsewhere. **http://scim.ag/Q12Survey**

New bird flu strain in Europe

AMSTERDAM | A highly pathogenic bird flu strain named H5N8 that had never been seen in Europe has struck the continent three times this month, triggering cullings of poultry, tight control measures, and worries about further spread. Since 6 November, the H5N8 avian influenza strain has caused outbreaks at a turkey plant in Germany, a chicken facility in the Netherlands, and a duck breeding farm in the United Kingdom. H5N8 caused outbreaks in Japan, South Korea, and China earlier this year; migratory birds may have carried it westward. Although virologists can't rule out human infections with H5N8, no such cases have ever been found and the European Centre for Disease Prevention and Control has deemed the public health risk "very low."

U.S. plans two supercomputers

WASHINGTON, D.C. | The United States Department of Energy announced last week that it will spend $325 million on two extreme-scale computers to be delivered to national labs in Oak Ridge, Tennessee, and Livermore, California, in 2017. The agency will spend another $100 million to improve software and

PHOTO: JAN KOCIAN

Downloaded from www.sciencemag.org on November 22, 2014

Published by AAAS

applications that will run on the new machines. Though the specifications for the computers are still in flux, they're expected to run at speeds of between 100 and 300 petaflops (10^{15} floating point operations per second). That could make them nearly 10 times faster than China's Tianhe-2, crowned the world's fastest supercomputer in the TOP500 list released 17 November. The jump would mark a key milestone toward the goal of creating the first "exascale" (10^{18} flops) supercomputer, the next major landmark in high-performance computing. http://scim.ag/USsupercomp

E.U. closer to enabling GM bans

BRUSSELS | Members of the European Parliament agreed 11 November on draft rules allowing individual governments to ban cultivation of genetically modified (GM) crops in their territory, even if the products have been authorized at the European level. The European Food Safety Authority has sanctioned several GM crops, but many consumers spurn these foods, and some national governments have tried outlawing them. Disagreement among states has crippled regulatory decisions; to avoid such impasses, the plan gives more power to national governments—at the expense of pan-European market congruence. Biotech companies and plant scientists alike have warned that the proposal sets a negative precedent. But GM opponents have praised the Parliament's latest version of the bill for trying to give governments more solid rights to ban GM cultivation in their territory. http://scim.ag/GMcropsinEU

NEWSMAKERS

Rush Holt to lead AAAS

Rush Holt, a physicist and eight-term Democratic member of Congress, has been named the new CEO of AAAS (publisher of *Science*). He will succeed Alan Leshner, a neuroscientist who is stepping down in February after leading AAAS since 2001. Holt, 66, has represented a New Jersey district since 1999 and was part of an unofficial, bipartisan "physics caucus" in Congress that, at its peak, totaled three members who held physics Ph.D.s. In February, he announced he would not seek another term, but would continue his efforts "to bring more scientific thinking to public policy and to American society in general. I think it's important to maintain freedom of inquiry and to make sure that we have support not just for research but also for scientific communication."



PHOTO: VLADIMIR PUSHKAREV/RUSSIAN CENTRE OF ARCTIC EXPLORATION/COURTESY OF *THE SIBERIAN TIMES*

A team member from the Russian Centre of Arctic Exploration descending into the sinkhole last week.

Scientists explore mysterious Siberian crater

Earlier this year, oil and gas technicians flying over northern Siberia's Yamal Peninsula spied a mysterious, newly formed sinkhole 60 meters across. Yamal is Russia's main production area for natural gas; the crater is located about 30 kilometers from the Bovanenkovo gas field. Some scientists have theorized that the collapse that formed the up-to-70-meter-deep hole may have been triggered by a chain reaction caused by the release of methane hydrates in the ice as a result of global warming. Last week, a team of scientists from the Russian Centre of Arctic Exploration and other institutes decided to take a closer look, climbing into the hole and descending to the base of the crater, a frozen-over lake more than 10 meters deep. Along with soil and ice samples, the team collected an array of stunning images of the crater, the largest of three new sinkholes on the peninsula.

BY THE NUMBERS

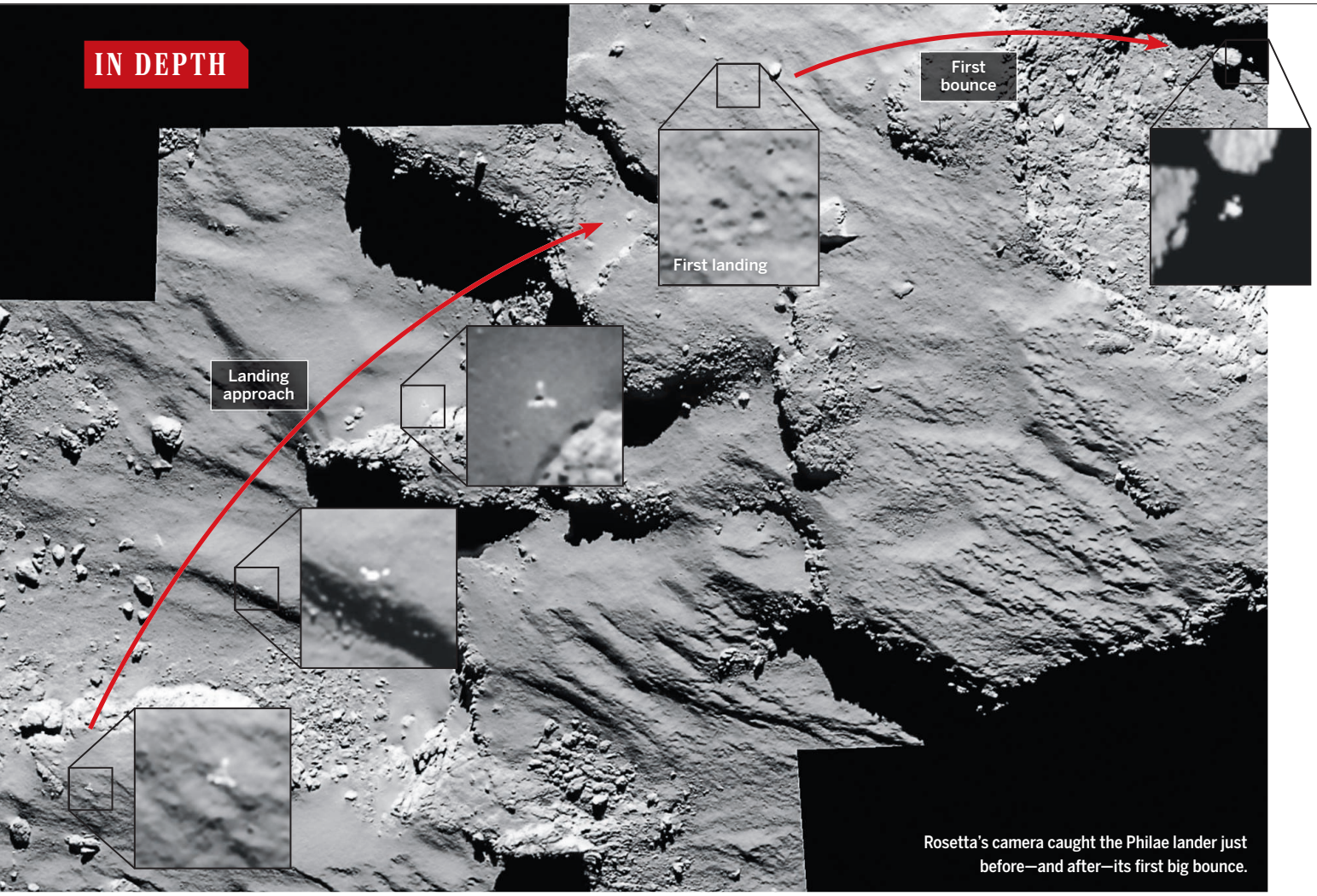
80 million

Number of bacteria that can be transmitted during a 10-second kiss, according to a study in *Microbiome*.

$1 million

New prize amount for the Association for Computing Machinery's Turing Award. The boost—four times the previous prize—is courtesy of Google.

Published by AAAS



Rosetta's camera caught the Philae lander just before—and after—its first big bounce.

PLANETARY SCIENCE

Philae probe makes bumpy touchdown on a comet

Elation and disappointment as lander goes into early hibernation, curtailing experiments

By **Eric Hand**, *in Darmstadt, Germany*

After the Philae probe bounced its way to a tenuous, unanchored perch on a comet—a bittersweet victory for the European Space Agency (ESA) and its Rosetta mission—Fred Jansen cried in the control room. Hours later, Jansen, the Rosetta project manager at ESA's European Space Research and Technology Centre in Noordwijk, the Netherlands, took himself to his hotel bar, bleary and hoarse. Colleagues asked to join him, but he brushed them off and drank two glasses of white wine alone. "I didn't know you could feel this bad and be so happy at the same time," he says. "Emotions are still running through my system in a way that is unbelievable."

Jansen had reason to feel joyful. Until last week, robots had landed on just six bodies: the moon, Venus, Mars, Saturn's moon Titan, and the asteroids Eros and Itokawa. Philae had added another locale to the list: a comet. "It's a great day," said ESA Director General Jean-Jacques Dordain in a postlanding briefing. "Not only for ESA but, I think, for the world." But it was not the perfect landing that Jansen and others had hoped for, against admittedly long odds. A series of glitches had doomed Philae to a short life and left its scientific harvest uncertain.

On 12 November, the Rosetta comet orbiter dropped Philae from an altitude of 22.5 kilometers. It took about 7 hours for the washing machine–sized probe to drift to the surface of 67P/Churyumov-Gerasimenko, a duck-shaped comet about 4 kilometers long. First came a big bounce, a sign that the comet's black crust of dust, organic molecules, and ice is harder than thought. Philae rebounded at the speed of a slow walk. In the weak gravity, it reached a height of a kilometer and may have flown laterally another kilometer. After a second, smaller bounce, it finally came to awkward stop—tipped up on its side and sitting in the shadows of some sort of cliff wall, with scant sunlight to recharge its batteries.

Scientists made the most of their new home. They tried to gather data from its 10 instruments for 57 hours, before the lander's batteries were exhausted and it fell into hibernation. It could be many weeks before scientists understand what the lander data tell them about the formation and composition of 67P, which, like all comets, is a relatively pristine object that dates to the early days of the solar system.

PHOTOS: ESA/ROSETTA/MPS FOR OSIRIS TEAM (6)

Downloaded from www.sciencemag.org on November 22, 2014

Published by AAAS

Just getting to 67P had been an immense challenge. Rosetta spent a decade after its 2004 launch wheeling through the solar system, traveling 6.5 billion kilometers before finally meeting up with its target in August. The long, intricate voyage has shown that ESA can manage a €1.4 billion mission with many moving parts and competing national interests. For example, Philae was built primarily by France and Germany, and its instruments were managed from control rooms in Toulouse, France, and Cologne, Germany—which in turn relayed instrument commands to Rosetta via ESA's main control room in Darmstadt, Germany.

The Rosetta orbiter will continue to orbit 67P for the next 13 months, monitoring the comet as it draws closer to the sun and ever more of its subsurface ice sublimes, or outgasses, driving jets of gas and dust. But, the landing was always going to be the mission's climax. It almost didn't come to pass. Two days before the attempt, controllers had trouble turning on the lander. The next day, engineers discovered that reverse thrusters, meant to keep Philae pinned to the surface after touchdown, were unlikely to work. Mission managers came within a hair's breadth of postponing the landing. "You can imagine the four-letter words," Jansen says.

Deciding that a delay would solve nothing, managers went ahead with the attempt. The problems multiplied at touchdown: Not only did the reverse thrusters not thrust, but two harpoons meant to fasten the probe also failed to fire, leaving Philae to bounce across the comet into rugged terrain.

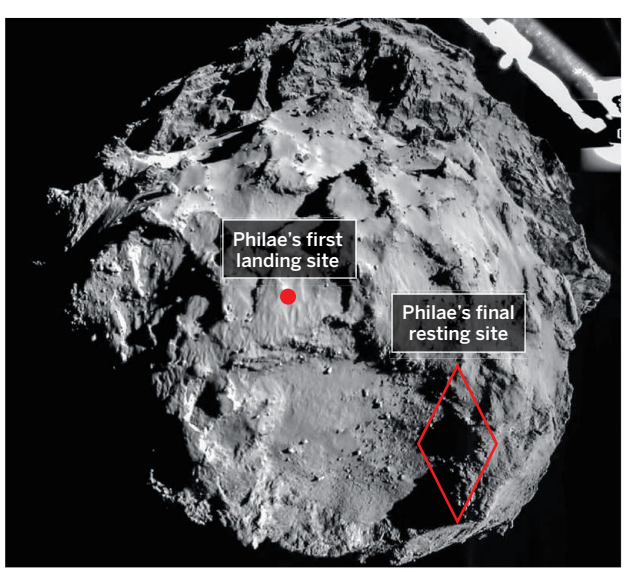
With just 1.5 hours of daylight a day falling on Philae in its shadowed position, hopes for recharging its batteries were dim. The elation of landing quickly turned into a frantic effort to wring science from the limited time. Not all turned out well. A rod meant to measure heat flow broke while the lander was attempting to hammer it into the comet's surprisingly tough surface. The shutters to another instrument—one that measures composition by bombarding materials with x-rays—did not open, so the instrument measured mostly the titanium and copper of the shutters. And the most sought-after result—an attempt to measure the composition of a subsurface sample obtained by a drill—did not come to pass. Fred Goesmann, principal investigator for one of two sample analysis instruments at the Max Planck Institute for Solar System in Göttingen, Germany, says the drill appeared to move down and up correctly. It also seemed to have delivered something to one of Goesmann's ovens. His ovens duly heated up. But the data show nothing. "It's indistinguishable from not having received a sample," Goesmann says. He doesn't know whether the problem was with the drilling or with his instrument.

There are still plenty of data to be thankful for. Both sample analysis instruments were able to "sniff" the gases present near the surface. Goesmann says one of his sniffs—just after the big bounce—seems richer than the others, perhaps a sign that dust was stirred up by the landing and sucked into his machine. The other sample analysis instrument, called Ptolemy, used its last moments to analyze a sniff chamber that had been trapping and concentrating ambient gases. Ptolemy's principal investigator, Ian Wright, of the Open University in Milton Keynes, U.K., hopes concentrations are high enough for researchers to measure rare isotopes of hydrogen, oxygen, and nitrogen. "We were pretty pleased at how things turned out," he says.

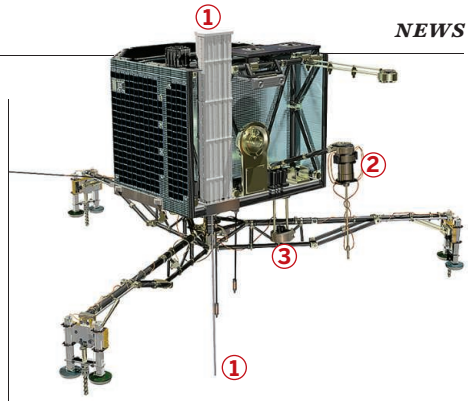
For Gerhard Schwehm, former project scientist for Rosetta, Philae was always going to be the cherry on top of a very big cake. The Rosetta orbiter remains entirely healthy and powerful, he says. Already, scientists are making significant findings. At a planetary science conference last week in Tucson, Arizona, members of the orbiter's camera team presented images that showed arcs of dust emanating from jets—a finding that could help them understand the mechanisms of outgassing. A radar instrument, working in concert with a receiver on Philae, got data about the interior of the comet that could help unravel a major question: Does 67P have its duck head and body because two separate cometesimals came together? Or was 67P stretched and nearly broken apart—perhaps by a gravitational perturbation from Jupiter?

And ROSINA, a Rosetta instrument that uses spectrometers to measure gas abundances, has obtained a highly sought after result: the so-called deuterium-to-hydrogen ratio of water in the comet's thin atmosphere, or coma. The measured value for 67P is much higher than the ratio in Earth's oceans and higher than in other comets, says ROSINA principal investigator Kathrin Altwegg, of the University of Bern. Three years ago, the comet Hartley-2 was found to have a D-to-H ratio near that of Earth's oceans—sparking interest in the notion that comet impacts delivered much of Earth's water. Altwegg says the result for 67P could make asteroids the primary suspect again.

In one of their last commands to Philae, controllers made the lander turn by 35° and lifted it up several centimeters, in hopes of putting Philae's solar panels in a more favorable position. Goesmann says he is still optimistic that they will get to do science again with Philae. As 67P approaches the sun and the comet's orientation changes, more light could reach its solar panels. He says the emotional roller coaster of last week is over for now, but not for good. "The battle's over, we're still alive," Goesmann says. "Did we win? I don't know." ■



A camera on the belly of Philae took this image 3 kilometers above the comet's surface. Scientists are still searching for the lander's final resting place.



Out in the cold

Philae tried to use all 10 of its instruments during its 57 hours on the surface, but some encountered problems.

1. SD2: Philae's drill tried to deliver a subsurface sample to an oven, but data indicate nothing was in the sample.

2. MUPUS: This heat-measuring device broke during attempts to penetrate the comet.

3. APXS: The shutters to this x-ray experiment never opened.

IMAGES: ESA (2)

Published by AAAS

HUMAN BEHAVIOR

New support for 'gay gene'

Replication of 1993 study highlights same region on X chromosome, but some still call evidence inconclusive

By **Kelly Servick**

Dean Hamer finally feels vindicated. More than 20 years ago, in a study that triggered both scientific and cultural controversy, the molecular biologist offered the first direct evidence of a "gay gene" by identifying a stretch on the X chromosome likely associated with homosexuality. Several subsequent studies failed to confirm Hamer's suspicion that a gene there subtly influences a person's predisposition to be gay, but the largest independent replication effort so far, looking at 409 pairs of gay brothers, has now fingered the same region on the X. "When you first find something out of the entire genome, you're always wondering if it was just by chance," says Hamer, who conducted research at the National Institutes of Health in Bethesda, Maryland, before formally retiring in 2011. The new research, he says, "clarifies the matter absolutely."

> ***"When you first find something out of the entire genome, you're always wondering if it was just by chance."***
>
> **Dean Hamer**, molecular biologist

Others, however, continue to doubt Hamer's result, contending that the latest evidence is weak. And the study still doesn't identify a specific gene whose role in homosexuality could be more closely examined.

Back in 1993, Hamer's original study led some to speculate that a genetic test for homosexuality would soon be at hand and could lead to more discrimination. Others attacked the premise that being gay has a biological basis. "For a long while, if you Googled my name, you would find right-wing religious Web pages saying that I was a liar," Hamer says.

The new analysis, published online this week in *Psychological Medicine*, was led by J. Michael Bailey, a psychologist at Northwestern University, and Alan Sanders, a psychiatrist at NorthShore University HealthSystem Research Institute, both in Evanston, Illinois. Bailey says he went into the project skeptical, largely because Hamer had studied just 38 pairs of gay brothers. "I thought that Dean did a fine but small study, but if I had to bet, I would have bet against our being able to replicate it."

In 2004, Bailey began to recruit families with at least two gay male siblings, planning to perform genetic linkage analysis, which searches family members for genetic markers consistently inherited by people with a common trait. DNA analysis revealed markers linked to homosexuality on both Xq28 and a region of chromosome 8, which Hamer had also highlighted.

Psychiatric geneticist Kenneth Kendler of Virginia Commonwealth University in Richmond, who is an editor at *Psychological Medicine*, says it was somewhat surprising to receive a genetic linkage study. The approach has been largely superseded by so-called genome-wide association (GWA) studies, which can home in on specific genes that contribute to a trait. "Seeing linkage studies in this world of GWAs is rare," Kendler says, but he maintains that the study "really moves the field along."

Still, Sanders acknowledges that at least one journal rejected the work. And geneticist Neil Risch of the University of California, San Francisco, notes that the linkages Bailey and Sanders report don't rise to statistical significance. Risch collaborated on a 1999 study that found no association of homosexuality with Xq28.

Sanders admits that the strongest linkage identified from an isolated genetic marker on Xq28 doesn't clear the threshold for significance. But he contends that the case is bolstered by neighboring markers, which appear to be shared at higher rates between pairs of gay brothers. "The convergence of the evidence pointed towards" Xq28 and chromosome 8, he asserts.

Bailey and Sanders may soon have more data to back their claim—or refute it. They are now working on a GWA study that includes genetic data from the just-published work plus DNA samples from more than 1000 additional gay men. Based on the results published this week, "it looks promising for there being genes in both of these regions," Bailey says, "but until somebody finds a gene, we don't know." ■

Downloaded from www.sciencemag.org on November 22, 2014

Published by AAAS



U.S. President Barack Obama and Chinese President Xi Jinping shake on a climate deal last week in Beijing.

PHOTO: AP PHOTO/PABLO MARTINEZ MONSIVAIS

CLIMATE POLICY

China's peak carbon pledge raises pointed questions

Modelers move to analyze implications of largest emitter's commitment to stabilize emissions by 2030

By **David Malakoff**

Five years ago, the sight of a rainbow delighted a group of Chinese and American climate policy experts gathered in Washington, D.C. The rainbow wasn't real: Instead, the colorful graph of arcing curves showed predictions for how China's carbon dioxide emissions, now rising fast, might flatten out and fall over the next 50 years.

The delight, however, was genuine. At the time, it wasn't clear how China could curb its spiraling emissions of greenhouse gases, which threatened to undermine global efforts to curb climate change, without enormous economic cost. But the rainbow showed that modeling teams were converging on a relatively optimistic conclusion: China could stop its emissions growth by the 2030s—and then begin making cuts—through a combination of ambitious but economically prudent energy policies and inexorable demographic change.

Last week's news that China has vowed to stabilize its greenhouse emissions by 2030 suggests that its leaders paid attention to such calculations. And despite calls for more radical cuts from some quarters, climate experts aren't minimizing the importance of the joint U.S.-China announcement on 12 November, which came as President Barack Obama visited Beijing. (He pledged that the United States will emit 26% to 28% percent less carbon in 2025 than it did in 2005.) "To tell the truth, we did not expect [China to set] such clear targets," says climate specialist Qi Ye, director of the Brookings-Tsinghua Center for Public Policy, a think tank in Beijing. China's goal is "relatively ambitious" and "implies a meaningful effort beyond business-as-usual," said Lynn Price, a leading modeler with the China Energy Group at the Lawrence Berkeley National Laboratory (LBNL) in California, in a statement. For example, to achieve its goal, China said that by 2030 at least 20% of its power will come from sources other than fossil fuels, up from about 10% today.

But the haziness of China's emissions pledge has sent many modelers scurrying back to their computers, eager to understand the implications and the obstacles. Critics of the bilateral deal, including leading Republican lawmakers in the United States, have been quick to point out that China is simply pledging to halt the growth of emissions, not cap them at a particular tonnage. That, they argue, could allow China to rapidly increase emissions over the next decade—by building fleets of new coal-fired power plants, for instance—in order to make the 2030 peak as high as possible.

But that scenario "flies in the face" of other realities, including the government's growing desire to reduce air pollution and diversify its power sources, says Deborah Seligsohn, a former U.S. diplomat who specialized in China's climate policy. Although China will certainly build some new coal-fired power plants, she says, the pledge means "it wouldn't make sense to build a bunch of new power plants that you then … take offline in 2030."

Indeed, models that include data on the falling prices of renewable power technologies, China's aging and stagnating population, and the nation's growing urbanization suggest that China could substantially lower the peak of its annual emissions—now about 7 billion tons (7 gigatons)—compared with existing scenarios. In 2030, the peak would fall from as much as 18 Gt to as little as 14 Gt, suggests one forecast by Climate Action Tracker, an alliance of four European research groups. Other studies suggest that if China adopts even more aggressive policies, as it says it might, emissions in 2030 could top out at just 8 or 10 Gt.

At the global level, modelers say the China and U.S. pledges would make a noticeable dent in carbon pollution, especially on top of a commitment earlier this year by 28 European nations to cut emissions by at least 40% below 1990 levels by 2030. In 2100, annual global emissions of carbon dioxide would be 80 Gt, about 20 Gt less than under existing trends, estimate researchers at Climate Interactive, a nonprofit in Washington, D.C. Still, the team notes that the reduction would neither prevent average global temperatures from rising nor keep warming below the 2°C threshold that many scientists say is desirable.

And despite China's apparent political will, the government may struggle to meet its pledge. Concerns about sustaining its rapid buildup of nuclear power and connecting solar and wind power to the national electrical grid could explain the relatively cautious 20% goal for nonfossil energy, said Nan Zhou, the deputy group leader of LBNL's China Energy Group, in a statement. Restraining emissions from transportation as a growing middle class demands cars may also be a challenge, Seligsohn says.

Stabilizing emissions by 2030 could shave 1% to 3.7% off China's gross domestic product, estimates Wang Yi, deputy director-general of the Institute of Policy and Management at the Chinese Academy of Sciences in Beijing. That could hamper government efforts to pull millions of people out of poverty. But China's willingness to risk that slowdown—and Obama's decision to move in parallel—"could have global reverberations" as nations prepare to finalize a new international climate agreement next year in Paris, says Joanna Lewis, a China scholar at Georgetown University in Washington, D.C. "There is no doubt," she says, "that the other major economies are carefully considering these announcements." ■

With reporting by Eli Kintisch and Ling Xin.

Downloaded from www.sciencemag.org on November 22, 2014

Published by AAAS

EUROPE

Exit of E.U. science adviser triggers furor

New European Commission says it hasn't decided how it will organize its scientific advice

By **Tania Rabesandratana**, *in Brussels*

If the European Commission's new boss, Jean-Claude Juncker, had hoped to build a good relationship with the scientific community, his first moves haven't helped. Last week, European scientists reacted angrily after it became clear that Juncker has effectively put an end to the position of the chief scientific adviser (CSA) to the commission, created only 3 years ago. Prominent researchers and science policy leaders called the move "an enormous blow," a "deep disappointment," and a "backward step."

But some observers say those reactions are premature because Juncker hasn't said exactly how the new commission wants to use scientific advice. They argue that the change of administration is a good time to rethink the commission's science advice system, because the position of CSA—so far held by Scottish biologist Anne Glover—was poorly defined.

Glover herself has become a lame duck. Her position expired when the previous commission, led by José Manuel Barroso, left office on 31 October; she still has a salary until February, but Glover says she can no longer speak on behalf of the commission and has canceled her engagements. Glover sent an e-mail last week to scientists and colleagues, saying that her position would not continue and bidding the scientific community farewell. She wrote that she was proud of what she had achieved.

Her announcement triggered a series of dismayed comments, many of them from the United Kingdom, which has had government science advisers for decades. (In most other European countries, national academies or other groups play that role.) Scrapping the CSA "would be a retrograde step," says James Wilsdon, a professor at the Science Policy Research Unit of the University of Sussex in the United Kingdom, because the role gives science a privileged, high-level voice. But he adds that instead of offering constructive thoughts on the science advice system, some British commenters appear to have used the opportunity to "have a go at Greenpeace or have a go at Europe." Some U.K. media outlets, for example, wrongly reported that Glover had been dismissed over her public support for transgenic crops, which she denies.



Anne Glover, who became science adviser to the European Commission in 2012, is a lame duck.

PHOTO: NEWSLINE MEDIA LIMITED

What exactly will happen now is unclear. Juncker announced on 5 November that the Bureau of European Policy Advisers, which housed Glover's office, will be scrapped—one of several changes he is making to the commission's bureaucracy—and replaced by a new European Political Strategy Centre. Glover says she has been told that this new center will not have a CSA position, and Juncker has so far dodged specific questions about science advice. "President Juncker believes in independent scientific advice," but has not yet decided how to "institutionalize" that function, says his representative. In an e-mail to *Science*, Glover expressed hope that the position Barroso gave her will somehow live on.

Indeed, Juncker's steps so far don't necessarily bode ill for the status of scientific advice, says Alberto Alemanno, a professor of E.U. law at HEC Paris in France. Juncker needs time to come up with a solid plan after two recent controversies turned scientific advice into a "sensitive issue," he says.

The first happened this summer, when Greenpeace and other nongovernmental organizations urged Juncker—then president-elect—to scrap the CSA's single-headed role, which they deem opaque and vulnerable to industry lobbying. In response, furious scientists told him to save Glover's post (*Science*, 1 August, p. 500). Later, Juncker sparked outrage when he proposed shifting responsibility for the science-based assessment and oversight of drugs from the health commissioner to the industry commissioner. Many scientists, consumer organizations, and members of the European Parliament opposed the plan because they worried public health recommendations would take a back seat to business concerns—and Juncker relented.

The position of CSA wasn't well thought out, Alemanno argues. "We never really asked what it would bring, but the added value was very limited," he says, and this summer's controversy caused severe "reputational damage" to the commission. Glover's job description was both vague and narrow, leaving her "in an institutional black hole." Even Glover herself told *Science* this summer that her position was sometimes frustrating, for instance because her budget and staff were very limited.

Whatever Juncker decides, science needs a clear entrance point to the commission, says Sofie Vanthournout, head of the Brussels office of the European Academies Science Advisory Council. "The CSA has been good for us," Vanthournout says, "but we're not saying there can't be any other model." ■

Published by AAAS

PHOTO: NASA, ESA, M. ROBBERTO (SPACE TELESCOPE SCIENCE INSTITUTE/ESA) AND THE HUBBLE SPACE TELESCOPE ORION TREASURY PROJECT TEAM

Downloaded from www.sciencemag.org on November 22, 2014

THE MYSTERY OF THE DEAD GALAXIES

Astronomers thought they knew why all galaxies eventually redden and die. They were wrong

By **Ann Finkbeiner**

A locked room, a dead body, and no apparent cause of death. It's the classic setup for a mystery. And it is effectively what astronomers found a few years ago when they used the Hubble Space Telescope's new Cosmic Origins Spectrograph (COS) to look at a handful of large galaxies within a few billion light-years of Earth.

Because the galaxies shone with the cool red light of old age rather than the hot blue light of youth, scientists knew they had stopped making new stars. Such "red, dead" galaxies make up roughly half of all the galaxies in the universe. For decades, researchers assumed that red galaxies are burning their way toward senescence and extinction because they have run out of the gas needed for star formation. But the COS data showed something quite different. In fact, the dying galaxies were surrounded by hydrogen and helium gas that, to all

Cool gas, the lifeblood of a galaxy, is condensing into hot young stars in the Orion Nebula, a star-forming region in the Milky Way.

appearances, should have been falling into the galaxies where it could make stars. But for some reason, it wasn't falling. "The gas is still out there waiting," says Molly Peeples of the Space Telescope Science Institute (STScI) in Baltimore, Maryland, a member of the so-called COS-Halos team. "Something has to not let the gas in."

That observation touched off a quest that continues today, as astronomers apply computer models and ever more refined observations to understand why red galaxies stay dead even though they have an abundant supply of gas. The answer, when it comes, will not only solve a nagging puzzle about how galaxies die, but will also deepen astronomers' understanding of how galaxies live and make stars.

"The tale of the galaxy," Peeples says, "is really the tale of the gas." Astronomers think the story goes like this: Galaxies are born in clouds of gas, which, here and there, condense into stars. Stars, in turn, blow gas out of their galaxy in fierce stellar winds when they are born and in violent blasts at the end of their lives, when some explode as supernovae. The gas hangs around the galaxy in a roughly spherical halo a few hundred thousand light-years across—about 20 times the size of the galaxy we see. Gravitationally bound to the galaxy, the gas in the so-called circumgalactic medium (CGM) cools until it falls back into the galaxy. There, it fuels new stars, the lives and deaths of which blow the gas back out. Over billions of years, the cycle repeats until the galaxy runs out of fresh gas; and as its stars burn through the remaining gas, the galaxy begins its long death.

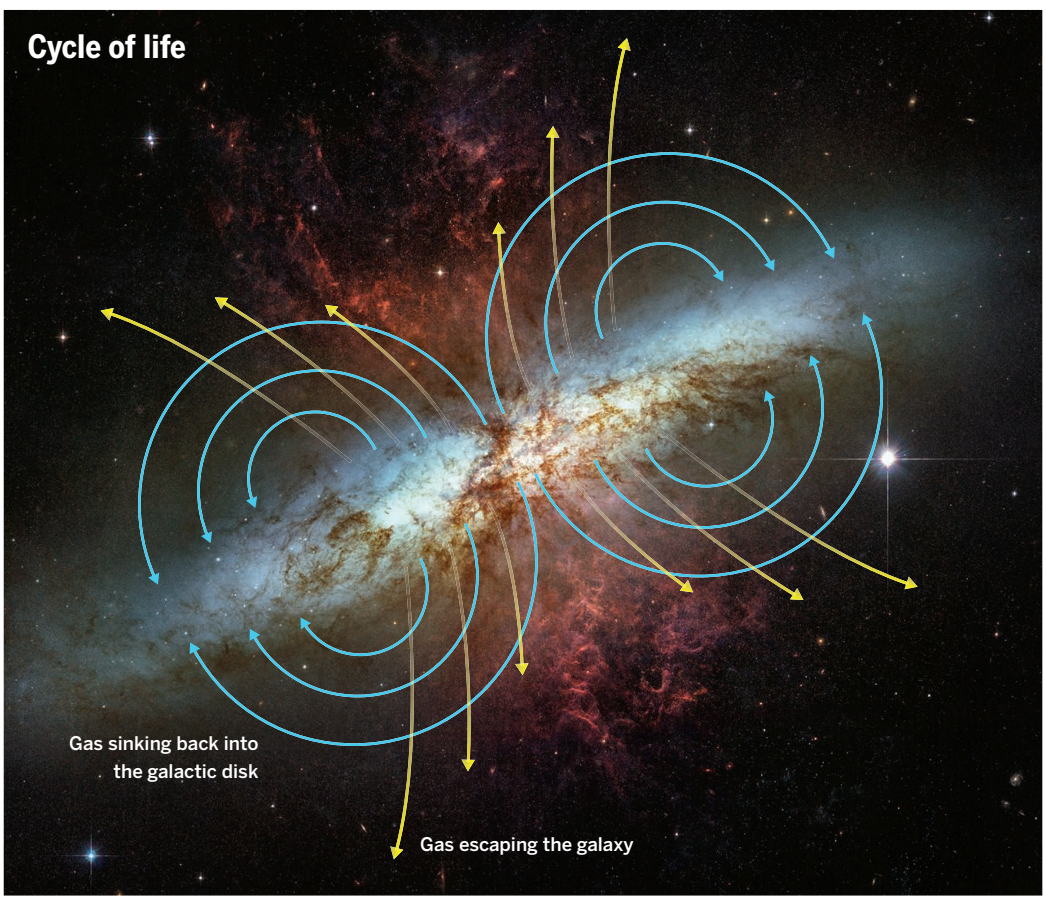
That storyline accounts for the two general families of galaxies, which astronomers identified more than a century ago. The spiral galaxies are blue, full of gas and newborn stars so hot that they produce floods of ultraviolet radiation. The elliptical galaxies are red; they have depleted their gas, their stars have aged and cooled, and their light has reddened. Astronomers believe that galaxies are born blue and die red. And because galaxies live by recycling gas, says STScI's Jason Tumlinson, head of the COS-Halos team, "the problem of galaxies going red is solved only by studying gas."

> ***"The tale of the galaxy is really the tale of the gas."***
>
> **Molly Peeples**, Space Telescope Science Institute

The ability to do that was a long time coming. One obstacle was cultural: The astronomers who studied galaxies were traditionally a separate community from those who studied gas. The latter community was small and specialized in reading the spectra of distant, brilliant galaxies called quasars. The quasars act as backlights for gas along the line of sight to Earth. As their light passes through the gas, some of it gets absorbed, causing its spectrum to show dark absorption lines that reveal the gas's abundance and properties, including its temperature and motion. By contrast, the galaxy people studied the relatively nearby universe, and at conferences on the days when gas talks were scheduled, says astronomer Charles Steidel of the California Institute of Technology (Caltech) in Pasadena, "the galaxy people went home."

Gas in the CGM is also hard to study. It is rarified—the CGM has a density of about one atom per cubic meter—and it emits very little light of its own. As a result, observing gas around red galaxies requires both fortuitously placed quasars and spectrographs, only recently available, that have high sensitivity and resolution and can observe more than one small field at a time. As a result, Tumlinson says, just in the past decade "are the threads coming together."

BY NOW, these observations have confirmed parts of the galaxy life cycle. In galaxies with newly forming stars, observers have traced swift outflows of hot gas. Steidel, an early crossover between the communities of gas and galactic astronomers, has spent the last 30 years gathering evidence on the relationship between the gas seen in quasar absorption spectra and the impossibly faint galaxies of the early universe, which were forming stars at prodigious rates. In well over 1000 of these blue, star-bursting galaxies, Steidel, along with Gwen Rudie at the Carnegie Observatories in Pasadena and other colleagues, saw gas at about 10,000 K flowing out of the galaxies at about 800 kilometers per second.



Gas erupts from M82, a spiral star-forming galaxy, driven by supernovae and a central black hole. Some moves fast enough to escape the galaxy altogether (yellow arrows), whereas other gas cools and sinks back into the galactic disk (blue arrows).

PHOTO: NASA, ESA, AND THE HUBBLE HERITAGE TEAM STSCI/AURA; ACKNOWLEDGMENT: J. GALLAGHER (UNIVERSITY OF WISCONSIN), M. MOUNTAIN (STSCI), AND P. PUXLEY (NSF)

Published by AAAS

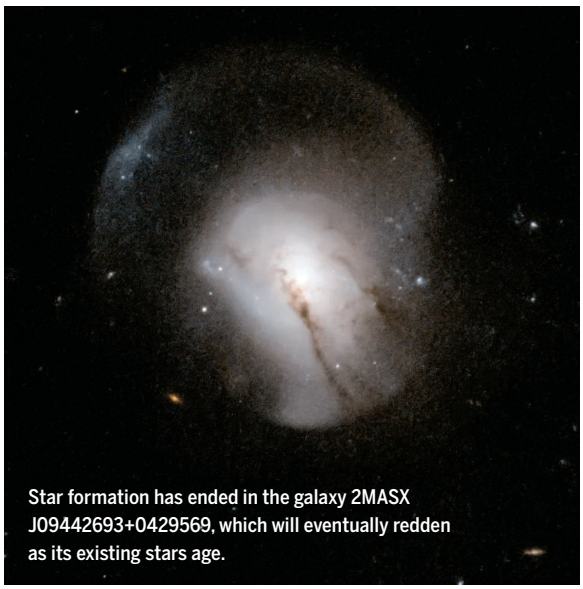
More recently, at intermediate distances, another team, led by Crystal Martin of the University of California, Santa Barbara, found gas at the same 10,000 K flowing at several hundred kilometers a second out of about half of 200 star-forming galaxies. Astronomers now think outflows from star-forming galaxies are ubiquitous.

Driving the outflows, theorists and observers agree, are probably supermassive black holes in galactic centers, supernovae exploding in galactic disks, or both. Black holes live in most galaxies and were probably born with them. When a black hole is pulling in surrounding material, its immense gravity fiercely heats the infalling material, turning a galaxy into a quasar and sending out enormous jets of radiation and gas. Massive stars at the ends of their lives explode into supernovae, making shock waves that send bubbles and fountains of gas out of the galaxy. The outflows are spectacular: Around living, star-forming galaxies, astronomers have detected as much gas in the CGM as is in the galaxies' stars. The blue star-bursting galaxies that Steidel saw in the early universe, full of short-lived, massive stars, are extreme cases, says STScI's Tumlinson: "Some lift off most of the gas they have."

The composition of the gas in the CGM confirms that it was flung out of galaxies. Steidel and colleagues found that the gas surrounding their distant blue galaxies was enriched in the heavy elements—magnesium, silicon, oxygen, iron—that are created by thermonuclear fusion in the cores of stars. And around 50 relatively nearby blue galaxies, the COS-Halos team found that the gas was similarly enriched, indicating that it had once been inside the galaxies' stars.

THE FLOWS CAN'T BE ONE-WAY. If they were, the galaxies would have all lost their gas and died long ago. Our own Milky Way, for instance, has been forming stars for 10 billion years on a 1-billion-year supply of gas. Clearly, the gas has to be falling back in.

That's exactly what physics says it should do: Gas lingering in the CGM cools and condenses until gravity pulls it in. In theory, inflows ought to form narrow rivers, relatively slow and cold. In practice, infall is difficult both to find and to differentiate from the broad outflows—partly because a thin ribbon of gas is unlikely to fall within a quasar sightline. Nevertheless, separate teams led by Kate Rubin of the Harvard-Smithsonian Center for Astrophysics and by Martin have found a total of 15 galaxies at intermediate distances that showed evidence of infalling gas. And in the Milky Way, Joshua Peek of STScI and Mary Putman of Columbia University are among several observers who have mapped clouds of gas falling toward the galaxy's spiral disk.



Star formation has ended in the galaxy 2MASX J09442693+0429569, which will eventually redden as its existing stars age.

PHOTO: ESA/HUBBLE & NASA

The gas around young, blue galaxies seems to be poised to fall back in. Some of it has cooled to less than 10,000 K—a temperature at which it can sink back into its parent galaxy. There it should cool further, to about 10 K, and condense into the raw material for new star formation.

That only underscores the puzzle of the red galaxies, where the gas seems equally ready to fall back in and fuel new star birth. In 2012, the COS-Halos team found that the CGM of 16 nearby red, dead galaxies held almost as much mass in gas as those galaxies had in stars—and it was near the 10,000 K threshold.

Yet the red and dead galaxies that COS-Halos observed have stopped recycling. "They're the huge mystery," Peek says. As far as astronomers can tell, that gas has no reason not to fall in. Something must be either blocking its reentry or otherwise spoiling it for starmaking. Peeples says: "The galaxies toss the ball up. It stays up there."

So far, computer simulations haven't supplied many leads toward explaining the levitating gas. "No model works," says Romeel Davé of the University of the Western Cape in Cape Town and a theorist on the COS-Halos team. One problem, he says, is that current simulations—though large and sophisticated—can't simultaneously cover the range of scales relevant to galaxies' life cycles, from the CGM down to galaxies' interiors, let alone include the messy physics of exploding stars and accreting black holes. As a result, models can't account for important pieces of the puzzle. For example, Davé says, he and colleagues ran a simulation that successfully stopped infalling gas by heating the CGM—but it didn't specify where the heat might come from.

Undeterred, theorists have proposed a number of ideas for why red galaxies are quenched. Maybe gas from the CGM actually does fall back into them but can't form stars once it arrives. The spoiler might be gravity: The red, dead galaxies are the universe's largest and most massive. Perhaps their gravitational pull heats any infalling gas enough to prevent it from condensing into stars.

Or maybe the same mechanisms that drive outflows keep some galaxies too warm for stars to form. For instance, a supermassive black hole might blow a lot of gas out of a galaxy and then switch to a more quiescent state—"bubbling at a low level," as Caltech theorist Philip Hopkins puts it, and warming the gas as it returns.

Or maybe the CGM isn't homogeneous. It is a "complex, dynamic, superbusy place," Peeples says, and might be generally hot but riddled with pockets of dense, cold gas. That would make the COS data on red galaxies easier to understand, but would leave the mystery of how so much cold gas can coexist with the hot gas long enough for us to see it.

In coming decades, the current best telescopes and instruments—COS on the Hubble Space Telescope and instruments called HIRES and LRIS on the 10-meter Keck telescopes—will give way to a new generation of instruments mounted on telescopes as big as 12 meters in space and 30 meters on the ground. They should be able to trace the details of gas recycling in galaxies just beginning to die, Tumlinson says, to "catch them in the act of going from blue to red."

That might explain the mysterious deaths of the red galaxies. Unfortunately, solving the mystery won't stop the bodies from piling up. The universe as a whole has only so much gas and is using it up. The earliest galaxies were more than 50% gas; today's galaxies, like the Milky Way, are only 10% gas and, Steidel says, "we're about out of it." Star formation in blue galaxies peaked about 11 billion years ago. Over the past 8 billion years, the total mass bound up in red, dead galaxies has doubled. With time, their numbers, like the numbers of people in cemeteries, will do nothing but grow. ■

Ann Finkbeiner is a science writer in Baltimore, Maryland.

Published by AAAS



Downloaded from www.sciencemag.org on November 22, 2014

A DOSE OF REALITY

Does any treatment work against Ebola? Researchers may soon find out, if they can overcome daunting ethical and practical challenges

By **Jon Cohen** *and* **Kai Kupferschmidt**

On 2 October, Ashoka Mukpo left his father a voice mail from Monrovia, saying he had "unwelcome but not unexpected news." Mukpo, an American freelance cameraman for NBC News, had tested positive for Ebola virus. Mukpo's father, Mitchell Levy, a pulmonologist who heads critical care at Rhode Island Hospital in Providence, immediately helped arrange his son's transfer to the Nebraska Medical Center in Omaha, one of four specialized Ebola centers in the United States.

The big question then was how to treat the patient.

The medical team, which included Levy, planned to intensively monitor Mukpo and give him intravenous replacement of fluids and electrolytes, antibiotics to combat secondary infections, and drugs to slow diarrhea and vomiting. But it also had three unproven treatments available. TKM-Ebola, which inhibits viral RNA, has worked beautifully in monkeys, the best animal model. Kent Brantly, a missionary doctor in Liberia who developed Ebola and recovered, offered to donate plasma removed from his blood, which contained antibodies that might help. And there was brincidofovir, a drug being developed for other viral infections that has been shown to stop Ebola virus in test tubes. (The most famous drug candidate, ZMapp, was not available at the time.)

After careful consideration, Mukpo and his doctors opted to use the serum—a proven intervention with other viruses—and brincidofovir, which has a substantial safety record. But they decided to forgo TKM-Ebola, despite its promise, because of worries that it could trigger overproduction of cytokines, a dangerous inflammatory response also caused by the Ebola virus, and scant data from human trials. "I was not quite on my deathbed and didn't need to take any huge risks," Mukpo says. His doctor father had reached a similar conclusion. "I didn't have a high degree of confidence that brincidofovir was going to work, but I was loath to try an investigational agent with no data," Levy says.

Mukpo survived, but no one has any idea whether the experimental treatments helped him, did nothing, or even slowed his

Workers at the ELWA3 hospital in Monrovia, where many Ebola patients are being treated.

PHOTO: DOMINIQUE FAGET/AFP/GETTY IMAGES

Published by AAAS

recovery. The same is true for Brantly and 17 other Ebola patients who received experimental interventions in the United States and Europe. (One other Ebola patient was treated in Germany without any experimental interventions.) Many, like Mukpo, were given several treatments at the same time, making it hard to unravel the impact of any one of them. The fact that they were taken care of in modern, well-staffed hospitals may also help explain why 75% have survived (see sidebar, p. 911). "Probably the best we can say is that the experimental treatments are not killing anyone," says Michael Kurilla, who heads the Office of Biodefense Research Resources and Translational Research at the National Institute of Allergy and Infectious Diseases (NIAID) in Rockville, Maryland.

Now, that's about to change. As early as next month, researchers will begin trials in West Africa to find a solid answer to the key question: Do the treatments work? Carried out in makeshift emergency hospitals by researchers wearing full protective gear in the middle of a deadly epidemic, these will be some of the most unusual drug trials ever done. And they also raise major ethical and practical questions, some of which were intensely debated at a World Health Organization (WHO) meeting in Geneva, Switzerland, on 11 and 12 November.

Perhaps the most important one: Is it right to do randomized controlled trials (RCTs), in which some people don't get the novel intervention? Doctors Without Borders (MSF), which has led the medical response to the outbreak, says no—not with a disease as deadly as Ebola. Instead, on 13 November MSF said it will take part in three trials that will use an alternative design in which everyone who enrolls receives the untested treatment. But others argue that such setups may not give clear answers and squander a precious scientific opportunity.

It's an uncomfortable and complex debate held under extreme time pressure. "Everyone has stepped outside of their comfort zone in a big way," says Peter Horby of the University of Oxford in the United Kingdom, who is leading one of the upcoming trials and attended the WHO meeting.

UNTIL THE CURRENT EPIDEMIC began, development of Ebola treatments was painfully slow. Since the first recognized outbreak in 1976, the virus has surfaced two dozen times, but until 2014, it had sickened fewer than 2500 people altogether. That didn't make for an attractive market for private companies, leaving most research to be funded by the U.S. government, which worries that hostile nations or bioterrorists may stage gruesome attacks with the virus. And because traditional containment efforts have stopped every outbreak to date within a few months, researchers have had few opportunities to test novel treatments.

Among the candidates, the two frontrunners are TKM-Ebola, an RNA inhibitor of the virus packaged in a lipid nanoparticle, and ZMapp, a laboratory-made cocktail of three Ebola antibodies that shot to fame in August when it was given to Brantly. (A breathless CNN report called it a "secret serum that likely saved his life.") These drugs have worked better than all others in monkey studies, which puts them "light-years ahead" of other treatments, says Thomas Geisbert of the University of Texas Medical Branch in Galveston, who conducted many of the key experiments. "If I were exposed to Ebola I'd take ZMapp or Tekmira's drug and I wouldn't worry," he says.



Recovered Ebola patient Ashoka Mukpo with his father, Mitchell Levy, a pulmonologist who helped guide Mukpo's treatment.

PHOTO: TAYLOR WILSON/NEBRASKA MEDICAL CENTER

"Everybody keeps talking about ZMapp," says Annick Antierens, who heads work on investigational Ebola drugs at MSF in Geneva. But both ZMapp and TKM-Ebola are relatively difficult to make, and despite aggressive efforts to ramp up their production, fewer than a thousand doses of each may be ready by the end of the year. Both are also difficult to test in the affected countries, as they require intravenous infusions.

Other candidates are more easily manufactured and administered—but the data supporting their use are weaker. Brincidofovir was designed to interfere with viral DNA replication, and it's now in ongoing phase III trials against cytomegalovirus and adenovirus infections; about 1000 people have received it. This spring, Chimerix, the manufacturer, had two outside labs test the drug against Ebola; they found that the drug did indeed inhibit the virus in test-tube studies. Brincidofovir cannot be tested in monkeys because an enzyme in the animals rapidly inactivates the drug, but Chimerix says studies in guinea pigs and mice are ongoing.

Another option is favipiravir, an influenza drug licensed in Japan that protected mice from Ebola when administered 6 days after they were exposed to the virus. But unlike monkeys, mice only develop mild disease from Ebola strains, so the experiment relied on a mouse genetically engineered to lack immune defenses against viruses. That makes the result harder to interpret.

Antibody-containing whole blood or the plasma component could theoretically be harvested from thousands of recovered Ebola patients, but "convalescent serum" has not worked well in monkey experiments. One published report shows that seven out of eight people who received whole blood from survivors during a 1995 Ebola outbreak in the Democratic Republic of the Congo survived, but they were treated late in the course of disease, and some researchers believe they likely would have recovered without the serum. A horse serum that contains Ebola antibodies is being developed, too.

Drugs that target only Ebola symptoms, rather than the virus itself, might also help. Doctors in Germany, for instance, have treated two patients with an experimental treatment named FX06 that aims to stop fluid leaking from blood vessels, a major problem in patients with advanced Ebola infections. One of the patients recovered, the other died.

Many other ideas have been floated. Kurilla is setting up a database for WHO to publish negative findings to discourage researchers from pursuing compounds that don't pass muster in screening assays or animal experiments. "We are getting inundated with people who are suggesting the same thing over and over again," he says. A doctor in Liberia in particular has received widespread attention for touting the HIV drug lamivudine, but there is zero evidence from lab tests that it has anti-Ebola activity.

NOW RESEARCHERS HAVE an unprecedented chance to test candidate treatments systematically. At last week's WHO meeting in Geneva, researchers who want to con-

Published by AAAS

Headed for trials

Selected Ebola treatments under development

TREATMENT	COMPANY	WHAT IS IT?	WHAT'S THE EVIDENCE?
TKM-Ebola	Tekmira Pharmaceuticals (Vancouver, Canada)	RNA inhibitor in lipid nanoparticle	Solid protection in monkeys
ZMapp	Mapp Biopharmaceutical (San Diego, California)	Ebola antibody cocktail	Solid protection in monkeys
Brincidofovir	Chimerix (Durham, North Carolina)	Small molecule with broad antiviral activity	Blocks Ebola in test tubes
AVI-7537	Sarepta Therapeutics (Cambridge, Massachusetts)	Antisense oligonucleotide that cripples Ebola mRNA	Partial protection in monkeys
Favipiravir	Fujifilm (Tokyo)	Small molecule; influenza drug. Broadly targets RNA polymerase enzyme	Solid protection in mice
Convalescent serum	None	Antibodies from recovered patients' blood or plasma	Failed in monkeys; may have helped in small human study

duct clinical trials for Ebola treatments met with regulators, pharmacologists, and representatives from the three most affected countries to work out how to move from anecdotes to hard evidence—and which drugs to test. More than 120 products have been put forward as possible treatments, but far too few clinics are qualified to participate in trials, the attendees were told. And given the lack of supply, ZMapp and TKM-Ebola are not on the table for the moment. Instead, the less promising treatments are moving ahead first.

An international consortium led by Johan van Griensven of the Institute of Tropical Medicine in Antwerp, Belgium, plans to test convalescent serum in Conakry, the Guinean capital. The French biomedical research agency INSERM will lead a trial of favipiravir in Guéckédou, Guinea. And brincidofovir will be put to the test in a study led by Oxford, in either Sierra Leone or Liberia. The three clinical trials will share a simple form to collect the most basic of data; recording anything is exceedingly cumbersome when health care workers are wearing bulky personal protective gear.

The ethical issues surrounding the trials have roiled the scientific and humanitarian community—and were "vigorously debated" at the meeting, according to WHO. MSF has said that for the moment it won't participate in trials that randomly decide who would receive the treatment. "If an outbreak like this with such a high fatality rate would be happening in Europe, I don't think randomizing patients would be acceptable," says MSF's Antierens. "I certainly would not want to get standard of care if there is a promising drug available." A much discussed editorial published online on 10 October in *The Lancet*, signed by prominent ethicists and scientists from 11 countries, made the same point. Some worry that RCTs could even trigger protests and violent reactions from the families of patients and their communities.

But others say trials without an untreated control group raise ethical problems of their own. "I don't know whether these agents might be harmful, and given a disease with mortality as high as this one, you might not be able to detect that harm" without a control arm, says Clifford Lane, clinical director at NIAID in Bethesda, Maryland. RCTs also reduce confusion introduced by variables such as how sick people are when treatment begins and whether patients in a trial also receive better care. Randomization, Lane says, is the only effective way to "make sense of anything."

The three studies that will start first, all at MSF centers, will not have a randomized design. Instead, all patients will get the treatment; their survival rate 14 days later will be compared with survival in earlier patients who didn't receive the treatment. (The convalescent serum trial will also have a "concurrent" control arm that eludes the ethical problems: Some patients won't be treated because there is no donor with a matching blood type.)



Patients in the spare Ebola treatment unit in Kenema, Sierra Leone, in August.

PHOTO: WHO EBOLA RESPONSE TEAM

Published by AAAS

Antierens agrees that such trials may not detect small effects of a drug, but says the goal is to determine whether an intervention is worthless or clearly works. "We are not interested in whether some liver enzymes are a little bit higher," she says. "We are looking for a significant change in survival." For the brincidofovir trial, for example, the researchers have agreed to define survival below 50% as "failure" and above 80% "success." If the data are ambiguous, an RCT could be considered, she adds.

The horrific nature of the epidemic has led to other arrangements rarely seen in clinical studies. The researchers conducting the favipiravir study initially wanted to target adults within the first 2 days of their illness. MSF asked for the design to be changed so no one would be refused the drug—including people who have been sick longer and children. "People from the field said, 'What are we going to do when a family arrives? We treat the parents and not the child?' " says Xavier de Lamballerie of Aix-Marseille University in France, who is leading the study. The brincidofovir study will enroll up to 140 people, and at MSF's request it will continue offering the drug while data from the trial are being analyzed to make sure that no patient misses out on a potentially effective treatment.

PROPONENTS OF RCTS are aggressively pushing ahead with trial plans, too. Luciana Borio of the U.S. Food and Drug Administration in Silver Spring, Maryland, who attended the WHO meeting; NIAID's Lane; and others have developed a protocol that would test multiple interventions—including ZMapp and TKM-Ebola—in a single large RCT, using sophisticated Bayesian statistics to get an answer as fast as possible. Lane is now negotiating with the Liberian government about setting up several of these studies. Liberia is not opposed to RCTs, says Stephen Kennedy, an investigator at the University of Liberia–Pacific Institute for Research and Evaluation Africa Center in Monrovia, who advises the country's ministry of health about its oversight of Ebola clinical research. "We have to use the gold standard," Kennedy says. "We understand the issues and know what is appropriate for Liberia."

Borio well understands the concerns about randomization, but says that not getting a clear answer would be worse. The nonrandomized trials announced last week have a "significant risk of not generating interpretable data," Borio says. "It is so important to get this right. It's important for patients who will become affected during this epidemic, and also for generations to come, since future outbreaks will surely occur." ■



A room reserved for Ebola patients at the University Medical Center Groningen in the Netherlands.

PHOTO: REMKO DE WAAL/AFP/GETTY IMAGES

Saving lives without new drugs

By **Jon Cohen**

When people from the United States and Europe working in West Africa have developed Ebola, time and again the first thing they wanted to take was not an experimental drug. It was an airplane that would cart them home.

Care for Ebola patients in Liberia, Sierra Leone, and Guinea varies greatly at different clinics, but it never matches what wealthy countries provide. This partly explains why the Ebola epidemic has had a case fatality rate (CFR) of 70%, according to World Health Organization calculations. Too few Ebola patients have been treated outside Africa to make scientifically valid comparisons—and they may have been healthier before falling ill—but only five out of 20 to date have died, a CFR of 25%.

Now, there's a push to improve care in West Africa. Just a handful of basic interventions to fight the killer effects of Ebola, including dehydration and secondary infections, could dramatically lower the CFR there, says Michael Callahan, an infectious disease specialist at Massachusetts General Hospital in Boston. A case in point appeared online on 5 November in *The New England Journal of Medicine* (*NEJM*): Relatively intensive care in Conakry led to a CFR of 43%.

With so much room for improvement in supportive care, the current international focus on drugs is "misguided," says Callahan, who has recently worked in Monrovia and provided care in four previous Ebola outbreaks. "While we wait for months for forthcoming experimental therapies, many lives can be saved, certainly hundreds and possibly thousands, using inexpensive and simple therapies," he says.

Callahan is helping an international team develop guidelines dubbed Maximum Use of Supportive Therapy (MUST), aimed at keeping more patients alive. It includes intravenous (IV) drips to replace massive fluid loss from diarrhea and vomiting, a risk factor for shock; balancing of electrolytes such as calcium or potassium, which prevents kidney and heart failure; nasogastric tubes for feeding; and testing and treatment of secondary infections such as malaria. Introducing MUST will also make it easier to study new treatments, Callahan says: Randomized controlled trials—ethically fraught because only some patients get the novel treatment (see main story, p. 908)—will be much more acceptable if everyone receives high-level care. In addition, MUST might reveal side effects of new drugs that would otherwise be masked by Ebola symptoms, and it could reduce the rate of complications that might be incorrectly blamed on a drug.

It's an important proposal, but Ebola clinics will need more resources to offer MUST, says John Fankhauser, an American clinician who has worked at the ELWA hospital in Monrovia since before the outbreak surfaced. Overwhelmed by patients and logistical challenges, many clinics have provided minimal supportive care. "We are able to give IV hydration, but the testing is limited to malaria and Ebola," Fankhauser says. Tests for electrolytes and other types of monitoring MUST calls for are simply beyond reach, he says. Callahan says the additional measures cost less than $600 extra per patient at a Monrovia clinic in August.

Armand Sprecher of Doctors Without Borders (MSF) in Brussels, who co-authored the *NEJM* report, concedes that the standard of care dropped when Ebola exploded this summer. But Sprecher, who is "very supportive of supportive care," says MSF clinics have corrected several problems and now doubts that MUST can save many more lives. "I'm less optimistic than some people about how much of an effect we're going to have," he says. "I hope I'm wrong." ■

Published by AAAS

INSIGHTS

Tectonics in the driving seat *p. 918*

When to take your medicine *p. 921*



PERSPECTIVES



The ancient Great Wall.

PHOTO: ZHU DIFENG/THINKSTOCK

ECOSYSTEMS MANAGEMENT

Rethinking China's new great wall

Massive seawall construction in coastal wetlands threatens biodiversity

By **Zhijun Ma,[1]* David S. Melville,[2] Jianguo Liu,[3] Ying Chen,[1] Hongyan Yang,[4,5,6] Wenwei Ren,[7] Zhengwang Zhang,[8] Theunis Piersma,[5,6] Bo Li[1]**

China's position as the world's second largest economy is largely due to its rapid economic growth in the coastal region, which composes only 13% of China's total land area, yet contributes 60% of the gross domestic product (GDP). To create extra land for the rapidly growing economy, coastal wetlands have been enclosed by thousands of kilometers of seawalls, whose length exceeds that of China's famous ancient "Great Wall" (see photos and map). This new "Great Wall," covering 60% of the total length of coastline along mainland China (*1*), caused a dramatic decline in internationally shared biodiversity and associated ecosystem services and will threaten regional ecological security and sustainable development. Here, we outline these problems, analyze the drivers behind wetland reclamation, and propose measures for effective wetland management.

POLICY

IMPORTANCE OF COASTAL WETLANDS. China's coastal wetlands, with an area of 5.8 million ha, support abundant biodiversity and provide the foundation for regional development. For example, 230 waterbird species, over 25% of the global total, inhabit China's coastal wetlands. Millions of migrating birds refuel on the wetlands that connect countries in the south with those in the north (*2*). The wetlands produced 28 million tons of fishery products in 2011, nearly 20% of the global total, as well as providing spawning and nursery grounds for many aquatic organisms that maintain marine ecosystem health and serve as the base for offshore fisheries. Coastal wetlands help to absorb pollutants that are increasingly discharged from land and are ecological barriers against extreme weather events, such as typhoons, protecting people living along the coast (*3*). Coastal wetlands also provide enormous direct and indirect ecosystem services, including nutrient cycling, carbon storage, and tourism and recreation. Although the area of coastal wetlands accounts for <1% of all ecosystem area in China, the values of ecosystem services they provide amount to U.S. $200 billion annu-

Downloaded from www.sciencemag.org on November 22, 2014

Published by AAAS

ally for the country, accounting for a 16% share of the country's total (*4*).

CHANGING COASTLINES AND CONSEQUENCES. Globally, coastlines have undergone enormous change. Seawall construction has played a crucial role since ancient times (*5*). Although the seawalls were used traditionally for coastal defenses, such as erosion control and protecting human habitation from tides and waves, they have been increasingly used to enclose coastal wetlands for agricultural and industrial uses over the past several centuries (*6*, *7*). This has caused a great loss of coastal wetlands and their myriad of ecological services.

Over the past decades, the importance of coastal wetlands has been increasingly recognized by the public and governments. Management policies have been established in some countries, e.g., the "Integrated Coastal Zone Management" strategy in Europe and the "no-net-loss" policy in the United States, resulting in a decreasing rate of loss and even an increase in wetland area in certain countries (*6*, *8*).

In contrast, reclamation of coastal wetlands has been accelerating in China. From 1950 to 2000, the enclosed wetland area increased by an average of 24,000 ha year^{-1}, which led to a loss of 50% of the coastal wetlands (*9*). The reclamation rate has increased dramatically to 40,000 ha year^{-1} during 2006–2010 to support rapid urbanization and economic development through constructing industrial zones, ports, and other infrastructure (see chart). The length of such seawalls has increased 3.4 times (from 18 to 61% of the total 18,000 km) over the past two decades, reaching 11,000 km in 2010 (*1*).

Such massive coastal reclamation, often implemented by introduction of sedimentation-promoting exotic plants (e.g., *Spartina alterniflora*) and sand pumping, has severely reduced biodiversity and associated ecosystem services, and more serious consequences are expected in the foreseeable future. The loss of coastal wetlands in China has contributed to the rapid decline of waterbird populations in the East Asian–Australasian flyway, which currently is the migratory path for the highest proportion (19%) of threatened waterbird populations among the global flyways (*2*). Upon reclamation, coastal wetlands are converted from pollutant sinks to sources, producing pollutants from ports and factories; nutrients and pesticides from croplands; and chemicals, such as antibiotics, from aquacultures; resulting in deterioration of inshore and oceanic environments (*10*). Loss of coastal saltmarsh wetlands makes people highly vulnerable to extreme weather events, especially in times of predicted climate change and sea level rise. Reclamation of China's coastal wetlands is estimated to cause a loss of U.S. $31 billion of ecosystem services annually, about 6% of the gross marine products in China (*10*).

DRIVERS BEHIND WETLAND RECLAMATION. Multiple drivers contribute to the loss of China's coastal wetlands. They include the lack of national legislation for wetland conservation, overemphasis on GDP growth, conflicting goals among government agencies and between central and local governments, underappreciated values of wetlands, and inappropriate definitions of wetlands in laws and regulations.

China's central government has taken measures to conserve the wetlands. For example, the National Wetland Conservation Action Plan was promulgated in 2000, and the National Wetland Protection Plan was approved in 2004. Thirty-five national nature reserves were established along China's coasts and 14 coastal wetlands have been designated as Wetlands of International Importance (Ramsar sites) (table S1). However, China's coastal wetlands are managed by multiple agencies (table S2). This "fragmentation of bureaucratic authority" (*11*) results



The "new Great Wall." A seawall that is being built in the Yangtze estuary. Seawalls such as this are creating land and reducing ecosystem services along the coastal wetlands of China. (Right) The ancient Great Wall (yellow line) and the 11,000-km seawall on the coasts of mainland China (red line). The discontinuity of the walls is not visible because of the map resolution.



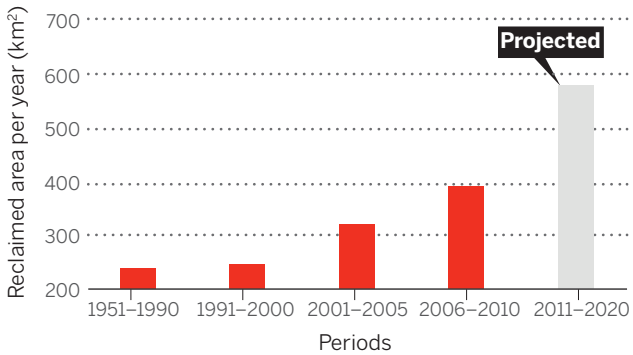
PHOTO: W. WU

Published by AAAS

in conflicts and overlapping functions. Moreover, relevant laws and regulations are often inadequate to protect coastal wetlands. In practice, wetland destruction carries no or negligible penalties; land administration law still classifies coastal wetlands as "unused lands," and, thus, exploitation of coastal wetlands is encouraged. In addition, environmental impact assessments for coastal wetland reclamation projects focus on the potential loss of fisheries, environmental pollution, and other direct impacts on people but largely ignore the loss of biodiversity or associated ecosystem services.

Since China's reform in the late 1970s, GDP growth has been the main criterion for assessing the achievements of local governments, and, hence, local officials favor projects that result in immediate and direct economic benefits. Although the central government has recently proposed to add environmental performance to the assessment criteria, the effectiveness of such a proposed change remains to be seen. Coastal wetlands provide essential services, most of which are indirect and long-term, and are therefore vastly underappreciated. By contrast, enclosing coastal wetlands to create land for various enterprises produces direct and immediate economic benefits. Moreover, because land is owned by the state in China, local governments can obtain huge profits from selling the use right of land created by coastal reclamation.

The huge economic returns from reclamation have prompted local governments to "bypass" regulations issued by the central government. For example, the State Council of the People's Republic of China ruled that reclamation projects over 50 ha must be approved by the central government. To evade this, local governments simply divide large projects into smaller ones (*1*, *9*). Some local governments have compelled coastal nature reserves to change their boundaries so that wetlands previously within the reserves can be legally reclaimed. Because of a lack of integrated planning at the national level and coordination between coastal provinces, there are substantially redundant and overlapping development projects, making macroregulations difficult at the national level (*9*).



The extent of Chinese seawall building. The amount of reclamation of coastal wetlands divided into time periods (*1*, *9*, *10*, *12*).

FUTURE TRENDS AND COUNTER MEASURES. In 2012, the State Council of China approved National Marine Function Zoning (2011–2020) "to strengthen the management of reclamation projects and to rationally control the reclamation scale." However, according to the Marine Function Divisions formulated by coastal provinces, 250,000 ha of coastal wetlands will be enclosed for infrastructure development and more wetlands for other purposes (e.g., agriculture) by 2020 (*12*). The reclamation rate is expected to increase to 60,000 ha $year^{-1}$ during 2010–2020 (see the chart). The loss of coastal wetlands is unlikely to slow down unless more effective measures are urgently taken.

First, legislation is required to set a mandatory minimum area for coastal wetlands at both national and local levels to achieve a target of "no net loss." This should be based on comprehensive research on ecological, hydrological, and socioeconomic conditions of coastal regions to clarify the importance, sensitivity, and vulnerability of each region and to answer the questions of where, when, and how much coastal wetland can be enclosed without damaging the integrity of coastal wetlands.

Second, an effective agency directly under the State Council is needed to coordinate the functions and responsibilities among the many government agencies involved in wetland management. Overall, reclamation projects should be planned at the national level to achieve the target of sustainable development. Strict environmental impact assessments must be performed on reclamation projects, in which cumulative ecological impacts of multiple reclamations for different regions should be considered.

Third, mechanisms must be established for government authorities to be accountable for ecological losses. For the local governments, it is important to change the model of economic development to decrease their heavy dependence on increasing land area but to increase the added value and the efficiency of existing land.

Finally, outreach and education about ecosystem services and sustainable development are needed to raise public awareness and compliance for conserving coastal wetlands.

In conclusion, adverse socioeconomic and ecological consequences of over-reclamation of coastal wetlands have already emerged (*2*). To meet the targets of "ecological civilization" (*13*) and to support sustainable development, Chinese governments at all levels must place a high priority on the conservation of coastal wetlands and their ecosystem services. It is time to think again about China's new "Great Wall" that is built on the coastal wetlands. ■

[1]*Ministry of Education Key Laboratory for Biodiversity Science and Ecological Engineering, Institute of Biodiversity Science, Fudan University, Shanghai 200438, China.* [2]*No. 1261 Dovedale Road, Rural Delivery 2, Wakefield, Nelson, 7096, New Zealand.* [3]*Center for Systems Integration and Sustainability, Department of Fisheries and Wildlife, Michigan State University, East Lansing, MI 48823, USA.* [4]*College of Nature Reserve, Beijing Forestry University, Beijing 100083, China.* [5]*Chair in Global Flyway Ecology, Centre for Ecological and Evolutionary Studies, University of Groningen, Post Office Box 11103, 9700 CC Groningen, Netherlands.* [6]*Department of Marine Ecology, Royal Netherlands Institute for Sea Research (NIOZ), Post Office Box 59, 1790 AB Den Burg, Texel, Netherlands.* [7]*World Wildlife Fund China Shanghai Office, No. 121 Zhongshan North Road, Shanghai 200083, China.* [8]*Ministry of Education Key Laboratory for Biodiversity Science and Ecological Engineering, College of Life Sciences, Beijing Normal University, Beijing 100875, China.* **Corresponding author. zhijunm@fudan.edu.cn*

REFERENCES AND NOTES

1. D. M. Guan, D. A, *Study on the National Marine Function Zonation* [in Chinese] (Ocean Press, Beijing, 2013).
2. J. MacKinnon *et al.*, "IUCN situation analysis on East and Southeast Asian intertidal habitats, with particular reference to the Yellow Sea (including the Bohai Sea)" (IUCN, Gland and Cambridge, 2012).
3. E. B. Barbier *et al.*, *Ecol. Monogr.* **81**, 169 (2011).
4. Z. X. Chen, X. S. Zhang, *Chin. Sci. Bull.* **45**, 17 (2000) [in Chinese].
5. M. L. Kirwan, J. P. Megonigal, *Nature* **504**, 53 (2013).
6. L. Airoldi, M. W. Beck, *Oceanogr. Mar. Biol.* **45**, 345 (2007).
7. H. K. Lotze *et al.*, *Science* **312**, 1806 (2006).
8. K. B. Gedan, B. R. Silliman, M. D. Bertness, *Annu. Rev. Mar. Sci.* **1**, 117 (2009).
9. Consultation Group of Academic Division of Earth Science of Chinese Academy of Sciences, in *2011 Science Development Report*, CAS Ed. [in Chinese] (Science Press, Beijing, 2011), pp. 344–349.
10. China Council for International Cooperation on Environment and Development, *Annual Policy Report: Ecosystem Management and Green Development* (China Environmental Science Press, Beijing, 2010), pp. 113–158.
11. K. Lieberthal, M. Oksenberg, *Policy Making in China: Leaders, Structures, and Processes* (Princeton Univ. Press, Princeton, NJ, 1988).
12. Marine function zoning plans (2011–2020) of coastal provinces [in Chinese]; www.gov.cn/zwgk/.
13. G. He *et al.*, *Science* **341**, 133 (2013).

SUPPLEMENTARY MATERIALS

www.sciencemag.org/content/346/6212/912/suppl/DC1

ACKNOWLEDGMENTS

Supported by the National Basic Research Program of China (2013CB430404), the National Natural Science Foundation of China (31071939, 31272334), World Wide Fund for Nature, the Paulson Institute, National Science Foundation, and Michigan AgBioResearch. We thank J. Qiu for helpful comments.

10.1126/science.1257258

Published by AAAS

NEUROSCIENCE

His brain, her brain?

Research exploring sex differences in the human brain must overcome "neurosexist" interpretations

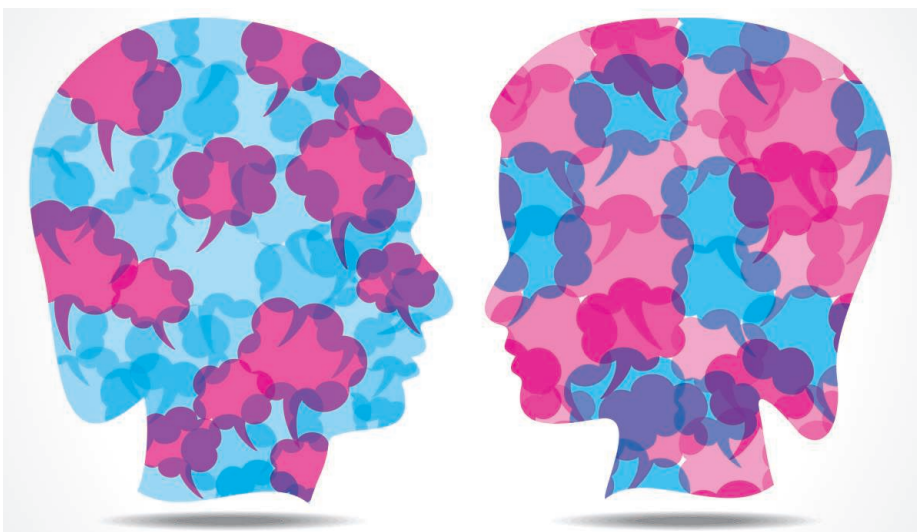
By **Cordelia Fine**

There is a long history of scientific inquiry about what role biological sex plays in differences between brain function in human males and females. Greater knowledge of the influence of biological sex on the human brain promises much-needed insights into brain function and especially dysfunctions that differentially affect the sexes (*1*). Certainly, advancing technologies and an increasing wealth of data (with more sophisticated analyses) should prompt robust future research—carefully conducted and well replicated—that can elucidate sex effects in the brain. However, this field of research has spurred an equally long history of debate as to whether inherent differences in brains of males and females predispose the sexes to stereotypical behaviors, or whether such claims reinforce and legitimate traditional gender stereotypes and roles in ways that are not scientifically justified—so-called neurosexism. Although this topic remains controversial, a commonly held belief is that the psyches of females and males are highly distinct. These differences are perceived as natural, fixed, and invariant across time and place (*2*), presumably due to unique female versus male brain circuitry that is largely fixed by a sexually differentiated genetic blueprint. A major challenge in the field is to crtically view previous experimental findings, as well as design future studies, outside the framework of this dichotomous model. Here, gender scholarship can hasten scientific progress by revealing the implicit assumptions that can give rise to inadvertent neurosexism.

Contemporary gender research, mainly across the disciplines of psychology and sociology, has overturned many old views of gendered behavior—traits (e.g., aggression), abilities (e.g., empathic accuracy), attitudes (e.g., sexual), interests (e.g., in science), and roles (e.g., caregiving)—as polarized and immutable (*3*). Rather, female-male distributions substantially overlap on the majority of gender characteristics (*3*, *4*). Moreover, these different feminine and masculine characteristics are only weakly intercorrelated, if at all. Thus, rather than falling neatly into masculine and feminine clusters, males and females possess a complex mosaic of both characteristics (*5*). And gendered behavior is mutable: Female-male differences and individual behavior vary across time, place, group, and context (*3*).

Also transformed is our understanding of brain development, with a growing appreciation that it is a dynamic developmental process that interacts with experience. Thus, nonhuman research demonstrates that biological sex interacts in complex ways with many other factors that influence brain development (*6*). For example, work on rats has shown that brief exposure to stress can reverse a sex difference in a hippocampal brain characteristic (the density of neuronal dendritic spines) in one region and create a sex difference in a second hippocampal region, while having no effect elsewhere (*7*). Sex influences therefore give rise not to distinctive male and female brains, but rather to unique mosaics of "male" and "female" characteristics (*6*).

These research advances in behavior, neuroanatomy, and sexual differentiation of the brain indeed challenge "essentialist" assumptions of distinctive, fixed sex differences in behavior and brains. Nonetheless, research that examines the human brain can still sometimes be designed and reported in the context of this outdated model. For example, a recent study used diffusion tensor imaging technology to assess sex differences in neuronal connectivity in about 1000 children and young adults (*8*). The data indicated that on average there is greater connectivity within each hemisphere in males and greater connectivity between the hemispheres in females. Notably, the connectivity differences were of degree, not of kind. And in the larger sample from which the participants were a subset, the sexes showed highly similar performance on a battery of psychological measures (*9*). Yet the connectivity differences were speculated to underpin psychological differences between the sexes. Brain-behavior correlations were not explored, nor was theoretical or empirical attention given to the possible influence of gendered differences in male and female participants' past experiences (hobbies, sports participation, and subjects studied, for instance) on brain and behavior. Thus, neurosexist interpretation of research that is taken as scientific proof of "hardwired" sex differences can support old stereotypes, which can obscure the actual findings (*10*).



Research can be influenced by essentialist assumptions, albeit more implicitly. A review of all functional magnetic resonance imaging–based studies conducted in 2009 and 2010 on sex differences (*11*), for example, found that nearly three-quarters of the studies had fewer than 16 participants in each experimental cell. Although this would be unproblematic if brain function in females versus males were highly distinctive, the low reliability of small samples creates conditions for both false-negative and false-positive errors. More than two-thirds of the surveyed studies speculated on behavioral implications of reported sex differences in brain activations—most often either in the absence of data showing relevant behavioral differences between the sexes, or despite

Melbourne School of Psychological Sciences, Melbourne Business School & Centre for Ethical Leadership, University of Melbourne, Australia. E-mail: cfine@unimelb.edu.au

CREDIT: GRAPHICSDUNIA4YOU/THINKSTOCK. ADAPTED BY V. ALTOUNIAN/*SCIENCE*

Published by AAAS

contradictory data. All the studies made single "snapshot" comparisons of the sexes, even though contemporary gender research indicates the importance of asking why, how, in whom, and when differences occur (*3*). Thus, the snapshot approach does not allow challenge to the notion of stable, universal sex differences in the brain.

Although the scientific and/or popular impact of most studies in this field may be modest, the overall outcome is a scientific literature that can be viewed as subtly biased toward a presentation of sex differences in the brain as more dichotomous, fixed, and functionally important in stereotype-consistent ways than is warranted (*11*). And while scientists have rallied to redress popular misrepresentations of their research (*12*), it is worth considering how research implicitly entrenched in essentialist assumptions may reinforce and legitimate traditional gender stereotypes and roles (*13*). Moreover, potentially productive research strategies may be overlooked or unnoticed. However, new approaches are indicated by, for example, recent recommendations as to how insights from contemporary gender research can be incorporated into neuroscientific research design, analysis, and interpretation (*14*), and the study of sex interactions in the development of psychopathology (*15*).

"His brain, her brain?" The assumptions brought to bear on this topic not only can influence public understanding of research but may also influence how the research itself is approached. The time is opportune to integrate the continually advancing tools of neuroscience with the insights of gender scholarship, and attend to the problem of neurosexism with rigorous science and discussion. ■

REFERENCES

1. M. M. McCarthy, A. P. Arnold, G. F. Ball, J. D. Blaustein, G. J. De Vries, *J. Neurosci.* **32**, 2241 (2012).
2. N. Haslam, L. Rothschild, D. Ernst, *Br. J. Soc. Psychol.* **39**, 113 (2000).
3. J. S. Hyde, *Annu. Rev. Psychol.* **65**, 373 (2014).
4. D. I. Miller, D. F. Halpern, *Trends Cogn. Sci.* **18**, 37 (2014).
5. J. T. Spence, *J. Pers. Soc. Psychol.* **64**, 624 (1993).
6. D. Joel, *Biol. Sex Differ.* **3**, 27 (2012).
7. T. J. Shors, C. Chua, J. Falduto, *J. Neurosci.* **21**, 6292 (2001).
8. M. Ingalhalikar *et al.*, *Proc. Natl. Acad. Sci. U.S.A.* **111**, 823 (2014).
9. D. Joel, R. Tarrasch, *Proc. Natl. Acad. Sci. U.S.A.* **111**, E637 (2014).
10. C. O'Connor, H. Joffe, *PLOS ONE* **9**, e110830 (2014).
11. C. Fine, *Neuroethics* **6**, 369 (2013).
12. D. F. Halpern *et al.*, *Science* **333**, 1706 (2011).
13. C. Fine, *Delusions of Gender: How Our Minds, Society, and Neurosexism Create Difference* (Norton, New York, 2010)
14. G. Rippon, R. Jordan-Young, A. Kaiser, C. Fine, *Front. Hum. Neurosci.* **8**, 650 (2014).
15. D. Joel, R. Yankelevitch-Yahav, *Br. J. Pharmacol.* **171**, 4620 (2014).

10.1126/science.1262061

NUCLEAR MATERIALS

Taking the measure of molten uranium oxide

Levitated droplets of uranium oxide reveal a complex structure below and above the melting point

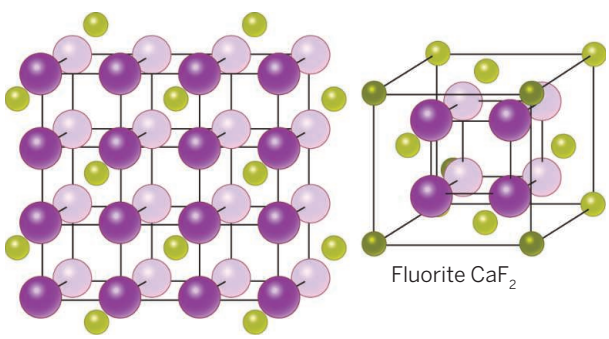
By **Alexandra Navrotsky**

Uranium dioxide (UO_2) occurs as the mineral uraninite and is the most common fuel in nuclear reactors. Its high melting point (near 3140 K) makes studying its properties near, at, and above this temperature difficult for both experimental and theoretical approaches, but understanding molten UO_2 is critical for understanding how the melt would interact with the container materials of a nuclear reactor. However, the sensitivity of stoichiometry of UO_2 to oxygen content in the atmosphere and, most importantly, the lack of unreactive container materials also make experiments challenging. Nonetheless, on page 984 of this issue, Skinner *et al.* (*1*) use sample levitation and laser heating combined with synchrotron x-ray diffraction to study the structure of UO_2 both just below and directly above its melting point.

Crystalline UO_2 has the fluorite structure, in common with that of the oxides of cerium, thorium, plutonium and, at high temperature, zirconium and hafnium (see the first figure). This cubic structure provides eightfold cation coordination (U^{4+}) and fourfold anion coordination (O^{2-}). There is only one type of cation site and one cation-anion bond length, but at temperatures near the melting point, many fluorite-type compounds undergo disordering in the anion sublattice in the solid state that can lead to high ionic conductivity, excess heat capacity, and changes in other properties.

Theory and experiment need to complement one another in benchmarking fundamental properties of refractory materials at high temperatures, but the number of physical observables that can be measured accurately above 2500 K is small. The properties of molten UO_2 and their relation to those of the solid are important for applications as well. Modeling of solid-liquid phase equilibria in UO_2-containing systems—for example, by standard CalPhaD formalisms (computer coupling of phase diagrams and thermochemistry)—requires knowledge of its melting thermodynamics and melt properties. The temperature dependence of density and heat capacity must also be estimated, both above and below the melting point (the latter in the supercooled liquid). Structural changes in the melt can profoundly affect these temperature-dependent properties.

For predicting and understanding "fuel meltdown" and the formation of both small highly radioactive particles that could be easily transported in the atmosphere and corrosive bulk melts containing uranium (e.g., the Chernobyl "lavas") during a runaway loss-of-coolant nuclear accident (*2*, *3*), one must understand melt properties in multicomponent systems. Uranium oxide can mix in the molten state with several other components, including zirconium oxide from oxidized zircalloy cladding, iron oxide from steel, and calcium, aluminum, silicon, and other oxides from cement, concrete, and sand. The lowest–melting point mixtures (deep eutectics) and their crystallization, viscosity, rheology, thermal expansion, and thermal conductivity are all critically important parameters that are still poorly constrained. Melt structure is a major determinant of such properties. Understanding multicomponent systems starts



Schematic of fluorite structure. UO_2 and other actinide dioxides have the same structure as CaF_2.

ILLUSTRATION: P. HUEY/*SCIENCE*

Peter A. Rock Thermochemistry Laboratory and NEAT ORU, University of California, Davis, Davis, CA 95616, USA. E-mail: anavrotsky@ucdavis.edu

Published by AAAS

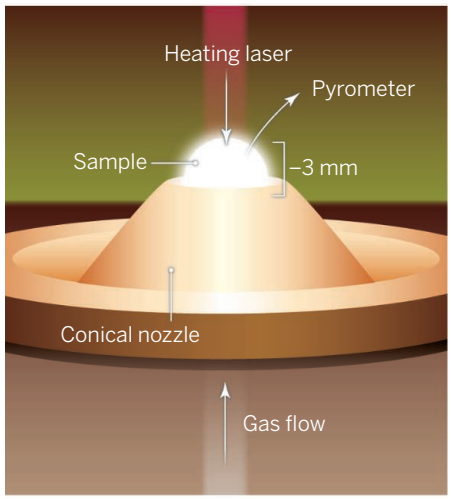
with understanding the single-component systems (e.g., UO_2), as well as binary (e.g., UO_2-ZrO_2) and ternary (e.g., UO_2-ZrO_2-SiO_2) systems. The severity and progression of a nuclear accident will depend on how far a UO_2-rich melt travels, how strongly it reacts with its surroundings, and how quickly it becomes viscous or crystallizes.

The starting point for answering such questions is the melting of UO_2, so the study by Skinner *et al.* is of both fundamental and technological importance. Small spheres of sample were suspended aerodynamically—they floated in an argon gas stream—so that the laser and the x-ray beam could interact with UO_2 without contamination from a container (see the second figure). The synchrotron x-ray studies (see the third figure) permit the calculation of pair distribution functions, which in turn allow calculations of bond lengths and coordination numbers, and comparison of solid and melt.

This solid state transition, sometimes called sublattice melting, can subsume as much as half of the entropy of the overall melting process, and so the remaining entropy measured at the melting point itself can appear to be anomalously low. The λ transition in UO_2 at 2670 K is thought to be caused by sublattice melting and presumably accounts for the development of high thermal and ionic conductivity (*4*). Skinner *et al.* confirmed that the fluorite structure remains through the transition and that the U^{4+} sublattice remains relatively rigid. However, the O^{2-} sublattice shows disorder, supporting a molecular dynamics model proposed by Yakub *et al.* (*4*). This disorder causes the average U-O distance to contract, although the unit cell and molar volumes continue to increase with increasing temperature. As disorder increases, there appear to be two groups of U-O distances, shorter and longer, perhaps related to the positions of oxygen vacancies and interstitials created by the anion disorder, although the average uranium coordination number remains about eight. Thus, a disordered and dynamic crystalline structure, still based on fluorite, exists between 2500 and 3300 K. The structural findings support the λ transition being sublattice melting and leading to low enthalpy and entropy of fusion at the melting point.

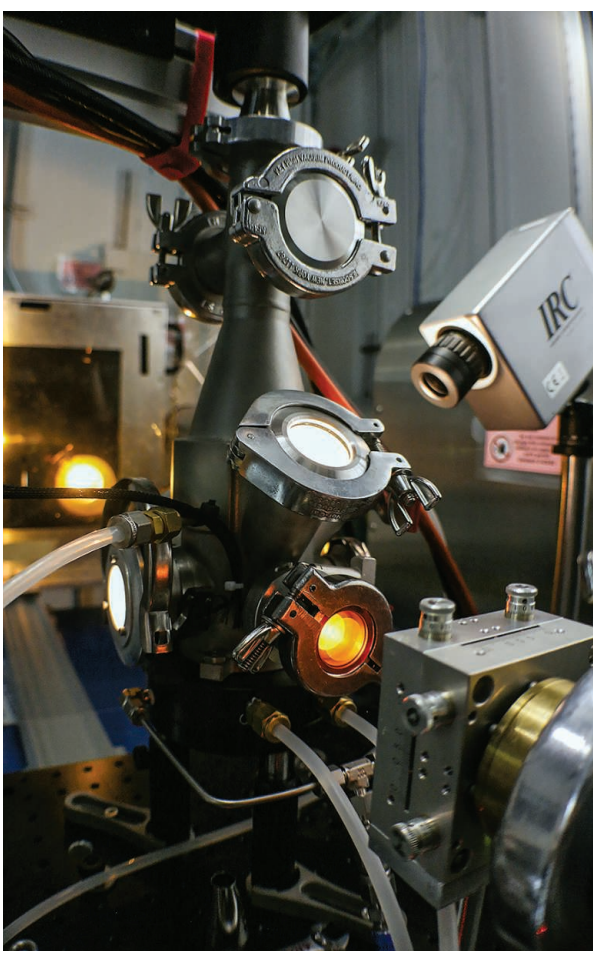
The U-O distance increases normally with increasing temperature in the melt. Melting produces a decrease of about 16% in the average U coordination number. The lower-coordinated liquid contains predominantly UO_7, and UO_6, polyhedra with some UO_8, and UO_5. These polyhedra are not linked rigidly to each other, and there is no evidence, either from the x-ray data or from molecular dynamics simulations, of clustering of like polyhedra. This random mixture of species is dynamic, and the average structure is temperature dependent. As already seen in the solid near melting, the anions jump rapidly between polyhedra centered by different U atoms. The U atoms move somewhat more slowly, but their polyhedra rearrange and exchange atoms quickly, presumably leading to a melt of low viscosity, rapid flow, and high chemical reactivity.

Skinner *et al.* have shown that the UO_2 liquid contains a variety of loosely connected polyhedra. It is reasonable to speculate that the liquid could readily incorporate other components. In the initial stages of an accident such as the Chernobyl event, in which rapid heating leads to fuel rod melting, the molten UO_2 could rapidly incorporate polyhedra containing other tetravalent cations, for example, Zr^{4+} from oxidation of the cladding. Probably both excess oxygen and excess metal could be accommodated, because the parent molten UO_2 structure is disordered and dynamic. Structural and simulation studies of such substitutions would be of great interest. ■





Floating on argon. The images show the aerodynamic levitation apparatus that floats a spherical sample on a gas stream that flows through the conical nozzle. The sample, which in the study of Skinner *et al.* is studied by x-ray diffraction, is laser heated, and temperature is measured from sample brightness by a pyrometer.



Under analysis. The apparatus for the studying the heated UO_2 sample by x-ray diffraction.

PHOTOS: LAWRIE SKINNER/STONY BROOK UNIVERSITY; TOP ILLUSTRATION, LEFT PANEL: P. HUEY/*SCIENCE*

REFERENCES

1. L. B. Skinner *et al.*, *Science* **346**, 984 (2014).
2. P. Burns, R. Ewing, A. Navrotsky, *Science* **335**, 1184 (2012).
3. B. E. Burakov *et al.*, *Proc. MRS* **465**, 1297 (1996).
4. E. Yakub, C. Ronchi, D. Staicu, *J. Chem. Phys.* **127**, 094508 (2007).

10.1126/science.aaa0163

Published by AAAS

GEOPHYSICS

Can erosion drive tectonics?

Data from the eastern Himalaya challenge the idea that climate-driven erosion can control tectonics

By **Kelin X. Whipple**

Can climate-modulated erosion affect the location, rate, and style of tectonic deformation in Earth's crust and thus seismic hazards? Particularly in the Himalaya, there are clear correlations between rugged topography and high rates of rainfall, erosion, and rock uplift (*1*, *2*), but a vigorous cause-and-effect debate continues, with new papers presenting evidence for (*1*–*4*) and against (*5*–*7*) erosional control of tectonics (see the figure). Although much field data are consistent with predicted associations among topography, erosion, climate, and deformation, unambiguous evidence has proven elusive (*8*). By focusing on a simple diagnostic test, Wang *et al.* show on page 978 of this issue (*9*) that the zone of rugged topography and extreme erosion rates where the Tsangpo-Brahmaputra River cuts through the Namche Barwa massif (see the figure)—often argued to reflect a dynamic tectonic response to river incision (*2*)—records, instead, a passive landscape response to tectonics over the past ~2 to 2.5 million years. The data threaten to undermine one of the most dramatic examples of a proposed tectonic response to erosion.

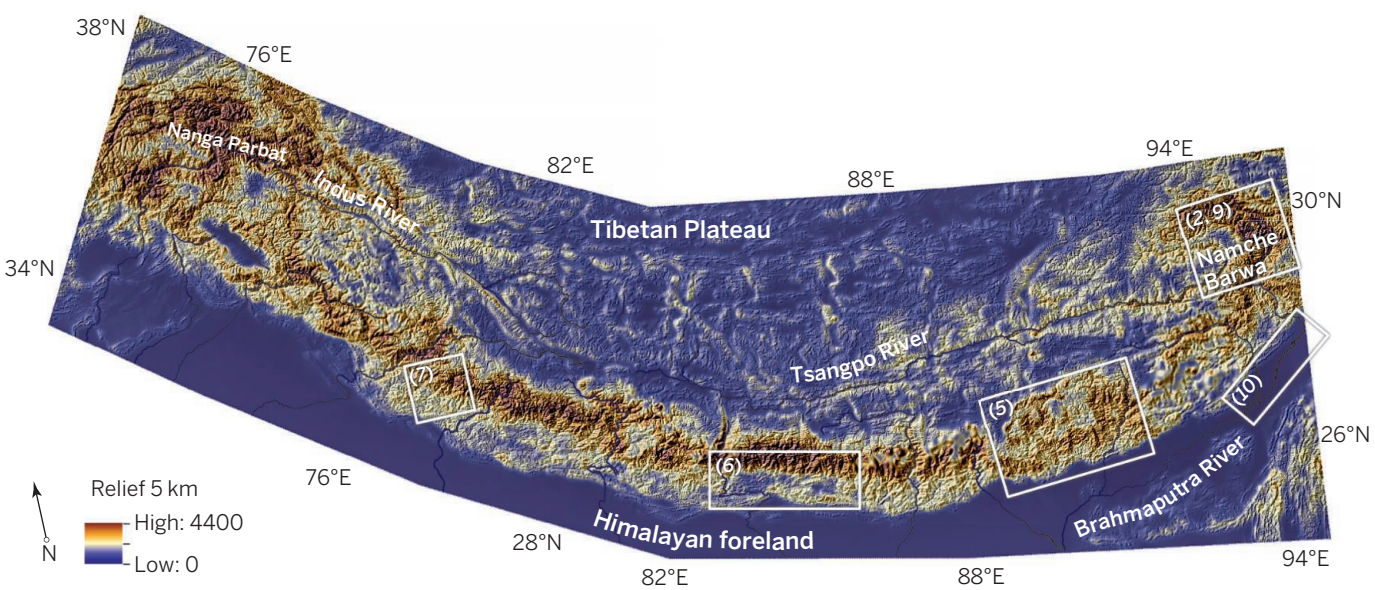
School of Earth and Space Exploration, Arizona State University, Tempe, AZ 85287, USA. E-mail: kxw@asu.edu

Perhaps the best known field examples of possible erosional control of tectonics are the "tectonic aneurysms" at both ends of the Himalaya, at Nanga Parbat and Namche Barwa. In these ~100-km-wide regions, extreme rates of rock uplift are thought to be induced by a positive feedback among erosion, heat advection, rock strength, and deformation (*2*). The case for erosion-triggered rock uplift at Namche Barwa rests mainly on three factors: the spatial coincidence over millions of years of high erosion rates, extreme relief, and rapid exhumation (7 to 10 km per million years) of rocks from deep in the crust; the coincidence of the deformation zone with a greatly oversteepened reach (a "knickzone") involving a 2-km drop in elevation over 100 km along the large, powerful Tsangpo-Brahmaputra River; and geodynamic models showing the proposed mechanism to be feasible (*2*).

The ability of this large river to trigger the positive feedback is an essential component of the tectonic aneurysm hypothesis. A postulated recent (about 4 to 10 million years ago) rerouting of the Tsangpo down a shorter, steeper path in response to headward erosion by the Brahmaputra (termed a river capture) is a favored, though not strictly required, triggering event (*2*). Wang *et al.* now corroborate the finding (*10*) that any such capture event occurred more than 21 million years ago, thus eliminating river capture as a mechanism to induce a sudden increase in erosion rate.

Further, the authors test whether the knickzone through the Tsangpo Gorge formed in response to accelerated tectonic rock uplift. To maintain its course over an imposed zone of rapid uplift, a river must build up a sedimentary wedge of sufficient thickness to match the elevation gain on the developing knickzone through the uplifting region (*11*). No such sedimentary wedge would form if the uplift occurred as a dynamic response to rapid river incision focused on a preexisting knickzone, as has been proposed (*2*). From a series of drill cores along the Tsangpo immediately upstream of the zone of rapid uplift, Wang *et al.* document the 1-km-thick sedimentary wedge predicted for a passive response of a large river to a zone of rapid rock uplift. They date the onset of sediment accumulation and thus the acceleration of rock uplift to between ~2 and 2.5 million years ago.

This finding is a serious challenge to the tectonic aneurysm hypothesis, but the jury is still out. Wang *et al.*'s clear demonstration of a tectonic driver only applies to the past 2.5 million years. Could the pulse of uplift revealed by the authors have been itself triggered by the preceding period of rapid, but not extreme, erosion and deep exhumation



Tectonics, topography, climate, and erosion: Cause and effect? This hillshade map is colored by relief within a 5-km radius. Erosion and rock uplift rates are high in the narrow (~100 km) band of high relief along the Himalayan arc and near the Nanga Parbat and Namche Barwa massifs at its ends. Several recent studies have investigated whether erosion controls tectonics in particular areas (white boxes) (*2*, *5*–*7*, *10*); others used data from the full arc of the Himalaya (*1*, *3*, *4*). Wang *et al.* (*9*) now show that at least in the past 2.5 million years, tectonics have been the main driver in the Namche Barwa massif, contrary to earlier interpretations.

Published by AAAS

that began ~8 million years earlier (2)? This scenario would require the deformational response to the earlier erosional exhumation to be sufficiently nonlinear to induce rock uplift rates much larger than the triggering erosion rate. It remains to be shown whether such a nonlinear response is mechanically plausible. To remain viable for the Namche Barwa massif, the tectonic aneurysm hypothesis must pass this test.

Surface processes however, have likely influenced the evolution of the Namche Barwa massif, and the Himalaya in general, regardless of the debate over erosional triggering of uplift. Simple physics dictates that rock uplift rates of 5 to 10 km per million years could not be sustained over millions of years as observed (*2*) without vigorous erosional removal; vertical movement of rock would otherwise slow and the zone of deformation would broaden in response to the increasing work against gravity involved in uplifting the massif. Thus, even if erosion did not trigger the increase in uplift 2.5 million years ago (*9*), erosion was critical for sustaining the extreme rate of uplift to the present.

Motivated by clear associations of relief, rainfall, and exhumation rate in the Himalaya and elsewhere, I and many others have speculated about possible manifestations of a climatic control on tectonics. However, the spatial coincidence of rugged terrain, high rainfall rates, high erosion rates, and active tectonic uplift is an insufficient test of such climatic control. Hard data and robust tests of specific model predictions—like that provided by Wang *et al.* and the further tests their data demand—are now sorely needed. Seeking evidence for a temporal change in tectonics attributable to climate change remains a promising avenue (*2*, *3*, *8*). However, erosional control of tectonics does not necessarily equate to climatic control of tectonics. Quantification of the influence of climate on erosion rates or erosional rate constants in the Himalaya and elsewhere is a high priority given recent evidence that this coupling may be weaker or more complex than generally thought (*6*, *7*). ■

REFERENCES

1. R. C. Thiede, T. A. Ehlers, *Earth Planet. Sci. Lett.* **371-372**, 278 (2013).
2. P. K. Zeitler *et al.*, *Spec. Pap. Geol. Soc. Am.* **507**, 23 (2014).
3. F. Herman *et al.*, *Nature* **504**, 423 (2013).
4. J. Hirschmiller *et al.*, *Geology* **42**, 247 (2014).
5. I. Coutand *et al.*, *J. Geophys. Res.* **119**, 1446 (2014).
6. V. Godard *et al.*, *Geology* **42**, 243 (2014).
7. D. Scherler, B. Bookhagen, M. R. Strecker, *J. Geophys. Res.* **119**, 83 (2014).
8. K. X. Whipple, *Nat. Geosci.* **2**, 97 (2009).
9. P. Wang *et al.*, *Science* **346**, 978 (2014).
10. K. A. Lang, K. W. Huntington, *Earth Planet. Sci. Lett.* **397**, 145 (2014).
11. N. F. Humphrey, S. K. Konrad, *Geology* **28**, 43 (2000).

10.1126/science.aaa0887



IMMUNOLOGY

Charting the life-course epidemiology of influenza

How does influenza immunity develop over one's lifetime?

By **Justin Lessler**

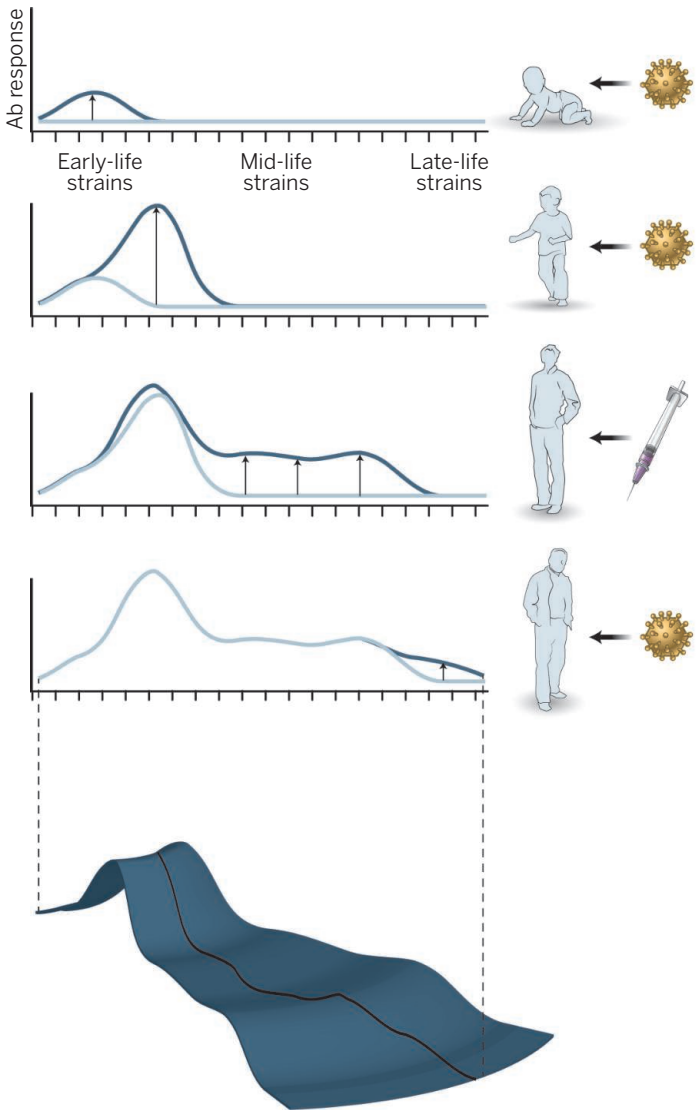
Interaction between the human immune system and influenza virus is predominantly driven by antigenic drift. In this process, ongoing mutation of the virus slowly changes its antigenic signature, eventually allowing the virus to infect people with immunity to earlier versions of the virus. Along with antigenic shifts, through which extreme changes in influenza A lead to pandemics (most often when genes from two or more different strains of influenza reassort to form a new subtype), antigenic drift is the dominant driver of influenza epidemiology. One of the most important results of antigenic drift is the need to periodically reformulate and annually administer influenza vaccine. On page 996 of this issue, Fonville *et al.* (*1*) use a technique called "antibody landscapes" to characterize antibody protection from the full spectrum of influenza strains, illuminating the interaction between new influenza exposures and past immunity.

Fonville *et al.* extend previous work on "antigenic cartography," a method for creating maps to quantify and visualize the antigenic distance (i.e., the immunological cross-reactivity) between influenza strains (*2*). The authors move from simply mapping the antigenic relationship between viruses, to characterizing the immune response developed by individuals (or populations) over a lifetime of exposure to influenza infection and vaccination. The basic approach is to use antigenic cartography to establish a planar map of the antigenic relationship between influenza strains, and then add "altitude" based on the strength of an individual's (or a population's) antibody response to each strain on the map. The resultant topology characterizes a person's immunological response to all strains of a particular influenza subtype, including those not included in the testing used to produce the landscape. The display of these antibody landscapes can be further simplified by tracing the altitude along the dominant path of influenza's antigenic evolution, producing a two-dimensional summary akin to the elevation profiles provided for race routes or hiking trails (see the figure).

Because of antigenic drift, the life-course epidemiology of influenza infection is complex. Without vaccination, nearly everyone would be infected with influenza multiple times over a lifetime; and vaccination results in additional exposures to influenza antigen. The immune system takes years to fully develop, and eventually degrades as we age. Hence, individuals will differ in their response to antigen based upon the age at which they are exposed. Likewise, previous exposures affect how the body responds to infection or to vaccination with similar strains. Antibody landscapes show promise

Department of Epidemiology, Johns Hopkins Bloomberg School of Public Health, Baltimore, MD, USA. E-mail: justin@jhu.edu

Published by AAAS



A lifetime of infection. Most people experience their first influenza infection before age 3. Infections at 5 to 10 years of age elicit a vigorous antibody (Ab) response. Later in life, there may be antibody responses to the infecting strain, vaccine, or previously infecting strains (back-boosting). As people age, it may be less common to see a vigorous antibody response. A two-dimensional chart of antibody titer summarizes a multidimensional immunological landscape that is created by potentially complex interactions between the immune system and influenza antigen over a lifetime of vaccination and infection.

as a method for visualizing and analyzing the immunologic patterns that develop over a life course, particularly in understanding how new infections or vaccination interacts with a person's existing immunological profile. Fonville *et al.* discuss one such interaction, a phenomenon that they call "back-boosting."

Back-boosting refers to a process whereby infection with a novel strain of influenza boosts antibody titers to strains circulating earlier in an individual's life. Described as far back as 1941 (*3*), back-boosting has traditionally been interpreted as evidence for "original antigenic sin" (*4*), whereby the first strain that an individual was infected with has a privileged place in their immune response, and subsequent strains elicit a reduced response while boosting antibodies to the first infecting strain. The rich characterization that is possible using antibody landscapes makes it clear that the original antigenic sin explanation is inadequate, and that back-boosting affects all previous strains to which an individual has a measurable titer. Several biological explanations are consistent with this observation, and Fonville *et al.* suggest stimulation of immune memory B cells and antibody recall (antibody production by memory B cells that is recalled from previous encounters with a strain through infection or vaccination) as the likely cause. However, without more biological and molecular evidence, this question cannot be definitively answered.

Back-boosting alone should lead people to have the highest titers of antibodies to strains that they were exposed to earlier in their lives, because antibodies to these strains have had more opportunities to be boosted. This is indeed the case (perhaps an "antigenic seniority"), but the peak in titers does not necessarily correspond to the timing of the first influenza infection. Numerous studies have shown that most people will experience their first influenza infection by 3 years of age (*5*), but Fonville *et al.* find that well over half the population has peak titers to a later strain (though age 3 is the modal peak), with the population average being highest to strains circulating when individuals were between 5 and 10 years old (*6*). This suggests differences in the immunological response to first infections, whether due to an immature immune system or because it is a first infection.

Antibody landscapes are an exciting new analytic technique, but Fonville *et al.*'s illustrative study is somewhat limited—only 294 individuals were examined. This included 69 people who were monitored (blood samples examined for antibody titers) for infection over 6 years, and 225 people of varying ages who were monitored once before and once after vaccination. Further development is needed for this landscaping approach to have an appreciable impact on the field. For antibody landscapes to be reliable, some sufficient sampling density of antibody titers must be obtained, but Fonville *et al.* offer little guidance on the number of strains needed. How to measure uncertainty and the importance of differences between landscapes also remain open questions.

There is much we still do not understand about how influenza immunity develops over an individual's life course. Immunological patterns may change as the primary mode of exposure changes from natural infection to vaccination. Antibody landscapes are an important analytic and visualization tool for exploring these issues, but are ineffective without sufficient data to create them.

Taking a life-course view of influenza immunity requires a change in the way we approach studies of influenza infection and immunity, which usually involve tests for antibodies against only a few strains of interest. Broader characterization has been rare in part because influenza antibody testing is labor intensive and expensive, primarily using methods that have changed little over the past half-century. The findings of Fonville *et al.* may signal a renewed interest in sero-epidemiology. Validation and general availability of new technologies for quickly quantifying antibodies to a wide range of influenza strains are needed for the antibody landscapes approach to be widely adopted. Such a life-course approach may yield unexpected insights into how a lifetime of interaction with influenza virus changes our immune system and influences our health. ■

REFERENCES

1. J. M. Fonville *et al.*, *Science* **346**, 996 (2014).
2. D. J. Smith *et al.*, *Science* **305**, 371 (2004).
3. F. L. Horsfall, E. R. Rickard, *J. Exp. Med.* **74**, 433 (1941).
4. T. Francis, *Proc. Am. Philos. Soc.* **104**, 572 (1960).
5. R. Bodewes *et al.*, *Clin. Vaccine Immunol.* **18**, 469 (2011).
6. J. Lessler *et al.*, *PLOS Pathog.* **8**, e1002802 (2012).

10.1126/science.aaa0613

ILLUSTRATION: V. ALTOUNIAN/*SCIENCE*

Published by AAAS

CIRCADIAN RHYTHMS

Temporal targets of drug action

A circadian gene expression atlas shows that time of day is relevant to the oscillation of drug targets and the effects of medications

By **Garret A. FitzGerald**

It has long been known that certain drug targets and many drug-metabolizing enzymes and cellular transporters are subject to variation in their abundance and activity during roughly 24-hour cycles. Indeed, variability in drug exposure and disposition following drug administration at different times of day has been appreciated for more than 40 years (*1*). However, this has had little impact on clinical practice, aside from some influence on cancer chemotherapy (*2*). A recent study by Zhang *et al.* (*3*) serves as a valuable corrective.

There are reasons to believe that our circadian clock is a biological network of considerable importance. This molecular system is highly conserved—from cyanobacteria to humans—and is tightly regulated through a series of transcriptional feedforward and feedback loops, layered with translational and post-translational levels of control (*4*). Core clock genes encode transcription factors that include BMAL1, which partners with CLOCK or NPAS2, to drive cyclical gene expression and downstream physiological processes. Indeed, the system exhibits a high level of redundancy; when clock gene expression is reduced or absent, substitutes often stand at the ready (*5*).

Orchestration of organismal biology by molecular clocks—most notably to drive circadian rhythms—is also complex. The master clock (or zeitgeber) is entrained to a 24-hour cycle by light. It resides in the suprachiasmatic nucleus (SCN) of the hypothalamus, where it can emanate neural and systemic signals to influence behavior of clocks in peripheral tissues (*6*, *7*). However, peripheral clocks, aside from such direction, may also exhibit autonomy and send signals back to the master clock to modify central behavior (*8*, *9*). Molecular clocks are highly represented among those biological networks that integrate function across tissues, so it is not surprising that genetic disruptions of clock components in mice result in disordered metabolism, inflammatory disease, and premature aging (*10*). In higher organisms, molecular clocks afford an oscillatory context upon which environmental influences, such as times, amounts, and qualities of feeding and sleeping, stress exposures, and alterations in behavioral cycles resulting from jet lag or shift work, impinge.



Medicine, in time. Oscillation in the expression of genes that are drug targets, across tissues and over time, indicates the need for evaluating the varied timing of drug administration.

Zhang *et al.* (*3*) remind us again of why we should care about our circadian rhythms. Sampling multiple tissues from mice, the authors used DNA arrays at 2-hour intervals and next-generation RNA sequencing technology every 6 hours to develop a circadian gene expression atlas. This comprehensive catalog makes the variable of time relevant to the study of biological processes. Nearly half of the known protein-coding transcripts were found to undergo circadian variation in abundance, and most do so in a tissue-specific fashion. Whereas core clock genes oscillate in phase across tissues, most other genes that are influenced by the master and peripheral clocks do not. For example, the expression of 1400 genes is phase-shifted more than 6 hours with respect to themselves across two tissues, implicating organ-specific regulation of timing that is positioned between the operation of the core clock of a tissue and the output genes. Many constituents of discrete cell signaling pathways oscillate, although in some cases they are rhythmic only in a single organ despite functioning systemically. In many tissues (but not heart and lung), gene expression was found to peak at "rush hours" before subjective dusk or dawn in bimodal (e.g., brown fat) or unimodal (e.g., liver) fashions. Zhang *et al.* also detected a diverse set of noncoding RNAs that exhibited rhythmic expression. A similar proportion of protein-coding genes and noncoding RNAs conserved between mouse and human oscillate, suggesting their functional importance. Likewise, their differential abundance over a 24-hour cycle in the 12 tissues examined also suggests organ-specific regulation.

Almost 175 drugs target oscillating genes, including 56 of the top 100 best-selling drugs in the United States. When one layers onto this the variability in disposition of drugs whose targets do not oscillate, it provokes a fundamental reconsideration of therapeutic practice. For example, half of the 56 "top 100" drugs have half-lives of 6 hours or less, yet many drugs are prescribed (or taken) only once a day. Indeed, patient compliance drops off with multiple daily dosing and is optimal when drugs are administered in the morning. An example of a common disease where this may be relevant is essential hypertension (a form with no identifiable cause), where up to 40% of patients fail to drop their blood pressure at night. Adverse cardiovascular clinical outcomes have long been noted in such "non-dippers." However, only now is controlled evaluation of varied timing of antihypertensive drug administration under way.

The data amassed by Zhang *et al.* point to several things that could be examined easily in human patients. For example, the gene targeted for cholesterol-lowering efficacy

Department of Systems Pharmacology and Translational Therapeutics, Perelman School of Medicine, University of Pennsylvania, Philadelphia, PA 19104, USA. E-mail: garret@upenn.edu

ILLUSTRATION: V. ALTOUNIAN/*SCIENCE*

Published by AAAS

of statins oscillates 12 hours out of phase with a gene associated with statin-induced myopathy. Perhaps timing of dosing could broaden the therapeutic index of statins in some patients.

There is much still to be learned about our circadian clocks. The 2014 Nobel Prize in Physiology or Medicine recognized the role of the hypothalamus in orienting us in space. How does our orientation in time, in the same brain region, intersect with this system? The range of integrative signals between the master clock in the hypothalamus and peripheral tissue clocks also remains unclear. Zhang *et al.* noted that developmentally related organs (such as the liver and kidney or white and brown fat) share genes that oscillate; how do the developmental and molecular clocks interact and how might this impinge on life span? As compounds emerge that can amplify, dampen, and phase-shift rhythms, can we safely tinker with such an integrative oscillatory system, perhaps in an organ-specific fashion? Clock genes in the testis fail to oscillate (unlike in other mammalian peripheral organs), despite their influence on fertility (*11*), but it is not clear why this is necessary or important. Intriguingly, genes in human heart and lung cluster in their expression at unconventional rush hours—why is this?

The development of a wide range of remote-sensing techniques—such as lab-on-a-chip, monitoring of human breath for metabolic data, and the documentation of diet, activity, and temperature—should allow real-time exploration of diurnal variation in human biological processes (*12*, *13*). Such advances will ease characterization of the human "chronobiome" (*9*). For now, we can try to parse differential patterns of oscillating gene expression to improve both the effectiveness and safety of commonly used drugs (see the figure), as we tentatively explore the pharmacology of new compounds aimed directly at components of the clock. ■

REFERENCES

1. G. K. Paschos, J. E. Baggs, J. B. Hogenesch, G. A. FitzGerald, *Annu. Rev. Pharmacol. Toxicol.* **50**, 187 (2010).
2. R. Kondratov, *Ann. Med.* **46**, 189 (2014).
3. R. Zhang, N. F. Lahens, H. I. Ballancea, M. Hughes, J. B. Hogenesch, *Proc. Natl. Acad. Sci. U.S.A.* 10.1073/pnas.1408886111 (2014).
4. C. L. Partch, C. B. Green, J. S. Takahashi, *Trends Cell Biol.* **24**, 90 (2014).
5. J. E. Baggs *et al.*, *PLOS Biol.* **7**, e52 (2009).
6. P. McNamara *et al.*, *Cell* **105**, 877 (2001).
7. A. Gerber *et al.*, *Cell* **152**, 492 (2013).
8. G. K. Paschos *et al.*, *Nat. Med.* **18**, 1768 (2012).
9. A. Kohsaka *et al.*, *Cell Metab.* **6**, 414 (2007).
10. G. Yang *et al.*, *Sci. Transl. Med.* **5**, 212rv3 (2013).
11. X. Liang *et al.*, *J. Biol. Rhythms* **28**, 208 (2013).
12. S. Carrara *et al.*, *Sensors* (Basel) **12**, 11013 (2012).
13. P. M. Sinues, M. W. Kohler, R. Zenobi, *Anal. Chem.* **85**, 369 (2013).

10.1126/science.aaa2285

DEVELOPMENTAL BIOLOGY

How a long-lived fungus keeps mutations in check

Specific mechanisms of somatic growth protect long-lived fungi and plants from deleterious mutations

By **Duur K. Aanen**

An individual of the mushroom-forming fungus *Armillaria bulbosa* is among the largest and oldest of all living organisms: More than 1500 years old, it covers more than 15 ha and weighs more than 10,000 kg (*1*). Some trees can also reach ages of thousands of years (*2*). How can such long-lived organisms keep the number of deleterious mutations during somatic growth in check? In a recent paper in *Mycologia*, Anderson and Catona (*3*) report extremely low genetic variation, and by inference a very low mutation rate, in a long-lived individual of another fungus, *Armillaria gallica* (see the photo). This genomic stability is puzzling and unexpected, because the sequenced samples come from locations that are more than 100 m apart and presumably separated by many rounds of cell division.

Fungi of the genus *Armillaria* are persistent tree root pathogens. An individual originates from a single mating between two haploid gametes. The resulting diploid then grows vegetatively to occupy a territory. Dispersal from one tree to another occurs through formation of root-like structures called rhizomorphs, which consist of bundles of hyphae. This growth mode leaves a spatial record of growth over time within which mutations can be localized.

By comparing the full genome sequences of multiple samples of a single individual that covers an area of roughly 200 m by 60 m, Anderson and Catona identified somatic mutations and mapped these onto the individual to localize these mutations in space and time. Consistent with expansion of this individual from a single point of origin, the genotypes occurred in a spatially coherent pattern. With this pattern of mutant sectors, the authors could estimate the mutation rate per year. Two samples separated by 100 m differed at an estimated 60 positions in their genomes, giving a haploid mutation rate of $\sim 6 \times 10^{-10}$ per site per year (*4*). The number of cell divisions separating two samples can be estimated on the basis of an average compartment length of 10 μm and the assumption that growth exclusively occurs at the tip cells. The resulting estimate of 10 million mitotic divisions separating the samples (*1*) gives a mutation rate of $\sim 3 \times 10^{-14}$ per mitotic division—some three orders of magnitude below the mutation rates estimated for filamentous fungi.

To explain this extremely low variation, Anderson and Catona propose that the effective number of cell divisions is reduced. They hypothesize that the rhizomorphs of this

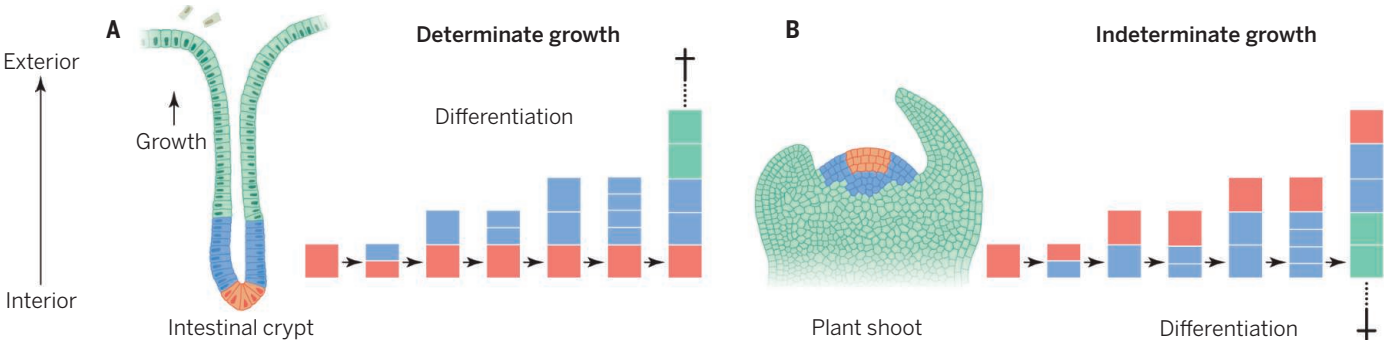
Department of Plant Sciences, Laboratory of Genetics, Wageningen University, 6708 PB Wageningen, Netherlands. E-mail: duur.aanen@wur.nl



Bulbous honey fungus—*Armillaria gallica*

PHOTO: NEIL HARDWICK/ALAMY

Published by AAAS



Position matters. Somatic growth is fundamentally different between animals (**A**) and plants and fungi (**B**). In both groups there is a small group of undifferentiated stem cells (red), which divide asymmetrically into a new stem cell and a rapidly dividing transit-amplifying cell (blue), ultimately differentiating into the various tissues (green). However, the position of the stem cells is on opposite sides of the growth front in these organism groups. In animals, the relatively mutation-free stem cells should remain on the inside to reduce the risk of cancer. In contrast, fungi and plants have indeterminate growth, implying that relatively mutation-free cells should remain at the growth front. This requires that stem cells remain at the growth front and that mitotic divisions primarily occur just below this cell, as proposed by Anderson and Catona (*3*). In plant roots and shoots, most mitotic divisions take place in the subapical region, below the stem cells. For simplicity, cells involved in the maintenance of stem cells, such as Paneth cells in intestinal crypts (*14*) and the organizing center in the plant shoot (*15*), are not shown.

fungus grow like a plant shoot, where most cell divisions take place just below the apex, reducing the number of new mutations in the apical zone and thus sheltering the population from accumulating new mutations (see the figure). In plants, this mechanism minimizes the number of cell divisions (*5*).

Long-lived fungi and plants continue to increase in size throughout their lives. Therefore, relatively mutation-free cells should remain on the outside of the individual, that is, at the growth front. This is fundamentally different from long-lived animals, where superficial tissues such as the epidermis or the intestine are continuously discarded and renewed from internal, basal cell layers (*6*). Because somatic mutations in animals may give rise to cancer, the mutation-free cells of self-renewing tissues should remain inside. As early as 1975, Cairns (*7*) proposed that this was achieved by asymmetric division of stem cells, giving rise to a new stem cell and a differentiating cell; the latter divides further to form the tissue, which ultimately is disposed and renewed from the inside. Reducing the number of stem cell divisions, and instead maximizing the number of cell divisions of the disposable transit cells, is one mechanism to reduce the number of stem cell mutations (*7*).

In addition, Cairns proposed the "immortal-strand hypothesis," according to which sister chromatids segregate nonrandomly during mitosis. The stem cell preferentially receives the old templates, thus preserving the original genetic information, while the other sister cell receives the copied strands (*7*). Although there is evidence that template strands segregate nonrandomly to daughters of a dividing cell, there is no direct proof for the assumption that most mutations arise in the newly synthetsized strand. An alternative explanation is that nonrandom segregation of sister chromatids epigenetically regulates cell fate. For fungi, asymmetric cell division could reduce the mutation rate, provided the slowly dividing totipotent stem cells remain at the growth front (*8*). There is evidence for this hypothesis in the fungus *Aspergillus nidulans*, where nuclei containing the original template DNA are concentrated at the growth front (*9*).

Anderson and Catona's study contributes to an emerging picture of the specific adaptations through which long-lived species in all three main groups of multicellular organisms reduce the somatic mutation rate. In animals, long-lived species are better able to maintain relatively mutation-free somatic cells. For example, animals with 1000 times as many cells as humans (such as whales) do not exhibit an increased cancer risk, showing that natural mechanisms can suppress cancer vastly more effectively than is done in human cells (*10*). In plants, the finding that taller species tend to have lower rates of molecular evolution than small species supports the hypothesis that long-lived plants have a reduced somatic mutation rate (*5*).

In fungi, there is also extreme variation in the longevity of individuals, ranging from 1500-year-old individuals of *Armillaria* to *Podospora anserina*, which lives for only 2 to 3 weeks. The life span of the latter species is extrinsically limited because of its ephemeral habitat, a herbivore dropping. When artificially grown for a time that exceeds its maximal life span in nature, this fungus shows signs of aging, leading to colony death (*11*). The observation that aging progresses fastest on the edge of the colony indicates that there is asymmetrical cell division—but in this case with the "wrong" orientation of the rejuvenated stem cells, namely on the inside of the colony. This result shows that predictable, extrinsic mortality can take away the selective pressure to keep mutation-free cells at the growth front of an individual.

Whatever the exact mechanism, asymmetric cell division seems to be a key to slowing down the accumulation of somatic mutations in long-lived fungi and plants. In contrast to growth of renewable tissues in animals, the stem cells should remain at the growth front of the individual. Even in unicellular organisms, careful experimentation has demonstrated asymmetric cell division, with one daughter cell rejuvenated and one aged (*12*). This asymmetry has been attributed to the accumulation of physiological damage. However, there may also be asymmetries in the expected mutation frequency among the sister cells—for example, because only one of the two cells acquires the "immortal" template strand. With the advent of new techniques to detect mutations in living cells (*13*), testing this hypothesis may come within reach. ■

REFERENCES AND NOTES

1. M. L. Smith, J. N. Bruhn, J. B. Anderson, *Nature* **356**, 428 (1992).
2. H. Thomas, *New Phytol.* **197**, 696 (2013).
3. J. B. Anderson, S. Catona, *Mycologia* **106**, 642 (2014).
4. Assuming the average growth rate of rhizomorphs of 0.2 m per year (*1*), these samples have been separated for at least 500 years. Given a genome size of ~10^8 base pairs, this gives a haploid mutation rate of ~6×10^{-10} per site per year [$60/(2 \times 500 \times 10^8)$].
5. R. Lanfear *et al.*, *Nat. Commun.* **4**, 1879 (2013).
6. S. A. Frank, M. A. Nowak, *BioEssays* **26**, 291 (2004).
7. J. Cairns, *Nature* **255**, 197 (1975).
8. A. Gladfelter, J. Berman, *Nat. Rev. Microbiol.* **7**, 875 (2009).
9. R. F. Rosenberger, M. Kessel, *J. Bacteriol.* **96**, 1208 (1968).
10. A. F. Caulin, C. C. Maley, *Trends Ecol. Evol.* **26**, 175 (2011).
11. A. D. van Diepeningen *et al.*, *Philos. Trans. R. Soc. B* **369**, 20130447 (2014).
12. E. J. Stewart, R. Madden, G. Paul, F. Taddei, *PLOS Biol.* **3**, e45 (2005).
13. M. Elez *et al.*, *Curr. Biol.* **20**, 1432 (2010).
14. L. Li, H. Clevers, *Science* **327**, 542 (2010).
15. R. Heidstra, S. Sabatini, *Nat. Rev. Mol. Cell Biol.* **15**, 301 (2014).

ACKNOWLEDGMENTS

I thank J. Anderson, F. Debets, A. de Visser, and D. Vreugdenhil for fruitful discussions.

10.1126/science.1261401

ILLUSTRATION: ADAPTED BY P. HUEY/*SCIENCE*

Published by AAAS

BOOKS *et al.*



PHOTO: THINKSTOCK

RESTORATION ECOLOGY

A walk on the wild side

By **Christine Griffiths**

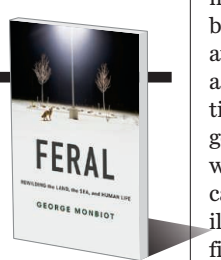
The term "rewilding" evokes everything from fear to outrage in the minds of the public, as they imagine lions and elephants haphazardly released into city streets. The term first appeared in print in 1998 and was used to describe conservation methods that focused on reducing habitat loss and fragmentation by promoting "cores, corridors, and carnivores" (*1*). Much literature has indeed focused on reintroducing large herbivores and apex carnivores to North America and Europe, because these keystone species play crucial roles in maintaining the structure and integrity of ecological communities

In *Feral: Rewilding the Land, the Sea, and Human Life*, author George Monbiot challenges the reader to think more deeply on the subject of rewilding. He maintains that understanding how ecological communities persisted in the past and why they are degraded today is necessary to identify and set appropriate targets for restoration.

Monbiot's dream is to rewild the world, starting with the barren and bleak British landscape and the depleted oceans.

The reviewer is at the School of Biological Sciences, University of Bristol, Bristol, UK. E-mail: christine.griffiths@bristol.ac.uk

Feral
Rewilding the Land, the Sea, and Human Life
George Monbiot
University of Chicago Press, 2014. 341 pp.



Monbiot bemoans how much of the British landscape that is perceived as wild and largely unspoiled is in fact damaged by overgrazing deer and sheep and argues that misguided local, national, and regional land management policies are to blame. His panacea is to supplant archaic subsidies that support unsustainable farming practices with an economy based on walking and wildlife.

Throughout the text, Monbiot presents compelling evidence that the benefits of rewilding—including its effects on carbon sequestration, tourism, hunting, recreation, soil recovery, water regulation, and quality of life—far outweigh the costs. But he insists that rewilding should not take place without public consensus.

Challenging public opinion that the restoration of rainforest or coral reefs, or the reintroduction of large herbivores and predators, is needed only in tropical areas or vast uninhabited lands, he envisions restoring small corners and pockets of urban environments to their original states as well. Rewilding, according to Monbiot, can occur everywhere and on many scales.

Because humans now shape the future of the planet, the conservation and restoration of fauna and flora depend on our vision as much as on science. Yet, as Monbiot laments, our shifting expectations about what a healthy ecosystem looks like—an affliction referred to as "shifting baseline syndrome"—curtails our ability to identify problems and implement restoration efforts to protect biodiversity. Reconnecting with nature and examining our ecological history, he argues, is essential to appreciating what has been lost and is critical for repairing damaged ecosystems.

Throughout the book, Monbiot's lyrical and provocative tales of his efforts to reengage with the wild stimulate the senses and arouse an innate urge to affiliate with nature. His efforts are reminiscent of those of biologist Edward O. Wilson, who theorizes that contact with nature is needed to reverse what he sees as a growing dissatisfaction and emptiness in our lives (*2*).

In *Feral,* Monbiot takes you on an emotional roller coaster, at times plunging you into troughs of despair as he discusses the bleak plight of much of our wildlife and, at others, raising you up on peaks of hope as he discusses how much of the degradation can be reversed. Though daunting, his goals of renewing the public's engagement with nature and raising perceived ecological baselines may ultimately be more easily tackled than other challenges in the field of restoration ecology. Convincing the public that certain critical ecosystem functions may only be restored by introducing functionally similar exotic species or by species de-extinction (by means of cloning technologies and/or synthetic biology), for example, might prove more difficult.

Part personal journal, part restoration ecology primer, *Feral* popularizes the concept of rewilding and will likely prompt wildlife managers, landowners, policymakers, and the general public to question their perception of the natural world and its role in our lives. In addition to stressing the inherent need to restore ecological interactions, Monbiot's thesis—that rewilding is in our own best interest—could become the catalyst for a rewilding movement.

REFERENCES

1. M. Soule, R. Noss, *Wild Earth* **8**, 19 (1998).
2. E. O. Wilson, *Biophilia* (Harvard Univ. Press, Cambridge, MA, 1984).

10.1126/science.1262000

Downloaded from www.sciencemag.org on November 22, 2014

Published by AAAS

EXHIBITION

Steampunk science

By **Deborah Dixon**



Longitude Punk'd
Heloise Finch-Boyer, Curator
Flamsteed House,
Royal Observatory Greenwich
10 April 2014 to 4 January 2015.
www.rmg.co.uk/whats-on/events/longitude-punkd

Longitude Punk'd is part of an exhibit at the Royal Observatory in Greenwich that celebrates the 300th anniversary of the United Kingdom's Longitude Act, an act of Parliament that established the British Board of Longitude and offered a monetary prize to anyone who could develop a practical method for determining a ship's longitude while at sea.

The exhibition features the works of nine artists from the United Kingdom who relied on historical accounts and resources from the observatory to create a fictional retelling of the longitude prize competition. The exhibit is done in "steampunk" style—an



aesthetic known for futuristic inventions rendered in the style of the British Victorian era. The result is an often whimsical and amusing, while always clever, series of installations.

The Royal Observatory has played an authoritative role in providing precise and accurate observations of both space and time, and the artists playfully satirize this authority by appropriating the observatory's inventory and exhibition spaces to set the scene. The intent is not to blur fact and fiction but to create new stories of hubris and derring-do in the vein of Jules Verne and H. G. Wells.

The reviewer is at the School of Geographical and Earth Sciences, University of Glasgow, East Quadrangle, University Avenue, Glasgow G12 8QQ, Scotland. E-mail: deborah.dixon@glasgow.ac.uk

The organizing conceit of the exhibition is the story of a fictional navigator, the Commodore, created by author Robert Rankin, who exploits the geographical awareness of kiwi birds to win the Board of Longitude's competition. Excerpts from "The Rime of the Ancient Commodore," a whimsical poem about his experience, appear on a series of signposts throughout the exhibit, creating a narrative for visitors to follow.

The upstairs rooms of the observatory's Flamsteed House, where part of the exhibit is displayed, are preserved as the apartments of previous Royal Astronomers and their families—with a twist. The rooms now feature reimagined costumes for occupants and visitors of the day, created by artists Jema Hewitt and Karen Grover. In the Octagon Room, for example, is Hewitt's Orrery Gown, a garment that combines period dress detail with a new model of the solar system, where all revolves around the moon. Downstairs, the usual contents of the "Time and Longitude" gallery have been replaced with fictional entries to the Board of Longitude competition. An example is artist Ian Crichton's "Precise Longitudinal Beacon," a traditional Georgian mansion with a steampunk slant. Crichton imagines a series of these stately homes hoisted 50 miles above the equator and adorned with flashing lights to indicate the lines of longitude.

The highlight of the exhibition, however, is Geof Banyard's alternative history project, which provides new titles and captions for paintings, sketches, and artifacts in the Royal Observatory's permanent collection. Simon de Vlieger's sublime oil painting, *A Ship Wrecked off a Rocky Coast* (1640), for example, is now called *From BENEATH you, it DEVOURS*—an homage to horror author H. P. Lovecraft.

In contrast to the National Maritime Museum's exhibition on the same subject, Longitude Punk'd does not purport to educate visitors about the realities of the past; rather, it emphasizes how a history of science can be told in a way that instills wonder and curiosity.

10.1126/science.aaa0415

IMAGE: © JEMA HEWITT

Downloaded from www.sciencemag.org on November 22, 2014

LETTERS

Edited by **Jennifer Sills**

Tropical crops: Cautious optimism

IN THEIR PERSPECTIVE "A double-edged sword for tropical forests" (3 October, p. 38), L. R. Carrasco *et al*. warn that the development of high-yielding tropical crops such as oil palm may accelerate tropical deforestation. We believe that the situation may not be as dire as it seems.

The genetic yield potential of oil palm does not currently limit production in Malaysia, Indonesia, or the countries in which Malaysian and Indonesian companies are expanding (such as Liberia). The main constraint to production is labor availability. In Malaysia, a large part of the plantation workforce is hired on a daily ad hoc basis. Given that ripened fruit needs to be harvested and milled within 48 hours, a lack of harvesters on any particular day delays processing and compromises fruit quality and yield. Consequently, the yield potential of oil palm is rarely fully realized in existing plantations.

Citing a modeling study by Villoria *et al*. (*1*), Carrasco *et al*. argued that by closing the oil palm yield gap, Indonesia and Malaysia are projected to lose 65,000 ha of forests to oil palm under current global oil crop demand. However, this figure assumes no yield increases for other oil crops globally or for oil palm outside of Indonesian and Malaysia. Under a more realistic scenario that incorporates plausible yield increases for all crops, 1,800,000 ha of forest are spared globally, including both Indonesia and Malaysia (*1*).

Of greater concern to us—and noted by Carrasco *et al*.—is the possibility that genetic "improvements" will increase the temperature and moisture ranges at which oil palm can profitably be grown. Such improvements would indeed open up previously spared ecosystems to agricultural conversion. This, far more than boosting the yields of oil palm in already-planted areas, strikes us as the critical threat to biodiversity.

Xingli Giam,[1]* Lian Pin Koh,[2] David S. Wilcove[3]

[1]School of Aquatic and Fishery Sciences, University of Washington, Seattle, WA 98105, USA. [2]School of Earth and Environmental Sciences and The Environment Institute, University of Adelaide, Adelaide SA 5005, Australia. [3]Woodrow Wilson School and Ecology and Evolutionary Biology, Princeton University, Princeton, NJ 08544, USA.

*Corresponding author. E-mail: xgiam@uw.edu

REFERENCE

1. N. B. Villoria, A. Golub, D. Byerlee, J. Stevenson, *Am. J. Agric. Econ.* **95**, 1301 (2013).



Oil palm harvest in Malaysia.

Response

GIAM *ET AL*. SUGGEST that the labor constraints oil palm production faces are more influential in determining current yields than genetic constraints. Although we agree that oil palm production is limited by a range of constraints, including labor, technological advances associated with genetically improved new varieties could relax this constraint in the future. These advances could include distinctive pigmentation when ripened (*1*), synchronized ripening, higher fruit quality to increase oil extraction rates, lower content of free fatty acids allowing more flexibility of post-harvest processing (*2*), and more uniform tree height and architecture facilitating the eventual mechanization of harvest (*3*).

However, a focus on labor constraints in oil palm production misses our key point: Current global models ignore the interactions between crops, which feed through into uneven distributions of new fronts of deforestation. We will only see how genetically improving yields, relaxing labor constraints, or both will affect land use if we understand how such feedbacks filter through the system. In this respect, we agree with Giam *et al*.; we need models that can link global market effects with realities on the ground (*4*, *5*).

As highlighted in our Perspective and reiterated by Giam *et al*., the potential for genetic improvements enabling producers to open up new tropical frontiers to conversion in the Amazon and Africa is a major concern. But ascertaining whether this or overall yield improvements is the most severe threat to biodiversity requires the development of models that can capture global market feedbacks [e.g., (*6*)] and local realities.

L. R. Carrasco,[1]* C. Larrosa,[1,2] E. J. Milner-Gulland,[2] D. P. Edwards[3]

[1]Department of Biological Sciences, National University of Singapore, Singapore 117543. [2]Department of Life Sciences, Silwood Park Campus, Imperial College London, UK. [3]Department of Animal and Plant Sciences, University of Sheffield, Sheffield, S102TN, UK.

*Corresponding author. E-mail: dbsctlr@nus.edu.sg

REFERENCES

1. R. Singh *et al.*, *Nat. Commun.* **5**, 4106 (2014).
2. F. Morcillo *et al.*, *Nat. Commun.* **4**, 2160 (2013).
3. D. J. Murphy, *J. Oil Palm Res.* **26**, 1 (2014).
4. E. F. Lambin, P. Meyfroidt, *Proc. Natl. Acad. Sci. U.S.A.* **108**, 3465 (2011).
5. J. Weinzettel, E. G. Hertwich, G. P. Peters, K. Steen-Olsen, A. Galli, *Glob. Environ. Change* **23**, 433 (2013).
6. T. W. Hertel, N. Ramankutty, U. L. C. Baldos, *Proc. Natl. Acad. Sci. U.S.A.* **111**, 13799 (2014).

Rewarding academic innovation

WE COULD NOT agree more with the conclusion of the 10 October Editorial ("Five years of translation," K. L. Kelner and M. McNutt, p. 145) that "[a]s a science community, we should be creating more opportunities for facilitating the transfer of science in the service of society." One way to accomplish this is to recognize performance through honors and awards, which can motivate faculty to get involved in patenting and commercialization activities by providing peer validation and recognition (*1*–*3*). Unfortunately, the awards landscape for the academic inventor is sparse. As pointed out by D. Normile ("Physicists change the light bulb," In Depth, 10 October, p. 149), it was very surprising to see the Nobel Prize for Physics awarded for an invention rather than for basic discovery. We hope the future brings more such awards.

The National Research Council recently compiled an extensive list of faculty

PHOTO: CRAIG MOREY/FLICKR

Downloaded from www.sciencemag.org on November 22, 2014

Published by AAAS

awards and honors (*4*). Of the nearly 1500 awards and honors listed, fewer than a dozen can be stretched to recognize and reward excellence in academic invention and technology transfer specifically. For the most accomplished academic inventors, there are avenues for national-level recognition, such as the National Medal of Technology and Innovation, the Lemelson-MIT Prize, the National Inventors Hall of Fame, and the newly instituted AAAS-Lemelson Invention Ambassadors program (*5*). However, these awards touch very few academic inventors annually.

The National Academy of Inventors (NAI) Fellows program provides an award open to a larger number of academic inventors than the awards listed above. The NAI defines Fellow status as "a high professional distinction accorded to academic inventors who have demonstrated a highly prolific spirit of innovation in creating or facilitating outstanding inventions that have made a tangible impact on quality of life, economic development, and the welfare of society." At the end of its second year, the NAI Fellows consisted of 244 academic inventors worldwide who collectively hold more than 9000 issued U.S. patents and represent 216 universities and governmental and nonprofit research institutions. These fellows are recognized by the U.S. Patent and Trademark Office (USPTO) at an annual ceremony, listed on plaques displayed at USPTO headquarters, and recorded each year in the Congressional Record of the U.S. House of Representatives (*6*).

In addition to recognizing individual faculty members, we need to recognize and celebrate best practices at institutions. Recognizing this, the Association of Public and Land-Grant Universities recently created the Innovation and Economic Prosperity designation (*7*) "to recognize universities that are leaders in spurring and promoting regional economic development." These kinds of peer recognition help build institutional confidence and provide models for others to follow as universities respond to societal demands to play a more central role in economic development.

Paul R. Sanberg, Judy Genshaft, Sudeep Sarkar

University of South Florida System, Tampa, FL, 33620, USA.

*Corresponding author. E-mail: psanberg@usf.edu

REFERENCES

1. K. N. Huggett, R. B. Greenberg, D. Rao, B. Richards, S. W. Chauvin, *Med. Teach.* **34**, 907 (2013).
2. N. Baldini, R. Grimaldi, M. Sobrero, "Motivations and incentives for patenting within universities: A survey of Italian inventors," paper presented at the 65th Annual Meeting of the Academy of Management, Honolulu, Hawaii, 9 August 2005.
3. A. Lam, *What Motivates Academic Scientists to Engage in Research Commercialization: 'Gold', 'Ribbon' or 'Puzzle'?* (School of Management, Royal Holloway University of London, Working Paper Series, 2010).
4. National Academy of Sciences, Awards and Honors: Data Collection and Methodology (http://sites.nationalacademies.org/PGA/Resdoc/PGA_044718).
5. American Association for the Advancement of Science, About the AAAS-Lemelson Invention Ambassadors Program (www.aaas.org/page/about-aaas-lemelson-invention-ambassadors-program).
6. National Academy of Inventors, About the NAI Fellows Program (http://academyofinventors.org/fellows.asp).
7. Association of Public and Land-Grant Universities, 2014 Innovation and Economic Prosperity Universities Designation and Awards Program (www.aplu.org/page.aspx?pid=2680).

Older scientists get their due

IN THE IN DEPTH News story "A call for NIH youth movement" (J. Kaiser, 10 October, p. 150), Representative Andy Harris (R–MD) raises concerns about the "plight of young biomedical scientists," especially the fact that they "now are often in their 40s before they win their first [National Institutes of Health (NIH)] grant." He claims that he "saw firsthand how the most innovative thinking frequently came from younger scientists."

There are two major problems with Harris's claims. First, research suggests that scientists are most productive, and most productive of innovative research, when they are middle-aged, not when they are under 35 (*1*, *2*). Second, the trends that are captured in the graph accompanying Kaiser's story can be explained without suggesting that young scientists are being robbed of opportunities. The growth rate of science is decreasing. The scientific workforce is no longer growing at a rate of 5% per year. In fact, it is growing at less than half that rate and has been for some decades (*3*). Scientists are also remaining in the workforce longer (*4*). As a result of these two trends, the percentage of the scientific workforce that is under the age of 35 is now much lower. Hence, relative to the whole population of working scientists, there are proportionally fewer young scientists applying for NIH grants (*5*). As we would expect, more older scientists are getting NIH grants.

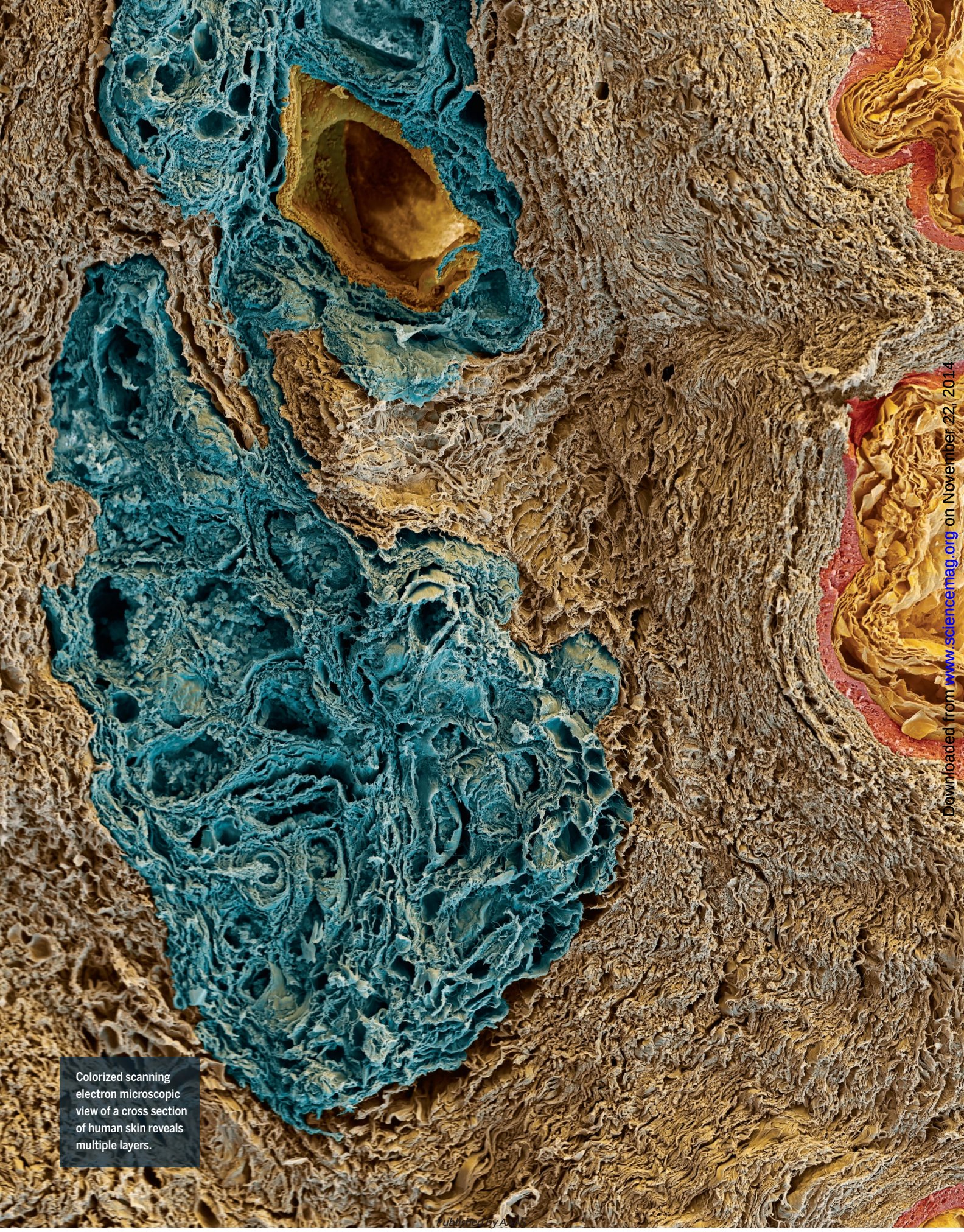
K. Brad Wray

State University of New York, Oswego, Oswego, NY 13126, USA. E-mail: kwray@oswego.edu

REFERENCES

1. D. K. Simonton, *Creativity in Science: Chance, Logic, Genius, and Zeitgeist* (Cambridge Univ. Press, Cambridge, 2004).
2. K. B. Wray, *Scientometrics* **81**, 757 (2009).
3. National Science Foundation, Science and Engineering Indicators 2000 (NSF, 2000), Appendix table 4-21; www.nsf.gov/statistics/seind00/access/c4/c4s4.htm.
4. J. Kaiser, *Science* **322**, 848 (2008).
5. S. Arbesman *et al.*, *Social Studies Sci.* **43**, 282 (2013).

Published by AAAS



Colorized scanning electron microscopic view of a cross section of human skin reveals multiple layers.

Downloaded from www.sciencemag.org on November 22, 2014

Published by AAAS



Skin

From bench to bedside

by **Stella Hurtley**, **Pamela J. Hines**, **Kristen L. Mueller**, *and* **Elizabeth Culotta**

Skin is frequently referred to as the largest organ in the body. Our skin protects us from the elements; it is through our skin that we interact with our environment, and it is a crucial part of how we present ourselves to the world, from tanning and tattoos to scars and wrinkles (see linked videos). The basic biology of the skin (Watt, p. 937) involves a multitude of cell types, all of which cooperate to form the organ we all inhabit. When skin is wounded, a repair process is instigated to breach the gap, and ancient and modern approaches to promoting wound healing have saved countless lives (Sun *et al.*, p. 941). Anthropologist Nina Jablonski, profiled by Ann Gibbons (p. 934), studies the evolution of skin color and has found that a surprising number of people face health consequences from having a skin tone poorly adapted to their current environment. A stark example of this is malignant melanoma. Melanomas often appear on exposed skin, and new approaches are finally starting to provide hope for successful treatments (Lo and Fisher, p. 945). Our sense of touch is key to how we respond to and interact with our environment. Different types of nerve endings within the skin provide us with a variety of sensations, from pleasurable to painful (Zimmerman *et al.*, p. 950). Besides protecting us, our skin also provides a habitat for a host of microbes—many helpful, some less so (Belkaid and Segre, p. 954). In this special issue of *Science*, we present an overview of some of the basic aspects of skin biology and how advances in our understanding are leading to positive benefits in the treatment of skin conditions, wounds, and diseases.

INSIDE

NEWS

Shedding light on skin color *p. 934*

REVIEWS

Mammalian skin cell biology: At the interface between laboratory and clinic *p. 937*

Advances in skin grafting and treatment of cutaneous wounds *p. 941*

The melanoma revolution: From UV carcinogenesis to a new era in therapeutics *p. 945*

The gentle touch receptors of mammalian skin *p. 950*

Dialogue between skin microbiota and immunity *p. 954*

RELATED ITEMS

- ▸ VIDEOS
- ▸ sciencemag.org/special/skin

PHOTO: EYE OF SCIENCE/SCIENCE SOURCE

Published by AAAS



Shedding light on SKIN COLOR

Nina Jablonski explores how it evolved—and what happens when it does not match the environment

By **Ann Gibbons**

A few years ago, anthropologist Nina Jablonski faced off with comedian Stephen Colbert on his late-night talk show. He proclaimed that his skin was so white, he could hide in a snow bank. Was it really true, he asked her, that *his* ancestors had dark skin?

Certainly, Jablonski said. If researchers were to "dissect his DNA" they would find evidence that he was descended from black Africans. Colbert, in his conservative persona, feigned shock: "Is it possible that I am blacker than Barack Obama?"

In her 7 minutes on the show, Jablonski, a biological anthropologist at Pennsylvania State University (Penn State), University Park, got her point across: "Skin color is not about race," she told Colbert. "It's about sun and how close our ancestors lived to the equator." As modern humans spread out of Africa in the past 60,000 years, they adapted to the varying natural light they encountered, from the twilight of northern winters to the blazing sun of the equator, and their dark skin evolved into a sepia rainbow. It's a story Jablonski has told in countless radio and TV interviews, two popular books, and a TED talk viewed by nearly 700,000 people online (http://bit.ly/1tx8Jbs).

Although skin color is a poor way to classify humans, Jablonski says it does have real implications for health. She argues that in the modern era, as humans of various shades have moved rapidly across hemispheres, their skin has not had time to adapt to different amounts of ultraviolet (UV) light. "You have this lovely gradient of skin color—then, people start moving around," she says. "Often we're unaware that we're living in environments to which our skin is inherently poorly adapted."

Most white people know that if they live near the equator, they risk skin cancer unless they use sunscreen. But Jablonski argues that other consequences of skin color played crucial roles in its evolution. In the tropics, she says, light-skinned people may face a higher risk of having babies with birth defects, because intense sunlight can destroy folate in the blood. Meanwhile, dark-skinned people who bundle up in frigid northern winters or stay indoors all day in the tropics risk vitamin D deficiency, making them susceptible to rickets, infectious diseases, heart disease, and other health problems. "You can have a desk job in Nairobi, or be a woman wearing the veil in Yemen, or any number of fairly serious scenarios where you don't get enough vitamin D," Jablonski says. "This is an enormous game changer for health."

Some of Jablonski's ideas remain unproven. Yet her work is injecting a shot of evolutionary perspective into medicine and influencing researchers to test how sunlight affects health. Jablonski has "opened my eyes to so many things I hadn't thought about," says perinatal epidemiologist Lisa Bodnar of the University of Pittsburgh in Pennsylvania. Radiation epidemiologist Michael Kimlin of the Queensland University of Technology in Brisbane, Australia, agrees. "We have this brand-new field in which people are suggesting that when we put our bodies in the sun, there are complex interactions," he says. "What Nina's doing is not only contributing to evolutionary science … she's creating ripples in [biomedical] science and giving people like me hypotheses to test."

IF YOU HAD TOLD Jablonski when she was a girl that she would travel the world giving lectures and be a sought-after speaker on TV, she wouldn't have believed it. Painfully shy, she grew up collecting butterflies and fossils near her family's farm, half a mile from the nearest neighbor in western New York. She flubbed her first organized

PHOTO: BRIAN STRAUSS

Downloaded from www.sciencemag.org on November 22, 2014

Published by AAAS

talk—a 4-H presentation on how to make a crudité tray—because she was so nervous.

Encouragement from her mother and female mentors, including those at Bryn Mawr College, where she earned her undergraduate degree in biology, boosted her confidence and speaking skills. In graduate school at the University of Washington, Seattle, she studied how extinct monkeys in the *Theropithecus* genus, which includes baboons, adapted to grazing on grass. Then she worked at universities in Asia and Australia, studying fossil monkeys in China and Africa for clues to how they adapted to their environment. She became "the reigning expert on Old World monkeys," says paleoanthropologist Jay Kelley of Arizona State University, Tempe.

In 1990, a colleague asked her to give a class lecture on an unfamiliar topic: the evolution of skin. As she prepared, Jablonski was surprised by how little was known. Back in the 1930s, researchers had proposed that light skin evolved to provide vitamin D where sunlight was scarce. Skin needs to be struck by sunlight to synthesize the vitamin—essential for bone strength and other aspects of health—and dark skin contains melanin, a remarkably effective natural sunscreen that also reduces vitamin D synthesis. As for dark skin, many researchers believed protection from sunburn and skin cancer was its key advantage.

But Jablonski, like other evolutionists before her, quickly spotted the flaw in that logic: Skin cancer strikes people late in life, after the age when they reproduce. Why would natural selection favor dark skin?

A few weeks after giving her talk, Jablonski heard a lecture on how neural tube birth defects such as spina bifida are linked to deficiencies in folate, a naturally occurring form of vitamin B; she also read that sunlight can destroy folate circulating in the tiny blood vessels of the skin. In a flash of insight, she realized that sunlight would be more likely to zap folate in light-skinned people than in people with dark skin, protected by melanin. Thus natural selection would favor darker skin in environments with strong sunlight. "I sat there literally bouncing around in my chair," Jablonski recalls. "This is a connection between pigmentation and reproductive success."

She and her husband, geographer George Chaplin, also of Penn State, compared the worldwide distribution of skin tone with that of ground-level UV light, mapped from satellite data (see graphic, p. 936). In a paper in 2000, they were able to show quantitatively that skin color is darkest where light is most intense, and palest in dim high latitudes. In Africa, for example, people in humid and cloudy environments are a lighter shade of brown than those at high altitude or along the coasts, where glare from the water boosts UV light. The match between skin tone and UV intensity within the tropics also disproved then-current theories that dark skin evolved in the tropics because it was a better barrier to microbes.

In that paper, Jablonski proposed an evolutionary scenario for dark skin: Like chimpanzees, our ancient ancestors in Africa originally had fair skin covered with hair. When they lost body hair in order to keep cool through sweating, perhaps about 1.5 million years ago, their naked skin became darker to protect it from folate-destroying UV light.



Nina Jablonski measures the light reflected by a Cape Town woman's skin to test how skin tone can affect vitamin D levels.

PHOTO: ANNA COUSSENS

This idea is still controversial. "It's a valid theory and it's intriguing, but it's obscure to the folate community," says Robert Berry, a pediatric epidemiologist at the Centers for Disease Control and Prevention in Atlanta. "There's virtually no evidence to prove it or disprove it." In medical circles, the idea that dark skin is an adaptation to skin cancer is still received wisdom, Kimlin says. But Jablonski says that the circumstantial evidence for her hypothesis is growing. One 1996 study found that several women exposed to UV light in tanning beds had babies with spina bifida. Then in February, Kimlin and colleagues reported that the more time healthy white women in Queensland spent in the sun, the less folate circulated in their blood. Given these and other studies, Kimlin concludes, "the idea that darker skin tones could have developed in order to protect folate makes sense."

Meanwhile, additional research continues to confirm that light skin was favored in dimmer regions, presumably to boost vitamin D synthesis. For example, recent genetic studies show that in the past 70,000 years, Europeans, Asians, and Neandertals independently evolved white skin, using at least three different genes, says Penn State geneticist Mark Shriver, whose team dated when those genes arose. Jablonksi is spreading an evolutionary perspective that many still haven't quite absorbed, says Harvard University immunologist Barry Bloom. "The message that people still don't understand that just knocks your socks off is that we were all born white on the planet and then we all became black," he says. Then "some of us got to Europe where being black wasn't a great advantage, and we became white again."

These days, though, people do not always live in the conditions for which evolution equipped them.

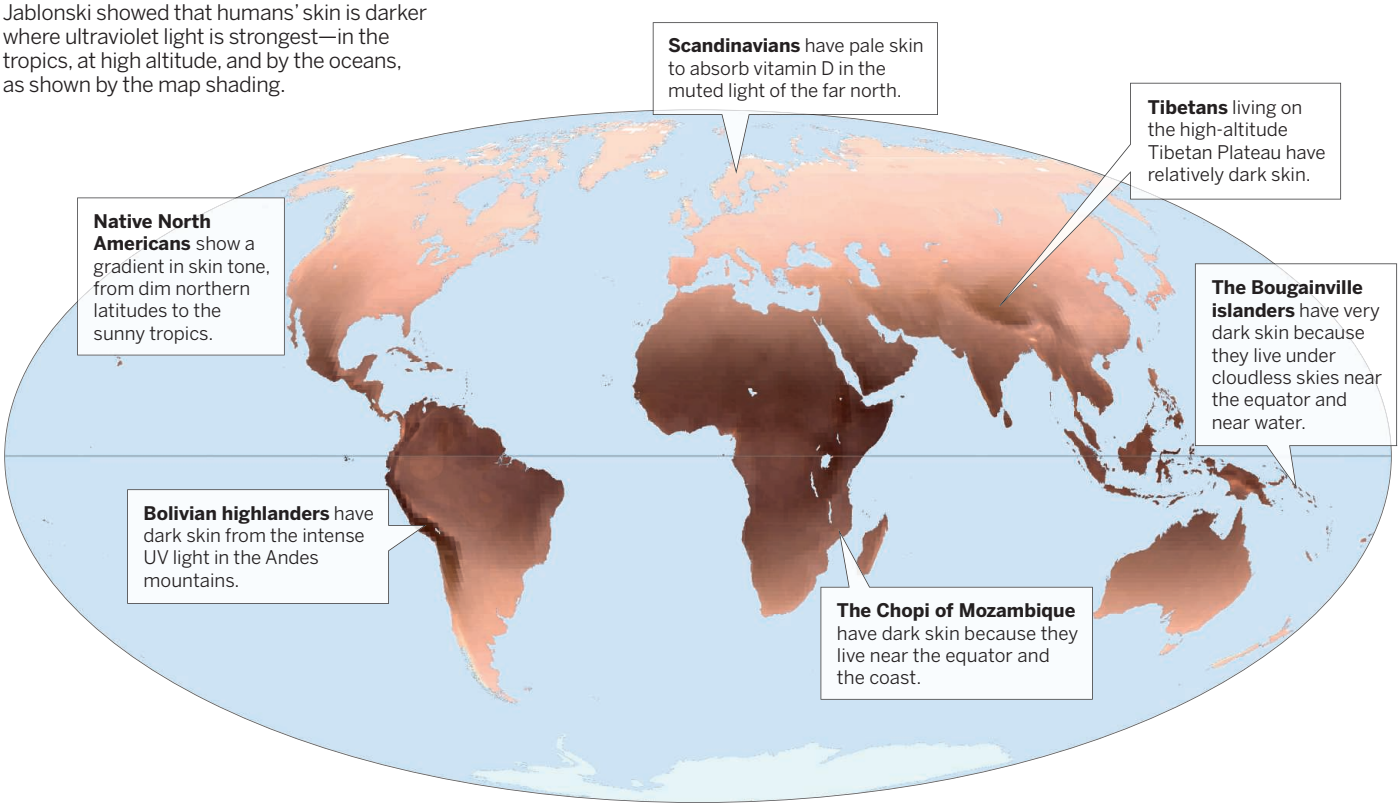
STRUNG ALONG THE MAIN highway leading to the international airport in Cape Town are the Cape Flats townships, where 600,000 people crowd into makeshift houses of tin, cardboard, and wood. These vast slums, first settled during apartheid when black Africans moved to Cape Town to find work and were forced to live in tents or huts, have improved in the last 20 years. But they are still dangerous, with rampant crime and diseases such as tuberculosis (TB) and AIDS. "This is not a garden spot," Jablonski says. But it has provided a natural laboratory to test portions of her hypotheses.

In the winter, sandstorms blast the flimsy houses and streets sometimes flood, forcing people inside day and night. The lack of sunshine may explain an additional health hazard facing dark-skinned people in the townships: They have too little vitamin D in their blood, according to an 8-year study of 370 township dwellers. In the study, published in 2011 in the *Proceedings of the National Academy of Sciences*, vitamin D dropped by a mean of 46% in 63% of participants during the winter months of July to September. Then, from October to December, just after these seasonal declines in vitamin D, TB surged citywide, according to study leaders Adrian Martineau and infectious disease physician Robert Wilkinson, both of the MRC National Institute for Medical Research in London. South Africa is third in the world for TB cases, and Cape Town has the nation's highest incidence.

Published by AAAS

Sunshine and skin color

Jablonski showed that humans' skin is darker where ultraviolet light is strongest—in the tropics, at high altitude, and by the oceans, as shown by the map shading.



Lower vitamin D weakens the immune response to the mycobacterium that causes TB, Wilkinson explains. Earlier this year, Harvard's Bloom and his colleagues identified a new molecular pathway in the immune response that requires vitamin D to kill tuberculosis (http://scim.ag/Montoyaetal). Wilkinson believes the seasonal drop in vitamin D is a "significant factor" in TB among black Africans, as it is in Europeans.

As in most major cities around the world, Cape Town is home to a spectrum of skin tones. Jablonski predicted that darker skinned township dwellers exposed to little sunlight would produce less vitamin D and get more TB and other infectious diseases than lighter skinned people in the same environments. "This is an evolutionary problem that has very high stakes for health," she says.

Her team joined Wilkinson's in 2012, and they designed a new study, now under way, to test this prediction. Khayelitsha Clinic health care workers draw blood and interview young dark-skinned and moderately pigmented Cape Flats residents about their diet, clothing, work hours, time spent indoors and outdoors, and other factors. The team also measured how much UV radiation hits the ground close to the Cape Flats.

Jablonski, now analyzing the data, predicts that seasonal fluctuations in UV light will be more important than diet for vitamin D levels, because few people in the study supplement their diet with vitamin D–rich foods, such as oily fish. Surprisingly, many doctors in South Africa have not realized how important it is for dark-skinned people to get enough vitamin D, she says.

She also predicts that the team may end up recommending that South Africa fortify dairy foods with vitamin D, as is done in the United States, or make cheap vitamin D supplements available. (Some researchers question how well supplements work, however [*Science*, 21 September 2012, p. 1476].)

> ***"Often we're unaware that we're living in environments to which our skin is inherently poorly adapted. … This is an enormous game changer for health."***
>
> **Nina Jablonski**, Pennsylvania State University

Back in the United States, "overwhelming" data now show that African-Americans are more likely to be deficient in vitamin D than white people and that the health consequences can hit pregnant women particularly hard, says the University of Pittsburgh's Bodnar. In a large analysis of vitamin D levels in 50,000 pregnant women in the United States in the 1960s, she found that low vitamin D was common in blacks—but not whites—and was associated with preterm birth.

Such information needs to be spread more widely, Jablonski says. She and Harvard historian Henry Louis Gates Jr. have teamed up to help teach middle school kids about evolution; as part of the project, they are spreading the message that dark-skinned African-Americans are still paying a health price for being moved to North America. That's true even for those at the highest levels. As Jablonski noted in her TED talk, President Obama, with his "moderately pigmented skin," has a desk job indoors. "So let's all wish for his great health and his awareness of his own skin pigmentation." ■

MAP: ADAPTED FROM GEORGE CHAPLIN

Published by AAAS

REVIEW

Mammalian skin cell biology: At the interface between laboratory and clinic

Fiona M. Watt*

Mammalian skin research represents the convergence of three complementary disciplines: cell biology, mouse genetics, and dermatology. The skin provides a paradigm for current research in cell adhesion, inflammation, and tissue stem cells. Here, I discuss recent insights into the cell biology of skin. Single-cell analysis has revealed that human epidermal stem cells are heterogeneous and differentiate in response to multiple extrinsic signals. Live-cell imaging, optogenetics, and cell ablation experiments show skin cells to be remarkably dynamic. High-throughput, genome-wide approaches have yielded unprecedented insights into the circuitry that controls epidermal stem cell fate. Last, integrative biological analysis of human skin disorders has revealed unexpected functions for elements of the skin that were previously considered purely structural.

Skin research has made spectacular progress over the past 30 years (Box 1). In 1975, the ability to culture cells efficiently from biopsies of human epidermis, the outer covering of the skin, was reported (*1*). This quickly opened up opportunities to expand cell sheets for transplantation onto burn victims, to characterize genes that are differentially expressed in different epidermal layers, and to analyze tissue assembly in cell culture (*2*). Cloning the genes that encode epidermal keratins led to a second major advance: Gene promoters could drive transgene expression in specific layers of the skin and, subsequently, perform targeted gene knockouts and lineage analysis in mice (*3*). Even with the power of the in vitro and in vivo laboratory-based approaches, skin research would not be in its current vibrant state had it not been for the major contributions of the dermatology community. Eminent clinicians in the early 1980s taught scientists the fundamentals of skin structure and function and called attention to rare skin conditions, such as Epidermolysis bullosa, that at the time were of unknown etiology. As a result, the molecular basis of many human genetic skin disorders was quickly determined and validated in mouse models, laying the foundation for ongoing efforts to treat them by means of gene correction and other approaches (*4*).

Here, I highlight recent advances in our understanding of skin cell biology. A variety of technologies are illuminating cellular heterogeneity, the extrinsic and intrinsic controls that regulate cell behavior and tissue architecture, and the surprising role of structural elements of the epidermis in regulating skin function.

Skin architecture

Mammalian skin forms the outer covering of the body and consists of two major layers (Fig. 1) (*5*). The upper layer is an epithelium called the epidermis, and the lower layer is a connective tissue called the dermis. The epidermis comprises a multilayered epithelium, the interfollicular epidermis (IFE), and associated (adnexal) structures—hair follicles, sebaceous glands, and sweat glands. The distribution of adnexal structures differs in different body sites, as does the thickness of the IFE.

Key functions of the epidermis are the formation of a protective interface with the external environment, lubrication of the skin with lipids, and thermoregulation by hairs and sweat. Each function depends on nondividing, terminally differentiated keratinocytes that die and are shed from the body. These differentiated cells are replenished through a variety of stem cell populations in different epidermal locations (Fig. 1) (*6*). Under steady-state conditions, each stem cell compartment produces a subset of differentiated epidermal cells, but when the cells are transplanted or the skin is damaged or otherwise manipulated experimentally, most stem cells can contribute to the full range of differentiated epidermal lineages.

The epidermis is separated from the dermis by a basement membrane, an extracellular matrix (ECM) that is rich in type IV collagen and laminin. The main resident cell type of the dermis is the fibroblast. The dermis is organized into three layers (Fig. 1). The layer closest to the epidermis is the papillary layer, and beneath that lies the reticular layer. Fibroblast density is higher in papillary dermis, and the reticular dermis is characterized by an abundance of fibrillar collagen. The deepest dermal layer, historically termed the hypodermis, is characterized by a thick layer of white adipocytes. In addition to the three main dermal layers, there are two other mesenchymal structures in the dermis that are important for skin function. These are the dermal papilla (DP), a cluster of cells at the base of the hair follicle that control the hair follicle cycle, and the arrector pili muscle (APM), a smooth muscle that inserts into the basement membrane at a specific point

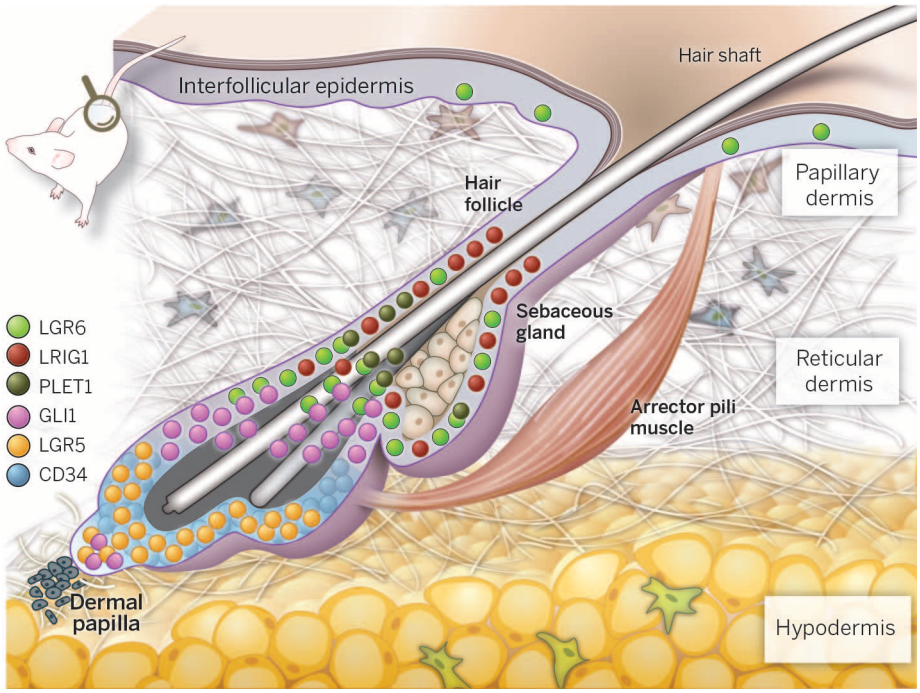


Fig. 1. Mouse back skin. Markers of different epidermal stem cell populations (LGR6, LRIG1, PLET1, GLI1, LGR5, and CD34) are shown. LGR6 and LRIG1 are expressed in the hair follicle isthmus, whereas CD34 and LGR5 are bulge markers. The three dermal layers (boxed) are the reticular dermis, papillary dermis, and hypodermis/white adipose tissue. The dermal papilla and arrector pili muscle constitute two specialized populations of dermal mesenchymal cells. The hair is shown in the resting phase of the hair growth cycle. [Redrawn from (*60*).]

King's College London Centre for Stem Cells and Regenerative Medicine, 28th Floor, Tower Wing, Guy's Hospital, Great Maze Pond, London SE1 9RT, UK.
*Corresponding author. E-mail: fiona.watt@kcl.ac.uk

in the hair follicle and, on contraction, causes the hair follicles to become erect.

Although epidermal epithelial cells (keratinocytes) and dermal fibroblasts are the most abundant cell types in the skin, there are several other key cell types that are either permanent residents of the tissue or traffic through the skin. These include the cells of the peripheral nervous system (*7*) and blood vessels, melanocytes (*8*), and cells of the innate and adaptive immune system (*9*).

Single-cell approaches to skin cell biology

Cell behavior is regulated by a combination of intrinsic and extrinsic mechanisms. Local extrinsic signals are provided by the cellular microenvironment, or niche, and include interactions with neighboring cells, secreted factors, extracellular matrix (ECM) proteins, physical parameters such as tissue stiffness, and environmental conditions such as hypoxia (*10*). The ability to isolate and culture single stem cells from human epidermis allows analysis of stem cell–niche interactions at the single-cell level (Fig. 2). One approach is to capture cells on ECM-coated micropatterned islands and direct them to adopt specific shapes (*11*). Another is to seed cells on hydrogels that differ in bulk stiffness or on composite substrates containing gold nanoparticles that change the way that ECM proteins are anchored to the substrate and thereby influence cell attachment (*12*). In both cases, activator protein 1 (AP1) factors are activated to execute the terminal differentiation program, but the signal transduction pathways are different. It remains unclear which of the alternative pathways—one dependent on serum response factor and the other on extracellular signal–regulated kinase (ERK) mitogen-activated protein kinase (MAPK)—operates in vivo, and whether other pathways—in particular, the Hippo pathway, which is mechanosensitive and active in regulating epidermal differentiation (*13*, *14*)—are also involved.

The same type of reductionist approach has provided new insights into how individual cells assemble into a multilayered epithelium. As few as 10 cells are sufficient to form a stratified epidermis, a process that requires actin polymerization and assembly of two of the major classes of epidermal intercellular adhesive junction: adherens junctions and desmosomes (*15*, *16*). Cells can assemble an epidermis even when there are discontinuities in the underlying ECM (*15*, *16*) by forming multicellular bridges held together by intercellular adhesions that are under tension (*16*). The ability of keratinocytes to form these bridges may play a role in wound healing (*16*).

There is clear evidence for extensive interactions between different types of adhesive junction and different cytoskeletal elements within the epidermis. For example, cadherin-mediated adhesions modulate forces transmitted to the ECM so that keratinocytes in a cohesive colony localize traction forces to the colony periphery (*17*) and the desmosomal plaque protein desmoplakin regulates assembly and function of gap junctions (*18*). Understanding the dynamics of these interactions has been facilitated by mathematical modeling, as in the case of the impact of actin and keratin filaments on keratinocyte cell spreading (*19*) and how epidermal stem cells self-organize within stratified cell sheets (*17*, *20*).

There has also been recent progress in modeling dermal fibroblast-niche interactions. Recent in vitro approaches have elucidated reciprocal signaling between dermal subsets and keratinocytes, such as identifying soluble factors secreted by keratinocytes that promote adipocyte differentiation and fibroblast factors that stimulate keratinocyte differentiation (*21*, *22*). In addition, the keratinocyte ECM protein nephronectin promotes differentiation of a subset of fibroblasts into APM cells in vitro (*23*). Both epidermis and dermis have been reconstituted by directed differentiation of human iPS cells (*24*), which opens up a new approach for understanding tissue organization and also for disease modeling.

To date, stem cell characterization has relied largely on enrichment of cell populations with specific markers. Single-cell global gene expression profiling provides much higher resolution and the potential to understand how much cell-to-cell variation is stochastic versus functionally important (*25*). In cultured human keratinocytes, single-cell global gene expression profiling has revealed cell-to-cell variation in the relative abundance of transcripts of two previously reported markers of human epidermal stem cells: the Notch ligand Delta-like 1 (DLL1) and the epidermal growth factor receptor antagonist LRIG1 (*26*). Cells that express high levels of DLL1 also have elevated expression of genes associated with endocytosis, integrin-mediated adhesion, and receptor tyrosine kinase signaling, and there was some evidence that expression of these genes is not independently regulated (*26*). The two cell states may be reinforced by virtue of their influence on how keratinocytes interact with the microenvironment. For example, one of the genes up-regulated in cells with high levels of DLL1 is caveolin-1, which is known to couple β1 integrin, Notch1, and receptor tyrosine kinase signaling. The desmosomal cadherin Desmoglein-2 associates with caveolin-1, an interaction that is believed to regulate proliferation (*27*).

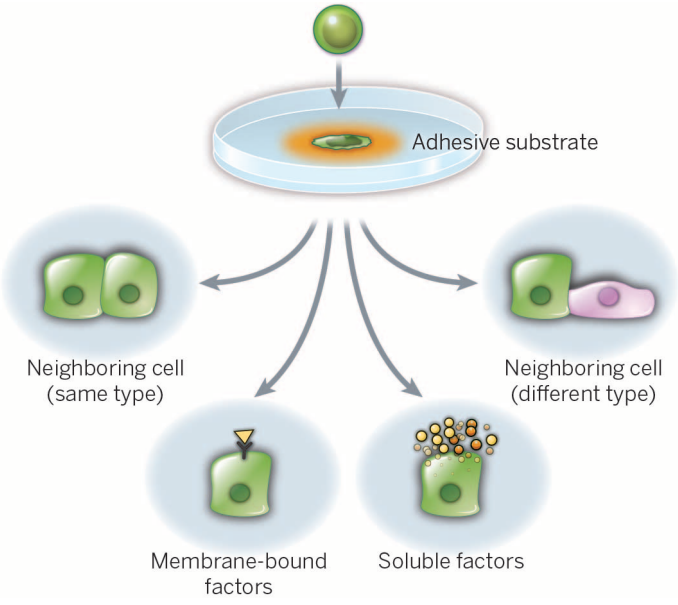


Fig. 2. Reconstructing the epidermal stem cell niche at single-cell resolution. A single stem cell (green) is shown interacting with different components of the microenvironment: the extracellular matrix supporting substrate adhesion, interactions with neighboring cells of the same or different type, intercellular adhesion and signaling molecules that can be membrane-bound, or soluble factors.

Cell behavior in the context of the intact tissue

The way epidermal stem cells behave under steady-state conditions can be quite different from how they behave after tissue damage or upon isolation and transplantation (*6*). This conclusion is based, in part, on extensive lineage tracing of the progeny of different mouse epidermal stem cell populations (Fig. 1). Most recently, lineage-tracing has also been performed in the dermis (*28*–*31*). The results indicate that the fibroblasts in different dermal regions (Fig. 1) arise from different lineages during embryonic development and can be modulated by epidermal Wnt signaling (*30*, *31*). Bone marrow–derived cells do not appear to contribute to dermal mesenchyme (*28*, *31*). Dermal fibroblast subpopulations express different genes at different stages of development (*31*).

Because skin is on the surface of the body, cell behavior can be analyzed noninvasively. Serial optical sections from the skin of anesthetized mice obtained by using two-photon laser scanning microscopy (*32*) have revealed coordinated cell movements during hair follicle growth. With laser-induced cell-ablation of fluorescently labeled dermal papilla cells, the importance of the dermal papilla for initiation of hair growth has been confirmed (*32*). Conversely, after hair follicle stem cell ablation, neighboring keratinocytes repopulate the niche, allowing hair follicle growth to proceed (*7*, *33*).

Optogenetic tools have been used to resolve a long-standing controversy about how the epidermal mechanosensory cells, called Merkel cells, communicate with nerve cells. By stimulating Merkel cells that express a light-sensitive hyperpolarizing

proton pump, it has been established that Merkel cells form a functional, excitatory connection with sensory neurons in the skin (*34*).

High-throughput/genome-wide approaches

Single-cell studies are complemented by genome-wide approaches to skin biology. Cultured human keratinocytes have previously been used to screen compound libraries for drugs that stimulate or inhibit terminal differentiation, and the same assay format has been adapted for high-throughput small interfering RNA–based genetic screens. A screen of more than 300 chromatin regulatory genes (*35*) identified a network of five chromatin factors that regulate genes involved in keratinocyte-ECM interactions and revealed how intrinsic controls of gene expression affect stem cell–niche interactions (*35*). A further application of high-throughput approaches is a screen of more than 9000 recombinant proteins for direct binding to the long noncoding RNA terminal differentiation-induced noncoding RNA (TINCR), which plays a role in regulating keratinocyte terminal differentiation (*36*). This led to identification of Staufen1 protein, which in concert with TINCR stabilizes a subset of mRNAs required for epidermal differentiation.

High-throughput approaches are also being used to knock out epidermal genes in the mouse. Ultrasound-guided in utero infection introduces fluorescently labeled lentiviral vectors into mouse embryos, resulting in efficient, selective, and stable transduction of the epidermis. This approach has been used to screen short hairpin RNA libraries for genes that confer a selective growth advantage or disadvantage on keratinocytes in embryonic and postnatal life and to identify genes that modulate epidermal responses to oncogenic H-Ras (*37*, *38*).

Whole-mount imaging of mouse tail epidermis has been used for a large-scale screen of more than 500 knockout mouse mutants via confocal microscopy (*39*). Roughly 10% of mutants had an epidermal phenotype, several of which mapped to known human genetic conditions. Some mutant genes were expressed in the skin, whereas others were not, indicating systemic effects that could not have been found by selectively targeting the epidermis.

In keeping with the observation that gene deletion can have direct or indirect effects on skin function, integrative biology approaches are being used to explore disease mechanisms in skin conditions that affect more than one cell type. For example, the benign skin condition psoriasis is characterized by epidermal hyperproliferation, disturbed differentiation and tissue architecture, and a dermal inflammatory infiltrate (*40*). By integrating transcriptomic data sets with data from biological models such as mouse knockouts and human psoriatic skin xenografts on mice, it has been possible both to identify, and validate, IL-22 as a new target in the treatment of psoriasis.

New functions for structural proteins

A key function of the interfollicular epidermis is to act as a protective interface between the body and the external environment, and it contains several architectural elements that enable it to fulfill this function (Fig. 3). The basal layer of the epidermis is anchored to the basement membrane by cell-extracellular matrix receptors, including the β1 integrins and α6β4, which are found in focal adhesions and hemidesmosomal junctions, respectively (*41*). Integrins are down-regulated with the onset of terminal differentiation, and this is accompanied by changes in intercellular adhesion, notably down-regulated expression of P-cadherin, increased expression of E-cadherin, and changes in the number and composition of desmosomal junctions (*42*). In addition, the keratin filaments change in composition with the onset of terminal differentiation (*43*). Last, a structure known as the cornified envelope replaces the plasma membrane in the outermost epidermal layers and consists of insoluble, transglutaminase–cross-linked proteins and lipids (*44*).

All of these elements of the epidermis play active roles in regulating skin function, which might not have been anticipated from their role in maintaining skin integrity. For example, integrins not only mediate adhesion to the basement membrane but also control initiation of terminal differentiation (*41*). Misexpression of integrins in the suprabasal layers of hyperproliferative epidermis is linked to up-regulation of ERK MAPK signaling, altered cancer susceptibility, and inflammation. Differentiating epidermal cells in which ERK MAPK signaling is activated can recruit cells in the underlying basal layer to become hyperproliferative and can promote wound-induced tumor formation via signaling to macrophages and γδ T cells (*45*). Suprabasal epidermal expression of α6β4 integrin is a feature of human skin squamous cell carcinomas and increases susceptibility to chemically induced tumor formation in mice. Suprabasal α6β4 integrin expression stimulates secretion of pro-inflammatory molecules such as CXCL5 and M-CSF and stimulates a protumorigenic skin microenvironment by augmenting the influx of immunosuppressive granular cells during tumor promotion (*46*).

Proteins that mediate keratinocyte intercellular adhesion also play an active role in regulating proliferation and differentiation. Intercellular adhesion and ECM adhesion are closely coupled. The desmosome protein plakophilin 2 affects cell migration by modulating focal adhesion dynamics and integrin protein expression (*47*), coupling actomyosin remodeling to desmosomal plaque assembly via RhoA (*48*). Kazrin, a cytoplasmic protein that binds the desmosomal protein periplakin, also regulates cell shape, cytoskeletal organization, and terminal differentiation via Rho-dependent and -independent mechanisms (*49*). Epidermal ablation of α-catenin, a key cytoplasmic component of adherens junctions, selectively induces apoptosis in suprabasal differentiating keratinocytes, altering ECM adhesion and growth factor signaling in the underlying basal layer (*50*). In humans, mutations in integrins and desmosome components are associated with a variety of diseases (*4*). Intriguingly, Desmoglein 1 deficiency has recently been linked to severe dermatitis, multiple allergies, and metabolic wasting in humans (*51*).

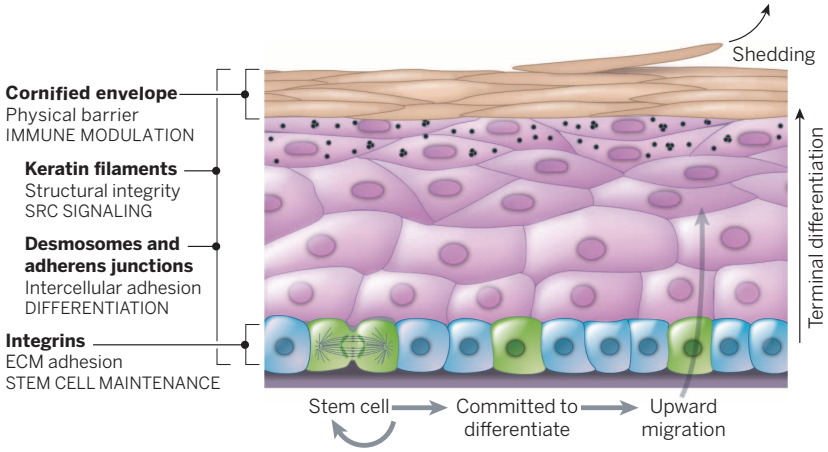


Fig. 3. Structural components of the interfollicular epidermis. Each component of human epidermis is listed, together with its structural and signaling properties. The location of each component is indicated by brackets. [Redrawn from (*41*).]

In the same way as integrins and desmosomes have functions that extend beyond cell adhesion, keratin filaments have roles in cell proliferation, apoptosis, and inflammation (*43*). For example, genetic ablation of keratin 6 in mice results in activation of Src kinase, and as a result, keratinocyte migration is stimulated (*52*). Mutations in keratins 6 and 16 underlie a skin condition called Pachyonychia congenita, and gene expression profiling has revealed coregulation of these keratins with genes involved in skin barrier maintenance and innate immunity (*53*).

Not surprisingly, mutations in structural proteins of the cornified envelope and associated structures result in a defective epidermal barrier. Mutations in the keratin filament–associated protein Filaggrin are linked to ichthyosis vulgaris (dry, flaky skin) and increased risk of atopic dermatitis in humans (*54*). Another structural protein, the transmembrane protein Tmem79, which is a component of lamellar granules, is mutated in some patients with atopic dermatitis and is

Box 1. Timeline of some of the advances in skin cell biology.

Year (reference)*	Discovery	Technology
1970 (*31*)	Reconstitution of skin from disaggregated cells	Chamber implanted onto back of mouse
1975 (*1*)	Clonal growth of human epidermal cells in culture	Keratinocyte culture on feeder layer
1984 (*2*)	Autologous sheets of keratinocytes treat large burn wounds	Cell expansion under good manufacturing practices conditions
1988 (*11*)	Directed differentiation of single keratinocytes	Microfabrication technology
1989 (*3*)	Promoters to drive gene expression in specific epidermal layers	Transgenesis
1990 (*60*)	Stem cells in the hair follicle bulge	DNA label–retaining cells
1991 (*4*)	Keratin mutations in Epidermolysis bullosa	Mouse knockouts; human genomics
1993 (*26*)	Markers of human epidermal stem cells	Flow cytometry
1998 (*60*)	Wnt pathway activation in skin tumors	Transgenics; human genomics
2006 (*54*)	Humans lacking filaggrin predisposed to atopic dermatitis	Human genomics
2009 (*60*)	Multiple stem cell populations in mouse epidermis	Lineage-tracing
2010 (*37*)	Genome-wide knockdown of epidermal gene expression	In utero lentiviral knockdown

*Where the original reference is not cited, the more recent reference contains the relevant information.

linked to defective stratum corneum formation (*55*). Recent studies indicate a link between the epidermal barrier and skin cancer. Studies in a mouse model of atopic dermatitis, in which three epidermal barrier proteins have been deleted—envoplakin, periplakin, and involucrin—show a high resistance to developing benign tumors (*56*). The mechanism is believed to involve at least two elements. One is a reduction in the transit time of keratinocytes through the epidermis, which has previously been shown to be tumor-suppressive in oncogene-driven skin carcinogenesis (*57*). The second is an exacerbated inflammatory response to the phorbol ester 12-*O*-tetradecanoylphorbol-13-acetate (TPA) as a result of which keratinocytes release high levels of chemokines and T helper 2 (T_H2)–T_H17 cytokines, including thymic stromal lymphopoietin, which has previously been shown to be tumor-suppressive in skin (*58*, *59*).

Thus, terminally differentiated cells within the epidermis play an ongoing role in regulating cell behavior and act via communication with stem cells in the basal layer, as well as other skin cell types, particularly cells of the immune system. In the case of epidermal tumor formation, these interactions can either be tumor-promoting or tumor-protective, depending on the context.

Conclusion

Skin cell research benefits from the integration of complementary technologies and disciplines. As we learn ever more about the cell biology of the tissue, we are gaining a wider appreciation about how skin function is regulated and how it may be possible to intervene to treat a variety of skin conditions.

Future directions

Future research in skin biology will see an increasing emphasis on holistic approaches, combining in vitro and in vivo data and data from mouse models and clinical material. There will be increasing use of computational biology to interrogate existing publicly available databases, such as genome-wide chromatin immunoprecipitation–sequencing and gene expression data sets, to validate and extend conclusions from individual screens (*35*). Second, by collating information about phenotypes in multiple tissues for single-gene knockouts, hypothesis building can be initiated without the need to generate mouse models in-house (*39*). There is every reason to expect that the next 30 years of skin cell biology will be just as exciting as the past 30 years.

REFERENCES AND NOTES

1. J. G. Rheinwatd, H. Green, *Cell* **6**, 331–343 (1975).
2. H. Green, *BioEssays* **30**, 897–903 (2008).
3. C. Byrne, M. Tainsky, E. Fuchs, *Development* **120**, 2369–2383 (1994).
4. J. Uitto, A. M. Christiano, W. H. McLean, J. A. McGrath, *J. Invest. Dermatol.* **132**, 820–828 (2012).
5. F. M. Watt, H. Fujiwara, *Cold Spring Harb. Perspect. Biol.* **3**, a005124 (2011).
6. T. Schepeler, M. E. Page, K. B. Jensen, *Development* **141**, 2559–2567 (2014).
7. A. Zimmerman, L. Bai, D. D. Ginty, *Science* **346**, 950 (2014).
8. J. A. Lo, D. E. Fisher, *Science* **346**, 945 (2014).
9. Y. Belkaid, J. A. Segre, *Science* **346**, 954 (2014).
10. S. W. Lane, D. A. Williams, F. M. Watt, *Nat. Biotechnol.* **32**, 795–803 (2014).
11. J. T. Connelly *et al.*, *Nat. Cell Biol.* **12**, 711–718 (2010).
12. B. Trappmann *et al.*, *Nat. Mater.* **11**, 642–649 (2012).
13. G. Halder, S. Dupont, S. Piccolo, *Nat. Rev. Mol. Cell Biol.* **13**, 591–600 (2012).
14. M. Aragona *et al.*, *Cell* **154**, 1047–1059 (2013).
15. J. E. Gautrot *et al.*, *Biomaterials* **33**, 5221–5229 (2012).
16. S. R. Vedula *et al.*, *Nat. Mater.* **13**, 87–96 (2014).
17. A. F. Mertz *et al.*, *Proc. Natl. Acad. Sci. U.S.A.* **110**, 842–847 (2013).
18. D. M. Patel, A. D. Dubash, G. Kreitzer, K. J. Green, *J. Cell Biol.* **206**, 779–797 (2014).
19. J. S. Kim, C. H. Lee, B. Y. Su, P. A. Coulombe, *Biophys. J.* **103**, 1828–1838 (2012).
20. A. M. Klein, V. Nikolaidou-Neokosmidou, D. P. Doupé, P. H. Jones, B. D. Simons, *J. R. Soc. Interface* **8**, 1815–1824 (2011).
21. G. Donati *et al.*, *Proc. Natl. Acad. Sci. U.S.A.* **111**, E1501–E1509 (2014).
22. M. Schumacher *et al.*, *J. Invest. Dermatol.* **134**, 1332–1341 (2014).
23. H. Fujiwara *et al.*, *Cell* **144**, 577–589 (2011).
24. M. Itoh *et al.*, *PLOS One* **8**, e77673 (2013).
25. A. C. Oates, *Development* **138**, 601–607 (2011).
26. D. W. M. Tan *et al.*, *Development* **140**, 1433–1444 (2013).
27. D. Brennan *et al.*, *Oncogene* **31**, 1636–1648 (2012).
28. Y. Rinkevich, P. Lindau, H. Ueno, M. T. Longaker, I. L. Weissman, *Nature* **476**, 409–413 (2011).
29. B. A. Schmidt, V. Horsley, *Development* **140**, 1517–1527 (2013).
30. M. Takeo *et al.*, *Nature* **499**, 228–232 (2013).
31. R. R. Driskell *et al.*, *Nature* **504**, 277–281 (2013).
32. P. Rompolas *et al.*, *Nature* **487**, 496–499 (2012).
33. P. Rompolas, K. R. Mesa, V. Greco, *Nature* **502**, 513–518 (2013).
34. S. Maksimovic *et al.*, *Nature* **509**, 617–621 (2014).
35. K. W. Mulder *et al.*, *Nat. Cell Biol.* **14**, 753–763 (2012).
36. M. Kretz *et al.*, *Nature* **493**, 231–235 (2013).
37. S. Beronja, G. Livshits, S. Williams, E. Fuchs, *Nat. Med.* **16**, 821–827 (2010).
38. S. Beronja *et al.*, *Nature* **501**, 185–190 (2013).
39. K. Liakath-Ali *et al.*, *Nat. Commun.* **5**, 3540 (2014).
40. G. K. Perera *et al.*, *Sci. Transl. Med.* **6**, 223ra22 (2014).
41. S. M. Janes, F. M. Watt, *Nat. Rev. Cancer* **6**, 175–183 (2006).
42. O. Nekrasova, K. J. Green, *Trends Cell Biol.* **23**, 537–546 (2013).
43. X. Pan, R. P. Hobbs, P. A. Coulombe, *Curr. Opin. Cell Biol.* **25**, 47–56 (2013).
44. E. Candi, R. Schmidt, G. Melino, *Nat. Rev. Mol. Cell Biol.* **6**, 328–340 (2005).
45. E. N. Arwert *et al.*, *Proc. Natl. Acad. Sci. U.S.A.* **107**, 19903–19908 (2010).
46. S. W. Maalouf, S. Theivakumar, D. M. Owens, *J. Dermatol. Sci.* **66**, 108–118 (2012).
47. J. L. Koetsier, E. V. Amargo, V. Todorović, K. J. Green, L. M. Godsel, *J. Invest. Dermatol.* **134**, 112–122 (2014).
48. L. M. Godsel *et al.*, *Mol. Biol. Cell* **21**, 2844–2859 (2010).
49. L. M. Sevilla, R. Nachat, K. R. Groot, F. M. Watt, *J. Cell Sci.* **121**, 3561–3569 (2008).
50. G. Livshits, A. Kobielak, E. Fuchs, *Proc. Natl. Acad. Sci. U.S.A.* **109**, 4886–4891 (2012).
51. L. Samuelov *et al.*, *Nat. Genet.* **45**, 1244–1248 (2013).
52. J. D. Rotty, P. A. Coulombe, *J. Cell Biol.* **197**, 381–389 (2012).
53. J. C. Lessard *et al.*, *Proc. Natl. Acad. Sci. U.S.A.* **110**, 19537–19542 (2013).
54. S. J. Brown, W. H. McLean, *J. Invest. Dermatol.* **132**, 751–762 (2012).
55. T. Sasaki *et al.*, *J. Allergy Clin. Immunol.* **132**, 1111–1120.e4 (2013).
56. S. Cipolat, E. Hoste, K. Natsuga, S. R. Quist, F. M. Watt. *eLife* **2014**, 3e01888 (2014).
57. J. Guinea-Viniegra *et al.*, *J. Clin. Invest.* **122**, 2898–2910 (2012).
58. S. Demehri *et al.*, *Cancer Cell* **22**, 494–505 (2012).
59. M. Di Piazza, C. S. Nowell, U. Koch, A. D. Durham, F. Radtke, *Cancer Cell* **22**, 479–493 (2012).
60. K. Kretzschmar, F. M. Watt, *Cold Spring Harb. Perspect. Med.* **4**, a013631 (2014).

ACKNOWLEDGMENTS

I am most grateful to the Medical Research Council and the Wellcome Trust for funding, and to all members of my laboratory, collaborators, and colleagues for their input.

10.1126/science.1253734

REVIEW

Advances in skin grafting and treatment of cutaneous wounds

Bryan K. Sun,[1] Zurab Siprashvili,[1] Paul A. Khavari[1,2]*

The ability of the skin to repair itself after injury is vital to human survival and is disrupted in a spectrum of disorders. The process of cutaneous wound healing is complex, requiring a coordinated response by immune cells, hematopoietic cells, and resident cells of the skin. We review the classic paradigms of wound healing and evaluate how recent discoveries have enriched our understanding of this process. We evaluate current and experimental approaches to treating cutaneous wounds, with an emphasis on cell-based therapies and skin transplantation.

Protection and renewal are among the major functions of epithelial tissues, the sheets of cells that line the surfaces and cavities of the body. The skin, as the body's external epithelium, sustains and repairs injuries throughout a lifetime. This vital role is affected by a wide variety of factors that influence skin wounding and the speed and quality of healing (Table 1). These factors include a number of common diseases and medications, underscoring the broad relevance of cutaneous wound healing to medicine, public health, and the global burden of disease (*1*).

Surgical incisions, thermal burns, and chronic ulcers are among the conditions in which wound healing plays a critical role. More than 70 million surgical procedures are performed in the United States every year (*2*), with more than one-third resulting in hypertrophic scarring or keloid formation. Burn injuries affect >11 million people worldwide annually (*3*). The time to burn wound closure is closely correlated with susceptibility to infection, pain duration, length of hospital stay, and incidence of scarring (*4*). In addition to acute wounds, there has been a steady rise in chronic skin wounds such as pressure ulcers and diabetic foot ulcers, which now affect more than 1% of all people during their lifetime (*5*). The prevalence of diabetes, obesity, and vascular disease in an aging population is fueling a surge in chronic skin wounds, which affect >6 million people in the United States alone at a cost of >$25 billion per year (*2*). Advances in understanding the molecular and cellular basis of cutaneous wound healing will be important for improved wound therapy and prevention.

Enduring paradigms of cutaneous wound healing

Cutaneous wound healing is classically divided into four overlapping stages: hemostasis, inflammation, proliferation, and remodeling. Each stage is characterized by key molecular, cellular, and physiologic events, which are orchestrated in large part by signaling among hematopoietic, immunologic, and resident skin cells. These stages have been reviewed in detail (*6*) and are summarized in Fig. 1.

Immediately after skin injury, multiple physiologic responses are triggered to stop blood loss. Local vascular smooth muscle cells constrict vessels to reduce blood flow. Platelets and coagulation cascade factors form a hemostatic fibrin clot, which serves as a scaffold for the migration of cells, including leukocytes, keratinocytes, and fibroblasts, into the wound (*7*). The inflammatory stage initiates within hours after injury and is fueled by platelet-derived mediators, bacterial by-products, and secreted chemoattractants. Neutrophils infiltrate the injury site first, killing bacteria and degrading damaged matrix proteins (*8*). Monocytes arrive within 24 hours and transform into macrophages to kill microbes, remove tissue debris, destroy remaining neutrophils, and pave the way for angiogenesis and tissue granulation (*9*).

Macrophages also assist in the transition to the proliferation stage, a process whereby newly produced cells fill the wound defect, by releasing a host of growth factors and chemokines including platelet-derived growth factor (PDGF), fibroblast growth factors (FGFs), vascular endothelial growth factor (VEGF), and transforming growth factor–α and –β (TGFα and TGFβ), which induce cell migration, cell proliferation, and matrix formation (*10*). Stem cell reservoirs in the hair follicle bulge, isthmus, and interfollicular epidermis release keratinocytes, which proliferate and migrate to achieve wound coverage, then undergo stratification and differentiation to rebuild the epidermal barrier (*11*, *12*). In concert with epidermal repair, angiogenesis begins, stimulated by multiple growth factors including VEGF and FGF-2. The admixture of newly formed blood vessels with fibroblasts, macrophages, and matrix proteins forms "granulation tissue," the soft, pink material that appears at the base of a healing wound. Toward the end of the proliferative stage, fibroblasts differentiate into actin-rich, contractile myofibroblasts (*13*), which pull together the wound edges.

The remodeling phase involves a transition of the dermis from type III to type I collagen predominance, in concert with removal of cells from earlier stages. Collagen remodeling involves matrix metalloproteinases (MMPs) and altered collagen synthesis to produce a scar (*14*). The tensile strength of wounded skin increases during this phase, regaining ~40% of its original strength at 1 month and ~70% by 1 year (*15*). Failure to initiate, terminate, or regulate any particular stage results in pathologic wound healing and manifests in cutaneous entities such as pyogenic granulomas (overgrowth of granulation tissue), hypertrophic scars and keloids (excessive fibrotic response), or chronic ulcers (prolonged inflammation and inability to re-epithelialize).

Evolving concepts in wound healing

Recent discoveries have expanded our understanding of how wound healing stages are regulated. Studies in zebrafish, *Xenopus*, and *Drosophila* reveal that the immediate aftermath of tissue injury results in a burst of damage response signals that are critical to activation of the repair process (*16*), including a hydrogen peroxide gradient that is formed within minutes after injury, which is essential for recruitment of immune cells to the wound (*17*–*19*). In *Drosophila*, the generation of hydrogen peroxide is dependent

Wound-specific variables	Systemic variables	Medications and exposures	Diseases and conditions
Body site	Nutrition	Cancer chemotherapeutic agents	Diabetes
Infection	Age	Nonsteroidal anti inflammatory agents	Autoimmune diseases
Vascular supply	Sex	Glucocorticoids	Venous stasis
Oxygenation	Psychological stress	Radiation therapy	Predisposition to keloids
Mechanical stress	Immobility	Smoking	Some genetic skin diseases
Desiccation		Alcohol and recreational drugs	Immunocompromised state (AIDS, cancer)
Edema			Obesity, vasculitis, neuropathy, some infectious diseases

Table 1. Factors that affect wound healing.

[1]Program in Epithelial Biology, Stanford University, Stanford, CA 94305, USA. [2]Veterans Affairs Palo Alto Healthcare System, Palo Alto, CA 94304, USA.
*Corresponding author. E-mail: khavari@stanford.edu

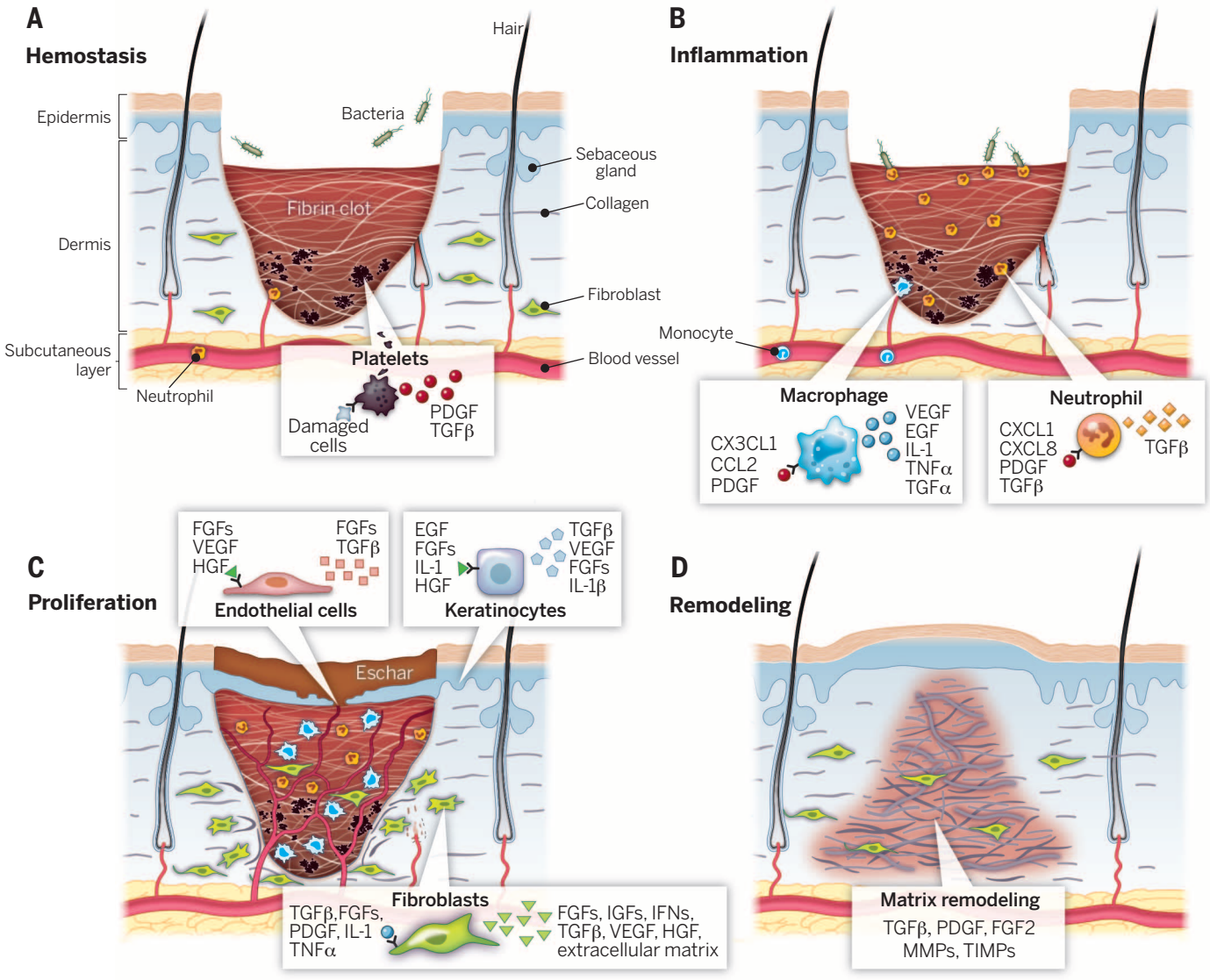


Fig. 1. Stages of wound healing. Wound healing is classically divided into four stages: (**A**) hemostasis, (**B**) inflammation, (**C**) proliferation, and (**D**) remodeling. Each stage is characterized by key molecular and cellular events and is coordinated by a host of secreted factors that are recognized and released by the cells of the wounding response. A representative subset of major factors are depicted. PDGF, platelet-derived growth factor; TGF, transforming growth factor; FGFs, fibroblast growth factors; IL-1, interleukin-1; TNF, tumor necrosis factor; KGF, keratinocyte growth factor; IGF, insulin-like growth factor; IFN, interferon; VEGF, vascular endothelial growth factor; HGF, hepatocyte growth factor; MMP, matrix metalloproteinase; TIMP, tissue inhibitor of metalloproteinase.

on a burst of calcium that is induced upon wounding (*18*). These findings establish calcium and hydrogen peroxide as the earliest known wound response signals.

The downstream effects of other early damage response signals have been described as well. In *Caenorhabditis elegans*, elevated epidermal calcium concentration produced upon injury fosters actin polymerization and wound contraction (*20*). In mice, apoptotic wound keratinocytes upregulate prostaglandins PGH_2 and PGE_2, which stimulate progenitor cell proliferation (*21*). Together, these discoveries illustrate the multifaceted response that occurs in the first minutes after injury. They also raise the possibility that immediate response signals may serve as future targets for therapeutic intervention in the acute wound.

The relationship between inflammation and scarring has also been an active focus in wound biology. Adult human dermal wounds result in scarring that increases with progressive injury depth. However, it has long been recognized that early-stage human fetuses undergo scarless skin healing (*22*). In addition, wounds of the oral mucosa also heal with much less scarring than cutaneous wounds. One notable difference is a markedly attenuated inflammatory response in fetal and oral mucosal wounds relative to adult skin wounds (*22*, *23*), which suggests that inflammation in adult cutaneous wounds may have evolved as a compromise to combat microbial infection at the expense of scarring. Consistent with this, PU.1-null mice deficient for neutrophils and macrophages heal without scarring (*24*). The relationship between inflammatory cells and scarring, however, is complex. Ablating macrophages at different stages of mouse wound healing demonstrated that macrophages promote scarring during early stages but subsequently promote vascular proliferation and transition to tissue remodeling (*25*), which indicates that inflammatory cells play roles that depend on spatial and temporal contexts (*26*). Understanding these context-specific roles will be essential to deciphering the molecular and cellular relationship between inflammation and healing.

Although studies of the inflammatory wound healing response have tended to focus on the role of neutrophils and macrophages, recent work has identified additional contributors, including γδ T lymphocytes. Human epidermal γδ T cells secrete

soluble factors that promote leukocyte recruitment and keratinocyte proliferation after injury (*27*). In mice, dermal γδ T lymphocytes induce hair follicle neogenesis through Fgf9 release and Wnt pathway induction after wounding (*28*). This discovery has potential implications in human skin regeneration, because adnexal structures such as hair follicles are lost upon healing from deep cutaneous wounds. γδ T lymphocytes are much less abundant in human than in mouse dermis, raising the possibility that human follicular regeneration could be induced by repletion of the proper signaling factors.

Therapeutic approaches to wound healing

Improved understanding of cutaneous healing has guided more sophisticated and targeted approaches to enhancing injury repair. As a foundation to treating all wounds, optimization of controllable healing factors (Table 1) remains a central principle. This can include nutritional support, smoking cessation, blood perfusion and fluid drainage, infection clearance, and mechanical protection. Simple techniques such as maintaining a clean but moist wound environment with occlusive dressings (*29*) help to accelerate re-epithelialization and alter the inflammatory milieu to favor better healing. Mechanical support at sites of high skin tension reduces the development of hypertrophic scars and keloids (*30*). Electric stimulation has proved beneficial by establishing electric fields that guide cells to migrate into the wound (*31*).

In addition to optimizing global and environmental variables, one targeted approach involves applying growth factors to the wound to promote healing. Experimental delivery of factors such as PDGF-BB, endothelial growth factor (EGF), FGF-2, and granulocyte-macrophage colony-stimulating factor (GM-CSF) has shown promise in animal models of wounding. However, clinical efficacy of single-factor therapy in humans has been more limited, with the exception of topical PDGF-BB (becaplermin), which is FDA-approved for treatment of diabetic ulcers and improves healing in clinical trials (*32*), and topical FGF-2, approved for use in China and Japan. One challenge is that these growth factors are administered onto a protease-rich, inflamed wound environment that makes them susceptible to rapid breakdown and clearance. This problem has been addressed by embedding growth factors within an extracellular matrix (ECM), where they can reside and act physiologically. A fibronectin domain–based ECM has been used to deliver PDGF-BB and VEGF-A to a mouse diabetic wound (*33*); the presence of the matrix potentiated the effects of both growth factors on the wound and promoted wound repair. Other approaches to improve delivery include liposomal transfection, particle-mediated transfer, and viral transfer (*34*). However, because wounds and cancer share a number of features (*35*, *36*), application of mitogenic growth factors to wounds may carry some risk. The FDA placed a cancer risk warning on becaplermin in 2008, highlighting a potential drawback of direct growth factor–based therapeutics in wound healing.

The challenge to develop successful wound healing therapies reinforces the complex nature of the process itself, which involves a dynamic interplay of cell types, growth factors, cytokines, and matrix components interacting in an environment in which pH, oxygenation, temperature, and moisture all contribute to the healing wound. This complexity makes the prospect of cell- and graft-based therapies an attractive alternative approach.

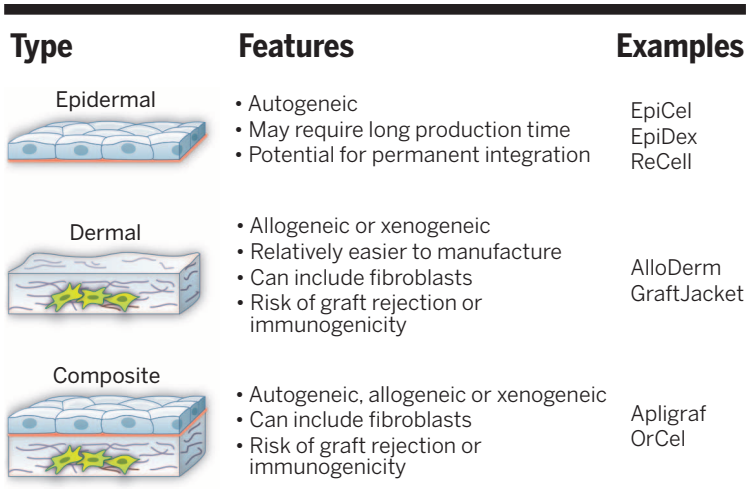


Fig. 2. Bioengineered skin substitutes. Available products can be classified into epidermal, dermal, or composite grafts. Individual products differ according to the source of the cellular material, method of delivery, and presence of supplementary substrates such as fibroblasts or matrix proteins. See table S1 for a comprehensive list of skin substitutes.

Skin grafting: A time-tested approach

The origin of skin grafting, in which skin tissue is removed from one site and transferred to another, is credited to Hindu surgeons circa 800 BCE who described methods of free skin grafts used to repair the nasal mutilations of individuals punished for theft or adultery (*37*). This practice saw a revival in European medicine during the 18th century, and the basic principles of grafting have carried into the modern era. Living skin grafts can be classified as split-thickness skin grafts (STSGs), consisting of the epidermis and part of the dermis, or full-thickness skin grafts (FTSGs), consisting of the epidermis and full-thickness dermis (*38*). STSGs can be meshed for expanded area coverage and are able to survive at graft sites with less vascularity. However, they suffer from contracture during healing. FTSGs require a better vascular bed for survival, but they contract less than STSGs and are preferred for exposed areas of the body, such as the face or neck.

A second classification of grafts is based on donor origin. Grafts from one site to another within the same individual are autografts; grafts where the donor and recipient are different individuals of the same species are allografts; and grafts from one species to another are xenografts. Autografts have capacity for full integration into the donor site, whereas allografts and xenografts undergo immunologic rejection with time and thus serve as temporary "biologic dressings." Despite this, several weeks of graft presence can be indispensable in the treatment of burns, ulcers, and difficult wounds, as these temporary biological dressings can limit infections, reduce substrate losses, and improve survival.

Innovations in surgical grafting techniques have advanced the art and science of skin grafting, but living grafts are still imperfect (*39*). Autologous grafts are inherently limited to the size of available donor sites and are insufficient for global burn injuries. Allografts and xenografts, while offering larger amounts of material, are only temporary. An ideal grafting solution would generate unlimited grafting tissue that is well tolerated by the patient, does not suffer from immune rejection, and provides all the therapeutic benefit and function of real skin.

Bioengineered skin equivalents: Are we closer to perfect skin substitutes?

The limitations of living skin grafts have prompted the development of transplantable bioengineered skin of many variations that are now approved for human clinical use (table S1). The ideal bioengineered skin substitute should be safe, have high clinical efficacy, be simple to produce, and be easy to handle and administer. These bioengineered equivalents can be classified into epidermal, dermal, or composite categories according to their structure and the degree of their functional resemblance to normal skin (Fig. 2).

Epidermal substitutes consist classically of a sheet of autologous keratinocytes, isolated from a donor and expanded in vitro. Generating epidermal sheets is time-consuming and costly, and the resulting products have a short shelf life (<24 hours). However, autologous epidermal grafts can be life-saving and have enjoyed numerous innovations at various stages of production, including improvements to cell culture techniques, differentiation techniques, and support/scaffolding assembly (*40*, *41*). Today, autologous epidermal grafts capable of covering the entire surface area of the body can be generated from a 3-cm^2 biopsy (*42*). In contrast, dermal substitute

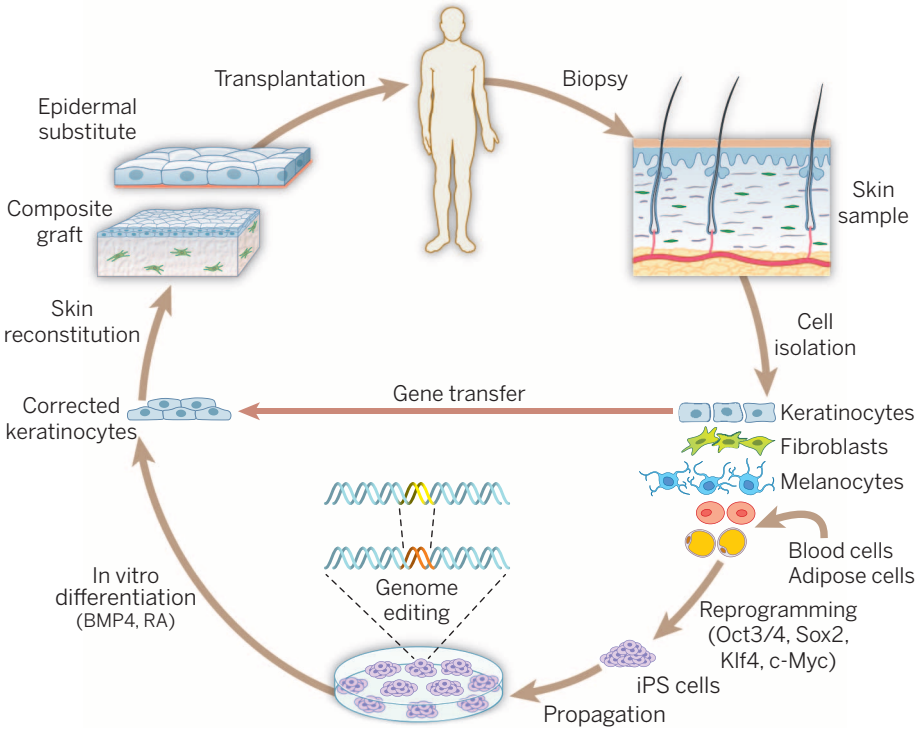


Fig. 3. Genetically engineered skin grafts. Advances in stem cell biology, genome editing capabilities, and grafting techniques have improved the efficacy and applicability of skin grafting in wound healing. Cells of different origins can be harvested from skin or other tissues and either directly altered by gene transfer or reprogrammed into induced pluripotent stem cells (iPS cells) to facilitate genomic editing on larger numbers of cells. The genetically engineered cells are reconstituted into skin tissue as epidermal or composite grafts, then transplanted onto the subject.

products are largely acellular and are prepared from allogeneic, xenogeneic, or synthetic material. Composite substitutes usually consist of allogeneic keratinocytes and fibroblasts, and have the benefit of providing growth factors, cytokines, extracellular matrix, and other elements along with a temporary wound cover. They are easier to manufacture than cell-containing substitutes and readily incorporate into wounds without rejection. However, they do not revascularize well; they have found a role in reconstructive surgery but not as dermal replacement material. Like living dermal composites, they ultimately undergo immune rejection in 3 to 4 weeks (*43*).

Cell-based skin therapies and genetically modified tissue transplantation

A wide variety of experimental approaches have been developed to incorporate stem cell–based therapies in cutaneous wound healing. Stem cells can be delivered in conjunction with skin composites or by various other methods, including direct application. For skin wounds, major efforts have focused on the use of epidermal progenitor cells, mesenchymal stroma/stem cells (MSCs), adipose tissue–derived stem cells (ASCs), and induced pluripotent stem cells (iPS cells).

The robust capacity of epidermal progenitor cells has created new opportunities to improve the performance of autologous epidermal grafts by means of genetically modified keratinocytes expressing factors that promote healing (Fig. 3). This concept closely parallels ongoing efforts using engineered grafts to treat genetic skin disorders such as epidermolysis bullosa (EB), a family of blistering disorders characterized by genetic mutations affecting epidermal-dermal adhesion, which affects 400,000 to 500,000 people worldwide (*44*). Successful skin transplantation of genetically engineered autologous keratinocyte grafts has been achieved in a patient with laminin 332–deficient non–Herlitz junctional EB (*45*). Autologous epidermal keratinocytes were transduced ex vivo with a retrovirus expressing normal laminin cDNA, and cultured epidermal grafts transplanted onto the patient's legs. More than 6 years later, the transgenic epidermis persists, is fully functional, and is virtually indistinguishable from normal epidermis (*46*). For recessive dystrophic epidermolysis bullosa (RDEB), caused by mutations in type VII collagen, a phase I clinical trial is under way using autologous epidermal sheets with wild-type collagen VII delivered by retroviral infection (*47*).

In addition to epidermal progenitors, stem cells including MSCs and ASCs have shown promise in promoting wound healing both by direct transfer onto wounds and by delivery embedded in scaffolds (*48*, *49*). Early studies indicate that both MSCs and ASCs secrete factors that attenuate inflammation, stimulate angiogenesis, and lead to faster wound closure. Both cell types have the potential for harvesting from autologous sites, and ASCs are relatively abundant and easy to obtain. Although clinical translation of MSC- or ASC-based wound therapy is still in the early stages, the potential use of these cells holds great promise.

Finally, advances in iPS cell technology allow patient- and disease-specific stem cells to be used for research and development of therapeutics, including transplantation medicine. iPS cells have been successfully derived from multiple epidermal cell types, including the fibroblasts of a patient with dyskeratosis congenita (*50*), as well as fibroblasts and keratinocytes from individuals with RDEB (*51*). Similar to human embryonic stem cells (hESCs), iPS cells can be reprogrammed to keratinocytes (*52*). Moreover, unlike somatic cells, they have a high proliferation potential, allowing genetic manipulations to be conducted. New therapeutic approaches are emerging that include (i) generation of iPS cells from different sources, including epidermal keratinocytes, fibroblasts, and melanocytes; (ii) insertion of desirable genes or correction of deleterious mutations based on homologous recombination or current genome editing tools such as the CRISPR-Cas9 system; (iii) differentiation of altered iPS cells into desired cell types, including keratinocytes; and (iv) generation of functional skin equivalents using iPS-derived keratinocytes and bioengineered dermal substitutes. A goal of regenerative medicine is to replace or regenerate whole body organs. For skin grafting, this would mean the restoration of all functional components, including hair follicles, sweat glands, and nerves. Although there is no perfect skin substitute currently available, rapid developments in understanding skin development and wound repair, together with advances in stem cell and tissue bioengineering, provide hope that such a product represents a tractable goal in the future.

REFERENCES AND NOTES

1. R. J. Hay *et al.*, *J. Invest. Dermatol.* **134**, 1527–1534 (2014).
2. C. K. Sen *et al.*, *Wound Repair Regen.* **17**, 763–771 (2009).
3. M. D. Peck, *Burns* **37**, 1087–1100 (2011).
4. K. L. Butler *et al.*, *J. Burn Care Res.* **31**, 874–881 (2010).
5. J. E. Jones, E. A. Nelson, A. Al-Hity, *Cochrane Database Syst. Rev.* **1**, CD001737 (2012).
6. G. C. Gurtner, S. Werner, Y. Barrandon, M. T. Longaker, *Nature* **453**, 314–321 (2008).
7. R. A. Clark, *Ann. N.Y. Acad. Sci.* **936**, 355–367 (2001).
8. R. Ross, G. Odland, *J. Cell Biol.* **39**, 152–168 (1968).
9. T. J. Koh, L. A. DiPietro, *Expert Rev. Mol. Med.* **13**, e23 (2011).
10. S. Werner, R. Grose, *Physiol. Rev.* **83**, 835–870 (2003).
11. M. Ito *et al.*, *Nat. Med.* **11**, 1351–1354 (2005).
12. C. Blanpain, E. Fuchs, *Science* **344**, 1242281 (2014).
13. J. J. Tomasek, G. Gabbiani, B. Hinz, C. Chaponnier, R. A. Brown, *Nat. Rev. Mol. Cell Biol.* **3**, 349–363 (2002).
14. S. E. Gill, W. C. Parks, *Int. J. Biochem. Cell Biol.* **40**, 1334–1347 (2008).

15. S. M. Levenson *et al.*, *Ann. Surg.* **161**, 293–308 (1965).
16. J. V. Cordeiro, A. Jacinto, *Nat. Rev. Mol. Cell Biol.* **14**, 249–262 (2013).
17. P. Niethammer, C. Grabher, A. T. Look, T. J. Mitchison, *Nature* **459**, 996–999 (2009).
18. W. Razzell, I. R. Evans, P. Martin, W. Wood, *Curr. Biol.* **23**, 424–429 (2013).
19. N. R. Love *et al.*, *Nat. Cell Biol.* **15**, 222–228 (2013).
20. S. Xu, A. D. Chisholm, *Curr. Biol.* **21**, 1960–1967 (2011).
21. F. Li *et al.*, *Sci. Signal.* **3**, ra13 (2010).
22. B. J. Larson, M. T. Longaker, H. P. Lorenz, *Plast. Reconstr. Surg.* **126**, 1172–1180 (2010).
23. A. M. Szpaderska, J. D. Zuckerman, L. A. DiPietro, *J. Dent. Res.* **82**, 621–626 (2003).
24. P. Martin *et al.*, *Curr. Biol.* **13**, 1122–1128 (2003).
25. T. Lucas *et al.*, *J. Immunol.* **184**, 3964–3977 (2010).
26. J. M. Daley, S. K. Brancato, A. A. Thomay, J. S. Reichner, J. E. Albina, *J. Leukoc. Biol.* **87**, 59–67 (2010).
27. W. L. Havran, J. M. Jameson, *J. Immunol.* **184**, 5423–5428 (2010).
28. D. Gay *et al.*, *Nat. Med.* **19**, 916–923 (2013).
29. W. H. Eaglstein, *Dermatol. Surg.* **27**, 175–181 (2001).
30. R. Ogawa, *Plast. Reconstr. Surg.* **125**, 557–568 (2010).
31. M. Zhao *et al.*, *Nature* **442**, 457–460 (2006).
32. D. L. Steed, *Plast. Reconstr. Surg.* **117**, 143S–149S (2006).
33. M. M. Martino *et al.*, *Sci. Transl. Med.* **3**, 100ra89 (2011).
34. L. K. Branski, G. G. Gauglitz, D. N. Herndon, M. G. Jeschke, *Burns* **35**, 171–180 (2009).
35. E. N. Arwert, E. Hoste, F. M. Watt, *Nat. Rev. Cancer* **12**, 170–180 (2012).
36. H. F. Dvorak, *N. Engl. J. Med.* **315**, 1650–1659 (1986).
37. J. S. Davis, *Ann. Surg.* **113**, 641–656 (1941).
38. A. Andreassi, R. Bilenchi, M. Biagioli, C. D'Aniello, *Clin. Dermatol.* **23**, 332–337 (2005).
39. K. S. Petkar *et al.*, *Burns* **37**, 925–929 (2011).
40. J. W. Oh, T.-C. Hsi, C. F. Guerrero-Juarez, R. Ramos, M. V. Plikus, *J. Invest. Dermatol.* **133**, e14 (2013).
41. H. Seland, C.-J. Gustafson, H. Johnson, J. P. E. Junker, G. Kratz, *Burns* **37**, 99–108 (2011).
42. D. L. Chester, D. S. Balderson, R. P. G. Papini, *J. Burn Care Rehabil.* **25**, 266–275 (2004).
43. N. Morimoto *et al.*, *J. Surg. Res.* **125**, 56–67 (2005).
44. S. Ferrari, G. Pellegrini, T. Matsui, F. Mavilio, M. De Luca, *Expert Opin. Biol. Ther.* **6**, 367–378 (2006).
45. F. Mavilio *et al.*, *Nat. Med.* **12**, 1397–1402 (2006).
46. L. De Rosa *et al.*, *Stem Cell Rep.* **2**, 1–8 (2014).
47. Z. Siprashvili *et al.*, *Hum. Gene Ther.* **21**, 1299–1310 (2010).
48. W. M. Jackson, L. J. Nesti, R. S. Tuan, *Stem Cells Transl. Med.* **1**, 44–50 (2012).
49. H. Mizuno, M. Tobita, A. C. Uysal, *Stem Cells* **30**, 804–810 (2012).
50. S. Agarwal *et al.*, *Nature* **464**, 292–296 (2010).
51. J. Tolar *et al.*, *J. Invest. Dermatol.* **131**, 848–856 (2011).
52. H. Guenou *et al.*, *Lancet* **374**, 1745–1753 (2009).

ACKNOWLEDGMENTS

Supported by U.S. Department of Veterans Affairs Office of Research and Development Merit Award BX001409 (P.A.K.), National Institute of Arthritis and Musculoskeletal and Skin Diseases (NIAMS) grants R01 AR055914 and R01 AR045192 (P.A.K.), NIAMS training grant F32 AR063508 (B.K.S.), and the Epidermolysis Bullosa Research Foundation.

SUPPLEMENTARY MATERIALS

www.sciencemag.org/content/346/6212/941/suppl/DC1
Table S1

10.1126/science.1253836

REVIEW

The melanoma revolution: From UV carcinogenesis to a new era in therapeutics

Jennifer A. Lo and David E. Fisher*

Melanoma, the deadliest form of skin cancer, is an aggressive disease that is rising in incidence. Although melanoma is a historically treatment-resistant malignancy, in recent years unprecedented breakthroughs in targeted therapies and immunotherapies have revolutionized the standard of care for patients with advanced disease. Here, we provide an overview of recent developments in our understanding of melanoma risk factors, genomics, and molecular pathogenesis and how these insights have driven advances in melanoma treatment. In addition, we review benefits and limitations of current therapies and look ahead to continued progress in melanoma prevention and therapy. Remarkable achievements in the field have already produced a paradigm shift in melanoma treatment: Metastatic melanoma, once considered incurable, can now be treated with potentially curative rather than palliative intent.

Melanoma is among the most aggressive and treatment-resistant human cancers. In 2014, an estimated 76,100 new cases and 9710 deaths are expected in the United States, with melanoma accounting for 75% of all skin cancer deaths (*1*). Although these stark numbers highlight the need for improved prevention strategies and treatments, the explosion of discovery and concrete clinical advances in the melanoma field have brought great optimism in recent years. From identification of cancer genes to successes of new drugs in clinical trials, progress in understanding melanoma is now leading the way for other malignancies.

Cells of origin: Melanocytes

Melanomas arise from malignant transformation of melanocytes, the melanin-producing cells of the skin, eye, mucosal epithelia, and meninges that are responsible for pigmentation and photoprotection. Several common subtypes of melanoma are shown in Fig. 1. Melanocytes are derived from neural crest progenitors, and their development is modulated by the receptor tyrosine kinase (RTK) c-KIT and microphthalmia-associated transcription factor (MITF) (*2*).

Melanocytes produce two main types of pigment: brown/black eumelanin and red pheomelanin. Eumelanin is the photoprotective pigment that provides ultraviolet radiation (UVR) attenuation. Pigment synthesis is stimulated by binding of α-melanocyte–stimulating hormone (α-MSH) to melanocortin 1 receptor (MC1R) on melanocytes (Fig. 2). MC1R activates cyclic adenosine monophosphate (cAMP) production and cAMP response element–binding protein (CREB)–mediated transcriptional activation of MITF. MITF in turn promotes transcription of pigment synthesis genes and melanin production. MC1R is a major determinant of pigmentation, and loss-of-function polymorphisms result in impaired eumelanin production, with the most severe loss-of-function alleles producing red hair and fair skin (*2*). In addition to basal pigmentation, acquired pigmentation can be elicited by stimuli such as UVR (Fig. 4) (*3*).

Cutaneous Biology Research Center, Department of Dermatology and MGH Cancer Center, Massachusetts General Hospital, Harvard Medical School, Boston, MA 02114, USA.
***Corresponding author. E-mail: dfisher3@partners.org**

Melanoma risk factors

The strongest melanoma risk factors are family history, multiple moles, fair skin, immunosuppression, and UVR. Epidemiologic studies have implicated intense intermittent UVR exposure and severe sunburns during childhood in conferring the highest risk (*4*). Indoor artificial tanning devices that deliver UVR to the skin have also been linked to dose-dependent melanoma risk (*5*). UVR has multiple effects on the skin, including genetic changes, induction of reactive oxygen species (ROS), alterations in cutaneous immune function, and production of growth factors [reviewed in (*6*)]. Recent mouse model studies have shown that UVR induces inflammatory responses involving macrophages and neutrophils that can promote melanocytic cell survival, immunoevasion, and perivascular invasion (*7*, *8*).

The red hair/fair skin phenotype, characterized by fair skin, freckling, and inability to tan, is associated with the highest melanoma risk of all pigmentation phototypes (*9*), an observation traditionally attributed to reduced UVR protection. However, a recent study demonstrated that pheomelanin synthesis contributes to melanomagenesis through a UVR-independent mechanism thought to involve elevated ROS (*10*). Thus, high melanoma susceptibility in red hair/fair skin individuals is likely attributable to intrinsic carcinogenic effects of pheomelanin synthesis as well as UVR.

The mutational landscape of melanoma

Over the past two decades, there have been revolutionary changes in the methodologies used

to characterize melanoma genomes. Early insights came from familial melanoma and genome-wide association studies that identified melanoma risk loci such as cyclin-dependent kinase inhibitor 2A (CDKN2A) (*11*) and pigment-related genes including MC1R and tyrosinase (*12*). In a 2002 genome-wide screen, BRAF point mutations were discovered at high frequency in melanomas and lower frequencies in other cancers, such as those of the thyroid and colon. Most oncogenic BRAF mutations cause valine-to–glutamic acid substitutions at codon 600 (V600E) that constitutively activate the kinase domain (*13*). In recent years, next-generation sequencing of melanomas has become increasingly accessible through declining costs and improving technologies and informatics platforms. Since the first melanoma genome was published in 2010 (*14*), sequencing studies have identified numerous novel melanoma genes involved in the regulation of mitogen-activated protein kinase (MAPK) and other signaling pathways (*15*–*17*).

Molecular heterogeneity and high mutational loads present major challenges in comprehensive analyses of melanoma genomes. Next-generation sequencing has confirmed that rates of somatic base mutation in melanoma are among the highest of any cancer type. This elevated mutation rate reduces the statistical power to detect true driver mutations, and creating a complete catalog of melanoma oncogenes and tumor suppressors mutated in at least 2% of patients will require an estimated 5300 melanoma samples (*18*).

The high mutation rate in melanoma is largely attributed to mutagenic effects of UVR. Cytosines in UVB-generated cyclobutane pyrimidine dimers are prone to hydrolytic deamination that can result in C-to-T mutations at the 3′ base of a pyrimidine. Such UVB signature mutations account for most of the elevated mutational burden in melanoma (*14*). However, not all C-to-T events are products of UVB damage. A recent computational study of 30 cancer types identified three mutational signatures characterized by C-to-T transitions in melanoma, each attributable to a distinct source: UVR, age, or chemotherapeutics (*19*). Although UVB signature mutations dominate melanoma genomes, it is important not to overlook the contribution of UVB-independent processes. The other classic UV signature mutation is G-to-T transversion resulting from UVA-associated oxidative damage. UVA light is absorbed by endogenous photosensitizers like pheomelanin, leading to ROS amplification and subsequent ROS-induced DNA lesions. The best studied of these is 8-oxoguanine, which mispairs with adenosine and produces G-to-T mutations (*20*).

"Melanomas arise from malignant transformation of melanocytes, the melanin-producing cells of the skin, eye, mucosal epithelia, and meninges that are responsible for pigmentation and photoprotection."

Despite progress in understanding mechanisms of UVR-induced DNA damage, the scope of biologically meaningful UVR-associated mutations remained elusive until the advent of next-generation sequencing. A 2012 analysis of whole-exome sequences found that 46% and 9% of melanoma driver mutations can be attributed to C-to-T or G-to-T mutations, respectively (*16*). Most of these occur in tumor suppressor genes, including CDKN2A, PTEN, and TP53. In rarer instances, recurrent UVR signature mutations are found at hot spots in oncogenes such as ras-related C3 botulinum toxin substrate 1 (RAC1) and the telomerase reverse transcriptase (TERT) promoter (*16*, *17*, *21*). Consistent with the human data, UVR accelerates melanomagenesis and produces UVB signature mutations in a $BRAF^{V600E}$-mutant melanoma mouse model (*22*).

The most common mutation in melanoma, $BRAF^{V600E}$, is enriched in melanomas of sun-exposed versus sun-shielded skin. This prompted early speculation that BRAF mutation might be linked to UVR. Indeed, the rarer $BRAF^{V600K}$ mutation is associated with older age and chronic sun damage and may be attributable to UVB-induced mutagenesis (*23*). However, most oncogenic BRAF and NRAS mutations are not UVR signature mutations. Moreover, $BRAF^{V600E}$ melanomas are less common in chronically versus intermittently sun-exposed areas (*24*). These observations suggest that, although UVR accounts for many driver mutations, other mutagenic mechanisms are likely important in melanoma development. For instance, ROS are known to produce a host of oxidative DNA base lesions not limited to 8-oxoguanine. Although sunscreen has shown significant protection against melanoma (*25*), the protection it affords may be incomplete, particularly given evidence of UVR-independent melanomagenesis (*10*). Elucidating UVR-independent mechanisms of mutagenesis has potential implications for improving melanoma prevention.

Common genetic alterations in melanoma

Signaling molecules

The most common genetic targets in melanoma, BRAF and NRAS, are mutated in two-thirds of melanomas and result in MAPK pathway hyperactivation (*13*, *26*). Other recurrent genetic alterations include amplification of AKT3 and loss of PTEN by epigenetic silencing or deletion (*27*, *28*). Both events lead to constitutive phosphatidylinositol 3-kinase (PI3K) signaling (Fig. 2).

In some melanomas, MAPK and PI3K pathway dysregulation results from overexpression or hyperactivation of growth factor receptors such as c-KIT, MET, and epidermal growth factor receptor (EGFR) (*29*–*31*) or inactivating mutations in neurofibromin 1 (NF1), a negative regulator of Ras (*32*). c-KIT–activating mutations and amplifications are most common in melanomas arising on hairless (acral), mucosal, and chronically sun-damaged skin (*31*). The dominant genetic lesions in ocular (uveal) melanomas are activating mutations in GNAQ and GNA11, two G protein α subunits involved in MAPK signaling (*33*).

Cell cycle and proliferation regulators

The CDKN2A locus encodes two tumor suppressors, $p14^{ARF}$ and $p16^{INK4a}$, which regulate the

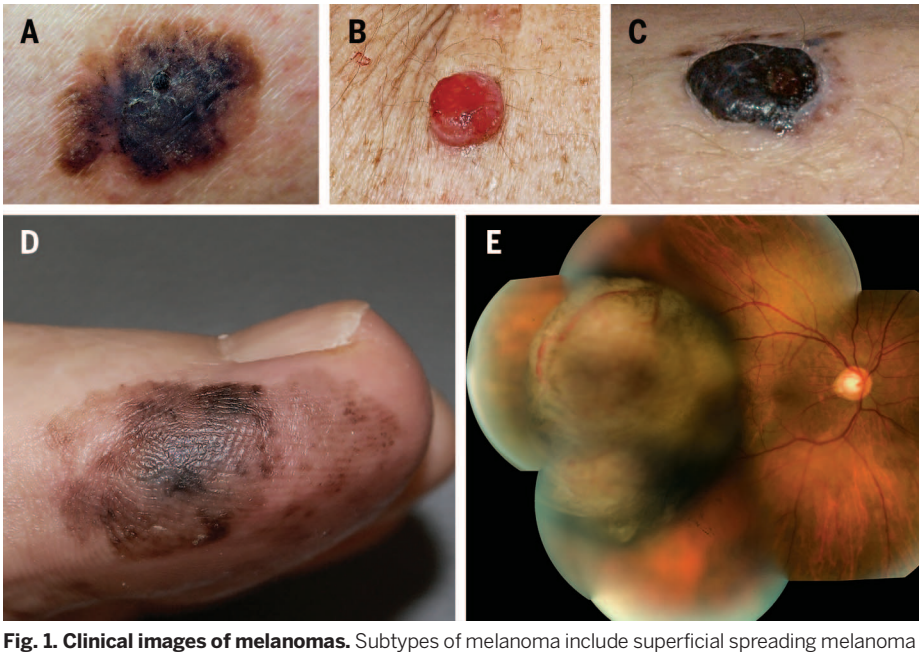


Fig. 1. Clinical images of melanomas. Subtypes of melanoma include superficial spreading melanoma (**A**), amelanotic melanoma (**B**), nodular melanoma (**C**), acral lentiginous melanoma (**D**), and uveal melanoma (**E**). Images courtesy of H. Tsao, C.H. Won, and I. Kim.

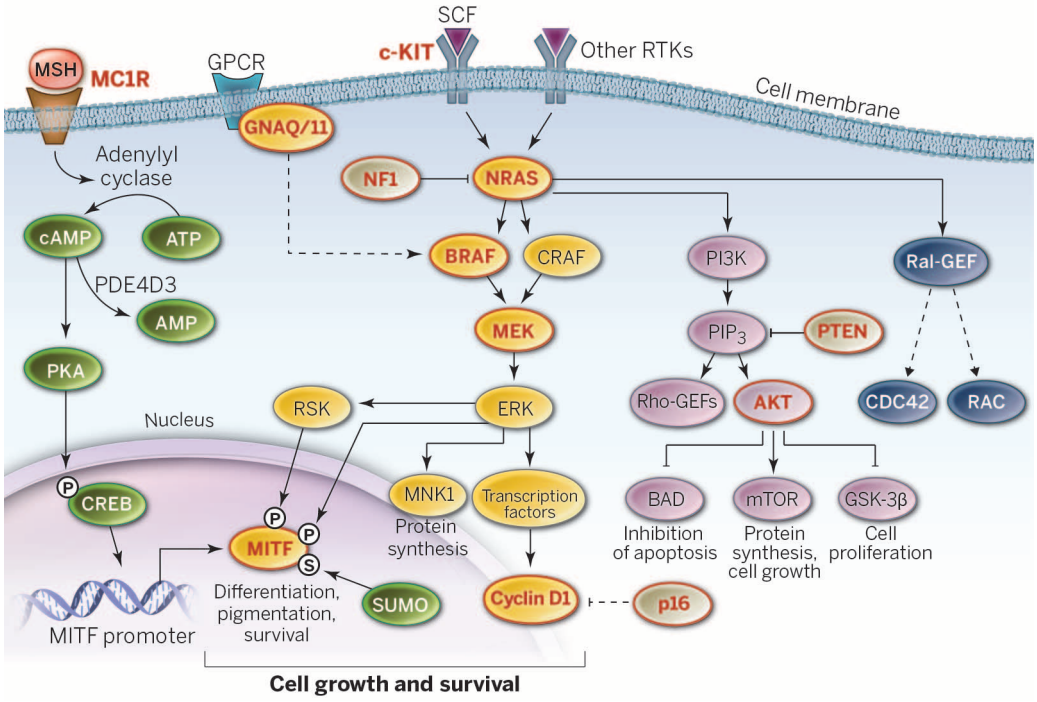


Fig. 2. Signaling pathways in melanoma. MAPK signaling promotes cell growth and survival and is constitutively active in most melanomas. RAS family members are activated by RTKs and signal through effector proteins, including RAF kinases, PI3K, and Ral-GEFs. Oncogenic BRAF and NRAS are found in 40 to 60% and 10 to 30% of melanomas, respectively. c-KIT signaling is essential for melanocyte development and is associated with melanomas arising on acral, mucosal, and chronically sun-damaged skin. Mutations in GNAQ and GNA11, two G protein α subunits involved in MAPK signaling, are the dominant genetic lesions in uveal melanomas. MITF, the master transcriptional regulator in melanocytes and lineage-specific oncogene, is expressed in response to MC1R signaling. Loss-of-function variants of MC1R are associated with the red hair/fair skin phenotype and increased melanoma susceptibility. Known melanoma oncogenes and tumor suppressors are labeled in red. Dotted lines represent omitted pathway components.

p53 and RB (retinoblastoma) pathways. Loss of the p53 cell cycle checkpoint and apoptotic pathway in melanoma can result from deletion or mutations in $p14^{ARF}$ or TP53, as well as rarer amplifications of mouse double minute 2 homolog (MDM2). Loss of the RB pathway can result from $p16^{INK4a}$ lesions, cyclin-dependent kinase 4 (CDK4) point mutations or amplifications, retinoblastoma 1 (RB1) mutations, and cyclin D1 (CCND1) amplifications [reviewed in (*34*)]. TERT promoter mutations are common and produce MAPK-responsive expression (*21*).

Transcription factors and epigenetic regulators

Although MITF is essential for melanocyte differentiation and pigmentation, it can alternatively act as a lineage-specific oncogene, likely through up-regulation of targets that promote cell cycle progression and survival. MITF is amplified in many sporadic melanomas (*35*), and a germline variant that confers gain-of-function activity is associated with familial melanoma (*36*). The related oncogene MYC is also occasionally amplified (*37*). Nuclear β-catenin, a mediator of canonical Wnt pathway activation, is detected in about one-third of melanomas (*38*), although the mechanism of its nuclear activation is not well understood. Inactivating mutations in BRCA1-associated protein-1 (BAP1) deubiquitinase are present in half of uveal melanomas and confer increased metastatic risk (*39*). Loss-of-function mutations in ARID1a and -2, components of the SWI/SNF chromatin-remodeling complex, have been reported in cutaneous melanomas (*16*).

Targeted therapies in melanoma

The first targeted therapy to demonstrate substantial efficacy against melanoma was vemurafenib, an adenosine triphosphate–competitive BRAF inhibitor (*40*). In the phase III clinical trial, vemurafenib conferred a survival advantage compared to dacarbazine chemotherapy in patients with $BRAF^{V600E}$-mutant melanomas, with an overall response rate of 48% (*41*). Dabrafenib, another BRAF inhibitor, provides similar clinical benefit (*42*). Vemurafenib and dabrafenib were approved by the U.S. Food and Drug Administration (FDA) for treatment of advanced BRAF-mutant melanoma in 2011 and 2013, respectively (Fig. 3).

A remarkable feature of mutant BRAF inhibitors is their ability to trigger paradoxical CRAF hyperactivation in cells containing wild-type BRAF and upstream MAPK pathway activation (*43*). The emergence of low-grade squamous carcinomas in sun-exposed skin is not uncommon after single-agent vemurafenib or dabrafenib therapy and is believed to involve drug-induced MAPK pathway hyperactivation in keratinocytes harboring RAS mutations (*44*). This paradoxical activation provides an opportunity for a combination of BRAF and MAPK kinase (MEK) inhibition. When administered together, dabrafenib and the MEK inhibitor trametinib achieve increased clinical benefit with fewer toxicities relative to single-agent treatment (*45*).

Vemurafenib and dabrafenib are impressive examples of bench-to-bedside translation in melanoma and produce rapid initial disease stabilization. However, their efficacy is restricted to the subset of patients with $BRAF^{V600}$-mutant melanomas and has only transient durability. Regressions on BRAF and MEK inhibitors are almost inevitably followed by emergence of drug resistance and disease progression, with median progression-free survival limited to 5 to 7 months (*41*, *42*, *46*).

Mechanisms of resistance to targeted therapy include those that can be predicted from pretreatment analysis and those that are later acquired or selected. Pretreatment factors that predict early resistance are mediators of apoptosis, growth, and cell cycle progression. They include BCL2A1 expression, PTEN loss, and CCND1 activation (*47*–*49*). Most cases of acquired resistance to BRAF inhibitors involve reactivation of MAPK signaling. Such mechanisms include MEK1-activating mutations, COT/MAP3K8 up-regulation, and $BRAF^{V600E}$ splicing variants (*50*–*52*). NRAS mutation and loss of NF1 have also been described (*53*, *54*). Although NRAS and NF1 act upstream of BRAF in the MAPK pathway, hyperactive NRAS can nevertheless restore MAPK signaling in the context of BRAF inhibition via paradoxical activation of CRAF. Most MAPK pathway–independent mechanisms of acquired resistance involve activation of PI3K signaling through up-regulation of RTKs (*53*).

Although many mechanisms of resistance to BRAF and MEK inhibitors have been observed in vitro, it is crucial to elucidate which mechanisms are clinically relevant. Results from next-generation sequencing of patient-matched melanoma biopsies before therapy, during response to therapy, and after disease progression are starting to emerge, revealing the kinetics and spectrum of in vivo resistance mechanisms (*55*). Melanomas with acquired resistance to targeted therapies show evidence of branched evolution and a high degree of genomic heterogeneity, even within single tumor sites. Sequencing has also uncovered new resistance mechanisms, including $BRAF^{V600E}$ amplifications

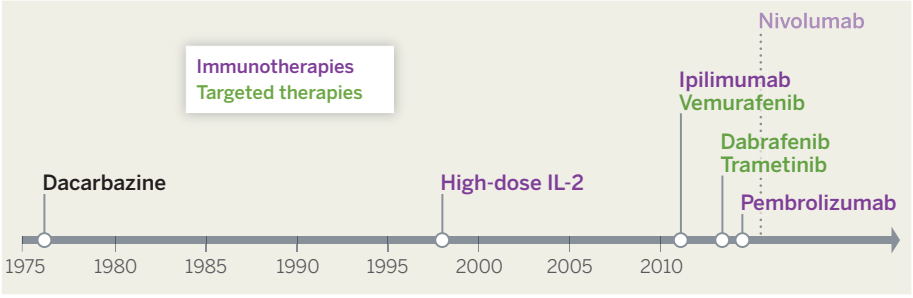


Fig. 3. Timeline of FDA regulatory approval for metastatic melanoma. Between 1976 and 2011, dacarbazine chemotherapy (1976) and high-dose IL-2 (1998) were the only approved agents for the treatment of advanced melanoma. The number of approved agents more than tripled in the past 3 years with the approvals of ipilimumab (antibody to CTLA-4) and vemurafenib (BRAF inhibitor) in 2011, dabrafenib (BRAF inhibitor) and trametinib (MEK inhibitor) in 2013, and pembrolizumab (antibody to PD-1) in 2014. FDA approval of nivolumab (antibody to PD-1) is anticipated in the near future. Targeted therapies are labeled in green; immunotherapies are labeled in purple.

and MEK2-activating mutations (*55*, *56*). Comprehensively cataloging the landscape of BRAF inhibitor resistance will enable more accurate prediction of drug response patterns and guide future therapeutic strategies.

Although there has been considerable progress in the melanoma targeted-therapy field, a major challenge continues to be forestalling the emergence of resistant disease. A combination of BRAF and MEK inhibitors provides some delay in disease progression, but most patients still relapse within a year (*45*). Efforts to improve durability of responses will likely include other double, triple, and quadruple drug regimens.

Melanoma immunotherapies

The importance of immune responses in melanoma has long been appreciated, with reports of spontaneous melanoma regressions published more than 50 years ago (*57*). The cancer immunosurveillance hypothesis, which posits that adaptive immunity can prevent cancer development and progression, was supported by observation of higher melanoma incidence in immunosuppressed patients (*58*). Early discovery of immune infiltrates and tumor-specific antibodies as positive prognostic factors provided additional evidence of immune interactions with melanoma (*59*, *60*).

Although immunotherapy has historically been an active area of research, major successes were elusive until recently. Melanoma vaccines and treatments with nonspecific immune stimulants like Bacillus Calmette-Guerin (BCG) have thus far failed to deliver predictable major clinical benefit. High-dose interleukin-2 (IL-2), a type I cytokine that activates cytotoxic T cells, became the first nonchemotherapeutic FDA-approved therapy for advanced melanoma in 1998. Although its use is limited by high toxicity and low response rates, IL-2 can produce long-term remissions in a small subset of patients (*61*).

Another treatment that can yield durable responses is adoptive cell transfer with autologous T cells, in which lymphocytes are harvested from patient tumors, expanded and activated ex vivo, and reinfused (*62*). Combination with complementary modalities such as dendritic cell immunization and BRAF inhibition is under investigation. There is also interest in the related technologies of transgenic T cell receptor therapy and chimeric antigen receptor therapy. Both involve adoptive transfer of peripheral T cells that have been genetically modified to target specific tumor-associated antigens.

The most successful immunotherapy approach to date has been immune checkpoint inhibition. T cell activation requires T cell receptor recognition of an antigenic peptide/major histocompatibility complex on the surface of an antigen-presenting cell (APC) and a costimulatory interaction between the T cell and APC. The second costimulation step can be mediated by either stimulatory or inhibitory receptor-ligand pairs known as "immune checkpoints" (*63*). Two of the best-studied checkpoints involve cytotoxic T lymphocyte antigen-4 (CTLA-4) and programmed cell death-1 (PD-1), two coinhibitory T cell receptors that mediate immune tolerance. Interestingly, activated T cells can induce up-regulation of PD-1 ligands PD-L1 and PD-L2 in many peripheral tissues and APCs. One important example of tumor-mediated immune evasion is PD-L1 up-regulation on cells in inflammatory tumor microenvironments (*64*).

Ipilimumab, a humanized CTLA-4 blocking monoclonal antibody, was the first treatment to prolong survival in advanced melanoma and was approved by the FDA in 2011 (Fig. 3). Although ipilimumab responses were limited to 11% of patients in the phase III trial, many of these responses were durable (*65*). Monoclonal antibodies that antagonize PD-1 or PD-L1 have been even more impressive in clinical studies, with higher response rates and fewer autoimmune toxicities (*66*, *67*). The PD-1–blocking antibody pembrolizumab won FDA approval this year, and approval of another PD-1 antibody, nivolumab, is expected in the near future.

With the successes of ipilimumab, nivolumab, pembrolizumab, and several additional checkpoint inhibitors in the pipeline, the past few years have been a time of accelerated progress in immunotherapy. Striking durable responses and curative outcomes have established immune checkpoint inhibitors as the most promising treatments available for metastatic melanoma. Efforts are now focused on increasing the proportion of patients who respond to checkpoint blockade, with great interest in potential synergy of combinatorial therapies.

One immunotherapy combination under investigation is coinhibition of CTLA-4 and PD-1/PD-L1, because the two checkpoints are known to play nonredundant roles in the regulation of

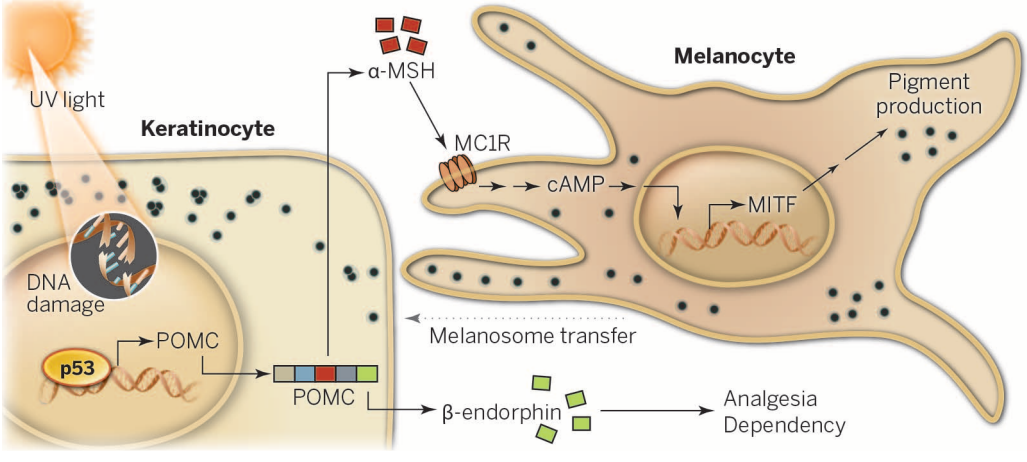


Fig. 4. Cutaneous response to UVR. Tanning involves p53 activation in keratinocytes in response to UVR-induced DNA damage, leading to p53-mediated up-regulation of proopiomelanocortin (POMC). Posttranslational cleavage of POMC produces β-endorphin and α-MSH. Secreted α-MSH stimulates MC1R on adjacent melanocytes, resulting in melanin synthesis and eventual transfer of melanin-containing vesicles (melanosomes) to keratinocytes. Chronic UVR results in elevated circulating β-endorphin levels, leading to analgesia and physical dependence.

immune responses (*68*). Another compelling strategy is combination of immune checkpoint inhibitors with BRAF or MEK inhibitors. Preclinical data suggest that MAPK pathway inhibition may enhance immune cell function and increase melanocytic antigen expression (*69*). Although the phase I trial of ipilimumab plus vemurafenib was closed due to severe hepatotoxicity (*70*), several trials with other combinations of targeted therapies, checkpoint inhibitors, and cytokines are ongoing.

Future prospects

Although skin is the most common site of cancer, its malignancies are likely to be among the most preventable. A well-established carcinogen, UVR, is responsible for a large fraction of melanomas and can be limited or avoided to dramatically reduce melanoma risk. Thus, it is of particular concern that melanoma incidence is on the rise (*1*). Despite convincing evidence that indoor tanning increases skin cancer risk (*5*), tanning devices are increasingly popular in many countries, and the FDA estimates that they are used by more than 30 million Americans every year.

In addition to an aesthetic preference for tanned skin (*71*), an emerging factor believed to contribute to the popularity of tanning is its addictive potential. Many tanners meet CAGE (Cut down, Annoyed, Guilty, Eye-opener) Questionnaire and Diagnostic and Statistical Manual of Mental Disorders, Fourth Edition (DSM-IV), criteria for substance abuse with respect to UVR (*72*). A recent study reported that UVR-induced β-endorphin production in skin mediates addiction to UV light in mice (*73*), suggesting that there is an endogenous opiate-mediated mechanism for primordial UV addiction (Fig. 4). Biological addiction may help to explain the risky UVR-associated behaviors of some melanoma survivors. In a 2012 study, less than half of survivors reported regular sunscreen use and sun avoidance, and 6% continued to tan indoors after their melanoma diagnosis (*74*). Future skin cancer prevention efforts may benefit from considering UVR-seeking behavior in the context of biological addiction.

Another major opportunity lies in understanding the mechanisms of UVR-independent or UVR-synergistic melanoma susceptibility. Elucidating such processes, perhaps involving oxidative stress, could provide targets for intervention. In combination with protection from UVR, these additional strategies may achieve optimal melanoma prevention in vulnerable populations.

Despite challenges remaining in melanoma prevention, the past 3 years have been a time of remarkable achievement. Five drugs have gained FDA approval for the treatment of advanced melanoma, with approval of several others anticipated in the near future. The arrival of these therapeutics has been accompanied by major strides in our understanding of the molecular events in melanomagenesis. Ongoing deep-sequencing projects are uncovering new information about not only genomic alterations but also epigenomic and transcriptomic changes that underlie melanoma development, progression, and drug resistance. These discoveries have profound implications for the development of targeted therapies that may complement existing treatment modalities.

Interestingly, the preponderance of UVR-induced mutations that is implicated in melanomagenesis offers an immunotherapeutic opportunity. Somatic mutations can produce altered proteins that, in the context of immune surveillance, are distinct from self proteins and are not protected by central tolerance. These new mutant "neoantigens" can potentially serve as targets of immune responses, and studies have reported that some melanoma neoantigens are recognized by tumor-infiltrating lymphocytes (*75*). Efforts are under way to target melanoma neoantigens through personalized approaches such as vaccination.

Although identifying strategies to overcome resistance to targeted therapies and increase the proportion of responders to immunotherapies remains an important next step in melanoma research, recent breakthroughs have already produced a paradigm shift in melanoma treatment. Metastatic melanoma, which was once considered incurable, can now be treated with potentially curative rather than palliative intent. Moving forward, complementary insights from melanoma and immunology research will continue to drive the development of melanoma therapies and help to determine optimal therapeutic sequences and combinatorial strategies, likely relevant to many malignancies.

REFERENCES AND NOTES

1. R. Siegel, J. Ma, Z. Zou, A. Jemal, *CA Cancer J. Clin.* **64**, 9–29 (2014).
2. J. Y. Lin, D. E. Fisher, *Nature* **445**, 843–850 (2007).
3. R. Cui *et al.*, *Cell* **128**, 853–864 (2007).
4. D. C. Whiteman, C. A. Whiteman, A. C. Green, *Cancer Causes Control* **12**, 69–82 (2001).
5. M. Boniol, P. Autier, P. Boyle, S. Gandini, *BMJ* **345**, e4757 (2012).
6. L. Garibyan, D. E. Fisher, *Curr. Oncol. Rep.* **12**, 319–326 (2010).
7. M. R. Zaidi *et al.*, *Nature* **469**, 548–553 (2011).
8. T. Bald *et al.*, *Nature* **507**, 109–113 (2014).
9. J. L. Rees, *Annu. Rev. Genet.* **37**, 67–90 (2003).
10. D. Mitra *et al.*, *Nature* **491**, 449–453 (2012).
11. C. J. Hussussian *et al.*, *Nat. Genet.* **8**, 15–21 (1994).
12. D. T. Bishop *et al.*, *Nat. Genet.* **41**, 920–925 (2009).
13. H. Davies *et al.*, *Nature* **417**, 949–954 (2002).
14. E. D. Pleasance *et al.*, *Nature* **463**, 191–196 (2010).
15. M. S. Stark *et al.*, *Nat. Genet.* **44**, 165–169 (2011).
16. E. Hodis *et al.*, *Cell* **150**, 251–263 (2012).
17. M. Krauthammer *et al.*, *Nat. Genet.* **44**, 1006–1014 (2012).
18. M. S. Lawrence *et al.*, *Nature* **505**, 495–501 (2014).
19. L. B. Alexandrov *et al.*, *Nature* **500**, 415–421 (2013).
20. E. Kvam, R. M. Tyrrell, *J. Invest. Dermatol.* **113**, 209–213 (1999).
21. F. W. Huang *et al.*, *Science* **339**, 957–959 (2013).
22. A. Viros *et al.*, *Nature* **511**, 478–482 (2014).
23. A. M. Menzies *et al.*, *Clin. Cancer Res.* **18**, 3242–3249 (2012).
24. J. A. Curtin *et al.*, *N. Engl. J. Med.* **353**, 2135–2147 (2005).
25. A. C. Green, G. M. Williams, V. Logan, G. M. Strutton, *J. Clin. Oncol.* **29**, 257–263 (2011).
26. A. P. Albino, R. Le Strange, A. I. Oliff, M. E. Furth, L. J. Old, *Nature* **308**, 69–72 (1984).
27. J. M. Stahl *et al.*, *Cancer Res.* **64**, 7002–7010 (2004).
28. M. Stark, N. Hayward, *Cancer Res.* **67**, 2632–2642 (2007).
29. K. A. Furge *et al.*, *Proc. Natl. Acad. Sci. U.S.A.* **98**, 10722–10727 (2001).
30. N. Bardeesy *et al.*, *Mol. Cell. Biol.* **25**, 4176–4188 (2005).
31. J. A. Curtin, K. Busam, D. Pinkel, B. C. Bastian, *J. Clin. Oncol.* **24**, 4340–4346 (2006).
32. O. Maertens *et al.*, *Cancer Discov.* **3**, 338–349 (2013).
33. C. D. Van Raamsdonk *et al.*, *Nature* **457**, 599–602 (2009).
34. H. Tsao, L. Chin, L. A. Garraway, D. E. Fisher, *Genes Dev.* **26**, 1131–1155 (2012).
35. L. A. Garraway *et al.*, *Nature* **436**, 117–122 (2005).
36. S. Yokoyama *et al.*, *Nature* **480**, 99–103 (2011).
37. G. M. Kraehn *et al.*, *Br. J. Cancer* **84**, 72–79 (2001).
38. D. L. Rimm, K. Caca, G. Hu, F. B. Harrison, E. R. Fearon, *Am. J. Pathol.* **154**, 325–329 (1999).
39. J. W. Harbour *et al.*, *Science* **330**, 1410–1413 (2010).
40. K. T. Flaherty *et al.*, *N. Engl. J. Med.* **363**, 809–819 (2010).
41. P. B. Chapman *et al.*, *N. Engl. J. Med.* **364**, 2507–2516 (2011).
42. A. Hauschild *et al.*, *Lancet* **380**, 358–365 (2012).
43. S. J. Heidorn *et al.*, *Cell* **140**, 209–221 (2010).
44. F. Su *et al.*, *N. Engl. J. Med.* **366**, 207–215 (2012).
45. K. T. Flaherty *et al.*, *N. Engl. J. Med.* **367**, 1694–1703 (2012).
46. K. T. Flaherty *et al.*, *N. Engl. J. Med.* **367**, 107–114 (2012).
47. R. Haq *et al.*, *Proc. Natl. Acad. Sci. U.S.A.* **110**, 4321–4326 (2013).
48. K. H. T. Paraiso *et al.*, *Cancer Res.* **71**, 2750–2760 (2011).
49. K. S. M. Smalley *et al.*, *Mol. Cancer Ther.* **7**, 2876–2883 (2008).
50. C. M. Emery *et al.*, *Proc. Natl. Acad. Sci. U.S.A.* **106**, 20411–20416 (2009).
51. C. M. Johannessen *et al.*, *Nature* **504**, 138–142 (2013).
52. P. I. Poulikakos *et al.*, *Nature* **480**, 387–390 (2011).
53. R. Nazarian *et al.*, *Nature* **468**, 973–977 (2010).
54. S. R. Whittaker *et al.*, *Cancer Discov* **3**, 350–362 (2013).
55. E. M. Van Allen *et al.*, *Cancer Discov* **4**, 94–109 (2014).
56. H. Shi *et al.*, *Nat. Commun.* **3**, 724 (2012).
57. W. H. Cole, T. C. Everson, *Ann. Surg.* **144**, 366–383 (1956).
58. M. H. Greene, T. I. Young, W. H. Clark Jr., *Lancet* **317**, 1196–1199 (1981).
59. D. Morton, F. R. Eilber, R. A. Malmgren, W. C. Wood, *Surgery* **68**, 158–163 (1970).
60. C. G. Clemente *et al.*, *Cancer* **77**, 1303–1310 (1996).
61. M. B. Atkins *et al.*, *J. Clin. Oncol.* **17**, 2105–2116 (1999).
62. S. A. Rosenberg *et al.*, *Clin. Cancer Res.* **17**, 4550–4557 (2011).
63. A. H. Sharpe, *Immunol. Rev.* **229**, 5–11 (2009).
64. T. F. Gajewski, H. Schreiber, Y. X. Fu, *Nat. Immunol.* **14**, 1014–1022 (2013).
65. F. S. Hodi *et al.*, *N. Engl. J. Med.* **363**, 711–723 (2010).
66. S. L. Topalian *et al.*, *N. Engl. J. Med.* **366**, 2443–2454 (2012).
67. O. Hamid *et al.*, *N. Engl. J. Med.* **369**, 134–144 (2013).
68. J. D. Wolchok *et al.*, *N. Engl. J. Med.* **369**, 122–133 (2013).
69. A. Boni *et al.*, *Cancer Res.* **70**, 5213–5219 (2010).
70. A. Ribas, F. S. Hodi, M. Callahan, C. Konto, J. Wolchok, *N. Engl. J. Med.* **368**, 1365–1366 (2013).
71. M. R. Albert, K. G. Ostheimer, *J. Am. Acad. Dermatol.* **47**, 930–937 (2002).
72. C. E. Mosher, S. Danoff-Burg, *Arch. Dermatol.* **146**, 412–417 (2010).
73. G. L. Fell, K. C. Robinson, J. Mao, C. J. Woolf, D. E. Fisher, *Cell* **157**, 1527–1534 (2014).
74. D. Mayer, A. Layman, J. Carlson, *J. Am. Acad. Dermatol.* **66**, e9–e10 (2012).
75. P. F. Robbins *et al.*, *Nat. Genet.* **19**, 747–752 (2013).

ACKNOWLEDGMENTS

We thank H. Tsao, C.-H. Won, and I. Kim for clinical images and K. Robinson and K. Flaherty for useful comments and discussions. We extend our sincere apologies to those colleagues whose studies were not cited due to space constraints. This work was supported by the NIH under award numbers T32GM007753 (J.A.L.), P01CA163222, R01AR043369, and R01CA150226 and by grants from the Melanoma Research Alliance, the U.S.-Israel Binational Science Foundation, and the Dr. Miriam and Sheldon G. Adelson Medical Research Foundation (D.E.F.).

10.1126/science.1253735

REVIEW

The gentle touch receptors of mammalian skin

Amanda Zimmerman,[1] Ling Bai,[1,2] David D. Ginty[1]*

The skin is our largest sensory organ, transmitting pain, temperature, itch, and touch information to the central nervous system. Touch sensations are conveyed by distinct combinations of mechanosensory end organs and the low-threshold mechanoreceptors (LTMRs) that innervate them. Here we explore the various structures underlying the diverse functions of cutaneous LTMR end organs. Beyond anchoring of LTMRs to the surrounding dermis and epidermis, recent evidence suggests that the non-neuronal components of end organs play an active role in signaling to LTMRs and may physically gate force-sensitive channels in these receptors. Combined with LTMR intrinsic properties, the balance of these factors comprises the response properties of mechanosensory neurons and, thus, the neural encoding of touch.

The skin, our largest organ, encompasses the entire body and mediates our sense of touch. Neurophysiologically complex, the skin is innervated by a wide variety of sensory neuron subtypes, including nociceptors, which sense painful stimuli; pruriceptors, which convey itch; thermoreceptors, which register temperature information; and low-threshold mechanoreceptors (LTMRs), which encode non-painful mechanical stimuli, or touch. We use our sense of touch to recognize and manipulate objects, to communicate and socially interact with one another, to appreciate the textures of the foods we eat, for procreation and sexual pleasure, and in maternal nursing. The cutaneous end organs and the mechanosensory neurons that innervate them have evolved to underlie a range of sensory functions, as evidenced by the multitude of skin type specializations that are each innervated by a distinct array of sensory neuron subtypes, reflecting the diversity of functions of touch neurons.

Mammalian skin comprises both hairy and nonhairy, or glabrous, skin. Glabrous skin is predominantly found on the hands and feet of most mammals. In this context, glabrous skin is specialized for discriminative touch, determining texture and shape to accurately recognize objects and providing feedback to the central nervous system to mediate proper grip control, reaching, and locomotion. Hairy skin covers more than 90% of the body surface. It also serves a discriminative touch role, albeit with considerably lower spatial acuity as compared with nonhairy skin. Hairy skin is strongly associated with affective touch—that is, touch that evokes an emotional response, such as during nurturing. Other types of skin are highly specialized for the functional roles they play. The genitalia, specifically the glans penis and glans clitoris, are specialized forms of glabrous skin, fine-tuned for sexual pleasure sensation and reproductive reflexes. The skin of the lips, tongue, and inner cheeks are specialized to aid in food localization and movement and to define textural components of taste. In mammalian females, milk secretion is triggered by suckling stimulation of the nipples. Moreover, some species have evolved skin that is highly specialized for particular functions. Mystacial pads of nocturnal rodents have long whiskers and are specialized for navigation and spatial orientation. The snouts of star-nosed moles and the bills of tactile-foraging birds are specialized for locating prey. These particular skin regions are associated with different combinations of LTMRs, making each region neurophysiologically and functionally distinct.

Key to our understanding of the neurobiological basis of touch is determining how LTMR end organs encode complex forms of tactile stimulation and how this encoding is then integrated and processed within the central nervous system. LTMR subtype central projections terminate within somatotopic columns in the dorsal horn of the spinal cord, with a subset also sending collaterals to the dorsal column nuclei of the brainstem (*1*). Dorsal horn columns contain interneurons that are thought to process touch information, as well as projection neurons that carry this processed information to the brainstem and higher cortical areas [for a review of central processing, see (*2*)]. Here we explore the mechanosensory end organs of the skin, focusing on the physiological, morphological, and ultrastructural properties of LTMRs and their associated non-neuronal cells, and we hypothesize how different end organs give rise to the distinct response properties and functions that define mammalian touch neurons.

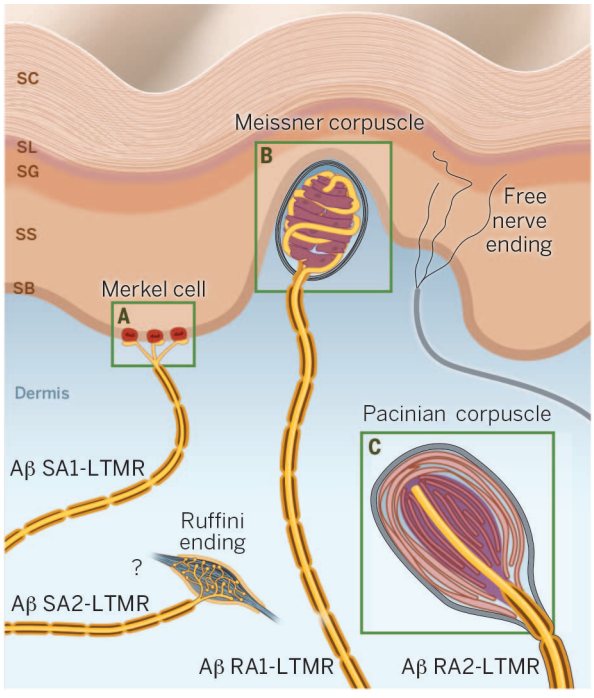


Fig. 1. LTMR innervation of glabrous skin. Glabrous skin is innervated by Aβ LTMRs, including Aβ SA1-LTMRs terminating in Merkel cells, Aβ SA2-LTMRs hypothesized to end in Ruffini endings, Aβ RA1-LTMRs innervating Meissner corpuscles, and Aβ RA2-LTMRs ending in Pacinian corpuscles. Green boxed regions are shown in greater detail in Fig. 3 (here, the letters "A," "B," and "C" correspond to panels with the same names in Fig. 3). SC, stratum corneum; SL, stratum lucidum; SG, stratum granulosum; SS, stratum spinosum; SB, stratum basale.

LTMRs of hairy and glabrous skin

The LTMRs are a heterogeneous group of sensory neurons. Just as the gustatory system has distinct sensory receptors optimally tuned to detect sweet, sour, salty, umami, or bitter tastants, LTMRs are divided into subtypes distinguished by their distinct sensitivities, conduction velocities, and adaptation to sustained mechanical stimulation. For example, slowly-adapting (SA) touch receptors are indentation detectors, firing continuously during a sustained stimulus, whereas rapidly-adapting (RA) touch receptors are velocity detectors that respond only to the onset and offset of indentation. In glabrous skin, four types of LTMRs with fast conduction velocity (Aβ LTMRs) have been defined (Fig. 1), each with a distinct terminal

[1]Department of Neurobiology, Howard Hughes Medical Institute, Harvard Medical School, 220 Longwood Avenue, Boston, MA 02115, USA. [2]The Solomon H. Snyder Department of Neuroscience and Howard Hughes Medical Institute, Johns Hopkins University School of Medicine, Baltimore, MD 21205, USA.
*Corresponding author. E-mail: david_ginty@hms.harvard.edu

morphology and tuning property (*3*–*5*): (i) Aβ SA1-LTMRs innervate Merkel cells in the basal epidermis and report the static nature of touch stimuli, (ii) Aβ SA2-LTMRs are hypothesized to terminate in Ruffini corpuscles in the dermis and are particularly sensitive to skin stretch, (iii) Aβ RA1-LTMRs innervate Meissner's corpuscles in dermal papillae and are sensitive to movement across the skin, and (iv) Aβ RA2-LTMRs terminate in Pacinian corpuscles deep in the dermis and are tuned to high-frequency vibration (*6*–*8*).

In hairy skin, several LTMRs form specialized terminals associated with hair follicles, allowing the sense of touch to extend beyond the skin surface (Fig. 2). Aβ SA1-LTMRs and Merkel cells form complexes called touch domes to detect skin indentation (*9*, *10*). The hair follicle shaft is supplied by collars of mechanoreceptor terminals, including at least three LTMR subtypes that exhibit longitudinal lanceolate endings and one type that has circumferential endings. These subtypes differ in their sensitivities, adaptation properties, and conduction velocities (*1*, *11*). The neck of the hair follicles and the adjacent epidermis are penetrated by unmyelinated LTMRs with free nerve endings (*12*). At least one type of unmyelinated, slowly-conducting LTMR has endings localized solely to hairy skin and is implicated in pleasurable touch sensation in humans (*13*). Thus, morphological and neurophysiological differences in glabrous- and hairy-skin LTMRs define the distinct sensory functions of glabrous and hairy skin.

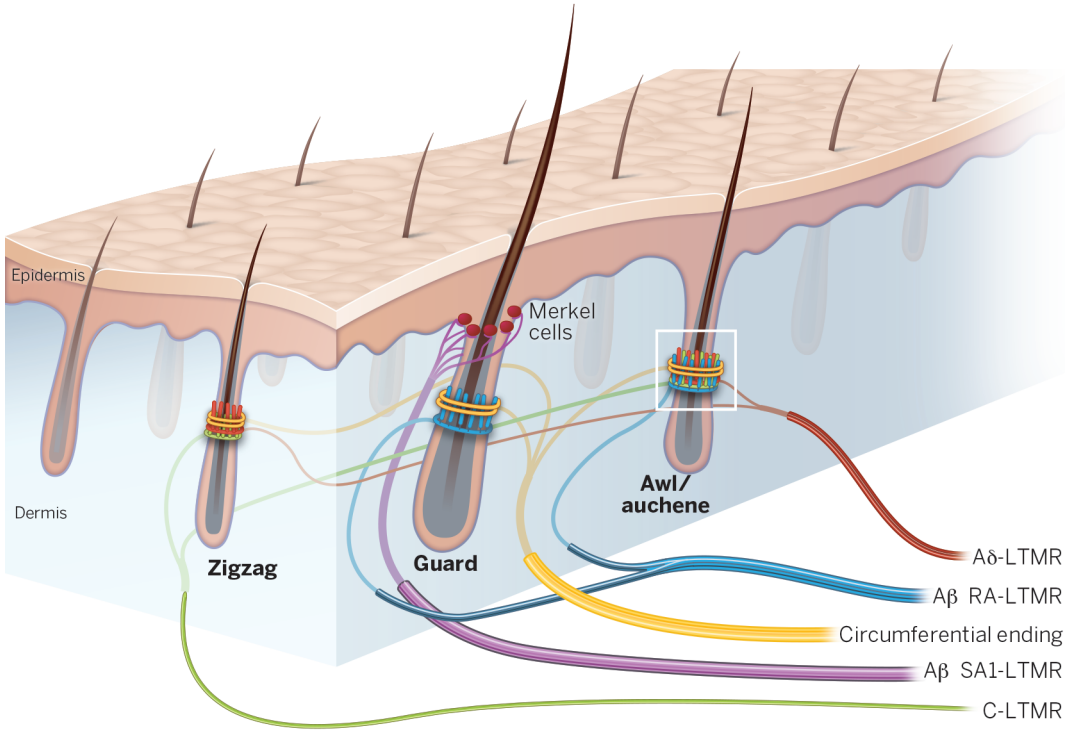


Fig. 2. LTMR innervation of hairy skin. Hairy skin in rodents is innervated by distinct combinations of LTMRs. Touch domes of Merkel cells and associated Aβ SA1-LTMRs are found above the level of the sebaceous glands of guard hair follicles. Guard hairs are also innervated by Aβ RA-LTMR lanceolate endings. Awl/auchene hairs are innervated by all three types of lanceolate-ending LTMRs: Aβ RA-LTMRs, Aδ-LTMRs, and C-LTMRs. Zigzag hairs, the most numerous, are innervated by Aδ-LTMRs and C-LTMRs. Circumferential endings encircle the longitudinal lanceolate endings of all three types of hair follicles. The white boxed region is shown in greater detail in Fig. 4.

The form that underlies function of cutaneous touch receptors

Merkel cell/Aβ SA1-LTMR mechanotransduction

How do ultrastructural features of mechanosensory end organs in hairy and glabrous skin underlie LTMR response properties and functions? It is instructive to first consider the end organ that is shared by hairy and glabrous skin, the Merkel cell/Aβ SA1-LTMR complex. Originally described as "touch corpuscles" by Friedrich Merkel in 1875, they are a group of specialized oval cells in the epidermis of glabrous skin that are innervated by sensory fibers and were thus reasoned to mediate mechanosensation. Later termed "Merkel cells," clusters of these cells are observed in the basal layer of the epidermis of many specialized skin types, including a dome-shaped bulge close to guard hairs of rodent hairy skin, mammalian glabrous skin, the noses of moles, the wings of bats, whisker pads, the mucosa of the mouth and lips, and elsewhere (*14*). These complexes are infrequent or absent in skin regions in which spatial acuity is not paramount, such as the genitalia (*15*, *16*). Aβ SA1-LTMR responses to static indentation include a high-frequency dynamic phase during initial skin indentation and lower-frequency, tonic firing during prolonged indentation. Functionally, studies mainly performed in humans and other primates indicate that the glabrous-skin Merkel cell/Aβ SA1-LTMR complex conveys information about texture, curvature, and object shape with high spatial acuity (*7*, *17*).

The Merkel cell is anchored within the epidermis by thin cytoplasmic protrusions projecting to keratinocytes and by desmosomes (*9*). These physical connections link movement and compression of the skin to mechanical stress on Merkel cells. Aβ SA1-LTMR endings exhibit stereotyped discoid enlargement and connect to the dermal side of each Merkel cell. Synapse-like structures at the junction between Aβ SA1-LTMR endings and Merkel cells have been described in multiple species and include a postsynaptic-like thickening of Aβ SA1-LTMR axon terminal membranes and the presence of presynaptic protein and neurotransmitter in the Merkel cells (*18*–*20*). However, small, clear synaptic vesicles typically associated with fast neurotransmission are absent in Merkel cells, and instead dense-core vesicles are seen clustered near the presumptive postsynaptic region of axonal endings (Fig. 3A). These dense-core vesicles are hypothesized to release neuropeptides rather than classical neurotransmitters, thus modulating Aβ SA1-LTMR responses.

Taste receptor cells in the gustatory system and hair cells of the auditory system are prominent examples of non-neuronal cells participating in stimulus transduction (*21*, *22*), yet it was only recently shown that an analogous situation occurs in touch sensation. Merkel cells, both in culture and ex vivo, exhibit mechanically activated currents, which are absent after loss of the mechanically activated cation channel Piezo2 (*23*, *24*). Moreover, optogenetic activation of Merkel cells is alone sufficient to evoke a SA discharge in Aβ SA1-LTMRs, whereas ablation or functional inactivation of Merkel cells leads to a reduction in both the dynamic and static phases of Aβ SA1-LTMR firing in response to skin indentation (*24*, *25*). Thus, both Merkel cells and Aβ SA1-LTMRs directly respond to mechanical force applied to the skin, and Merkel cells signal to Aβ SA1-LTMRs to achieve optimal activation of the LTMR. A new principle, that non-neuronal components of cutaneous touch complexes detect stimuli and potentiate LTMR responses, has thus begun to emerge.

Glabrous corpuscle LTMR transduction mechanisms

Do non-neuronal cells of the skin mediate mechanotransduction in other cutaneous mechanosensory

end organs? We explore two different corpuscles, both of which are rapidly adapting end organs discovered more than 150 years ago. Nestled within dermal papillae of glabrous skin, Meissner corpuscles are composed of flattened lamellar cells that form an ellipsoid structure perpendicular to the skin surface, with one or more tortuous Aβ RA1-LTMR axons meandering throughout (*26*, *27*). In contrast, the larger Pacinian corpuscles are found deep in the dermis of glabrous skin and, in some species, in hairy skin and noncutaneous tissues including the mesentery and periosteum. Pacinian corpuscles are oval-shaped, contain layered lamellae, and reach up to 3 to 4 mm in length in adult human hands (*28*, *29*). Both Meissner and Pacinian corpuscles are innervated by RA LTMRs tuned to vibration and motion across the skin, in contrast to the static mechanical indentation encoded by Merkel cells/Aβ SA1-LTMRs. Psychophysical studies in humans have described two coding channels of vibration, with low-frequency sinusoids perceived as flutter and high-frequency stimulation detected as vibration (*8*). Aβ RA1-LTMRs, which are tuned to low-frequency vibrations under 40 Hz, can detect the slip of an object in the hand (*5*, *8*, *30*) and may be essential for reflex grip control. On the other hand, Pacinian corpuscle afferents, or Aβ RA2-LTMRs, are tuned to high-frequency stimulation, with optimal activation around 200 Hz, and thus are involved in detecting vibration of held objects (*3*, *31*, *32*).

The non-neuronal components of Meissner and Pacinian corpuscles are quite distinct, and their arrangement within the corpuscle offers clues about how vibration and dynamic movement across the skin are encoded. Each disc-like unit of the Meissner corpuscle consists of an unmyelinated axon terminal swelling surrounded by flattened Schwann cell–derived lamellar cells (*26*, *33*). These discoid units are serrated on their external surfaces and smooth on their inner surfaces and are connected to collagen fibers that traverse the surrounding fibroblast capsule (Fig. 3B) (*27*, *34*). Substantial convergence occurs, as a single Aβ RA1-LTMR innervates multiple Meissner corpuscles (*6*). During indentation, force is transduced via collagen fibers connected to the serrated edges of the lamellar cells, which leads to bending of Aβ RA1-LTMR axon terminals until the smooth lamellar cell middle compresses. This compression generates action potentials during stimulus onset and produces a RA response (*33*, *34*). How this mechanism results in Meissner corpuscle sensitivity at the low end of the frequency stimulation range is unknown.

"We use our sense of touch to recognize and manipulate objects, to communicate and socially interact with one another, to appreciate the textures of the foods we eat, for procreation and sexual pleasure, and in maternal nursing."

In contrast to the layered lamellae organization of Meissner corpuscles, the non-neuronal components of Pacinian corpuscles are arranged in concentric lamellae, consisting of an inner core, an intermediate layer or growth zone, and an outer zone. The inner core is composed of tightly packed, bilaterally symmetric hemilamellar cells distributed along both sides of the Aβ RA2-LTMR axon terminal, with small-diameter collagen fibers coursing longitudinally in the clefts between them (*6*, *35*). The outer zone, about three times thicker than the inner core, is composed of concentrically arranged, flattened, and overlapping lamellar cells interspersed with circularly oriented type II collagen fibers in the fluid-filled extracellular space (*35*, *36*). A single heavily myelinated axon penetrates each corpuscle. Its unmyelinated axonal branches, or filopodia, project radially into the clefts between the inner-core hemilamellar cells (Fig. 3C) (*29*, *37*). The lamellar composition is believed to be responsible for the Aβ RA2-LTMR's encoding of high-frequency vibration, postulated in a model proposed more than 50 years ago: Pacinian corpuscle outer-core lamellar cells and surrounding fluid act as a high-pass filter that dampens low-frequency mechanical stimuli while allowing the slightest high-frequency vibration to reach axonal filopodia via interconnected collagen fibers. The depolarizing generator potentials of the filopodia converge and summate on the primary axon (*38*). Therefore, the cylindrically layered ultrastructure of Pacinian corpuscles facilitates the high-frequency sensitivity of Aβ RA2-LTMRs.

Do corpuscle lamellar cells actively govern Aβ RA1-LTMR and Aβ RA2-LTMR responses, analogous to what is observed in Merkel cell/Aβ

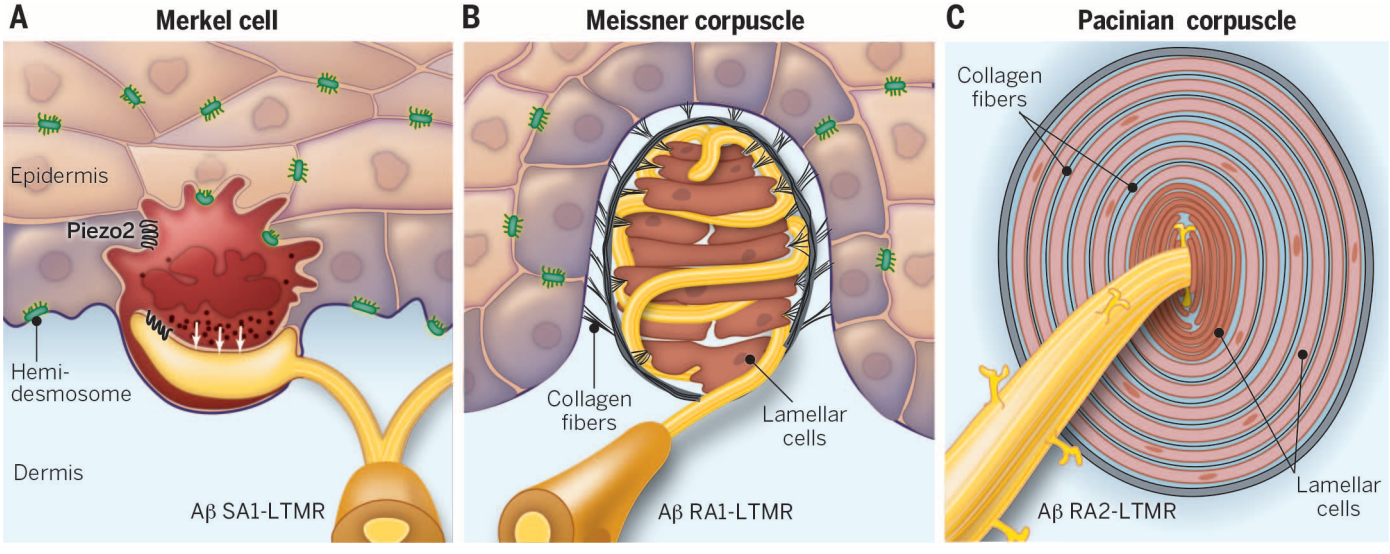


Fig. 3. LTMR end organs of glabrous skin. (**A**) Merkel cells are located within the basal layer of the epidermis, innervated by a single Aβ SA1-LTMR. Cytoplasmic protrusions of the Merkel cell and hemidesmosomes physically link Merkel cells to surrounding epithelial cells. Dense-core vesicles are located inside the Merkel cell in close proximity to the enlarged axon terminal and are thought to be involved in signaling between the Merkel cell and the neurite. Recent evidence revealed Merkel cells to be mechanically sensitive and to play an active role in mechanotransduction (white arrows). (**B**) Meissner corpuscles are located within dermal papillae and are innervated by one or more Aβ RA1-LTMRs. The external capsule is linked to both the lamellar cells and the epidermis via collagen fibers. (**C**) Pacinian corpuscles are located in the deep dermis, contain layered lamellar cells, and are innervated by a single Aβ RA2-LTMR. Axonal protrusions project from the neurite into the cleft between inner-core lamellar cells and are thought to be the sites of generator potentials. Longitudinal and circumferential collagen fibers anchor the inner core and outer zone, respectively.

SA1-LTMRs, or do they simply serve a structural role, positioning the respective LTMR endings to detect vibration and movement within the dermis? For the Pacinian corpuscle, studies in cats have revealed that inner-core lamellar cells have glutamate and γ-aminobutyric acid (GABA) receptors, vesicular glutamate transporters, synaptic proteins, synapse-like thickenings, and clear-core vesicles on both sides of the area adjacent to axonal filopodia and lamellae intersections. Glutamate and GABA receptor antagonists modulate electrophysiological responses of Aβ RA2-LTMRs (*39*, *40*). These findings suggest that Pacinian corpuscle lamellar cells can modulate Aβ RA2-LTMR responses and potentially even transduce force directly. Future studies are needed to determine whether an active role of non-neuronal cells of cutaneous LTMR end organs is the rule rather than the exception during mechanotransduction.

Hair follicle LTMR mechanotransduction mechanisms

Hair follicles are neurophysiologically complex mechanosensory organs. Apart from the SA1/Merkel cell complex, hair follicles are innervated by collars of LTMR terminals located just below the level of the sebaceous gland in both rodents and primates. The outer region of this sensory collar contains circumferential endings, whose physiological properties and functions remain unknown (*11*, *41*). The inner region is composed of three types of longitudinal lanceolate terminals, comb-like protrusions aligned parallel to the hair follicle. These longitudinal lanceolate endings—belonging to Aβ RA-LTMRs, Aδ-LTMRs, and C-LTMRs—are all sensitive to hair deflection and light touch of the skin, yet they have distinct conduction velocities (with Aβ > Aδ > C) (*1*, *42*, *43*). Similar to Aβ RA1-LTMRs associated with Meissner corpuscles in glabrous skin, lanceolate Aβ RA-LTMRs and Aδ-LTMRs are rapidly adapting and sensitive to movement and low-frequency vibration, despite slight differences in tuning properties (*43*–*45*). In rodent trunk skin, lanceolate C-LTMRs are intermediately adapting. Their electrophysiological properties resemble those of C-LTMRs in humans, which are optimally tuned to stroking of the skin at rates that are deemed pleasurable, thus implicating C-LTMRs in "emotional touch" (*46*, *47*).

Despite their differences in sensitivity and encoding, the three types of lanceolate-ending LTMRs have virtually identical terminal structures (Fig. 4) (*1*, *48*). All lanceolate terminals are shaped like flattened cylinders and are sandwiched between two or three terminal Schwann cell processes. The inner face of the axon directly abuts the basal lamina of hair follicle outer root sheath cells, with no intervening Schwann cell process, enabling a close apposition of LTMR axon terminal membranes and hair follicle keratinocytes. Longitudinally oriented collagen fibers fill the extracellular space between and around each lanceolate ending–terminal Schwann cell unit, which may provide structural support for the lanceolate complex (*48*, *49*).

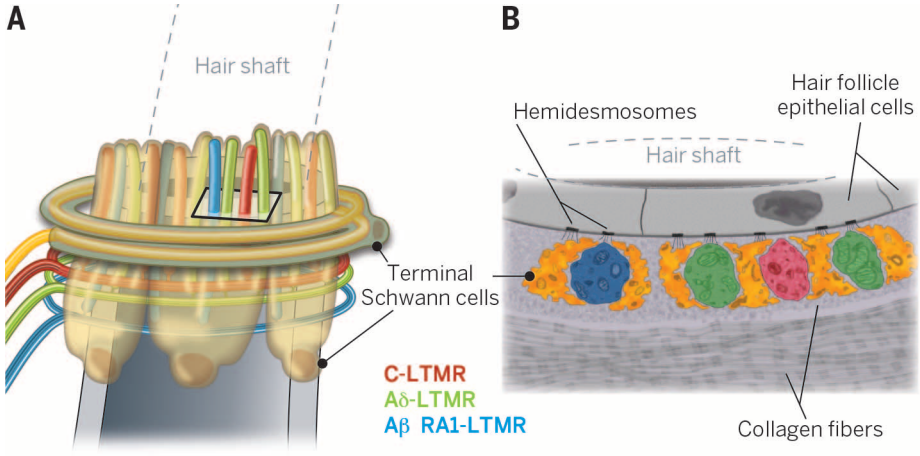


Fig. 4. LTMRs associated with mouse hair follicles. (**A**) Innervation pattern of Awl/auchene hair follicles. Terminal Schwann cells surround all three types of interdigitated lanceolate endings, as well as the circumferential ending(s). (**B**) Cross-sectional view of (A), based on electron microscopic analysis. Terminal Schwann cells surround lanceolate endings on either side, with a gap in coverage facing the hair follicle hair cells. Putative protein tethers may connect hair follicle epithelial cells with LTMRs and terminal Schwann cells, while both longitudinal and circumferential collagen fibers provide a supporting role.

How does hair deflection result in excitation of LTMR lanceolate endings and, subsequently, LTMR firing? Electron microscopy has been used to demonstrate that large numbers of hemidesmosomes are distributed along hair follicle epithelial cell membranes and that fine filaments appear to project from these hemidesmosomes to directly contact both LTMR lanceolate endings and terminal Schwann cell processes (Fig. 4B) (*48*). These filaments may serve to either simply anchor axon terminals to hair follicles or perhaps function as a kind of protein tether necessary for mechanotransduction of lanceolate-ending LTMRs. The protein tether hypothesis posits a mechanism analogous to that seen in the auditory system, in which tip links that connect stereocilia of cochlear hair cells transduce stereocilia movements to the opening of force-gated ion channels (*22*). In support of such a model for hair follicle lanceolate endings, protein tethers extend between cultured somatosensory neuron axons and fibroblasts, and chemical ablation of these tethers leads to a loss of mechanically activated currents (*50*). Thus, a physical connection between hair follicle epithelial cells and LTMR lanceolate endings may underlie LTMR excitation during hair deflection. Future challenges include understanding the contributions of hair follicle epithelial cells, terminal Schwann cells, and putative mechanical tethers in the transduction of hair deflection to LTMR excitation.

Cutaneous LTMRs and the neural encoding of touch

Like individual instruments in an orchestra, each LTMR subtype conveys a specific feature of the forces acting on the skin, collectively culminating in a musical symphony of neural impulses that the brain translates as a touch. Each LTMR end organ has similar basic components: sensory axon terminals, associated non-neuronal components (e.g., lamellar cells, Merkel cells, epithelial cells, and/or terminal Schwann cells), and contacts between them and the surrounding cells of the skin. Deciphering the underlying principles that govern transduction at LTMR axon terminals in the skin will reveal the mechanisms by which LTMR subtypes are tuned to deliver distinct components of touch sensation.

As neuroscientists, our instinct is to focus on how intrinsic physiological properties of neurons define their diverse tuning properties. As in the case of distinguishing lanceolate-ending LTMRs from one another, intrinsic determinants appear to be a predominant factor underlying physiological differences of LTMR subtypes [for a detailed discussion, see (*45*)]. Yet the ultrastructure of mechanosensory end organs plays an equal, if not more important, role in defining the responses of LTMRs. Be it structural filtering, physical tethering, or active propagation or modulation of force sensation, non-neuronal end organ components contribute heavily to the neural dialogue between the skin and the brain. The challenge for future research is to explore how the balance of intrinsic LTMR physiological properties and structural features of LTMR end organs underlies the neural encoding of each LTMR subtype. Ultimately, it is the combination of distinctively constructed touch end organs, highly specialized for each skin type, that produces myriad ensembles of LTMR activity patterns that are represented and processed in the spinal cord and brain and enables the richness of touch perceptions.

REFERENCES AND NOTES

1. L. Li *et al.*, *Cell* **147**, 1615–1627 (2011).
2. V. E. Abraira, D. D. Ginty, *Neuron* **79**, 618–639 (2013).
3. A. Iggo, H. Ogawa, *J. Physiol.* **266**, 275–296 (1977).

4. W. Jänig, *Brain Res.* **28**, 203–216 (1971).
5. R. S. Johansson, *J. Physiol.* **281**, 101–125 (1978).
6. M. Paré, A. M. Smith, F. L. Rice, *J. Comp. Neurol.* **445**, 347–359 (2002).
7. D. T. Blake, S. S. Hsiao, K. O. Johnson, *J. Neurosci.* **17**, 7480–7489 (1997).
8. W. H. Talbot, I. Darian-Smith, H. H. Kornhuber, V. B. Mountcastle, *J. Neurophysiol.* **31**, 301–334 (1968).
9. A. Iggo, A. R. Muir, *J. Physiol.* **200**, 763–796 (1969).
10. C. J. Woodbury, H. R. Koerber, *J. Comp. Neurol.* **505**, 547–561 (2007).
11. D. Biemesderfer, B. L. Munger, J. Binck, R. Dubner, *Brain Res.* **142**, 197–222 (1978).
12. S. Vrontou, A. M. Wong, K. K. Rau, H. R. Koerber, D. J. Anderson, *Nature* **493**, 669–673 (2013).
13. H. Olausson *et al.*, *Nat. Neurosci.* **5**, 900–904 (2002).
14. Z. Halata, M. Grim, K. I. Bauman, *Anat. Rec. A Discov. Mol. Cell. Evol. Biol.* **271A**, 225–239 (2003).
15. Z. Halata, B. L. Munger, *Brain Res.* **371**, 205–230 (1986).
16. C. Shih, C. J. Cold, C. C. Yang, *J. Sex. Med.* **10**, 1783–1789 (2013).
17. S. M. Maricich *et al.*, *Science* **324**, 1580–1582 (2009).
18. W. Hartschuh, E. Weihe, *J. Invest. Dermatol.* **75**, 159–165 (1980).
19. M. Mihara, K. Hashimoto, K. Ueda, M. Kumakiri, *J. Invest. Dermatol.* **73**, 325–334 (1979).
20. B. M. Fagan, P. M. B. Cahusac, *Neuroreport* **12**, 341–347 (2001).
21. T. E. Finger *et al.*, *Science* **310**, 1495–1499 (2005).
22. M. LeMasurier, P. G. Gillespie, *Neuron* **48**, 403–415 (2005).
23. R. Ikeda *et al.*, *Cell* **157**, 664–675 (2014).
24. S.-H. Woo *et al.*, *Nature* **509**, 622–626 (2014).
25. S. Maksimovic *et al.*, *Nature* **509**, 617–621 (2014).
26. N. Cauna, *Am. J. Anat.* **99**, 315–350 (1956).
27. C. Idé, *Am. J. Anat.* **147**, 329–355 (1976).
28. M. Bentivoglio, P. Pacini, *Brain Res. Bull.* **38**, 161–165 (1995).
29. N. Cauna, G. Mannan, *J. Anat.* **92**, 1–20 (1958).
30. M. Knibestöl, *J. Physiol.* **232**, 427–452 (1973).
31. A. J. Brisben, S. S. Hsiao, K. O. Johnson, *J. Neurophysiol.* **81**, 1548–1558 (1999).
32. M. Sato, *J. Physiol.* **159**, 391–409 (1961).
33. N. Cauna, L. L. Ross, *J. Biophys. Biochem. Cytol.* **8**, 467–482 (1960).
34. H. Takahashi-Iwanaga, H. Shimoda, *J. Neurocytol.* **32**, 363–371 (2003).
35. D. C. Pease, T. A. Quilliam, *J. Biophys. Biochem. Cytol.* **3**, 331–342 (1957).
36. L. Pawson, N. B. Slepecky, S. J. Bolanowski, *Somatosens. Mot. Res.* **17**, 159–170 (2000).
37. P. S. Spencer, H. H. Schaumburg, *J. Neurocytol.* **2**, 217–235 (1973).
38. W. R. Loewenstein, R. Skalak, *J. Physiol.* **182**, 346–378 (1966).
39. L. Pawson, A. K. Pack, S. J. Bolanowski, *Somatosens. Mot. Res.* **24**, 85–95 (2007).
40. L. Pawson *et al.*, *J. Neurosci.* **29**, 2695–2705 (2009).
41. F. L. Rice, B. L. Munger, *J. Comp. Neurol.* **252**, 186–205 (1986).
42. A. Iggo, *J. Physiol.* **152**, 337–353 (1960).
43. A. G. Brown, A. Iggo, *J. Physiol.* **193**, 707–733 (1967).
44. M. Koltzenburg, C. L. Stucky, G. R. Lewin, *J. Neurophysiol.* **78**, 1841–1850 (1997).
45. S. G. Lechner, G. R. Lewin, *Physiology* **28**, 142–150 (2013).
46. L. S. Löken, J. Wessberg, I. Morrison, F. McGlone, H. Olausson, *Nat. Neurosci.* **12**, 547–548 (2009).
47. A. Vallbo, H. Olausson, J. Wessberg, U. Norrsell, *Brain Res.* **628**, 301–304 (1993).
48. L. Li, D. D. Ginty, *eLife* **3**, e01901 (2014).
49. T. Yamamoto, *J. Electron Microsc.* **15**, 158–166 (1966).
50. J. Hu, L.-Y. Chiang, M. Koch, G. R. Lewin, *EMBO J.* **29**, 855–867 (2010).

ACKNOWLEDGMENTS

We thank members of the Ginty laboratory for helpful discussions and comments on this manuscript. Our research addressing the organization and function of LTMRs and their circuits is supported by NIH grants R01 NS34814 and R01 DE022750 (to D.D.G.). D.D.G. is an investigator of the Howard Hughes Medical Institute.

10.1126/science.1254229

REVIEW

Dialogue between skin microbiota and immunity

Yasmine Belkaid[1]* and Julia A. Segre[2]*

Human skin, the body's largest organ, functions as a physical barrier to bar the entry of foreign pathogens, while concomitantly providing a home to myriad commensals. Over a human's life span, keratinized skin cells, immune cells, and microbes all interact to integrate the processes of maintaining skin's physical and immune barrier under homeostatic healthy conditions and also under multiple stresses, such as wounding or infection. In this Review, we explore the intricate interactions of microbes and immune cells on the skin surface and within associated appendages to regulate this orchestrated maturation in the context of both host physiological changes and environmental challenges.

Multicellular organisms exist as metaorganisms composed of both the macroscopic host and symbiotic commensal microbiota. Compartmentalized barrier tissues such as the skin are a complex composite of microbes and host structural, hormonal, nervous, and immunological networks. The development of defined arms of the immune system, particularly adaptive immunity, has coincided with the acquisition of complex microbiota, suggesting that a large fraction of this host complexity has evolved to maintain this symbiotic relationship. In turn, microbiota can regulate multiple aspects of the immune system. However, this alliance may also come at a price when extrinsic and intrinsic factors, such as diet, indoor heating, and use of antibiotics, change rapidly. Profound changes in the microbiota and as a direct result, the immune system, are now believed to contribute to the dramatic and rapid increase in chronic inflammatory and autoimmune disorders seen in high-income countries. Indeed, while each inflammatory disease is associated with specific genetic and biological mechanisms, many inflammatory diseases are also associated with shifts in the resident microbiota from a "healthy" to a "diseased" state. These diseases can therefore be viewed as dysbiotic host-microbial metaorganismal states.

Skin microbial diversity and plasticity

The skin is home to a myriad of microbial communities residing on the tissue surface, as well as in associated appendages, such as hair follicles and sebaceous glands (*1*–*3*). Skin is a stratified, cornified epithelium of basal stem cells that undergo a 4-week process of terminal differentiation to become enucleated cross-linked sacs of proteins cemented together by extruded lipids (*4*, *5*). Across the 1.8 m^2 of skin surface, 1 million bacteria reside per square centimeter for a total of over 10^{10} bacterial cells covering a human (*6*). However, the skin's surface is quite diverse, consisting of different microenvironments with distinct pH, temperature, moisture, sebum content, and topography (*1*). These niche-specific physiologic differences influence the resident bacteria (*2*, *3*) and fungi (*7*); oily surfaces like the forehead support lipid-loving bacteria that differ from dry, low-biomass sites like the forearm (Fig. 1).

Surveys of discrete skin sites, selected for predilection to microbial infections, demonstrated that skin physiology (moist, dry, or sebaceous) is the organizing principle of bacterial communities. Sebaceaous sites are dominated by lipophilic *Propionibacterium* species, while humidity-loving *Staphylococcus* and *Corynebacterium* species are abundant in moist areas. Fungi of the genus *Malassezia* dominate core-body and arm sites, while foot sites, which are major sites of fungal infection, are colonized by a more diverse combination of *Malassezia*, *Aspergillus*, *Cryptococcus*, *Rhodotorula*, *Epicoccum*, and others (*7*) (Fig. 1).

The vast majority of the human-associated microbes reside within the rich gut milieu. By contrast, the skin habitat is less hospitable and nutrient poor (*8*) (Table 1 and Fig. 2). The skin surface is cool, acidic, desiccated, and bathed in sweat with only sebum and skin stratum corneum peptides and lipids as nutrients. Moreover, sweat is salt-laden and replete with antibacterial molecules, such as free fatty acids and antimicrobial peptides (AMPs), natural antibiotics that represent an evolutionarily ancient arm of protective responses (*8*). Yet humans and their commensal microbial communities have coevolved to provide mutual benefit. Some strains of the predominant skin symbiotic *Staphylococcus* are tolerant of high salt and may even utilize the urea present in sweat as a nutrient (*9*). Sebaceous glands secrete lipid-rich sebum, a hydrophobic coating that protects and lubricates hair and skin.

[1]Program in Barrier Immunity and Repair and Mucosal Immunology Section, Laboratory of Parasitic Diseases, National Institute of Allergy and Infectious Disease, National Institute of Health (NIH), Bethesda, MD, USA. [2]Microbial Genomics Section, Translational and Functional Genomics Branch, National Human Genome Research Institute, NIH, Bethesda, MD, USA.
***Corresponding author. E-mail: ybelkaid@niaid.nih.gov (Y.B.); jsegre@nhgri.nih.gov (J.A.S.)**

Although sebum generally serves as an antibacterial coating, *Propionibacterium acnes* hydrolyzes triglycerides present in sebum, releases free fatty acids that promote bacterial adherence, and then colonizes sebaceous units (*10*). Many *Malassezia* and *Corynebacterium* species do not produce their own lipids and must obtain them from their environment, which makes them well-suited to reside on skin whose most abundant resource is the lipid-rich content of sebum and skin stratum corneum.

The gut microbiota eventually converge toward an adultlike profile during the first years of life with dramatic transient shifts, presumably when a new microbe is ingested or other normal developmental processes (*11*, *12*). For the skin, one might imagine shifts associated with the exploration of new environments through crawling, walking, and increased socialization. Examination of a birth cohort's skin microbial succession awaits further study. Major shifts are occurring during the first few years of human life, which is also the time when the immune system is maturing and being educated. Gut communities are perturbed by antibiotics, after which the individual may return to their previous state or a "new normal" (*13*, *14*). Skin bacterial communities, however, go through a major shift with sexual maturation and the transition through puberty (Table 1). The skin microbiome of young children and adolescent/postadolescent individuals clustered into two distinct groups. *Streptococcus*, *Betaproteobacteria*, and *Gammaproteobacteria* dominated the microbial communities of children (*15*). In contrast, postadolescent young adults had few to none of these taxa; their microbiomes were dominated instead by lipophilic bacteria, including *Propionibacterium* and *Corynebacterium*. Subsets within the larger immune system of skin are functionally distinct in younger individuals and may permit the colonization and growth of a wider range of bacteria, consistent with the higher community-wide diversity observed in younger children.

Very recent work has moved beyond amplicon-based studies to direct sequencing of all microbial DNA (shotgun metagenomics) to analyze more fully the functional and taxonomic landscape of the human skin microbiome as shaped by the local biogeography (*16*). This inclusive, relational analysis of the bacterial, fungal, and viral communities showed not only site specificity but also unique individual signatures. Similar to results from amplicon studies, shotgun metagenomics confirmed that microbial communities were shaped primarily by the microenvironment in which differential abundance of taxa such as *P. acnes*, commensal staphylococci, and *Corynebacterium* contributed most significantly to variation both between and within individuals. However, with more genomic information, relationships between different microbial communities were apparent. For example, Fungi, primarily *Malassezia,* represented a small fraction of the community, except near the ears and forehead, which had a higher fungal presence. The feet had low fungal relative abundance (<1%) despite high diversity observed in amplicon-based studies (*7*) (Fig. 1).

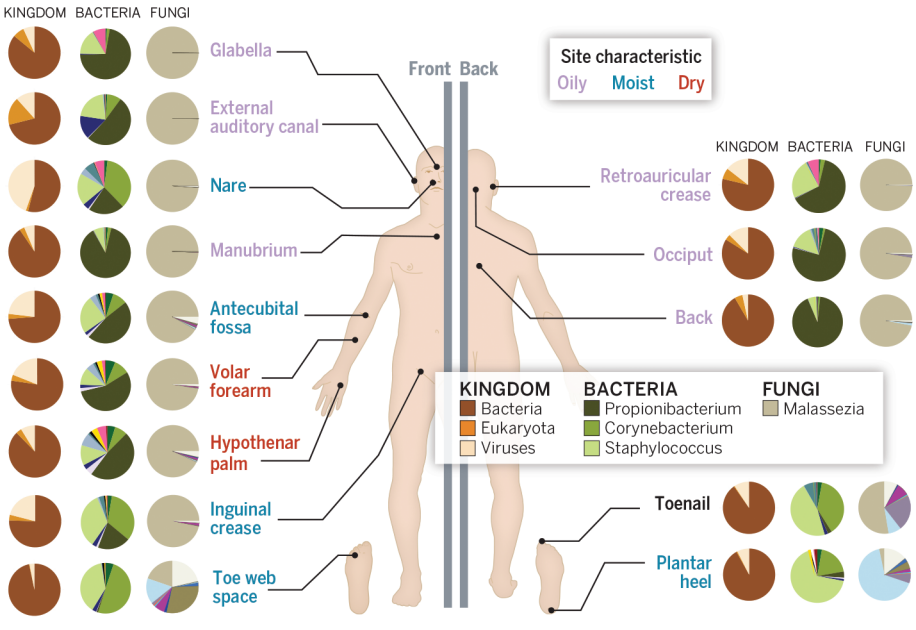


Fig. 1. Skin shotgun metagenomics defines relative abundance of viral, bacterial, and fungal components of the microbial community. Sites represent three microenvironments: sebaceous (blue), dry (red), and moist (green). Toenail (black) is a site that does not fall under these major microenvironments and is treated separately. Pie charts represent consensus relative abundance of the different categories kingdom, bacteria, and fungi. For bacteria and fungi, major taxa colors are identified in the legend. Relative proportion of minor taxa are colored to represent relative proportion.

Shotgun metagenomic sequencing now empowers studies of interkingdom interactions (e.g., bacterial-fungal) to explore how these relationships exacerbate disease severity or facilitate a transition between opportunism and pathogenicity (*17*). Moreover, shotgun metagenomic sequencing demonstrates the extensive strain-level diversity for dominant skin bacterial species, suggesting that both the individual and the microenvironment differentially shape subspecies variation. While *P. acnes* strains were more individual-specific, *S. epidermidis* strains were significantly more site-specific with diminished interindividual variation. Strains of species may vary dramatically in their genome content, their ability to perform critical microbial functions, and their relationship with the immune system. For example, the variable component of the genome of *S. epidermidis* was enriched in genes encoding functions such as repair, transcriptional regulators, and defense mechanisms, all gene pools that one could imagine impact intermicrobial and microbial-host interactions (*18*).

With increasing concerns of antibiotic-resistant microorganisms, shotgun metagenomics also empowers an exploration of the reservoir of antibiotic resistance genes in the skin. Although skin is physically compartmentalized from other body sites, cross-inoculation remains a risk factor. For example, the nares can harbor methicillin-resistant *Staphylococcus aureus* (MRSA), which causes skin and soft-tissue infections (*19*). Antibiotic resistance potential is host- and site-specific, such as multi-antimicrobial extrusion efflux pump genes found only on specific healthy individuals, whereas lincosamide resistance genes were found across multiple individuals, specifically on the three foot sites examined (*16*). While resistance activity may differ in vivo, these studies point to the pervasive antimicrobial resistance potential encoded in healthy humans.

The extent to which the human host benefits from resident microbes remains under investigation. For example, the commensal skin bacterium *S. epidermidis* was shown to inhibit both nare colonization and biofilm formation by *S. aureus*. A subset of *S. epidermidis* expresses the *Esp* gene, which can synergize with a human-expressed AMP to interfere with *S. aureus* colonization (*20*). Meanwhile, MRSA colonization may have been enhanced when the now dominant USA300 strain acquired the arginine catabolic mobile element horizontally from *S. epidermidis* (*21*). Although better described for gut microbiota, skin microbiota are likely to compete for resources with pathogenic microbes for defined metabolites in a process referred to as colonization resistance (Table 1) (*22*–*24*). Commensals can also promote the establishment of an environment hostile to pathogen establishment by affecting the local pH (*25*).

Skin microbiota–immunity dialog

The skin is equipped with a highly sophisticated system of immune surveillance that results from the combined action of a rich network of epithelial

cells, lymphocytes, and antigen-presenting cells that populate the epidermis and the dermis (*26*). When operating optimally, the skin immune system interweaves the innate and adaptive arms of immunity in a dialogue that selects, calibrates, and terminates responses in the most appropriate manner. One of these fundamental processes involves tissue repair, a response that can be controlled by defined components of the skin microbiota. Acute skin damage releases ligands that activate keratinocytes and trigger the release of inflammatory mediators (*27*). In these settings, a defined product of *S. epidermidis*, lipoteichoic acid, can mitigate inflammation and promote wound healing through its capacity to bind to the innate immune receptor, Toll-like receptor (TLR) 2 (*27*).

In contrast to the known role of the gut microbiota in the control of the development of gut-associated lymphoid structures, skin commensals are not required for the seeding of immune cells and overall organization of the tissue (Table 1) (*28*, *29*). However, skin-resident microbes do control the expression of various innate immune factors, including AMPs (*9*). Epithelial cell AMPs belong to multiple protein families, which in the skin are dominated by cathelicidins and β-defensins (*9*). These molecules can rapidly kill or inactivate a diverse range of skin pathogens, including Gram-negative and Gram-positive bacteria, fungi, viruses, and parasites (*30*). Whereas some of these molecules are constitutively expressed, the expression of others is controlled by defined members of the microbiota such as Propionibacterium species (*31*, *32*). How AMPs, and more particularly the ones induced by the microbiota, shape microbial communities remains unclear, but this dialogue is likely to play a fundamental role in the skin microbial ecology.

The skin microbiota also promotes the expression of other potent and highly conserved pathways of host defense. For instances, skin-resident microbes can increase expression of components of the complement system. This system is composed of a large number of proteins that react with one another to opsonize pathogens and induce inflammatory responses that promote clearance of pathogens. In mice raised in the absence of live microbes (germ-free), impaired expression of the complement component C5aR results in decreased expression of antimicrobial peptides and proinflammatory factors, alterations that are associated with dysbiosis of skin-resident microbes (*33*). The skin microbiota also controls the level of expression of interleukin-1 (IL-1), a cytokine involved in the initiation and amplification of immune responses (*28*). Of note, AMPs, the complement system, and IL-1 all represent ancient arms of the innate immune system, suggesting that these pathways may have arisen as early mediators of host skin-commensal interaction.

Table 1. Comparison of skin and gut microbial communities and effect on the immune system.

	Gut	Skin
Density	10^{12}/g of intestinal matter	10^{6}/cm^{2}
Diversity	Bacteria dominant 7–8 phyla of bacteria ~100 species/individual Fungi and virus (non-phage) rare	Bacteria dominant 7–8 phyla of bacteria ~40 species/individual Up to 10% fungi and 40% viral/phage colonization
Niche	Mucus Epithelial surfaces Crypts	Strateum corneum (surface) Appendages (sebaceous glands, hair follicle, sweat glands)
Community establishment	Early life	Early life Puberty
Nutrients	Rich Dietary (sugars, proteins, lipids) Bacterial metabolic products Mucus	Poor Sweat Sebum Stratum corneum (peptides, lipids)
Effect on the immune system	Secondary lymphoid structure development Adjuvant effect (innate immune activation) Regulation Functional Tuning Colonization resistance	Functional tuning Colonization resistance
Range of the effect	Local Systemic (e.g arteries, bone marrow)	Local ?

Control of adaptive immunity by skin commensals

A downstream consequence of the effect of the skin microbiota on innate immunity is enhanced activation of lymphocytes both at steady state and during infection and an overall increase of adaptive immunity (*28*). As such, the skin microbiota acts as an endogenous adjuvant of the skin immune system. Skin commensals modulate the function of local T cells through their capacity to tune the local innate immune milieu and in particular IL-1 production (*28*). This action of skin commensals results in increased potential for the production of cytokines involved in both host defense and inflammatory diseases such as IL-17-A and interferon-γ (IFN-γ) by dermal T cells. The skin flora controls immune homeostasis and responses to infection in an autonomous manner and independently of the gut flora (*28*), suggesting that under steady-state conditions or in the context of local inflammation, each barrier site is likely to be controlled independently of other commensal niches. Furthermore, commensals may have evolved to specifically control the immunological network associated with their ecological niches. This compartmentalization and specialization of responses may have evolved as a mechanism to constrain the adjuvant properties of commensals and unwanted consequences associated with systemic inflammatory responses.

Because of the extraordinary pressure exerted by the microbiota on the immune system, the highest number of immune cells in the body is at sites colonized by commensals. In particular, the healthy human skin harbors ~20 billion effector lymphocytes, making it one of the largest reservoirs of memory T cells in the body (*34*). We speculate that a large fraction of tissue-resident lymphocytes may recognize skin microbiota-derived antigens. Indeed, recent observations reveal that, in the gastrointestinal tract, a large fraction of T helper 17 (T_H17) cells are specific for commensals (*35*–*37*). In an analogous manner, IL-17 produced by skin commensal-specific T cells could reinforce skin immunity through its action on keratinocytes' antimicrobial function. In support of this, mice lacking adaptive immunity fail to efficiently contain their skin microbiota, leading to microbial dissemination to the regional lymph node (*38*). Collectively, these results reveal that through their capacity to promote various aspects of innate and adaptive

responses, the skin microbiota not only limit pathogenic microbial invasion but also reinforce its own stability and containment.

In the gastrointestinal tract, defined microbes and products of microbial metabolism can promote immune homeostasis by controlling the induction, function, and homeostasis of the regulatory immune network (*29*). Albeit less documented in the skin, a few examples suggest that this may be also true for environmental microbiota that can interface with the skin. For instance, epicutaneous exposure to a lysate of *Vitreoscilla filiformis*, a Gram-negative bacterium originally found in thermal spa water, can promote the induction of tissue-resident regulatory T cells and inhibit T cell proliferation during cutaneous inflammation in mice (*39*, *40*). Thus, the immune landscape of the skin may not be under the sole control of its resident microbes—transient partners may also play an important role in setting the skin threshold of activation.

How skin commensal products or antigens are recognized by the immune system and the cellular mediators involved in this dialogue remain largely unknown. We could speculate that analogous to the gastrointestinal tract (*41*), tissue-resident dendritic cells, surrounding the rich commensal communities associated with appendages such as the hair follicle, may be able to directly capture microbes or microbial products. Further, microbial secreted metabolites or their downstream products may be able to diffuse from these niches and be captured or sensed by neighboring cells (Fig. 2).

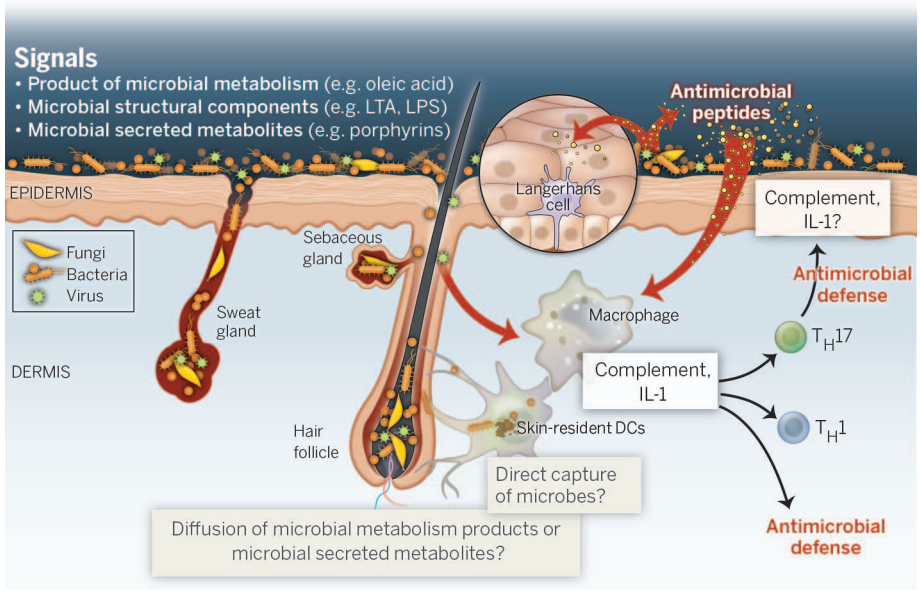


Fig. 2. Cross-talk between the microbiota and the skin immune system. Microorganisms (virus, fungi, bacteria) cover the skin surface and reside in appendages (hair follicle, sebaceous glands, and sweat glands). These microbes can directly produce antimicrobial peptides and control the production of antimicrobial peptides by keratinocytes, as well as the production of cardinal mediators of immunity such as complement and IL-1. These molecules can directly or indirectly enhance skin immunity by promoting cytokine production, enhancing cell microbicidal function, and promoting the recruitment of effector cells. Enhanced production of IL-17 by the microbiota may promote keratinocyte effector function against invading microbes. Skin-resident microbes may exert their function via the release of defined products or metabolites and/or could be directly captured by skin-resident dendritic cells (DCs).

Immune regulation of microbiota in human primary immunodeficiency patients

Although landmark studies have shown that microbiota activate and educates host immunity, how the immune system shapes microbial communities and contributes to disease is less-well characterized. An open question is the extent to which symbiotic bacteria are selected for mutualistic interactions with the human host based on the limited ecological niches of human tissues versus a more active modulation of microbial communities by the immune system. Studying primary immunodeficiency (PID) patients provides a unique perspective on the degree to which altered immunity may influence the human microbiome and how, in turn, microbiota may interact with the host to develop disease. Skin of PID patients displayed increased ecological permissiveness with decreased site specificity and temporal stability, and colonization with microbial species not observed in controls, such as *Clostridium* species and *Serratia marcescens* (*42*). The overarching theme of increased ecological permissiveness in PID skin was counterbalanced by the maintenance of a phylum barrier in which colonization remained restricted to the typical human-associated phyla. Extending these studies into mouse models of immune deficiency could begin to tease apart the functional role of immunity in shaping microbial communities under homeostatic conditions and the stress of infection.

Potential association of the microbiota with skin inflammatory disorders

Common skin disorders such as psoriasis, atopic dermatitis, and acne have all been associated with dysbiosis of the skin flora (*43*). While understanding the initiating event is crucial to early disease diagnosis and molecular interventions, breaking the escalating danger signals that cycle between skin microbial, structural, and immunologic cells can also provide clinical benefit. Atopic dermatitis (AD; commonly known as eczema) has long been associated with *S. aureus* skin colonization or infection and is typically managed with regimens that include antimicrobial therapies. However, the role of microbial communities in the pathogenesis of AD is incompletely characterized. A longitudinal study of microbial diversity of AD showed that the proportion of *Staphylococcus* and in particular *S. aureus* was greater during disease flares (episodic exacerbation) and correlated with worsened disease severity (*44*). However, the clinical effectiveness of AD treatments does not rely on the total elimination of *S. aureus*, suggesting that therapeutic modalities may act to recalibrate the diversity of the skin microbiome. AD patients using no treatment during flares exhibited markedly reduced bacterial diversity on affected sites, leading to the hypothesis that lesional skin requires continued intensive treatment to sufficiently reduce the inflammatory response. Increases in diversity associated with AD treatments may be due to therapies that preferentially kill *S. aureus*, promote growth of microbes that control *S. aureus* predominance, or reduce bacterial biomass, followed by rapid repopulation with a diverse community.

The prevalence of AD has more than doubled in industrialized countries with no clear cause (*45*, *46*) and at a high cost (*47*). More than half of children with moderate to severe AD develop hay fever and/or asthma, atopic disorders associated with substantial morbidity and rare mortality, a phenomena called the "atopic march." Mutations in *FLG*, the gene encoding the skin barrier protein filaggrin, are associated with AD, particularly in patients who subsequently develop asthma or hay fever (*48*). Since FLG is not expressed in nasal or lung epithelia, this genetic association suggests that skin microbial exposure sets the stage for other atopic disorders later in life. A question of active investigation is whether, in the context of inflammation, the skin microbiota could act distally and prime the subsequent immune response observed in lungs and nasal passages. Such an effect could be mediated by diffusion of microbial products or metabolites or through direct means, whereby

skin microbes may be seeding lung and nasal epithelium. These types of distal effects of the gut microbial communities on atherosclerosis and hematopoiesis have been some of the most intriguing recent findings in the field (*49*, *50*),

Lesional psoriasis is a chronic T cell–mediated skin disease affecting ~1 to 3% of the U.S. and European populations (*51*). Notably, lesional skin from plaque psoriatic patients is more diverse, enriched in *Streptococcus* spp. with reduced *P. acnes* (*52*). Although most studies have focused on the common psoriasis vulgaris, only the subtype of guttate psoriasis has been associated with a microbial streptococcal infections (*53*).

The classic feature of teenage acne vulgaris is sebaceous hyperplasia and lipid release into the follicular lumen, which leads to a clogged pore (*54*). This process results in follicular wall rupture, triggering neutrophil influx and pustule formation, a process that is further amplified by the capacity of *P. acnes* to activate keratinocytes (*55*). However, the confounding issue of assigning a causative role to *P. acnes* in disease initiation is that *P. acnes* predominates on both normal and disease-associated skin (*56*, *57*). Genomic comparison of *P. acnes* strains explored whether there might be functional differences of *P. acnes* in functioning as a commensal in healthy skin and as a pathogen in diseases (*57*, *58*). However, elucidation will require longitudinal studies to track adolescents transitioning through puberty and functional studies performed in animal models.

As previously discussed, the skin microbiota can promote responses (IL-1, IL-17A, complement) that play an important role in host defense but also contribute to the etiologies of various inflammatory disorders. For instance, the IL-1 pathway that is promoted by skin-resident commensals is also linked to a multitude of chronic inflammatory disorders, including psoriasis and other cutaneous disorders (*59*). Psoriatic plaques are also characterized by marked infiltration of activated T cells, producing inflammatory cytokines and in particular cytokines of the IL-17 family such as IL-17A that have been recently associated with the pathogenesis of the disease (*60*, *61*). Some of the pathogenic role of IL-17A results from its capacity to amplify various inflammatory pathways in the skin, leading to keratinocyte hyperproliferation and lesion formation in psoriasis (*62*, *63*). Additionally, in the context of inflammation, changes in barrier permeability and enhanced contact with commensals could further promote the local inflammatory process. Given the capacity of the microbiota to control both innate and adaptive immunity, resident microbes are likely primary drivers and amplifiers of skin pathologies (Fig. 3).

Whether alterations of the microbial composition described in various disease states are the results of inflammation rather than the cause remains difficult to evaluate. Furthermore, an important point to consider when exploring the potential role of the microbiota in inflammation is that pathogenicity is, in most cases, a contextual state. Indeed, the capacity of a given microbe to trigger or promote disease is highly dependent on the state of activation of the host, the host's genetic predisposition, the localization of the particular microbe, or the coexistence of other microbial members (*64*) (Fig. 3). Thus, the culprit microbe may remain elusive in most cases. Nonetheless, we could envision several mechanisms by which microbes or microbial communities could contribute to the initiation or amplification of skin pathologies (Fig. 3). For instance, local expansion of defined commensals with enhanced inflammatory potential could trigger disease states in susceptible individuals. For example, colonization of the skin with *S. aureus* triggers local allergic responses by releasing δ-toxin, which directly induces the degranulation of dermal mast cells and in turn promotes both innate and adaptive type 2 immune responses (*65*). In addition to the relative enrichment of defined microbes, increase in microbial load itself may be sufficient to trigger aberrant production of AMPs and keratinocyte proliferation, or as previously discussed, promote the local production of inflammatory mediators. Increased bacterial density can be observed in the context of chronic diabetic wounds in a murine model of type 2 diabetes where nonhealing wounds are associated with increased abundance of *Staphylococcus* spp. (*66*). Thus, in the context of defined metabolic diseases, altered nutrient availability and sustained inflammatory states could contribute to the emergence and dominance of bacteria that either qualitatively or quantitatively alter the local inflammatory milieu and promote local pathologies. All of these effects could be amplified in the context of altered barrier integrity mediated

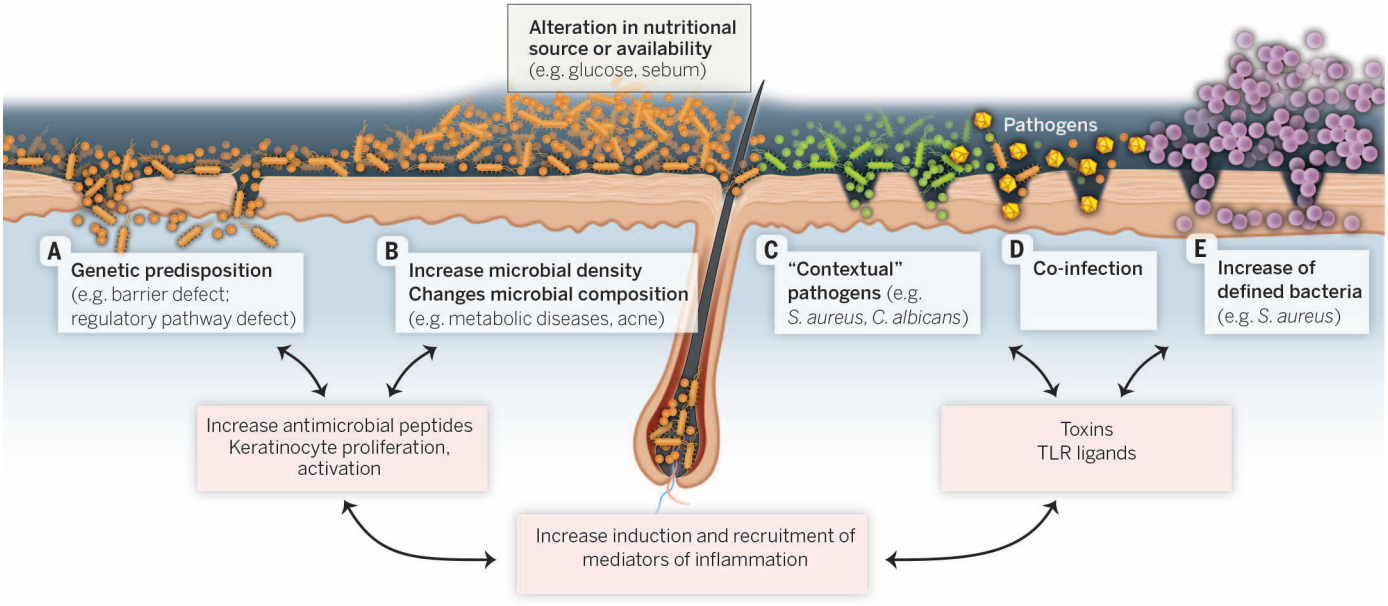


Fig. 3. Potential mechanisms by which the skin microbiota may initiate or amplify skin disorders. (**A**) Enhanced sensing or translocation of the microbiota can be mediated by host genetic predispositions (e.g., filaggrin, IL-23, IL-10 mutation). (**B**) Metabolic diseases (e.g., diabetes) associated with alteration of nutrients could lead to enhanced microbial density and dysbiosis. (**C**) In the context of barrier breach, normal constituents of the microbiota could act as pathogens. (**D**) In the context of infection, skin microbes may contribute to inflammation and tissue damage. (**E**) Microbes with inflammatory potential may dominate, an event that can also be promoted by antibiotic treatment or environmental alterations. In most settings, combinations of the various scenarios are likely required to trigger pathologies. In turn, enhanced inflammation can alter microbial communities, a process that can further amplify tissue damage.

by inflammation and/or genetic predisposition (Fig. 3).

Future therapeutic potential to modulate skin immunologic and microbial constituency

Although the relationships between microbiota, host, and disease are complex, investigators have long relied upon Koch's postulates to impute causation between microorganism and disease. However, the requirement that disease-causing microorganisms uniformly recapitulate disease in healthy individuals was compromised when Koch discovered asymptomatic carriers of *Vibrio cholera* and *Salmonella typhi*, revealing the important distinction between apparent colonization and infection (*67*). Potential pathogenicity of bacteria that colonize humans is likely influenced by host immunologic factors and the native microbial community. This paradigm requires that diseases with microbial involvement must be investigated within the context of their microbial community, host factors, and immunity.

Longitudinal plasticity of the microbial and immunologic communities is one of the great complications of this research, but also one of the greatest potential benefits for designing probiotic or prebiotic therapies. Studies of metabolic capacity, pathogenicity islands, and virulence genes in disease states, with our catalog from healthy skin, will uncover biomarkers associated with transmission, recurrence, and severity of disease. Finally, characterization and tracking of surprisingly pervasive antibiotic resistance elements will remain clinically relevant, as skin sites can serve as a taxonomic and genetic reservoir for pathogens. We envision a new therapeutic landscape leveraging unique metagenomic profiles with tailored clinical interventions that reshape our microbial communities. Notably, because of the scarcity of nutrients available for the skin microbiota, the opportunity for prebiotic-based therapy in this tissue may be unmatched. In these arid conditions, subtle alterations in defined nutrient availability may have a dramatic impact on the skin microbiota composition and when rationally designed could provide a powerful advantage for microbes endowed with regulatory or protective properties. While humans typically use creams to moisturize their skin and improve barrier function, this product is also fertilizing the microbial garden. As such, topical products could be designed to specifically shape microbial communities.

Finally, the capacity of skin-resident and potentially transient partners to modulate local immunity could be harnessed. One major impediment in the development of vaccine adjuvants for clinical use is associated unacceptable amounts of inflammation. As previously discussed, the skin microbiota is likely to have coevolved with its host to finely tune the unique requirements of this tissue. Consequently, these microbes may release or engage highly adapted tissue-specific adjuvants. A search for these products and mechanisms associated with the stimulatory effect of the microbiota may allow development of a novel class of adjuvants capable of boosting local immunity while preserving tissue homeostasis. Further, as our arsenal of antimicrobial weapons falls short in the battle against multidrug-resistant pathogens, perhaps therapeutics derived from microorganisms themselves offer promise as viable alternatives.

Conclusions

While we can now imagine how to characterize the language encoded by the representative cell types, how is context encoded into the language spoken by the microbes and immune cells? A classic feature of dermatologic disorders of microbial etiology is their manifestation at stereotypical sites and at different times of human development such as AD in the bend of the elbow during early childhood, acne on forehead and back during puberty, and psoriasis on the outer elbow with onset in the second or third decade of life. While long appreciated that the rolls of skin of a baby's neck are quite different from the oily forehead of a teenager, only the last few years of research have begun to tease out the specificity of the microbial and immunologic cells that inhabit these very specific skin niches.

Language differs from communication in that language is deeply entrenched in human culture. Humans acquire language through social interaction in early childhood, and children generally speak fluently when they are about 3 years old. However, specificity and fine-tuning of language continue throughout life with specialization. By analogy, microbial communities acquired at birth are very dynamic for early years of life, and immune cells mature during postnatal development. Just as children begin to appreciate the context of their words on the playground versus the dinner table, immune-microbe interactions are context dependent. In addition to its strictly communicative uses, language also has many social and cultural uses, such as signifying group identity, and social stratification. Analogously, studies are just beginning to explore how cohabitation or early microbial exposures may link humans across space and time.

REFERENCES AND NOTES

1. E. A. Grice, J. A. Segre, *Nat. Rev. Microbiol.* **9**, 244–253 (2011).
2. E. A. Grice *et al.*, *Science* **324**, 1190–1192 (2009).
3. E. K. Costello *et al.*, *Science* **326**, 1694–1697 (2009).
4. C. Blanpain, E. Fuchs, *Science* **344**, 1242281 (2014).
5. F. M. Watt, *Science* **346**, 937–940 (2014).
6. E. A. Grice *et al.*, *Genome Res.* **18**, 1043–1050 (2008).
7. K. Findley *et al.*, *Nature* **498**, 367–370 (2013).
8. T. C. Scharschmidt, M. A. Fischbach, *Drug Discov. Today Dis. Mech.* **10**, e83–e89 (2013).
9. R. L. Gallo, L. V. Hooper, *Nat. Rev. Immunol.* **12**, 503–516 (2012).
10. R. R. Marples, D. T. Downing, A. M. Kligman, *J. Invest. Dermatol.* **56**, 127–131 (1971).
11. C. Palmer, E. M. Bik, D. B. DiGiulio, D. A. Relman, P. O. Brown, *PLOS Biol.* **5**, e177 (2007).
12. J. E. Koenig *et al.*, *Proc. Natl. Acad. Sci. U.S.A.* **108** (suppl. 1), 4578–4585 (2011).
13. L. Dethlefsen, S. Huse, M. L. Sogin, D. A. Relman, *PLOS Biol.* **6**, e280 (2008).
14. T. Yatsunenko *et al.*, *Nature* **486**, 222–227 (2012).
15. J. Oh, S. Conlan, E. C. Polley, J. A. Segre, H. H. Kong, *Genome Med* **4**, 77 (2012).
16. J. Oh *et al.*, *Nature* **514**, 59–64 (2014).
17. A. Y. Peleg, D. A. Hogan, E. Mylonakis, *Nat. Rev. Microbiol.* **8**, 340–349 (2010).
18. S. Conlan *et al.*, *Genome Biol.* **13**, R64 (2012).
19. C. von Eiff *et al.*, *N. Engl. J. Med.* **344**, 11–16 (2001).
20. T. Iwase *et al.*, *Nature* **465**, 346–349 (2010).
21. B. A. Diep *et al.*, *Lancet* **367**, 731–739 (2006).
22. C. G. Buffie, E. G. Pamer, *Nat. Rev. Immunol.* **13**, 790–801 (2013).
23. D. Van der Waaij, J. M. Berghuis-de Vries, J. E. C. Lekkerkerk-van der Wees, *J. Hyg. (Lond.)* **69**, 405–411 (1971).
24. N. Kamada, G. Y. Chen, N. Inohara, G. Núñez, *Nat. Immunol.* **14**, 685–690 (2013).
25. Y. Turovskiy, K. Sutyak Noll, M. L. Chikindas, *J. Appl. Microbiol.* **110**, 1105–1128 (2011).
26. M. Pasparakis, I. Haase, F. O. Nestle, *Nat. Rev. Immunol.* **14**, 289–301 (2014).
27. Y. Lai *et al.*, *Nat. Med.* **15**, 1377–1382 (2009).
28. S. Naik *et al.*, *Science* **337**, 1115–1119 (2012).
29. Y. Belkaid, T. W. Hand, *Cell* **157**, 121–141 (2014).
30. Y. Lai, R. L. Gallo, *Trends Immunol.* **30**, 131–141 (2009).
31. I. Nagy *et al.*, *Microbes Infect.* **8**, 2195–2205 (2006).
32. D. Y. Lee *et al.*, *J. Invest. Dermatol.* **128**, 1863–1866 (2008).
33. C. Chehoud *et al.*, *Proc. Natl. Acad. Sci. U.S.A.* **110**, 15061–15066 (2013).
34. R. A. Clark *et al.*, *J. Immunol.* **176**, 4431–4439 (2006).
35. Y. Yang *et al.*, *Nature* **510**, 152–156 (2014).
36. Y. Goto *et al.*, *Immunity* **40**, 594–607 (2014).
37. E. Lécuyer *et al.*, *Immunity* **40**, 608–620 (2014).
38. W. Shen *et al.*, *Proc. Natl. Acad. Sci. U.S.A.* **111**, E2977–E2986 (2014).
39. T. Volz *et al.*, *J. Invest. Dermatol.* **134**, 96–104 (2014).
40. T. Nakatsuji, R. L. Gallo, *J. Invest. Dermatol.* **134**, 11–14 (2014).
41. M. Rescigno *et al.*, *Nat. Immunol.* **2**, 361–367 (2001).
42. J. Oh *et al.*, *Genome Res.* **23**, 2103–2114 (2013).
43. J. A. Sanford, R. L. Gallo, *Semin. Immunol.* **25**, 370–377 (2013).
44. H. H. Kong *et al.*, *Genome Res.* **22**, 850–859 (2012).
45. M. I. Asher *et al.*, *Lancet* **368**, 733–743 (2006).
46. T. E. Shaw, G. P. Currie, C. W. Koudelka, E. L. Simpson, *J. Invest. Dermatol.* **131**, 67–73 (2011).
47. D. R. Bickers *et al.*, *J. Am. Acad. Dermatol.* **55**, 490–500 (2006).
48. A. D. Irvine, W. H. McLean, D. Y. Leung, *N. Engl. J. Med.* **365**, 1315–1327 (2011).
49. R. A. Koeth *et al.*, *Nat. Med.* **19**, 576–585 (2013).
50. A. Khosravi *et al.*, *Cell Host Microbe* **15**, 374–381 (2014).
51. F. O. Nestle, D. H. Kaplan, J. Barker, *N. Engl. J. Med.* **361**, 496–509 (2009).
52. Z. Gao, C. H. Tseng, B. E. Strober, Z. Pei, M. J. Blaser, *PLOS ONE* **3**, e2719 (2008).
53. R. J. Chalmers, T. O'Sullivan, C. M. Owen, C. E. Griffiths, *Br. J. Dermatol.* **145**, 891–894 (2001).
54. W. D. James, *N. Engl. J. Med.* **352**, 1463–1472 (2005).
55. S. Jugeau *et al.*, *Br. J. Dermatol.* **153**, 1105–1113 (2005).
56. S. Fitz-Gibbon *et al.*, *J. Invest. Dermatol.* **133**, 2152–2160 (2013).
57. S. Tomida *et al.*, *MBio* **4**, e00003–e00013 (2013).
58. M. Bek-Thomsen, H. B. Lomholt, M. Kilian, *J. Clin. Microbiol.* **46**, 3355–3360 (2008).
59. J. E. Sims, D. E. Smith, *Nat. Rev. Immunol.* **10**, 89–102 (2010).
60. C. Leonardi *et al.*, *N. Engl. J. Med.* **366**, 1190–1199 (2012).
61. K. A. Papp *et al.*, *N. Engl. J. Med.* **366**, 1181–1189 (2012).
62. Y. Zheng *et al.*, *Nature* **445**, 648–651 (2007).
63. Y. Lai *et al.*, *Immunity* **37**, 74–84 (2012).
64. M. Otto, *Nat. Rev. Microbiol.* **7**, 555–567 (2009).
65. Y. Nakamura *et al.*, *Nature* **503**, 397–401 (2013).
66. E. A. Grice *et al.*, *Proc. Natl. Acad. Sci. U.S.A.* **107**, 14799–14804 (2010).
67. R. Koch, *BMJ* **2**, 403–407 (1884).

ACKNOWLEDGMENT

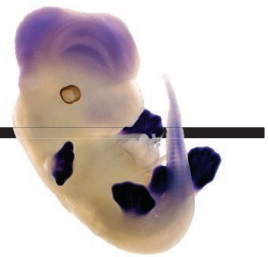
This work was supported by the Division of Intramural Research, National Institute of Allergy and Infectious Diseases, and National Human Genome Research Institute, National Institutes of Health. We thank A. Byrd, V. Ridaura, and T. Hand for discussion about the manuscript and help with the preparation of the figures. We apologize to our colleagues for not having cited all papers relevant to this expanding field because of space constraints.

10.1126/science.1260144

RESEARCH

Dissecting *Hox* gene regulation in mouse development

Lonfat et al., *p. 1004*



IN *SCIENCE* JOURNALS

Edited by **Stella Hurtley**



Tsangpo Gorge, Tibet

GEOMORPHOLOGY

Tibetan gorge avoids a tectonic aneurysm

Rapid tectonic uplift was responsible for the immense Tsangpo Gorge on the eastern edge of the Tibetan plateau 2.5 million years ago. Wang *et al*. found a buried canyon upstream from the gorge along the Yarlung Tsangpo River that began filling with sediments after sudden uplift. Drill cores of the buried canyon sediments show the same river gradient as found downstream of the gorge. The constant river gradient strongly suggests a rapid uplift event created the gorge, rather than river incision as previously believed. — BG

Science, this issue p. 978

CHROMOSOMES

A cohesin ring around two DNA strands

Holding together homologous sister chromosome pairs is a vital requirement during cell division and DNA repair. A special complex, called cohesin, forms a ring made of three different proteins and functions to hold together the two sister DNA strands. Gligoris *et al*. and Huis in `t Veld *et al*. identified a specific protein-protein interface within the cohesin ring that forms a DNA exit gate. Mutations in this interface prevented cohesion between sister chromatids. Thus, the cohesin ring must indeed encircle the two DNA strands to hold them together. — GR

Science, this issue p. 963, p. 968

OPTICS

Compensating optical loss for laser gain

Optical loss is thought to be detrimental to the operation of a laser, typically resulting in poor beam quality, multimode emission, and low efficiencies. Now results that take their cue from theoretical ideas of parity-time symmetry and implement them into the design of coupled laser components show that loss and gain can actually work together. Feng *et al*. and Hodaei *et al*. designed laser systems based on microring cavities to carefully control the amount of loss and gain within each component. The interplay between the loss and gain resulted in enhanced and cleaner emission from their lasers. — ISO

Science, this issue p. 972, p. 975

LIQUID STRUCTURE

Containing the nuclear elephant's foot

Molten nuclear fuel composed of large amounts of uranium dioxide is extremely dangerous. Liquid UO_2 has a high melting temperature and is very reactive, making it difficult to find a suitable sample container within which to study it. Skinner *et al*. bypassed the container and used instead a laser to heat beads of UO_2 levitated in a synchrotron x-ray beam with inert gas. They found an unexpected increase in the fluidity of molten nuclear fuel caused by a fall in the number of oxygen atoms surrounding each uranium cation. These findings are important when considering how to contain nuclear fuel during an accident. — BG

Science, this issue p. 984

EBOLA EPIDEMIOLOGY

Recharging Ebola mitigation measures

Effective drugs and vaccines for Ebola virus are not available, so what can be done? Pandey *et al*. used a mathematical model to analyze transmission in different scenarios: the community, hospitals, and at funerals. Achieving full compliance with any single control measure, such as case isolation, is impossible under prevailing conditions. However, with a minimum of 60% compliance, a combination of case isolation, hygienic burial, and contact tracing could reduce daily case numbers to single figures in 5 to 6 months. Success will also require persistence and sensitivity to local customs. — CA

Science, this issue p. 991

Downloaded from www.sciencemag.org on November 22, 2014

PHOTOS: (TOP TO BOTTOM) LONFAT *ET AL*.; FENG WEI PHOTOGRAPHY/GETTY IMAGES

Published by AAAS

TUBERCULOSIS

Using a diabetes drug to treat tuberculosis

The increasing prevalence of drug-resistant strains of *Mycobacteria tuberculosis*—the bacterium that causes tuberculosis (TB)—has led to a paradigm shift in the search for new drugs. Rather than targeting the bacterium itself, researchers are trying to augment host defenses. Now, Singh *et al.* report that the FDA-approved drug metformin, currently used to treat type 2 diabetes, can improve the immune response to *M. tuberculosis* infection. Metformin inhibited the growth of *M. tuberculosis* by enhancing specific immune responses in vitro and in infected mice. Furthermore, in human diabetic patients with TB, metformin treatment decreased TB severity. — ACC

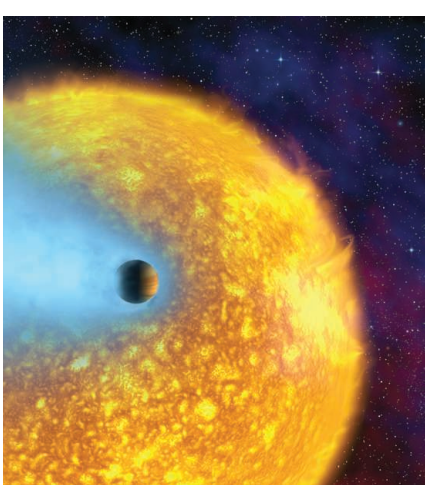
Sci. Transl. Med. **6**, 263ra159 (2014).

EXOPLANET MAGNETISM

Transit marked by magnetosphere effects

Life on Earth exists under the protective sheath of our magnetosphere that deflects charged particles blown out by the Sun. Kislyakova *et al.* calculated the strength of the magnetic field of a well-studied hot-Jupiter–type exoplanet that produces similar effects. During the planet's transit in front of its host star, HD 209458, hydrogen atoms leave a peculiar asymmetric signature in the transmitted spectrum. — MMM

Science, this issue p. 981



Transit observations of an exoplanet reveal its atmospheric and magnetic properties

METABOLISM

Making the brain promote fat loss in mice

Obesity is a growing global problem associated with diabetes and metabolic syndrome. Signals from the brain regulate whole body metabolism and can trigger adipose tissue to burn fat. Perino *et al.* found that mice that expressed catalytically inactive forms of two phosphoinositide 3-kinases (PI3Kβ and PI3Kγ) were leaner, burned more fat, and expended more energy than normal mice. Fat loss also occurred in mice that received inhibitors of PI3Kβ and PI3Kγ delivered specifically into the brain. Thus, drugs that block these enzymes in the brain could potentially help to fight obesity. — WW

Sci. Signal. **7**, ra110 (2014).

INFLUENZA IMMUNOLOGY

Hills and valleys of influenza infection

Each one of us may encounter several different strains of the ever-changing influenza virus during a lifetime. Scientists can now summarize such histories of infection over a lifetime of exposure. Fonville *et al.* visualize the interplay between protective responses and the evasive influenza virus by a technique called antibody landscape modeling (see the Perspective by Lessler). Landscapes reveal how exposure to new strains of the virus boost immune responses and indicate possibilities for optimizing future vaccination programs. — CA

Science, this issue p. 996; see also p. 919

IN OTHER JOURNALS

Edited by **Kristen Mueller** *and* **Jesse Smith**



Scanning electron micrograph of *Trichomonas vaginalis*

MICROBIOLOGY

Mycoplasma doubles the cost of an STD

It's cruel enough to acquire one sexually transmitted infection, but gaining two for one is harsh. Trichomoniasis is a very common protozoal infection of the vagina that causes symptoms ranging from urogenital inflammation to pregnancy complications. Fettweis *et al.* analyzed the microbiomes from vaginal samples collected from more than 1300 women and now report that a previously unknown mycoplasma (a type of bacteria) tightly associates with trichomonas organisms. The genome of the new mycoplasma (called candidatus *Mycoplasma girerdi*) encodes proteins similar to known virulence factors, which suggests that the mycoplasma might be contributing to trichomoniasis disease. — CA

PLOS One **9**, e110943 (2014).

BIOTECHNOLOGY

Disorder enhances binding cooperativity

Some natural proteins, such as hemoglobin, bind their ligands in a cooperative manner, whereby the binding of the first ligand alters the structure of the protein, favoring binding of subsequent ligands. Taking inspiration from this mechanism, Simon *et al.* created unstructured receptors from DNA. Upon binding their ligand, the disordered receptors become structured, forming sites for further ligands to bind. Because

CREDITS: (LEFT TO RIGHT) EUROPEAN SPACE AGENCY/ALFRED VIDAL-MADJAR/INSTITUT D'ASTROPHYSIQUE DE PARIS/CNRS; FRANCE/NASA; DAVID PHILLIPS/VISUALS UNLIMITED, INC.

Published by AAAS

ALSO IN *SCIENCE* JOURNALS

Edited by **Stella Hurtley**

EBOLA MOUSE MODEL

Variety of Ebola symptoms in mice

Apart from monkeys, there are no animal models available that show the same symptoms of Ebola virus infection as those of humans. Rasmussen *et al*. tested the effects of Ebola virus in mice with defined genetic backgrounds in a series of painstaking experiments performed under stringent biosafety conditions. Resistance and susceptibility to Ebola virus was associated with distinct genetic profiles in inflammation, blood coagulation, and vascular function. This panel of mice could prove valuable for preliminary screens of candidate therapeutics and vaccines. — CA

Science, this issue p. 987

INFLAMMATION

HIV drugs can dampen inflammation, too

Nucleoside reverse transcriptase inhibitors (NRTIs) stop HIV in its tracks by blocking reverse transcription, a process critical for HIV to replicate its genome. Fowler *et al.* found that in mice, these drugs also block inflammation caused by a large protein complex called the NLRP3 inflammasome. This activity is independent of the drugs' ability to block reverse transcription. Instead, the drugs block the activity of the ion channel P2X7, which activates the NLRP3 inflammasome. NRTIs improved outcomes in several NLRP3 inflammasome-dependent mouse models of inflammation, including age-related macular degeneration and graft-versus-host disease. — KLM

Science, this issue p. 1000

HOX LOCI REGULATION

Similar regulation of digit and genital development

Hox proteins help set up the vertebrate and invertebrate body plan and also specify segment identity, such as leg versus antennae. Lonfat *et al.* examined *Hox* gene regulation in mouse limb and genitals. Although the limb and genitals have widely differing structure and function, they display common features for *Hox* regulation during development. Transcription at these anatomical sites depends upon gene enhancers within a shared chromatin topological domain. It is likely that this regulatory landscape provided genomic niches for enhancer evolution. — BAP

Science, this issue p. 1004

MOUSE GENOMICS

Rewiring the gene regulatory landscape

DNAse I hypersensitive sites (DHSs) correlate with genomic locations that control where messenger RNA is to be produced. DHSs differ, depending on the cell type, developmental stage, and species. Viestra *et al*. compared mouse and human genome-wide DHS maps. Approximately one-third of the DHSs are conserved between the species, which separated approximately 80 million years ago. Most DHSs fell into tissue-specific cohorts; however, these were generally not conserved between the human and mouse. It seems that the majority of DHSs evolve because of changes in the sequence that gradually change how the region is regulated. — LMZ

Science, this issue p. 1007

AGING

How a fungus can live for centuries

Some species of fungi and plants can live for a thousand years or more. How do these species avoid harmful mutations over these long time spans? In a Perspective, Aanen highlights a recent study that reports extremely low genetic variation in an individual of a long-lived fungus. The manner in which stem cells divide differs between fungi, plants, and animals. These differences may allow certain fungi and plants to avoid accumulation of harmful mutations at the growth front, enabling them to grow particularly old. — JFU

Science, this issue p. 922

Published by AAAS

IN OTHER JOURNALS

Edited by **Kristen Mueller** *and* **Jesse Smith**



Scanning electron micrograph of *Trichomonas vaginalis*

MICROBIOLOGY

Mycoplasma doubles the cost of an STD

It's cruel enough to acquire one sexually transmitted infection, but gaining two for one is harsh. Trichomoniasis is a very common protozoal infection of the vagina that causes symptoms ranging from urogenital inflammation to pregnancy complications. Fettweis *et al.* analyzed the microbiomes from vaginal samples collected from more than 1300 women and now report that a previously unknown mycoplasma (a type of bacteria) tightly associates with trichomonas organisms. The genome of the new mycoplasma (called candidatus *Mycoplasma girerdi*) encodes proteins similar to known virulence factors, which suggests that the mycoplasma might be contributing to trichomoniasis disease. — CA

PLOS One **9**, e110943 (2014).

TUBERCULOSIS

Using a diabetes drug to treat tuberculosis

The increasing prevalence of drug-resistant strains of *Mycobacteria tuberculosis*—the bacterium that causes tuberculosis (TB)—has led to a paradigm shift in the search for new drugs. Rather than targeting the bacterium itself, researchers are trying to augment host defenses. Now, Singh *et al.* report that the FDA-approved drug metformin, currently used to treat type 2 diabetes, can improve the immune response to *M. tuberculosis* infection. Metformin inhibited the growth of *M. tuberculosis* by enhancing specific immune responses in vitro and in infected mice. Furthermore, in human diabetic patients with TB, metformin treatment decreased TB severity. — ACC

Sci. Transl. Med. **6**, 263ra159 (2014).

EXOPLANET MAGNETISM

Transit marked by magnetosphere effects

Life on Earth exists under the protective sheath of our magnetosphere that deflects charged particles blown out by the Sun. Kislyakova *et al.* calculated the strength of the magnetic field of a well-studied hot-Jupiter–type exoplanet that produces similar effects. During the planet's transit in front of its host star, HD 209458, hydrogen atoms leave a peculiar asymmetric signature in the transmitted spectrum. — MMM

Science, this issue p. 981

METABOLISM

Making the brain promote fat loss in mice

Obesity is a growing global problem associated with diabetes and metabolic syndrome. Signals from the brain regulate whole body metabolism and can trigger adipose tissue to burn fat. Perino *et al.* found that mice that expressed catalytically inactive forms of two phosphoinositide 3-kinases (PI3Kβ and PI3Kγ) were leaner, burned more fat, and expended more energy than normal mice. Fat loss also occurred in mice that received inhibitors of PI3Kβ and PI3Kγ delivered specifically into the brain. Thus, drugs that block these enzymes in the brain could potentially help to fight obesity. — WW

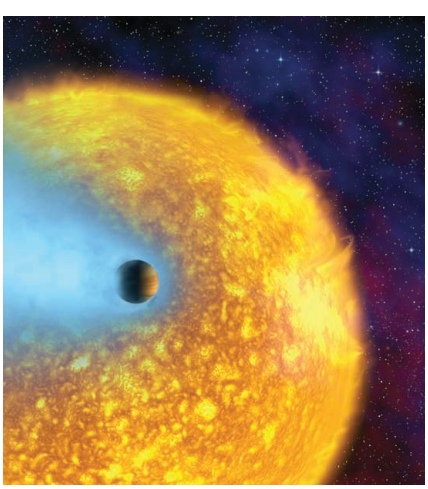
Sci. Signal. **7**, ra110 (2014).

INFLUENZA IMMUNOLOGY

Hills and valleys of influenza infection

Each one of us may encounter several different strains of the ever-changing influenza virus during a lifetime. Scientists can now summarize such histories of infection over a lifetime of exposure. Fonville *et al.* visualize the interplay between protective responses and the evasive influenza virus by a technique called antibody landscape modeling (see the Perspective by Lessler). Landscapes reveal how exposure to new strains of the virus boost immune responses and indicate possibilities for optimizing future vaccination programs. — CA

Science, this issue p. 996; see also p. 919



Transit observations of an exoplanet reveal its atmospheric and magnetic properties

BIOTECHNOLOGY

Disorder enhances binding cooperativity

Some natural proteins, such as hemoglobin, bind their ligands in a cooperative manner, whereby the binding of the first ligand alters the structure of the protein, favoring binding of subsequent ligands. Taking inspiration from this mechanism, Simon *et al.* created unstructured receptors from DNA. Upon binding their ligand, the disordered receptors become structured, forming sites for further ligands to bind. Because

CREDITS: (LEFT TO RIGHT) EUROPEAN SPACE AGENCY/ALFRED VIDAL-MADJAR/INSTITUT D'ASTROPHYSIQUE DE PARIS/CNRS; FRANCE/NASA; DAVID PHILLIPS/VISUALS UNLIMITED, INC.

Downloaded from www.sciencemag.org on November 22, 2014

Published by AAAS



MATERIALS SCIENCE

Climbing up the walls like a gecko

The Tokay gecko scurries across ceilings with the help of tiny hair on its feet, which generate weak intermolecular forces that add up to a secure foothold. Scientists have recreated dry gecko-like adhesion using silicones, plastics, carbon nanotubes, and other materials, but they've run into a scaling problem: The stickiness drops rapidly with increasing surface area. Hawkes *et al*. offer a solution: an adhesive consisting of 24 tiles that distribute loads evenly among themselves, offering the same adhesive strength for sizes from a square millimeter to the area of a human hand. The adhesive works even if one tile fails to stick. Wearing hand-sized adhesives, a 70-kilogram human can climb a vertical glass wall, the team showed. — JY

J. R. Soc. Interface, 10.1098/rsif.2014.0675.

ligands bind more favorably to these sites than to the unstructured receptor, the binding of subsequent ligands is enhanced. Relatively small changes in ligand concentration can therefore lead to an all-or-none binding response, a feature that could prove useful for artificial biotechnologies. – MDC

Proc. Natl. Acad. Sci. U.S.A. 10.1073/pnas.1410796111 (2014).

QUANTUM COMMUNICATION

Symmetric photons make good communicators

Future communication networks will be based on quantum mechanics and will rely on the ability to store quantum information in quantum nodes and transfer that information between them. Photons offer the ability to transfer information over long distances, but that requires that single photons be emitted and detected reliably at each end of the communication channel—a feat that requires the photons to be symmetric. Using a superconducting-based quantum circuit, Pechal *et al.* demonstrate how to generate the symmetric microwave photons that will be necessary to carry quantum information successfully. — ISO

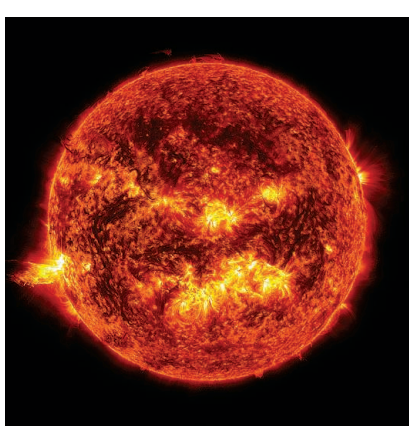
Phys. Rev. X **4**, 041010 (2014).

COSMOLOGY

Dark matter may yield x-ray glow nearby

Dark matter often has been observed to influence the dynamics of galaxies. Still, astrophysicists have great difficulty demonstrating the presence of dark matter with some type of direct detection. Now, observations made by the European XMM-Newton satellite of what should be blank sky instead show a variable background x-ray signal that could result from axions, a proposed component of dark matter. Fraser *et al.* explain that these candidate particles—a billionth the mass of an electron—could be produced by the Sun and then converted into x-rays by Earth's magnetic field. This step toward understanding dark matter still may be supported or refuted by further x-ray measurements with other observatories. — MMM

Mon. Not. Roy. Astron. Soc. 10.1093/mnras/stu1865 (2014).



AAA+ ATPASES

Redox regulation of Lon protease

Bacteria and other organisms use so-called AAA+ proteases to degrade cytosolic proteins. The Lon protease is the main protease used by bacteria to degrade damaged or misfolded cytosolic proteins, which can be toxic to the cell. Both too much and too little Lon protease activity is bad for survival. Nishii *et al.* asked how cells keep Lon activity levels just right. By examining the crystal structure of Lon from *Escherichia coli* they identified conserved cysteine residues that acted as a redox switch. The exit pore changed in size depending on whether the bacteria were growing in the presence or absence of oxygen: Reducing its size decreased products from passing through the pore and therefore the activity of the enzyme. –SMH

Nat. Chem. Biol. 10.1038/nchembio.1688 (2014).

EDUCATION

Follow scientists, not the lab notebook

Scientific experiments rarely go as planned. Despite following the scientific method, experiments often double back, repeat a step, or move in a new direction. Why then, do classroom laboratory exercises present students with a linear set of tasks resulting in a known outcome? To create a more authentic experience, Alaimo *et al*. redesigned four undergraduate organic chemistry labs to allow students to generate reliable data through repeating experiments, participate in authentic data analysis, and receive instruction in data-driven decision-making. These changes shifted the lab from an exercise in following directions to an exercise of learning the iterative process of a scientific study. — MM

J. Chem. Educ. 10.1021/ed400510b (2014).

HUMAN IMMUNOLOGY

A (w)holistic approach to track T cells

Immunologists know a lot about mouse T cells: how they develop, respond to infection, form memory cells, and where they reside. But whether this knowledge holds true for human T cells is still a black box because of the difficulty in obtaining samples from anywhere other than the blood. To gain more insight into human T cell biology, Thome *et al*. performed multidimensional, quantitative analyses on T cells obtained from the blood, lymph nodes, spleen, and mucosal tissues of 56 individual organ donors aged 3 to 73 years. They find that the distribution and maintenance of different T cell subsets depends on the differentiation state of the T cell and its location within the body. — KLM

Cell **159**, 814 (2014).

PHOTOS: (TOP TO BOTTOM) HAWKES *ET AL.*; NASA/SDO

Published by AAAS

RESEARCH ARTICLES

CHROMOSOMES

Closing the cohesin ring: Structure and function of its Smc3-kleisin interface

Thomas G. Gligoris,[1] Johanna C. Scheinost,[1] Frank Bürmann,[2] Naomi Petela,[1] Kok-Lung Chan,[1,3] Pelin Uluocak,[1,4] Frédéric Beckouët,[1] Stephan Gruber,[2] Kim Nasmyth,[1]* Jan Löwe[5]*

Through their association with a kleisin subunit (Scc1), cohesin's Smc1 and Smc3 subunits are thought to form tripartite rings that mediate sister chromatid cohesion. Unlike the structure of Smc1/Smc3 and Smc1/Scc1 interfaces, that of Smc3/Scc1 is not known. Disconnection of this interface is thought to release cohesin from chromosomes in a process regulated by acetylation. We show here that the N-terminal domain of yeast Scc1 contains two α helices, forming a four-helix bundle with the coiled coil emerging from Smc3's adenosine triphosphatase head. Mutations affecting this interaction compromise cohesin's association with chromosomes. The interface is far from Smc3 residues, whose acetylation prevents cohesin's dissociation from chromosomes. Cohesin complexes holding chromatids together in vivo do indeed have the configuration of hetero-trimeric rings, and sister DNAs are entrapped within these.

A vital member of the Smc/kleisin family is the eukaryotic cohesin complex, which confers sister chromatid cohesion, facilitates the repair of double-strand breaks, and modulates the structure and transcription of interphase chromatin (*1*, *2*). Cohesin contains a dimer of two related Smc proteins, Smc1 and Smc3, whose association with an α-kleisin subunit (Scc1/Rad21) has the potential to form an extended tripartite ring (*3*) within which sister DNAs could be entrapped (*4*). It has been suggested that the cohesin ring has separate DNA entry and exit gates, located at the Smc1/Smc3 "hinge" (*5*) and Smc3/kleisin interfaces, respectively (*6*). To understand how the latter's disconnection by the regulatory subunits Wapl, Pds5, and Scc3 releases cohesin from chromatin and how Smc3 acetylation locks rings shut (*6*), we have determined the structure of the Smc3-kleisin interface.

Structure of the Smc3-Scc1 interface

Because in vivo photo–cross-linking experiments (*7*) showed that Scc1's N-terminal domain (NTD) binds to the coiled coil emerging from Smc3's adenosine triphosphatase (ATPase) head (figs. S1 and S2), we coexpressed in *Escherichia coli* Scc1's first 115 residues (Scc1-N) with a version of the Smc3 ATPase head containing a 75-residue-long section of its coiled coil (Smc3hdCC). This yielded a complex suitable for x-ray crystallography (fig. S2D). Diffraction data were obtained to a resolution of 3.3 Å from crystals grown in the presence of adenosine 5′-*O*-(3-thiotriphosphate) (ATP-γ-S), and their structure was solved by a combination of molecular replacement and selenomethionine (SeMet) single-wavelength anomalous diffraction (SAD) phasing. The structure (Fig. 1A) reveals nearly one third of Smc3's coiled coil, including a pronounced and highly conserved kinked region between L991 and F999 (fig. S3C). The structure of the Smc3 ATPase domain is most closely related to that of Smc1 of all structures currently deposited in the Protein Data Bank (PDB) [root mean square deviation (RMSD) ~ 2.2 Å] (Fig. 1B). (Single-letter abbreviations for the amino acid residues are as follows: A, Ala; C, Cys; D, Asp; E, Glu; F, Phe; G, Gly; H, His; I, Ile; K, Lys; L, Leu; M, Met; N, Asn; P, Pro; Q, Gln; R, Arg; S, Ser; T, Thr; V, Val; W, Trp; and Y, Tyr. In the mutants, other amino acids were substituted at certain locations; for example, L1019R indicates that leucine at position 1019 was replaced by arginine.)

Scc1's NTD is folded into three helices: α1, α2, and α3 (Fig. 1, A and C). The most prominent is the 34-residue α3 (R69-M102), which forms a long helical bundle with Smc3's coiled coil. The C-terminal end of α3 almost reaches the coiled coil's pronounced kink, while the N-terminal end extends to Smc3's ATPase head. Helices α2 and α3 together form a compact four-helix bundle with Smc3's coiled coil, and there is no contact with the ATPase head itself. The very different manner by which N- and C-terminal domains interact with Smc ATPase heads (Fig. 1B) means that the path of Scc1 central domain's polypeptide is complex and possibly influenced by its association with Pds5 and Scc3. Sequences responsible for recruiting Pds5 are situated between H124 and L138 (*7*), close to the top of α3 (Fig. 1D). This proximity is striking because Pds5 has a key role in releasing cohesin from chromatin, presumably by dissociating the Scc1/Smc3 interface, as well as shutting off this process during *S* phase by promoting Smc3K113 acetylation.

Conservation of the Scc1-N/Smc3 interface

The entire surface of Smc3's coiled coil facing Scc1's α3 is highly conserved, whereas the opposing surface is not (Fig. 2A). The face of Scc1's α3 that contacts Smc3's coiled coil is similarly conserved (Fig. 1C and fig. S4, A and D). Scc1's α2 helix is in general less conserved than α3. In a *Bacillus subtilis* complex (*8*), ScpA sequences corresponding to the N-terminal half of Scc1 α3 form a three-helix bundle with the Smc coiled coil similar to that observed between Scc1-N and Smc3, but the structure of the rest of ScpA's NTD differs substantially from that of Scc1 (fig. S4B). Several of the characteristics of α3 are found in β- and γ-kleisins from condensin. Thus, hydrophobic residues such as L75, Y82, L89, and L97, which seem to have a role in contacting Smc3's coiled coils, are present at the same positions within β-kleisins (condensin II) and for the most part also γ-kleisins (condensin I) (fig. S4D). The equivalent residues in *B. subtilis* ScpA are also hydrophobic and have a similar juxtaposition to their Smc partner (*8*).

Testing the structure by use of thiol-specific cross-linking

We created a series of pairwise cysteine substitutions within Scc1 and Smc3 and, using the homo-bifunctional sulfhydryl active reagent dibromobimane (bBBr), measured the efficiency with which these are cross-linked (*9*). Treatment of native cohesin complexes after immunoprecipitation revealed the expected pattern of cross-linking between cysteines within Smc3's coiled coil and cysteines within Scc1's α3 (Fig. 2, B and C). This included cross-linking between Scc1I100C and Smc3F1005C, which confirms that Scc1's α3 extends further up the Smc3 coiled coil than that observed for ScpA (fig. S4B). We also observed efficient cross-linking between Scc1K48C and Smc3K1032C, confirming the observed juxtaposition of α2 with Smc3's coiled coil. In contrast, cross-linking occurred rarely if at all between residues predicted to be nonadjacent (fig S4E). Cysteine pairs involving α2 and α3 can be cross-linked in vivo, and the cross-linked species were acetylated, implying that the interactions revealed by the Smc3/kleisin structure actually exist in complexes engaged in holding sister DNAs together.

Because of the presence of prolines (*10*), it is unlikely that α3 from bacterial kleisins extends as far up the coiled coil as is the case for Scc1. This difference between the cohesin and bacterial structures may therefore be genuine. To assess

[1]Department of Biochemistry, University of Oxford, Oxford, OX1 3QU, UK. [2]Max-Planck-Institut für Biochemie, 82152, Martinsried, Germany. [3]Medical Research Council (MRC) Genome Damage and Stability Centre, University of Sussex, Brighton BN1 9RQ, UK. [4]Dunn School of Pathology, University of Oxford, Oxford OX1 3RF, UK. [5]MRC Laboratory of Molecular Biology, Cambridge, CB2 0QH, UK.
*Corresponding author. E-mail: kim.nasmyth@bioch.ox.ac.uk (K.M.); jyl@mrc-lmb.cam.ac.uk (J.L.)

the N-terminal differences, we designed cysteine pairs, ScpAE39C-SmcH1043C and ScpAL42C-SmcQ1039C, which should be cross-linked if ScpA adopts the conformation observed in the ScpA/Smc crystal, and an alternative pair, E39C-Q1020C, which should be cross-linked only if they adopted the Smc3/Scc1 conformation. Our observation that, in *B. subtilis*, bis-maleimidoethane (BMOE) induces efficient cross-linking in vivo between the latter but not the former pairs suggests that ScpA binds to the Smc coiled coil by forming a four-helix bundle similar to that formed by Scc1 and Smc3 (fig. S4F).

Interaction between Scc1's NTD and Smc3's coiled coil is essential

The adverse effects of mutations within Scc1's NTD that affect its association with Smc3 (*11*) are explained by the structure. Three highly conserved leucine residues—L68, L75, and L89—line the surface of α3 that faces Smc3's coiled coil (Fig. 3A). In each case, substitution by lysine causes lethality, reduces association between Scc1 and Smc3 (*11*), and abrogates (in the cases of L75K and L89K) cohesin's association with centromeres (*12*). As expected, Scc1L89K abolished cross-linking between S1043C-C56 cysteine pairs (Fig. 3C). To address whether these defects arise from defective interaction with Smc3's coiled coil, we created a series of mutations intended to alter its surface without affecting coiled-coil formation per se (a comprehensive list of mutants and related phenotypes is provided in Fig. 3F). Lethality was caused by three mutations—L1019R, I1026R, and L1029R—that replaced hydrophobic side chains with charged ones on the surface of the coiled coil facing Scc1's α2 and α3 (Fig. 3B and fig. S5A). None of these mutations altered Smc3 levels or prevented Scc1's association with Smc1/Smc3 heterodimers in vivo (fig. S5B), presumably because association between Scc1's CTD and Smc1's ATPase head recruits the kleisin to heterodimers even when interaction between its NTD and Smc3 is compromised (*11*). Smc3L1029R also disrupted interaction with Scc1-N when coexpressed in *E. coli* (fig. S5F). In yeast cells, the same mutation reduced ultraviolet-induced cross-linking between Smc3A181bpa and Scc1 (fig. S5D) as well as cross-linking between Scc1Q76C and Smc3A181C (fig. S5C). Disruption of the hydrophobic nature of Smc3's coiled coil by Smc3L1019R, I1026R, and L1029R abrogated cohesin's ability to associate with centromeric DNAs in vivo and prevented acetylation of Smc3 by Eco1 (Fig. 3D and fig. S5E).

Introduction of charged residues into a hydrophobic interface precludes evaluation of the role of individual residues. For a more nuanced analysis, we focused on Y82, a conspicuous feature of α-, β-, and γ-kleisins (fig. S4D). Tetrad analysis revealed that Scc1Y82A caused slow growth at 30°C and lethality at 32°C (Fig. 3E and fig. S6A). Scc1Y82I had no obvious effect on proliferation but was synthetic lethal with a temperature-sensitive allele of *ECO1* (Eco1G211D). We conclude that insertion at this position in Smc3's coiled coil of a large aromatic residue has an important role in stabilizing its association with Scc1's NTD.

Although crucial, these hydrophobic interactions are insufficient. For example, lethality is also caused by substitution with glutamic acid of the highly conserved Smc3R1015 (Fig. 3B and fig. S6B)), which interacts with the equally conserved D92 within Scc1's α3. Contrary to previous observations, which were made on a version of Scc1 that was doubly tagged and contained a TEV protease cleavage site, D92K is in fact not lethal per se, although it does cause slow growth at 30°C and lethality at 37°C when Smc3 is tagged at its C terminus by PK3 (fig. S6C). Last, the finding that lethality is also caused by Scc1A47K (*11*), which alters a highly conserved alanine within Scc1's α2, confirms the importance of α2 (fig. S4A).

The KKD strand within the Smc3 ATPase head

The Smc3 ATPase heads have an irregular β strand at the top of their N-terminal lobe that contains an invariant aspartic acid residue (D114) next to a

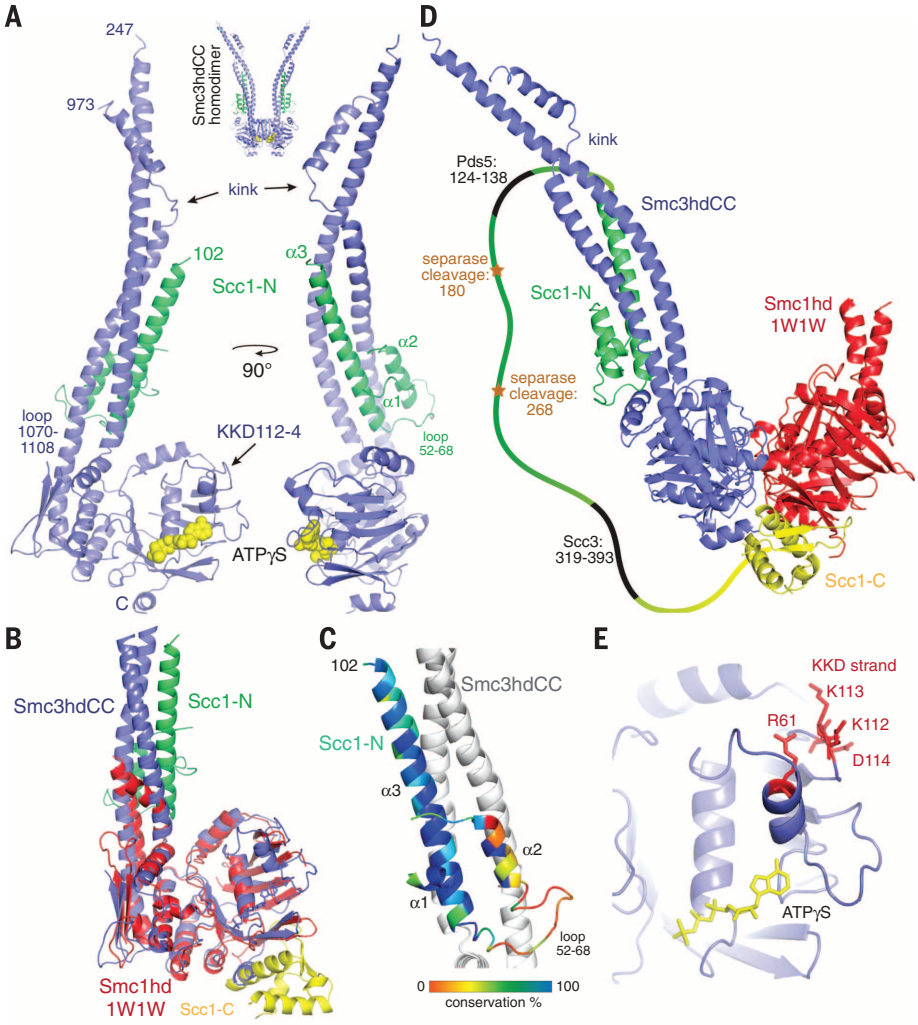


Fig. 1. Crystal structure of the Smc3hdCC:Scc1-N complex. (**A**) The coiled-coil segment of Smc3 (blue) is interrupted by a "kink." The NTD of Scc1, Scc1-N (green), binds to the coiled-coil segment of Smc3, leading to a four-stranded helical arrangement. (Inset) Aberrant homodimer formation of Smc3 head domains in the crystals. (**B**) A superposition of the Smc3hdCC:Scc1-N crystal structure (blue and green, respectively; this work) with Smc1hdCC:Scc1-C (red and yellow, respectively; PDB 1W1W) reveals that in addition to the ATPase fold, the position of the coiled-coil segments is conserved. Crucially, Scc1 binding is completely different for Smc3 and Smc1. (**C**) Sequence conservation of Scc1's NTD. (**D**) ATP binding leads to sandwich dimer formation of the head domains of Smc1 and Smc3, closing the ring temporarily. According to the ring model, Scc1 more permanently bridges the two head domains, which can be released through separase-mediated cleavage of Scc1 or in a separase-independent pathway through opening of the Smc3:Scc1 gate. Scc1 contains many more residues in the middle domain. Separase cleavage sites, Pds5 (*7*) and Scc3 binding sites are highlighted (*28*). (**E**) Detail of the KKD strand, whose acetylation by Eco1 reduces separase-independent cohesin release. It is far away from the nucleotide binding site on the head domain, but the acetylation state may influence the nucleotide binding site through the helix containing R61.

pair of highly conserved lysine residues (K112 and K113) whose acetylation by Eco1 is essential for sister chromatid cohesion (*13*, *14*). Our structure also reveals an adjacent α helix (R58-L64) whose base abuts the nucleotide and potentially links the latter to the KKD strand (Fig. 1E). The KKD strand, as well as other highly conserved Smc3-specific residues (S75, R107, and G110) in its vicinity (*15*), has a role in releasing cohesin from chromatin in a process dependent on cohesin's Wapl, Pds5, and Scc3 regulatory subunits. Acetylation of K112 and K113 by Eco1 neutralizes this activity and stabilizes cohesin's association with chromatin. Given that release is thought to involve transient dissociation of Scc1's NTD from Smc3, creating a gate through which DNA exits the ring, it is striking that the KKD strand is situated some distance (minimal 25 Å) from the part of Smc3 that binds Scc1, its coiled coil.

To address the function of the R58-L64 helix, we investigated the role of two highly conserved Smc3-specific residues (fig. S4C), Smc3R61 and E59. Replacement of R61 by glutamic acid or glutamine was lethal, whereas replacement by isoleucine or alanine was not (fig. S6D). In contrast, replacement of E59 by either alanine or arginine had little or no effect on cell proliferation. To address whether cohesin containing Smc3R61Q loads onto chromosomes, we compared the distribution of green fluorescent protein (GFP)–tagged Smc3R61Q and wild-type Smc3 in living cells carrying an untagged endogenous Smc3 gene. Smc3R61Q-GFP failed to accumulate at kinetochores or to form pericentromeric barrels during G2/M, implying that the mutant protein cannot load onto chromosomes, at least in the vicinity of centromeres (Fig. 3D). R61 is close to K112 and K113 (Fig. 1E), whose acetylation by Eco1 not only blocks release but also very possibly blocks cohesin's ability to engage in a loading reaction capable of producing cohesion (*16*). It is conceivable, therefore, that R61 has some role in relaying the state of modification of the KKD strand to Smc3's nucleotide binding pocket. Because the Smc3K112Q K113Q double mutation is also lethal and reduces cohesin's loading onto chromosomes (*13*, *17*), it is possible that in their unmodified form, K112 and K113 have a role in promoting cohesin loading and that they do so by influencing Smc3's ATPase activity in a manner involving R61. Thus, the KKD strand might be concerned with Scc2/4–mediated loading of cohesin onto chromosomes as well as Wapl-mediated release.

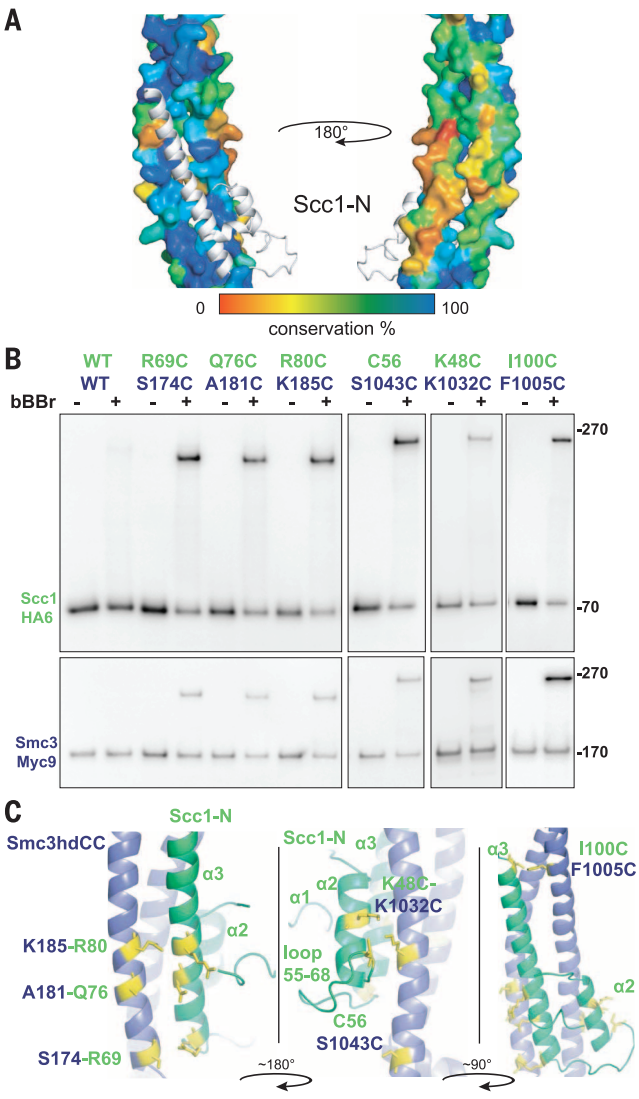


Fig. 2. Testing the Smc3-kleisin crystal structure. (**A**) Conservation of Smc3's coiled coil. The surface associated with Scc1 is highly conserved, but the solvent-exposed side is not. (**B**) Thiol-specific cross-linking (bBBr) between α2 and α3 of Scc1-N and Smc3's coiled coil (CC) after immunoprecipitation of Scc1-HA6. Cross-linking specific to K48C-K1032C was observed in cells expressing C56S (K19796, K19769, K19727, K19732, K19764, K23102, and K23103). All mutations were functional, and all observed cross-links were dependent on a pair of cysteine substitutions. (**C**) Scc1-N α2 and α3 helices (green), Smc3 coiled coil (Smc3CC, blue), and substituted residues (yellow).

Cohesin trimers hold sister DNAs together in live cells

To address whether simultaneous interaction of the three Smc/kleisin interfaces actually creates rings in vivo, living cells expressing Smc1-myc9, Scc1-PK6, and Smc3-Halo were incubated with BMOE to cross-link one, two, or three interfaces. Scc1-PK6 was then immunoprecipitated. In the presence of the tetramethylrhodamine (TMR) ligand, Smc3-Halo becomes labeled and fluorescent and was visualized after SDS–polyacrylamide gel electrophoresis by scanning gels at 545 nm (Fig. 4B). Smc1-myc9 and Scc1-PK6 were detected by means of Western blotting (fig. S7A). Dimeric molecules were created if cysteine pairs were present at single interfaces, and trimers were created when cysteine pairs were present at two interfaces (Fig. 4B). Cross-linking cohesin containing cysteines at all three interfaces generated a new form form (Ci) whose electrophoretic mobility was slower than that of all three trimeric forms created by cross-linking at merely two out of the three interfaces. This form presumably arises from the creation of circular molecules owing to the simultaneous cross-linking of all three interfaces of tripartite rings. The fraction of linear and circular trimers was roughly consistent with cross-linking at each of the three interfaces occurring independently (fig. S7C). Similar results were obtained by cross-linking with bBBr after immunoprecipitation (fig. S7B). Thus, most cohesin inside living yeast cells has the form of a heterotrimeric ring. Western blotting by using antibodies specific for acetylated Smc3 (*17*) showed that the Ci form was acetylated to a degree similar to that of molecules that had not been chemically circularized (Fig. 4B, last lane). Acetylation was detected in cross-linked species created in vivo by several different cysteine pairs (Fig. 4A). Because cohesion is mediated only by acetylated complexes (*13*, *14*), these data suggest that the cohesin complexes responsible for holding sister DNAs together are also circular Smc1/Smc3/Scc1 heterotrimers.

It has been suggested that Scc1 links the ATPase heads of different Smc1/Smc3 heterodimers, creating dimeric rings or multimeric chains (*18*). According to this scenario, the Ci form could conceivably be a tetramer containing Smc subunits from two Smc1/3 heterodimers. To address whether Ci contains more than one Smc3 molecule, we compared the amount of Halo-tagged Ci associated with PK- and hemagglutinin (HA)–tagged proteins from Scc1-PK6/Scc1-PK6, Smc3-HA6/Smc3-Halo diploids after in vivo cross-linking. This showed that little or no Smc3-Halo is present in Ci molecules that had

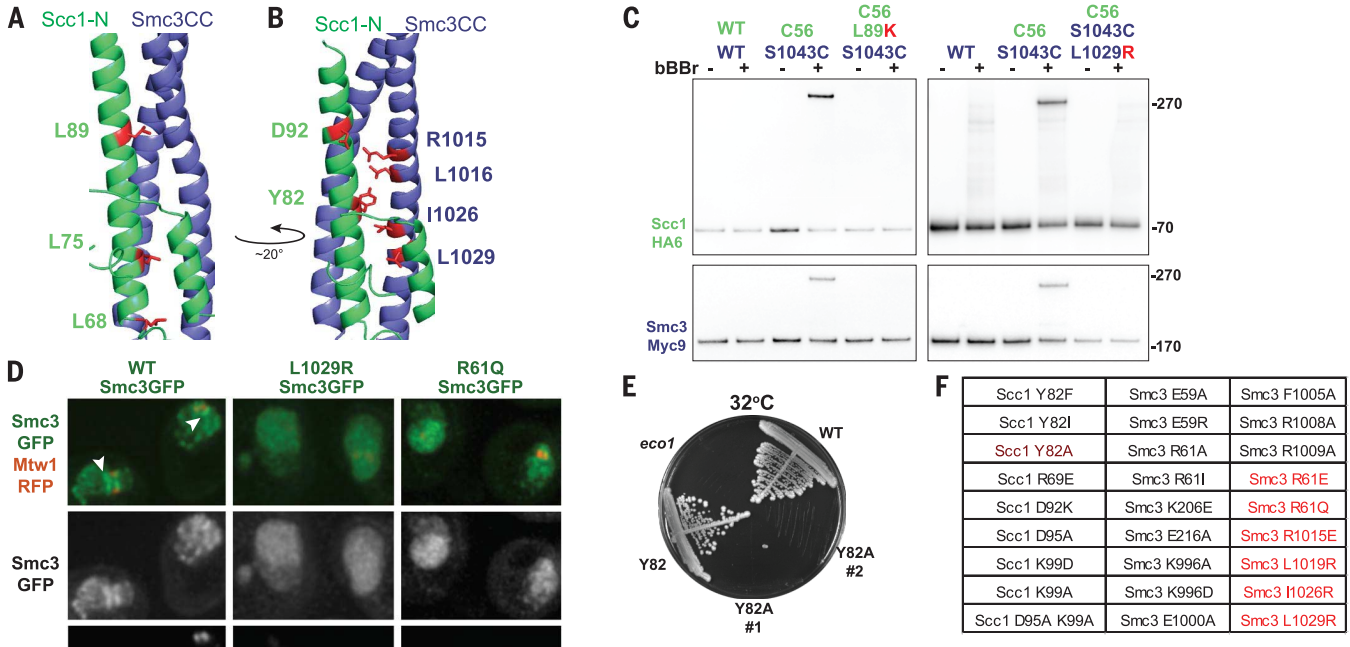


Fig. 3. Functional analysis of the Smc3-kleisin structure. (**A**) Essential Scc1-N residues (*11*) situated within the Smc3-kleisin interface. (**B**) Conserved residues in Scc1-N (D92 and Y82) and Smc3CC (R1015, L1019, I1026, and L1029), whose mutation disrupts interaction and causes lethality. (**C**) Abolition of Scc1-N/Smc3CC cross-linking by Scc1L89K (K19796, K23144, and K23145) and Smc3L1029R (K23146, K23128, and K23129) as measured by cross-linking C56-S1043C with bBBr after immunoprecipitation of Scc1-HA6. Western blots of Smc3-myc9 and Scc1-HA6 are shown. (**D**) Diploid cells expressing ectopic WT or mutant Smc3-GFP, with white arrowheads pointing at the cohesin pericentromeric barrel structure absent in the case of L1029R and R61Q (K23107-23109). (**E**) Scc1Y82A is lethal at 32°C (K699, K16296, and K23105-6). (**F**) A summary of mutations created and characterized. Lethal (red) and temperature-sensitive (brown) mutations, both in Scc1 and Smc3, were found. Shown is the viability of Scc1D95A, K99D, K99A, and D95A K99A mutants (K23111-23117).

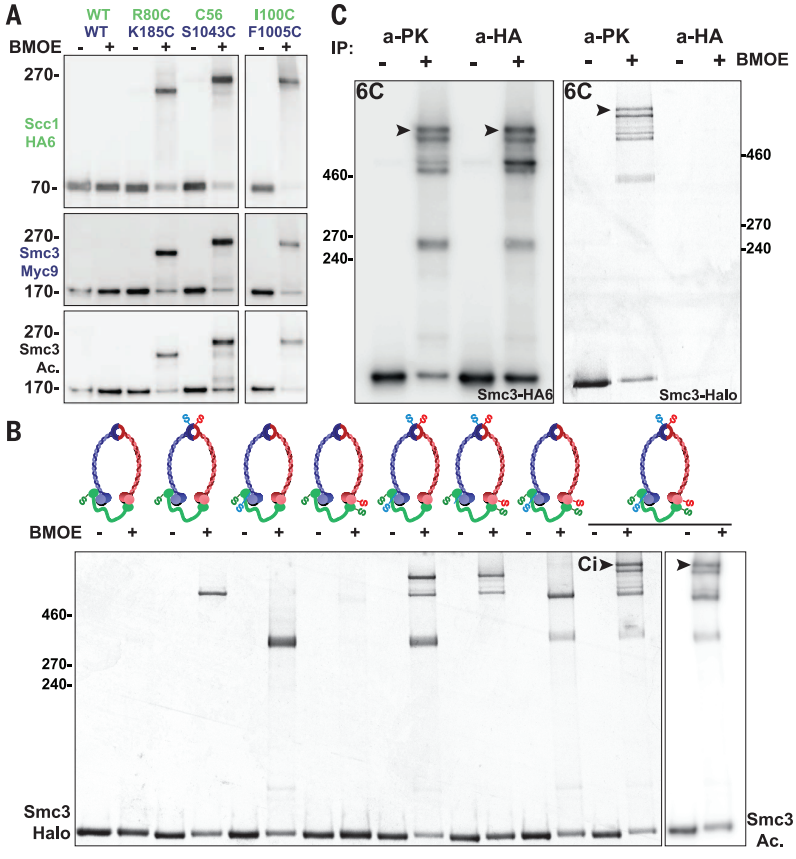


Fig. 4. Cohesin forms heterotrimeric rings in vivo. (**A**) In vivo thiol-specific cross-linking (BMOE) between α2 and α3 of Scc1-N and the Smc3 coiled coil (CC) followed by immunoprecipitation of Scc1-HA6. In all shifted bands, Smc3 is acetylated (K19796, K19732, K19764, and K23103). (**B**) In vivo thiol-specific cross-linking of the three Smc1/Smc3/Scc1 interfaces followed by immunoprecipitation of Scc1-PK6 and observation of TMR fluorescence associated with Smc3-Halo. A circular form (Ci) only appears when all three interfaces are linked (black arrowheads). Western blotting by use of an antibody specific for acetylated K113 shows that Ci is acetylated (last lane) (strains K22013-K22020). (**C**) Cohesin forms heterotrimeric rings but not higher-order complexes. Halo-tagged Ci (black arrowhead) is associated with PK- and HA-tagged proteins from Scc1-PK6/Scc1-PK6, Smc3-HA6/Smc3-Halo diploids after in vivo cross-linking. No Smc3-Halo is present in form Ci molecules that had been immunoprecipitated with HA antibodies, implying that they are circular trimers, not tetramers (K22590).

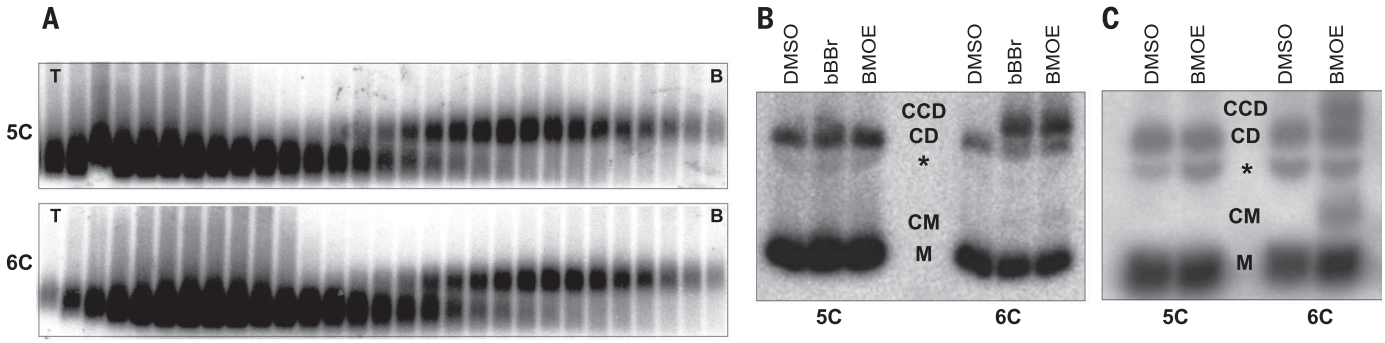


Fig. 5. Heterotrimeric cohesin rings trap sister DNAs both in vitro and in vivo. (**A**) Dimers of a 2.3-kb circular minichromosome were isolated by using sucrose gradients (T, top; B, bottom) from strains containing five (5C) or six (6C) cysteines within the Smc1/Smc3/Scc1 interfaces (K20300 and K20279). (**B**) Electrophoresis of dimers denatured with SDS after isolation from sucrose gradients and cross-linking with bBBr or BMOE. DNAs detected by means of Southern blotting. (**C**) Electrophoresis of Scc1-PK6 immunoprecipitated DNAs denatured with SDS after in vivo BMOE cross-linking of cycling cells. DNAs detected by means of Southern blotting. M, monomeric circles: CM, catenated monomers; asterisk, nicked DNA; CD, catenated dimers; and CCD, cohesin catenated dimers (K20280 and K20279).

been immunoprecipitated with HA antibodies, implying that they are circular heterotrimers and not tetramers or multimers (Fig. 4C). We used a similar method, albeit without cross-linking, to show that acetylated wild-type Smc3 cannot be co-immunoprecipitiated by a myc-tagged version when extracts were prepared from Smc3/Smc3-myc18 diploids (fig. S7E).

Sister DNAs are entrapped by cohesin trimers

To test whether cross-linking all three interfaces of the cohesin ring entraps sister DNAs in a covalent topological embrace, we isolated dimers of a 2.3-kb circular minichromosome (Fig. 5A), treated them with bBBr or BMOE, and subjected them to gel electrophoresis after denaturation (*19*). In the absence of cross-linker, most minichromosome DNAs detected with Southern blotting migrated as closed circular monomers (Fig. 5B, M), whereas 10 to 20% migrated as monomeric nicked circles or catenated supercoils (CD). With cysteine pairs at all three interfaces, both cross-linkers caused the appearance of dimers (CCD) that migrate more slowly than catenated supercoils (Fig. 5B) (*9*). No such dimers were formed when minichromosomes were isolated from a strain lacking a single one of the six "interface" cysteines (Fig. 5B). We estimated that the fraction of monomeric DNAs converted to dimers by cross-linking was ~25%, which is similar to the efficiency of cohesin's chemical circularization in vivo (Fig. 4B) and in vitro (fig. S7B). Crucially, sister (CCD) as well as monomeric (CM) DNAs were catenated in this manner by chemically circularized cohesin when living yeast cells were treated with BMOE (Fig. 5C), indicating that cohesin rings entrap sister DNAs in vivo.

Discussion

Our crystal structure of an Smc3/Scc1 complex provides a mechanism by which a single Scc1 polypeptide links the ATPase heads of Smc1/Smc3 heterodimers, creating a heterotrimeric ring structure. Using thiol-specific chemical cross-linking, we demonstrate that cohesin complexes holding sister chromatids together in vivo do indeed have the configuration of heterotrimeric rings and that sister minichromosome DNAs are entrapped within these in vivo. The interactions between Smc1/3 hinges, Smc1 ATPase/Scc1-C, and Smc3CC/Scc1-N are all very stable (*4*, *20*, *21*). Intact cohesin rings are therefore likely to be extremely durable in the absence of specific mechanisms to disrupt them. Such a feature is desirable for a complex that must hold sister DNAs together for extended periods of time, which may last for several decades in the case of human oocytes.

Two mechanisms are known to remove cohesin from chromosomes. Best understood is cleavage of the central domain of Scc1 (*22*) and its meiotic counterpart Rec8 (*23*) by separase, an event that triggers sister chromatid disjunction at the onset of anaphase. The simplest explanation for this phenomenon is that the three interactions that create tripartite cohesin rings are both necessary and sufficient to entrap sister DNAs, and separase merely destroys topological entrapment. The second mechanism is separase-independent, occurs throughout the cell cycle, and is especially active during prophase, when most cohesin is removed from chromosome arms (*24*, *25*). The releasing activity responsible for this phenomenon is associated with cohesin itself; involves its Wapl (*26*, *27*), Pds5, and Scc3 subunits (*15*); and is blocked by fusion of Smc3 to Scc1. Our finding that Smc3 R61 possibly links the KKD strand to the Smc3's adenosine 5´-triphosphate (ATP) binding pocket raises the possibility that acetylation, which blocks releasing activity, may directly regulate ATPase activity and vice versa.

Sequence comparisons suggest that most if not all eukaryotic Smc/kleisin complexes have a configuration similar to that of cohesin's ring. Because all three interfaces of cohesin's ring and those of bacterial Smc/kleisin complexes are structurally homologous, this class of complex must have been present in the last common ancestor of all living organisms and may be an indispensable feature of DNA genomes.

REFERENCES AND NOTES

1. J. M. Peters, A. Tedeschi, J. Schmitz, *Genes Dev.* **22**, 3089–3114 (2008).
2. K. Nasmyth, *Nat. Cell Biol.* **13**, 1170–1177 (2011).
3. S. Gruber, C. H. Haering, K. Nasmyth, *Cell* **112**, 765–777 (2003).
4. C. H. Haering, J. Löwe, A. Hochwagen, K. Nasmyth, *Mol. Cell* **9**, 773–788 (2002).
5. S. Gruber *et al.*, *Cell* **127**, 523–537 (2006).
6. K. L. Chan *et al.*, *Cell* **150**, 961–974 (2012).
7. K. L. Chan *et al.*, *Proc. Natl. Acad. Sci. U.S.A.* **110**, 13020–13025 (2013).
8. F. Bürmann *et al.*, *Nat. Struct. Mol. Biol.* **20**, 371–379 (2013).
9. C. H. Haering *et al.*, *Nature* **454**, 297–301 (2008).
10. A. Schleiffer *et al.*, *Mol. Cell* **11**, 571–575 (2003).
11. P. Arumugam *et al.*, *Curr. Biol.* **16**, 1998–2008 (2006).
12. B. Hu *et al.*, *Curr. Biol.* **21**, 12–24 (2011).
13. E. Unal *et al.*, *Science* **321**, 566–569 (2008).
14. T. Rolef Ben-Shahar *et al.*, *Science* **321**, 563–566 (2008).
15. B. D. Rowland *et al.*, *Mol. Cell* **33**, 763–774 (2009).
16. F. Beckouët *et al.*, *Mol. Cell* **39**, 689–699 (2010).
17. T. Sutani *et al.*, *Curr. Biol.* **19**, 492–497 (2009).
18. C. E. Huang, M. Milutinovich, D. Koshland, *Philos. Trans. R. Soc. London B Biol. Sci.* **360**, 537–542 (2005).
19. D. Ivanov, K. Nasmyth, *Mol. Cell* **27**, 300–310 (2007).
20. C. H. Haering *et al.*, *Mol. Cell* **15**, 951–964 (2004).
21. A. Kurze *et al.*, *EMBO J.* **30**, 364–378 (2011).
22. F. Uhlmann *et al.*, *Nature* **400**, 37–42 (1999).
23. S. B. Buonomo *et al.*, *Cell* **103**, 387–398 (2000).
24. A. Losada *et al.*, *Genes Dev.* **12**, 1986–1997 (1998).
25. I. Sumara *et al.*, *J. Cell Biol.* **151**, 749–762 (2000).
26. R. Gandhi *et al.*, *Curr. Biol.* **16**, 2406–2417 (2006).
27. S. Kueng *et al.*, *Cell* **127**, 955–967 (2006).
28. M. B. Roig *et al.*, *FEBS Lett.* **16**, 3692–3702 (2014).

ACKNOWLEDGMENTS

T.G.G. is supported by a European Molecular Biology Organization long-term fellowship (ALTF 2008-127) and the John Fell Fund (132/108). The work was funded by the Medical Research Council (U10518432 to J.L., C573/A11625 to J.C.S.), the Wellcome Trust (095514/Z/11/Z to J.L., 091859/Z/10/Z to K.N.), Cancer Research UK (C573/A 12386 to K.N.), and the MitoSys project (FP7/2007-2013 under grant agreement 241548 to K.N.).

SUPPLEMENTARY MATERIALS

www.sciencemag.org/content/346/6212/963/suppl/DC1
Materials and Methods
Figs. S1 to S7
Tables S1 to S2
References (*29*–*36*)

3 June 2014; accepted 26 September 2014
10.1126/science.1256917

CHROMOSOMES

Characterization of a DNA exit gate in the human cohesin ring

Pim J. Huis in 't Veld,[1] Franz Herzog,[2,3] Rene Ladurner,[1] Iain F. Davidson,[1] Sabina Piric,[1] Emanuel Kreidl,[1] Venugopal Bhaskara,[1] Ruedi Aebersold,[2] Jan-Michael Peters[1]*

Chromosome segregation depends on sister chromatid cohesion mediated by cohesin. The cohesin subunits Smc1, Smc3, and Scc1 form tripartite rings that are thought to open at distinct sites to allow entry and exit of DNA. However, direct evidence for the existence of open forms of cohesin is lacking. We found that cohesin's proposed DNA exit gate is formed by interactions between Scc1 and the coiled-coil region of Smc3. Mutation of this interface abolished cohesin's ability to stably associate with chromatin and to mediate cohesion. Electron microscopy revealed that weakening of the Smc3-Scc1 interface resulted in opening of cohesin rings, as did proteolytic cleavage of Scc1. These open forms may resemble intermediate states of cohesin normally generated by the release factor Wapl and the protease separase, respectively.

To ensure proper chromosome segregation during cell division, sister chromatids must be held together from the onset of DNA replication until the metaphase-to-anaphase transition. This sister chromatid cohesion is mediated by cohesin, a protein complex also implicated in chromatin organization, gene regulation, and DNA repair. Cohesin malfunction can result in genetic disorders such as Cornelia de Lange syndrome, and it has been found to correlate with age-related female infertility and tumorigenesis (*1*). The core of human cohesin is composed of the subunits Smc1, Smc3, Scc1 (also known as Rad21 or Mcd1), and SA1 or SA2. Because Smc1 and Smc3 contain long coiled coils, dimerize through their hinge domain at one end, and are bridged by the kleisin Scc1 at their nucleotide-binding domains (NBDs), the cohesin core complex has a ring-like appearance (*2*–*4*). According to the embrace model, cohesin uses this characteristic subunit topology to physically entrap DNA (*5*). The loading of cohesin onto DNA depends on the Scc2-Scc4 complex and adenosine triphosphate hydrolysis (*6*–*8*). It has been proposed that this reaction involves a transient opening of the Smc1-Smc3 hinge, because artificial stabilization of this interface abolishes cohesin's loading onto DNA (*9*, *10*). Cohesin complexes that mediate sister chromatid cohesion must dissociate from DNA to allow chromosome segregation at the metaphase-to-anaphase transition. This removal involves cleavage of cohesin's Scc1 subunit by separase (*11*, *12*). Cohesin is also released from DNA in a proteolysis-independent manner that occurs throughout the cell cycle and depends on the cohesin-associated protein Wapl (*13*–*15*). An intramolecular fusion of Scc1 and Smc3 renders cohesin refractory to this activity, which suggests that Wapl acts on the Scc1-Smc3 interface (*10*, *16*, *17*). Cohesin rings

[1]Research Institute of Molecular Pathology (IMP), Vienna Biocenter (VBC), 1030 Vienna, Austria. [2]Department of Biology, Institute of Molecular Systems Biology, Eidgenössische Technische Hochschule (ETH) Zürich, 8093 Zurich, Switzerland. [3]Department of Biochemistry, Gene Center, Ludwig-Maximilian University, 81377 Munich, Germany.
*Corresponding author. E-mail: peters@imp.ac.at

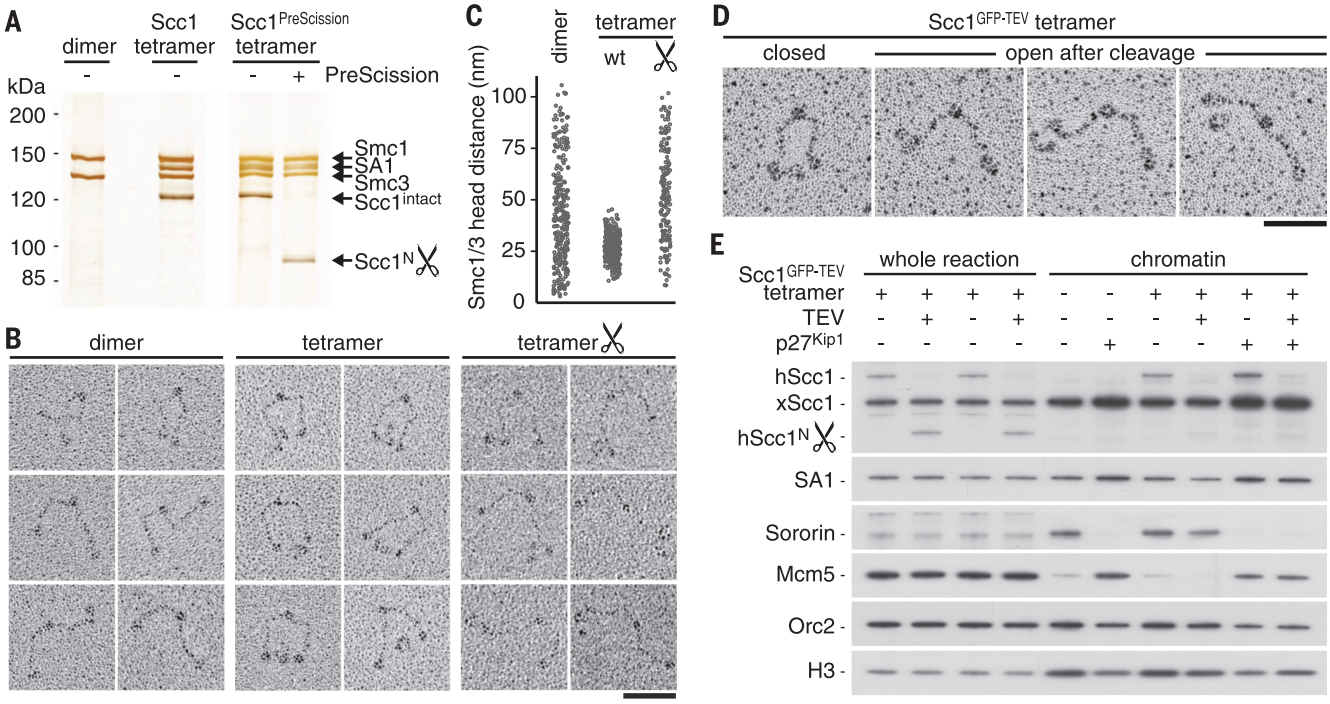


Fig. 1. Cleavage of Scc1 opens cohesin rings and releases cohesin from chromatin before and after DNA replication. (**A**) Silver staining of purified recombinant human cohesin dimers and tetramers after SDS–polyacrylamide gel electrophoresis (PAGE). Scc1^{PreScission} is efficiently cleaved by PreScission protease. (**B**) Representative micrographs of cohesin dimers, tetramers, and cleaved tetramers after low-angle Pt/C rotary shadowing. Scc1 bridges the heads of Smc1 and Smc3 to form ring-like structures that rearrange upon Scc1 cleavage. Scale bar, 50 nm. (**C**) Distance between the heads of Smc1 and Smc3 for dimers (n = 274), tetramers (n = 304), and cleaved tetramers (n = 168). (**D**) Cohesin tetramers with Scc1$^{GFP-TEV}$ adopt an open conformation after cleavage by TEV protease. Scale bar, 50 nm. (**E**) *Xenopus* sperm chromatin, purified human cohesin, and interphase *Xenopus* egg extract were incubated for 75 min. TEV protease was then added for 15 min to cleave Scc1$^{GFP-TEV}$. Chromatin-bound material was analyzed by immunoblotting. Human and *Xenopus* Scc1 can be distinguished by the GFP-induced mobility shift. Mcm5 accumulates on chromatin when DNA replication is inhibited by p27^{Kip1}, whereas sororin binds to cohesin on replicated DNA.

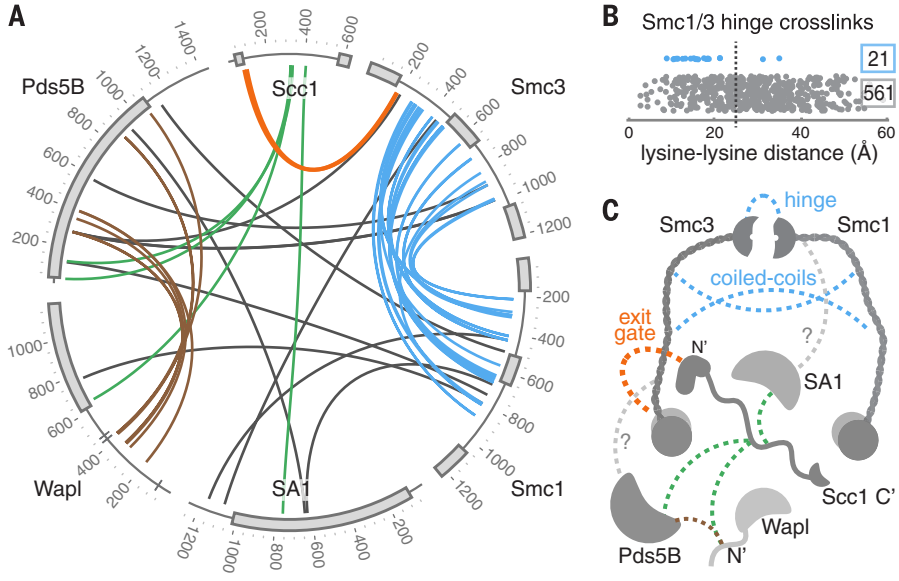


Fig. 2. A cohesin proximity map generated by cross-linking followed by mass spectrometry. (**A**) Intermolecular cross-links (n = 51) are shown in a Circos diagram. Gray boxes illustrate the NBDs and hinge domains of Smc1 and Smc3, the α-helical regions in Scc1, and the α-helical repeats of SA1, Wapl, and Pds5B. The three dashes indicate FGF motifs in the N-terminal part of Wapl. (**B**) The Cα-Cα distance of all lysines (gray, n = 561) in the Smc1-Smc3 hinge domain was compared to the experimentally observed lysine-lysine cross-links in this region (blue, n = 21). (**C**) Schematic representation of the cohesin proximity map.

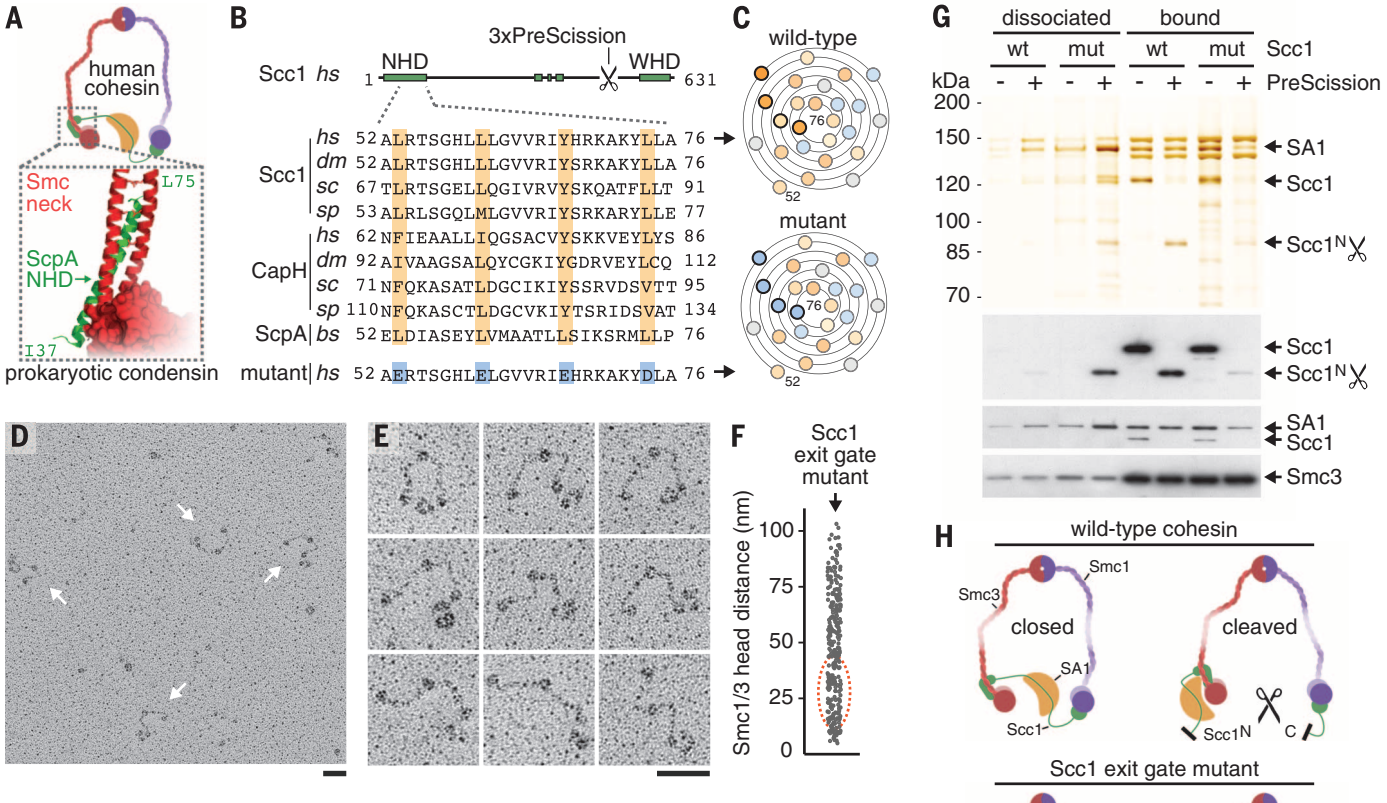


Fig. 3. Scc1 binds the coiled coil of Smc3 to close the cohesin ring. (**A**) Cartoon of cohesin tetramers and structure of the prokaryotic Smc (red) and ScpA (green) interaction (PDB ID 3ZGX). (**B**) Sequence alignment of the second part of the NHD in ScpA (prokaryotic condensin), Scc1 (cohesin), and CapH (condensin) from human (hs), fly (dm), budding yeast (sc), fission yeast (sp), and *B. subtilis* (bs). Predicted α helices (green boxes) and the introduced PreScission recognition site are shown. (**C**) Top-down helical wheel representation of wild-type and mutant Scc1^{NHD}. Hydrophobic (orange) and hydrophilic (blue) amino acids are indicated. (**D** and **E**) Tetramers with mutated Scc1 were visualized by rotary shadowing EM. Scale bars, 50 nm. (**F**) Distance between the heads of Smc1 and Smc3 in mutant complexes (n = 283). The dashed circle indicates the distribution of wild-type tetramers (see Fig. 1C). (**G** and **H**) Tetramers containing wild-type (wt) or mutant (mut) Scc1^{PreScission} were bound to anti-FLAG beads through Smc3^{FLAG} and exposed to PreScission protease. Supernatant (dissociated) and peptide eluates after extensive washing (bound) were analyzed by silver staining (top panel) and immunoblotting (lower panels) after SDS-PAGE. Upon cleavage, mutant Scc1^{N} and SA1 dissociated from Smc1-Smc3.

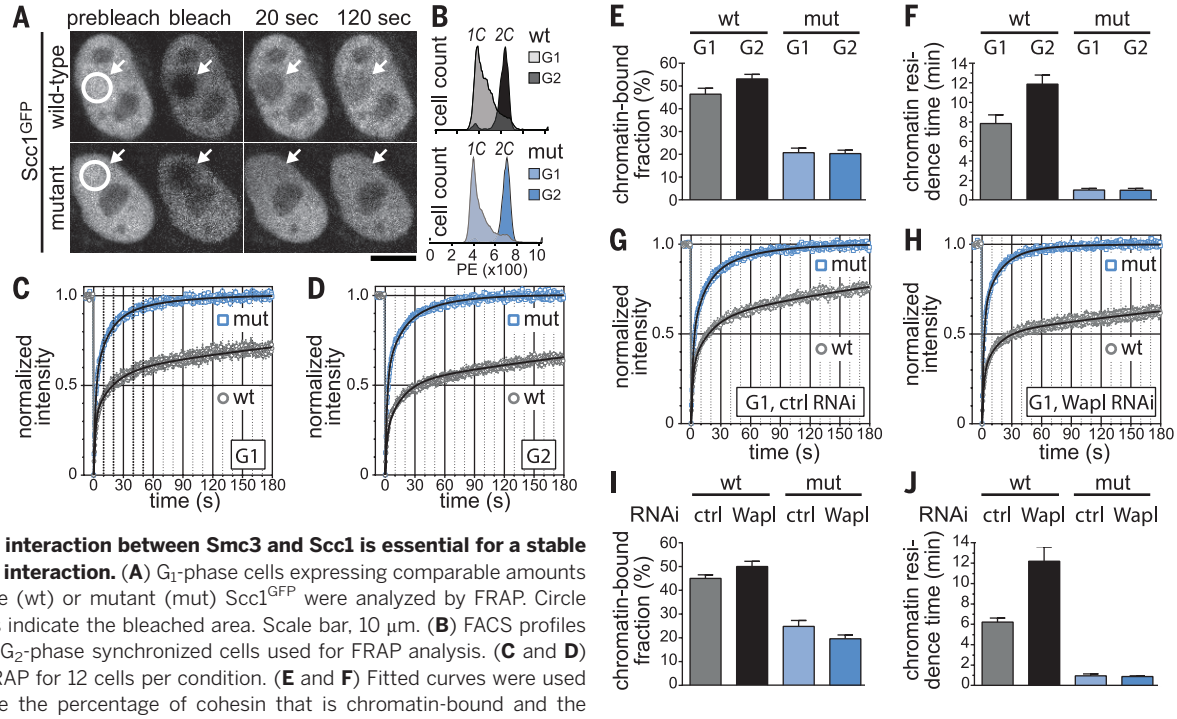


Fig. 4. The interaction between Smc3 and Scc1 is essential for a stable chromatin interaction. (**A**) G_1-phase cells expressing comparable amounts of wild-type (wt) or mutant (mut) $Scc1^{GFP}$ were analyzed by FRAP. Circle and arrows indicate the bleached area. Scale bar, 10 μm. (**B**) FACS profiles of G_1- and G_2-phase synchronized cells used for FRAP analysis. (**C** and **D**) Average FRAP for 12 cells per condition. (**E** and **F**) Fitted curves were used to calculate the percentage of cohesin that is chromatin-bound and the residence time of chromatin-bound cohesin. (**G** and **H**) Cells were treated with control or Wapl siRNA and synchronized in G_1. Cells expressing comparable amounts of wild-type or mutant $Scc1^{GFP}$ were analyzed by FRAP. The average FRAP for 12 cells per condition is shown. (**I** and **J**) Fitted curves were used to calculate the percentage of cohesin that is chromatin-bound and the residence time of chromatin-bound cohesin. Error bars represent SEM.

are thus suggested to be opened at distinct interfaces to allow entry and exit of DNA.

Reconstitution and visualization of the human cohesin complex

To obtain insight into how cohesin rings might open to entrap and release DNA, we reconstituted human cohesin complexes and used low-angle Pt/C rotary shadowing followed by transmission electron microscopy (henceforth rotary shadowing EM) to visualize them. Pure and stoichiometric Smc1-Smc3 heterodimers (283 kD) and cohesin complexes containing Smc1, Smc3, Scc1, and SA1 (500 kD) were obtained from baculovirus-infected insect cells (Fig. 1A). Smc1-Smc3 dimers appeared as a "pair of cherries" with a combined coiled-coil length of 98 ± 10 nm (n = 578). The additional presence of Scc1 and SA1 resulted in closed ring-like structures. SA1 was observed at varying positions, possibly reflecting the flexibility of its unstructured binding partner Scc1 (Fig. 1B). Whereas cohesin purified from HeLa cells was reported to contain a single kink in one of the coiled coils (*3*), we observed complexes with none, one, or two irregularities in the coiled coils.

Cleavage of Scc1 opens cohesin rings and releases cohesin from chromatin

It is well established that cleavage of Scc1 by separase at the metaphase-to-anaphase transition, as well as artificially induced cleavage of Scc1 by other proteases, leads to cohesin's release from DNA (*4*, *11*). However, the structural consequences of Scc1 cleavage have not been analyzed. We therefore generated recombinant cohesin with a triple tobacco etch virus (TEV) or human rhinovirus (PreScission) protease recognition site near the C-terminal end of Scc1. Rotary shadowing EM showed that cleaved cohesin tetramers resembled Smc1-Smc3 dimers with respect to flexibility (Fig. 1, B to D, and fig. S1). This confirms, as had been assumed, that Scc1 provides the physical connection between the NBDs of Smc1 and Smc3 and that Scc1 cleavage opens the cohesin ring.

We next used *Xenopus* egg extract to test whether reconstituted cohesin could be loaded onto chromatin. Binding of endogenous *Xenopus* cohesin is abolished by the addition of geminin, an inhibitor of prereplication complex assembly, but not by the addition of the Cdk inhibitor $p27^{Kip1}$ which prevents DNA replication (*18*, *19*). Purified human cohesin was loaded in a similar manner and was released from chromatin upon TEV protease–induced proteolysis of Scc1. When DNA replication was inhibited, Scc1 cleavage still released cohesin from chromatin (Fig. 1E and figs. S2 and S3). Cohesin's ring structure is thus essential for the association with DNA before and after replication.

A cohesin proximity and interaction map

We used chemical cross-linking and mass spectrometry to generate a lysine proximity map of cohesin and probe its topology. In a series of experiments using cohesin core complexes, a complex of Wapl and its binding partner Pds5B, and cohesin bound to Pds5B-Wapl, 51 unique intermolecular and 185 unique intramolecular cross-links were obtained (Fig. 2, fig. S4, and tables S1 and S2). We generated a distance map using high-resolution information from a murine Smc1-Smc3 hinge domain crystal structure (*20*). Of the 21 lysine-lysine pairs that were detected within this region, 19 bridged amino acids fewer than 24 Å apart. This distance reflects spatial constraints imposed by the cross-linker and thus validates our proximity map (Fig. 2B and fig. S4).

The majority of inter- and intramolecular cross-links in Smc1 and Smc3 were found in their coiled coils, likely as a consequence of solvent accessibility. Most cross-links in Pds5B and Wapl were also found within their unstructured and solvent-accessible regions. Consistently, regions in Pds5B that did not contain cross-linked lysines were also resistant to proteolysis by trypsin (fig. S4). For Scc1, only six intermolecular and two intramolecular cross-links were obtained, despite its predicted lack of secondary structure. Residues in the middle of Scc1 (Lys^{323}, Lys^{335}, and Lys^{406}) formed cross-links to SA1, Pds5B, and Wapl. This confirms Scc1's central region as a docking point for these proteins (*21*, *22*). Binding studies using recombinant proteins showed that the HEAT repeats of Pds5B and, as previously reported (*21*, *23*), the unstructured N-terminal half of Wapl associate with cohesin through Scc1 and SA1, respectively (fig. S5).

Scc1 binds the coiled coil of Smc3 to close the cohesin ring

Two residues that reside near the end of Scc1's N-terminal helical domain (NHD), Lys^{72} and Lys^{86}, form cross-links to Lys^{185} and Lys^{188} in

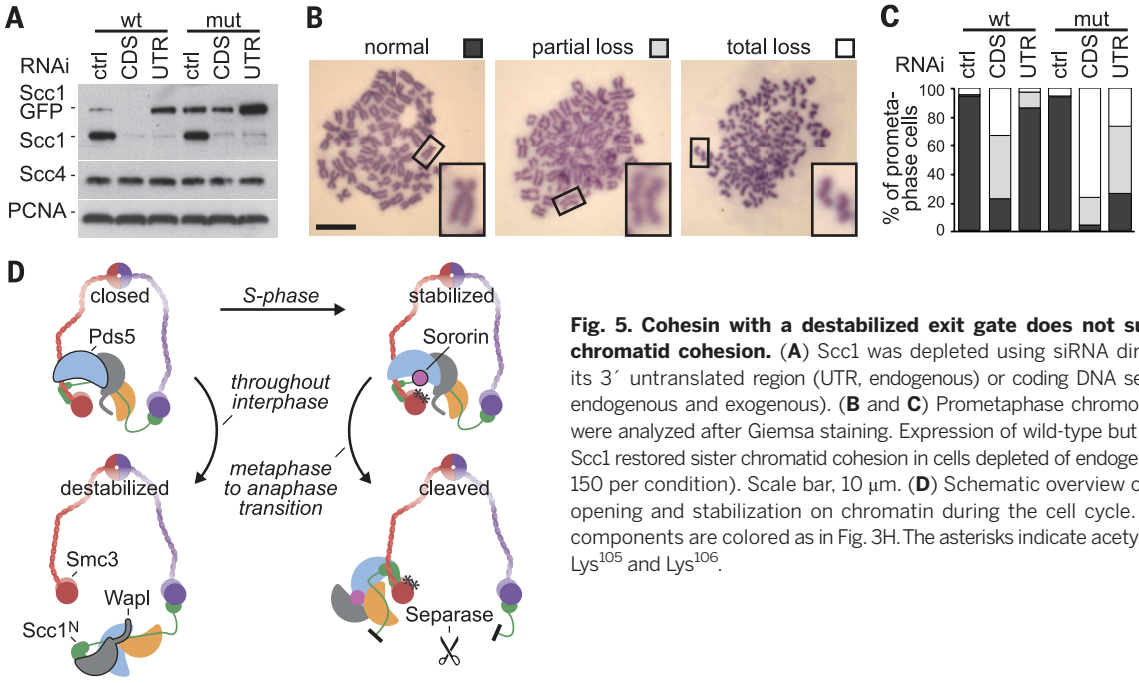


Fig. 5. Cohesin with a destabilized exit gate does not support sister chromatid cohesion. (**A**) Scc1 was depleted using siRNA directed against its 3′ untranslated region (UTR, endogenous) or coding DNA sequence (CDS, endogenous and exogenous). (**B** and **C**) Prometaphase chromosome spreads were analyzed after Giemsa staining. Expression of wild-type but not of mutant Scc1 restored sister chromatid cohesion in cells depleted of endogenous Scc1 (n = 150 per condition). Scale bar, 10 μm. (**D**) Schematic overview of cohesin ring opening and stabilization on chromatin during the cell cycle. Cohesin core components are colored as in Fig. 3H. The asterisks indicate acetylation of Smc3 Lys^{105} and Lys^{106}.

Smc3, respectively. These residues are located at the onset of Smc3's coiled coil, which suggests that Scc1's NHD binds Smc3 through a mechanism that differs from the interaction between Scc1's C-terminal winged-helix domain (WHD) and Smc1's NBD (*24*). An α helix in ScpA has been shown to interact with the onset of the Smc coiled coil in the bacterial *Bacillus subtilis* condensin complex (*25*) (Fig. 3A). Our cross-linking proximity map suggested analogous contacts in human cohesin—a notion further supported by the conserved amphiphilic nature of the NHD in Scc1 and condensin's kleisin CapH (Fig. 3B) and by the observation that point mutations in the NHD of yeast Scc1 reduced binding to Smc3 and compromised viability (*26*). To test the importance of this amphiphilicity, we generated cohesin complexes containing four point mutations in Scc1 (Fig. 3C). Rotary shadowing EM showed that most of these mutated complexes adopted an open conformation reminiscent of the cohesin complexes in which Scc1 was proteolytically cleaved (Fig. 3, D to F). Cohesin's proposed exit gate is thus formed by hydrophobic interactions between Scc1's NHD and the onset of Smc3's coiled coil, and this interaction is essential to keep cohesin rings closed.

Consistent with results obtained for yeast cohesin (*4*), Scc1 cleavage fragments ($Scc1^N$ and $Scc1^C$) and SA1 remained stably bound to Smc1-Smc3 after Scc1 proteolysis (Fig. 3G and fig. S6). If mutations in Scc1's NHD disturb its interaction with Smc3, $Scc1^N$ is predicted to dissociate from cohesin upon Scc1 cleavage. When tested, most $Scc1^N$ and SA1 did indeed dissociate, indicating that the Scc1 exit gate mutant bound the Smc1-Smc3 dimer through its C-terminal WHD before cleavage. Despite their similar appearance after rotary shadowing EM, this experiment thus confirmed that complexes with mutated Scc1 or cleaved Scc1 are topologically distinct (Fig. 3, G and H). Note that our in vitro results show that Scc1 cleavage fragments can remain associated with cohesin in the absence of Smc3 acetylation, unlike a previous proposal (*27*) (fig. S6).

The Scc1-Smc3 interaction is essential for a stable chromatin interaction

To test the in vivo effects of a disrupted Smc3-Scc1 interaction, we generated stably transfected HeLa cell lines in which wild-type and exit gate mutant Scc1 tagged with green fluorescent protein ($Scc1^{GFP}$) could be expressed at near-endogenous levels. Wild-type and mutant $Scc1^{GFP}$ were incorporated into cohesin complexes and could be purified from nuclease-digested chromatin (fig. S7). Mutations in Scc1's NHD did thus not disrupt cohesin's ability to interact with chromatin, despite their profound effect on cohesin's structure. Consistently, these mutations did reduce but not abolish cohesin's binding to sperm chromatin in *Xenopus* egg extract (fig. S8). Because exit gate mutants, as well as complexes in which Scc1 was proteolytically cleaved, are active adenosine triphosphatases, the reduced recruitment to chromatin is not caused by a reduction of cohesin's enzymatic activity (fig. S9).

To further investigate how the cohesin exit gate mutant binds to chromatin, we used the GFP tag on Scc1 to measure its fluorescence recovery after photobleaching (FRAP). For wild-type $Scc1^{GFP}$, reduced GFP levels were still detectable several minutes after bleaching, indicating a chromatin residence time of 7 to 9 min. In contrast, the residence time of mutant $Scc1^{GFP}$ was in the range of 1 min (Fig. 4, A to F). This chromatin interaction was sensitive to depletion of the Scc2-Scc4 complex by RNA interference, indicating that the loading of the exit gate mutant still depends on the cohesin loading machinery (fig. S10). Cohesin complexes that contain mutant Scc1 can thus interact with chromatin, but not in a stable manner. This residual chromatin association could reflect cohesin recruitment to the loading complex, or it could indicate that these mutants can still close their exit gates transiently.

Cohesin with a destabilized exit gate does not support sister chromatid cohesion

To test whether Wapl can still destabilize the transient association of the cohesin exit gate mutant with chromatin, we analyzed wild-type and mutant $Scc1^{GFP}$ by FRAP after depletion of Wapl by RNA interference. Whereas the residence time of wild-type complexes on chromatin doubled when Wapl was depleted, exit gate mutants were not stabilized (Fig. 4, G to J, and fig. S11). The effect of mutations at the Smc3-$Scc1^N$ interface thus resembles continuous destabilization by Wapl. Consistently, the binding dynamics of mutant $Scc1^{GFP}$ did not differ between G_1 and G_2 phase, whereas the residence time of wild-type $Scc1^{GFP}$ on chromatin increased after DNA replication, as previously described (*28*) (Fig. 4, A to F).

The marked reduction in chromatin binding and acetylation of Smc3 (fig. S7) raised the question of whether exit gate mutants could support sister chromatid cohesion. To test whether ectopically expressed Scc1 supported cohesion, we specifically depleted endogenous Scc1 by RNA interference (Fig. 5A and fig. S12). Under these conditions, expression of wild-type $Scc1^{GFP}$ rescued cohesion defects, whereas expression of mutated $Scc1^{GFP}$ did not (Fig. 5, B and C). Cohesin complexes that do not stably close their

exit gates are thus unable to mediate sister chromatid cohesion.

Conclusion

It has long been postulated that cohesin forms rings that can be opened to mediate entry and exit of DNA. Here, we used electron microscopy to demonstrate the existence of such open forms, generated either by proteolytic cleavage of Scc1 (mimicking the effect of separase at the metaphase-to-anaphase transition) or by weakening the interaction between Scc1's NHD and the coiled coil of Smc3 (mimicking the opening of cohesin's DNA exit gate). Because the latter is thought to be achieved by Wapl, our exit gate mutant may resemble an otherwise transient intermediate in the ring opening and closure cycle (Fig. 5D). We identified residues at the outside of the solenoid-like Pds5B that reside in direct proximity to Wapl and the Smc3-Scc1 interaction interface (fig. S13), implying that Wapl and Pds5 control the exit gate through direct interactions. However, it remains to be addressed at a mechanistic level how Wapl promotes ring opening and how this is coordinated by Pds5, antagonized by sororin, and regulated by phosphorylation events.

REFERENCES AND NOTES

1. S. Remeseiro, A. Losada, *Curr. Opin. Cell Biol.* **25**, 63–71 (2013).
2. C. H. Haering, J. Löwe, A. Hochwagen, K. Nasmyth, *Mol. Cell* **9**, 773–788 (2002).
3. D. E. Anderson, A. Losada, H. P. Erickson, T. Hirano, *J. Cell Biol.* **156**, 419–424 (2002).
4. S. Gruber, C. H. Haering, K. Nasmyth, *Cell* **112**, 765–777 (2003).
5. C. H. Haering, A. M. Farcas, P. Arumugam, J. Metson, K. Nasmyth, *Nature* **454**, 297–301 (2008).
6. R. Ciosk *et al.*, *Mol. Cell* **5**, 243–254 (2000).
7. P. Arumugam *et al.*, *Curr. Biol.* **13**, 1941–1953 (2003).
8. S. Weitzer, C. Lehane, F. Uhlmann, *Curr. Biol.* **13**, 1930–1940 (2003).
9. S. Gruber *et al.*, *Cell* **127**, 523–537 (2006).
10. J. Buheitel, O. Stemmann, *EMBO J.* **32**, 666–676 (2013).
11. F. Uhlmann, F. Lottspeich, K. Nasmyth, *Nature* **400**, 37–42 (1999).
12. S. Hauf, I. C. Waizenegger, J. M. Peters, *Science* **293**, 1320–1323 (2001).
13. R. Gandhi, P. J. Gillespie, T. Hirano, *Curr. Biol.* **16**, 2406–2417 (2006).
14. S. Kueng *et al.*, *Cell* **127**, 955–967 (2006).
15. A. Tedeschi *et al.*, *Nature* **501**, 564–568 (2013).
16. K. L. Chan *et al.*, *Cell* **150**, 961–974 (2012).
17. C. S. Eichinger, A. Kurze, R. A. Oliveira, K. Nasmyth, *EMBO J.* **32**, 656–665 (2013).
18. P. J. Gillespie, T. Hirano, *Curr. Biol.* **14**, 1598–1603 (2004).
19. T. S. Takahashi, P. Yiu, M. F. Chou, S. Gygi, J. C. Walter, *Nat. Cell Biol.* **6**, 991–996 (2004).
20. A. Kurze *et al.*, *EMBO J.* **30**, 364–378 (2011).
21. K. Shintomi, T. Hirano, *Genes Dev.* **23**, 2224–2236 (2009).
22. N. Zhang *et al.*, *PLOS ONE* **8**, e69458 (2013).
23. Z. Ouyang *et al.*, *Proc. Natl. Acad. Sci. U.S.A.* **110**, 11355–11360 (2013).
24. C. H. Haering *et al.*, *Mol. Cell* **15**, 951–964 (2004).
25. F. Bürmann *et al.*, *Nat. Struct. Mol. Biol.* **20**, 371–379 (2013).
26. P. Arumugam, T. Nishino, C. H. Haering, S. Gruber, K. Nasmyth, *Curr. Biol.* **16**, 1998–2008 (2006).
27. M. A. Deardorff *et al.*, *Nature* **489**, 313–317 (2012).
28. D. Gerlich, B. Koch, F. Dupeux, J. M. Peters, J. Ellenberg, *Curr. Biol.* **16**, 1571–1578 (2006).

ACKNOWLEDGMENTS

We thank O. Hudecz, K. Mechtler, G. Schmauss, K. Uzunova, M. Brandstetter, H. Kotisch, G. Resch, and A. Schleiffer for excellent technical support and I. Berger for an introduction to MultiBac. P.J.H. was supported by the Austrian Science Fund (W1221) and received funding from the European Community (FP7/2007-2013, no. 227764). Research in the laboratory of J.-M.P. is supported by Boehringer Ingelheim, the Austrian Science Fund (SFB-F34 and Wittgenstein award), the Austrian Research Promotion Agency (FFG Laura Bassi), the Vienna Science and Technology Fund (WWTF LS09-13), and the European Community (FP7/2007-2013, no. 241548, MitoSys).

SUPPLEMENTARY MATERIALS

www.sciencemag.org/content/346/6212/968/suppl/DC1
Materials and Methods
Figs. S1 to S13
Tables S1 and S2
References (*29*–*49*)

3 June 2014; accepted 26 September 2014
10.1126/science.1256904

REPORTS

OPTICS

Single-mode laser by parity-time symmetry breaking

Liang Feng,[1]* Zi Jing Wong,[1]* Ren-Min Ma,[1]* Yuan Wang,[1,2] Xiang Zhang[1,2]†

Effective manipulation of cavity resonant modes is crucial for emission control in laser physics and applications. Using the concept of parity-time symmetry to exploit the interplay between gain and loss (i.e., light amplification and absorption), we demonstrate a parity-time symmetry–breaking laser with resonant modes that can be controlled at will. In contrast to conventional ring cavity lasers with multiple competing modes, our parity-time microring laser exhibits intrinsic single-mode lasing regardless of the gain spectral bandwidth. Thresholdless parity-time symmetry breaking due to the rotationally symmetric structure leads to stable single-mode operation with the selective whispering-gallery mode order. Exploration of parity-time symmetry in laser physics may open a door to next-generation optoelectronic devices for optical communications and computing.

Laser cavities support a large number of closely spaced modes because their dimensions are typically much larger than an optical wavelength. As a result, the outputs from such lasers are subject to random fluctuations and instabilities because of mode competition for limited gain. During recent decades, effective mode manipulation and selection strategies have been intensively explored to achieve single-mode operation with both spatial and spectral controllability—a requirement for enhanced laser performance with higher monochromaticity, less mode competition, and better beam quality. Obtaining single-mode operation depends on sufficiently modulated gain and loss, but such modulation is impeded by factors such as inhomogeneous gain saturation. Several approaches have been developed that make use of an additional cavity for the intracavity feedback (*1*), distributed feedback gratings (*2*), an enlarged free spectral range through mode size reduction (*3*, *4*), or spatially varied optical pumping (*5*). However, these approaches are applicable to specific configurations; what is desired is a general design concept with flexible control of cavity modes.

Recent explorations of parity-time (PT) symmetry offer an opportunity to advance laser science by strategically manipulating gain and loss in order to control light transport. PT symmetry was initially proposed in quantum mechanics as an alternative criterion for non-Hermitian Hamiltonians $\hat{H}^{+} \neq \hat{H}$ that possesses a real eigenspectrum (*6*). Because of the equivalence between the Schrödinger equation in quantum mechanics and the electromagnetic wave equation, optics has become an ideal platform for studying the fundamentals of PT symmetry (*7*–*16*), with non-Hermiticity denoted by optical gain and loss. An intriguing PT phase transition has been demonstrated (*11*, *12*), enabling unique optical phenomena such as unidirectional light transport (*13*–*15*) and novel devices including low-power optical diodes (*16*). The strategic modulation of gain and loss in the PT symmetry–breaking condition can fundamentally broaden optical science at both semiclassical and quantum levels (*17*–*23*).

Using the PT symmetry–breaking concept, we delicately manipulated the gain and loss of a microring resonator and observed single-mode laser oscillation of a whispering-gallery mode (WGM). We exploited the continuous rotational symmetry of the microring structure to facilitate unique

[1]NSF Nanoscale Science and Engineering Center, University of California, Berkeley, CA 94720, USA. [2]Materials Sciences Division, Lawrence Berkeley National Laboratory, Berkeley, CA 94720, USA.
*These authors contributed equally to this work. †Corresponding author. E-mail: xiang@berkeley.edu

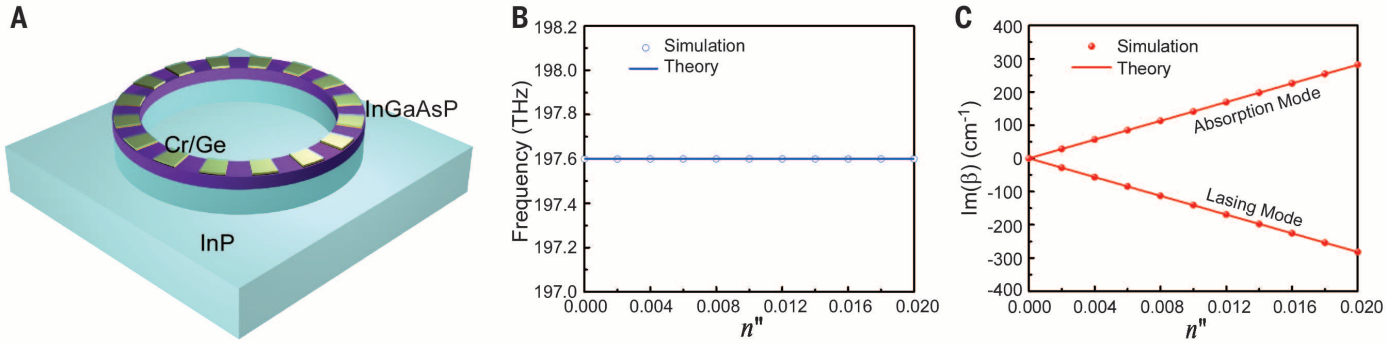


Fig. 1. Design of PT microring lasers. (**A**) Schematic of the PT microring laser, which consists of Cr/Ge bilayer structures arranged periodically in the azimuthal direction on top of the InGaAsP/InP microring resonator to mimic a pure gain/loss modulation. The diameter and width of the microring resonator are 8.9 μm and 900 nm, respectively. The microring also extends 1 μm deeper into the InP substrate. Here, the designed azimuthal order is m = 53 to achieve the resonant wavelength around 1500 nm. (**B** and **C**) The same eigenfrequency (197.6 THz) and complex conjugate imaginary eigenspectra for the two modes at m = 53 determined by numerical simulations (circles and dots) and theoretical calculations (solid lines). The onset in (C) indicates thresholdless PT symmetry breaking.

thresholdless PT symmetry breaking. This thresholdless PT symmetry breaking was valid only for the desired WGM order and enabled two energy-degenerate modes—the non-oscillating loss mode and the oscillating gain mode—whereas all other WGM modes experienced balanced gain/loss modulation and thus remained below the lasing threshold, leading to single-mode lasing.

The PT-synthetic microring resonator was designed with 500-nm-thick InGaAsP multiple quantum wells (MQWs) on an InP substrate (Fig. 1A). InGaAsP MQWs have a high material gain coefficient (>1000 cm^{-1}) around 1500 nm (*24*). The gain/loss modulation, satisfying an exact PT symmetry operation, was periodically introduced using additional Cr-Ge structures on top of the InGaAsP MQW along the azimuthal direction (φ):

$$\Delta n = \begin{cases} n_{\text{gain}} = -in'' \left[\frac{l\pi}{m} < \varphi < \frac{(l+1/2)\pi}{m}\right] \\ n_{\text{loss}} = in'' \left[\frac{(l+1/2)\pi}{m} < \varphi < \frac{(l+1)\pi}{m}\right] \end{cases} \quad (1)$$

where n'' denotes the index modulation in only the imaginary part; m is the azimuthal order of the desired WGM in the microring; and l = 0, 1, 2, ..., $2m$ – 1 divides the microring into $2m$ periods (i.e., $4m$ sections of gain and loss in total). The PT modulation is designed using bilayers on top of the gain material that introduces loss and exactly reverses the sign of the imaginary part of the local modal index while maintaining the same real part (in practice, the deposition of Cr/Ge also slightly modifies the real part on the order of 0.01%). The wave numbers of the eigenmodes in our PT microring resonator are $\beta = \beta_0 \pm i\kappa n''$, where β_0 is the intrinsic wave number of the WGM without gain or loss, and κ denotes the coupling between the clockwise and counterclockwise traveling waves through PT modulation in the microring resonator (*25*) (see supplementary text). Evolution of PT symmetry of the m = 53 WGM in the microring resonator as a function of imaginary part–index modulation can be seen from the corresponding

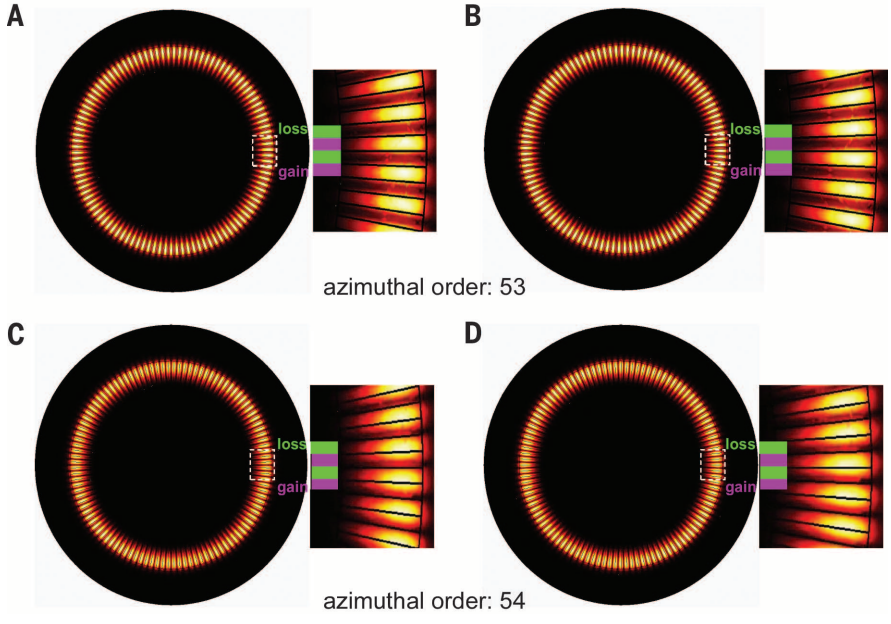


Fig. 2. WGMs of different azimuthal orders in the PT microring laser. (**A** and **B**) Eigen–electric field intensity distributions of paired lasing and absorption modes at m = 53. Fields are confined in the gain (A) and loss (B) sections, resulting in conjugate modal gain/loss coefficients: effective gain of 268 cm^{-1} [Im(β) = –134 cm^{-1}] for the lasing mode (A) and effective loss of –268 cm^{-1} [Im(β) = 134 cm^{-1}] for the absorption mode (B). (**C** and **D**) Eigen–electric field intensity distributions of paired WGMs at m = 54. The two modes share the same eigenfrequency of 200.9 THz and a similar modal loss coefficient of –8 cm^{-1} [Im(β) = 4 cm^{-1}].

complex eigenspectra (Fig. 1, B and C). Two WGMs are energy-degenerate at the same resonant eigenfrequency, but their modal wave numbers are complex conjugates of each other, corresponding to PT symmetry breaking with a simultaneous coexistence of lasing and absorption eigenmodes.

The microring resonator goes into the PT-broken phase with a bifurcation in the imaginary spectrum even if the strength of gain/loss modulation is infinitesimal. This thresholdless feature in our PT phase transition is attributable to the continuous rotational symmetry associated with the desired WGM order in the absence of a real-index modulation (see supplementary text and fig. S1). This feature is distinct from the previously studied coupled PT waveguide systems, including the recently developed coupled gain/loss WGM resonators (*16*, *23*). In those systems, there are no continuous symmetries, such that PT symmetry breaking requires a finite strength of the gain/loss modulation (*20*). Although our design is based on a linear model by assuming a steady lasing state with a certain gain coefficient of InGaAsP (*3*, *4*, *19*, *21*, *26*), it is worth noting that lasing itself is an intrinsic nonlinear process. However, this thresholdless PT symmetry breaking in our system is robust against optical nonlinearity and its induced PT phase transition (*10*). In the experiment, a slight deviation from the desired perfectly balanced gain/loss modulation

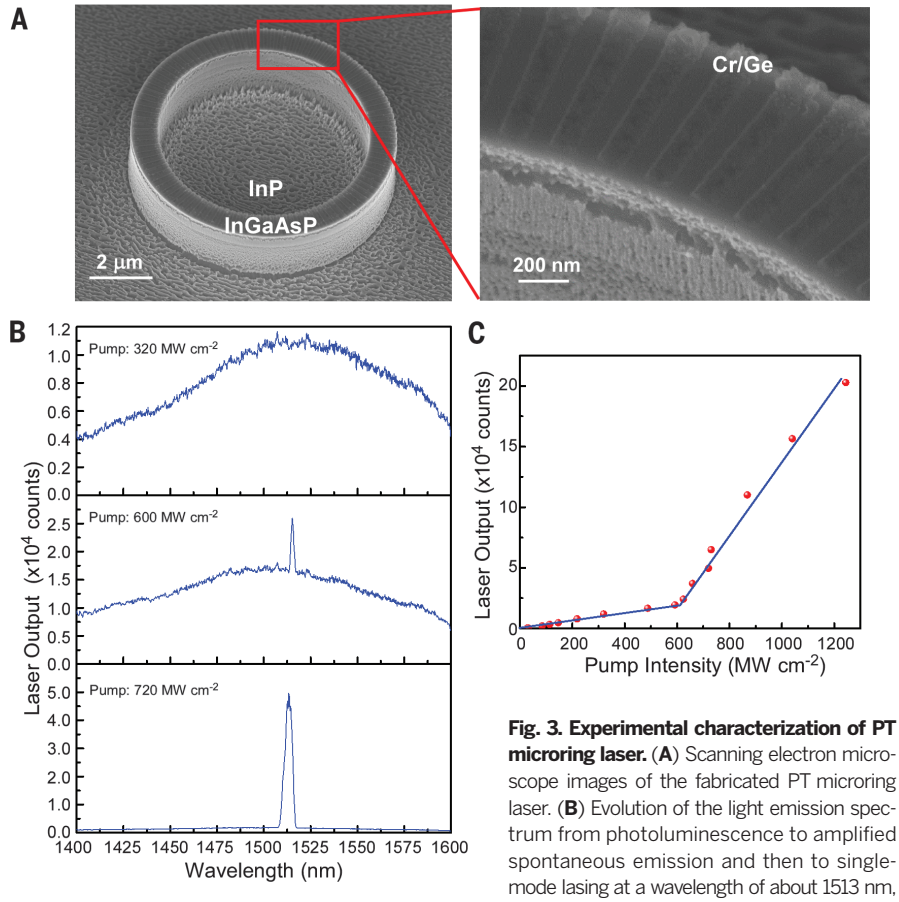


Fig. 3. Experimental characterization of PT microring laser. (**A**) Scanning electron microscope images of the fabricated PT microring laser. (**B**) Evolution of the light emission spectrum from photoluminescence to amplified spontaneous emission and then to single-mode lasing at a wavelength of about 1513 nm, shown as the peak power density of pump light was increased from 320 MW cm^{-2} to 600 MW cm^{-2} and then to 720 MW cm^{-2}. (**C**) Light-light curve of the PT microring laser shows the power relationship between the lasing emission and the pump light. A clear onset of the intrinsic single-mode lasing appears at a threshold slightly larger than 600 MW cm^{-2}.

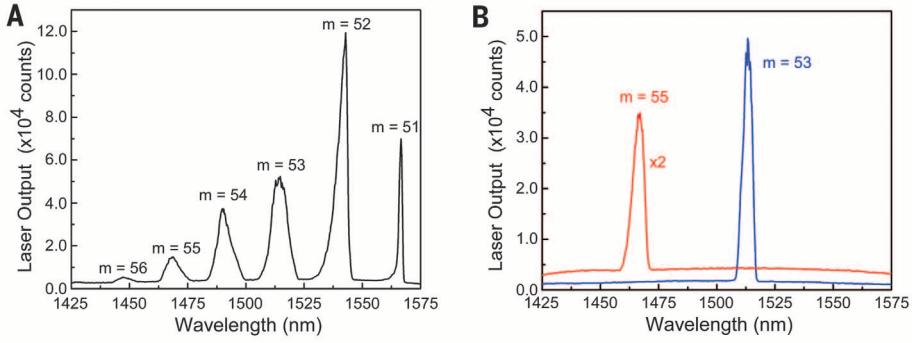


Fig. 4. Comparison between PT laser and typical microring laser. (**A**) Multimode lasing spectrum observed from the typical microring WGM laser, showing a series of lasing modes corresponding to different azimuthal orders. (**B**) Single-mode lasing spectra of the PT microring lasers operating at the m = 53 and m = 55 azimuthal orders, consistent with the lasing wavelength for the same azimuthal orders in (A). This confirms that our PT microring laser does not alter original WGMs but efficiently selects the desired lasing mode.

is possible, but the thresholdless PT symmetry–breaking feature is still preserved (see supplementary text and fig. S2).

Figure 2, A and B, shows the modal intensity distribution of the lasing and absorption modes in the PT microring resonator with 15 nm of Cr and 40 nm of Ge on top (corresponding to the InGaAsP MQW material gain coefficient of 800 cm^{-1} for the presumed ideal balanced gain/loss modulation). In the lasing mode, electric fields are confined mainly in the amplification sections, exhibiting a net modal gain coefficient of 268 cm^{-1}, whereas the absorption mode is loss-dominant with electric fields mainly under the Cr/Ge sections, with a loss coefficient of −268 cm^{-1}. Their eigenfrequencies are energy-degenerate but their gain/loss coefficients are opposite one another, consistent with the features of PT symmetry breaking. For other WGMs, for instance m = 54, electric fields in both energy-degenerate WGMs are uniformly distributed in gain and loss regimes. As a result, gain and loss are averaged out, creating modal wave numbers without net gain or loss (simulations show both modes have a similarly small loss coefficient of about −8 cm^{-1}) (Fig. 2, C and D). In this case, WGMs fall into the PT symmetric phase for the nondesired azimuthal orders (see supplementary text). It is therefore clear that only the lasing mode at the desired order contains a positive effective gain coefficient above the lasing threshold, enabling single-mode lasing. All other WGMs are suppressed by the intentionally introduced loss from the PT modulation. This unique single-mode operation is valid even with an arbitrarily wide gain spectrum because of its stringent mode selectivity, which is inherently different from the conventional single-mode microring lasers that use real-index coupling and modulation to achieve the mode splitting in eigenfrequencies and are limited by the bandwidth of the gain media (*27*, *28*).

The PT microring laser with Cr/Ge modulations (Fig. 3A) was fabricated using overlay electron beam lithography and plasma etching. Under optical pumping with a femtosecond laser (see supplementary text and fig. S3), a broad photoluminescence emission around 1500 nm was first observed at low pump power densities. As the pump power was increased, the transition to amplified spontaneous emission and full laser oscillation was clearly observed from the rapidly increasing spectral purity of the cavity mode (Fig. 3B). At higher pumping intensities well above the lasing threshold, the single-mode lasing peak is seen at the wavelength of 1513 nm, confirming our theoretical prediction of the single WGM lasing operation of the PT microring laser. The lasing linewidth is about 1.7 nm around the transparency pump power, corresponding to a quality factor of about 890 that is limited by the surface roughness of the sample. In Fig. 3C, the light-light curve corresponding to single-mode emission clearly shows a slope change corresponding to a lasing threshold at peak pump power density of about 600 MW cm^{-2}. The lasing mode (m = 53) in the PT-broken phase emerges above the lasing threshold, creating pronounced single-mode lasing with an extinction ratio of more than 14 dB, whereas other WGMs are all below the lasing threshold and are strongly suppressed.

For comparison, a control sample of a WGM laser was fabricated consisting of the same-sized InGaAsP/InP microring resonator without additional Cr/Ge index modulation. As expected, we observed a typical multimode lasing spectrum with different WGM azimuthal orders distributed over the gain spectral region (Fig. 4A). Relative to the PT microring laser, it can be seen that

under a similar pumping condition, the resonance peak for the same azimuthal order of m = 53 well matches the single-mode lasing of the PT ring resonator at a wavelength of 1513 nm (Fig. 4B). The power efficiency and the lasing threshold are also similar because the introduced loss in the PT microring laser minimally affects the desired lasing mode. We also fabricated an additional PT microring laser with a different azimuthal PT modulation for the order of m = 55. Its lasing emission at 1467 nm (Fig. 4B) also agrees well with the multimode lasing spectrum of the conventional WGM laser for the same azimuthal order (Fig. 4A). It is evident that instead of altering the WGM in the microring resonator, the introduced PT gain/loss modulation selects the lasing WGM in the PT-broken phase over a broad spectral band. By changing the desired azimuthal order of the structured PT modulation, the single-mode lasing frequency can be efficiently selected. Although we demonstrated lasing for only two WGM orders, this mode selection concept is general and in principle valid for arbitrary gain spectra. In applications, the demonstrated stable single-mode lasing can be efficiently routed, using a bus waveguide through the evanescent ring-waveguide coupling, to photonic integrated circuits for on-chip signal amplification and processing.

We have demonstrated a PT microring laser by delicate exploitation of optical loss and gain. Such a microring laser is intrinsically single-mode regardless of the gain spectral bandwidth. This is because the continuous rotational symmetry of PT modulation enables the thresholdless PT symmetry breaking only for the desired mode. More important, our PT laser demonstration is a major step toward unique photonic devices such as a PT-symmetric laser-absorber that coincides lasing and anti-lasing [i.e., coherent perfect absorption (*29*, *30*)] simultaneously.

REFERENCES AND NOTES

1. D. C. Hanna, B. Luther-Davies, R. C. Smith, *Electron. Lett.* **8**, 369 (1972).
2. H. Ghafouri-Shiraz, *Distributed Feedback Laser Diodes and Optical Tunable Filters* (Wiley, New York, 2003).
3. M. T. Hill *et al.*, *Nat. Photonics* **1**, 589–594 (2007).
4. R. M. Ma, R. F. Oulton, V. J. Sorger, G. Bartal, X. Zhang, *Nat. Mater.* **10**, 110–113 (2011).
5. S. F. Liew, B. Redding, L. Ge, G. S. Solomon, H. Cao, *Appl. Phys. Lett.* **104**, 231108 (2014).
6. C. M. Bender, S. Böttcher, *Phys. Rev. Lett.* **80**, 5243–5246 (1998).
7. K. G. Makris, R. El-Ganainy, D. N. Christodoulides, Z. H. Musslimani, *Phys. Rev. Lett.* **100**, 103904 (2008).
8. S. Klaiman, U. Günther, N. Moiseyev, *Phys. Rev. Lett.* **101**, 080402 (2008).
9. A. E. Miroshnichenko, B. A. Malomed, Y. S. Kivshar, *Phys. Rev. A* **84**, 012123 (2011).
10. Y. Lumer, Y. Plotnik, M. C. Rechtsman, M. Segev, *Phys. Rev. Lett.* **111**, 263901 (2013).
11. A. Guo *et al.*, *Phys. Rev. Lett.* **103**, 093902 (2009).
12. C. E. Rüter *et al.*, *Nat. Phys.* **6**, 192–195 (2010).
13. Z. Lin *et al.*, *Phys. Rev. Lett.* **106**, 213901 (2011).
14. A. Regensburger *et al.*, *Nature* **488**, 167–171 (2012).
15. L. Feng *et al.*, *Nat. Mater.* **12**, 108–113 (2013).
16. B. Peng *et al.*, *Nat. Phys.* **10**, 394–398 (2014).
17. H. Schomerus, *Phys. Rev. Lett.* **104**, 233601 (2010).
18. G. Yoo, H. S. Sim, H. Schomerus, *Phys. Rev. A* **84**, 063833 (2011).
19. S. Longhi, *Phys. Rev. A* **82**, 031801(R) (2010).
20. Y. D. Chong, L. Ge, A. D. Stone, *Phys. Rev. Lett.* **106**, 093902 (2011).
21. M.-A. Miri, P. LiKamWa, D. N. Christodoulides, *Opt. Lett.* **37**, 764–766 (2012).
22. M. Liertzer *et al.*, *Phys. Rev. Lett.* **108**, 173901 (2012).
23. M. Brandstetter *et al.*, *Nat. Commun.* **5**, 4034 (2014).
24. M. Körbl, A. Gröning, H. Schweizer, J. L. Gentner, *J. Appl. Phys.* **92**, 2942 (2002).
25. J. Wiersig, S. W. Kim, M. Hentschel, *Phys. Rev. A* **78**, 053809 (2008).
26. A. Mizrahi *et al.*, *Opt. Lett.* **33**, 1261–1263 (2008).
27. L. Shang, L. Liu, L. Xu, *Opt. Lett.* **33**, 1150–1152 (2008).
28. A. Arbabi, Y. M. Kang, C. Y. Lu, E. Chow, L. L. Goddard, *Appl. Phys. Lett.* **99**, 091105 (2011).
29. Y. D. Chong, L. Ge, H. Cao, A. D. Stone, *Phys. Rev. Lett.* **105**, 053901 (2010).
30. W. Wan *et al.*, *Science* **331**, 889–892 (2011).

ACKNOWLEDGMENTS

Supported by Office of Naval Research Multidisciplinary University Research Initiative program grant N00014-13-1-0649. We thank Y.-L. Xu and K. O'Brien for helpful discussions.

SUPPLEMENTARY MATERIALS

www.sciencemag.org/content/346/6212/972/suppl/DC1
Supplementary Text
Figs. S1 to S3

8 July 2014; accepted 17 October 2014
Published online 30 October 2014;
10.1126/science.1258479

OPTICS

Parity-time–symmetric microring lasers

Hossein Hodaei, Mohammad-Ali Miri, Matthias Heinrich,*
Demetrios N. Christodoulides, Mercedeh Khajavikhan†

The ability to control the modes oscillating within a laser resonator is of fundamental importance. In general, the presence of competing modes can be detrimental to beam quality and spectral purity, thus leading to spatial as well as temporal fluctuations in the emitted radiation. We show that by harnessing notions from parity-time (PT) symmetry, stable single–longitudinal mode operation can be readily achieved in a system of coupled microring lasers. The selective breaking of PT symmetry can be used to systematically enhance the maximum attainable output power in the desired mode. This versatile concept is inherently self-adapting and facilitates mode selectivity over a broad bandwidth without the need for other additional intricate components. Our experimental findings provide the possibility to develop synthetic optical devices and structures with enhanced functionality.

Since the early days of the laser, enforcing single-mode operation in a given arrangement has been one of the primary goals of cavity design (*1*). At first glance, one might expect these challenges to become less acute in the course of miniaturization, as the separation of resonances, or free spectral range, scales inversely with size. However, despite their smaller size, mode management in semiconductor lasers is still demanding because of their large inhomogeneously broadened gain bandwidth (*2*). In such broadband gain environments, the lasing of the desired mode does not prevent the neighboring resonances from also experiencing amplification. Consequently, additional steps must be taken to suppress the competing parasitic modes. This can be accomplished in a number of ways, as, for example, coupling to detuned external cavities (*3*), by including intracavity dispersive elements such as distributed feedback gratings or distributed Bragg mirrors (*4*–*6*), by spatially modulating the pump (*7*), or more recently by extreme confinement of light in subwavelength structures using metallic cavities (*8*–*10*). However, not all of these schemes are practically compatible with every type of resonator, and each of them introduces further demands in terms of design complexity and fabrication tolerances. Clearly, of importance will be to identify alternative strategies through which mode selection can be established not only in a versatile manner, but also without any negative impact on the overall efficiency.

A prominent class of integrated laser arrangements is based on microring resonators (*11*, *12*). By virtue of their high refractive index contrast, such configurations can support whispering gallery modes that exhibit high quality factors and small footprints, thus making them excellent candidates for on-chip integrated photonic applications. However, like many other microscale resonators, these cavities tend to support multiple longitudinal modes with almost similar quality factors throughout their gain bandwidth, while offering little control in terms of mode discrimination with conventional techniques.

CREOL, The College of Optics and Photonics, University of Central Florida, Orlando, FL 32816-2700, USA.
*Present address: Institute of Applied Physics, Abbe Center of Photonics, Friedrich-Schiller-Universität Jena, Max-Wien-Platz 1, 07743 Jena, Germany. **†Corresponding author. E-mail: mercedeh@creol.ucf.edu**

This inherent multimode operation drastically limits the prospects of these lasers for on-chip applications.

A number of studies have suggested that notions taken from parity-time symmetry—first developed within the framework of quantum field theories—can be observed and used in the field of optics (*13*–*27*). In general, a nonconservative optical system is considered to be PT-symmetric provided the gain-loss distribution is spatially balanced, in which case, its associated Hamiltonian commutes with the parity-time ($\mathcal{PT}$) operator (*28*). Under these conditions, the spectrum of this non-Hermitian system can be entirely real-valued, even though gain and loss are present (*13*–*16*, *28*–*30*). However, above a certain gain-loss contrast threshold, PT symmetry can be spontaneously broken, in which case the spectrum becomes partially complex (*17*–*23*, *31*, *32*). In this regime, some of the modes experience either gain or loss, while the rest remains neutral (*16*, *23*).

We show that PT symmetry breaking can be elegantly exploited to establish single-mode operation in inherently multimoded microring lasers. This is accomplished in a coupled arrangement of two structurally identical ring resonators, with one experiencing gain while the other provides an equal amount of loss. The key idea behind this mechanism is that the threshold of symmetry breaking depends solely on the relation between gain/loss and coupling. Whereas any active resonator can generally display single-wavelength operation when the pump power is reduced, selective breaking of PT symmetry can be used to systematically enhance the maximum attainable gain of this mode. This is possible even if a large number of competing longitudinal or transverse resonator modes fall within the amplification bandwidth of the inhomogeneously broadened active medium. Consequently, our approach naturally exhibits a type of broadband self-adaptive behavior and is, in principle, applicable to any active resonator configuration.

We consider two coupled microrings. The small structure size associated with such devices necessitates a high refractive index contrast. The interaction between two adjacent rings is mediated by the mutual overlap of their fields in the narrow region of greatest proximity, and the coupling coefficient κ determines the frequency splitting $\delta\omega$ between mode pairs. As is well known, the free spectral range, or mode spacing, of a ring with radius R and effective group index n_g is given by $\Delta\omega = c/Rn_g$. Assuming an active medium with an inhomogeneously broadened amplification profile $g(\omega)$, each and every mode whose gain exceeds the resonator losses can lase (see schematic in Fig. 1A).

Following the equivalence between the mathematical frameworks of quantum mechanics and optics (*13*, *28*), PT symmetry can be established in photonic systems (*16*, *17*, *23*) provided that the complex refractive index distribution $n(\vec{r}) = n_R(\vec{r}) + in_I(\vec{r})$ obeys $n(\vec{r}) = n^*(-\vec{r})$, i.e., that the real and imaginary parts exhibit even and odd spatial distributions, respectively. In our coupled arrangement, this implies that the gain experienced in one ring is balanced by the loss in the other. If PT symmetry is unbroken, the modes neither decay nor grow, but rather remain neutral. By contrast, once the gain-loss contrast is increased beyond the coupling constant, this symmetry is broken and the respective modes experience gain or loss in conjugate pairs (*27*). This phase transition lies at the heart of our approach.

When two identical resonators are placed next to one another, the degeneracy between their respective modes is broken (see Fig. 1B). The frequency splitting $\delta\omega$ of the resulting supermode doublets $\omega_n^{(1,2)}$ is directly proportional to the coupling coefficient, i.e., $\delta\omega = 2\kappa$. The resulting eigenfrequencies of such an active system can in general be complex, and their imaginary part describes amplification or attenuation. Meanwhile, in PT-symmetric arrangements, the relationship

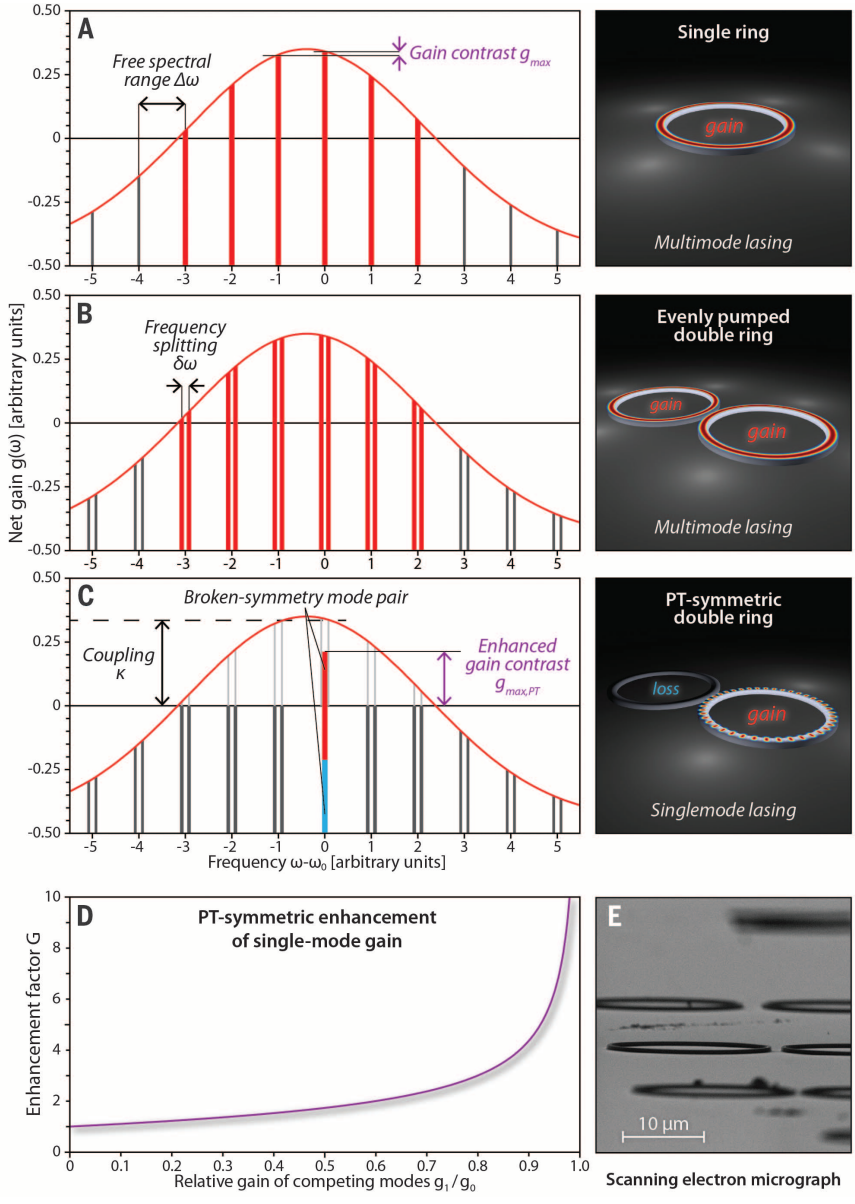


Fig. 1. Principle of mode suppression in PT-symmetric microring lasers. (**A**) An isolated ring resonator allows lasing of all longitudinal modes with positive net gain. To achieve single-mode operation, the maximum permissible gain is limited by the contrast between the resonances. (**B**) In a coupled arrangement of two identical and evenly pumped rings, the degeneracy of resonator modes is broken and mode pairs emerge. (**C**) PT-symmetric arrangement: As long as the coupling exceeds the amplification, loss and gain in the two respective rings balance each other, whereas above this threshold, PT symmetry breaking occurs. This mechanism can be exploited to enforce stable single-mode operation in otherwise highly multimoded resonators. (**D**) Enhancement factor G of the maximum achievable differential gain for single-mode operation in a PT-symmetric setting compared to a single active resonator. (**E**) Scanning electron microscope image of a typical set of coupled microring resonator pairs.

between eigenfrequencies and coupling is by nature different, as indicated by the following expression:

$$\omega_n^{(1,2)} = \omega_n \pm \sqrt{\kappa_n^2 - \gamma_n^2} \quad (1)$$

Any pair of modes, whose gain-loss contrast γ_n remains below the coupling coefficient κ_n, undergoes bounded neutral oscillations. However, as soon as γ_n exceeds κ_n, a conjugate pair of lasing and decaying modes emerges. Clearly, a judicious placement of this PT threshold will allow a complete suppression of all nonbroken mode pairs in favor of a single amplified mode associated with the aforementioned conjugate pair (see Fig. 1C). As the imaginary parts of the eigenvalues diverge, degeneracy between their real parts is restored. We emphasize that even in the absence of PT symmetry, any resonator with a spectrally nonuniform gain distribution $g(\omega)$ can in principle exhibit single-mode operation, provided that the losses overcompensate the gain for all but one resonance. However, in this regime, the amplification cannot exceed the gain contrast $g_{max} = g_0 - g_1$ (see Fig. 1A). Here, g_0 refers to the gain of the principal mode, whereas g_1, to that of the next-strongest competing resonance. Obviously, this approach will impose severe constraints on the operating parameters—especially in the case of broad gain windows and/or closely spaced resonator modes, where g_{max} is very small. By contrast, in a PT-symmetric setting, the coupling κ now plays the role of a virtual loss, and all undesirable modes must fall below its corresponding threshold. According to Eq. 1, we find that in this case, the maximum achievable gain differential is given by

$$g_{max,PT} = \sqrt{g_0^2 - g_1^2} = g_{max} \cdot \sqrt{\frac{g_0/g_1 + 1}{g_0/g_1 - 1}} \quad (2)$$

Given that $g_0 \geq g_1$, a selective breaking of PT symmetry can therefore systematically increase the available amplification for single-mode operation. The square-root behavior of this enhancement (a direct outcome of the PT symmetry breaking), as characterized by the factor $G = g_{max,PT}/g_{max}$, can provide substantially higher selectivity, especially when the initial contrast between adjacent modes is small ($g_1 \to g_0$, see Fig. 1D). This type of mode discrimination is resilient and remains valid even when PT symmetry does not exactly hold for all modes involved. On a fundamental level, the mechanism is related to the presence of an exceptional point in the system (*33*). Similar strategies have recently been proposed as means to boost the sensitivity of high-*Q* resonant nanoparticle detectors (*34*). The influence of deviations from ideal PT-symmetry conditions is discussed in the supplementary materials (*35*). The high mode confinement offered by our arrangement, as well as the strong coupling between rings, makes this arrangement relatively immune to local perturbations introduced by fabrication errors, nonlinearities, and/or temperature gradients (*36*).

We used electron beam lithographic techniques for the realization of active ring resonators based on InGaAsP (indium-gallium-arsenide-phosphide) quantum wells (Fig. 1E). More details on the sample fabrication are given in the supplementary materials (*35*). The gain and loss regions can be defined by selective optical pumping at 1064 nm. The gain bandwidth of the active medium spans the spectral region between 1260 and 1600 nm. In the following, the resonators were characterized by placing them within a circularly symmetric Gaussian pump beam to implement three possible configurations (single ring, evenly pumped double ring, and PT-symmetric ring arrangement). Accordingly, the effective pump powers were calculated from the geometric overlap between the active medium and the pump profile. After blocking remnants of the pump radiation by means of a notch filter, we

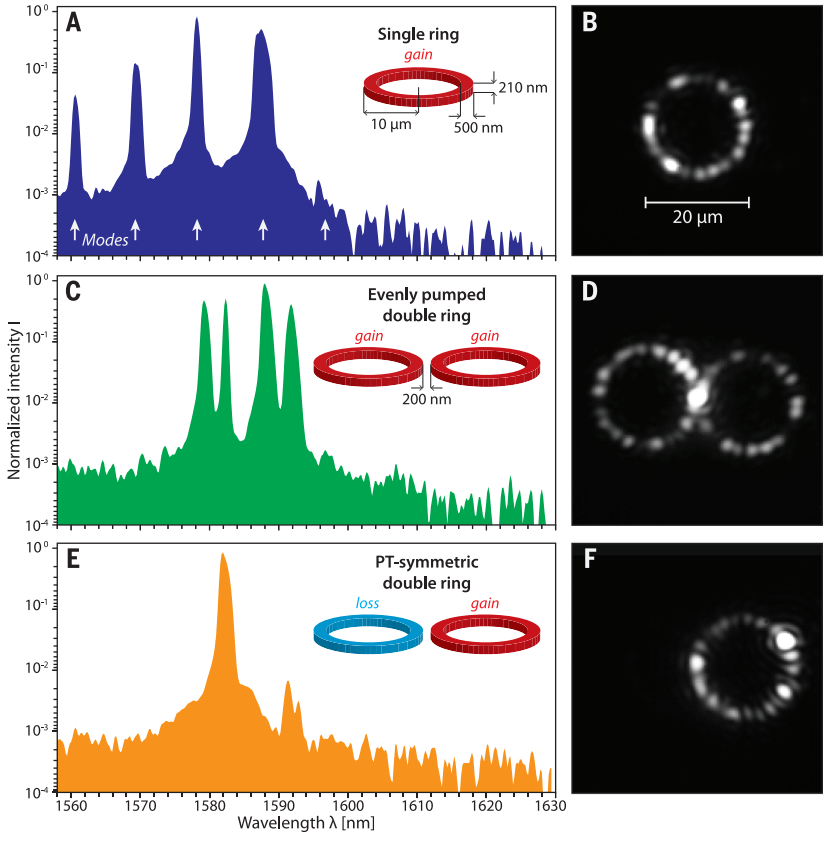


Fig. 2. Experimental observation of mode suppression by PT-symmetry breaking. (**A**) Emission spectrum of a single resonator (radius 10 µm, ring width 500 nm, height 210 nm) when exposed to a peak pump power of 4.9 mW. (**B**) Corresponding intensity pattern within the ring as observed from scattered light. (**C**) Spectrum obtained from an evenly pumped pair of such rings (4.9 mW + 4.9 mW). (**D**) The intensity pattern shows that both resonators equally contribute. (**E**) Single-moded spectrum under PT-symmetric conditions (0 mW + 4.9 mW pump). The mode suppression ratio exceeds 20 dB. (**F**) Lasing exclusively occurs in the active resonator. The single ring has a free spectral range of ~ 9.9 nm and a *Q*-factor of ~2×10^5. The measured linewidth of the single ring laser is ~ 0.12 nm, limited by the spectrometer resolution.

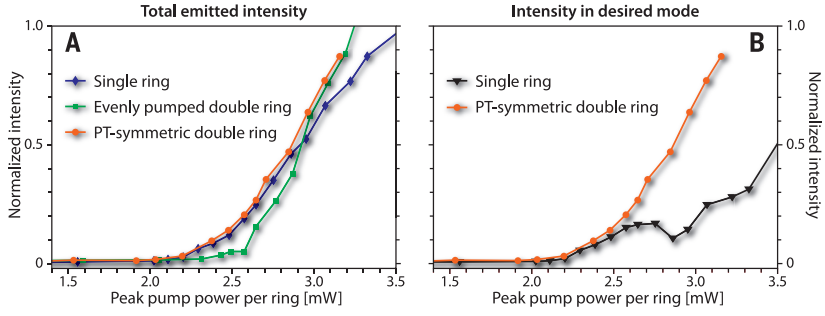


Fig. 3. Light-light characteristics. (**A**) Characteristic light-light graphs of the single, double, and PT-symmetric microring resonator arrangements shown in Fig. 2. The increased slope in the evenly pumped case is due to the doubled active area. (**B**) Spectrally resolved plots comparing the intensity emitted in the desired mode. The PT-symmetric configuration clearly offers superior performance. The onset of parasitic modes is indicated by the kinks in the single-ring graph.

simultaneously monitored the intensity profile and spectrum of the light oscillating in the microrings. Figure 2, A and B, illustrate the behavior of a single ring (radius 10 μm, ring width 500 nm, height 210 nm) when exposed to an effective peak pump power of 4.9 mW (15-ns pulses with a repetition rate of 290 kHz). Under these conditions, at least four modes contribute to lasing in the isolated ring. When two such rings are placed at a distance of 200 nm from one another, and both are exposed to the same pump power, the coupling-induced mode splitting can be seen (Fig. 2, C and D), which occurs symmetrically around the resonance wavelengths of each ring in isolation. In this coupled regime, both structures are contributing equally. Once PT symmetry is established by withholding the pump from one of the resonators (Fig. 2, E and F), lasing occurs exclusively in the active ring, where single-mode operation is now achieved. The presence of the lossy ring only serves to suppress the unwanted longitudinal modes with a contrast exceeding 20 dB. As the pump increases to very high levels, eventually the PT symmetry of other cavity modes will break, leading to multimode operation.

In the characteristic light-light curves for all three arrangements involving the 10-μm rings shown in Fig. 3A, the transition to the lasing regime, defined by the sudden onset of emission, is clearly visible. The evenly pumped double ring displays almost twice the slope of the single ring because of its larger pumped/emitting area. The PT-symmetric arrangement appears almost indistinguishable from the single ring, indicating that the presence of the lossy element does not necessarily decrease the overall efficiency. A spectrally resolved comparison of these two scenarios (Fig. 3B) reveals that the PT system offers superior performance, because the emission from the single ring includes contributions from several modes. In integrated photonic circuit applications, light from the PT-microring lasers can be optimally extracted using on-chip bus waveguides as output couplers.

Our results show that the selective breaking of PT symmetry can be used to enforce stable single-mode operation in microring laser resonators. In particular, the maximum achievable gain in PT-symmetric ring pairs can be systematically enhanced with respect to competing modes. This mechanism of mode selectivity is robust in terms of fabrication inaccuracies and can accommodate active media with wide gain spectra. Moreover, as the occurrence of PT symmetry breaking is exclusively determined by the relation between net gain and coupling, the proposed arrangement is by nature self-adapting. PT-symmetric arrangements offer superior performance in terms of efficiency. Although such designs can in principle be adopted for any type of laser cavity, they are particularly suited for the control of longitudinal modes in microring resonators, a previously challenging task. These results provide the possibility of developing classes of compact lasers that combine the advantages of multimode cavities and stable single-mode emission.

REFERENCES AND NOTES

1. A. L. Schawlow, C. H. Townes, *Phys. Rev.* **112**, 1940–1949 (1958).
2. M. Asada, A. Kameyama, Y. Suematsu, *IEEE J. Quantum Electron.* **20**, 745–753 (1984).
3. M. Fleming, A. Mooradian, *IEEE J. Quantum Electron.* **17**, 44–59 (1981).
4. H. Kogelnik, C. V. Shank, *J. Appl. Phys.* **43**, 2327 (1972).
5. M. Nakamura, K. Aiki, J. Umeda, A. Yariv, *Appl. Phys. Lett.* **27**, 403 (1975).
6. K. Iga, F. Koyama, S. Kinoshita, *IEEE J. Quantum Electron.* **24**, 1845–1855 (1988).
7. S. F. Liew, B. Redding, L. Ge, G. S. Solomon, H. Cao, *Appl. Phys. Lett.* **104**, 231108 (2014).
8. M. A. Noginov *et al.*, *Nature* **460**, 1110–1112 (2009).
9. R. F. Oulton *et al.*, *Nature* **461**, 629–632 (2009).
10. M. Khajavikhan *et al.*, *Nature* **482**, 204–207 (2012).
11. S. L. McCall, A. F. J. Levi, R. E. Slusher, S. J. Pearton, R. A. Logan, *Appl. Phys. Lett.* **60**, 289 (1992).
12. K. J. Vahala, *Nature* **424**, 839–846 (2003).
13. K. G. Makris, R. El-Ganainy, D. N. Christodoulides, Z. H. Musslimani, *Phys. Rev. Lett.* **100**, 103904 (2008).
14. R. El-Ganainy, K. G. Makris, D. N. Christodoulides, Z. H. Musslimani, *Opt. Lett.* **32**, 2632–2634 (2007).
15. S. Klaiman, U. Günther, N. Moiseyev, *Phys. Rev. Lett.* **101**, 080402 (2008).
16. A. Guo *et al.*, *Phys. Rev. Lett.* **103**, 093902 (2009).
17. C. E. Rüter *et al.*, *Nat. Phys.* **6**, 192–195 (2010).
18. S. Longhi, *Phys. Rev. A* **82**, 031801 (2010).
19. Y. D. Chong, L. Ge, A. D. Stone, *Phys. Rev. Lett.* **106**, 093902 (2011).
20. A. Szameit, M. C. Rechtsman, O. Bahat-Treidel, M. Segev, *Phys. Rev. A* **84**, 021806 (2011).
21. A. E. Miroshnichenko, B. A. Malomed, Y. S. Kivshar, *Phys. Rev. A* **84**, 012123 (2011).
22. E. M. Graefe, H. F. Jones, *Phys. Rev. A* **84**, 013818 (2011).
23. A. Regensburger *et al.*, *Nature* **488**, 167–171 (2012).
24. L. Feng *et al.*, *Nat. Mater.* **12**, 108–113 (2013).
25. M. Liertzer *et al.*, *Phys. Rev. Lett.* **108**, 173901 (2012).
26. M. Brandstetter *et al.*, *Nat. Commun.* **5**, 4034 (2014).
27. M.-A. Miri, P. LiKamWa, D. N. Christodoulides, *Opt. Lett.* **37**, 764–766 (2012).
28. C. M. Bender, S. Boettcher, *Phys. Rev. Lett.* **80**, 5243–5246 (1998).
29. T. Kottos, *Nat. Phys.* **6**, 166–167 (2010).
30. J. Schindler, A. Li, M. C. Zheng, F. M. Ellis, T. Kottos, *Phys. Rev. A* **84**, 040101 (2011).
31. B. Peng *et al.*, *Nat. Phys.* **10**, 394–398 (2014).
32. L. Chang *et al.*, *Nat. Photonics* **8**, 524–529 (2014).
33. D. D. Scott, Y. N. Joglekar, *Phys. Rev. A* **83**, 050102 (2011).
34. J. Wiersig, *Phys. Rev. Lett.* **112**, 203901 (2014).
35. More details on the breaking of PT symmetry in microring resonators, as well as additional information on the experimental techniques, can be found in the supplementary materials.
36. Y. Lumer, Y. Plotnik, M. C. Rechtsman, M. Segev, *Phys. Rev. Lett.* **111**, 263901 (2013).

ACKNOWLEDGMENTS

We gratefully acknowledge the nancial support from Army Research Office (grant W911NF-14-1-0543), NSF (grant ECCS-1128520), and Air Force Office of Scientific Research (grants FA9550-12-1-0148 and FA9550-14-1-0037). M.H. was supported by the German National Academy of Sciences Leopoldina (grant LPDS 2012-01). We thank M. Mills for helpful discussions.

SUPPLEMENTARY MATERIALS

www.sciencemag.org/content/346/6212/975/suppl/DC1
Materials and Methods
Supplementary Text
Figs. S1 to S8
References (*37*–*41*)

8 July 2014; accepted 17 October 2014
Published online 30 October 2014;
10.1126/science.1258480

GEOMORPHOLOGY

Tectonic control of Yarlung Tsangpo Gorge revealed by a buried canyon in Southern Tibet

Ping Wang,[1] Dirk Scherler,[2]*† Jing Liu-Zeng,[1] Jürgen Mey,[3] Jean-Philippe Avouac,[2]‡ Yunda Zhang,[4] Dingguo Shi[4]

The Himalayan mountains are dissected by some of the deepest and most impressive gorges on Earth. Constraining the interplay between river incision and rock uplift is important for understanding tectonic deformation in this region. We report here the discovery of a deeply incised canyon of the Yarlung Tsangpo River, at the eastern end of the Himalaya, which is now buried under more than 500 meters of sediments. By reconstructing the former valley bottom and dating sediments at the base of the valley fill, we show that steepening of the Tsangpo Gorge started at about 2 million to 2.5 million years ago as a consequence of an increase in rock uplift rates. The high erosion rates within the gorge are therefore a direct consequence of rapid rock uplift.

The topographic evolution of mountain ranges results from the competition between tectonic and erosive forces (*1*–*3*) and controls the organization of drainage and atmospheric-circulation systems (*4*–*6*). Although tectonics and erosion act in opposing directions, there may be feedbacks that couple the two (*7*, *8*). Prominent candidates for such coupling comprise the syntaxes regions (*9*, *10*), at either end of the Himalaya, where the two biggest rivers draining Tibet, the Indus and Yarlung Tsangpo, have cut deep gorges into very young metamorphic massifs (Fig. 1A) (*11*–*17*). In the so-called tectonic aneurysm model, it has been proposed that rapid incision within these gorges has thermally weakened the crust

and now sustains a positive feedback between uplift and erosion (*9*, *10*), but how and when this happened remains elusive.

Deeply incised gorges exist along the entire Himalaya and always coincide with very steep river gradients that have been related to zones of rapid rock uplift and incision (*18*–*20*). The most spectacular and emblematic gorge in the Himalaya, and probably on Earth, is the Tsangpo Gorge, where the Yarlung Tsangpo drops by 2 km in elevation as it cuts through the ~50-km-wide eastern Himalayan syntaxis where erosion rates are exceptionally high (Fig. 2B). The contorted and generally steep course of the gorge is often considered evidence for relatively young capture of the Yarlung Tsangpo by the headward incising Brahmaputra River, from a former course connecting it to the Parlung and Yigong rivers, which themselves might have been connected to rivers farther to the east (*5*, *6*, *9*, *18*). Provenance studies from the Himalayan foreland, however, indicate that a connection between the Yarlung Tsangpo and Brahmaputra River was already established before the Middle Miocene (*21*–*23*), emphasizing the stability of the gorge. More recently, the discovery of extensive lake deposits that have accumulated behind a river-blocking glacial dam upstream of the Tsangpo Gorge (*24*) has spurred the idea that glacial damming during the Quaternary inhibited headward incision of the Brahmaputra River and might have contributed to initiating rapid rock uplift (*25*).

Before entering its narrow gorge, the Yarlung Tsangpo flows for ~300 km across a broad alluvial plain that increases gradually in width toward the confluence with the Nyang River (Fig. 2A). Such downstream widening is typical for lakes that have drowned valleys upstream of dams. Five drillings recently conducted along the Yarlung Tsangpo (Fig. 1C) provide evidence of a thick sedimentary valley fill upstream of the gorge. The drillings were located near the valley center and reached bedrock at depths that increase from 70 m at the most upstream site (no. 1), to a maximum depth of 567 m (no. 3) at ~80 km upstream from the Nyang River confluence. Two more sites at distances of ~40 and 20 km upstream from the gorge yielded depths to bedrock of 510 (no. 4) and 230 m (no. 5), respectively.

Hillslopes bordering the valley floor are generally steep, with uniform slope angles of ~30°, comparable to hillslopes downstream of the Tsangpo Gorge (Fig. 2B) and suggestive of threshold hillslopes that are at their critical angle of stability (*14*). Simple projection of hillslopes into the subsurface predicts a depth to bedrock of ~1000 m near the Yarlung Tsangpo-Nyang River confluence (Fig. 2A), where the valley floor is widest. Based on the assumption that hillslopes below and above the valley fill are similar, we reconstructed the depth to bedrock (Figs. 1C and 2A) using an artificial neural network approach (*26*). Close correspondence of estimated and observed depths in drill cores provide us with confidence in the reconstruction, which confirms our initial notion of a steadily decreasing elevation of the former valley floor toward the Yarlung Tsangpo-Nyang River confluence. Downstream of the confluence, the valley floor remains ~4 km wide and deeply filled with sediments (Fig. 2A) until the river leaves the Indus-Yarlung Tsangpo Suture Zone and abruptly narrows to <2.5 km. Because no obvious spill-over toward other valleys exists near the deepest reach of the valley fill, we argue that the former Yarlung Tsangpo was following its present-day course and that uplift of the Namche Barwa and Gyala Peri massifs resulted in steepening of the river where it crosses the gorge and concurrent backfilling of upstream reaches (fig. S4).

Valley-fill sediments from the three sites closest to the Tsangpo Gorge (no. 3 to no. 5) (Figs. 1C and 2A) consist of clastic, mainly fluvial deposits that are dominated by pebbly gravel and sand (figs. S1 to S3). The cores from sites no. 3 and no. 4 both have coarse grain sizes in the lower half,

[1]State Key Laboratory of Earthquake Dynamics, Institute of Geology, China Earthquake Administration, Beijing 100029, P. R. China. [2]Division of Geological and Planetary Sciences, California Institute of Technology, Pasadena, CA 91125, USA. [3]Institute of Earth and Environmental Sciences, University Potsdam, 14476 Potsdam, Germany. [4]Chengdu Engineering Corporation, Chengdu 610072, P. R. China.
***Corresponding author. E-mail: scherler@caltech.edu** †Present address: GFZ German Research Centre for Geosciences, Section 3.4, Telegrafenberg, D-14473 Potsdam, Germany. ‡Present address: Department of Earth Sciences, University of Cambridge, Cambridge, UK

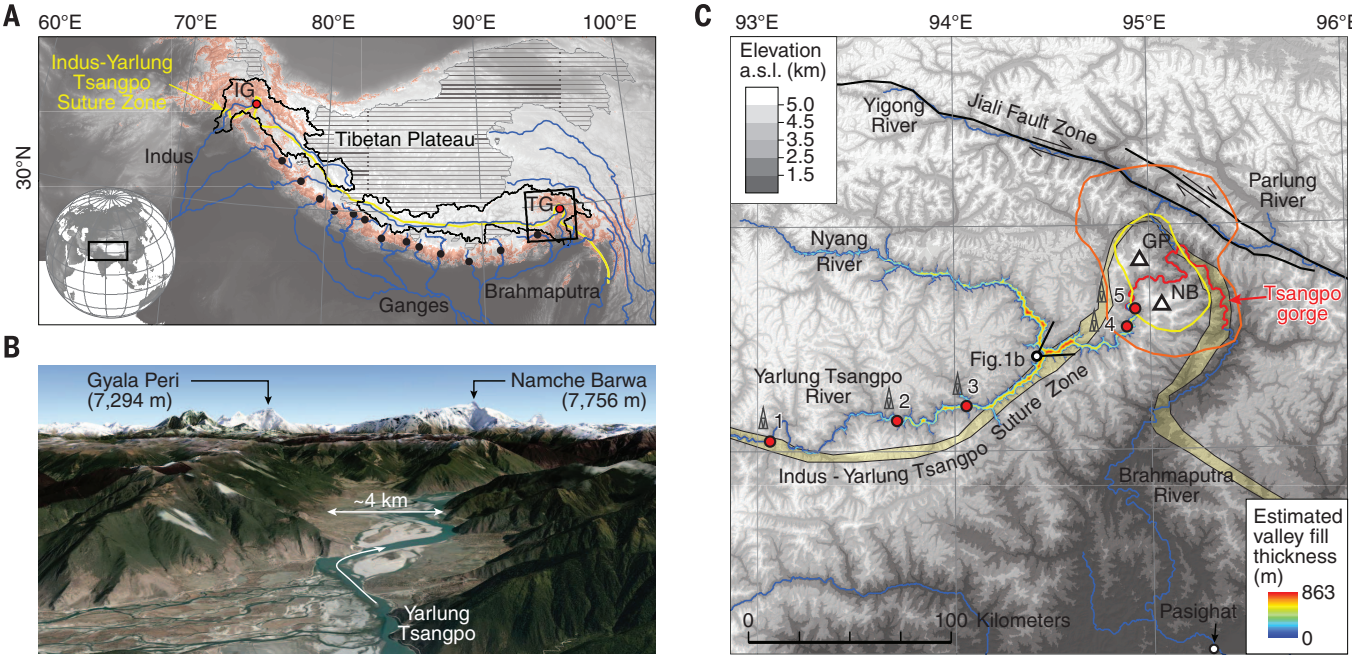


Fig. 1. River gorges in the Himalaya. (**A**) Geographical overview of Tibet and the Himalaya, with internally drained areas (horizontally hatched), major rivers, and gorges (red and black points) located within steep mountainous areas—i.e., where 5-km-radius local relief is >2 km (red). Black polygons show the mountainous drainage basins of the Indus River in the west and the Yarlung Tsangpo-Brahmaputra River in the east. The Indus-Yarlung Tsangpo Suture Zone separates the Eurasian (north) from the Indian plate (south) and is strongly distorted in the Indus Gorge (IG) and Tsangpo Gorge (TG). (**B**) Oblique northeastward aerial view of the Yarlung Tsangpo upstream of the Tsangpo Gorge (from Google Earth, www.google.com/earth). (**C**) Map of the eastern Himalayan syntaxis with the studied valley fill and drill core locations (red points). Contour lines show rapidly exhuming areas with young (<2 Ma) Zircon U/Th-He (orange), and Biotite $^{40}Ar/^{39}Ar$ ages (yellow) centered on the Tsangpo Gorge (*16*), which is marked by a red line.

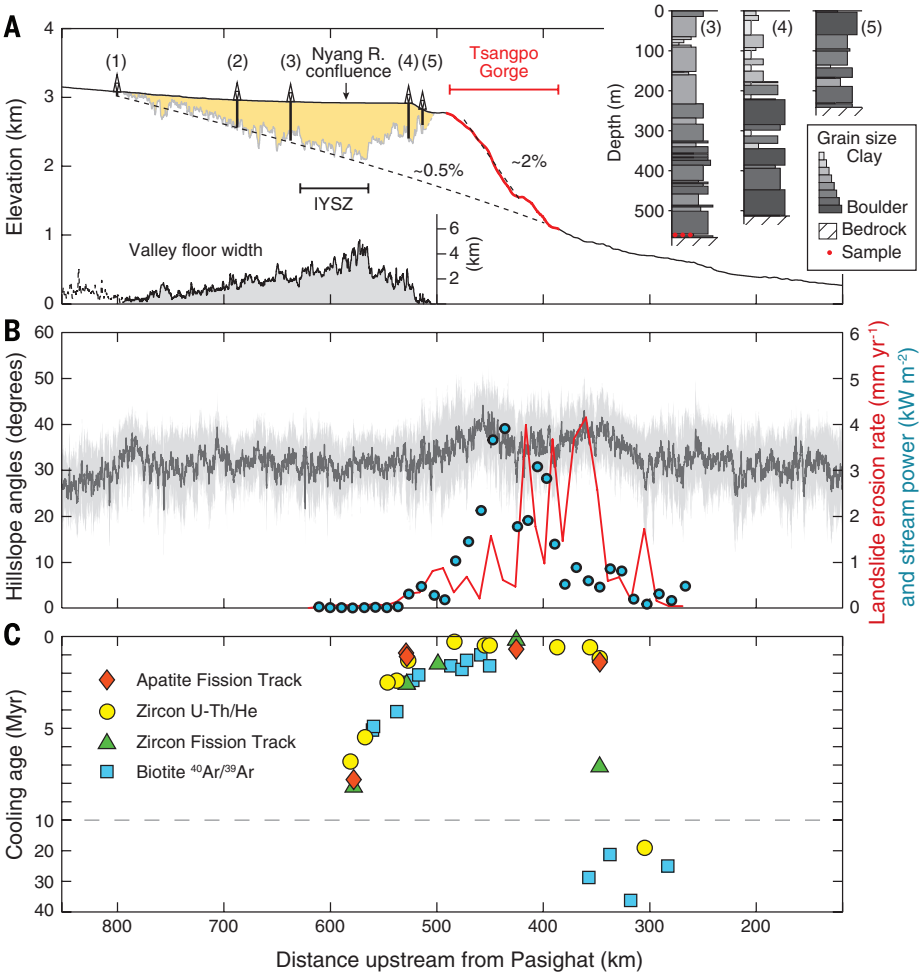


Fig. 2. Tsangpo Gorge and valley fill. (**A**) Longitudinal river profile showing present-day elevation (black; red where passing through Tsangpo Gorge), location of drill cores with observed depth to bedrock (vertical black bars), estimated depth to bedrock from artificial neural network (yellow area), and reconstructed valley bottom before uplift of Tsangpo Gorge (dashed line). IYSZ, Indus-Yarlung Tsangpo Suture Zone. Inset figures show present-day valley bottom width (lower left) and simplified drill core stratigraphy (upper right), with grain size variations (see fig. S1 for details) and sample locations (red points). (**B**) Hillslope angles within a 10-km distance from the river (mean ± 1σ), specific stream power (*12*), and landslide erosion rates (*17*). (**C**) Mineral cooling ages (*11*–*13*) within a 10-km distance from the river. See fig. S7 for spatial distribution of cooling ages.

including boulders up to 50 cm in diameter, and fine grain sizes in the upper half, including silt and clay that probably stems from lake periods (Fig. 2A and table S1). This fining upward sequence indicates a decrease in stream competency, consistent with lowered river gradients during backfilling upstream of the Tsangpo Gorge. The lack of upward fining in drill core no. 5, which is closer to the gorge and located ~120 m lower, may be related to erosion of its upper part during uplift and incision of the gorge (fig. S4). We collected three samples from near the base of drill core no. 3 for cosmogenic nuclide burial dating with in situ–produced ^{10}Be and ^{26}Al (*26*). Our samples yield consistent results that overlap within uncertainties (table S2) and indicate that deposition at this site initiated between ~2 and 2.5 million years ago (Ma) (figs. S5 and S6). Because site no. 3 is ~150 km upstream of the gorge and deposition may not have started immediately, it is likely that uplift and steepening of the gorge was initiated somewhat earlier.

Steepening of the Tsangpo Gorge requires either an increase in rock uplift rate or a decrease in erosional efficiency. Young crystallization and mineral cooling ages from bedrock within the gorge are consistent with an increase in rock uplift rates after ~4 Ma (Fig. 2C) (*11*–*13*). If rock uplift rates were constant and all surface uplift was due to changes in specific stream power [product of gravity, water density, channel slope, and discharge per unit width (*12*)], discharge would have to have decreased by more than a factor of four as channel slopes increased in the gorge (Fig. 2A). No observations exist to support discharge reductions of this magnitude, either due to climate change or drainage capture. River-blocking glacial dams (*25*) can also be excluded as causes of lowered erosional efficiency because the uplifted river reach was below ~2 km elevation, far from any glacial influence. Furthermore, the presence of >200 m of sediments beneath the moraines considered responsible for glacial damming (*24*) is incompatible with the reduced bedrock incision proposed previously (*25*).

Our results clearly show that ~2.5 Ma the Yarlung Tsangpo was able to erode back into the Tibetan Plateau and develop a nearly graded profile (Fig. 2A), which is consistent with provenance data from Miocene to Quaternary sediments in the Himalayan foreland of the Tsangpo Gorge (*23*). The reported increase of Eurasian-plate detritus in deposits of the Brahmaputra River between 7 and 3 Ma (*22*) could reflect the headward incision of the Yarlung Tsangpo into Tibet until uplift of the Namche Barwa and Gyala Peri massifs focused erosion to Indian-plate rocks within the Tsangpo Gorge (*12*). This scenario is consistent with an independently estimated onset of accelerated incision of the adjoining Parlung River at 4 to 9 Ma, based on detrital cooling ages (*27*), which most likely occurred as a result of capture by the Yarlung Tsangpo-Brahmaputra.

Striking similarities between the Indus and Tsangpo gorges have been noted previously (*9*–*11*) and suggest that the tectonic framework of the Himalayan syntaxes sets the stage for the exceptionally high rates of rock uplift (*11*, *28*). Even if positive feedbacks between erosion and uplift nowadays help to maintain these gorges in their current location (*9*, *10*), our results suggest that rapid incision within the Tsangpo Gorge is the result rather than the cause of rock uplift. A similar evolution could have taken place in the Indus Gorge, where mineral cooling and metamorphic ages (*9*, *10*, *14*) suggest equally high erosion rates, with some evidence for order-of-magnitude acceleration in exhumation by ~1.7 Ma (*15*). Notably, ponding of the Indus River upstream of the gorge and deposition of ~1200 m of fluvial and glacial deposits (*29*) apparently started before ~2.6 Ma (*30*) and might also reflect an increase in rock uplift in the western Himalayan syntaxis. Because new data are warranted, we leave it to future studies to test the suggested similarity and investigate the cause for synchronous initiation of rapid rock uplift of both Himalayan syntaxes.

REFERENCES AND NOTES

1. P. Tapponnier *et al.*, *Science* **294**, 1671–1677 (2001).
2. E. R. Sobel, G. E. Hilley, M. R. Strecker, *J. Geophys. Res.* **108**, 2344 (2003).
3. J. Liu-Zeng, P. Tapponnier, Y. Gaudemer, L. Ding, *J. Geophys. Res.* **113**, F04018 (2008).
4. P. Molnar, W. R. Boos, D. S. Battisti, *Annu. Rev. Earth Planet. Sci.* **38**, 77–102 (2010).
5. M. K. Clark *et al.*, *Tectonics* **23**, TC1006 (2004).
6. M. E. Brookfield, *Geomorphology* **22**, 285–312 (1998).
7. P. Molnar, P. England, *Nature* **346**, 29–34 (1990).
8. J.-P. Avouac, E. B. Burov, *J. Geophys. Res.* **101** (B8), 17747–17769 (1996).
9. P. Zeitler *et al.*, *GSA Today* **11**, 4–9 (2001).
10. P. O. Koons, P. K. Zeitler, B. Hallet, Tectonic Aneurysms and Mountain Building, in *Treatise on Geomorphology*, John F. Shroder, Ed. (Academic Press, San Diego 2013), pp. 318–349.
11. J. P. Burg *et al.*, *J. Asian Earth Sci.* **16**, 239–252 (1998).
12. N. J. Finnegan *et al.*, *Geol. Soc. Am. Bull.* **120**, 142–155 (2008).
13. D. Seward, J.-P. Burg, *Tectonophysics* **451**, 282–289 (2008).

14. D. W. Burbank *et al.*, *Nature* **379**, 505–510 (1996).
15. J. L. Crowley, D. J. Waters, M. P. Searle, S. A. Bowring, *Earth Planet. Sci. Lett.* **288**, 408–420 (2009).
16. E. Enkelmann, T. A. Ehlers, P. K. Zeitler, B. Hallet, *Earth Planet. Sci. Lett.* **307**, 323–333 (2011).
17. I. J. Larsen, D. R. Montgomery, *Nat. Geosci.* **5**, 468–473 (2012).
18. L. Seeber, V. Gornitz, *Tectonophysics* **92**, 335–367 (1983).
19. J. Lavé, J.-P. Avouac, *J. Geophys. Res. Solid Earth* **106** (B11), 26561–26591 (2001).
20. K. Hodges, J. M. Hurtado, K. X. Whipple, *Tectonics* **20**, 799–809 (2001).
21. S. E. Cina *et al.*, *Earth Planet. Sci. Lett.* **285**, 150–162 (2009).
22. F. Chirouze *et al.*, *Geol. Soc. Am. Bull.* **125**, 523–538 (2013).
23. K. A. Lang, K. W. Huntington, *Earth Planet. Sci. Lett.* **397**, 145–158 (2014).
24. D. R. Montgomery *et al.*, *Quat. Res.* **62**, 201–207 (2004).
25. O. Korup, D. R. Montgomery, *Nature* **455**, 786–789 (2008).
26. Materials and methods are available in the supplementary materials on *Science* Online.
27. A. R. Duvall, M. K. Clark, B. Avdeev, K. A. Farley, Z. W. Chen, *Tectonics* **31**, TC3014 (2012).
28. L. Seeber, A. Pecher, *Geology* **26**, 791–794 (1998).
29. V. S. Cronin, W. P. Johnson, N. M. Johnson, G. D. Johnson, Chronostratigraphy of the upper Cenozoic Bunthang sequence and possible mechanisms controlling base level in Skardu intermontane basin, Karkakoram Himalaya, Pakistan, in *Tectonics of the Western Himalayas*, L. L. Malinconico, R. J. Lillie, Eds. (Geological Society of America, Boulder, CO, 1989), pp. 295–309.
30. Y. B. Seong, *J. Korean Geogr. Soc.* **42**, 165–176 (2007).

ACKNOWLEDGMENTS

This work was supported by the National Natural Science Foundation of China (41372211 and 41172179) and the State Key Laboratory for Earthquake Dynamics (Project LED2013A07). D.S. was supported by the Alexander von Humboldt Foundation. Data presented here are archived with the supplementary materials. We thank four anonymous reviewers whose comments improved this paper and B. Hallet for insightful discussions.

SUPPLEMENTARY MATERIALS

www.sciencemag.org/content/346/6212/978/suppl/DC1
Materials and Methods
Supplementary Text
Figs. S1 to S7
Tables S1 to S3
References (*31*–*50*)

22 July 2014; accepted 1 October 2014
10.1126/science.1259041

EXOPLANET MAGNETISM

Magnetic moment and plasma environment of HD 209458b as determined from Lyα observations

Kristina G. Kislyakova,[1]* Mats Holmström,[2] Helmut Lammer,[1] Petra Odert,[3] Maxim L. Khodachenko[1,4]

Transit observations of HD 209458b in the stellar Lyman-α(Lyα) line revealed strong absorption in both blue and red wings of the line interpreted as hydrogen atoms escaping from the planet's exosphere at high velocities. The following sources for the absorption were suggested: acceleration by the stellar radiation pressure, natural spectral line broadening, or charge exchange with the stellar wind. We reproduced the observation by means of modeling that includes all aforementioned processes. Our results support a stellar wind with a velocity of ≈400 kilometers per second at the time of the observation and a planetary magnetic moment of ≈1.6 × 10^{26} amperes per square meter.

Hubble Space Telescope observations revealed a strong Lyα absorption of 15 ± 4% (1σ) during the transit of the exoplanet HD 209458b in front of its host star. This Lyα absorption significantly exceeded the 1.5% absorption in the visible (*1*). Shortly afterward, the data were reanalyzed, and a lower absorption depth of 8.9 ± 2.1% was reported (*2*), still present in both the blue and red wings of the Lyα line. The frequency f and velocity spectrum of neutral H atoms along the line of sight (LOS) v_x are connected through the relation

$$f = f_0 + v_x/\lambda_0 \quad (1)$$

where $\lambda_0 = 1215.65 \times 10^{-10}$m. Absorption in the wings of the Lyα line is a signature of neutral H atoms moving with high velocities toward (positive velocities along the LOS) and away from the star. Several interpretations for the excess absorption have been suggested: escaping neutral H atoms accelerated by the stellar radiation pressure (*1*), natural spectral line broadening (*3*), and energetic neutral atoms (ENAs) (*4*–*6*).

In the first scenario, neutral atoms are accelerated by the radiation pressure of stellar Lyα photons until the acceleration force is balanced by the gravity of the star.

Spectral line broadening arises because of the natural broadening mechanism and the spread of the particle velocities along the LOS. One must also account for the populations of nonthermal H accelerated by the radiation pressure and formed by charge exchange. Their broadening is nonsymmetric and is not described by the Voigt profile, which is the convolution of the Lorentz and Doppler profiles, as is the case for purely thermal populations.

ENAs are generally produced by charge exchange between ions and neutral atoms. In the exosphere, charge exchange occurs between high-velocity stellar wind protons and neutral atmospheric particles moving at thermal velocities. In this interaction, the electron is transferred to the proton. Because the initial velocities of the particles are almost conserved, the reaction produces a "slow" ion and a "fast" neutral. This mechanism generates ENA coronas around Earth and other solar system planets (*7*) and should operate in exoplanet systems as well (*4*).

None of the early studies considered all of these effects together. A later work (*8*) included all processes, but was still unable to explain the

Table 1. Parameters of HD209458 and HD209458b (*42*) and some simulation parameters.

Name	Symbol	Value	
Star mass	M_{st}	2.28×10^{30}kg	≈1.148 M_{Sun}
Star age		≈4 ± 2 Gyr	
Planet radius	R_{pl}	9.54×10^{7}m	≈0.71 M_{Jup}
Planet mass	M_{pl}	1.21×10^{27}kg	≈1.38 R_{Jup}
Orbital distance		7.1×10^{9}m	≈0.047 AU
Inner boundary radius	R_{ib}	2.7×10^{8}m	≈2.8 R_{pl}
Inner boundary temperature	T_{ib}	6×10^{3}K	
Inner boundary density	n_{ib}	2×10^{13}m^{-3}	
Obstacle standoff distance*	R_s	2.76×10^{8}m	≈2.9 R_{pl}
Obstacle width*	R_t	2.86×10^{8}m	≈3.0 R_{pl}
Photoionization rate	τ_{pi}	6.0×10^{-5}s^{-1}	
Electron impact ionization rate	τ_{ei}	1.25×10^{-4}s^{-1}	
Stellar wind density	n_{sw}	5×10^{9}m^{-3}	
Stellar wind velocity	u_{sw}	400×10^{3}m/s	
Stellar wind temperature	T_{sw}	1.1×10^{6}K	

*Assuming that the Alfvenic Mach number $M_A > 1$.

[1]Space Research Institute, Austrian Academy of Sciences, Schmiedlstrasse 6, A-8042 Graz, Austria. [2]Swedish Institute of Space Physics, PO Box 812, SE-98128 Kiruna, Sweden. [3]Institute of Physics, University of Graz, Universitätsplatz 5, A-8010 Graz, Austria. [4]Skobeltsyn Institute of Nuclear Physics, Moscow State University, Leninskie Gory, 119992 Moscow, Russia.
***Corresponding author. E-mail: kristina.kislyakova@oeaw.ac.at**

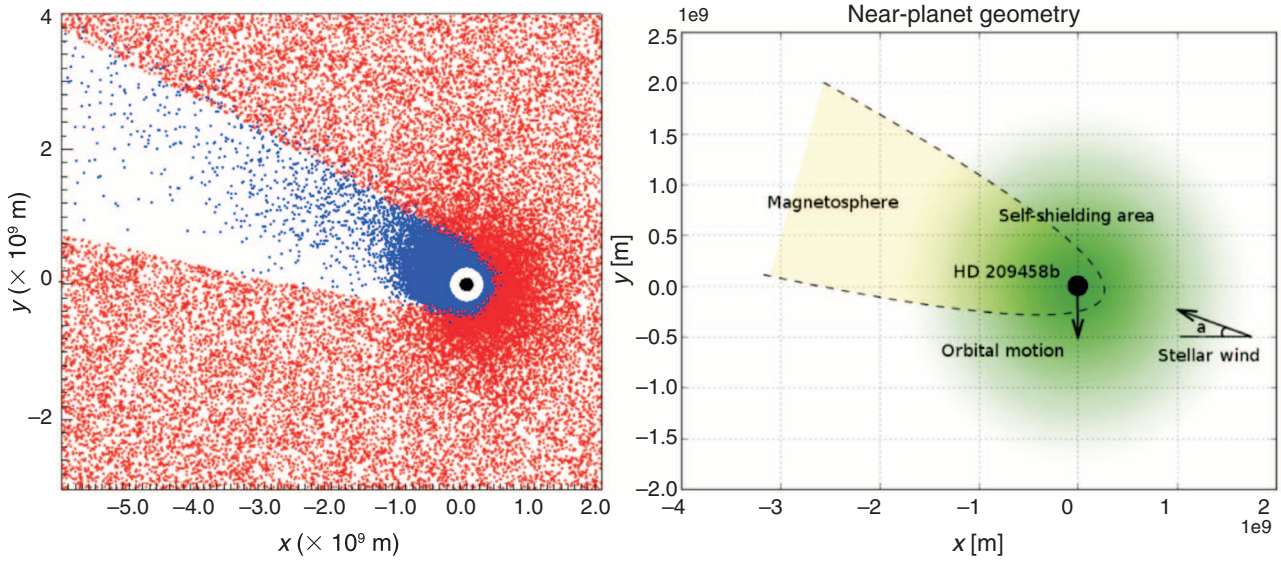


Fig. 1. (Left) Slice of modeled 3D atomic H corona around HD 209458b. Blue and red dots correspond to neutral H atoms and H ions, including stellar wind protons, respectively. The black dot represents the planet. The white area around the planet corresponds to the thermosphere below the inner simulation boundary at height R_{ib}. The star is on the right. The planetary magnetosphere is represented by an obstacle with a width R_t and a distance from the planet's center to substellar point R_s. We assume the atmosphere of HD 209458b to be dominated by atomic H at R_{ib} (*40*, *41*). Hydrogen atoms are launched from the inner boundary, assuming a number density n_{ib} and a temperature of T_{ib}, consistent with atmospheric models (*17*, *40*). Stellar wind protons are launched on the right side of the domain and cannot penetrate inside the magnetospheric obstacle. (**Right**) Illustration of near-planet geometry.

absorption in the red part of the line, which was recently observed again for another exoplanet, GJ 436b (*9*). The aforementioned work (*8*) includes a simplified natural broadening model. They used a Lorentzian broadening profile that is derived from the natural broadening of a Maxwellian gas. However, here we have a non-Maxwellian population of H atoms. They also used a too-coarse velocity grid when computing the naturally broadened profile. The computation has to be done on a grid that has much higher resolution to be accurate.

Here we show that the red part of the absorption can be explained by spectral broadening alone, whereas the blue part also reflects contributions from radiation pressure and ENAs.

With numerical modeling, we estimated how a neutral H cloud located in front of the star would affect the transit Lyα absorption of HD 209458b. Parameters of the system are summarized in Table 1. The orbit of HD 209458b is almost circular. The simulations were performed by using a direct simulation Monte Carlo code, which includes neutral H atoms and H ions. The comprehensive description of the model can be found in (*10*). The main processes and forces included for an exospheric atom are

1) Collision with an ultraviolet (UV) photon, which defines the velocity-dependent radiation pressure; self-shielding (*8*) is included.

2) Charge exchange with a stellar wind proton.

3) Elastic collision with another H atom.

4) Ionization by stellar photons or wind electrons. For a solar-type star, at an orbit of 0.047 astronomical units (AU), the electron impact ionization rate exceeds the photoionization rate by a factor of 2 (Table 1) because of a denser stellar wind, and thus cannot be neglected (*11*).

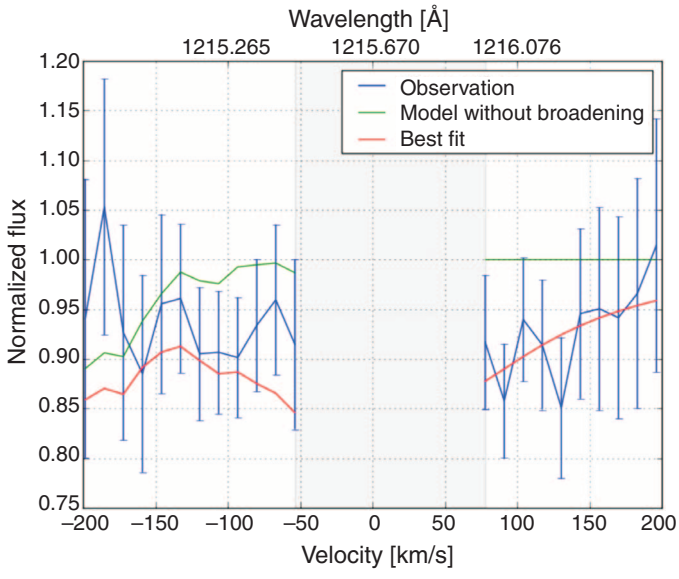


Fig. 2. Comparison of modeled and observed [according to Ben-Jaffel and Hosseini (*3*)] Lyα spectra at mid-transit. Blue, the observed in-transit profile, normalized by the out-of-transit profile. Red, the modeled profile, computed including charge exchange, radiation pressure with self-shielding, photo- and electron impact ionization, and natural broadening. The goodness of the best fit equals $\chi^2 = 0.081$. Green, the same as red, but excluding broadening, $\chi^2 = 0.139$. The abscissa is the H velocity along the x axis (away from Earth, toward the star). The region of contamination by geocoronal emission at low velocities is excluded and marked by the shaded area. One can clearly see that broadening affects both wings of the Lyα line, whereas other effects contribute to the absorption mainly on the blue wing produced by atoms moving away from the star. The details of computing the Lyα attenuation are given in (*10*).

5) The gravity of the star and planet and centrifugal, Coriolis, and tidal forces.

In this study, we used a velocity-dependent absorption coefficient of photons (*12*). The photon absorption rate has the same shape as the stellar Lyα line, so that the strongest acceleration of neutral H atoms occurs in the velocity domain between approximately $-100 \le v_x \le 100$ km s^{-1}. Self-shielding (*8*) is also included: In the optically thick regions in Lyα, the neutrals cannot collide with UV photons.

After the H corona was modeled, the Lyα in-transit attenuation was calculated. Natural broadening is accounted for at this stage. Doppler broadening is included automatically by accurately taking into account the velocities of the atoms.

Because HD 209458 is a solar-type star, we assumed the solar parameters at 0.047 AU for

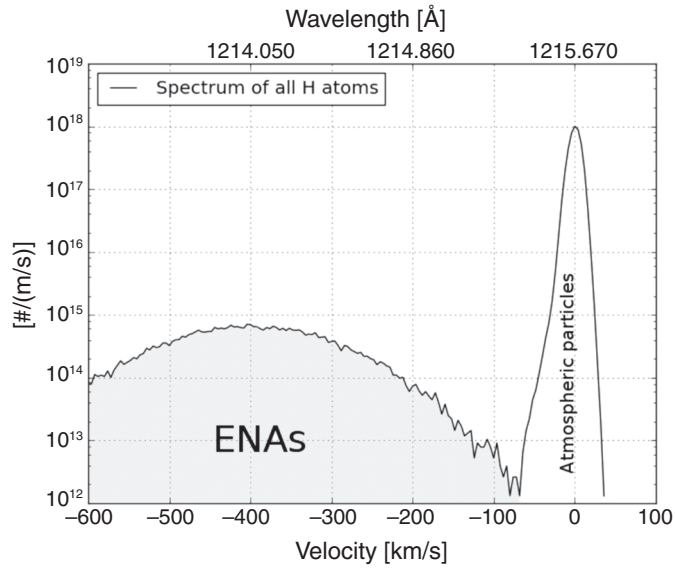


Fig. 3. The modeled best-fit *x* axis (planet-star) velocity spectrum of neutral H atoms in front of the star at mid-transit. One can see two H populations: the thermal population of the atmosphere (right peak) and the ENAs produced by charge exchange (left peak). The width of this part of the distribution is proportional to the stellar wind temperature. The thermal peak is slightly deformed and shifted toward negative velocities by the radiation pressure.

stellar wind density, temperature, and velocity and used scaled photo- and electron impact ionization rates from the Sun (*11*).

Our results show that an extended H corona exists around HD 209458b. We expect this to form when strong radiation pressure accelerates neutral H atoms and moves them out of the planetary magnetosphere, where they may undergo ionization either by charge exchange or by stellar wind electrons. Photoionization can occur in the whole nonshielded atmosphere outside the planet's shadow. The nonsymmetric form of the corona is defined by radiation pressure, charge exchange, and the Coriolis force. Our results show that one-dimensional (1D) atmospheric modeling (*3*) that assumes a symmetric upper atmosphere should be applied cautiously above the exobase to highly irradiated exoplanets.

Figure 1 illustrates the modeled H cloud around HD 209458b. The coordinate system is centered at the center of the planet, the x axis points toward the center of mass of the system, the y axis points in the opposite direction to the planet's velocity, and the z axis completes the right-hand coordinate system. Radiation pressure together with the tidal force lead to the formation of a cometary-like tail (*8*, *13*). One can clearly see the interaction area at the magnetospheric boundary revealed by an enhanced concentration of H^+ ions (red dots), where the neutrals underwent charge exchange. Figure 2 presents the observed (*3*) and modeled Lyα spectra with and without natural broadening normalized by the out-of-transit observation. Broadening plays the key role in absorption in the red wing of the line (positive v_x). This conclusion is in agreement with an early study (*3*), which, however, disregarded ENAs and radiation pressure contributing to absorption. Additionally, it was based on a 1D symmetric model of the atmosphere, whereas the modeled corona around HD 209458b shows significant asymmetry.

Finally, Fig. 3 depicts the velocity spectrum of neutral H atoms along the star-planet line with two populations of atoms: The left peak shows the ENAs, and the right higher peak shows the thermal atmospheric atoms.

In the velocity spectrum corresponding to our best fit, the ENA peak is located near –400 km s^{-1} due to a stellar wind (Fig. 3). We do not take into account the effects connected with the formation of a bow shock near the magnetospheric obstacle in the supersonic regime. In both cases when the bow shock is present or absent, there exists an ENA formation region. It is not easy to distinguish whether the estimated plasma parameters are from the undisturbed stellar wind or the slower and hotter shocked stellar wind. However, the best estimate we have of 400 km s^{-1} indicates that the ENAs are produced in an undisturbed (possibly deviated, but not shocked) stellar wind. The observation cannot be fitted with lower stellar wind velocities for any plausible planetary magnetic field (*10*). Because the ENAs maintain the velocity of the protons, fast stellar wind shifts their location out of the considered velocity range (–200 km $s^{-1} \le v_x \le$ 200 km s^{-1}, because the observed signal becomes too noisy beyond, see Fig. 2) to avoid overabsorption. However, ENAs play an important role in reducing the amount of neutrals in the velocity domain of interest, shaping the cloud and contributing to the absorption in the very blue part of the spectrum. Our search of realistic parameter space led us to conclude that the observations can be fitted only by using a very narrow and close-in magnetic obstacle with a substellar point located at $\approx 2.9 R_{pl}$ from the planet's center and an obstacle width of $\approx 3 R_{pl}$. In the case of a close-in obstacle, the exosphere interacts directly with the stellar wind. This diminishes the number of H neutrals, first by charge exchange and second by stellar wind electron impact ionization. A stronger intrinsic field shifts the magnetic boundary away from the planet and effectively protects the atmosphere from these processes. This dramatically increases the number of neutrals, which undergo acceleration by radiation pressure up to –200 km s^{-1} and leads to overabsorption in comparison to the in-transit observation. We could only fit the observations by including the self-shielding effect (*8*, *10*).

Assuming a dipole approximation, one can estimate the magnetic moment of HD 209458b using the formula (*14*)

$$\mathcal{M} = \left(\frac{8\pi^2 R_s^6 \rho_{sw} v_{rel}^2}{\mu_0 f_0^2} \right)^{1/2} \quad (2)$$

Here, R_s is the magnetospheric stand-off distance, μ_0 is the diamagnetic permeability of free space, $f_0 \approx 1.22$ is a form factor of the magnetosphere, ρ_{sw} is the mass density of the stellar wind, and v_{rel} is the relative velocity of the stellar wind plasma, including the planetary orbital velocity.

Adopting our best-fit simulation parameters, Eq. 2 yields $\mathcal{M} \approx 1.6 \times 10^{26}$ A × $m^2 \approx 0.1\ \mathcal{M}_{Jup}$ for HD 209458b, where $\mathcal{M}_{Jup} = 1.56 \times 10^{27}$ A× m2 (*15*). This value corresponds to the upper boundary predicted by the models of tidally locked close-in exoplanets (*15*, *16*), atmospheric models (*17*), and an empirical relationship (*18*), and is in agreement with the nondetection of the radio emission from HD 209458b at 150 MHz (*19*). Proximity of this value to a dipole field approximation indicates a negligible magnetodisk contribution, which is in agreement with the conclusion that HD 209458b probably cannot develop a significant magnetodisk (*14*). Our results do not support a larger magnetic moment that exceeds $\mathcal{M}_{Jup}$, as predicted by an energy flux scaling model (*20*, *21*).

In summary, our model predicts a fast stellar wind at the time of observation (≈ 400 km s^{-1}, $n_{sw} \approx 5 \times 10^9$ m^{-3}), stresses the importance of electron impact ionization in addition to photoionization, and infers a magnetic moment of HD 209458b of ≈10% $\mathcal{M}_{Jup}$.

REFERENCES AND NOTES

1. A. Vidal-Madjar *et al.*, *Nature* **422**, 143–146 (2003).
2. L. Ben-Jaffel, *Astrophys. J.* **671**, L61–L64 (2007).
3. L. Ben-Jaffel, S. S. Hosseini, *Astrophys. J.* **709**, 1284–1296 (2010).
4. M. Holmström *et al.*, *Nature* **451**, 970–972 (2008).
5. A. Ekenbäck *et al.*, *Astrophys. J.* **709**, 670–679 (2010).
6. P. Tremblin, E. Chiang, *Mon. Not. R. Astron. Soc.* **428**, 2565–2576 (2013).
7. H.-J. Fahr, H. Fichtner, K. Scherer, *Rev. Geophys.* **45**, RG4003 (2007).
8. V. Bourrier, A. Lecavelier des Etangs, *Astron. Astrophys.* **557**, A124 (2013).
9. J. R. Kulow, K. France, J. Linsky, R. O. P. Loyd, *Astrophys. J.* **786**, 132 (2014).
10. Supplementary materials.
11. T. E. Holzer, *Rev. Geophys. Space Phys.* **15**, 467 (1977).
12. K. G. Kislyakova *et al.*, *Astron. Astrophys.* **562**, A116 (2014).
13. C. Villarreal D'Angelo *et al.*, *Mon. Not. R. Astron. Soc.* **438**, 1654–1662 (2014).
14. M. L. Khodachenko *et al.*, *Astrophys. J.* **744**, 70 (2012).
15. J.-M. Grießmeier *et al.*, *Astron. Astrophys.* **425**, 753–762 (2004).
16. A. Sánchez-Lavega, *Astrophys. J.* **609**, L87–L90 (2004).
17. T. T. Koskinen, R. V. Yelle, P. Lavvas, N. K. Lewis, *Astrophys. J.* **723**, 116–128 (2010).
18. H. J. Durand-Manterola, *Planet. Space Sci.* **57**, 1405–1411 (2009).
19. A. Lecavelier des Etangs, S. K. Sirothia, Gopal-Krishna, P. Zarka, *Astron. Astrophys.* **533**, A50 (2011).

20. U. R. Christensen, V. Holzwarth, A. Reiners, *Nature* **457**, 167–169 (2009).
21. A. Reiners, U. R. Christensen, *Astron. Astrophys.* **522**, A13 (2010).
22. B. Fryxell *et al.*, *Astrophys. J. Suppl. Ser.* **131**, 273–334 (2000).
23. P. MacNeice, K. M. Olson, C. Mobarry, R. de Fainchtein, C. Parker, *Comput. Phys. Commun.* **126**, 330–354 (2000).
24. K. G. Kislyakova *et al.*, *Astrobiology* **13**, 1030–1048 (2013).
25. R. R. Hodges Jr., *J. Geophys. Res.* **99**, 23229 (1994).
26. B. E. Wood, H.-R. Müller, G. P. Zank, J. L. Linsky, S. Redfield, *Astrophys. J.* **628**, L143–L146 (2005).
27. B. E. Wood, S. Redfield, J. L. Linsky, H.-R. Müller, G. P. Zank, *Astrophys. J. Suppl. Ser.* **159**, 118–140 (2005).
28. S. Chandrasekhar, *Astrophys. J.* **138**, 1182 (1963).
29. A. L. Garcia, *Numerical Methods for Physics* (Prentice Hall, Upper Saddle River, NJ, 2000).
30. J. Candy, W. Rozmus, *J. Comput. Phys.* **92**, 230–256 (1991).
31. B. G. Lindsay, R. F. Stebbings, *J. Geophys. Res. Space Phys.* **110**, A12213 (2005).
32. V. V. Izmodenov *et al.*, *Astrophys. Space Sci.* **274**, 71–76 (2000).
33. G. A. Bird, *Molecular Gas Dynamics and the Direct Simulation of Gas Flows* (Clarendon Press, Oxford, 1976).
34. B. Semelin, F. Combes, S. Baek, *Astrophys. J.* **474**, 365 (2007).
35. P. J. E. Peebles, *Principles of Physical Cosmology* (Princeton Univ. Press, Princeton, NJ, 1993).
36. C. Lovis *et al.*, arXiv:1107.5325v1 (2011).
37. E. R. Priest, *Solar Magneto-Hydrodynamics* (D. Reidel Publishing, Dordrecht, Netherlands, 1982).
38. W. Baumjohann, R. A. Treumann, *Basic Space Plasma Physics* (Imperial College Press, London, 1996).
39. J. L. Linsky *et al.*, *Astrophys. J.* **717**, 1291–1299 (2010).
40. T. T. Koskinen, M. J. Harris, R. V. Yelle, P. Lavvas, *Icarus* **226**, 1678–1694 (2013).
41. V. I. Shematovich, *Sol. Syst. Res.* **44**, 96–103 (2010).
42. J. Southworth, *Mon. Not. R. Astron. Soc.* **408**, 1689–1713 (2010).

ACKNOWLEDGMENTS

This study was carried out with support by the Austrian Science Fund (FWF) Nationale Forschungsnetzwerke (NFN) project S116601-N16 "Pathways to Habitability: From Disk to Active Stars, Planets and Life" and the related FWF NFN subprojects S116 606-N16 and S116 607-N16. P.O. thanks FWF for grant P22950-N16. The research was conducted using computer resources provided by the Swedish National Infrastructure for Computing (SNIC) at the High Performance Computing Center North (HPC2N). The software was in part developed by the Flash Center at the University of Chicago. The authors thank L. Ben-Jaffel for providing the reprocessed Hubble Space Telescope observations, B. Wood for providing the processed Lyα profile, the team "Characterizing stellar and exoplanetary environments" for useful discussions, and C.P. Johnstone for his valuable comments on the stellar wind issue. The data are available in the supplementary materials.

SUPPLEMENTARY MATERIALS

www.sciencemag.org/content/346/6212/981/suppl/DC1
Supplementary Text
Figs. S1 to S12
Tables S1 to S2

23 June 2014; accepted 20 October 2014
10.1126/science.1257829

LIQUID STRUCTURE

Molten uranium dioxide structure and dynamics

L. B. Skinner,[1,2,3]* C. J. Benmore,[1] J. K. R. Weber,[1,3] M. A. Williamson,[4] A. Tamalonis,[1] A. Hebden,[4] T. Wiencek,[5] O. L. G. Alderman,[1,3] M. Guthrie,[6] L. Leibowitz,[4] J. B. Parise[2,7]

Uranium dioxide (UO_2) is the major nuclear fuel component of fission power reactors. A key concern during severe accidents is the melting and leakage of radioactive UO_2 as it corrodes through its zirconium cladding and steel containment. Yet, the very high temperatures (>3140 kelvin) and chemical reactivity of molten UO_2 have prevented structural studies. In this work, we combine laser heating, sample levitation, and synchrotron x-rays to obtain pair distribution function measurements of hot solid and molten UO_2. The hot solid shows a substantial increase in oxygen disorder around the lambda transition (2670 K) but negligible U-O coordination change. On melting, the average U-O coordination drops from 8 to 6.7 ± 0.5. Molecular dynamics models refined to this structure predict higher U-U mobility than 8-coordinated melts.

Nuclear power from fission currently accounts for about 10% of the global electricity supply. Compared with burning fossil fuels, nuclear power has prevented ~64×10^{12} kg of CO_2-equivalent emissions since 1971, corresponding to a saving of 1.84 million air pollution–related deaths (*1*). Because the majority of currently operating nuclear reactors use either UO_2 or mixed oxide fuel (typically 90% UO_2), understanding and predicting the behavior of UO_2 at extreme temperatures is of great importance to improved safety and optimization of this low-carbon electricity source.

Although no experimental structure measurement of molten UO_2 has been previously reported, some physical properties measurements (*2*, *3*) and several literature molecular dynamics (MD) models do exist for molten UO_2 (*4*–*9*). These models, which are often parameterized from solid-state properties, have large differences in their melt structures. The U-O bond length r_{UO}, for example, varies from 1.9 to 2.2 Å between UO_2 melt models (*4*–*9*). This structural uncertainty results in molten UO_2 models with differing physical properties, such as viscosity and compressibility, that are relevant to reactor safety. The present x-ray measurements, by contrast, find a precise value r_{UO} of 2.22 ± 0.01 Å (at 3270 K), which provides a new tool to test the validity of liquid UO_2 models. In addition, hot solid UO_2 undergoes a superionic lambda transition at 2670 K characterized by rapidly increasing oxygen disorder (*6*). Approaching this transition, there are steep rises in heat capacity and thermal conductivity (*2*). Although some MD models predict reduced U-O coordination through the lambda transition, other models retain their local structure into the melt (*4*), which is ~9.6% less dense than the hot solid (*2*).

Synchrotron x-ray diffraction measurements were performed on 3-mm depleted UO_2 spheroids that were laser heated while suspended in an aerodynamic levitator. Levitation negates any solid contact with the very hot sample, allowing high chemical purity to be maintained. Measured intensities provide the x-ray structure factor [$S_X(Q)$], where momentum transfer (Q) is $4\pi\sin(\theta)/\lambda$, 2θ is the scattering angle, and λ is the incident x-ray wavelength (*10*, *11*). Fourier transform of these $S_X(Q)$ provides pair distribution functions {$g(r)$, $D(r) = 4\pi\rho r[g(r) - 1]$, *or* $T(r) = 4\pi\rho r g(r)$}, where ρ is number density that describe the probability of finding atom pairs with a given separation r (*11*). Peak areas in these functions give coordination numbers, whereas peak width indicates local disorder.

The consistent Bragg peak positions and relative intensities of the measured $S_X(Q)$ patterns (Fig. 1A) indicate that the U-U positions of the CaF_2-like cubic structure are maintained above the lambda transition, whereas the reduced intensity of high-Q Bragg peaks at high temperatures indicates increasing disorder. The $D_X(r)$ patterns (Fig. 1B) confirm the consistent U-U periodicity, expansion, and increasing disorder with increasing temperature. The $D_X(r)$ of the Yakub MD model (*6*) (dotted lines, Fig. 1B) displays structure that matches the hot solid measurements more closely than other literature models investigated (*4*–*9*).

The measured U-O bond length, r_{UO}, contracts on heating up to the melting point, despite normal volume expansion, whereas r_{UU} expands (Fig. 2B). To understand what is happening as r_{UO} contracts, the running coordination numbers $n_{UO}(r)$, which give the average number of O atoms around each U within a distance r, are plotted (Fig. 2A). The Yakub MD simulations,

[1]X-ray Science Division, Argonne National Laboratory, Argonne, IL 60439, USA. [2]Mineral Physics Institute, Stony Brook University, Stony Brook, NY 11794-2100, USA. [3]Materials Development, Inc., 3090 Daniels Court, Arlington Heights, IL 60004, USA. [4]Chemical Science and Engineering, Argonne National Laboratory, Argonne, IL 60439, USA. [5]Nuclear Engineering, Argonne National Laboratory, Argonne, IL 60439, USA. [6]Geophysical Laboratory, Carnegie Institution of Washington, Washington, DC 20015, USA. [7]Photon Sciences, Brookhaven National Laboratory, Upton, NY 11973, USA
*Corresponding author. E-mail: lawrie.skinner@gmail.com

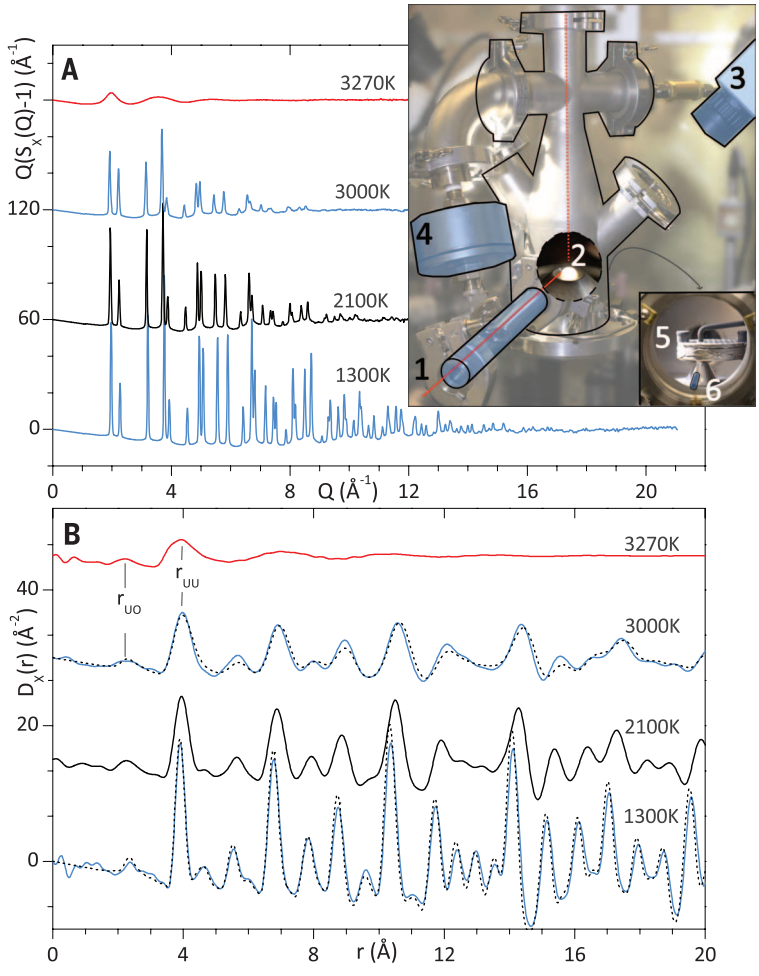


Fig. 1. X-ray diffraction measurements of UO_2. (**A**) UO_2 x-ray structure factors. Above 1300 K, the high-Q region (Q > 12 Å^{-1}) contained no structure. The setup diagram (inset) shows the incident x-rays passing through the collimator (1) and the hot sample (2). The temperature was measured with a pyrometer (3), and exhaust gas was filtered (4). The view through the exit window shows the sample loader (5) and beam stop (6), which absorbed exit window scattering. (**B**) X-ray pair distribution functions $D_X(r)$, generated from the patterns in (A). Dotted lines are from the Yakub MD model (*6*); red lines (3270 K) indicate the liquid state. As an approximate guide, these UO_2 x-ray diffraction patterns consist of pair contribution weightings of 73% U-U, 25% U-O, and 2% O-O (at Q = *0*).

which closely agree with the x-ray measurements, allow full isolation of U-U and U-O correlations (Fig. 2). These isolated $n_{UO}(r)$ and $n_{UU}(r)$ curves from the Yakub MD model also demonstrate the ambiguity in assigning a single number to average coordination. Although at low temperatures the n_{UO} and n_{UU} are unambiguously 8 and 12 respectively, as the temperature increases $n_{UO}(r)$ and $n_{UU}(r)$ no longer plateau, introducing cut-off dependence to the coordination numbers. Taking $n_{UO}(r)$ and $n_{UU}(r)$ up to their inflection points gives essentially constant coordination values of n_{UO} = 8 and n_{UU} = 12 below the melting point. There is, however, substantial rearrangement in this 2000 to 3300 K temperature range as short U-O neighbors (<2.8 Å), are exchanged for longer U-O neighbors (2.8 to 3.5 Å), with increasing temperature.

In the melt, we find a 16% decrease in U-O coordination compared with the hot solid (Fig. 2A). This U-O coordination drop is accompanied by large broadening and shortening of the U-U arrangements, with a small drop in U-U coordination on melting (Fig. 2, B and C). These results indicate a substantial change from the UO_8 cubic polyhedra of the solid and a very large disordering of the local U-U arrangements, which describe the connectivity of U-O polyhedra in the melt. Also, unlike the hot solid, the r_{UO} expands normally in the liquid state MD models investigated (Fig. 2B). Although this expansion of r_{UO} in the liquid cannot be confirmed by the single temperature point measured, first peak contraction behavior is not generally expected in oxide melts. Measurements on $CaAl_2O_4$, Al_2O_3, and SiO_2 liquids, for example, do not show contraction of r_{AlO}, r_{SiO} on heating (*12*–*14*). This behavior is in contrast to several liquid metals that have been shown to display contraction in the first peak in $g(r)$ on heating (*15*). The Yakub MD model displays r_{UO} expansion in the melt, while also reproducing the measured contraction of r_{UO} of the hot solid.

The UO_2 liquid structure measurements also give r_{UO} = 2.22 ± 0.01 Å, r_{UU} = 3.88 ± 0.10 Å, and n_{UO} = 6.7 ± 0.5Å; the latter two are matched within error by the Yakub MD model (Fig. 3). Discrepancies remain, however, in the first peaks of both $S_X(Q)$ and $g_X(r)$. To address these discrepancies, a simple pair potential model using the Morse functional form was refined against the measured liquid structure. The refined MD model essentially reproduces the $S_X(Q)$ measurement within error apart from the first peak in $S_X(Q)$, which remains slightly too sharp.

The CaF_2-like cubic crystal structure of UO_2 consists of UO_8 cubic polyhedra that share every edge with one of 12 neighboring polyhedra, such that looking out from each U through the faces of the UO_8 cube there is a gap to the next U that is a distance of $2r_{OO}$ away (Fig. 3C). After melting, the refined MD model finds the lower coordinated liquid to be ~40 ± 5% UO_6 and 40 ± 5% UO_7, with the remaining 20% being mainly UO_5 and UO_8. Accompanying this lower n_{UO} is the reduced sharing of oxygen, with ~2/3 of the O shared between just three, rather than four, UO_x polyhedra as in the crystal. Similarly, the connectivity of the UO_x polyhedra reduces from 100% edge-shared in the crystal to 60% corner-shared, 33% edge-shared, and 7% face-shared in the melt. Whether or not UO_6 and UO_7 polyhedra have a preference to cluster together is important to the properties and phase behavior of this melt. The MD simulations showed nearly random mixing with only a very slight degree of clustering of UO_6 and UO_7 polyhedra (*11*).

One explanation for the minimal clustering is rapid rearrangement of the local polyhedra. We investigated this rearrangement by measuring the rate at which atoms move out of the first coordination sphere (bond breaking) in the refined MD model. Counting the time for 50% of initially neighboring pairs to separate past a cut-off value (*11*) gives a neighbor "half-life" (τ_{50}). The τ_{50} value for U-O pairs in the supercooled melt at 3000 K was similar to the value for the crystalline solid at that temperature, 0.46 ps (liquid) versus 0.53 ps (crystal) (Fig. 3A). These short U-O τ_{50} times indicate that the U-O polyhedra do not move around as intact $UO_{6,7,8}$ units for any substantial amount of time. The U-U correlations, however, were found to swap neighbors more slowly, taking 1.6 ps in the 3000 K liquid and 8.3 ps in the crystalline solid at 3000 K (Fig. 3A). The increased U-U mobility in the liquid occurs with the collapse of the ordered U-U lattice, whereas the similarity of the U-O τ_{50} values is consistent with the disordered "liquid-like" O positions in the post–lambda transition hot solid. The atomic diffusion rates (refined MD model) follow a similar trend: Below the lambda transition (2670 K), there is negligible U or O diffusion on the ~100-ps time scales investigated. Above the lambda transition at 3000 K, the crystalline O diffusion increased to 5.1 nm^{2}s^{-1}, but the U

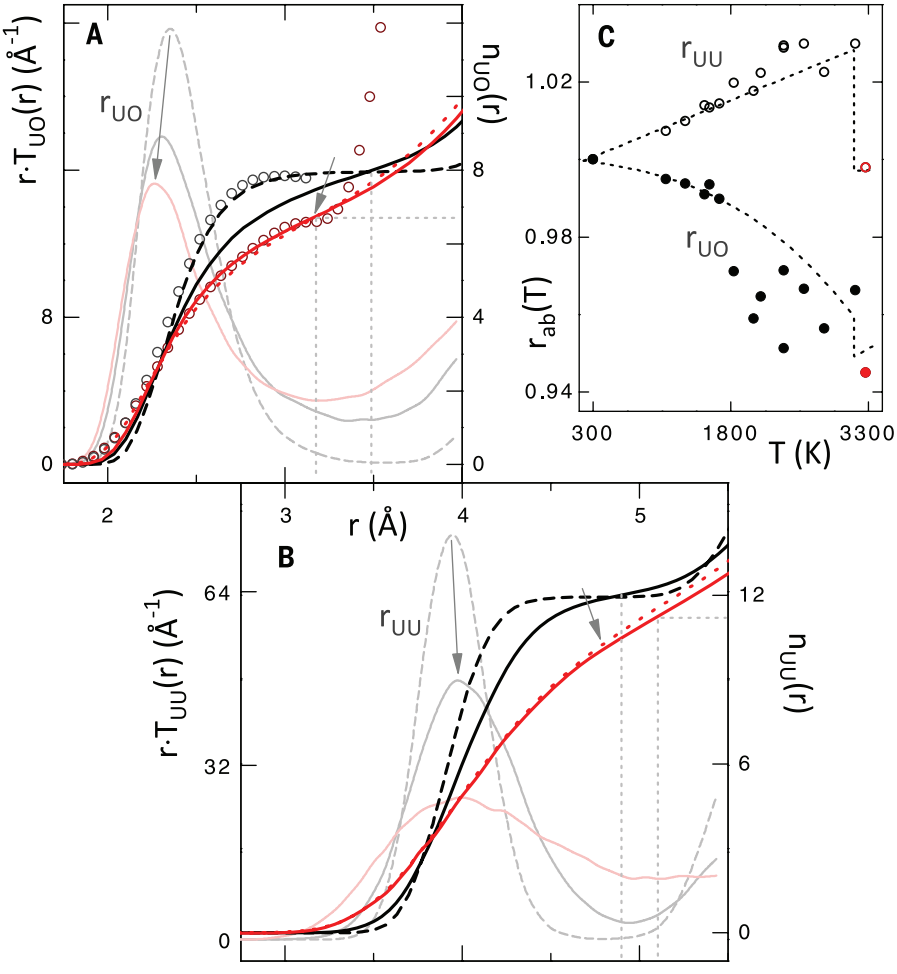


Fig. 2. UO_2 coordination numbers and bond lengths. (**A**) U-O pair distribution functions [$rT_{UO}(r)$] and running coordination numbers [$n_{UO}(r)$]. Open circles are $n_{UO}(r)$ from the x-ray measurements at 2100 K (black) and 3270 K (red). The above 3-Å U-U correlations also contribute to the measured $n_{UO}(r)$. (**B**) U-U pair distribution functions [$rT_{UU}(r)$] and running coordination numbers [$n_{UU}(r)$]. In both (A) and (B), light gray and light red curves are the $rT(r)$ and the thicker, darker curves are $n(r)$. The dashed or unbroken curves are from the Yakub MD model at three temperatures: 2100 K (dashed gray or black), 3000 K (unbroken gray or black), and 3270 K liquid (unbroken red or pink). The direction of the arrows indicates increasing temperature. The dotted red lines are the $n(r)$ curves from the refined MD model. The temperatures chosen are either side of the lambda transition in the hot solid (2100 K and 3000 K) and the stable liquid state (3270 K). (**C**) Measured r_{UO} (solid circles) and r_{UU} (open circles), normalized to the 300 K value. The dotted lines are the Yakub MD model. Red circles (3270 K) indicate the liquid state. Liquid UO_2 number density at 3270 K is 0.0593 Å^{-3} (*2*).

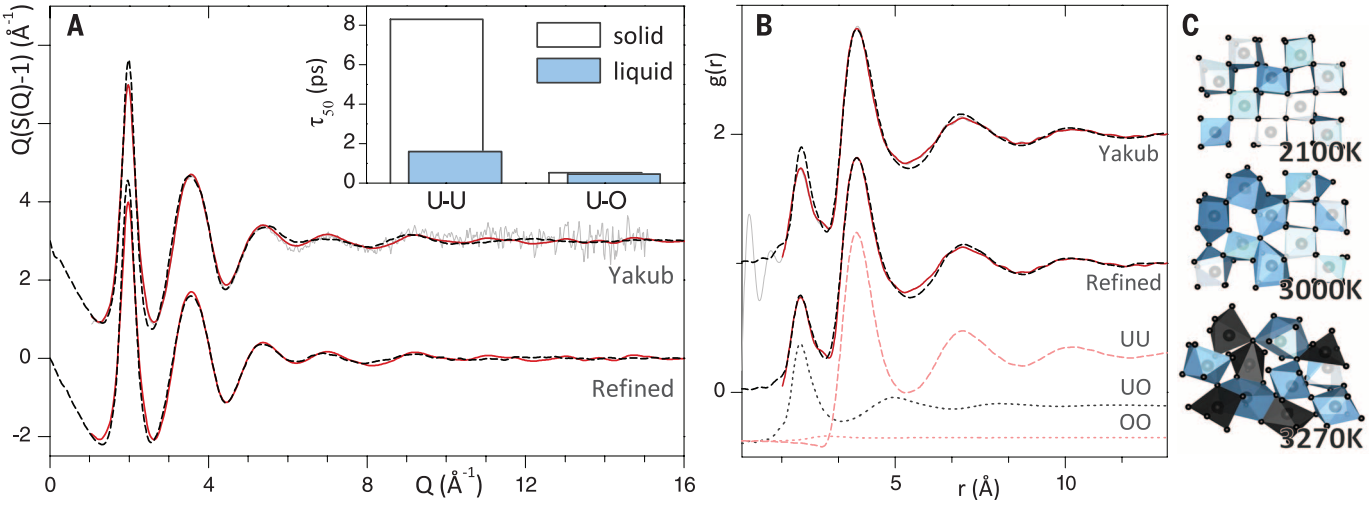


Fig. 3. Molten UO_2 structure measurements and MD simulations. Diffraction measurements (red), Yakub and refined MD models (black dashed). (**A**) The thin, light gray line on the upper pattern is the raw measurement, whereas the smoother red lines correspond to the solid red lines in (B). The inset shows times for 50% of bonds to be broken in the solid or supercooled liquid at 3000 K (light blue). (**B**) The solid red lines were filtered by Fourier transforming with an *r*-dependent modification function to reduce unphysical high-frequency noise (*13*, *19*), whereas the solid light gray line shows the unmodified transform. The lower dashed and dotted curves are the UU, UO, and OO partial contributions to the x-ray pattern. (**C**) Slices from the refined MD simulation (~15 by 12 by 3 Å) showing U-O polyhedra, above and below the lambda transition (2100 K and 3000 K) and in the liquid state (3270 K). The bottom slice shows the UO_6 drawn in black and the UO_7 in light blue (*11*).

diffusion remains below 10^{-4} nm^2s^{-1}. In the liquid state at 3270 K, the rates of U and O diffusion are of similar magnitude (3.7 versus 9.3 nm^2s^{-1}). Manara *et al.* measured a melting slope (dT_m/dP) that is a factor 1.5 to 2 steeper than expected from the recommended volume change on melting and enthalpy of fusion values (*11*, *16*). The rapid O exchange in these MD models results in a relatively low enthalpy of fusion, consistent with a relatively steep melting slope. Using pressure, an 8-coordinated UO_2 melt can be simulated at a number density of 0.074 $Å^{-3}$. The 8-coordinated melt has U and O diffusion rates slower by a factor of 3 (1.2 and 3.8 nm^2s^{-1}) than the low-coordinated melt, demonstrating the strong effect of local structure on the physical properties of this melt. The Andrade theory, for example, is often used to predict melt viscosity but assumes that the melt structure closely resembles that of the solid (*17*, *18*).

Portions of the hot solid and liquid UO_2 MD simulations illustrate the large oxygen disorder above the lambda transition and the different $UO_{6,7}$ coordination species that predominate in the melt (Fig. 3C). The structure and optimized interatomic potentials for UO_2 allow for accurate atomistic multiscale modeling. The x-ray data are important as an end-member benchmark for models of multicomponent systems, including corium melts and high-level waste glasses (*11*).

REFERENCES AND NOTES

1. P. A. Kharecha, J. E. Hansen, *Environ. Sci. Technol.* **47**, 4889–4895 (2013).
2. J. K. Fink, *J. Nucl. Mater.* **279**, 1–18 (2000).
3. D. Manara, C. Ronchi, M. Sheindlin, M. Lewis, M. Brykin, *J. Nucl. Mater.* **342**, 148–163 (2005).
4. S. D. Günay, Ü. Akdere, Ç. Taşseven, *J. Mol. Liq.* **173**, 124–129 (2012).
5. T. Arima, S. Yamasaki, Y. Inagaki, K. Idemitsu, *J. Alloys Compd.* **400**, 43–50 (2005).
6. E. Yakub, C. Ronchi, D. Staicu, *J. Chem. Phys.* **127**, 094508 (2007).
7. C. B. Basak, A. K. Sengupta, H. S. Kamath, *J. Alloys Compd.* **360**, 210–216 (2003).
8. N.-D. Morelon, D. Ghaleb, J.-M. Delaye, L. Van Brutzel, *Philos. Mag.* **83**, 1533–1555 (2003).
9. G. V. Lewis, C. R. A. Catlow, *J. Phys. C Solid State Phys.* **18**, 1149–1161 (1985).
10. H. E. Fischer, A. C. Barnes, P. S. Salmon, *Rep. Prog. Phys.* **69**, 233–299 (2006).
11. Materials and methods are available as supporting material on *Science* Online.
12. L. Hennet *et al.*, *J. Chem. Phys.* **126**, 074906 (2007).
13. L. B. Skinner *et al.*, *Phys. Chem. Chem. Phys.* **15**, 8566–8572 (2013).
14. S. Krishnan *et al.*, *Chem. Mater.* **17**, 2662–2666 (2005).
15. H. Lou *et al.*, *Proc. Natl. Acad. Sci. U.S.A.* **110**, 10068–10072 (2013).
16. D. Manara, C. Ronchi, M. Sheindlin, *Int. J. Thermophys.* **23**, 1147–1156 (2002).
17. E. N. C. Andrade, *Philosophical Mag.* **17**, 497–511 (1934).
18. F. Sudreau, G. Cognet, *Nucl. Eng. Des.* **178**, 269–277 (1997).

ACKNOWLEDGMENTS

X-ray diffraction data are available for download in the supplementary materials. We thank R. Spence, D. Robinson, and A. Hasozbek for technical support and useful discussions. This work was supported by the U.S. Department of Energy (DOE), Office of Basic Energy Sciences (BES), grant BES DE-FG02-09ER46650 (MD simulations, analysis, and manuscript preparation, L.B.S. and J.B.P.); DOE Small Business Innovation Research grant DE SC0007564 (x-ray experiment, J.K.R.W., A.T., and O.L.G.A.), and the Argonne Laboratory Directed Research and Development program (sample preparation and handling). M.G. (data analysis) was supported by EFree, an Energy Frontier Research Center funded by the DOE, BES, under award DE-SC0001057. The Advanced Photon Source, Argonne National Laboratory, is funded under U.S. DOE, BES, contract number DE-AC02-06CH11357.

SUPPLEMENTARY MATERIALS

www.sciencemag.org/content/346/6212/984/suppl/DC1
Materials and Methods
Fig. S1
Table S1
References (*19*–*29*)

6 August 2014; accepted 22 October 2014
10.1126/science.1259709

EBOLA MOUSE MODEL

Host genetic diversity enables Ebola hemorrhagic fever pathogenesis and resistance

Angela L. Rasmussen,*[1] Atsushi Okumura,*[1,4] Martin T. Ferris,[2] Richard Green,[1] Friederike Feldmann,[3] Sara M. Kelly,[1] Dana P. Scott,[3] David Safronetz,[4] Elaine Haddock,[4] Rachel LaCasse,[3] Matthew J. Thomas,[1] Pavel Sova,[1] Victoria S. Carter,[1] Jeffrey M. Weiss,[1] Darla R. Miller,[2] Ginger D. Shaw,[2] Marcus J. Korth,[1] Mark T. Heise,[2,5] Ralph S. Baric,[5] Fernando Pardo-Manuel de Villena,[2] Heinz Feldmann,[4] Michael G. Katze[1,6]†

Existing mouse models of lethal Ebola virus infection do not reproduce hallmark symptoms of Ebola hemorrhagic fever, neither delayed blood coagulation and disseminated intravascular coagulation nor death from shock, thus restricting pathogenesis studies to nonhuman primates. Here we show that mice from the Collaborative Cross panel of recombinant inbred mice exhibit distinct disease phenotypes after mouse-adapted Ebola virus infection. Phenotypes range from complete resistance to lethal disease to severe hemorrhagic fever characterized by prolonged coagulation times and 100% mortality. Inflammatory signaling was associated with vascular permeability and endothelial activation, and resistance to lethal infection arose by induction of lymphocyte differentiation and cellular adhesion, probably mediated by the susceptibility allele *Tek*. These data indicate that genetic background determines susceptibility to Ebola hemorrhagic fever.

A mouse-adapted strain of Ebola virus (MA-EBOV) does not cause hemorrhagic syndrome despite causing lethal disease in laboratory mice, and it cannot be used effectively to study Ebola hemorrhagic fever (EHF) pathogenesis, because the dissimilarity to human disease limits the ability to identify key correlates of viral pathogenesis or accurately assess the effect of vaccines or therapeutics. Pathogenesis studies of EHF have thus been restricted to macaques (*1*–*4*), guinea pigs (*5*, *6*), and Syrian hamsters (*7*). Although these models accurately recapitulate most of the disease features of EHF, practical and ethical concerns limit their use, including nonreproducible genetic backgrounds, cost, animal availability, and reagent availability. Epidemiologic studies of EBOV infection have identified a range of pathogenic phenotypes, which are not linked to specific mutations in the viral genome (*8*, *9*). This suggests that the host response may determine disease severity after EBOV infection.

We tested the role of host genetics in Ebola virus disease (EVD) using the Collaborative Cross (CC) resource, a genetically diverse panel of recombinant inbred (CC-RI) mice obtained through a systematic cross of eight inbred founder mouse strains, five of which are classic laboratory strains (C57BL/6J, A/J, 129S1/SvImJ, NOD/ShiLtJ, and NZO/H1LtJ) and three of which are wild-derived inbred strains (CAST/EiJ, PWK/PhJ, and WSB/EiJ) (*10*). The founders represent 90% of the common genetic variation across the three major *Mus musculus* subspecies (*M. m. musculus*, *M. m. domesticus*, and *M. m. castaneus)* (*11*). Different strains can be crossed with one another to generate CC-RI intercrossed (CC-RIX) F_1 progeny.

[1]Department of Microbiology, University of Washington, Seattle, WA, USA. [2]Department of Genetics, University of North Carolina, Chapel Hill, NC, USA. [3]Rocky Mountain Veterinary Branch, National Institute of Allergy and Infectious Diseases, National Institutes of Health, Rocky Mountain Laboratories, Hamilton, MT, USA. [4]Laboratory of Virology, National Institute of Allergy and Infectious Diseases, National Institutes of Health, Rocky Mountain Laboratories, Hamilton, MT, USA. [5]Department of Microbiology and Immunology, University of North Carolina, Chapel Hill, NC, USA. [6]Washington National Primate Research Center, Seattle, WA, USA.
*These authors contributed equally to this work. **†Corresponding author. E-mail: honey@uw.edu**

We recently observed a spectrum of pathogenic phenotypes in CC mice and identified genetic loci associated with influenza severity and disease outcome (*12*, *13*). Thus we tested whether a similar range of phenotypes would emerge after infecting CC-RIX animals with MA-EBOV.

To determine a phenotypic baseline, we challenged the eight CC founders intraperitoneally with MA-EBOV or the Mayinga strain of wild-type EBOV (WT-EBOV). MA-EBOV differs from the published WT-EBOV sequence by only 13 nucleotide changes, three of which are silent (*14*). MA-EBOV is pathogenic in guinea pigs and macaques (*1*) and causes lethal EHF in Syrian hamsters (*7*). Despite observing 25 to 100% mortality after MA-EBOV challenge at multiple doses (fig. S1), we found no evidence of hemorrhagic disease or susceptibility to lethal disease after infection with WT-EBOV. We assessed the pathogenic phenotype produced by intraperitoneal infection with 100 focus-forming units (FFUs) of MA-EBOV in 47 available CC-RIX lines (Table 1). We observed disease phenotypes ranging from complete resistance to lethal disease to severe EHF-associated pathology before death, as well as lines that showed lethal infection without symptoms of EHF but sometimes with hepatic discoloration.

We performed detailed studies on two representative lines, 13140x3015 (susceptible to lethal EHF) and 15156x1566 (resistant to lethal disease). Mice from both lines lost approximately 15% of their body weight over the first 5 days post-infection (p.i.) (Fig. 1A). However, susceptible mice succumbed to lethal infection on days 5 to 6 p.i., whereas resistant mice survived and fully recovered their body weight by day 14 (Fig. 1B). At day 5 p.i., susceptible mice presented pathological findings consistent with EHF, including prolonged blood coagulation, internal hemorrhage, coffee-colored blood, splenomegaly, and hepatic discoloration and softened texture (Fig. 1C). The resistant mice, however, had no evident gross pathology at the time of maximum body weight loss and no alteration in the appearance of the liver (Fig. 1D). Neither susceptible nor resistant mice developed observable clinical disease after challenge with WT-EBOV. We detected extremely low titers of virus at day 3 in the liver and spleen of animals after WT-EBOV infection, and these were 100 to 1000 times lower than organ titers detected in mice infected with MA-EBOV (fig. S2). We did not detect virus at day 5 in any organ or any mouse, indicating that WT-EBOV is not able to productively replicate in these mouse strains.

In liver and spleen from both mouse lines, equivalent levels of viral RNA were observed (Fig. 2, A and B). However, we observed 1 to 2 logs higher levels of infectious virus in susceptible liver and spleen than in resistant liver and spleen after virus titration by focus-forming assay when infectious virion production became detectable on day 3 (Fig. 2, C and D), suggesting that resistance may be associated with a defect in virion assembly, secretion, or other posttranscriptional processes. We confirmed this finding by staining liver sections from susceptible and resistant mice on day 5 p.i. for VP40, the viral matrix protein. We observed substantially less VP40 staining in resistant liver (Fig. 2, E and F) than in susceptible liver (Fig. 2, G and H, and fig. S3). Sequence analysis showed no nucleotide changes between virus genomes in either line, indicating that these effects cannot be readily attributed to the selection of quasispecies with different viral fitness (table S1). Despite significant differences in infectious virus titers between the two mouse lines, we observed similar levels of inflammation and apoptosis in the spleen and liver, although the two lines displayed distinct histopathology (figs. S4 to S6). Despite similar organ tropism, virus infection occurred in different hepatic cell types in the two mouse lines. Susceptible mice had viral antigen in essentially every hepatocyte (Fig. 2F and table S2); whereas in resistant mice, viral antigen was restricted to cells that lack typical hepatocyte morphology, most likely endothelial cells and Kupffer cells (Fig. 2G), consistent with low-pathogenicity Reston virus infection (*15*). Possibly in resistant mice, infected hepatic endothelial cell and macrophage responses limit virus production and control systemic inflammation and coagulopathy. Widespread hepatic infection in susceptible mice may explain how these animals both produce increased amounts of infectious virus and induce dysregulated coagulation pathways.

We quantified the extent of coagulopathy by measuring blood clotting times. On days 5 to 6 p.i., susceptible mice showed significantly prolonged thrombin time (TT), prothrombin time (PTT), and activated partial thromboplastin time (aPTT) compared to resistant and C57BL/6J mice (Fig. 3, A to C). An initial spike in serum fibrinogen levels in susceptible mice on day 3 p.i. was followed by a precipitous drop (Fig. 3D) before death. This

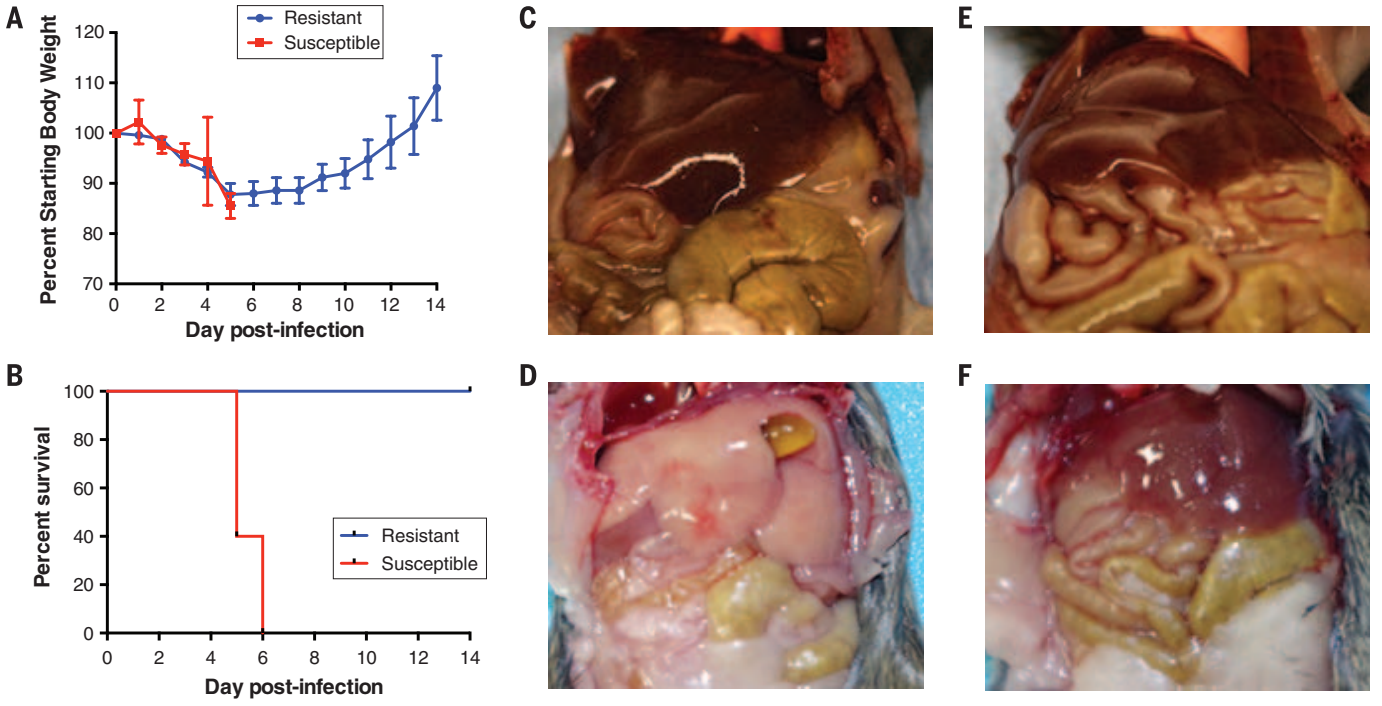


Fig. 1. Distinct morbidity and mortality after MA-EBOV infection in CC-RIX mouse lines. (**A**) Percent of starting body weight over the course of infection in susceptible (red squares) and resistant (blue circles) mice. Data shown are mean ± SEM from five mice per CC-RIX line. (**B**) Kaplan-Meier survival curve for susceptible (red) and resistant (blue) mice. Five mice were used for each CC-RIX line. (**C** to **F**) Gross appearance of liver at necropsy in uninfected susceptible (C) and resistant (D) mice and on day 5 p.i. in susceptible (E) and resistant (F) mice.

increase may be due to compensatory fibrinogen production in response to hepatic cell death and consequent clotting factor depletion, which is consistent with observations in other EHF models in which severe hemorrhage and coagulopathy typically peak within 48 hours preceding death (*3*, *7*).

We investigated transcriptional host responses linked to disease outcome in the CC-RIX lines. Significant differentially expressed genes relative to time-matched mock-infected samples (false discovery rate–adjusted P value <0.05; fold change >1.5) in both spleen and liver were 10 to 100 times higher in number in susceptible mice than in resistant mice (Fig. 4, A and B, and supplementary data files S2 and S3). These data suggest that EHF is characterized by earlier induction of a larger-magnitude transcriptional response. In susceptible mice relative to resistant mice, genes associated with EBOV infection were differentially induced. Early in infection in the spleens of susceptible mice at day 1 p.i., we observed enrichment of p38 mitogen-activated protein kinase and extracellular signal–regulated kinase signaling, processes that stimulate productive EBOV infection (*16*, *17*). Additionally, we observed increased nuclear factor κB expression and the induction of proinflammatory processes, which may reflect early targets of infection in the secondary lymphoid organs. By day 3 p.i. in both liver and spleen, inflammatory pathways became increasingly enriched in susceptible mice, as did pathways associated with cell death, including those associated with cytotoxicity and apoptosis in macrophages and endothelial cells. Both resistant and susceptible lines induced multiple immune pathways in the spleen. By day 5, although

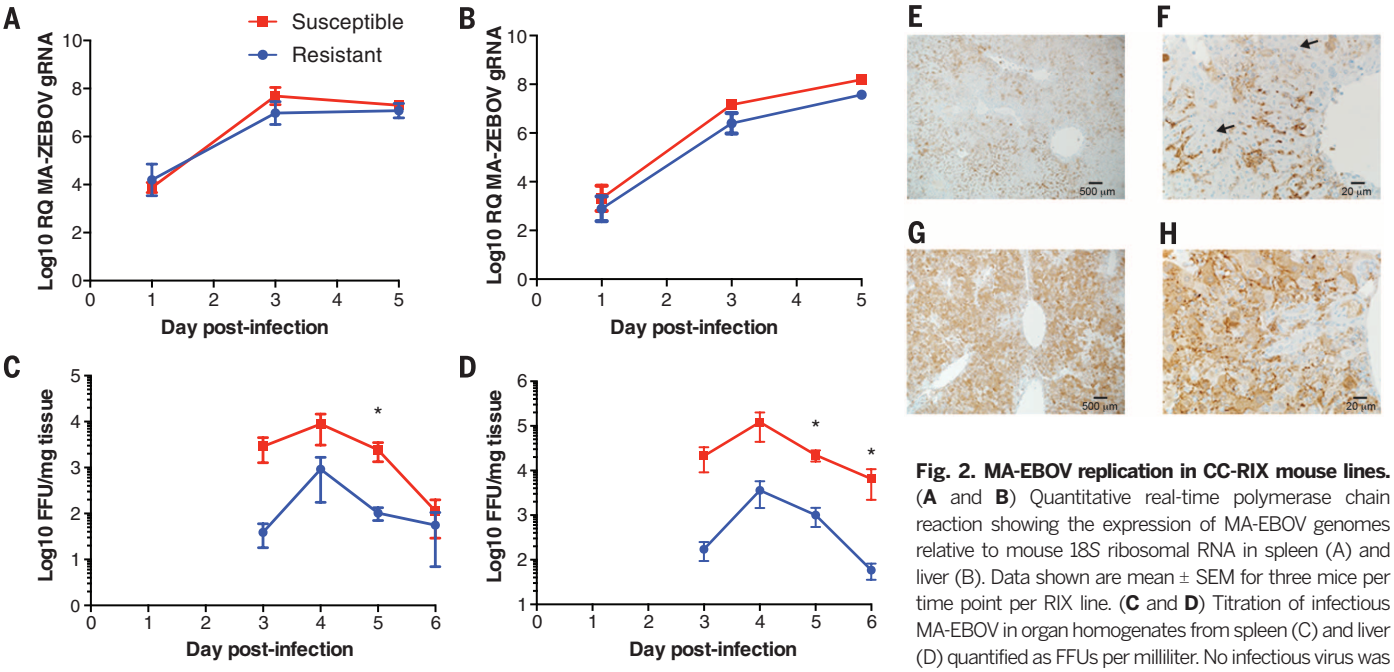


Fig. 2. MA-EBOV replication in CC-RIX mouse lines. (**A** and **B**) Quantitative real-time polymerase chain reaction showing the expression of MA-EBOV genomes relative to mouse 18S ribosomal RNA in spleen (A) and liver (B). Data shown are mean ± SEM for three mice per time point per RIX line. (**C** and **D**) Titration of infectious MA-EBOV in organ homogenates from spleen (C) and liver (D) quantified as FFUs per milliliter. No infectious virus was detected before day 3 p.i. Data shown are mean ± SEM from two experiments using two or three mice per time point per CC-RIX line. (**E** to **H**) Immunohistochemical staining for VP40 in resistant liver [(E) and (F)] and susceptible liver [(G) and (H)]. The arrows indicate representative hepatocyte morphology (*t* test, *P < 0.05).

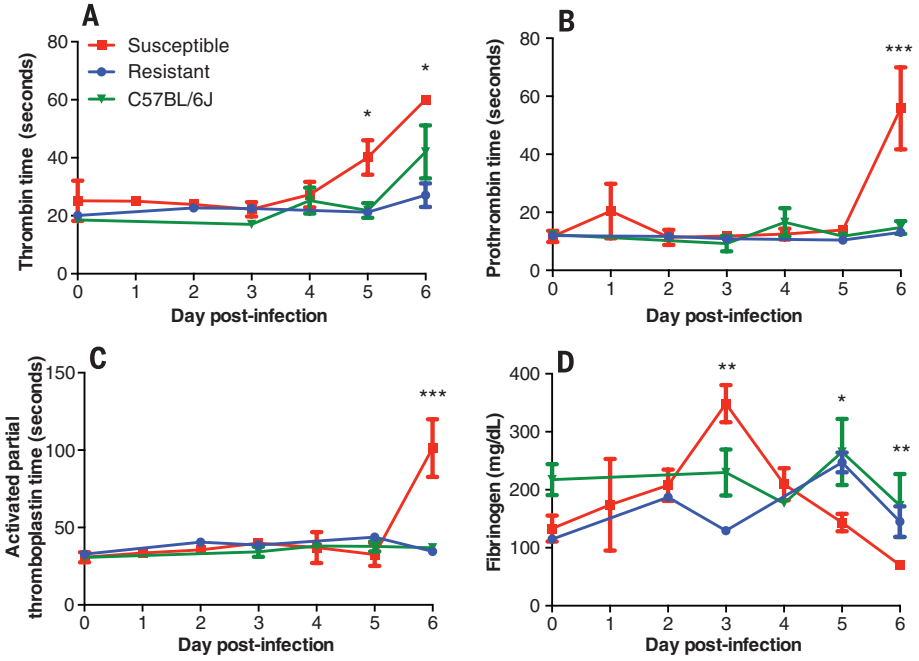


Fig. 3. Quantification of coagulopathy and hemorrhage in CC-RIX mouse lines. (**A** to **C**) Coagulation times in seconds for thrombin (A), prothrombin (B), and activated partial thromboplastin (C) over the course of MA-EBOV infection. (**D**) Serum fibrinogen levels in CC-RIX mice over the course of MA-EBOV infection. All data shown are the mean ± SEM for two experiments including two to five animals per time point. (ANOVA with Tukey's HSD post-hoc test; * P < 0.05, ** P < 0.05, *** P < 0.0000001).

differential gene expression peaked in both lines, the gene sets involved were distinct and probably reflected different courses of disease.

We identified differentially expressed genes unique to susceptible mice in the liver and observed enrichment in genes related to vascular integrity at days 3 and 5, including the endothelial tyrosine kinases *Tie1* and *Tek* (*Tie2*). *Tie1* and *Tek* expression was depressed as compared with levels in mock-infected animals at day 5, concurrent with the onset of coagulopathy. We used Ingenuity Pathway Analysis software to generate networks predicting molecular activity (*18*) and predicted the activation of processes associated with vascular differentiation and endothelial activation, interleukin-6–mediated inflammation and bleeding, and the inhibition of pathways associated with vascular integrity and inflammatory regulation in susceptible livers (fig. S7). TIE1 and TEK signaling promotes the activation of coagulation factors, such as thrombin (F2), tissue factor (F3), and protease-activated receptors 1, 3, and 4 (PAR1/F2R, PAR3/F2RL2, and PAR4/F2RL3) (*19*), which have been mechanistically implicated in coagulopathies mediated by EBOV and other viruses (*4*, *20*) and are differentially regulated in these mice (fig. S8). *Tie1* and *Tek* expression was consistently elevated in resistant mouse spleens, implying that endothelial signaling regulation and vascular leakage contribute to disease resistance in susceptible mice.

In livers from resistant mice at day 5, gene expression associated with vascular density and angiogenesis increased, suggesting that this line effectively controls vascular leakage, potentially through repair or structural maintenance of blood

Table 1. Distribution of phenotypes across CC-RIX lines. Boldface type indicates CC-RIX crosses used in this study.

Outcome of infection	Frequency of phenotype (%)	Phenotypic characteristics	CC-RIX line ID	Mortality (%)
Resistant	19 (9/47)	0% mortality	**15156x1566**	0
			3252x8042	0
			5119x8018	0
			3252x8002	0
			8034x8048	0
			8048x8026	0
			8026x5080	0
			1566x8043	0
			16012x15119	0
Partially resistant	11 (5/47)	<50% mortality	18042x3032	20
			15156x3252	20
			477x16912	40
			13140x16680	20
			16072x15119	20
Lethal	17 (8/47)	>50% mortality	3032x16188	80
			8004x8043	60
			8002x3032	60
			16188x8005	100
			8008x8016	100
			16441x8024	100
			16912x5489	100
			3415x16012	100
Lethal with hepatitis	19 (9/47)	>50% mortality, hepatic discoloration	8042x16513	60
			16513x15156	100
			16188x3252	75
			13067x16912	100
			5489x16557	80
			16912x16211	60
			16211x13140	80
			8024x8049	100
			8049x8010	100
Lethal with EHF	34 (16/47)	>50% mortality, severe coagulopathy (discolored blood, prolonged blood clotting)	3609x5119	60
			8018x3154	80
			13140x3015	100
			8016x8034	100
			16441x8005	100
			8010x16441	100
			3032x16441	60
			8005x8002	100
			3154x3609	100
			3609x5489	100
			16557x13067	100
			16513x16188	100
			15155x8054	100
			3393x8052	100
			8043x8008	80
			8048x15155	80

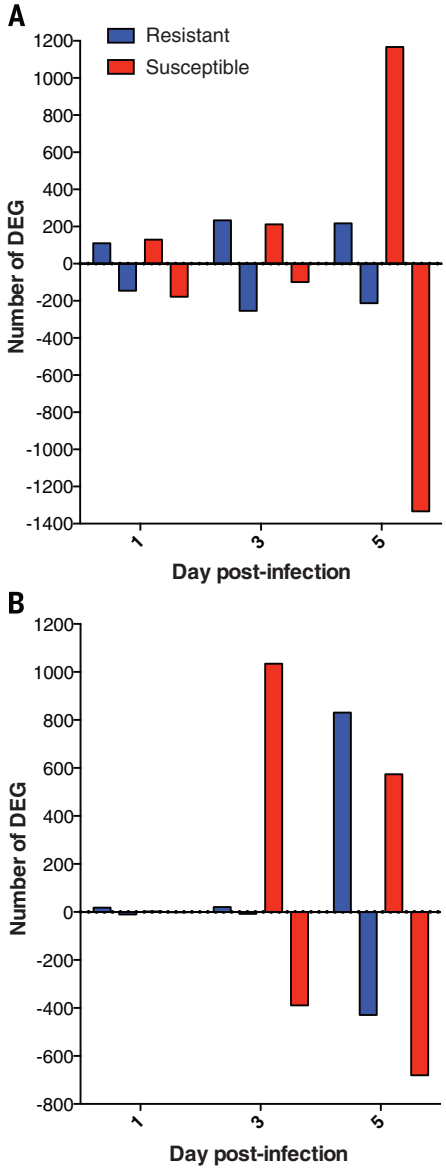


Fig. 4. Distinct host responses associated with disease phenotype. (**A** and **B**) Number of differentially expressed genes either up-regulated (positive *y* axis) or down-regulated (negative *y* axis) relative to time-matched mock-infected samples in spleen (A) and liver (B).

vessels. It seems likely that restriction of MA-EBOV infection to endothelial and Kupffer cells in resistant mice prevents the induction of hepatocyte-specific molecules that enhance systemic inflammation, thrombocytopenia, and coagulopathy.

We investigated the genomes and found that the *Tie1* alleles across the eight CC founders are from all three *M. musculus* subspecies and are highly divergent from one another (*21*), which prevented us from identifying significant relationships between *Tie1* alleles and phenotypes. In contrast, *Tek* alleles in the CC-RIX lines are derived from only two subspecies, *M. m. domesticus* and *M. m. musculus,* and are very different from one another. Distinct *Tek* alleles were previously associated with inflammatory coagulopathies and vascular dysfunction (*22*–*26*). In our preliminary analysis, we identified statistically significant relationships between subspecific *Tek* alleles and the initial onset of weight loss [analysis of variance (ANOVA), $F_{2,31} = 5.581$, $P = 0.0085$], average day of death (ANOVA, $F_{2,34} = 10.519$, $P = 0.00028$), and mortality (ANOVA, $F_{2,37} = 8.5553$, $P = 0.0008$) (fig. S9).

We reproduced EHF in a mouse model that will allow the linkage of specific genetic polymorphisms to tropism, infectious virus production, cell type–specific responses, and phenotypic outcome. The CC model provides a platform to map susceptibility alleles in the context of EHF pathogenesis and rapidly apply these findings to the development of candidate therapeutics and vaccines. Ongoing screening activities in CC-RIX mice will identify additional genetic loci that contribute to hemorrhagic disease, lethality, or resistance to severe disease.

The frequency of different pathological manifestations across the 47 CC-RIX lines screened so far is similar in variety and proportion to the spectrum of clinical disease observed in patients with EVD in the 2014 West Africa outbreak, with hemorrhagic symptoms appearing in 30 to 50% of patients (*27*, *28*). Although we cannot rule out the possibility that human survivors have preexisting immunity to EBOV or a related virus, our data suggest that genetic factors play a significant role in determining disease outcome in naïve individuals without prior exposure or immunologic priming.

Although we have not yet screened CC-RIX mice for susceptibility to other ebolavirus species, we anticipate that we would observe a similar distribution of pathogenic phenotypes after infection with viruses that are capable of replicating in mice. The current 2014 West Africa outbreak is caused by the same species of ebolavirus as the MA-EBOV used in this screen. There are also similarities in the spectrum of disease observed in CC-RIX mice infected with MA-EBOV and in clinical cases in the current outbreak. The model described in this paper can be implemented promptly to identify genetic markers, conduct meticulous pathogenesis studies, and evaluate therapeutic strategies that have broad-spectrum antiviral activity against all Zaire ebolaviruses, including the virus responsible for the current West Africa outbreak.

REFERENCES AND NOTES

1. M. Bray, S. Hatfill, L. Hensley, J. W. Huggins, *J. Comp. Pathol.* **125**, 243–253 (2001).
2. J. Y. Yen *et al.*, *J. Infect. Dis.* **204** (suppl. 3), S1043–S1052 (2011).
3. H. Ebihara *et al.*, *J. Infect. Dis.* **204** (suppl. 3), S991–S999 (2011).
4. T. W. Geisbert *et al.*, *J. Infect. Dis.* **188**, 1618–1629 (2003).
5. B. M. Connolly *et al.*, *J. Infect. Dis.* **179** (suppl. 1), S203–S217 (1999).
6. E. Ryabchikova *et al.*, *Arch. Virol.* **141**, 909–921 (1996).
7. H. Ebihara *et al.*, *J. Infect. Dis.* **207**, 306–318 (2013).
8. E. M. Leroy, S. Baize, E. Mavoungou, C. Apetrei, *J. Gen. Virol.* **83**, 67–73 (2002).
9. E. M. Leroy *et al.*, *Lancet* **355**, 2210–2215 (2000).
10. Collaborative Cross Consortium, *Genetics* **190**, 389–401 (2012).
11. A. Roberts, F. Pardo-Manuel de Villena, W. Wang, L. McMillan, D. W. Threadgill, *Mamm. Genome: Official J. Int. Mamm. Genome Soc.* **18**, 473 (2007).
12. D. Bottomly *et al.*, *Genes, Genomes, Genetics* **2**, 213 (2012).
13. M. T. Ferris *et al.*, *PLOS Pathog.* **9**, e1003196 (2013).
14. H. Ebihara *et al.*, *PLOS Pathog.* **2**, e73 (2006).
15. A. Groseth *et al.*, *PLOS Pathog.* **8**, e1002847 (2012).
16. J. C. Johnson *et al.*, *Antiviral Res.* **107**, 102–109 (2014).
17. J. E. Strong *et al.*, *Proc. Natl. Acad. Sci. U.S.A.* **105**, 17982–17987 (2008).
18. Supplementary text.
19. T. N. Sato *et al.*, *Nature* **376**, 70–74 (1995).
20. S. Antoniak, N. Mackman, *J. Cardiovasc. Transl. Res.* **7**, 203–211 (2014).
21. H. Yang *et al.*, *Nat. Genet.* **43**, 648–655 (2011).
22. P. Brouillard, B. R. Olsen, M. Vikkula, *Genomics* **67**, 96–101 (2000).
23. J. M. Flanagan *et al.*, *Blood* **117**, 6681–6684 (2011).
24. V. G. Nolan *et al.*, *Br. J. Haematol.* **133**, 570–578 (2006).
25. M. Vikkula *et al.*, *Cell* **87**, 1181–1190 (1996).
26. Q. Zheng *et al.*, *Gene* **523**, 195–198 (2013).
27. S. Baize *et al.*, *N. Engl. J. Med.* **371**, 1418–1425 (2014).
28. M. G. Dixon, I. J. Schafer; Centers for Disease Control and Prevention (CDC), *MMWR Morb. Mortal. Wkly. Rep.* **63**, 548–551 (2014).

ACKNOWLEDGMENTS

This study was supported in part by awards U54 AI081680, U19 AI109761, and U19 AI100625 from the National Institute of Allergy and Infectious Diseases, National Institutes of Health; P51 OD010425 from the Office of the Director, National Institutes of Health; and the Intramural Research Program of the National Institute of Allergy and Infectious Diseases, National Institutes of Health. Microarray data have been deposited with the Gene Expression Omnibus (www.ncbi.nlm.nih.gov/geo) (accession number GSE57214), and raw data can be obtained at https://www.ccebola.org/project/Supplemental/begin.view. Mice were developed by the Collaborative Cross Consortium, an international consortium of researchers who designed, planned, and implemented the Collaborative Cross project. Initial animals were provided by the Jackson Laboratory, and CC lines were developed independently at the Oak Ridge National Laboratories in Tennessee, USA; Tel Aviv University, Israel; and Geniad, Ltd., Australia. CC lines are currently produced and distributed at the University of North Carolina, Chapel Hill. A.L.R. designed the study, performed functional analysis of microarray data, and wrote the manuscript; A.O. performed infections, veterinary examinations, and necropsies and assessed phenotype, collected and processed samples, and titrated virus from organs by focus-forming assay; M.T.F., M.T.H., F.P.-M.V., and R.S.B. established systems for designing and breeding CC-RIX mouse populations and utilizing them for virus pathogenesis studies and contributed to strain selection and data analysis; R.G. performed microarray data normalization, batch correction, and differential expression analysis; S.M.K. and J.M.W. performed target preparation and hybridization of microarrays; R.L. coordinated veterinary care for experimental animals; D.P.S. performed histopathological staining and analyzed the histopathology data; F.F., D.S., and E.H. assisted with mouse procedures in high biocontainment; M.J.T. and R.G. performed sequencing and subsequent analysis of viral RNA; A.F. performed functional analysis of microarray data; P.S. quantified viral RNA by quantitative polymerase chain reaction; M.J.K. edited the manuscript; and H.F. and M.G.K. contributed significantly to study design, provided space and infrastructure for the experiments and analysis, assisted in data analysis, and edited the manuscript.

SUPPLEMENTARY MATERIALS

www.sciencemag.org/content/346/6212/987/suppl/DC1
Materials and Methods
Figs. S1 to S9
Tables S1 to S3
Data Files S1 to S7

4 August 2014; accepted 21 October 2014
Published online 30 October 2014;
10.1126/science.1259595

EBOLA EPIDEMIOLOGY

Strategies for containing Ebola in West Africa

Abhishek Pandey,[1]* Katherine E. Atkins,[1,2]* Jan Medlock,[3] Natasha Wenzel,[1] Jeffrey P. Townsend,[4] James E. Childs,[5] Tolbert G. Nyenswah,[6] Martial L. Ndeffo-Mbah,[1] Alison P. Galvani[1,5]†

The ongoing Ebola outbreak poses an alarming risk to the countries of West Africa and beyond. To assess the effectiveness of containment strategies, we developed a stochastic model of Ebola transmission between and within the general community, hospitals, and funerals, calibrated to incidence data from Liberia. We find that a combined approach of case isolation, contact-tracing with quarantine, and sanitary funeral practices must be implemented with utmost urgency in order to reverse the growth of the outbreak. As of 19 September, under status quo, our model predicts that the epidemic will continue to spread, generating a predicted 224 (134 to 358) daily cases by 1 December, 280 (184 to 441) by 15 December, and 348 (249 to 545) by 30 December.

A multinational Ebola outbreak of unprecedented magnitude was declared a Public Health Emergency of International Concern by the World Health Organization (WHO) on 8 August 2014 (*1*). From Guinea, the outbreak has spread to the neighboring nations of Liberia and Sierra Leone, subsequently expanding into Nigeria and Senegal (*2*). Imported Ebola cases have recently led to transmission in the United States and Spain (2). As of 15 October,

more than 9000 cases and 4000 fatalities have been reported, with the majority of both occurring in Liberia (*2*).

Initial Ebola symptoms include fever, malaise, myalgia, and headache, followed by pharyngitis, vomiting, diarrhea, and maculopapular rash (*3*). Severe and fatal stages are accompanied by hemorrhagic diathesis and multiple-organ dysfunction (*3*). Human-to-human transmission occurs primarily via contact with body fluids (*3*). Inadequate and improper use of personal protective equipment (PPE), compounded by staff shortages in isolation wards, poses major infection risks for health care workers (*4*, *5*), leading to nosocomial transmission that can cripple health services (*5*). Ebola transmission is further exacerbated by traditional West African funeral practices that may involve washing, touching, and kissing the body (*5*–*7*). Given the current lack of licensed therapeutic treatments and vaccines (*8*), near-term measures to curb transmission must rely on nonpharmaceutical interventions, including quarantine, case isolation, contact precautions, and sanitary burial practices that consist of disinfecting the cadaver before inclosure in a body bag that is further disinfected.

To evaluate the effectiveness of nonpharmaceutical interventions for curtailing the epidemic in Liberia, we developed a stochastic model of Ebola disease transmission that takes into account Ebola transmission within and between the community, hospitals, and funerals (fig. S1 and supplementary materials, materials and methods, section S1). We parameterized our model using epidemiological data on disease progression and on delay from symptom onset to hospital admission obtained from the current outbreak in Liberia (table S1) (*9*), as well as using demographic data from the 2008 National Housing Census of Liberia (*10*). In the absence of data on the number of infections due to funeral transmission for the current outbreak, we parameterized the elevated risk posed by funeral attendance using odds ratios calculated from data collected during a previous Ebola outbreak in the Democratic Republic of the Congo (*11*). We tracked the density of individuals in the following epidemiological classes: susceptible (S), latently infected (E), infected and infectious (I), deceased (F), recovered with sterilizing immunity (R), and buried (D). To account for heterogeneity in contact and transmission between individuals in different locations, we further stratified each epidemiological class into compartments that correspond to foci of Ebola transmission: the general community, hospitals, and funerals. Hospitals were further stratified into patients and hospital workers. We parameterized hospital visitors per patient and rate of funeral attendance per death based on the number of family members in a Liberian household (*10*).

To calibrate our model, we obtained data from Situation Reports provided by the Liberian Ministry of Health and Social Welfare (table S1) (*12*). Outbreak control measures were not coordinated on a national scale in Liberia until 8 August 2014, when the Armed Forces of Liberia established checkpoints to restrict the movement from affected regions (*13*). To avoid potential confounding of behavior change as a result of interventions, we used Ebola cases, deaths, health care worker infections, and hospitalizations from Liberia reported between 8 June and 7 August 2014 to calibrate our model (Fig. 1 and supplementary materials). Given intervention assistance from the international community deployed on 20 September (*14*), we validated our model by comparing data between 8 August and 19 September to our model projection over that time period (Fig. 1).

In our study, we evaluated whether four WHO-recommended nonpharmaceutical interventions can efficiently control the current Ebola epidemic: (i) transmission precautions for health care workers, (ii) sanitary burial, (iii) isolation of infectious Ebola patients, and (iv) contact-tracing with

[1]Center for Infectious Disease Modeling and Analysis, Yale School of Public Health, New Haven, CT, USA. [2]Department of Infectious Disease Epidemiology, London School of Hygiene and Tropical Medicine, London, UK. [3]Department of Biomedical Sciences, Oregon State University, Corvallis, OR, USA. [4]Department of Biostatistics, Yale School of Public Health, New Haven, CT, USA. [5]Department of Epidemiology of Microbial Diseases, Yale School of Public Health, New Haven, CT, USA. [6]Ministry of Health and Social Welfare, Monrovia, Liberia.
*These authors contributed equally to this work. **†Corresponding author. E-mail: alison.galvani@yale.edu**

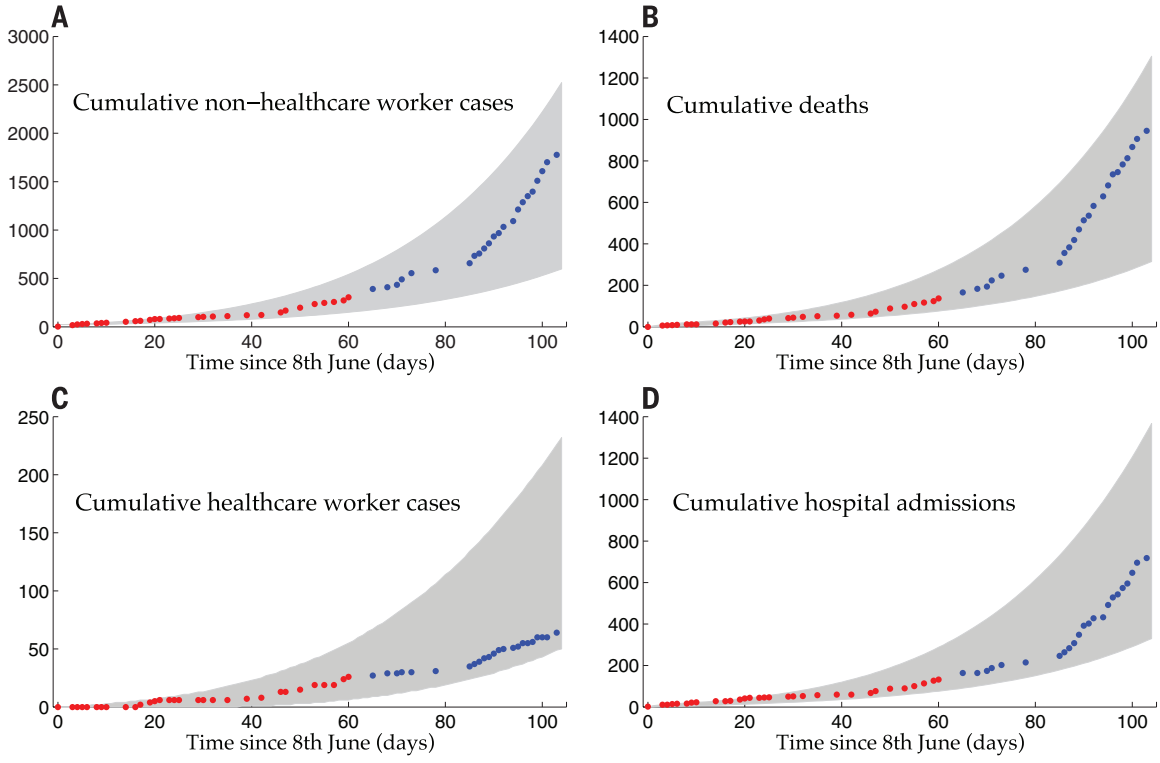


Fig. 1. Model fit to data. (**A**) Cumulative non–health care worker cases. (**B**) Cumulative deaths. (**C**) Cumulative health care worker cases. (**D**) Cumulative hospital admissions. Cumulative Ebola cases and fatalities were obtained from the Liberian Ministry of Health and Social Welfare Situation Reports nos. 10 to 89 (red circles), to which the model was fit. A 95% prediction interval was generated by 10,000 runs of the model, with parameters randomly sampled from within their confidence intervals (gray fill) (supplementary materials). Validation of the model predictions was provided by comparison with data of the cumulative Ebola cases and fatalities from Situation Reports nos. 89 to 127 (blue circles), representing 12 August 2014 to 19 September 2014, which were not used for model fitting.

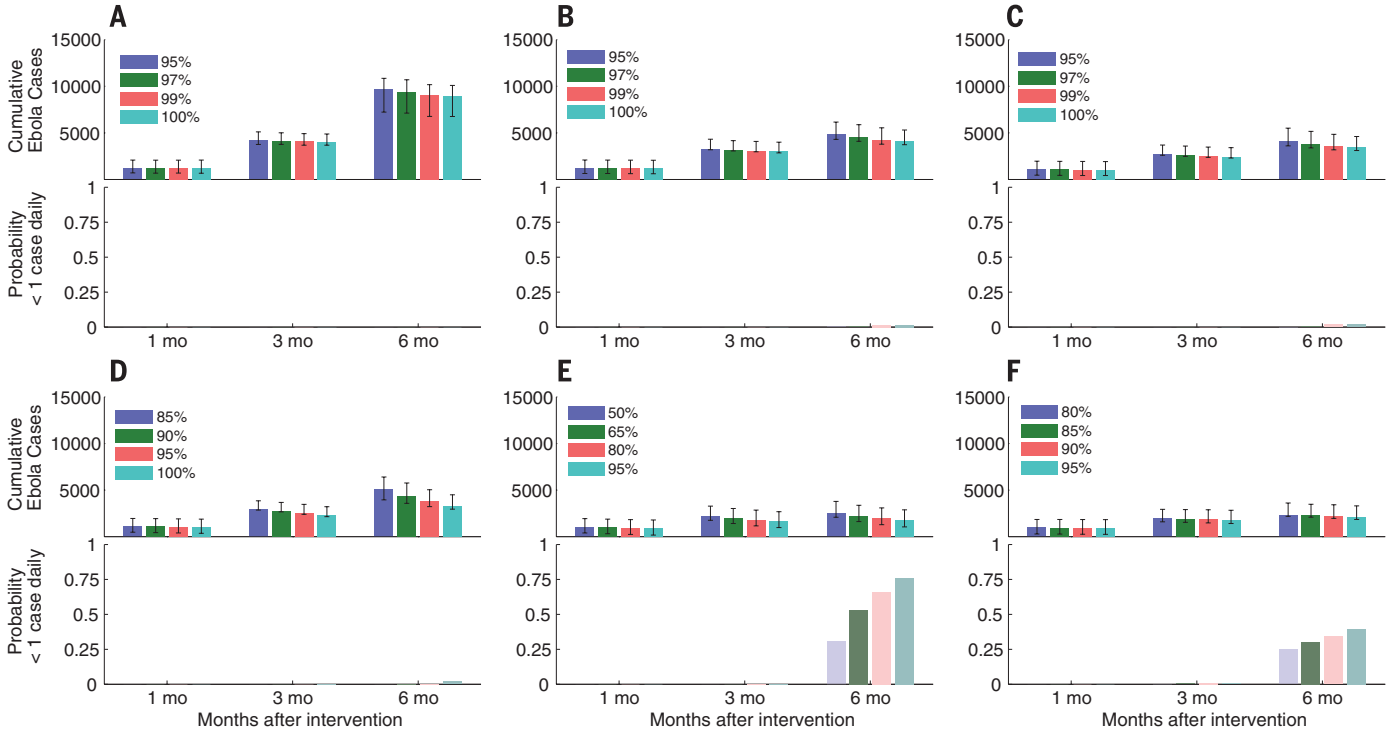


Fig. 2. Nonpharmaceutical intervention effectiveness. (**A** to **F**) Model predictions of the cumulative number of new cases after 1, 3, and 6 months after 20 September 2014, as well as the probability of fewer than one case daily after these months for (A) 80% reduction in transmission to health care workers combined with different reductions in community transmission, (B) increasing proportions of sanitary burial of hospital deaths, (C) increasing proportions of hospital case isolation, (D) 90% reduction in transmission to health care workers and increasing sanitary burial of hospital deaths, (E) 80% sanitary burial of hospitalized deaths with increasing sanitary burial of community deaths, and (F) 80% case isolation of hospitalized patients with concurrent contact-tracing and quarantine of infected contacts. One thousand simulations of the stochastic model were used to generate the cumulative case count error bars (95% prediction interval) and to estimate the probability of less than one new case per day.

follow-up and quarantine. Under no intervention strategies, our model assumes a status quo that reflects the control measures in place before 20 September. In addition, we also assessed a fifth intervention, enforcement of a cordon sanitaire, implemented by Liberian authorities. We calculated the basic reproductive number (R_0)—the average number of secondary cases generated by an average primary case in an entirely susceptible population (*15*)—and quantified the contribution of transmission arising from each of the community, hospital, and funeral settings.

We calculated R_0 for Ebola in Liberia to be 1.63 [95% confidence interval (CI), 1.59 to 1.66] before widespread interventions, which is consistent with other R_0 estimates for the current outbreak (*16*–*18*) but somewhat lower than those calculated for the previous outbreaks, which ranged between 1.8 and 2.7 (*19*–*21*). Our model structure allowed us to partition the contribution of different transmission routes in sustaining the epidemic. We calculated that in the absence of nosocomial transmission, R_0 = 1.48 (1.44 to 1.51); without community transmission, R_0 = 1.39 (1.35 to 1.42); if only funeral transmission were present and both nosocomial and community transmission were eliminated, R_0 = 1.16 (1.13 to 1.18); and if funeral transmission were absent but community and hospital transmis-

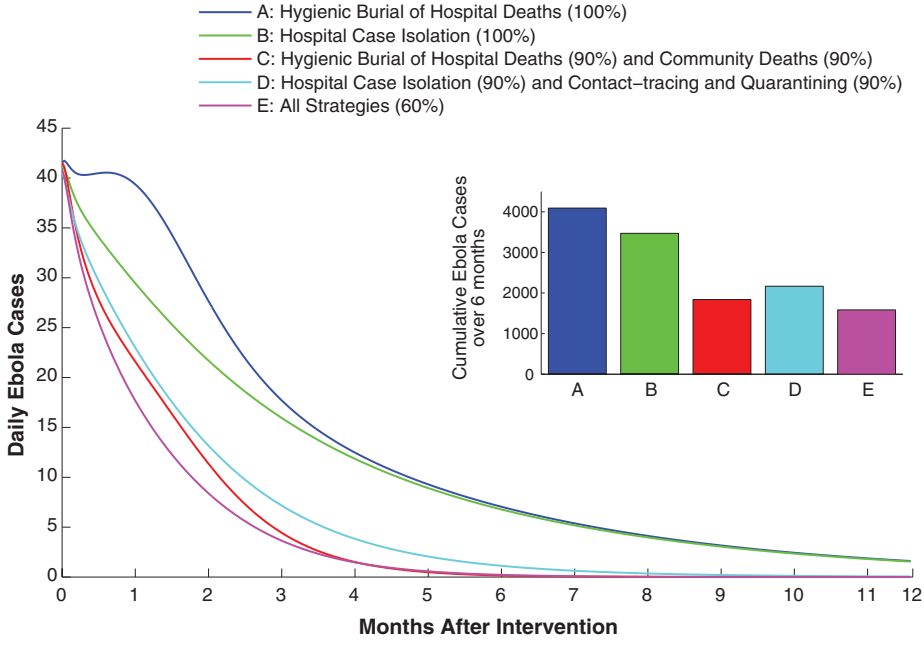


Fig. 3. Effectiveness comparison of individual and combined intervention strategies. Model predictions of the daily number of new and cumulative cases after 6 months for sanitary burial and hospital deaths, sanitary burial of community deaths, case isolation of hospitalized patients, contact-tracing in the community, and quarantine of infected contacts.

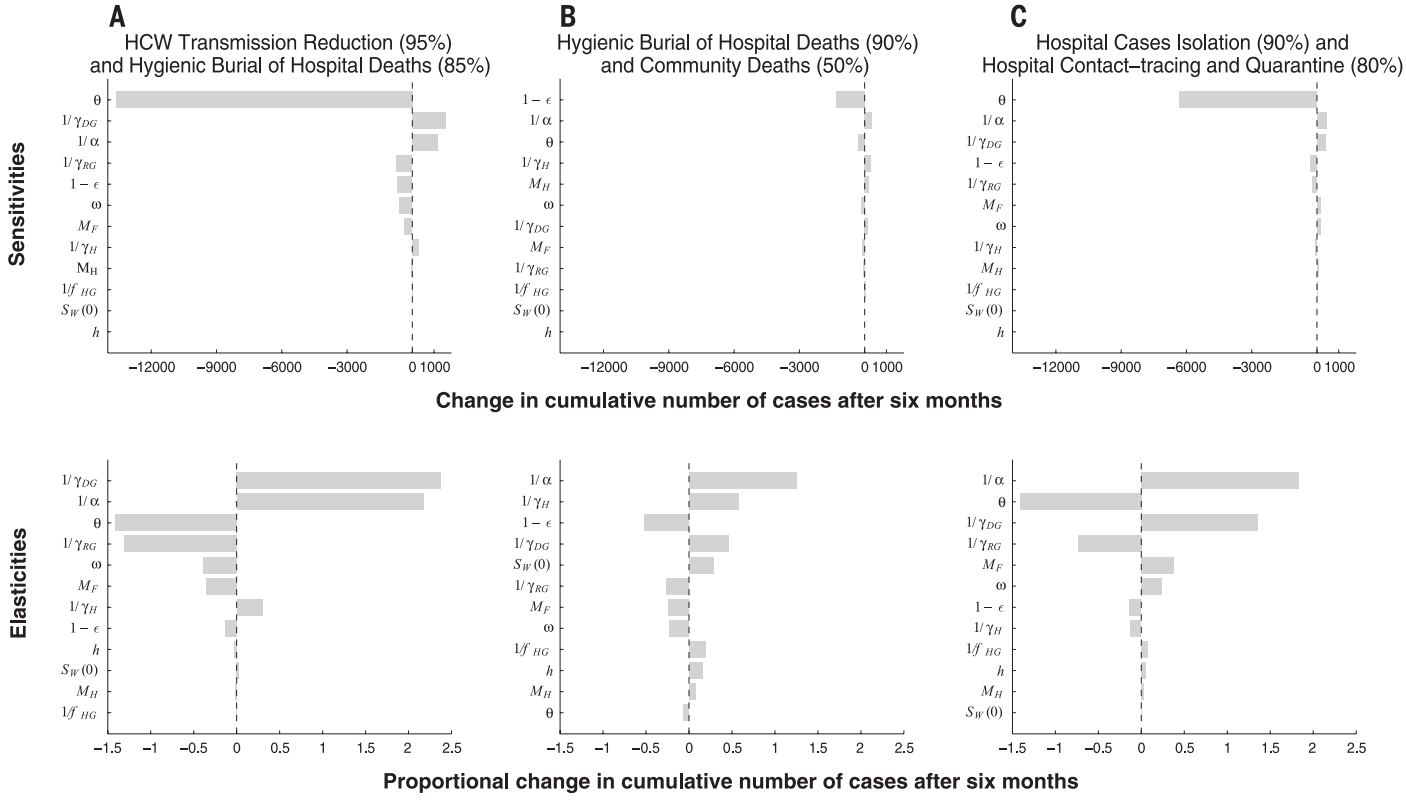


Fig. 4. Sensitivities and elasticities with respect to epidemiological parameters. (**A** to **C**) Sensitivities and elasticities of cumulative cases under (A) 85% successful sanitary burial of hospital deaths with 95% reduction in transmissibility to health care workers for 6 months (Fig. 2D, blue line); (B) successful sanitary funeral of 90% hospital deaths and 50% community deaths, respectively; and (C) 90% successful hospital case isolation with concurrent contact-tracing and quarantine of 80% infected contacts. We varied the number of pre-outbreak health care workers [$S_W(0)$], the incubation period ($1/\alpha$), the duration from symptom onset to death if not hospitalized ($1/\gamma_{DG}$), the duration from symptom onset to recovery if not hospitalized ($1/\gamma_{RG}$), the duration between symptom onset and hospitalization ($1/\gamma_H$), the hospitalization rate per person for reasons other than Ebola (h), the duration of hospitalization for reasons other than Ebola ($1/f_{HG}$), the number of funeral attendees with close contact to the body (M_F), the number of hospital visitors per patient (M_H), the transmission rate at funerals relative to general community (ω), the fraction of asymptomatic infections ($1-\epsilon$), and the hospital admission rate (θ). For each parameter varied, we recalibrated and reran the model.

sion were present, R_0 = 0.93 (0.87 to 0.99). These results for R_0 imply that reducing transmission in hospitals and the community is insufficient to stem the exponentially growing epidemic. To stem Ebola transmission in Liberia, it is imperative to simultaneously restrict traditional burials, which are effectively serving as superspreader events (*22*, *23*).

The close agreement between the epidemiological data and the temporal trajectory of our model between 8 August and 19 September suggests that the cordon sanitaire and curfews implemented in that period (*13*) have had little impact on the exponential increase of Ebola before 19 September (Fig. 1) and may have even been detrimental considering the civil unrest that was fueled by these measures (*24*). This result is underscored by our R_0 analysis that shows removal of community-based transmission only has a marginal impact on R_0 value.

Under the status quo scenario of no change in control measures from 20 September onward, our model predicts that the epidemic will continue to spread, generating a predicted 224 (134 to 358) daily cases by 1 December, 280 cases (184 to 441) by 15 December , and 348 cases (249 to 545) by 30 December. Reducing nosocomial transmission with the use of PPE is unquestionably fundamental to maintain medical infrastructure and to implement case isolation. Nevertheless, hospital-based measures alone, like community-based efforts alone, are insufficient to stem the Ebola outbreak in Liberia (Fig. 2, A to D). Instead, these efforts must be combined with sanitary burial practices (Fig. 2E) and ideally with contact-tracing (Fig. 2F) in order to achieve a reasonable likelihood of epidemic control over the next 6 months. The potential for rapid control depends on the efficacies that can be achieved for each intervention. For example, the combination of case isolation, sanitary burials of hospital deaths, and reduction in nosocomial transmission, each applied with an efficacy of 95%, would reduce the number of daily cases in Liberia to a projected 24 (15 to 41) by 1 December, whereas combining case isolation with contact-tracing and quarantine, each with an efficacy of 90%, is predicted to reduce the number of daily cases in Liberia to 9 (5 to 23) by 1 December. A strategy that achieves efficacies of 60% for sanitary burial, case isolation, and contact-tracing combined could reduce the number of daily Ebola cases to 7 (2 to 13) by 1 December and to 0 (0 to 3) by 15 March in Liberia (Fig. 3). Achieving efficacies in the region of 90% for any one intervention in Liberia would be challenging, if not unrealistic. Thus, combining all of the nonpharmaceutical approaches considered here offers the greatest promise for curtailing the epidemic.

To investigate the applicability of our national-scale results to a more local scale, we fit our model to data from Montserrado County (*12*). Here, too, our results show that swift control of the epidemic on a local level is only achievable through a combination of control strategies, which is consistent with our results on the national level (fig. S3).

Recent reports by WHO have suggested that cases in Liberia are underreported, although it is difficult to know by how much (*25*). To evaluate the impact of underreporting on our results, we refit our model to account for a range of plausible underreporting. In addition, we considered the possibility that underreporting differs between community and hospital settings. When we recalculated intervention effectiveness using these new model fits (fig. S2), we found that underreporting would reduce our

estimates of intervention effectiveness. For example, an underreporting rate of 20% predicts an average of 37 daily cases by 15 March compared with 8 daily cases for perfect reporting for the strategy of 80% case isolation as well as 50% contact-tracing and quarantining. Moreover, our results show that when only community cases are underreported (fig. S2, D to F), the effectiveness of nosocomial interventions is reduced (fig. S2D) because there is proportionally greater transmission within the community than observed. This possibility for lower effectiveness that arises when accounting for underreporting further argues for rapid application of diverse control interventions.

Underreporting might also manifest via asymptomatic infections, which have been observed in previous outbreaks (*26*). Although there is considerable empirical uncertainty regarding the proportion of infections that are asymptomatic, our sensitivity analysis indicates that the larger the proportion of asymptomatic infections, the greater the impact of intervention effectiveness (Fig. 4 and supplementary materials).

To evaluate the impact of uncertainty around epidemiological parameters on predicted outcomes, we analyzed the sensitivity and elasticity of intervention effectiveness to variation in epidemiological parameters (Fig. 4). Unsurprisingly, we find that lower transmissibility at funerals (ω) reduces the effectiveness of the funeral-based interventions (Fig. 4 and supplementary materials). More generally, the effectiveness of an intervention that reduces transmission to health care workers and increases sanitary burial of hospital cases is most sensitive and elastic to the incubation period ($1/\alpha$), the durations from symptom onset to death ($1/\gamma_{DG}$), and recovery ($1/\gamma_{RG}$) (Fig. 4A). In contrast, when the intervention scenario focuses on community transmission alone, there is less sensitivity to these parameters (Fig. 4, B and C).

Also to be considered is the impact of feasibility, human behavior, and likely adherence to recommendations (*27*) on the effectiveness of intervention strategies when making policy recommendations. As the epidemic unfolds, funeral attendance and traditional burial practices may decline with increased awareness of the disease, facilitating the enforcement of sanitary burial practices. In contrast, other behavior changes may hinder intervention efforts. For example, contact-tracing has recently become more challenging because of relocation of contacts from urban to rural communities (*28*). Additionally, case isolation outside of Monrovia is hampered by the scarcity of ambulances for prompt referral to Ebola-specific treatment centers (*29*). Similarly, the implementation of hospital-based interventions will depend on treatment center capacity and admission rates, in that an insufficient number of beds and low admission rates reduce the effectiveness of hospital-based interventions (Fig. 4, A and C). Because our model does not explicitly account for hospital capacity, our predicted outcomes regarding hospital-based interventions may be optimistic, further underscoring the importance of combining hospital-based interventions with contact-tracing and quarantine. Additionally, we stress the protection of health care workers as an essential component for maintaining the medical infrastructure and for implementing any response strategy. Although recent cumulative case data over October 2014 from Liberia suggest that the exponential growth that has characterized the epidemic for both communities and health care workers may be slowing down (*30*), it is too early to tell whether this apparent reduction in the effective reproductive number is a result of control measures initiated toward the end of September.

Although our predictions concur with an analysis of the 1995 Democratic Republic of Congo and 2000 Uganda outbreaks, suggesting that funeral transmission is an important driver of Ebola transmission (*20*), our study also reveals that at this point in the current Liberian outbreak, sanitary burial alone is insufficient to swiftly contain disease spread, unlike for past Ebola outbreaks. Other models assess countrywide intervention effectiveness (*16*, *31*) but do not explicitly parse the specific intervention strategies that are effective in particular settings. In contrast, our model has the complexity to demonstrate that a combination of case isolation in the hospital settings, contact-tracing in the community, and sanitary burials must be implemented to achieve a pronounced likelihood of controlling the outbreak over the next 6 months.

Until very recently, Ebola has been extremely neglected. Consequently, scarcity of data on both previous outbreaks and on the current outbreak limits the complexity of models that can be reasonably parameterized. In particular, there are no epidemiological data available with which to parameterize a spatially explicit model of Ebola transmission. Such data would be useful for predicting not only the scale of interventions required but also the geographical areas on which to focus control efforts and preparedness strategies.

Ebola poses an urgent threat not only to West Africa but also to the international community. The most effective approach to both limiting international spread of Ebola and minimizing local death toll is to control the disease at its source. We find that only a concerted suite of targeted nonpharmaceutical interventions has the potential to curtail the outbreak over the next few months. In the absence of immediate and effective multifaceted action, our predictions suggest that hundreds of new infections will be arising daily by early December in Liberia alone. The implementation of effective interventions needed to reverse the growth of the Ebola outbreak in impoverished West African countries will be logistically challenging even with substantial international aid, but impossible without it.

REFERENCES AND NOTES

1. World Health Organization, *WHO Statement on the Meeting of the International Health Regulations Emergency Committee Regarding the 2014 Ebola Outbreak in West Africa* (World Health Organization, 2014); available at www.who.int/mediacentre/news/statements/2014/ebola-20140808/en.
2. World Health Organization, *WHO: Ebola Response Roadmap Update—15 October 2014*. 1–11 (World Health Organization, 2014); available at http://apps.who.int/iris/bitstream/10665/136508/1/roadmapsitrep15Oct2014.pdf?ua=1.
3. American Public Health Association, in *Control Commun. Dis. Man.*, D. Heymann, Ed. (American Public Health Association, Washington, DC, 2008), pp. 204–206.
4. T. G. Ksiazek *et al*., *J. Infect. Dis.* **179** (suppl. 1), S177–S187 (1999).
5. A. S. Khan *et al*., *J. Infect. Dis.* **179** (suppl. 1), S76–S86 (1999).
6. B. S. Hewlett, R. P. Amola, *Emerg. Infect. Dis.* **9**, 1242–1248 (2003).
7. E. M. Leroy *et al*., *Science* **303**, 387–390 (2004).
8. A. P. Galvani, M. L. Ndeffo-Mbah, N. Wenzel, J. E. Childs, *Ann. Intern. Med.* 10.7326/M14-1904 (2014).
9. WHO Ebola Response Team, *N. Engl. J. Med.* **371**, 1481–1495 (2014).
10. Liberia Institute of Statistics and Geo-Information Services, *2008 National Population and Housing Census: Preliminary Results* (Government for the Republic of Liberia, Monrovia, Liberia, 2008).
11. T. H. Roels *et al*., *J. Infect. Dis.* **179** (suppl. 1), S92–S97 (1999).
12. Ministry of Health & Social Welfare, *Liberia Ebola SitRep no. 10-130* (2014); available at www.mohsw.gov.lr/content_display.php?sub=report2.
13. The Bureau of Public Affairs, Daily Media Summary, 08-08-2014. *Minist. Foreign Aff. Repub. Lib.* (2014); available at www.mofa.gov.lr/public2/2press.php?news_id=1226&related=7&pg=sp.
14. S. O. S. International, International SOS–Liberia. *Int. SOS* (2014); available at www.internationalsos.com/ebola/index.cfm?content_id=396&language_id=ENG.
15. R. M. Anderson, R. M. May, *Infectious Diseases of Humans: Dynamics and Control*. (Oxford University Press, 1991).
16. C. L. Althaus, *PLOS Curr.* 10.1371/currents.outbreaks.91afb5e0f279e7f29e7056095255b288 (2014).
17. M. F. C. Gomes *et al*., *PLOS Curr.* 10.1371/currents.outbreaks.cd818f63d40e24aef769dda7df9e0da5 (2014).
18. D. Fisman, E. Khoo, A. Tuite, *PLOS Curr.* 10.1371/currents.outbreaks.89c0d3783f36958d96ebbae97348d571 (2014).
19. L. F. White, M. Pagano, *Stat. Med.* **27**, 2999–3016 (2008).
20. J. Legrand, R. F. Grais, P. Y. Boelle, A. J. Valleron, A. Flahault, *Epidemiol. Infect.* **135**, 610–621 (2007).
21. G. Chowell, N. W. Hengartner, C. Castillo-Chavez, P. W. Fenimore, J. M. Hyman, *J. Theor. Biol.* **229**, 119–126 (2004).
22. J. O. Lloyd-Smith, S. J. Schreiber, P. E. Kopp, W. M. Getz, *Nature* **438**, 355–359 (2005).
23. A. P. Galvani, R. M. May, *Nature* **438**, 293–295 (2005).
24. Daily Media Summary, 08-18-2014. *Minist. Foreign Aff. Repub. Lib.* (2014); available at www.mofa.gov.lr/public2/2press.php?news_id=1246&related=7&pg=sp.
25. World Health Organization, *Why the Ebola outbreak has been underestimated* (World Health Organization, 2014); available at www.who.int/mediacentre/news/ebola/22-august-2014/en.
26. E. M. Leroy *et al*., *Lancet* **355**, 2210–2215 (2000).
27. C. T. Bauch, A. P. Galvani, *Science* **342**, 47–49 (2013).
28. Ministry of Health & Social Welfare, *Liberia Ebola SitRep no. 136* (2014); available at www.mohsw.gov.lr/documents/Liberia%20Ebola%20Sit%20Rep%20136%20Sept%2028,%202014.pptx%20New.pdf.
29. Ministry of Health & Social Welfare, *Liberia Ebola SitRep no. 135* (2014); available at www.mohsw.gov.lr/documents/Liberia%20Ebola%20Sit%20Rep%20135%20Sept%2027,%202014.pptx%20New.pdf.
30. H. Nishiura, G. Chowell, *Euro Surveill.* **19**, 20894 (2014).
31. Ministry of Health & Social Welfare, *Liberia Ebola SitRep no. 149* (2014); available at www.mohsw.gov.lr/documents/SITRep%20149%20Oct%2011th,%202014.pdf.

ACKNOWLEDGMENTS

The research was supported by the National Institutes of Health (NIH 2 U01 GM087719 and 5 U01 GM105627) and the Notsew Orm Sands Foundation. The data reported in this paper are tabulated in the supplementary materials. We thank S. G. Gaffney, A. Hofmann, and M. Traina for helpful feedback on the manuscript. All model code and data are available via https://github.com/abhiganit/EbolaCodes/tree/master/Science_Code.

SUPPLEMENTARY MATERIALS

www.sciencemag.org/content/346/6212/991/suppl/DC1
Materials and Methods
Figs. S1 to S3
Table S1
References (*32*–*42*)

29 August 2014; accepted 21 October 2014
Published online 30 October 2014;
10.1126/science.1260612

INFLUENZA IMMUNOLOGY

Antibody landscapes after influenza virus infection or vaccination

J. M. Fonville,[1,2,3]* S. H. Wilks,[1,2]* S. L. James,[1,2] A. Fox,[4] M. Ventresca,[1]† M. Aban,[5] L. Xue,[5] T. C. Jones,[1,2] Le N. M. H.,[4] Pham Q. T.,[6] Tran N. D.,[6] Y. Wong,[7] A. Mosterin,[1,2] L. C. Katzelnick,[1,2] D. Labonte,[8] Le T. T.,[6] G. van der Net,[3] E. Skepner,[1,2] C. A. Russell,[2,9] T. D. Kaplan,[10] G. F. Rimmelzwaan,[3] N. Masurel,[3]‡ J. C. de Jong,[3] A. Palache,[11] W. E. P. Beyer,[3] Le Q. M.,[6] Nguyen T. H.,[6] H. F. L. Wertheim,[4,12] A. C. Hurt,[5,13] A. D. M. E. Osterhaus,[3] I. G. Barr,[5] R. A. M. Fouchier,[3] P. W. Horby,[4,12] D. J. Smith[1,2,3]§

We introduce the antibody landscape, a method for the quantitative analysis of antibody-mediated immunity to antigenically variable pathogens, achieved by accounting for antigenic variation among pathogen strains. We generated antibody landscapes to study immune profiles covering 43 years of influenza A/H3N2 virus evolution for 69 individuals monitored for infection over 6 years and for 225 individuals pre- and postvaccination. Upon infection and vaccination, titers increased broadly, including previously encountered viruses far beyond the extent of cross-reactivity observed after a primary infection. We explored implications for vaccination and found that the use of an antigenically advanced virus had the dual benefit of inducing antibodies against both advanced and previous antigenic clusters. These results indicate that preemptive vaccine updates may improve influenza vaccine efficacy in previously exposed individuals.

Much of the global burden of infectious disease today is caused by antigenically variable pathogens, which escape immunity induced by prior infection or vaccination by changing the molecular structure recognized by antibodies. Human influenza viruses are notorious for their capacity to evolve and evade the adaptive immune response. This evolution has been progressive and stepwise (*1*), with antigenically similar viruses circulating for a few years before strains with related but novel antigenic characteristics replace them (*2*) (figs. S1 and S2). As a result, vaccine strain updates, based on analyses of circulating viruses, are necessary to maintain vaccine effectiveness.

[1]Center for Pathogen Evolution, Department of Zoology, University of Cambridge, Cambridge CB2 3EJ, UK. [2]World Health Organization (WHO) Collaborating Center for Modeling, Evolution, and Control of Emerging Infectious Diseases, Cambridge CB2 3EJ, UK. [3]Department of Viroscience, Erasmus Medical Center, Rotterdam 3015 CE, Netherlands. [4]Oxford University Clinical Research Unit and Wellcome Trust Major Overseas Programme, Hanoi, Vietnam. [5]WHO Collaborating Centre for Reference and Research on Influenza, Victorian Infectious Diseases Reference Laboratory at the Peter Doherty Institute for Infection and Immunity, Melbourne VIC 3000, Australia. [6]National Institute of Hygiene and Epidemiology, Hanoi, Vietnam. [7]Oxford University Museum of Natural History, Oxford OX1 3PW, UK. [8]Insect Biomechanics Group, Department of Zoology, University of Cambridge, Cambridge CB2 3EJ, UK. [9]Department of Veterinary Medicine, University of Cambridge, Cambridge CB3 0ES, UK. [10]bobblewire.com, Saint Louis, MO 63112, USA. [11]Abbott Laboratories, Weesp 1380 DA, Netherlands. [12]Nuffield Department of Clinical Medicine, Centre for Tropical Medicine, University of Oxford, Oxford OX3 7BN, UK. [13]Melbourne School of Population and Global Health, University of Melbourne, Parkville VIC 3010, Australia.
*These authors contributed equally to this work. †Present address: School of Industrial Engineering, Purdue University, West Lafayette, IN 47907 USA. ‡Deceased. §Corresponding author. E-mail: dsmith@zoo.cam.ac.uk

The current strategy for vaccine strain selection is to choose a virus that is antigenically representative of circulating viruses, mostly determined by using the hemagglutination inhibition (HI) assay to test a global selection of virus isolates against a panel of ferret antisera (*3*). The ferrets used in such studies are naïve to influenza before inoculation, and each antiserum has been raised by infection with only a single virus. Such postinoculation ferret antisera provide well-understood data for the characterization of antigenic differences between influenza viruses (*2*, *4*). However, this strategy does not account for the influence of prior immunity on the response induced by the vaccine when administered to humans.

The direct analysis of human serological data presents an opportunity to assess and understand immune responses in the context of differing background immunity and to use this information as the basis for improved vaccine strain selection and evaluation. Indeed, such data are already used to some extent in the vaccine strain selection process. Unfortunately, immunological patterns in human serological data are difficult to interpret because of complex, and usually unknown, exposure histories and the confounding factor of cross-reactivity due to antigenic relationships among strains. As a result, in-depth analyses of serological data have been difficult, and despite excellent cross-sectional seroepidemiology (*5*), our understanding of the typical characteristics of the human serological response to infection and vaccination has remained limited.

Results from the original (and seminal) studies on the antibody-mediated immune response to influenza virus infection and vaccination in humans (*6*–*9*) have often been interpreted as "original antigenic sin"—a hypothesis that proposes an anamnestic reinforcement of the level of antibody to the strain that first infected the individual that dampens the serologic response to the current virus (*9*–*11*). However, this definition is far from concrete, and the historical literature on the effect of immune memory on the generation of responses to variant antigens has been particularly equivocal.

To increase our ability to quantitatively study human serological data of antigenically variable pathogens, we present a methodology that enables detailed analyses and visualization of complex serological data by plotting antibody-mediated immunity as a function of the antigenic relationships among viruses. To achieve this, we first used antigenic cartography (*2*) to determine the antigenic relationships among a selection of 81 viruses spanning 43 years of influenza A/H3N2 evolution, using HI titrations of first-infection ferret sera (Fig. 1A, fig. S2, and tables S1 and S9). Human serum samples were then titrated against the same viruses and their HI titers plotted in an extra dimension added to the antigenic map (Fig. 1B).

We found that HI titers of a given serum are related for antigenically similar viruses (fig. S3), and thus a representative smooth surface could be fitted through these HI titers. The resulting antibody landscape represents an immune profile for each serum with elevations corresponding to regions in the antigenic map with higher antibody levels (figs. S4 and S5). Because the landscape at any given point is a function of surrounding data points, antibody levels can be inferred for viruses not included in the titration set. For antibody landscapes of influenza A/H3N2 based on the HI assay, we found that the landscape predicted omitted HI titers with a root mean square error of 1.3 $\log_2$ units, compared with an estimated error arising from HI assay repeatability alone of 0.9 (table S11 and figs. S6 to S11, S13, and S14).

To aid the visual comparison of multiple landscapes, we used a path on the antigenic map that passes through each antigenic cluster in chronological order (Fig. 1C). The corresponding values of the landscape along this summary path were used to represent the three-dimensional landscape in two dimensions (Fig. 1D and fig. S12).

We used this methodology to study serological data we generated from samples taken annually between 2007 and 2012 from unvaccinated individuals in the Ha Nam household cohort study in Vietnam (*12*). More than 10,000 HI titrations were performed to construct a total of 324 landscapes for 69 individuals born between 1917 and 2005, allowing us to assess the serological changes over time (Fig. 2, tables S3 and S4, and fig. S15). Titers were highest for influenza viruses that circulated when an individual was ~6 years old (figs. S42 and S43), corresponding with the time frame of first infection (*13*). Antibody levels against newly circulating viruses tended to be lower than those against strains circulating earlier in an individual's lifetime, as reported previously (*5*, *7*–*9*, *11*). In addition, previous results reported some cross-reactivity to

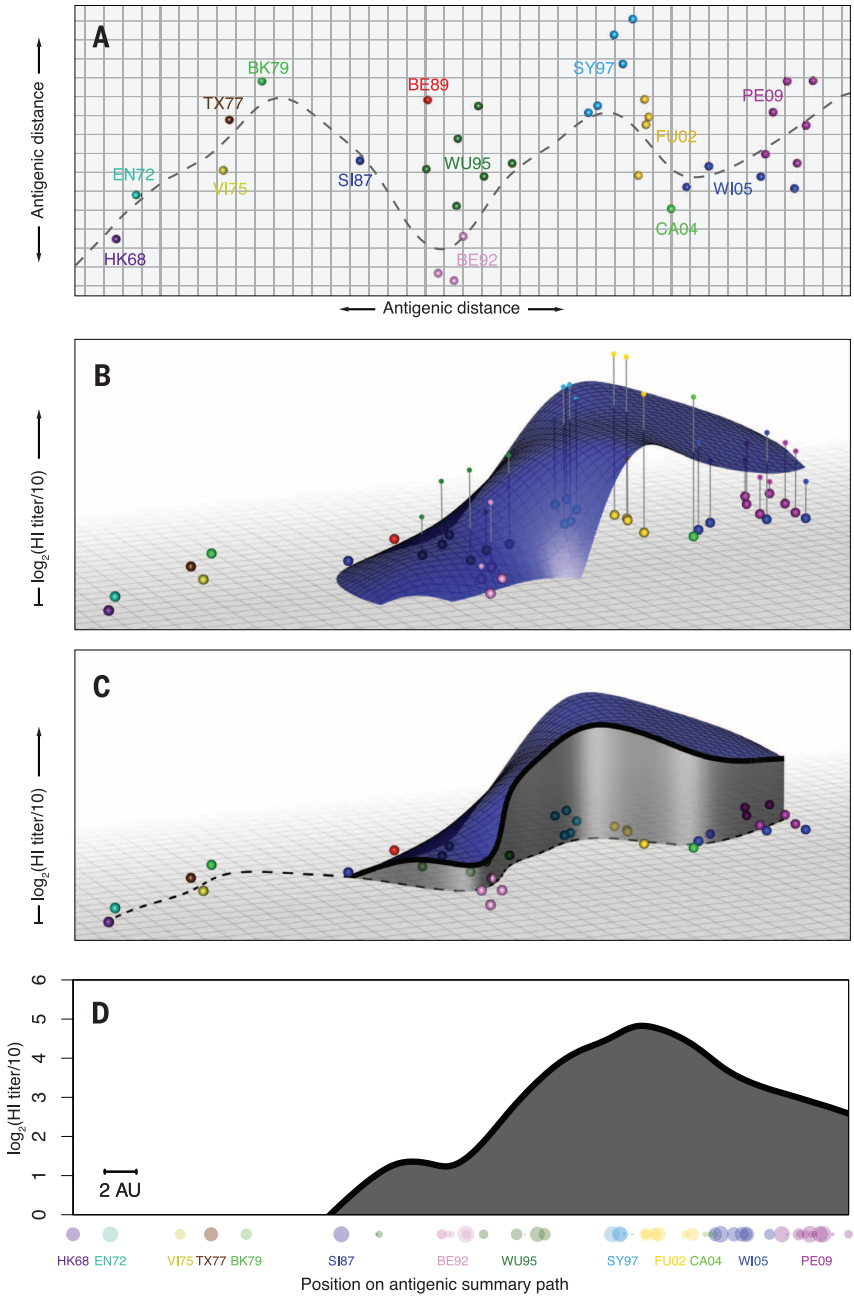


Fig. 1. Creating an antibody landscape. (**A**) Antigenic map of A/H3N2 showing virus strains color-coded by antigenic cluster. Both axes represent antigenic distance, and the spacing between grid lines is 1 antigenic unit, corresponding to a twofold dilution of antiserum in the HI assay. Two units correspond to fourfold dilution, three units to eightfold dilution, and so on (*2*). The gray dashed line shows a path through the antigenic clusters in chronological order calculated by fitting a smoothing spline (*1*). EN72, England 1972; VI75, Victoria 1975; TX77, Texas 1977; BK79, Bangkok 1979; SI87, Sichuan 1987; BE89, Beijing 1989; BE92, Beijing 1992; FU02, Fujian 2002; CA04, California 2004. (**B**) An additional dimension indicates the measured antibody titers as vertical impulses, and a smooth surface is fitted using locally weighted multiple linear regression to create the antibody landscape within the convex hull bounded by the viruses titrated (root mean square error of fit = 1.23 HI $\log_2$ units). (**C**) The height of the landscape along the path in (A) shows a slice through the landscape (*1*). (**D**) The height of the landscape along the antigenic summary path in (C) is plotted to create a rotation-independent two-dimensional summary visualization of the landscape. Titrated virus strains are shown in their corresponding positions along the *x* axis. The symbol radius is inversely proportional to the antigenic distance from the path; symbol color indicates antigenic cluster. The scale bar denotes 2 antigenic units (AU).

strains that circulated before an individual's birth (*5*, *7*–*9*, *14*), and based on the extent of detectable titers to viruses in circulation only before an individual's birth, we quantified this antibody cross-reactivity to be up to two antigenic clusters (table S12). There was substantial heterogeneity among the antibody landscapes of different individuals; however, each individual's landscape shape was typically stable from one year to the next and had distinctive individual features [within-person correlation coefficient r = 0.86 (SD ± 0.22); between-person r = 0.28 ± 0.21 (figs. S16 to S20)].

Infection with A/H3N2 resulted in a notably broad antibody response (Fig. 2 and figs. S21 and S22) that was typically governed by the extent of the preexposure antibody landscape (fig. S45). This antibody response far exceeded the extent of cross-reactivity typically produced in the response after primary exposure with one of the circulating viruses (figs. S44 and S47). For example, an individual born in 1970 and infected in 2009 (Fig. 2, fourth row) had a substantial long-distance response back to the Hong Kong 1968 (HK68) antigenic cluster and all clusters in between, even though these older viruses had not circulated for decades. To illustrate the substantial breadth of this "back-boost," there have been 13 antigenic cluster transitions from HK68 until Perth 2009 (PE09), each ~4.5 antigenic units (corresponding to a 24-fold dilution of antiserum in the HI assay). These antigenic changes have necessitated more than 20 vaccine strain updates and are the result of changes in 69 of the 346 amino acid positions in the HA1 domain of the hemagglutinin gene between HK68 and the PE09 vaccine strain, including substitutions in all of the seven key antigenic positions identified by Koel *et al.* (*15*).

Because of the range of this response and its dependence on the preexposure antibody landscape, we call it a "back-boost." The magnitude of back-boost response declined with antigenic distance from the likely infecting virus (fig. S46). Although the response to older viruses was substantial, titer increases were largest for viruses from the contemporary antigenic cluster, in contrast to a common interpretation of the original antigenic sin hypothesis (fig. S47). Infections with influenza B, A/H1N1, and A/H1N1(pdm09) often caused negligible changes in the A/H3N2 antibody landscape (fig. S23), indicating that the back-boost is specific to virus type and subtype.

Typically, the broad initial response was followed by a period of titer decay during which antibody titers stabilized to form an altered antibody landscape over the course of ~1 year (fig. S24). Comparison of the antibody landscapes of 2007 and 2012 (Fig. 2) shows that the antigenic region for which increased titers were maintained long-term was substantially narrower than that of the initial response to infection. This long-term persistence of increased antibody titers was more specific to the antigenic region of the likely infecting strain but still spanned multiple antigenic clusters (fig. S46).

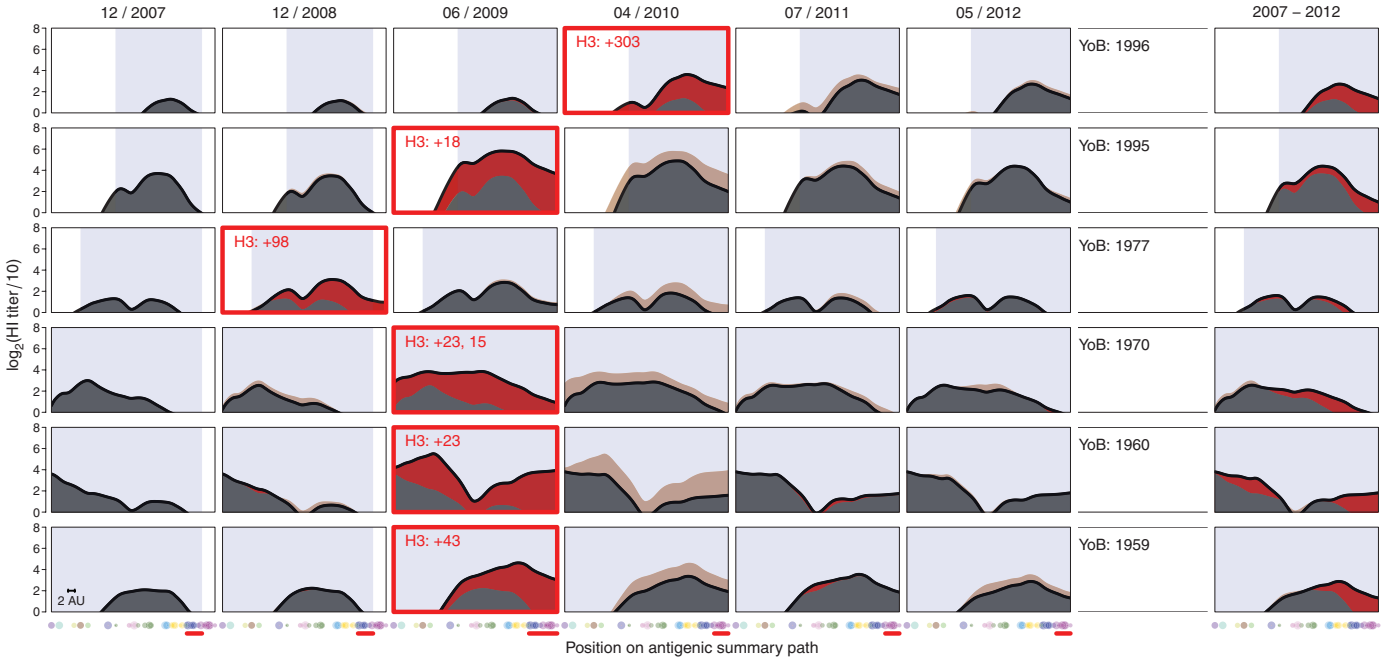


Fig. 2. Antibody landscapes from 2007 to 2012 for six individuals. The black lines represent the landscape height for each position on the antigenic summary path through the antigenic clusters from Fig. 1A. The first sample taken after a confirmed A/H3N2 influenza virus infection is marked with a red box, and the red number gives the days from the date of influenza-like illness–associated swab collection to serum collection. Red shading indicates increases, and beige decreases, compared with the previous year. The blue shaded rectangles indicate antigenic clusters that circulated during an individual's life span until sample collection (table S10). Dots along the *x* axis indicate the subset of 30 viruses used to generate these landscapes; contemporary strains, probably causing the infection, are indicated with red horizontal bars (table S2). The rightmost column shows the difference between the landscape in 2012 compared with 2007. The scale bar indicates 2 antigenic units. YoB, year of birth.

Next we investigated whether the back-boost observed after infection could be used to improve vaccine effectiveness. In the vaccine strain selection process, it is sometimes unclear whether currently circulating strains or antigenically novel strains are most likely to predominate in the next influenza season. The resulting dilemma is whether it is more beneficial to leave the vaccine strain unchanged or to preemptively update the vaccine to match a novel strain, without certainty over which antigenic cluster of viruses will actually circulate.

It would take a large, prospective, multiyear clinical trial comparing the two vaccination approaches to answer these questions definitively. However, we were able to retrospectively test the approach with the sera of 225 human vaccine recipients from two annual influenza vaccine reregistration studies, by identifying an antigenic cluster transition for which there was little circulation of the new cluster before a novel vaccine strain was first tested. Both groups had therefore received antigenically different vaccines, and yet there was no significant difference in the average prevaccination antibody landscapes of the two studies (figs. S30 and S31). Individuals in the first study (n = 102) (table S7), performed in 1997, received the A/Nanchang/933/95 vaccine from the Wuhan 1995 (WU95) antigenic cluster to which there had been some prior exposure, whereas individuals in the 1998 study (n = 123) (table S8) received the A/Sydney/5/97 vaccine from the antigenically advanced Sydney 1997 (SY97) cluster to which there was substantially less prevaccination immunity, thus mimicking a preemptive update.

Individual antibody landscapes were constructed from serum samples taken before vaccination and 4 weeks after vaccination (figs. S25 and S26 and tables S5 and S6) and combined to give overall pre- and postvaccination antibody landscapes (Fig. 3, A and B). As expected after a vaccine update, average vaccination responses were significantly greater against later antigenic clusters after vaccination with the antigenically advanced SY97 strain (figs. S32 to S35). The back-boost after infection was also observed for the vaccination studies, and interestingly, the magnitude and breadth of the response to infection and vaccination were comparable (figs. S27 to S29). The back-boost in the SY97 vaccine study resulted in a slightly larger response to WU95 viruses than the response in the WU95 vaccine study (Fig. 3C). These findings also held when studying only elderly individuals (fig. S36) and individuals with a low prevaccination titer against WU95, typically considered the most susceptible (figs. S37 and S38) (*16*). We further tested a subset of vaccination sera with a neutralization assay, and these data support the results from the HI assay (figs. S40 and S41). Despite differences in prevaccination landscapes, a second study of the Wisconsin 2005 (WI05)–PE09 cluster transition also demonstrated a similar back-boost upon vaccination (fig. S39 and tables S13 and S14).

The mechanism behind the broad back-boost is currently unknown, but we considered several hypotheses (*1*). In summary, rather than a result of the production of novel antibodies with extensive cross-reactivity, the back-boost appears most consistent with memory cell stimulation and antibody recall. This pattern of recall is consistent with raw data from mid–20th century studies on the response to infection or vaccination: Studies on antigenically different A/H1N1 strains also show a broad subtype-specific back-boost (*6*, *8*, *9*). However, this phenomenon was never quantified and put in relation to the antigenic difference among the viruses.

Whether the original antigenic sin hypothesis refers to higher preexposure antibody titers or also to a higher response to the first infecting virus is unclear, and both interpretations have been used over the past 60 years (*17*). We found no evidence for a predisposition in the antibody response toward the likely first infecting strain, and instead we demonstrate that the increase in antibody titers is greatest to the most recently encountered strain. We do, however, corroborate the finding that preexposure antibody reactivity tends to be highest against strains encountered earlier in life (figs. S42 and S43) (*5*, *7*–*9*, *11*). The presence of higher preexposure static titers, but not higher dynamic responses, to the first infecting strain may explain seemingly contradictory reports whereby cross-sectional studies have tended to describe a serological bias supportive of the original antigenic sin dogma (*5*, *11*),

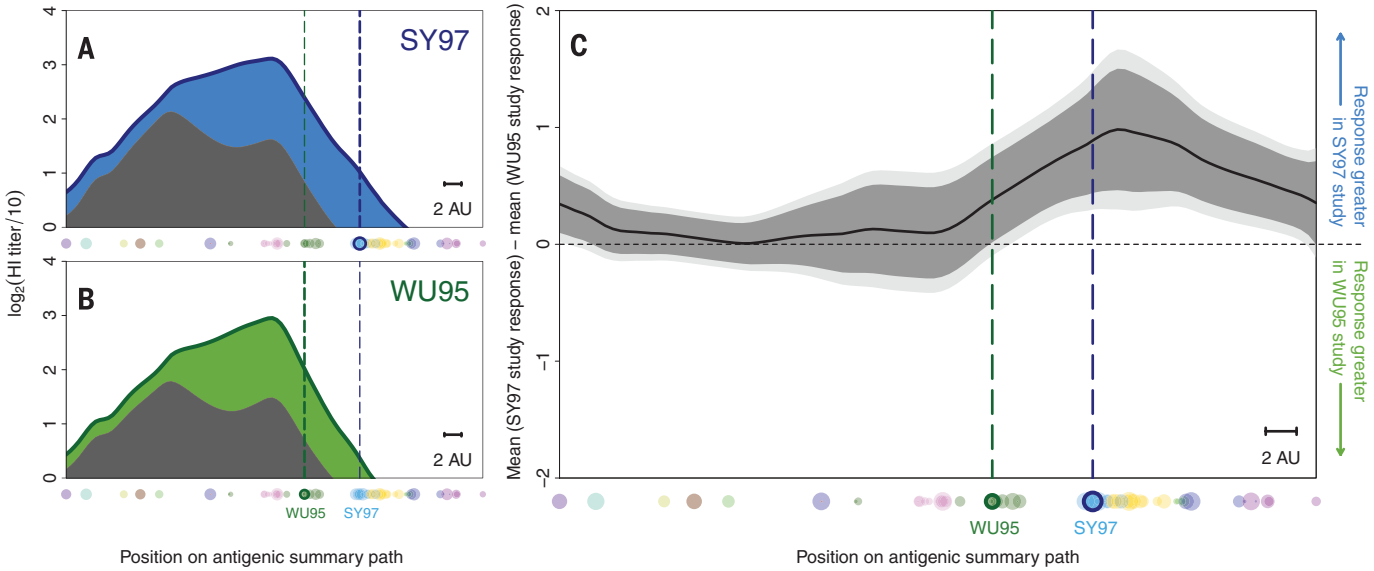


Fig. 3. Comparison of two different vaccines. (**A**) The mean prevaccination landscape (gray) and landscape after vaccination with A/Sydney/5/97 (blue) in the 1998 study (123 individuals) or (**B**) with A/Nanchang/933/95 (green) in the 1997 study (102 individuals) for each position on the antigenic summary path. Dots along the *x* axes indicate the subset of 70 viruses used to generate these landscapes. The vertical dotted lines indicate the position of the SY97 (blue) and WU95 (green) wild-type vaccine viruses. (**C**) Comparison of titer increase after vaccination with A/Nanchang/933/95 or A/Sydney/5/97 for each position along the antigenic summary path. When above the horizontal midpoint, the black line indicates a higher response in the group vaccinated with A/Sydney/5/97; when below the midpoint, it denotes a higher response in the group vaccinated with A/Nanchang/933/95. Data were calculated from the average titer increase between each individual's paired pre- and postvaccination titers, with 95% (dark gray) and 99% (light gray) *t* test–based confidence intervals. Scale bars indicate 2 antigenic units.

whereas investigations into actual responses upon exposure frequently oppose it (*17*, *18*).

These findings also shed light on the growth of the serological immunity over time. Although responses were often present against the oldest strains, these long-distance back-boosts were typically not maintained beyond a year (Fig. 2, rightmost panels, and fig. S24). This is evidence against the hypothesis of long-term and progressive reinforcement of antibody titers against earlier viruses upon exposure to each subsequent antigenic variant over time. Instead, the pattern of higher static titers against antigenic clusters encountered early in life may also be explained if the immune response to primary exposure is larger than the responses to subsequent exposures (fig. S48).

As others have speculated, it is plausible that the decreased antibody responses to subsequent exposures may be a result of "antigen trapping," a hypothesis according to which binding of antigen by preexisting cross-reactive antibodies and memory cells decreases the antigenic load available for priming naïve B cells and leads to a diminished novel response (*5*, *7*, *10*, *19*, *20*). This would also explain why the closest antigenic match between the vaccine strain and the circulating strains does not necessarily generate the best antibody response against the corresponding cluster: The mismatch of an antigenically advanced strain is compensated for by a greater novel response, as a result of reduced antigen trapping (*21*). The extent of interference by antigen trapping on the novel antibody response depends on the degree of antigenic relatedness and prior immunity (*22*). When individuals have no prior immunity to a subtype (such as young children, or in a pandemic), the best vaccine is probably the closest antigenic match, as there will be no prior immunity to avoid and no back-boost to exploit.

These findings highlight potentially important differences between the two types of vaccine mismatch in populations with prior immunity. Following a mismatch due to a delayed vaccine update (in which the vaccine strain, selected 10 to 14 months before the season in which it is used, lags behind influenza virus evolution), neither preexisting nor newly induced antibodies provide immunity against the novel strains. Consequently, such vaccines have poor effectiveness in this mismatch situation (*23*–*26*). However, if there was a vaccine mismatch due to an incorrectly timed, preemptive antigenic update of the vaccine, then the data from our retrospective surrogate study indicate that the extensive back-boost would still induce equivalent titers against previous antigenic strains. Such vaccines would have the dual advantage of being effective against the antigenically novel viruses to which they were targeted while remaining effective, or being even more effective, for contemporary viruses if they continued to circulate.

Our results underscore the importance of accounting for antigenic variation to better understand multiexposure sera; further, we provide a methodology for the direct visualization of otherwise complex serological patterns, allowing basic insights into the breadth of the adaptive humoral immune response to influenza and other antigenically variable pathogens. Antibody landscapes will be useful for the evaluation of evolutionary selection pressures (fig. S49) and the evaluation of different vaccination techniques, including the effect of adjuvants; vaccine composition; dose sparing; and the durability, breadth, and magnitude of responses to universal vaccines. Our results indicate that preemptive vaccine updates may substantially improve influenza vaccine effectiveness in previously exposed individuals. Prospective clinical trials will further test the breadth and longevity of the immunological response and protection provided by antigenically advanced vaccine strains.

REFERENCES AND NOTES

1. Materials and methods are available as supplementary materials on *Science* Online.
2. D. J. Smith *et al.*, *Science* **305**, 371–376 (2004).
3. G. K. Hirst, *J. Exp. Med.* **75**, 49–64 (1942).
4. I. G. Barr *et al.*, *Vaccine* **28**, 1156–1167 (2010).
5. J. Lessler *et al.*, *PLOS Pathog.* **8**, e1002802 (2012).
6. F. L. Horsfall, E. R. Rickard, *J. Exp. Med.* **74**, 433–439 (1941).
7. A. V. Hennessy, F. M. Davenport, T. Francis Jr., *J. Immunol.* **75**, 401–409 (1955).
8. F. M. Davenport, A. V. Hennessy, T. Francis Jr., *J. Exp. Med.* **98**, 641–656 (1953).
9. F. M. Davenport, A. V. Hennessy, *J. Exp. Med.* **104**, 85–97 (1956).
10. S. F. de St. Groth, R. G. Webster, *J. Exp. Med.* **124**, 331–345 (1966).
11. T. Francis Jr., *Proc. Am. Philos. Soc.* **104**, 572–578 (1960).
12. P. Horby *et al.*, *Am. J. Epidemiol.* **175**, 1062–1074 (2012).
13. R. Bodewes *et al.*, *Clin. Vaccine Immunol.* **18**, 469–476 (2011).
14. F. M. Davenport, A. V. Hennessy, C. H. Stuart-Harris, T. Francis Jr., *Lancet* **266**, 469–474 (1955).
15. B. F. Koel *et al.*, *Science* **342**, 976–979 (2013).
16. L. Coudeville *et al.*, *BMC Med. Res. Methodol.* **10**, 18 (2010).
17. C. D. O'Donnell *et al.*, *Clin. Vaccine Immunol.* **21**, 737–746 (2014).
18. J. Wrammert *et al.*, *Nature* **453**, 667–671 (2008).
19. J. H. Kim, I. Skountzou, R. Compans, J. Jacob, *J. Immunol.* **183**, 3294–3301 (2009).
20. M. S. Miller *et al.*, *Sci. Transl. Med.* **5**, 198ra107 (2013).

21. D. J. Smith, S. Forrest, D. H. Ackley, A. S. Perelson, *Proc. Natl. Acad. Sci. U.S.A.* **96**, 14001–14006 (1999).
22. K. Pan, *PLOS ONE* **6**, e23910 (2011).
23. T. Francis Jr., J. E. Salk, J. J. Quilligan Jr., *Am. J. Public Health Nations Health* **37**, 1013–1016 (1947).
24. E. A. Belongia *et al.*, *J. Infect. Dis.* **199**, 159–167 (2009).
25. D. M. Skowronski *et al.*, *J. Infect. Dis.* **199**, 168–179 (2009).
26. C. B. Bridges *et al.*, *JAMA* **284**, 1655–1663 (2000).

ACKNOWLEDGMENTS

We thank R. Bodewes, J. Bryant, D. Burke, N. Lewis, E. Selkov, B. Mühlemann, G. de Mutsert, and F. Pistoor. We also thank the staff of the Ha Nam Provincial Preventive Medicine Centre, the Hamlet health workers, and the National Institute for Hygiene and Epidemiology, Vietnam, for their support in conducting the fieldwork. We are indebted to the cooperation of the Ha Nam cohort and vaccine study participants. J.M.F. is supported by a Medical Research Council Fellowship (MR/K021885/1) and a Junior Research Fellowship from Homerton College, L.C.K. by the Gates-Cambridge Scholarship and the NIH Oxford-Cambridge Scholars program, and C.A.R. by a Royal Society University Research Fellowship (RG55423). We acknowledge the National Institute of Allergy and Infectious Diseases–NIH Centers of Excellence for Influenza Research and Surveillance contracts HHSN266200700010C and HHSN272201400008C, Nederlandse Organisatie voor Wetenschappelijk Onderzoek VICI grant 91896613, the European Union FP7 programs EMPERIE (223498) and ANTIGONE (278976), Human Frontier Science Program grant P0050/2008, the Wellcome Trust (WT087982MA), and NIH Director's Pioneer Award DP1-0D000490-01. The Melbourne WHO Collaborating Centre for Reference and Research on Influenza is supported by the Australian government Department of Health. A.D.M.E.O. (as Chief Scientific Officer of Viroclinics Biosciences BV) has advisory affiliations with GlaxoSmithKline, Novartis, and Roche. Sequences of the influenza viruses used in this study are available in GenBank with accession numbers: KM821278 to KM821358. Erasmus Medical Center (Rotterdam, the Netherlands) requires a materials transfer agreement for sharing viruses and antisera.

SUPPLEMENTARY MATERIALS

www.sciencemag.org/content/346/6212/996/suppl/DC1
Materials and Methods
Supplementary Text
Figs. S1 to S49
Tables S1 to S14
References (*27*–*35*)

23 May 2014; accepted 3 October 2014
10.1126/science.1256427

INFLAMMATION

Nucleoside reverse transcriptase inhibitors possess intrinsic anti-inflammatory activity

Benjamin J. Fowler,[1,2] Bradley D. Gelfand,[1,3,4] Younghee Kim,[1] Nagaraj Kerur,[1] Valeria Tarallo,[1,5] Yoshio Hirano,[1] Shoba Amarnath,[6] Daniel H. Fowler,[6] Marta Radwan,[7] Mark T. Young,[7] Keir Pittman,[8] Paul Kubes,[8] Hitesh K. Agarwal,[9] Keykavous Parang,[9] David R. Hinton,[10] Ana Bastos-Carvalho,[1] Shengjian Li,[1] Tetsuhiro Yasuma,[1] Takeshi Mizutani,[1] Reo Yasuma,[1] Charles Wright,[1] Jayakrishna Ambati[1,2]*

Nucleoside reverse transcriptase inhibitors (NRTIs) are mainstay therapeutics for HIV that block retrovirus replication. *Alu* (an endogenous retroelement that also requires reverse transcriptase for its life cycle)–derived RNAs activate P2X7 and the NLRP3 inflammasome to cause cell death of the retinal pigment epithelium in geographic atrophy, a type of age-related macular degeneration. We found that NRTIs inhibit P2X7-mediated NLRP3 inflammasome activation independent of reverse transcriptase inhibition. Multiple approved and clinically relevant NRTIs prevented caspase-1 activation, the effector of the NLRP3 inflammasome, induced by *Alu* RNA. NRTIs were efficacious in mouse models of geographic atrophy, choroidal neovascularization, graft-versus-host disease, and sterile liver inflammation. Our findings suggest that NRTIs are ripe for drug repurposing in P2X7-driven diseases.

Nucleoside reverse transcriptase inhibitors (NRTIs) are widely used to treat HIV. Age-related macular degeneration (AMD) is a leading cause of blindness in the elderly population worldwide (*1*, *2*). In geographic atrophy, the late stage of the prevalent and untreatable dry form of AMD, overabundance of noncoding *Alu* RNAs is implicated in cell death of the retinal pigment epithelium (RPE) (*3*–*5*). Because *Alu* sequences are noncoding retrotransposons that, like HIV, rely on reverse transcriptase for their life cycle (*6*), we hypothesized that NRTIs could block *Alu* RNA–induced cytotoxicity. Multiple NRTIs are typically administered orally to HIV patients at a total NRTI dose of up to 15 mg kg^{-1} day^{-1} (*7*) [equivalent dose in mice: 185 mg kg^{-1} day^{-1} (*8*)]. A clinically relevant dose (single daily oral administration of 150 mg kg^{-1}) of the NRTI stavudine (d4T), which is U.S. Food and Drug Administration–approved for the treatment of HIV infection, prevented *Alu*-induced RPE degeneration (*4*, *5*) in wild-type mice (Fig. 1A). A lower dose of oral d4T (50 mg kg^{-1} day^{-1}) also prevented *Alu*-induced degeneration, as did twice daily intraperitoneal administration of 50 mg kg^{-1} of the NRTI zidovudine (AZT) (Fig. 1B and fig. S1).

Alu RNA induces RPE cell death via activation of caspase-1 by the innate immune complex known as the NLRP3 inflammasome (*5*, *9*). Western blotting of RPE lysates from d4T-treated mice confirmed that d4T blocked caspase-1 activation (fig. S2A). Caspase-1, in turn, cleaves pro-interleukin-18 (IL-18) into its mature form, which induces RPE degeneration via IRAK4 phosphorylation (*5*); d4T also blocked IL-18 maturation and IRAK4 phosphorylation in vivo (fig. S2A). Consistent with the notion that d4T prevents RPE degeneration upstream of IL-18 by blocking caspase-1 activation, the protective effect of d4T in *Alu*-treated mice was overridden by subretinal injection of recombinant mature mouse IL-18 (fig. S2B). d4T also prevented *Alu*-induced caspase-1 activation (*10*) and IRAK4 phosphorylation in primary human (Fig. 1C) and wild-type mouse RPE cells (fig. S2C) without reducing *Alu* RNA levels (fig. S2D). Other clinically relevant NRTIs, including lamivudine (3TC) and abacavir (ABC), similarly blocked caspase-1 cleavage induced by *Alu* RNA (Fig. 1D).

To determine whether reverse transcriptase inhibition was required for inflammasome blockade by d4T, we synthesized a 5′-*O*-methyl–modified version of d4T (me-d4T) (figs. S3 to S5). Only the triphosphate forms of nucleoside analogs inhibit reverse transcriptase; the methyl modification at the 5′ position prevents phosphorylation and thus formation of nucleoside triphosphate (*11*). As predicted, me-d4T, unlike d4T, did not inhibit lentiviral vector transduction of green fluorescent protein (GFP) (fig. S6, A and B). Moreover, the triphosphate metabolite of some dideoxy nucleoside analogs causes depletion of mitochondrial DNA (*12*); we found that d4T, but not me-d4T, reduced mtDNA levels in RPE cells (Fig. 2A). Notably, despite its inability to inhibit polymerases, me-d4T still blocked caspase-1 activation and IRAK4 phosphorylation by *Alu* RNA in RPE cells (Fig. 2B). We confirmed that me-d4T also prevented *Alu*-induced RPE degeneration in wild-type mice (Fig. 2C). These data suggest that d4T can block caspase-1 activation and RPE degeneration independent of reverse transcriptase inhibition.

We also tested whether NRTIs blocked NLRP3 inflammasome activation by lipopolysaccharide/adenosine 5′-triphosphate (LPS/ATP), which is not known to signal via reverse transcriptase (*13*). d4T inhibited LPS/ATP-induced caspase-1 maturation in primary mouse bone marrow–derived macrophages (BMDMs) (Fig. 3A). To demonstrate that

[1]Department of Ophthalmology and Visual Sciences, University of Kentucky, Lexington, KY 40536, USA. [2]Department of Physiology, University of Kentucky, Lexington, KY 40536, USA. [3]Department of Microbiology, Immunology, and Human Genetics, University of Kentucky, Lexington, KY 40536, USA. [4]Department of Biomedical Engineering, University of Kentucky, Lexington, KY 40536, USA. [5]Angiogenesis Lab, Institute of Genetics and Biophysics, CNR, Naples, Italy [6]Experimental Transplantation and Immunology Branch, National Cancer Institute, National Institutes of Health, Bethesda, MD, USA. [7]School of Biosciences, Cardiff University, Cardiff CF10 3AX, UK. [8]Immunology Research Group, University of Calgary, Calgary, Alberta T2N 4N1, Canada. [9]Chapman University School of Pharmacy, 9401 Jeronimo Road, Harry and Diane Rinker Health Science Campus, Irvine, CA 92618, USA. [10]Departments of Pathology and Ophthalmology, Keck School of Medicine of the University of Southern California, Los Angeles, CA 90033, USA.
***Corresponding author. E-mail: jamba2@email.uky.edu**

LPS/ATP-induced inflammasome activation can be inhibited without reverse transcriptase inhibition, we used a cell system that is incapable of NRTI phosphorylation, which is required for reverse transcription inhibition. Although d4T metabolism is largely unaffected in thymidine kinase–deficient (Raji/TK$^-$) cells, AZT phosphorylation is severely impaired compared to thymidine kinase–expressing (TK$^+$) parental cells) (figs. S7 to S10) (*14*). One consequence of LPS/ATP-induced caspase-1 activation is the proteolytic cleavage and maturation of IL-1β. Even though AZT was not phosphorylated in TK$^-$ cells, it still inhibited LPS/ATP-induced caspase-1 and IL-1β maturation (Fig. 3B), indicating that AZT did not inhibit IL-1β and caspase-1 maturation via reverse transcriptase inhibition.

In support of the idea that NRTIs specifically impaired caspase-1 activation, levels of pro-caspase-1/IL-18 were not considerably changed (Fig. 1, C and D, fig. S2A, and Fig. 3, A and B), although AZT did diminish pro-IL-1β protein levels (Fig. 3B). Moreover, d4T did not reduce expression of *NLRP3* or *IL1B* mRNAs in RPE cells treated with *Alu* RNA (fig. S11). d4T also did not affect mRNA priming of noninflammasome genes (*Il6*, *Il12a*, *Tnf*) by LPS (fig. S12) in BMDMs. Consistent with this finding, and that LPS signaling occurs via IRAK4 phosphorylation, d4T did not reduce IRAK4 phosphorylation after LPS stimulation (fig. S13).

Alu RNA (*9*) and LPS/ATP (*15*) activate the NLRP3 inflammasome via the ATP receptor P2X7. d4T did not block extracellular release of ATP induced by *Alu* RNA in primary human RPE cells (fig. S14A). We therefore hypothesized that d4T blocks P2X7 or a P2X7-dependent pathway. Upon ATP binding, cell-surface P2X7 forms nonselective cation channels that can mediate inflammasome

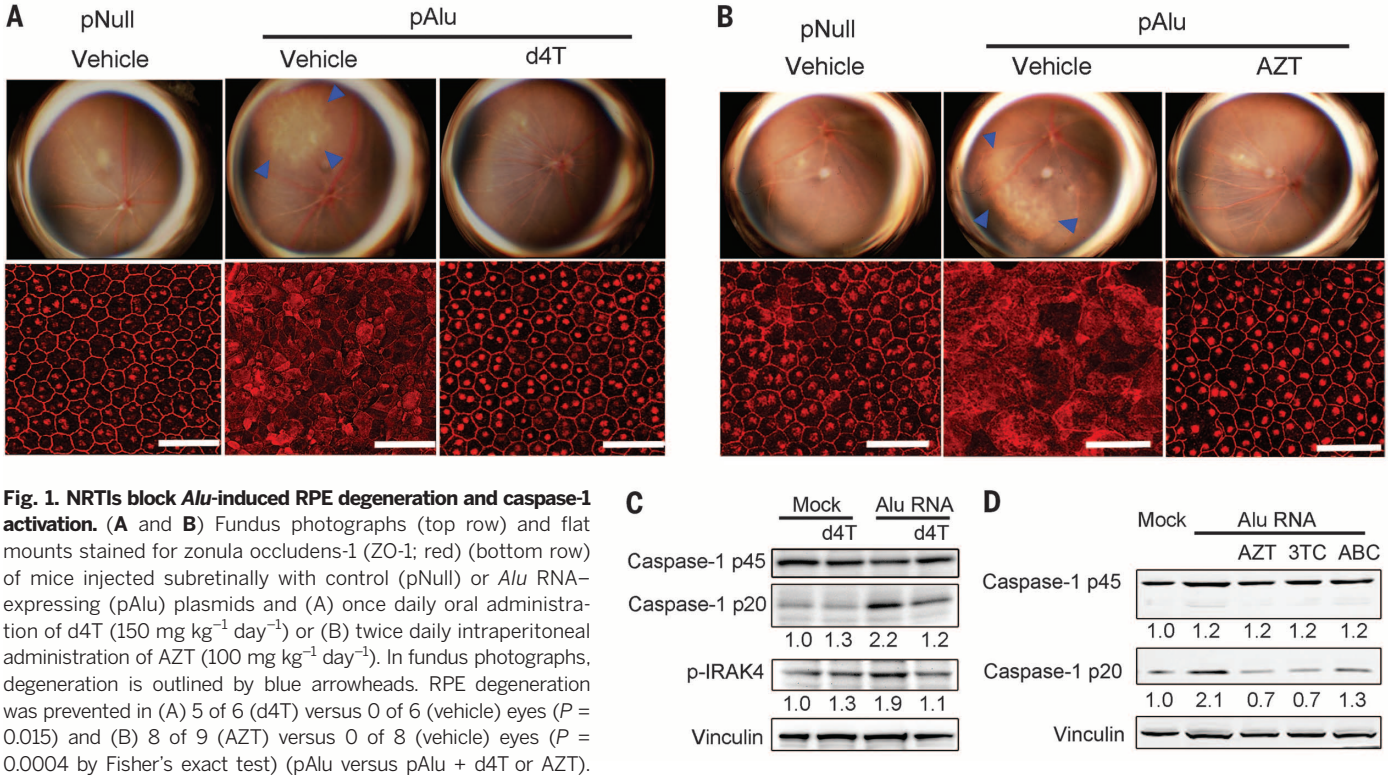


Fig. 1. NRTIs block *Alu*-induced RPE degeneration and caspase-1 activation. (**A** and **B**) Fundus photographs (top row) and flat mounts stained for zonula occludens-1 (ZO-1; red) (bottom row) of mice injected subretinally with control (pNull) or *Alu* RNA–expressing (pAlu) plasmids and (A) once daily oral administration of d4T (150 mg kg^{-1} day^{-1}) or (B) twice daily intraperitoneal administration of AZT (100 mg kg^{-1} day^{-1}). In fundus photographs, degeneration is outlined by blue arrowheads. RPE degeneration was prevented in (A) 5 of 6 (d4T) versus 0 of 6 (vehicle) eyes (P = 0.015) and (B) 8 of 9 (AZT) versus 0 of 8 (vehicle) eyes (P = 0.0004 by Fisher's exact test) (pAlu versus pAlu + d4T or AZT). Scale bars, 50 μm. See also fig. S1. (**C**) Western blot of caspase-1 activation (p20 subunit) or p45 pro-form and IRAK4 phosphorylation in primary human RPE cells transfected with *Alu* RNA ± d4T (100 μM). Fold change in densitometry compared to mock. (**D**) Western blot of caspase-1 pro (p45) and active (p20) forms in human RPE cells transfected with *Alu* RNA ± NRTIs (3TC, AZT, ABC) (100 μM). Fold change in densitometry compared to mock. Images representative of n = 6 to 9 (A and B) and n = 3 to 4 (C and D) experiments.

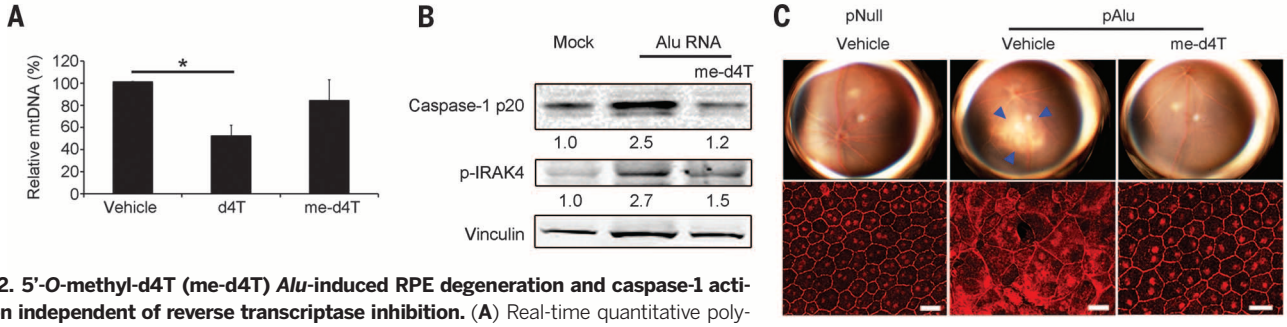


Fig. 2. 5′-*O*-methyl-d4T (me-d4T) *Alu*-induced RPE degeneration and caspase-1 activation independent of reverse transcriptase inhibition. (**A**) Real-time quantitative polymerase chain reaction for mitochondrial DNA normalized to chromosomal DNA exon-intron junction sequence of primary mouse RPE cells treated with unmodified d4T or me-d4T (100 μM both drugs). n = 4 experiments, *P < 0.05 by one-way analysis of variance (ANOVA) and Tukey's post-hoc test. (**B**) Western blot of caspase-1 activation (p20 subunit) and phosphorylated IRAK4 in primary human RPE cells transfected with *Alu* RNA ± me-d4T (100 μM). Fold change in densitometry compared to mock. (**C**) Fundus photographs (top row) and flat mounts stained for zonula occludens-1 (ZO-1; red) (bottom row) from mice treated with me-d4T (twice daily intraperitoneal injection; 50 mg kg^{-1} day^{-1}) (P = 0.029). In fundus photographs, degeneration outlined by blue arrowheads. Representative images of n = 4 experiments (B and C) shown. Scale bars: 20 μm.

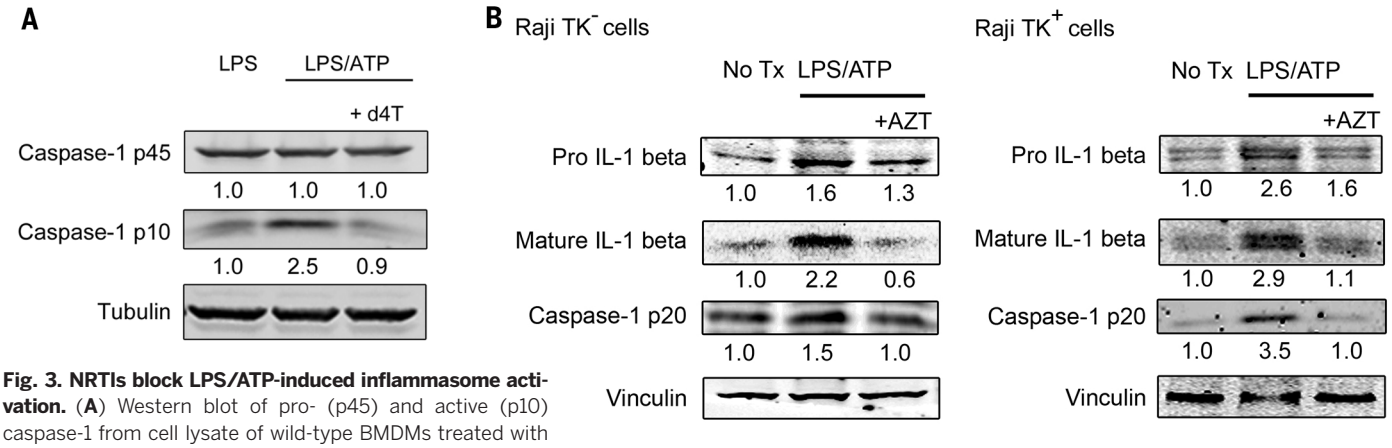


Fig. 3. NRTIs block LPS/ATP-induced inflammasome activation. (**A**) Western blot of pro- (p45) and active (p10) caspase-1 from cell lysate of wild-type BMDMs treated with LPS alone or LPS/ATP with or without d4T (50 μM). Fold change in densitometry compared to LPS alone. (**B**) Western blot of pro- and mature IL-1β and mature caspase-1 in cell lysates of Raji TK⁻ and TK⁺ cells untreated or with LPS ATP with or without AZT (100 μM). Fold change in densitometry compared to no treatment. Representative images of $n = 3$ to 4 experiments (A and B). See also figs. S7 to S10.

activation (*16*). However, d4T did not significantly modulate P2X7 cation channel function, as monitored by patch-clamp analysis of human embryonic kidney 293 (HEK293) cells expressing either the mouse or rat P2X7 receptor (fig. S14, B and C).

P2X7 activation also increases cell permeability to molecules of up to ~1000 daltons (*17*). We found that d4T and the known P2X7 antagonist A438079 inhibited P2X7-dependent uptake of YO-PRO-1 iodide (molecular mass 629 daltons) induced by the selective P2X7 agonist bzATP in human P2X7-expressing HEK293 cells (Fig. 4A and fig. S15). d4T only partially inhibited YO-PRO-1 uptake, whereas caspase-1 activation by *Alu* RNA was completely blocked by a peptide (^{10}Panx) targeting a P2X7-associated channel that inhibits P2X7-dependent dye uptake and LPS/ATP-induced inflammasome activation, but not cation flux (*18*) (Fig. 4B). These data are consistent with the notion that P2X7 activation leads to activation of multiple cell permeabilization pathways (*19*) and that inhibition of some but not all of these pathways by d4T is sufficient to fully block caspase-1 activation. Although a high concentration of ^{10}Panx peptide (*20*) was reported to induce cytotoxicity, the lower concentration used here did not (fig. S16A). Moreover, ^{10}Panx-treated human RPE cells could still synthesize other cytokines such as IL-6 (fig. S16B). *Alu* RNA activation of caspase-1 was unimpaired in *Panx1*$^{-/-}$ mouse RPE cells (fig. S16C), which parallels a previous report that pannexin-1 is not required for caspase-1 activation by LPS/ATP (*15*). The ^{10}Panx peptide can have nonspecific steric effects that alter cell permeability (*21*), possibly via overlapping mechanisms with P2X7-dependent pathways. Collectively, our data indicate that caspase-1 activation in RPE cells by *Alu* RNA occurs via a P2X7-dependent, pannexin-1–independent pathway.

Conversely, *Alu* RNA-induced caspase-1 activation in RPE cells was not inhibited by calmidazolium (fig. S16D), which has been shown to inhibit rat P2X7-mediated cation flux but not dye uptake (*22*) and to inhibit mouse P2X7-mediated cation flux but not cell death (*23*). We also found that calmidazolium blocked

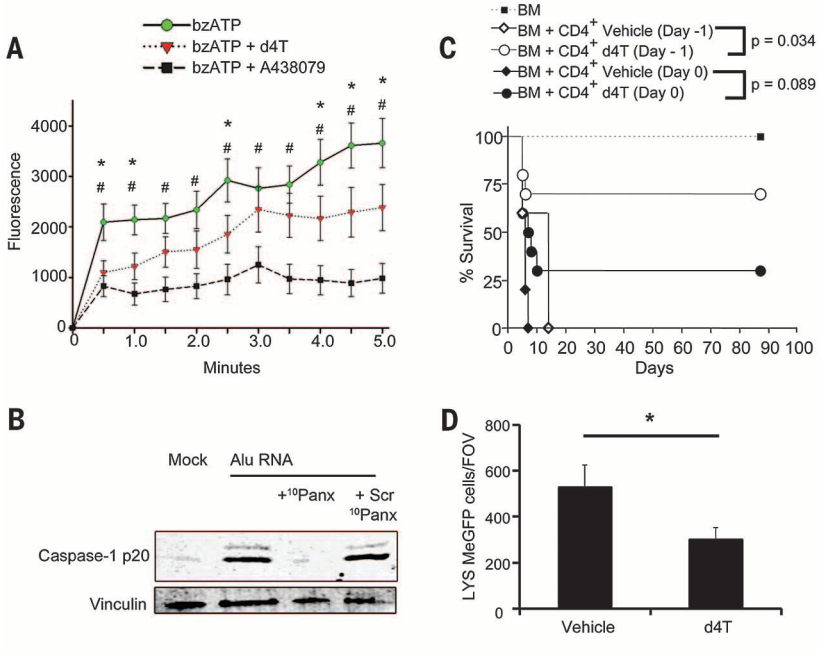


Fig. 4. NRTIs selectively block P2X7 pore function and P2X7-driven models of graft rejection and sterile liver inflammation. (**A**) P2X7-dependent YO-PRO-1 dye uptake induced by bzATP (100 μM) in HEK293 cells stably expressing the human P2X7 receptor and treated with d4T or A438079 (64 μM for both drugs). Fluorescence values are baseline subtracted from cells without bzATP treatment. (*) bzATP versus d4T; (#) bzATP versus A438079, $P < 0.05$ by two-way ANOVA and Student-Newman Keuls post-hoc test ($n = 12$ experiments). See also fig. S15. (**B**) Western blot of caspase-1 activation (p20 subunit) in primary human RPE cells transfected with *Alu* RNA with or without short peptide (^{10}Panx; 240 μM) that blocks P2X7 pore function but not cation flux (versus scrambled peptide: Scr ^{10}Panx; 240 μM). (**C**) Administration of d4T starting from day −1 pretransplant protects murine recipients from GVHD). BALB/c mice were subjected to total body irradiation (950 cGY) and then reconstituted with T cell–depleted bone marrow (TDBM) from B6 donors. Cohorts ($n = 10$ per cohort) received either BM alone or BM plus bulk CD4$^+$ T cells (2.5 M) on the same day as the irradiation. Cohorts that received BM and bulk CD4$^+$ T cells were additionally treated with either vehicle (saline) or drug (d4T) from day −1 or day 0 for a period of 10 days. Clinical manifestations of GVHD and overall survival were monitored after bone marrow transplant. Survival analysis was performed according to the Kaplan-Meier method, and survival between groups was compared by using the log-rank test. Results were pooled from two independent experiments. See also fig. S19. (**D**) LysMeGFP$^+$ cells per field of view (FOV) around a sterile focal hepatic lesion. d4T (400 mg kg^{-1}) or phosphate-buffered saline administered through the jugular vein 20 min before injury. Intravenous d4T inhibits neutrophil recruitment 60 min after injury. $n = 4$ experiments, error bars denote SEM, $P < 0.05$ by two-way ANOVA and Student-Newman Keuls post-hoc test. See also fig. S20.

caspase-1 activation by the cation-specific inflammasome agonist nigericin in these cells (fig. S16E), which supports the idea that the mode of action of calmidazolium involves the inhibition of cation flux (necessary for nigericin-induced inflammasome activation, but not for P2X7-induced inflammasome activation). Furthermore, the intracellular C terminus of P2X7 governs P2X7-associated dye uptake, and a version of d4T that is not cell permeable (*24*) did not block caspase-1 activation by *Alu* RNA in RPE cells (fig. S16, F and G). Consistent with antagonism downstream of P2X7 but preceding inflammasome activation, d4T blocked *Alu*-induced mitochondrial reactive oxygen species production (fig. S17, A and B) (*5*).

Supportive of the idea that d4T inhibits NLRP3 inflammasome activation via P2X7, d4T did not prevent caspase-1 activation in primary mouse BMDMs treated with nigericin or crystalline monosodium urate, NLRP3 agonists that do not signal via P2X7 (fig. S18, A and B) (*25*). Furthermore, d4T did not inhibit AIM2 inflammasome activation by poly(dA:dT) or NLRC4 inflammasome activation by flagellin (fig. S18, C and D). These findings suggest that d4T specifically inhibits P2X7-dependent inflammasome activation, because cytosolic flagellin and poly(dA:dT) activate these other inflammasomes independent of P2X7 (*26*, *27*).

To explore the therapeutic relevance of NRTIs beyond geographic atrophy, we hypothesized that NRTIs might be broadly useful in other P2X7-driven animal models of disease. Murine graft-versus-host disease (GVHD) is mediated by P2X7 (*28*); consistent with these results, irradiated BALB/c mice reconstituted with allogeneic (C57/Bl6) bone marrow and T cells showed improved survival when treated with d4T compared to saline-treated controls (Fig. 4C). We also found that at day 3 after transplant, d4T-treated mice had lower serum levels of interferon-γ, tumor necrosis factor–α, and IL-6 proteins compared to saline treatment (fig. S19). The increased abundance of these cytokines in serum is characteristic of allogeneic T cell transfer in murine models and thought to play a role in acute GVHD pathogenesis (*29*–*31*). Supporting the idea that d4T targets P2X7, serum levels of these three cytokines were also decreased in an acute GVHD model using P2X7-deficient host mice (*28*). Moreover, studies in a variety of other systems indicate that P2X7 regulates the expression of these cytokines (*32*–*34*). Further supporting the activity of d4T at the level of P2X7, in the P2X7-driven model of liver inflammation in which neutrophils are recruited from the circulation to a site of sterile injury (*35*), intravenous d4T reduced early neutrophil migration to the focus of hepatic necrosis (Fig. 4D and fig. S20). Finally, because P2X7 activation is known to increase tumor angiogenesis (*36*), we investigated whether NRTIs reduced choroidal neovascularization (CNV), which characterizes the "wet" form of AMD. In the laser-induced mouse model of CNV, we found that d4T and me-d4T reduced CNV volume in wild-type mice (fig. S21A), but not in P2X7-deficient mice (fig. S21B). These data suggest that NRTIs might be therapeutic for both dry and wet AMD and provide further evidence that these drugs work at the level of P2X7 in these systems.

NRTIs are a diverse, widely used, inexpensive class of small molecules, with extensive pharmacokinetic and safety data collected over several decades of human use. Our work, by illustrating a novel mechanism of action of NRTIs, paves a clear path for the broad repurposing of this drug class to address major unmet medical needs. Our data indicate that NRTIs could have dual therapeutic use in AMD in treating both geographic atrophy and neovascular AMD.

Because inflammasome inhibition by NRTIs can be achieved without their phosphorylation, the use of me-d4T or other phosphorylation-incompetent nucleoside analogs to treat disease could avoid dose-limiting toxicities associated with NRTI-triphosphate–mediated polymerase inhibition. It is not known whether long-term NRTI use is protective against developing AMD; however, as the population of aging HIV-positive individuals continues to grow, it might be possible to determine this predicted effect.

Recent work has shown caspase-1 activation by HIV in abortively infected T cells (*37*) and a role for NLRP3 in sensing HIV in macrophages and monocytes (*38*); such studies support the importance of inflammasome regulation by NRTIs. Also of note, HIV patients have increased plasma levels of the inflammasome effector IL-18 (*39*), which decreases after treatment with NRTI-containing highly active antiretroviral therapy (HAART) (*40*). Thus, while it is unclear whether suppression of viral replication by NRTIs or other components of HAART leads to the reduction of plasma IL-18 levels in these patients, our findings raise the possibility that inflammasome inhibition by NRTIs independent of reverse transcriptase inhibition could be responsible, at least in part, for modulation of HIV-induced cytokine expression.

REFERENCES AND NOTES

1. J. Ambati, B. K. Ambati, S. H. Yoo, S. Ianchulev, A. P. Adamis, *Surv. Ophthalmol.* **48**, 257–293 (2003).
2. J. Ambati, B. J. Fowler, *Neuron* **75**, 26–39 (2012).
3. S. Dridi *et al.*, *Proc. Natl. Acad. Sci. U.S.A.* **109**, 13781–13786 (2012).
4. H. Kaneko *et al.*, *Nature* **471**, 325–330 (2011).
5. V. Tarallo *et al.*, *Cell* **149**, 847–859 (2012).
6. M. Dewannieux, C. Esnault, T. Heidmann, *Nat. Genet.* **35**, 41–48 (2003).
7. Panel on Antiretroviral Guidelines for Adults and Adolescents, Guidelines for the use of antiretroviral agents in HIV-1-infected adults and adolescents. Department of Health and Human Services. Available at http://aidsinfo.nih.gov/ContentFiles/AdultandAdolescentGL.pdf. (2014).
8. Center for Drug Evaluation and Research, Center for Biologics Evaluation and Research (2002), Estimating the safe starting dose in clinical trials for therapeutics in adult healthy volunteers, U.S. Food and Drug Administration Rockville, MD, USA.
9. N. Kerur *et al.*, *Invest. Ophthalmol. Vis. Sci.* **54**, 7395–7401 (2013).
10. T. T. Yamin, J. M. Ayala, D. K. Miller, *J. Biol. Chem.* **271**, 13273–13282 (1996).
11. A. Nykänen, B. Haley, P. D. Zamore, *Cell* **107**, 309–321 (2001).
12. S. E. Lim, W. C. Copeland, *J. Biol. Chem.* **276**, 23616–23623 (2001).
13. F. Martinon, K. Burns, J. Tschopp, *Mol. Cell* **10**, 417–426 (2002).
14. J. Balzarini, P. Herdewijn, E. De Clercq, *J. Biol. Chem.* **264**, 6127–6133 (1989).
15. Y. Qu *et al.*, *J. Immunol.* **186**, 6553–6561 (2011).
16. J. M. Kahlenberg, G. R. Dubyak, *Am. J. Physiol. Cell Physiol.* **286**, C1100–C1108 (2004).
17. A. Surprenant, F. Rassendren, E. Kawashima, R. A. North, G. Buell, *Science* **272**, 735–738 (1996).
18. P. Pelegrin, A. Surprenant, *EMBO J.* **25**, 5071–5082 (2006).
19. A. Baroja-Mazo, M. Barberà-Cremades, P. Pelegrín, *Biochim. Biophys. Acta* **1828**, 79–93 (2013).
20. P. Pelegrin, C. Barroso-Gutierrez, A. Surprenant, *J. Immunol.* **180**, 7147–7157 (2008).
21. J. Wang, M. Ma, S. Locovei, R. W. Keane, G. Dahl, *Am. J. Physiol. Cell Physiol.* **293**, C1112–C1119 (2007).
22. C. Virginio, D. Church, R. A. North, A. Surprenant, *Neuropharmacology* **36**, 1285–1294 (1997).
23. E. Salas *et al.*, *J. Pharmacol. Exp. Ther.* **347**, 802–815 (2013).
24. H. K. Agarwal, K. Loethan, D. Mandal, G. F. Doncel, K. Parang, *Bioorg. Med. Chem. Lett.* **21**, 1917–1921 (2011).
25. N. Riteau *et al.*, *Cell Death Dis.* **3**, e403 (2012).
26. L. Franchi, T. D. Kanneganti, G. R. Dubyak, G. Núñez, *J. Biol. Chem.* **282**, 18810–18818 (2007).
27. T. Ichinohe, I. K. Pang, A. Iwasaki, *Nat. Immunol.* **11**, 404–410 (2010).
28. K. Wilhelm *et al.*, *Nat. Med.* **16**, 1434–1438 (2010).
29. X. Chen *et al.*, *Blood* **114**, 891–900 (2009).
30. H. Z. Hu, G. L. Li, Y. K. Lim, S. H. Chan, E. H. Yap, *Immunology* **98**, 379–385 (1999).
31. C. Schmaltz *et al.*, *Blood* **101**, 2440–2445 (2003).
32. I. P. Chessell *et al.*, *Pain* **114**, 386–396 (2005).
33. A. V. Gourine *et al.*, *Br. J. Pharmacol.* **146**, 139–145 (2005).
34. A. Solini, P. Chiozzi, A. Morelli, R. Fellin, F. Di Virgilio, *J. Cell Sci.* **112**, 297–305 (1999).
35. B. McDonald *et al.*, *Science* **330**, 362–366 (2010).
36. E. Adinolfi *et al.*, *Cancer Res.* **72**, 2957–2969 (2012).
37. G. Doitsh *et al.*, *Nature* **505**, 509–514 (2014).
38. M. A. Chattergoon *et al.*, *PLOS Pathog.* **10**, e1004082 (2014).
39. R. Ahmad, S. T. Sindhu, E. Toma, R. Morisset, A. Ahmad, *J. Virol.* **76**, 12448–12456 (2002).
40. E. Stylianou *et al.*, *Clin. Exp. Immunol.* **132**, 462–466 (2003).

ACKNOWLEDGMENTS

We thank B. K. Ambati, K. Ambati, A. M. Adams, A. M. Rao, and G. S. Rao for discussions; L. Toll, G. R. Pattison R. King, L. Xu, M. McConnell, C. Payne, D. Robertson, G. Botzet, and J. May for technical assistance; G. Dubyak for discussions and providing the HEK293-P2X7 cell line; and the University of Kentucky Viral Core (COBRE) for providing lentivirus-GFP. The data presented in this manuscript are tabulated in the main paper and in the supplementary materials. J.A. and B.J.F. are listed as inventors on a patent application for the therapeutic use of NRTIs and chemical derivatives filed by their employer, the University of Kentucky. J.A. is a cofounder of iVeena, Inc., which has licensed the technology described in this work. J.A. was supported by NIH grants (DP1GM114862, R01EY018350, R01EY018836, R01EY020672, R01EY022238, and R01EY024068), Doris Duke Distinguished Clinical Scientist Award, Burroughs Wellcome Fund Clinical Scientist Award in Translational Research, Ellison Medical Foundation Senior Scholar in Aging Award, Foundation Fighting Blindness Individual Investigator Research Award, Harrington Discovery Institute Scholar-Innovator Award, Dr. E. Vernon Smith and Eloise C. Smith Macular Degeneration Endowed Chair, and Research to Prevent Blindness departmental unrestricted grant; B.J.F. by NIH T32HL091812 and UL1RR033173; A.B.C. by the Programme for Advanced Medical Education (sponsored by Fundação Calouste Gulbenkian, Fundação Champalimaud, Ministério da Saúde and Fundação para a Ciência e Tecnologia, Portugal) and Bayer Global Ophthalmology Research Award; Y.H. by Alcon Japan Research award; N.K. by Beckman Initiative for Macular Research and NIH K99EY024336; B.D.G. by American Heart Association and International Retinal Research Foundation (IRRF); T.Y. by Fight for Sight postdoctoral award; and C.W. by The Loris and David Rich Postdoctoral Scholar Award (IRRF). D.H.F and S.A. are supported by the Center for Cancer Research, National Cancer Institute. The content is solely the responsibility of the authors and does not necessarily represent the official views of the NIH. M.T.Y. and M.R. are supported by Biotechnology and Biological Sciences Research Council (BBSRC) grant BB/J017345/1. D.R.H. is supported by NIH grants P30EY003040 and R01EY001545 and by the Arnold and Mabel Beckman Foundation. K.P. is supported by an Alberta Innovates Health Solutions Graduate Studentship, and M.R. by the BBSRC. me-d4T is available from the University of Kentucky via a Materials Transfer Agreement.

SUPPLEMENTARY MATERIALS

www.sciencemag.org/content/346/6212/1000/suppl/DC1
Materials and Methods
Supplementary Text
Figs. S1 to S21
References (*41*–*46*)

26 September 2014; accepted 24 October 2014
10.1126/science.1261754

REGULATION AT HOX LOCI

Convergent evolution of complex regulatory landscapes and pleiotropy at *Hox* loci

Nicolas Lonfat,[1]* Thomas Montavon,[1]† Fabrice Darbellay,[1] Sandra Gitto,[2] Denis Duboule[1,2]‡

Hox genes are required during the morphogenesis of both vertebrate digits and external genitals. We investigated whether transcription in such distinct contexts involves a shared enhancer-containing landscape. We show that the same regulatory topology is used, yet with some tissue-specific enhancer-promoter interactions, suggesting the hijacking of a regulatory backbone from one context to the other. In addition, comparable organizations are observed at both *HoxA* and *HoxD* clusters, which separated through genome duplication in an ancestral invertebrate animal. We propose that this convergent regulatory evolution was triggered by the preexistence of some chromatin architecture, thus facilitating the subsequent recruitment of the appropriate transcription factors. Such regulatory topologies may have both favored and constrained the evolution of pleiotropic developmental loci in vertebrates.

The evolution of vertebrates involved two rounds of genome duplications, which facilitated gene neofunctionalization (*1*) via novel regulatory sequences (*2*) and led to high pleiotropy for most known developmental genes, either coding for transcription factors or involved in signaling pathways (*3*, *4*). *Hox* genes illustrate such functional cooptations, and particular global regulations are associated with specific *Hox* gene clusters. For example, in addition to organizing the major body axis, both *HoxA* and *HoxD* genes are required for the development of digits and external genitals (*5*–*7*), two structures sharing genetic and embryological similarities (*8*–*10*) (Fig. 1A). Accordingly, the combined inactivation of *Hoxd13* and *Hoxa13* led to both digits and external genitals agenesis (*5*–*7*).

During digit development, *Hoxd13* is controlled by multiple enhancers located within an 800-kb flanking gene desert (Fig. 1B). This regulatory archipelago (*11*) matches a topologically associating domain (TAD), a chromatin structure in which both enhancer-promoter and structural interactions are enriched (*12*–*14*). Therefore, such a constitutive chromatin domain may be used as a template to support the necessary regulatory interactions between *Hoxd13* and the various digit enhancers. Indeed, although some interactions were detected only when target genes were transcribed, others were established regardless of the transcriptional status, thus forming a preorganized chromatin backbone (*11*, *15*).

We assessed whether transcription of *Hoxd13* during genitals outgrowth relies upon the same set of digit enhancers, within the same TAD, despite distinct developmental contexts. In transcription profiles from both fetal digits and genital tubercles (GT), *Hoxd13* transcripts were most abundant, whereas *Hoxd12* to *Hoxd8* showed progressively lower expression levels (Fig. 1A). This similarity extended to both histone H3K27 acetylation and trimethylation profiles (Fig. 1A), confirming that the regulation of these genes during GT and digit development is similar (*16*). We then analyzed the importance in GT of the digit regulatory landscape (*11*), using scanning deletions in vivo to compare *Hoxd13* transcription in digits and GT cells. Deletion of the entire gene desert reduced *Hoxd13* mRNAs in GT by 80% (Fig. 1, B and C), an effect close to that observed in digits (*11*). Using the Del(*rel1-rel5*) allele, which removes one-third of the regulatory landscape, including two digit enhancers (*17*), mRNAs were down by 40% in both digits and GT cells. When the adjacent 300 kb were removed [Del(*rel5-SB*)], a similar decrease was obtained in both cases. However, the 290-kb deletion, including the distal part of the landscape [Del(*SB-Atf2*)], had no effect on *Hoxd13* in GT cells, unlike in digits

[1]School of Life Sciences, Ecole Polytechnique Fédérale de Lausanne, 1015 Lausanne, Switzerland. [2]Department of Genetics and Evolution, University of Geneva, 1211 Geneva, Switzerland.
*Present address: Department of Genetics, Harvard Medical School, Boston, MA 02115, USA. †Present address: Department of Epigenetics, Max Planck Institute of Immunobiology and Epigenetics, 79108 Freiburg, Germany. ‡Corresponding author. E-mail: denis.duboule@epfl.ch

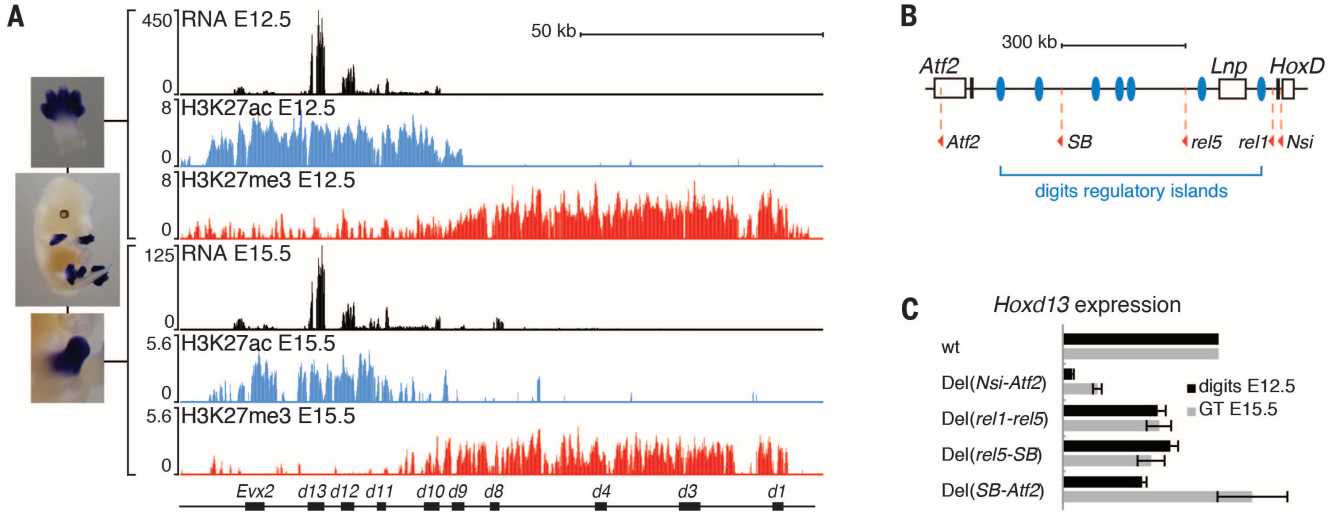


Fig. 1. Transcription of *Hoxd* genes in digits and genitals. (**A**) *Hoxd13* is transcribed in both developing digits (top) and genitals (bottom). Transcripts (black), H3K27ac (blue), and H3K27me3 (red) profiles show similar patterns between digits and genitals, with *Hoxd13* as the strongest expressed gene. Transcribed parts of the cluster are decorated with H3K27ac marks, and silent genes are H3K27me3 positive. (**B**) Scheme of the gene desert upstream from the *HoxD* cluster, including the seven digit regulatory islands (blue ovals) (*11*). The *loxP* sites used for deletions are shown in red along with the names of the alleles. (**C**) In vivo deletions within the *HoxD* regulatory landscape affect *Hoxd13* transcription in digits (*11*) and genitals (GT), although with slight differences. Names of deletions refer to (B).

where transcription was down to 50% (Fig. 1C). Therefore, although the digit regulatory landscape also controls *Hoxd13* transcription in external genitals, enhancers specific for either structure are organized with distinct topologies. We controlled the potential of this regulatory landscape in GT cells by using an inversion including a *Hoxd9lacZ* reporter transgene (fig. S1). In mutant embryos, both the digit enhancers and the reporter transgene are physically disconnected from their *Hoxd* targets. *LacZ* staining of mutant embryos revealed reporter staining into both GT and digit cells. Therefore, enhancers required for *Hoxd* transcription in GT and digit cells are located within the same regulatory landscape (fig. S1).

We compared the interaction profiles established by *Hoxd13* in digits and GT cells by circular chromosome conformation capture (4C). In GT cells, *Hoxd13* contacted mostly the centromeric gene desert, supporting the deletion approach. Interaction peaks extended over approximately 1 Mb and matched the TAD covering this region, as in digits (*12*, *15*) (Fig. 2, A and B). However, although the profiles shared many interactions, they also displayed differences with contacts observed in digits but not in GT and vice versa (Fig. 2C). *Hoxd13* interaction peaks were aligned with both evolutionary conserved noncoding sequences and the GT H3K27 acetylation profile (fig. S2). Potential regulatory sequences active either in GT only (GT1 and GT2), in digits only (Island II-1) (*11*), or in both (*Prox*) (*17*) were thus narrowed down and assayed in vivo using a *LacZ* reporter system (*18*) (Fig. 3). Accordingly, embryo transgenics for the GT2 sequence displayed strong activity in GT cells exclusively, whereas sequence II-1 triggered expression in digits but not in GT (Fig. 3). The staining elicited by GT1, however, was scored both in GT and in digits, perhaps reflecting the weak interaction peak between *Hoxd13* and GT1 in digit cells (Fig. 2C). As a control, the *Prox* element showed strong interactions with *Hoxd13* in both digit and GT cells, and staining was detected at both sites (Fig. 3). Islands I to IV did not trigger any staining in GT, even though all but island I were H3K27ac-positive in this tissue (fig. S2). Therefore, within this complex regulatory landscape, some intermingled enhancers are specific either for the genitals or for the digits, whereas others are used by both structures.

We asked whether the large spacing between these enhancers is necessary for their proper activities—for example, to isolate them from one another and prevent undesired regulatory interferences. We produced a reporter transgene containing 300 base pairs of the GT2-specific enhancer within digit island II-1. This chimeric DNA fragment elicited a strong additive staining in both digits and GT cells (Fig. 3), showing that each sequence could work autonomously and independently from its immediate neighborhood. Therefore, in this particular case, the TAD may not be critical to properly organize internal enhancers into a particular functional architecture.

Hoxa13 is also involved in the morphogenesis of both digits and external genitals with specificity and function similar to those of *Hoxd13* (*5*–*7*, *19*) (Fig. 4A). *Hoxa13* transcription in digits relies on several enhancers located within a regulatory landscape located telomeric to the *HoxA* cluster and containing some unrelated yet coexpressed genes (*20*, *21*). As for *Hoxd13*, this regulatory landscape matches a TAD—as defined by Hi-C, chromosome conformation capture carbon copy (5C), and 4C (*12*, *21*, *22*)—with a boundary located within the *HoxA* cluster, as for *HoxD*. To see whether in this case again, digit and genital enhancers were embedded into the same TAD, we generated and compared the *Hoxa13* 4C interaction profiles in developing genitals and digits. Both profiles extended over the same genomic distance, overlapping with the same TAD (Fig. 4, B and C, and fig. S3). Although some contacts involving known sequences were common to both cell types, others were clearly more prominent either in GT or in digit cells. The GTe2 sequence strongly interacted with *Hoxa13* in GT, whereas much weaker contacts were scored in digits. In contrast, the e16 DNA regulatory sequence

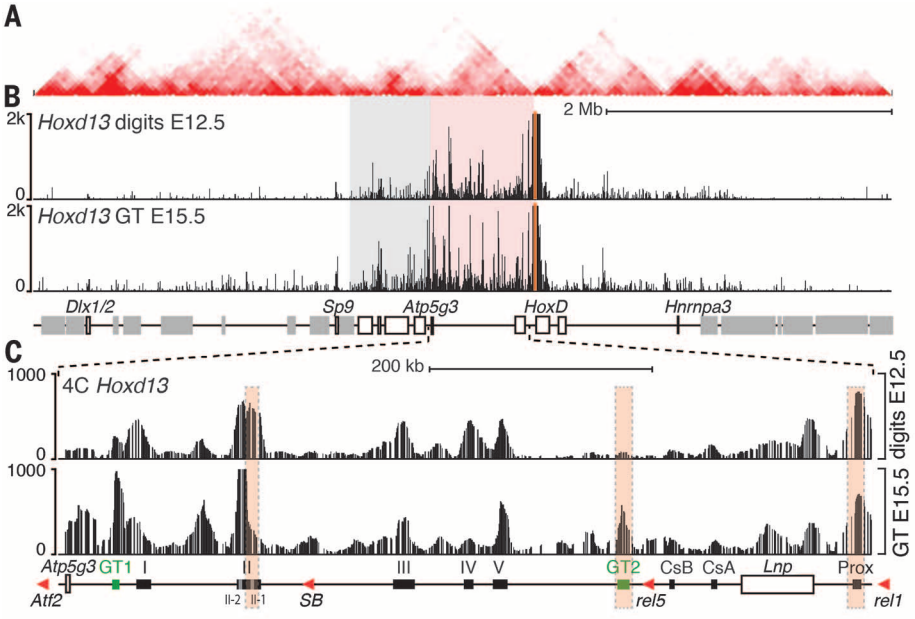


Fig. 2. 4C interaction profiles of *Hoxd13* in developing digits and genitals. (**A**) Distribution of TADs over a 6-Mb DNA interval, including the *HoxD* locus [embryonic stem cell data extracted from (*12*)]. (**B**) Interactions established by *Hoxd13* (orange bar) in E12.5 digits (top) and E15.5 genitals (bottom). Most contacts are observed over 1 Mb centromeric to the cluster (red shaded area), corresponding to the gene desert (below). In addition, weaker contacts are scored more centromeric (gray shaded area), in a gene-rich region. (**C**) Enlarged and smoothed interaction profiles covering the regulatory landscape. Selected islands of interaction (black and green boxes) and *loxP* sites (red triangles, used for the deletions in Fig. 1) are indicated.

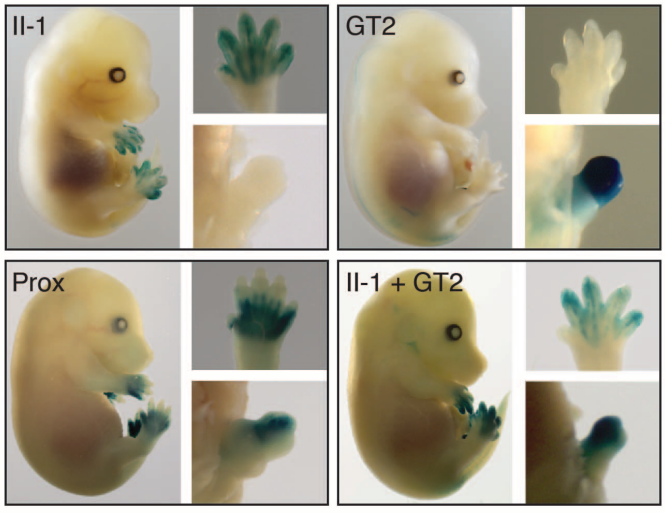


Fig. 3. *LacZ* staining of embryos transgenic for the island II-1, GT2, and Prox enhancers (Fig. 2, red areas) (*17*), as well as for a combination of both island II-1 and GT2 sequences. Displayed embryos are representatives of several integration events (see the supplementary materials).

[from (*21*)] displayed robust interactions with *Hoxa13* in digits, whereas contacts were reduced in GT cells (Fig. 4C). In transgenic mice, GTe2 triggered preferential expression in developing genitals, whereas e16 was active mostly in digits (Fig. 4D) (*20*, *21*). As a control, the GTe5 sequence contacted by *Hoxa13* in both contexts gave some staining in both structures (Fig. 4D). Therefore, the regulation of *Hoxa13* transcription in both digit and GT cells follows the same general principles as observed at the *HoxD* locus.

These similarities in size and organization of both enhancer landscapes are unexpected because the duplication of an ancestral *Hox* cluster occurred in a nonvertebrate animal, which had neither limbs nor external genitals (*23*, *24*) (fig. S4). Therefore, these related regulatory domains evolved independently, which may explain why only a few sequence homologies are found between *HoxA* and *HoxD* enhancers (*21*). Because digits and genitals were likely of high adaptive value for both locomotion and reproduction in a terrestrial environment, the parallel emergence of these morphological novelties may not be a surprise. However, the convergence between regulatory mechanisms is more difficult to explain. One possibility involves the presence in an ancestral *Hox* cluster of a constrained functionality or structure, which was used as a starting point to facilitate this convergence. In this view, a TAD might have been present before cluster duplications (fig. S4) and thus favored enhancer recruitment by providing the molecular and structural niches necessary to elicit productive interactions. Because group 13 HOX proteins were key to developing these appendices, any up-regulation of these genes during the evolution of digits and genitals—for example, via a response to appropriate signaling pathways (*9*, *25*)—may have been selected and further reinforced. The presence of a comparable organization in teleost fishes (*22*) supports the idea that these domains existed before the emergence of digits and genitals. Alternatively, convergent enhancer evolution may have driven the emergence of comparable TADs at both loci. We consider this as less probable because it implies the independent construction of comparable regulatory architectures without any prior constraint.

Our results suggest that TADs may act as genomic niches where tissue-specific factors can hijack global transcriptional readout from one cell type to the other. Although the use of the same regulatory landscape in digits and genitals indeed suggests that it was coopted from one context to the other, it is admittedly difficult to establish whether digits hijacked this regulation from genitals or vice versa. In this case, however, this particular situation may illustrate why many large regulatory landscapes accumulated pleiotropic regulations [e.g. (*26*)]. Accordingly, such well-defined topological domains may not be as clearly visible for genetic loci transcribed more constitutively or with a high cellular specialization. The case reported in this study might represent a permissive system where multiple and distinct inputs could all elicit a comparable transcriptional response. The latter situations, in contrast, would reflect a more instructive role of transcription factors in forming the spatial context necessary for transcribing target genes (*27*).

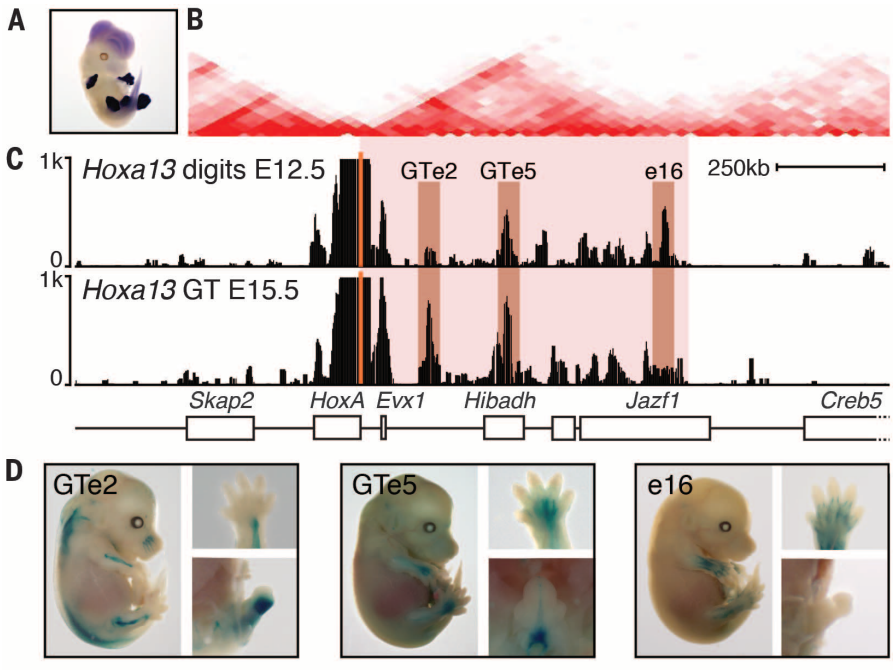


Fig. 4. 4C interaction profiles of *Hoxa13* in developing digits and genitals. (**A**) *Hoxa13* is transcribed in both developing digits and genitals, like *Hoxd13*. (**B**) Distribution of TADs over 2.5 Mb, including the *HoxA* locus [data from (*12*)]. (**C**) Interactions established by *Hoxa13* (vertical orange bar) in both E12.5 digits (top) and E15.5 genitals (bottom). Most contacts are observed within a 1-Mb regulatory landscape, telomeric to the cluster (red shaded area) in a gene-containing region, matching one TAD. The vertical dark shaded bars point to interaction peaks either present in genitals but weak in digits (GTe2), present in digits but weak in genitals (e16), or present in both tissues (GTe5). (**D**) *LacZ* staining of embryos transgenic for GTe2, GTe5, or e16. While GTe2 shows staining in the genitals, e16 transgene staining is mostly seen in proximal digits and absent from genitals. Embryos are representatives of several integration events (see the supplementary materials).

REFERENCES AND NOTES

1. S. Ohno, *Evolution by Gene Duplication* (Springer-Verlag, Heidelberg, 1970).
2. P. W. Holland, J. Garcia-Fernàndez, N. A. Williams, A. Sidow, *Dev. Suppl.* **1994**, 125–133 (1994).
3. D. Duboule, A. S. Wilkins, *Trends Genet.* **14**, 54–59 (1998).
4. M. Kirschner, J. Gerhart, *The Plausibility of Life: Resolving Darwin's Dilemma* (Yale Univ. Press, New Haven, CT, 2005).
5. C. Fromental-Ramain *et al.*, *Development* **122**, 2997–3011 (1996).
6. X. Warot, C. Fromental-Ramain, V. Fraulob, P. Chambon, P. Dollé, *Development* **124**, 4781–4791 (1997).
7. T. Kondo, J. Zákány, J. W. Innis, D. Duboule, *Nature* **390**, 29 (1997).
8. P. Dollé, J. C. Izpisúa-Belmonte, J. M. Brown, C. Tickle, D. Duboule, *Genes Dev.* **5**, 1767–1776 (1991).
9. M. J. Cohn, *Dev. Dyn.* **240**, 1108–1115 (2011).
10. S. Miyagawa *et al.*, *Development* **136**, 3969–3978 (2009).
11. T. Montavon *et al.*, *Cell* **147**, 1132–1145 (2011).
12. J. R. Dixon *et al.*, *Nature* **485**, 376–380 (2012).
13. E. P. Nora *et al.*, *Nature* **485**, 381–385 (2012).
14. T. Sexton *et al.*, *Cell* **148**, 458–472 (2012).
15. G. Andrey *et al.*, *Science* **340**, 1234167 (2013).
16. T. Montavon, J.-F. Le Garrec, M. Kerszberg, D. Duboule, *Genes Dev.* **22**, 346–359 (2008).
17. F. Gonzalez, D. Duboule, F. Spitz, *Dev. Biol.* **306**, 847–859 (2007).
18. M. Friedli *et al.*, *PLOS ONE* **5**, e15741 (2010).
19. H. Haack, P. Gruss, *Dev. Biol.* **157**, 410–422 (1993).
20. J. A. Lehoczky, J. W. Innis, *Evol. Dev.* **10**, 421–432 (2008).
21. S. Berlivet *et al.*, *PLOS Genet.* **9**, e1004018 (2013).
22. J. M. Woltering, D. Noordermeer, M. Leleu, D. Duboule, *PLOS Biol.* **12**, e1001773 (2014).
23. A. Amores *et al.*, *Science* **282**, 1711–1714 (1998).
24. V. Ravi *et al.*, *Proc. Natl. Acad. Sci. U.S.A.* **106**, 16327–16332 (2009).
25. K. Suzuki *et al.*, *Development* **130**, 6209–6220 (2003).
26. O. Symmons *et al.*, *Genome Res.* **24**, 390–400 (2014).
27. W. de Laat, D. Duboule, *Nature* **502**, 499–506 (2013).

ACKNOWLEDGMENTS

We thank D. Noordermeer, P. Fabre, G. Andrey, A. Necsulea, and all colleagues from the Duboule laboratories for their help and for reagents and discussions. We thank M. Docquier and the Geneva Genomics Platform, S. Verp and S. Offner for help with transgenic animals, and M. Leleu from the Bioinformatics and Biostatistics Core Facility (BBCF) of the Ecole Polytechnique Fédérale (EPFL). Computations were performed at Vital-IT center for high-performance computing of the Swiss Institute of Bioinformatics, using tools developed by the BBCF. This work was supported by funds from the Federal Institute of Technology (EPFL), the University of Geneva, the Swiss National Research Foundation (no. 310030B_138662), and European Research Council grant SystemsHox.ch (no. 232790). Data sets presented in this study are available with accession no. GSE62269.

SUPPLEMENTARY MATERIALS

www.sciencemag.org/content/346/6212/1004/suppl/DC1
Materials and Methods
Figs. S1 to S4
Table S1
References (*28*–*33*)

16 June 2014; accepted 10 October 2014
10.1126/science.1257493

MOUSE GENOMICS

Mouse regulatory DNA landscapes reveal global principles of cis-regulatory evolution

Jeff Vierstra,[1] Eric Rynes,[1] Richard Sandstrom,[1] Miaohua Zhang,[2] Theresa Canfield,[1] R. Scott Hansen,[3] Sandra Stehling-Sun,[1] Peter J. Sabo,[1] Rachel Byron,[2] Richard Humbert,[1] Robert E. Thurman,[1] Audra K. Johnson,[1] Shinny Vong,[1] Kristen Lee,[1] Daniel Bates,[1] Fidencio Neri,[1] Morgan Diegel,[1] Erika Giste,[1] Eric Haugen,[1] Douglas Dunn,[1] Matthew S. Wilken,[4] Steven Josefowicz,[5,6] Robert Samstein,[5,6] Kai-Hsin Chang,[7] Evan E. Eichler,[1,6] Marella De Bruijn,[8] Thomas A. Reh,[4] Arthur Skoultchi,[9] Alexander Rudensky,[5,6] Stuart H. Orkin,[6,10] Thalia Papayannopoulou,[7] Piper M. Treuting,[11] Licia Selleri,[12] Rajinder Kaul,[1,3] Mark Groudine,[2,13] M. A. Bender,[2,14] John A. Stamatoyannopoulos[1,15]*

To study the evolutionary dynamics of regulatory DNA, we mapped >1.3 million deoxyribonuclease I–hypersensitive sites (DHSs) in 45 mouse cell and tissue types, and systematically compared these with human DHS maps from orthologous compartments. We found that the mouse and human genomes have undergone extensive cis-regulatory rewiring that combines branch-specific evolutionary innovation and loss with widespread repurposing of conserved DHSs to alternative cell fates, and that this process is mediated by turnover of transcription factor (TF) recognition elements. Despite pervasive evolutionary remodeling of the location and content of individual cis-regulatory regions, within orthologous mouse and human cell types the global fraction of regulatory DNA bases encoding recognition sites for each TF has been strictly conserved. Our findings provide new insights into the evolutionary forces shaping mammalian regulatory DNA landscapes.

The laboratory mouse *Mus musculus* is the major model organism for mammalian biology and has provided extensive insights into human developmental and disease processes (*1*). At 2.7 Gb, the mouse genome is comparable to the 3.3-Gb human genome in size, structure, and sequence composition (*2*, *3*), and >80% of mouse genes have human orthologs (*1*, *4*). Human-to-mouse transgenic experiments have collectively demonstrated that the mouse is capable of recapitulating salient features of human gene regulation, often with striking precision and even in the case of human genes that lack mouse orthologs (*5*). By contrast, comparative analyses of regulatory regions governing individual gene systems (*6*), as well as the occupancy patterns of several TFs (*7*), have highlighted the potential for cis-regulatory divergence. However, broader efforts to identify and quantify the major forces shaping the evolution of the mammalian cis-regulatory landscape have been hampered by the lack of expansive and highly detailed regulatory DNA maps from diverse cell fates that can be directly compared between mouse and human.

Deoxyribonuclease I (DNase I)–hypersensitive sites (DHSs) mark all major classes of cis-regulatory elements in their cognate cellular context, and systematic delineation of DHSs across human cell types and states has provided fundamental insights into many aspects of genome control (*8*). In conjunction with the Mouse ENCODE Project (*9*), we undertook comprehensive mapping of DHSs in diverse mouse cell and tissue types and systematically compared the resulting maps to those from orthologous and non-orthologous human cells and tissues.

We mapped DHSs in 45 mouse cell and tissue types including adult primary tissues (n = 19), purified adult and primitive primary cells (n = 10), primary embryonic tissues (n = 4), embryonic stem cell lines (n = 4), and model immortalized primary (n = 3) and malignant (n = 5) cell lines (Fig. 1A, fig. S1A, and table S1). We identified between 74,386 and 218,597 DHSs per cell type at a false discovery rate threshold of 1%, and collectively delineated 1,334,703 distinct ~150–base pair DHSs, each of which was detected in one or more mouse cell or tissue types. The genomic distribution of DHSs relative to annotated genes and transcripts was similar to that observed in human (*8*) (fig. S1B). On average, 13.5% of DHSs marked promoters, with the remaining 86.5% distributed across the intronic and intergenic compartments in roughly equal proportions; the vast majority were located within 250 kb of the nearest annotated transcriptional start site (TSS) (fig. S1C). However, average intergenic DHS-to-TSS distances in the mouse genome were markedly compressed (median 48.7 kb versus 91.6 kb for human) relative to genome size (2.7 Gb versus 3.3 Gb), indicating differential rates of genome remodeling within DHS-rich regions (fig. S1D), with a pronounced difference in both size and density of distal elements (fig. S2, A and B).

To gain insight into the evolution of mammalian regulatory DNA, we comprehensively integrated the mouse DHS maps with human maps generated using the same methods from 232 cell or tissue types from the ENCODE Project (n = 103) (*8*) and the Roadmap Epigenomics Project (n = 126) (*10*). These human maps collectively encompass ~3 million distinct DHSs from primary cells, adult and fetal tissues, immortalized and malignant lines, and embryonic stem cells (table S2). We used high-quality pairwise alignments and a conservative reciprocal mapping and filtering strategy to project the genomic sequence underlying all mouse and human DHSs to the other species (Fig. 1, B and C, and fig. S3A). Collectively, 59.5% of mouse DHSs (52.5 to 78.8% per cell type) could be aligned with high confidence to the human genome, of which 35.6% (38.6 to 60% per cell type) coincided with a human DHS (Fig. 1B and table S3). The remaining 23.9% (13 to 22.7% per cell type) may correspond to human DHSs not yet defined, or to human lineage–specific extinction of an ancestral element. In support of the latter, mouse DHSs aligning outside of human DHSs showed excess sequence divergence, as evidenced by fewer alignable or identical nucleotides relative to mouse DHSs that aligned with human DHSs (fig. S3, B and C). A smaller proportion of human DHSs aligned with a mouse DHS (17.3%; fig. S3A and table S4); however, this was largely because there are more than twice as many DHSs identified in human. Given the breadth of mouse and human tissues analyzed, these values suggest upper and lower limits of regulatory DNA conservation between mouse and human.

To trace the evolutionary origins and dynamics of individual regulatory regions, we aligned all mouse and human DHS sequences to >30 vertebrate genomes spanning ~550 million years of evolutionary distance (fig. S4, A and B). Despite the deep sequence conservation of many DHSs, turnover of individual regulatory regions

[1]Department of Genome Sciences, University of Washington, Seattle, WA 98195, USA. [2]Fred Hutchinson Cancer Research Center, Seattle, WA 98109, USA. [3]Division of Medical Genetics, Department of Medicine, University of Washington, Seattle, WA 98195, USA. [4]Department of Biological Structure, University of Washington, Seattle, WA 98195, USA. [5]Immunology Program, Memorial Sloan-Kettering Cancer Center, New York, NY 10065, USA. [6]Howard Hughes Medical Institute. [7]Division of Hematology, Department of Medicine, University of Washington, Seattle, WA 98195, USA. [8]Medical Research Council (MRC) Molecular Haematology Unit, Weatherall Institute of Molecular Medicine, John Radcliffe Hospital, Oxford OX3 9DS, UK. [9]Department of Cell Biology, Albert Einstein College of Medicine, Bronx, NY 10461, USA. [10]Division of Hematology/Oncology, Children's Hospital Boston and Department of Pediatric Oncology, Dana-Farber Cancer Institute, Harvard Stem Cell Institute, Harvard Medical School, Boston, MA 02115, USA. [11]Department of Comparative Medicine, University of Washington, Seattle, WA 98195, USA. [12]Department of Cell and Developmental Biology, Weill Medical College of Cornell University, New York, NY 10065, USA. [13]Department of Radiation Oncology, University of Washington, Seattle, WA 98109, USA. [14]Department of Pediatrics, University of Washington, Seattle, WA 98195, USA. [15]Division of Oncology, Department of Medicine, University of Washington, Seattle, WA 98195, USA.
*Corresponding author. E-mail: jstam@uw.edu

within different branches of the evolutionary tree appeared frequently. Of the 80% of mouse DHS sequences that predate the divergence of humans from a common ancestor, only 58.5% were detectable in human, and comparison of mouse DHSs aligning to a human DHS or to a non-DHS region yielded nearly identical evolutionary profiles (fig. S4, A and B). Overall, the proportion of DHSs that encompassed evolutionarily conserved sequence elements increased with alignability and conservation of DNase I hypersensitivity (fig. S4B). Unexpectedly, however, ~40% of mouse-human shared DHSs lacked conserved sequence elements.

The aforementioned trends are also reflected in patterns of human variation. Analysis of nucleotide diversity (π) within DHSs indicated graded constraint depending on the extent of sequence and DHS conservation (fig. S5A). Notably, mean π within human-specific DHSs approximated that of fourfold synonymous sites within coding regions, compatible with relaxed (but not absent) nucleotide-level constraint. Despite decreased constraint (both evolutionary and recent), human-specific DHSs are significantly enriched (versus all DHSs) in disease- and trait-associated variants identified by genome-wide association studies (fig. S5B; permutation test, $P_{null} < 0.005$). The above results indicate that although mouse-human shared DHSs are collectively under selection over evolutionary time scales and within human populations, the sequence information with the cis-regulatory compartment is continuing to evolve rapidly in both mice and humans.

Whereas the overall density of mouse-human shared DHSs was higher in gene-proximal regions such as promoters, exons, and UTRs (Fig. 1D), the relative proportion of shared DHSs (to all DHSs) increased markedly with distance from the TSS (Fig. 1E and fig. S6). From 10 to 50 kb upstream of the TSS, the proportion of DHSs that are shared with human (average 27%) was lower than the average for intergenic regions (average 31%; Fig. 1E), whereas in far distal regions this proportion increased substantially to a plateau of ~38%. These data suggest that regulatory elements functioning over long range (>100 kb) (*11*) constitute a genomic compartment that may be operationally distinct from a more rapidly evolving gene-proximal region, and hence less buffered against evolutionary alteration.

The genesis of novel regulatory DNA sequences appears to have played a substantial role in shaping the DHS landscape of both mouse and human (Fig. 1B and fig. S2A). More than 50% of the mouse and human genomes consist of repetitive DNA (*2*, *3*), which is proportionately reflected in their respective DHS compartments (fig. S7, A and B). Species-specific DHSs were enriched (relative to all DHSs) for nearly all classes of repetitive elements (fig. S7C), and 5 to 10% of shared DHSs overlapped ancient repeats that predate mouse/human divergence (fig. S7D)—a finding compatible with an important role for transposons in the evolution of mammalian regulatory genomes.

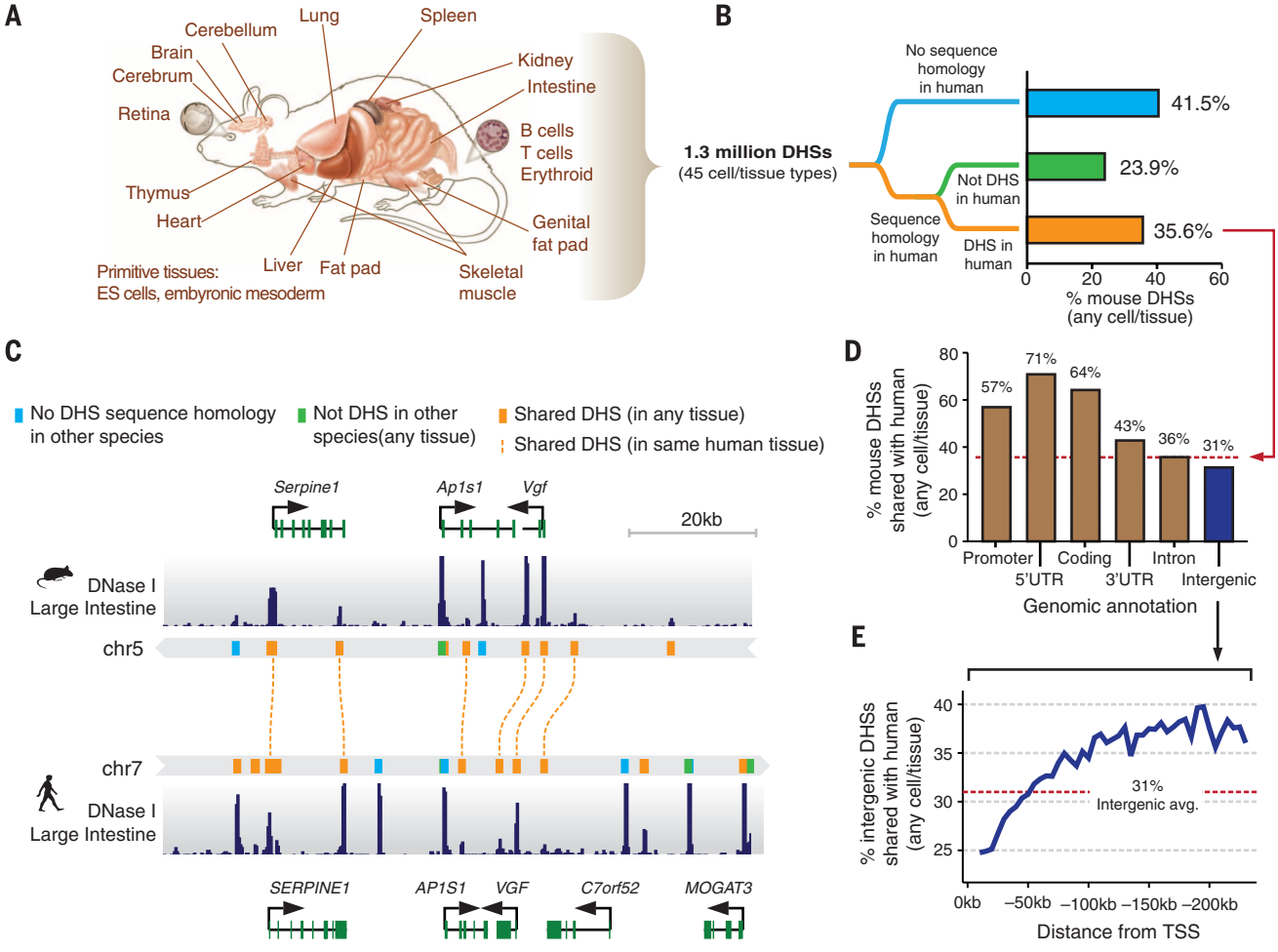


Fig. 1. Conservation of mouse regulatory DNA in humans. (**A**) The accessible landscape of the mouse was derived from 45 tissues and cell types. (**B**) Proportions of the mouse regulatory DNA landscape with sequence homology and functional conservation with human. (**C**) Example of the conservation of the cis-regulatory elements surrounding within the *Vgf/VGF* locus in mouse and human intestine. (**D**) Gene-proximal DHSs are more likely to be conserved than distal DHSs. Dashed red line indicates the average conservation of DHSs. (**E**) The rate of intergenic DHS conservation versus distance to nearest TSS indicates a rapidly evolving cis-regulatory domain.

Transposable elements have recently been implicated in the rapid expansion of TF recognition elements (*12*, *13*). To test the generality of this phenomenon, we estimated the total proportion of TF recognition sequences residing within species-specific DHSs that arose from transposon expansion during mouse and human evolution, which revealed substantial asymmetries (fig. S8, A to C). For example, the recognition motif for the pluripotency factor OCT4 (and other POU family TFs) has been greatly expanded in the murine lineage on a LTR/ERVL element (*12*), accounting for >25% of mouse-specific sites versus <5% in humans with a similar class of retroelement (fig. S8A). By contrast, expansions of CTCF (*13*) and retinoic acid receptor recognition elements (*14*) have been driven chiefly by short interspersed elements (SINEs) in both mouse and human (fig. S8, B and C). These results indicate that expansion of TF recognition sequences by repetitive elements is a general feature shaping mammalian cis-regulatory landscapes.

DHS patterns encode cellular fate and identity in a manner that reflects both current and future regulatory potential and informs an organism's developmental trajectory (*15*). To visualize cell- and tissue-selective activity patterns, we clustered shared DHSs by normalized DNase I cleavage measured in each of the 45 mouse cell and tissue types (Fig. 2A). The vast majority of shared DHSs (78.8%) displayed tissue-selective accessibility and were readily organized into distinct cohorts. A minority (21.2%) exhibited high accessibility across multiple tissue types, whereas <5% were constitutive (Fig. 2B). Tissue-selective shared DHSs were enriched in distal regions (fig. S9) and reflected both tissue organization and anatomic or functional compartments within tissues. For example, the 91,951 shared brain-selective DHSs in turn comprised four subclusters corresponding to distinct anatomical and developmental partitions (Fig. 2A, green box). Similarly, shared blood-selective DHSs were subcompartmentalized into major hematopoietic lineages, including T, B, myeloid, and erythroid cell cohorts (Fig. 2A, red boxes). Across all compartments, cell- or tissue-selective shared DHSs were preferentially localized around genes critical for the development and maintenance of their respective cell or tissue type (fig. S10).

We hypothesized that tissue-selective shared DHSs should encode information critical for basic mammalian regulatory processes such as development and differentiation, and that this would be reflected in their TF recognition sequence content. We thus computed, for each TF, the number of DHSs within each cluster that contained its recognition sequence, and compared this value to the overall distribution of recognition sequences within all shared DHSs. Tissue-selective DHSs showed pronounced enrichment for nearly all known lineage-specifying or cell

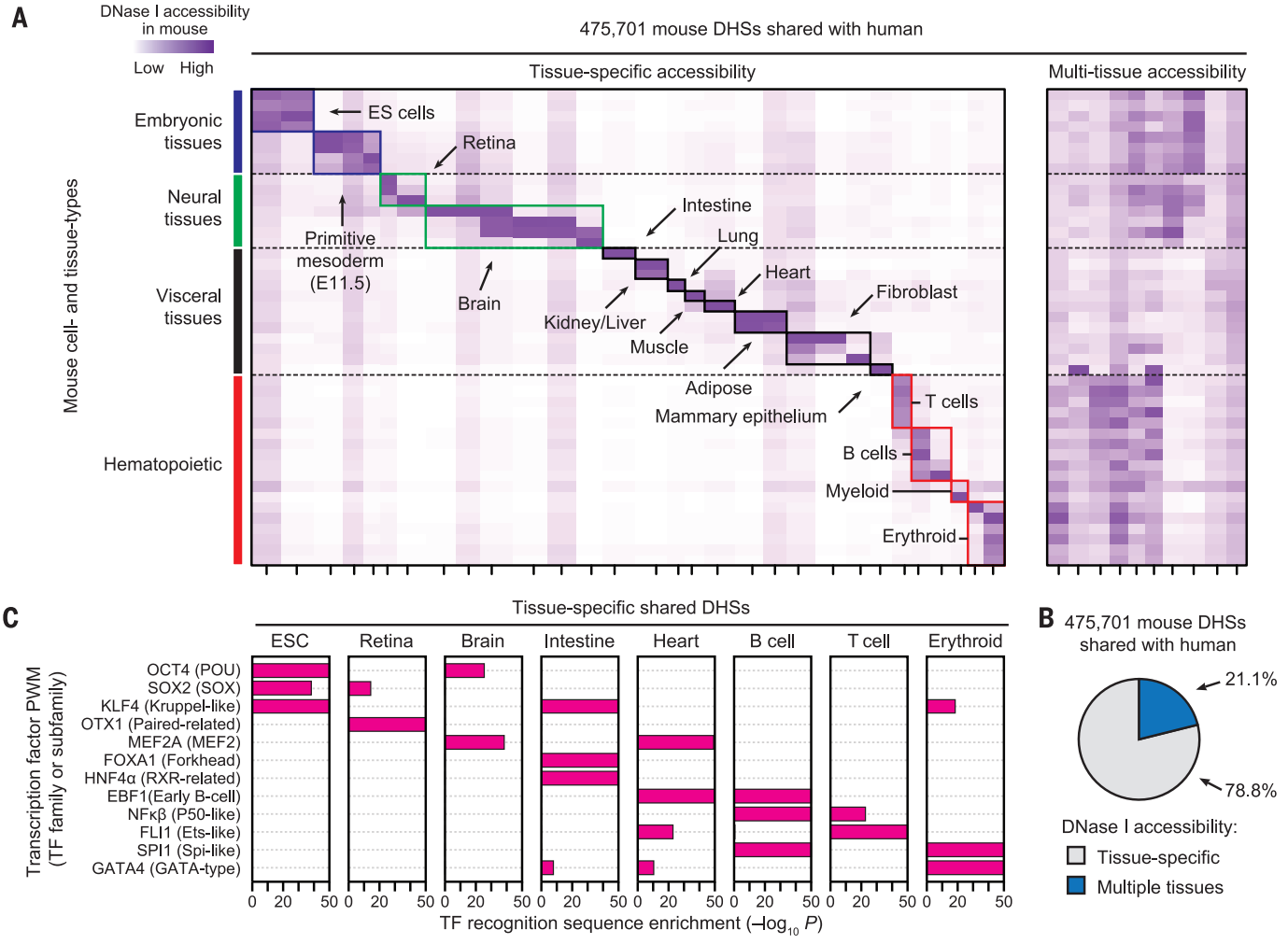


Fig. 2. Cell and tissue lineage encoding within shared regulatory elements. (**A**) *k*-means clustering of DHSs by accessibility at each of the 475,701 mouse DHSs shared with human. Columns correspond clusters of mouse DHSs that are also accessible in human; rows correspond to the 45 mouse cell or tissue types. Colors (axes and boxes) distinguish tissue groupings. Left, tissue-selective clusters; right, clusters containing DHSs active in multiple tissues. (**B**) Proportion of shared DHSs that are tissue-selective or active in multiple tissues. (**C**) Enrichment of TF recognition sequences within tissue-selective DHSs computed using the cumulative hypergeometric distribution.

identity–specifying regulators, which were further organized combinatorially into their respective functional compartments (Fig. 2C and fig. S11). For example, OCT4, SOX2, and KLF4 recognition sites were collectively concentrated within embryonic stem cell–selective shared DHS landscapes, consistent with coordinated expression of their cognate factors in embryonic stem cells. KFL4 recognition sites were also enriched within intestine- and erythroid-specific DHSs, consistent with the known role of Krüppel-like TFs (many of which share the KLF4 recognition sequence) in intestinal epitheliogenesis (*16*) and in erythropoiesis (*17*). Analogously, sequence elements recognized by the cardiac regulators MEF2A, EBF1, FLI1, and GATA4 (*18–20*) were enriched within heart-selective shared DHSs, compatible with important functions for these TFs or their cognates in defining their respective cell fates (*18*, *21*, *22*). Nonetheless, the tissue-selective enrichments we observed are consistent with the known cell-selective activity of TFs even after recognition sequences are systematically grouped by similarity (fig. S11). Together, these results indicate that mouse-human shared DHSs densely encode regulatory information fundamental to diverse cell and tissue specification programs, and thus collectively define a core mammalian regulon.

Because most shared DHSs showed strong cell or tissue selectivity in mouse, we next asked to what degree these patterns were preserved in human. Computing the Jaccard similarity index over all possible combinations of mouse and human cell types revealed surprisingly limited similarity in the tissue-selective usage of shared DHSs (fig. S12, A to C), even when accounting for variability in DNase I cleavage density and peak identification parameters (fig. S13). Unsupervised hierarchical clustering resulted in loose groupings of shared DHSs by cells or tissues derived from the same progenitor or developmental lineage (Fig. 3A).

Weak correspondence between orthologous tissues suggested that a substantial fraction of shared DHSs had undergone functional "repurposing" via alteration of tissue activity patterns from one tissue type in mouse to a different one in human (Fig. 3, B and C). Indeed, analysis of well-matched mouse and human tissue pairs confirmed substantial repurposing ranging from 22.9 to 69% of shared DHSs, depending on the tissue (Fig. 3B). For example, of the 77,060 shared DHSs active in mouse muscle, 59,658 (77.4%) were also DHSs in human muscle; the remaining 17,402 (22.6%) were DHSs in a different human tissue (Fig. 3B, 7th from top). Overall, we found that at least 35.7% of shared DHSs (12.7% of mouse DHSs overall) have undergone repurposing (Fig. 3D), chiefly affecting distal elements (fig. S14). Facile repurposing of regulatory DNA from one tissue context to another thus emerges as an important evolutionary mechanism shaping the mammalian cis-regulatory landscape.

To examine the conservation of individual TF recognition elements within the shared DHS compartment, we distinguished between elements that were positionally conserved versus those that were operationally conserved (i.e., have arisen independently at a different position within the DHS) (fig. S15A). In shared DHSs, 39.1% of TF recognition sequences were positionally conserved and 19.6% were operationally conserved (Fig. 4A). Both positional and operational conservation were significantly concentrated (χ^2 test, $P < 10^{-15}$) within shared DHSs that maintained their tissue activity profile (Fig. 4B and fig. S15B). Surprisingly, 41.3% of shared DHSs (chiefly repurposed DHSs) lacked any positionally or operationally conserved TF recognition elements (Fig. 4, A and B, and fig. S15, C and D). Additionally, the overall density of TF recognition elements did not differ substantially between shared DHSs with positionally, operationally, or nonconserved TFs (fig. S15E). This indicates that new regulatory features are

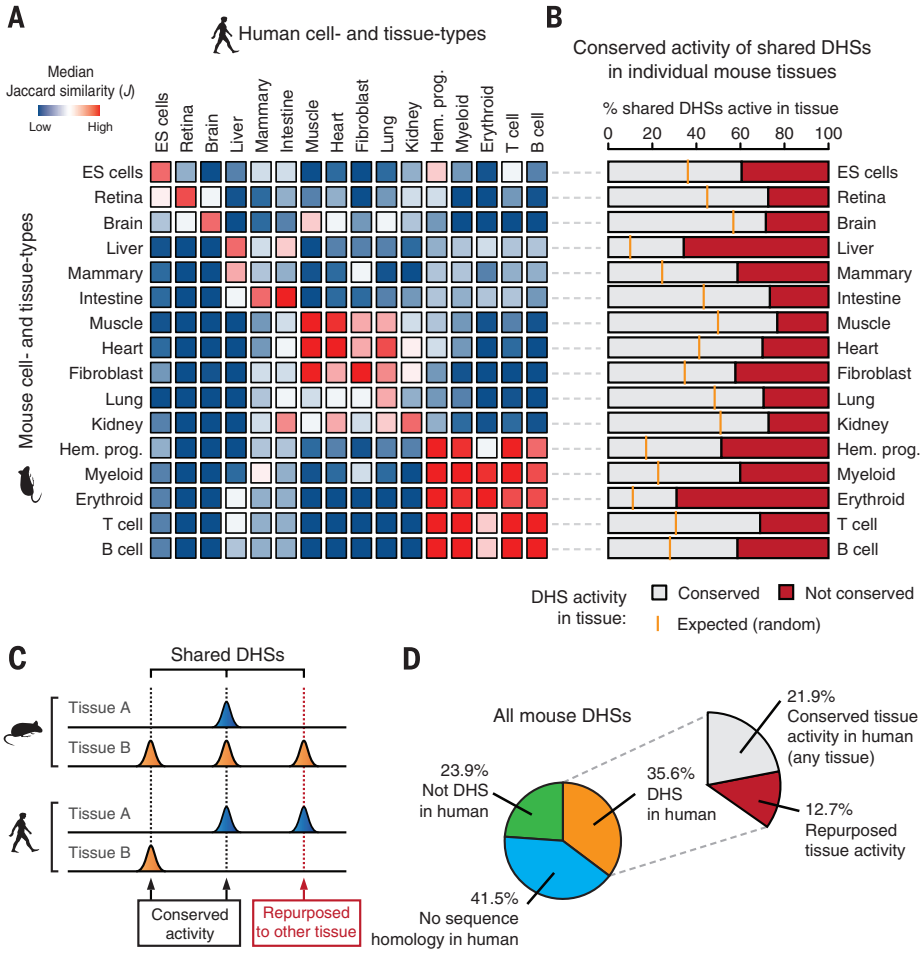


Fig. 3. Conservation and repurposing of regulatory DNA activity. (**A**) Pairwise comparison (median Jaccard distance) of shared DHS landscape usage between all mouse (rows) and human (columns) tissues largely mirrors their conserved morphological and embryological origins. (**B**) Conservation of mouse cis-regulatory DNA accessibility in human for individual tissue types. Orange ticks indicate the expected overlap of randomly selected DHSs. (**C**) The activity patterns of individual shared DHSs during mouse and human evolution may have been conserved (activity in at least one similar tissue) or repurposed to another tissue. (**D**) Overall conservation of tissue-level accessibility patterns of mouse DHSs shared with human.

continuously evolving within the same ancestral DNA segment.

We next elaborated the relationship between conservation of TF recognition sites and the maintenance of tissue accessibility patterns. Reasoning that known regulators of cell fate would play an outsized role in repurposing, we hypothesized that recognition sequences for such TFs would be preferentially maintained (or gained) in DHSs with conserved tissue activity spectra but would be preferentially lost at repurposed DHSs (fig. S16). We found this to be the case across a spectrum of lineage-regulating TFs. For example, recognition sites for the retinal master regulator OTX1 (and other paired-related homeodomain family TFs) within mouse retinal DHSs that had undergone repurposing in human were depleted by a factor of >4 relative to orthologous DHSs that had conserved retinal activity (Fig. 4C). Analogously, sequence elements recognized by the intestinal master regulator HNF1β (and by other POU-homeobox TFs) were selectively depleted in repurposed intestinal DHSs, and those recognized by the major erythroid regulator GATA1 (and by other GATA-type factors) were selectively depleted in repurposed erythroid DHSs (Fig. 4C). Overall, we found that recognition sites for cell fate–modifying TFs were consistently depleted within repurposed DHSs (Fig. 4D), linking the conservation and repurposing of DHSs to preservation versus turnover of specific TF recognition sequences.

The above results also suggest an incremental process whereby the composition of TFs within a given DHS is remodeled over evolutionary time via sequential small mutations (*23*) that could ultimately affect function and phenotype (*24*). The presence of a substantial population of shared DHSs without conserved TF recognition sites but with preserved tissue selectivity patterns highlights the plasticity of individual cis-regulatory templates. Such a finding indicates that the same higher-level regulatory outcome may be encoded by many different combinations of instructive TF recognition events.

To investigate how the marked plasticity of TF recognition elements within the evolving cis-regulatory landscape is reflected in global patterns of the types and quantities of such elements, we computed the global density of recognition sequences for each of 744 TFs within all mouse and human DHSs (separately, and irrespective of conservation status) from each cell or tissue type. This analysis revealed striking conservation of the proportion of the regulatory DNA landscape of each cell type devoted to recognition sites of each TF. Shown in Fig. 5, A and B, are examples for mouse versus human regulatory T cell DHSs and for mouse brain versus human fetal brain. In each case a linear relationship is observed, indicating that the proportion of the DHS compartment devoted to recognition sequences of each of the 744 TFs has been strictly conserved (Fig. 5A). It is noteworthy that this finding obtains across a wide spectrum of TFs that encompass diverse functional roles and biophysical mechanisms of DNA recognition. These findings are in marked contrast to the weak conservation (~25%) of individual mouse regulatory T cell and brain DHSs (Fig. 5, C and D). TF recognition sequence content varied between cell types and between tissue types, with effector TFs selectively enriched within their cognate cell type (fig. S17), and TF recognition sequence density was consistently more similar between orthologous cell or tissue pairs than between non-orthologous cells or tissues (Fig. 5E and fig. S18).

It has been proposed that in large genomes such as mouse and human, maximization of the occupancy of any given TF requires an excess of its recognition sites, so as to ensure high occupancy of sites with critical regulatory roles across a range of TF concentrations (*25*). Consistent with this model, the majority of DHSs in both the mouse and human genomes show relaxed sequence constraint over evolutionary distances (fig. S4C) and within human populations (fig. S5A). This model also predicts that the cis-regulatory programs of TF genes themselves should be more highly conserved than other gene classes. Comparing DHSs within 50 kb of the TSSs of TF genes (n = 911) relative to those of all orthologous genes (n = 14,666 with at least 10 identified DHSs in mouse) revealed an overall increase in the conservation of TF-linked DHSs (Wilcoxon rank sum test, $P < 10^{-15}$) (fig. S19), particularly for DHSs surrounding the TSSs of genes within canonical TF families, such as Hox and Sox factors. As such, TFs are distinguished from other trans-acting regulators in that their activity appears to directly shape their cis-regulatory landscape.

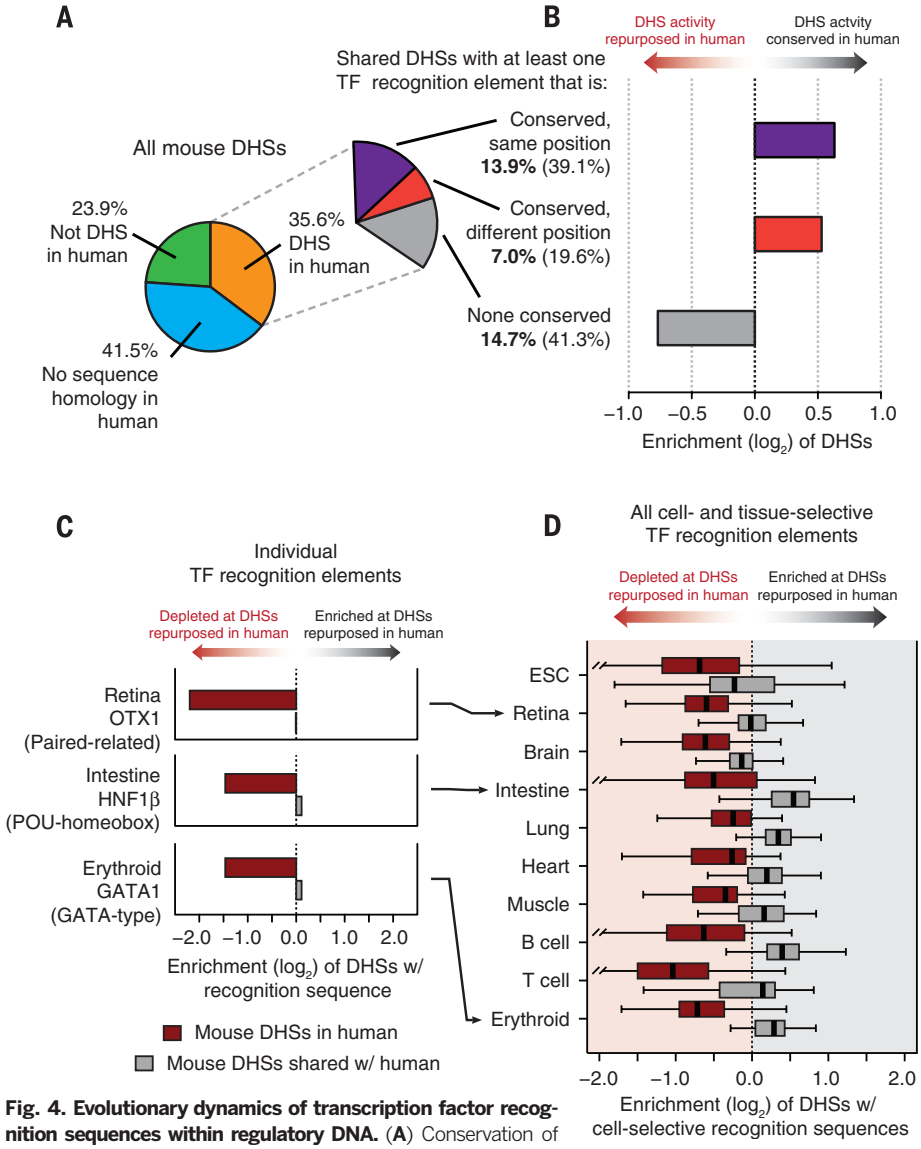


Fig. 4. Evolutionary dynamics of transcription factor recognition sequences within regulatory DNA. (**A**) Conservation of TF recognition sequences within shared DHSs. (**B**) Conserved TF recognition sequences (both positional and operational conservation) are enriched within DHSs that have conserved tissue activity patterns. (**C**) Recognition sequences for cell-selective TFs are preferentially lost at mouse DHSs that are repurposed in human but are maintained or gained in human. Representative examples of individual TF regulators in retina, intestine, and erythroid tissues are shown. (**D**) Same as (C) for recognition sequences of all cell-selective TF regulators (identified in Fig. 2C) within mouse DHSs repurposed in human.

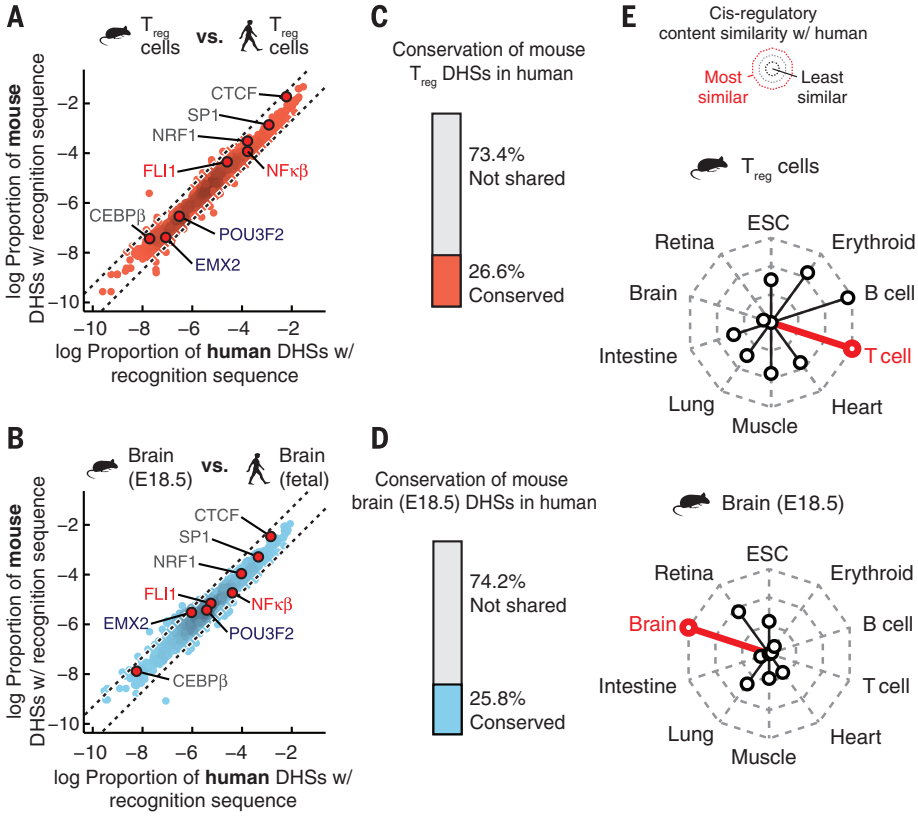


Fig. 5. Conservation of global cis-regulatory content predominates that of individual regulatory elements. (**A**) Density of individual TF recognition sequences in human (*x* axis) and mouse (*y* axis) regulatory T cells. Dotted black lines demarcate a factor of 2 difference in density between mouse and human. (**B**) Same as (A) for human and mouse brain. (**C** and **D**) Proportion of mouse DHSs that are conserved in a matched human tissue. Top, mouse regulatory T cell DHSs that are conserved in human regulatory T cells; bottom, mouse embryonic brain DHSs that are conserved in human fetal brain. (**E**) Radar plots showing the median similarity (Euclidean distance between the distributions of TF recognition sequence densities) of the cis-regulatory content between mouse and human tissues.

Taken together, our results have important implications for understanding the major mechanisms and forces governing the evolution of mammalian regulatory DNA. Performing genomic footprinting on 25 of the cell and tissue samples analyzed herein reveals that the effective in vivo recognition repertoires of human and mouse TFs are highly similar, and that the high turnover of individual TF occupancy sites within regulatory DNA is accompanied by striking evolutionary stability at the level of regulatory networks (*26*). As such, the combination of a highly conserved trans-regulatory environment with a large genome (under weakened selection) may function to potentiate both the de novo creation and the cis-migration of operational TF binding elements. We speculate that high cis-regulatory plasticity may be a key facilitator of mammalian evolution by increasing the potential for innovation of novel functions in the context of an evolutionarily inflexible trans-regulatory environment.

REFERENCES AND NOTES

1. S. N. Hardouin, A. Nagy, *Clin. Genet.* **57**, 237–244 (2000).
2. A. T. Chinwalla *et al.*, *Nature* **420**, 520–562 (2002).
3. E. S. Lander *et al.*, *Nature* **409**, 860–921 (2001).
4. J. L. Guénet, *Genome Res.* **15**, 1729–1740 (2005).
5. K. R. Peterson *et al.*, *Proc. Natl. Acad. Sci. U.S.A.* **90**, 11207–11211 (1993).
6. E. T. Dermitzakis, A. G. Clark, *Mol. Biol. Evol.* **19**, 1114–1121 (2002).
7. D. Schmidt *et al.*, *Science* **328**, 1036–1040 (2010).
8. R. E. Thurman *et al.*, *Nature* **489**, 75–82 (2012).
9. Mouse ENCODE Project Consortium, An integrated and comparative encyclopedia of DNA elements in the mouse genome. *Nature* 10.1038/nature13992 (2014).
10. B. E. Bernstein *et al.*, *Nat. Biotechnol.* **28**, 1045–1048 (2010).
11. L. A. Lettice *et al.*, *Hum. Mol. Genet.* **12**, 1725–1735 (2003).
12. G. Bourque *et al.*, *Genome Res.* **18**, 1752–1762 (2008).
13. D. Schmidt *et al.*, *Cell* **148**, 335–348 (2012).
14. D. Laperriere, T.-T. Wang, J. H. White, S. Mader, *BMC Genomics* **8**, 23 (2007).
15. A. B. Stergachis *et al.*, *Cell* **154**, 888–903 (2013).
16. J. M. Shields, R. J. Christy, V. W. Yang, *J. Biol. Chem.* **271**, 20009–20017 (1996).
17. Q. Xiong *et al.*, *BMC Genomics* **14**, 587 (2013).
18. S. Garel, F. Marín, R. Grosschedl, P. Charnay, *Development* **126**, 5285–5294 (1999).
19. D. G. Edmondson, G. E. Lyons, J. F. Martin, E. N. Olson, *Development* **120**, 1251–1263 (1994).
20. W. Schachterle, A. Rojas, S.-M. Xu, B. L. Black, *Dev. Biol.* **361**, 439–449 (2012).
21. M. K. Anderson, G. Hernandez-Hoyos, R. A. Diamond, E. V. Rothenberg, *Development* **126**, 3131–3148 (1999).
22. M. Merika, S. H. Orkin, *Mol. Cell. Biol.* **13**, 3999–4010 (1993).
23. J. L. Payne, A. Wagner, *Science* **343**, 875–877 (2014).
24. B. Prud'homme *et al.*, *Nature* **440**, 1050–1053 (2006).
25. S. Lin, A. D. Riggs, *Cell* **4**, 107–111 (1975).
26. A. B. Stergachis *et al.*, *Nature* 10.1038/nature13972 (2014).

ACKNOWLEDGMENTS

Supported by NIH grants U54HG007010 (J.A.S.), 1RC2HG005654 (J.A.S. and M.G.), R37DK44746 (M.G. and M.A.B.), and 2R01HD04399709 (L.S.) and by NSF Graduate Research Fellowship DGE-071824 (J.V.). E.E.E. is on the scientific advisory boards for Pacific Biosciences Inc., SynapDx Corp., and DNAnexus Inc. J.V. and J.A.S. designed the experiments and analysis; E.R., R.S., and R.E.T. aided in data analysis and management; all other authors participated in data generation and sample collection; and J.V. and J.A.S. wrote the manuscript with help from E.R. We thank H. Wang and E. K. Salinas for help with figures. All sequence data generated in this study can be accessed with GEO accession numbers found within tables S1 and S2.

SUPPLEMENTARY MATERIALS

www.sciencemag.org/content/346/6212/1007/suppl/DC1
Materials and Methods
Figs. S1 to S19
Tables S1 to S4
References (*27*–*52*)

25 September 2013; accepted 27 October 2014
10.1126/science.1246426

MOUSE GENOMICS

Mouse regulatory DNA landscapes reveal global principles of cis-regulatory evolution

Jeff Vierstra,[1] Eric Rynes,[1] Richard Sandstrom,[1] Miaohua Zhang,[2] Theresa Canfield,[1] R. Scott Hansen,[3] Sandra Stehling-Sun,[1] Peter J. Sabo,[1] Rachel Byron,[2] Richard Humbert,[1] Robert E. Thurman,[1] Audra K. Johnson,[1] Shinny Vong,[1] Kristen Lee,[1] Daniel Bates,[1] Fidencio Neri,[1] Morgan Diegel,[1] Erika Giste,[1] Eric Haugen,[1] Douglas Dunn,[1] Matthew S. Wilken,[4] Steven Josefowicz,[5,6] Robert Samstein,[5,6] Kai-Hsin Chang,[7] Evan E. Eichler,[1,6] Marella De Bruijn,[8] Thomas A. Reh,[4] Arthur Skoultchi,[9] Alexander Rudensky,[5,6] Stuart H. Orkin,[6,10] Thalia Papayannopoulou,[7] Piper M. Treuting,[11] Licia Selleri,[12] Rajinder Kaul,[1,3] Mark Groudine,[2,13] M. A. Bender,[2,14] John A. Stamatoyannopoulos[1,15]*

To study the evolutionary dynamics of regulatory DNA, we mapped >1.3 million deoxyribonuclease I–hypersensitive sites (DHSs) in 45 mouse cell and tissue types, and systematically compared these with human DHS maps from orthologous compartments. We found that the mouse and human genomes have undergone extensive cis-regulatory rewiring that combines branch-specific evolutionary innovation and loss with widespread repurposing of conserved DHSs to alternative cell fates, and that this process is mediated by turnover of transcription factor (TF) recognition elements. Despite pervasive evolutionary remodeling of the location and content of individual cis-regulatory regions, within orthologous mouse and human cell types the global fraction of regulatory DNA bases encoding recognition sites for each TF has been strictly conserved. Our findings provide new insights into the evolutionary forces shaping mammalian regulatory DNA landscapes.

The laboratory mouse *Mus musculus* is the major model organism for mammalian biology and has provided extensive insights into human developmental and disease processes (*1*). At 2.7 Gb, the mouse genome is comparable to the 3.3-Gb human genome in size, structure, and sequence composition (*2*, *3*), and >80% of mouse genes have human orthologs (*1*, *4*). Human-to-mouse transgenic experiments have collectively demonstrated that the mouse is capable of recapitulating salient features of human gene regulation, often with striking precision and even in the case of human genes that lack mouse orthologs (*5*). By contrast, comparative analyses of regulatory regions governing individual gene systems (*6*), as well as the occupancy patterns of several TFs (*7*), have highlighted the potential for cis-regulatory divergence. However, broader efforts to identify and quantify the major forces shaping the evolution of the mammalian cis-regulatory landscape have been hampered by the lack of expansive and highly detailed regulatory DNA maps from diverse cell fates that can be directly compared between mouse and human.

Deoxyribonuclease I (DNase I)–hypersensitive sites (DHSs) mark all major classes of cis-regulatory elements in their cognate cellular context, and systematic delineation of DHSs across human cell types and states has provided fundamental insights into many aspects of genome control (*8*). In conjunction with the Mouse ENCODE Project (*9*), we undertook comprehensive mapping of DHSs in diverse mouse cell and tissue types and systematically compared the resulting maps to those from orthologous and non-orthologous human cells and tissues.

We mapped DHSs in 45 mouse cell and tissue types including adult primary tissues (n = 19), purified adult and primitive primary cells (n = 10), primary embryonic tissues (n = 4), embryonic stem cell lines (n = 4), and model immortalized primary (n = 3) and malignant (n = 5) cell lines (Fig. 1A, fig. S1A, and table S1). We identified between 74,386 and 218,597 DHSs per cell type at a false discovery rate threshold of 1%, and collectively delineated 1,334,703 distinct ~150–base pair DHSs, each of which was detected in one or more mouse cell or tissue types. The genomic distribution of DHSs relative to annotated genes and transcripts was similar to that observed in human (*8*) (fig. S1B). On average, 13.5% of DHSs marked promoters, with the remaining 86.5% distributed across the intronic and intergenic compartments in roughly equal proportions; the vast majority were located within 250 kb of the nearest annotated transcriptional start site (TSS) (fig. S1C). However, average intergenic DHS-to-TSS distances in the mouse genome were markedly compressed (median 48.7 kb versus 91.6 kb for human) relative to genome size (2.7 Gb versus 3.3 Gb), indicating differential rates of genome remodeling within DHS-rich regions (fig. S1D), with a pronounced difference in both size and density of distal elements (fig. S2, A and B).

To gain insight into the evolution of mammalian regulatory DNA, we comprehensively integrated the mouse DHS maps with human maps generated using the same methods from 232 cell or tissue types from the ENCODE Project (n = 103) (*8*) and the Roadmap Epigenomics Project (n = 126) (*10*). These human maps collectively encompass ~3 million distinct DHSs from primary cells, adult and fetal tissues, immortalized and malignant lines, and embryonic stem cells (table S2). We used high-quality pairwise alignments and a conservative reciprocal mapping and filtering strategy to project the genomic sequence underlying all mouse and human DHSs to the other species (Fig. 1, B and C, and fig. S3A). Collectively, 59.5% of mouse DHSs (52.5 to 78.8% per cell type) could be aligned with high confidence to the human genome, of which 35.6% (38.6 to 60% per cell type) coincided with a human DHS (Fig. 1B and table S3). The remaining 23.9% (13 to 22.7% per cell type) may correspond to human DHSs not yet defined, or to human lineage–specific extinction of an ancestral element. In support of the latter, mouse DHSs aligning outside of human DHSs showed excess sequence divergence, as evidenced by fewer alignable or identical nucleotides relative to mouse DHSs that aligned with human DHSs (fig. S3, B and C). A smaller proportion of human DHSs aligned with a mouse DHS (17.3%; fig. S3A and table S4); however, this was largely because there are more than twice as many DHSs identified in human. Given the breadth of mouse and human tissues analyzed, these values suggest upper and lower limits of regulatory DNA conservation between mouse and human.

To trace the evolutionary origins and dynamics of individual regulatory regions, we aligned all mouse and human DHS sequences to >30 vertebrate genomes spanning ~550 million years of evolutionary distance (fig. S4, A and B). Despite the deep sequence conservation of many DHSs, turnover of individual regulatory regions

[1]Department of Genome Sciences, University of Washington, Seattle, WA 98195, USA. [2]Fred Hutchinson Cancer Research Center, Seattle, WA 98109, USA. [3]Division of Medical Genetics, Department of Medicine, University of Washington, Seattle, WA 98195, USA. [4]Department of Biological Structure, University of Washington, Seattle, WA 98195, USA. [5]Immunology Program, Memorial Sloan-Kettering Cancer Center, New York, NY 10065, USA. [6]Howard Hughes Medical Institute. [7]Division of Hematology, Department of Medicine, University of Washington, Seattle, WA 98195, USA. [8]Medical Research Council (MRC) Molecular Haematology Unit, Weatherall Institute of Molecular Medicine, John Radcliffe Hospital, Oxford OX3 9DS, UK. [9]Department of Cell Biology, Albert Einstein College of Medicine, Bronx, NY 10461, USA. [10]Division of Hematology/Oncology, Children's Hospital Boston and Department of Pediatric Oncology, Dana-Farber Cancer Institute, Harvard Stem Cell Institute, Harvard Medical School, Boston, MA 02115, USA. [11]Department of Comparative Medicine, University of Washington, Seattle, WA 98195, USA. [12]Department of Cell and Developmental Biology, Weill Medical College of Cornell University, New York, NY 10065, USA. [13]Department of Radiation Oncology, University of Washington, Seattle, WA 98109, USA. [14]Department of Pediatrics, University of Washington, Seattle, WA 98195, USA. [15]Division of Oncology, Department of Medicine, University of Washington, Seattle, WA 98195, USA.
*Corresponding author. E-mail: jstam@uw.edu

within different branches of the evolutionary tree appeared frequently. Of the 80% of mouse DHS sequences that predate the divergence of humans from a common ancestor, only 58.5% were detectable in human, and comparison of mouse DHSs aligning to a human DHS or to a non-DHS region yielded nearly identical evolutionary profiles (fig. S4, A and B). Overall, the proportion of DHSs that encompassed evolutionarily conserved sequence elements increased with alignability and conservation of DNase I hypersensitivity (fig. S4B). Unexpectedly, however, ~40% of mouse-human shared DHSs lacked conserved sequence elements.

The aforementioned trends are also reflected in patterns of human variation. Analysis of nucleotide diversity (π) within DHSs indicated graded constraint depending on the extent of sequence and DHS conservation (fig. S5A). Notably, mean π within human-specific DHSs approximated that of fourfold synonymous sites within coding regions, compatible with relaxed (but not absent) nucleotide-level constraint. Despite decreased constraint (both evolutionary and recent), human-specific DHSs are significantly enriched (versus all DHSs) in disease- and trait-associated variants identified by genome-wide association studies (fig. S5B; permutation test, $P_{null} < 0.005$). The above results indicate that although mouse-human shared DHSs are collectively under selection over evolutionary time scales and within human populations, the sequence information with the cis-regulatory compartment is continuing to evolve rapidly in both mice and humans.

Whereas the overall density of mouse-human shared DHSs was higher in gene-proximal regions such as promoters, exons, and UTRs (Fig. 1D), the relative proportion of shared DHSs (to all DHSs) increased markedly with distance from the TSS (Fig. 1E and fig. S6). From 10 to 50 kb upstream of the TSS, the proportion of DHSs that are shared with human (average 27%) was lower than the average for intergenic regions (average 31%; Fig. 1E), whereas in far distal regions this proportion increased substantially to a plateau of ~38%. These data suggest that regulatory elements functioning over long range (>100 kb) (*11*) constitute a genomic compartment that may be operationally distinct from a more rapidly evolving gene-proximal region, and hence less buffered against evolutionary alteration.

The genesis of novel regulatory DNA sequences appears to have played a substantial role in shaping the DHS landscape of both mouse and human (Fig. 1B and fig. S2A). More than 50% of the mouse and human genomes consist of repetitive DNA (*2*, *3*), which is proportionately reflected in their respective DHS compartments (fig. S7, A and B). Species-specific DHSs were enriched (relative to all DHSs) for nearly all classes of repetitive elements (fig. S7C), and 5 to 10% of shared DHSs overlapped ancient repeats that predate mouse/human divergence (fig. S7D)—a finding compatible with an important role for transposons in the evolution of mammalian regulatory genomes.

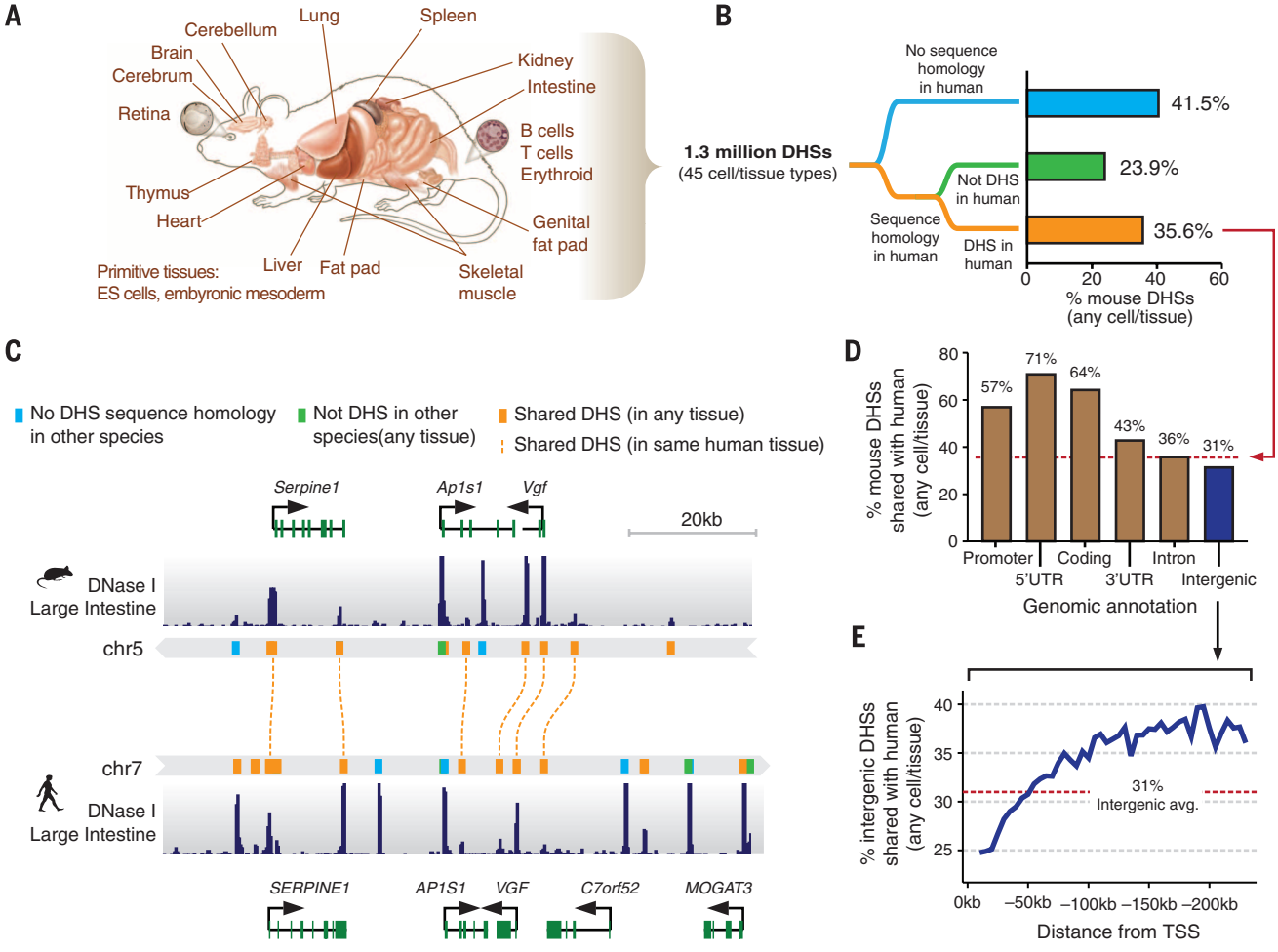


Fig. 1. Conservation of mouse regulatory DNA in humans. (**A**) The accessible landscape of the mouse was derived from 45 tissues and cell types. (**B**) Proportions of the mouse regulatory DNA landscape with sequence homology and functional conservation with human. (**C**) Example of the conservation of the cis-regulatory elements surrounding within the *Vgf/VGF* locus in mouse and human intestine. (**D**) Gene-proximal DHSs are more likely to be conserved than distal DHSs. Dashed red line indicates the average conservation of DHSs. (**E**) The rate of intergenic DHS conservation versus distance to nearest TSS indicates a rapidly evolving cis-regulatory domain.

Transposable elements have recently been implicated in the rapid expansion of TF recognition elements (*12*, *13*). To test the generality of this phenomenon, we estimated the total proportion of TF recognition sequences residing within species-specific DHSs that arose from transposon expansion during mouse and human evolution, which revealed substantial asymmetries (fig. S8, A to C). For example, the recognition motif for the pluripotency factor OCT4 (and other POU family TFs) has been greatly expanded in the murine lineage on a LTR/ERVL element (*12*), accounting for >25% of mouse-specific sites versus <5% in humans with a similar class of retroelement (fig. S8A). By contrast, expansions of CTCF (*13*) and retinoic acid receptor recognition elements (*14*) have been driven chiefly by short interspersed elements (SINEs) in both mouse and human (fig. S8, B and C). These results indicate that expansion of TF recognition sequences by repetitive elements is a general feature shaping mammalian cis-regulatory landscapes.

DHS patterns encode cellular fate and identity in a manner that reflects both current and future regulatory potential and informs an organism's developmental trajectory (*15*). To visualize cell- and tissue-selective activity patterns, we clustered shared DHSs by normalized DNase I cleavage measured in each of the 45 mouse cell and tissue types (Fig. 2A). The vast majority of shared DHSs (78.8%) displayed tissue-selective accessibility and were readily organized into distinct cohorts. A minority (21.2%) exhibited high accessibility across multiple tissue types, whereas <5% were constitutive (Fig. 2B). Tissue-selective shared DHSs were enriched in distal regions (fig. S9) and reflected both tissue organization and anatomic or functional compartments within tissues. For example, the 91,951 shared brain-selective DHSs in turn comprised four subclusters corresponding to distinct anatomical and developmental partitions (Fig. 2A, green box). Similarly, shared blood-selective DHSs were subcompartmentalized into major hematopoietic lineages, including T, B, myeloid, and erythroid cell cohorts (Fig. 2A, red boxes). Across all compartments, cell- or tissue-selective shared DHSs were preferentially localized around genes critical for the development and maintenance of their respective cell or tissue type (fig. S10).

We hypothesized that tissue-selective shared DHSs should encode information critical for basic mammalian regulatory processes such as development and differentiation, and that this would be reflected in their TF recognition sequence content. We thus computed, for each TF, the number of DHSs within each cluster that contained its recognition sequence, and compared this value to the overall distribution of recognition sequences within all shared DHSs. Tissue-selective DHSs showed pronounced enrichment for nearly all known lineage-specifying or cell

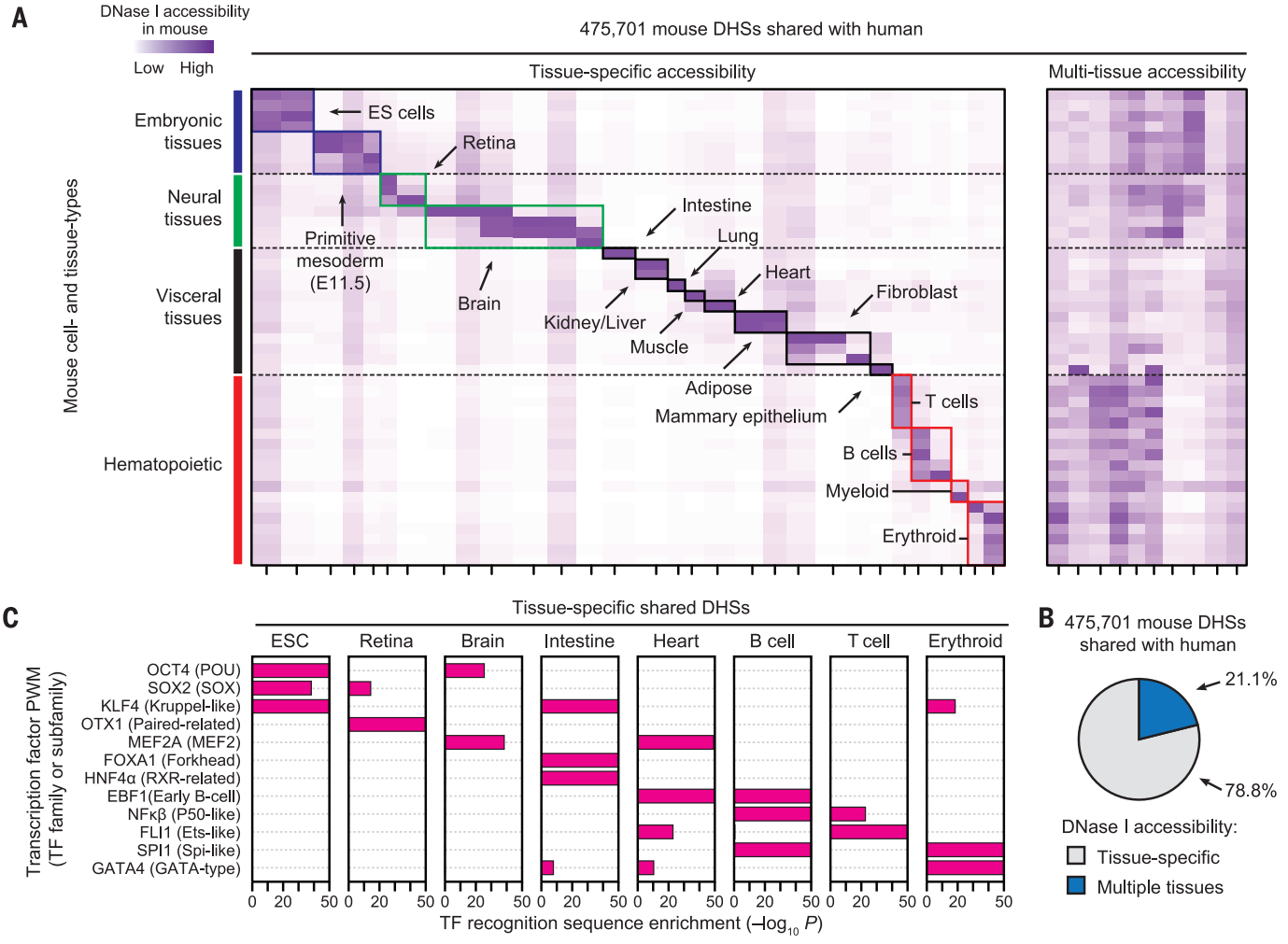


Fig. 2. Cell and tissue lineage encoding within shared regulatory elements. (**A**) *k*-means clustering of DHSs by accessibility at each of the 475,701 mouse DHSs shared with human. Columns correspond clusters of mouse DHSs that are also accessible in human; rows correspond to the 45 mouse cell or tissue types. Colors (axes and boxes) distinguish tissue groupings. Left, tissue-selective clusters; right, clusters containing DHSs active in multiple tissues. (**B**) Proportion of shared DHSs that are tissue-selective or active in multiple tissues. (**C**) Enrichment of TF recognition sequences within tissue-selective DHSs computed using the cumulative hypergeometric distribution.

identity–specifying regulators, which were further organized combinatorially into their respective functional compartments (Fig. 2C and fig. S11). For example, OCT4, SOX2, and KLF4 recognition sites were collectively concentrated within embryonic stem cell–selective shared DHS landscapes, consistent with coordinated expression of their cognate factors in embryonic stem cells. KFL4 recognition sites were also enriched within intestine- and erythroid-specific DHSs, consistent with the known role of Krüppel-like TFs (many of which share the KLF4 recognition sequence) in intestinal epitheliogenesis (*16*) and in erythropoiesis (*17*). Analogously, sequence elements recognized by the cardiac regulators MEF2A, EBF1, FLI1, and GATA4 (*18–20*) were enriched within heart-selective shared DHSs, compatible with important functions for these TFs or their cognates in defining their respective cell fates (*18*, *21*, *22*). Nonetheless, the tissue-selective enrichments we observed are consistent with the known cell-selective activity of TFs even after recognition sequences are systematically grouped by similarity (fig. S11). Together, these results indicate that mouse-human shared DHSs densely encode regulatory information fundamental to diverse cell and tissue specification programs, and thus collectively define a core mammalian regulon.

Because most shared DHSs showed strong cell or tissue selectivity in mouse, we next asked to what degree these patterns were preserved in human. Computing the Jaccard similarity index over all possible combinations of mouse and human cell types revealed surprisingly limited similarity in the tissue-selective usage of shared DHSs (fig. S12, A to C), even when accounting for variability in DNase I cleavage density and peak identification parameters (fig. S13). Unsupervised hierarchical clustering resulted in loose groupings of shared DHSs by cells or tissues derived from the same progenitor or developmental lineage (Fig. 3A).

Weak correspondence between orthologous tissues suggested that a substantial fraction of shared DHSs had undergone functional "repurposing" via alteration of tissue activity patterns from one tissue type in mouse to a different one in human (Fig. 3, B and C). Indeed, analysis of well-matched mouse and human tissue pairs confirmed substantial repurposing ranging from 22.9 to 69% of shared DHSs, depending on the tissue (Fig. 3B). For example, of the 77,060 shared DHSs active in mouse muscle, 59,658 (77.4%) were also DHSs in human muscle; the remaining 17,402 (22.6%) were DHSs in a different human tissue (Fig. 3B, 7th from top). Overall, we found that at least 35.7% of shared DHSs (12.7% of mouse DHSs overall) have undergone repurposing (Fig. 3D), chiefly affecting distal elements (fig. S14). Facile repurposing of regulatory DNA from one tissue context to another thus emerges as an important evolutionary mechanism shaping the mammalian cis-regulatory landscape.

To examine the conservation of individual TF recognition elements within the shared DHS compartment, we distinguished between elements that were positionally conserved versus those that were operationally conserved (i.e., have arisen independently at a different position within the DHS) (fig. S15A). In shared DHSs, 39.1% of TF recognition sequences were positionally conserved and 19.6% were operationally conserved (Fig. 4A). Both positional and operational conservation were significantly concentrated (χ^2 test, $P < 10^{-15}$) within shared DHSs that maintained their tissue activity profile (Fig. 4B and fig. S15B). Surprisingly, 41.3% of shared DHSs (chiefly repurposed DHSs) lacked any positionally or operationally conserved TF recognition elements (Fig. 4, A and B, and fig. S15, C and D). Additionally, the overall density of TF recognition elements did not differ substantially between shared DHSs with positionally, operationally, or nonconserved TFs (fig. S15E). This indicates that new regulatory features are

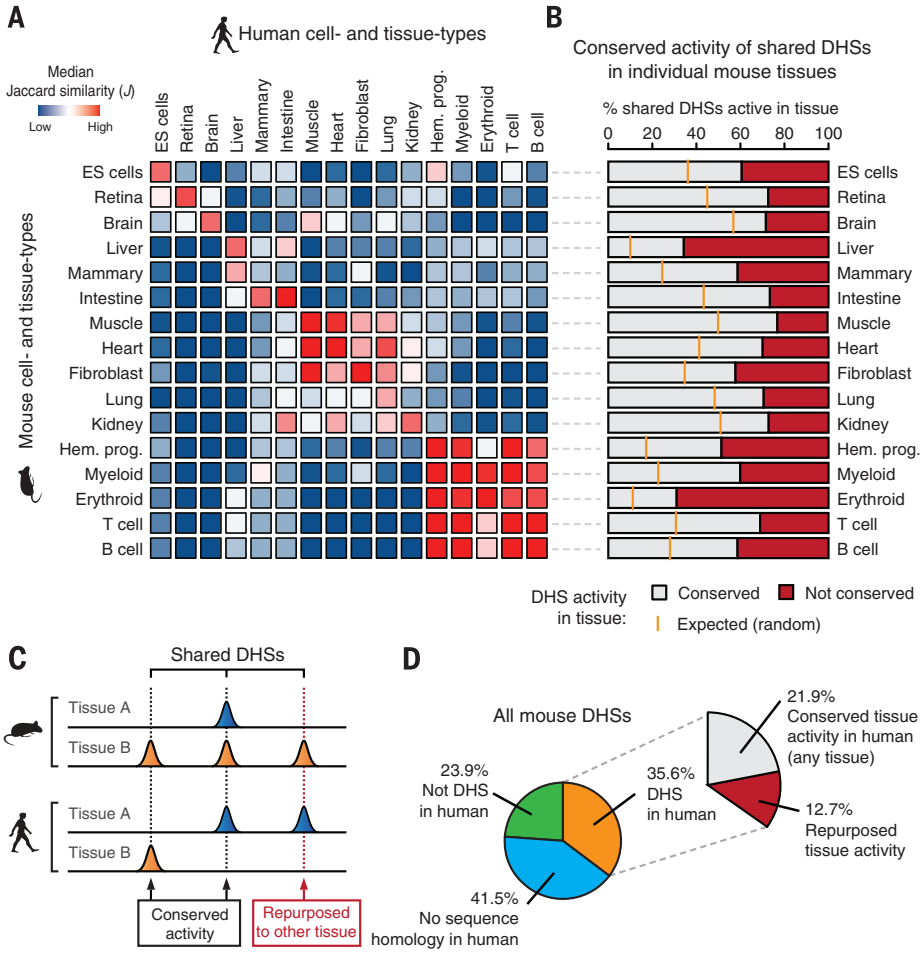


Fig. 3. Conservation and repurposing of regulatory DNA activity. (**A**) Pairwise comparison (median Jaccard distance) of shared DHS landscape usage between all mouse (rows) and human (columns) tissues largely mirrors their conserved morphological and embryological origins. (**B**) Conservation of mouse cis-regulatory DNA accessibility in human for individual tissue types. Orange ticks indicate the expected overlap of randomly selected DHSs. (**C**) The activity patterns of individual shared DHSs during mouse and human evolution may have been conserved (activity in at least one similar tissue) or repurposed to another tissue. (**D**) Overall conservation of tissue-level accessibility patterns of mouse DHSs shared with human.

continuously evolving within the same ancestral DNA segment.

We next elaborated the relationship between conservation of TF recognition sites and the maintenance of tissue accessibility patterns. Reasoning that known regulators of cell fate would play an outsized role in repurposing, we hypothesized that recognition sequences for such TFs would be preferentially maintained (or gained) in DHSs with conserved tissue activity spectra but would be preferentially lost at repurposed DHSs (fig. S16). We found this to be the case across a spectrum of lineage-regulating TFs. For example, recognition sites for the retinal master regulator OTX1 (and other paired-related homeodomain family TFs) within mouse retinal DHSs that had undergone repurposing in human were depleted by a factor of >4 relative to orthologous DHSs that had conserved retinal activity (Fig. 4C). Analogously, sequence elements recognized by the intestinal master regulator HNF1β (and by other POU-homeobox TFs) were selectively depleted in repurposed intestinal DHSs, and those recognized by the major erythroid regulator GATA1 (and by other GATA-type factors) were selectively depleted in repurposed erythroid DHSs (Fig. 4C). Overall, we found that recognition sites for cell fate–modifying TFs were consistently depleted within repurposed DHSs (Fig. 4D), linking the conservation and repurposing of DHSs to preservation versus turnover of specific TF recognition sequences.

The above results also suggest an incremental process whereby the composition of TFs within a given DHS is remodeled over evolutionary time via sequential small mutations (*23*) that could ultimately affect function and phenotype (*24*). The presence of a substantial population of shared DHSs without conserved TF recognition sites but with preserved tissue selectivity patterns highlights the plasticity of individual cis-regulatory templates. Such a finding indicates that the same higher-level regulatory outcome may be encoded by many different combinations of instructive TF recognition events.

To investigate how the marked plasticity of TF recognition elements within the evolving cis-regulatory landscape is reflected in global patterns of the types and quantities of such elements, we computed the global density of recognition sequences for each of 744 TFs within all mouse and human DHSs (separately, and irrespective of conservation status) from each cell or tissue type. This analysis revealed striking conservation of the proportion of the regulatory DNA landscape of each cell type devoted to recognition sites of each TF. Shown in Fig. 5, A and B, are examples for mouse versus human regulatory T cell DHSs and for mouse brain versus human fetal brain. In each case a linear relationship is observed, indicating that the proportion of the DHS compartment devoted to recognition sequences of each of the 744 TFs has been strictly conserved (Fig. 5A). It is noteworthy that this finding obtains across a wide spectrum of TFs that encompass diverse functional roles and biophysical mechanisms of DNA recognition. These findings are in marked contrast to the weak conservation (~25%) of individual mouse regulatory T cell and brain DHSs (Fig. 5, C and D). TF recognition sequence content varied between cell types and between tissue types, with effector TFs selectively enriched within their cognate cell type (fig. S17), and TF recognition sequence density was consistently more similar between orthologous cell or tissue pairs than between non-orthologous cells or tissues (Fig. 5E and fig. S18).

It has been proposed that in large genomes such as mouse and human, maximization of the occupancy of any given TF requires an excess of its recognition sites, so as to ensure high occupancy of sites with critical regulatory roles across a range of TF concentrations (*25*). Consistent with this model, the majority of DHSs in both the mouse and human genomes show relaxed sequence constraint over evolutionary distances (fig. S4C) and within human populations (fig. S5A). This model also predicts that the cis-regulatory programs of TF genes themselves should be more highly conserved than other gene classes. Comparing DHSs within 50 kb of the TSSs of TF genes (n = 911) relative to those of all orthologous genes (n = 14,666 with at least 10 identified DHSs in mouse) revealed an overall increase in the conservation of TF-linked DHSs (Wilcoxon rank sum test, $P < 10^{-15}$) (fig. S19), particularly for DHSs surrounding the TSSs of genes within canonical TF families, such as Hox and Sox factors. As such, TFs are distinguished from other trans-acting regulators in that their activity appears to directly shape their cis-regulatory landscape.

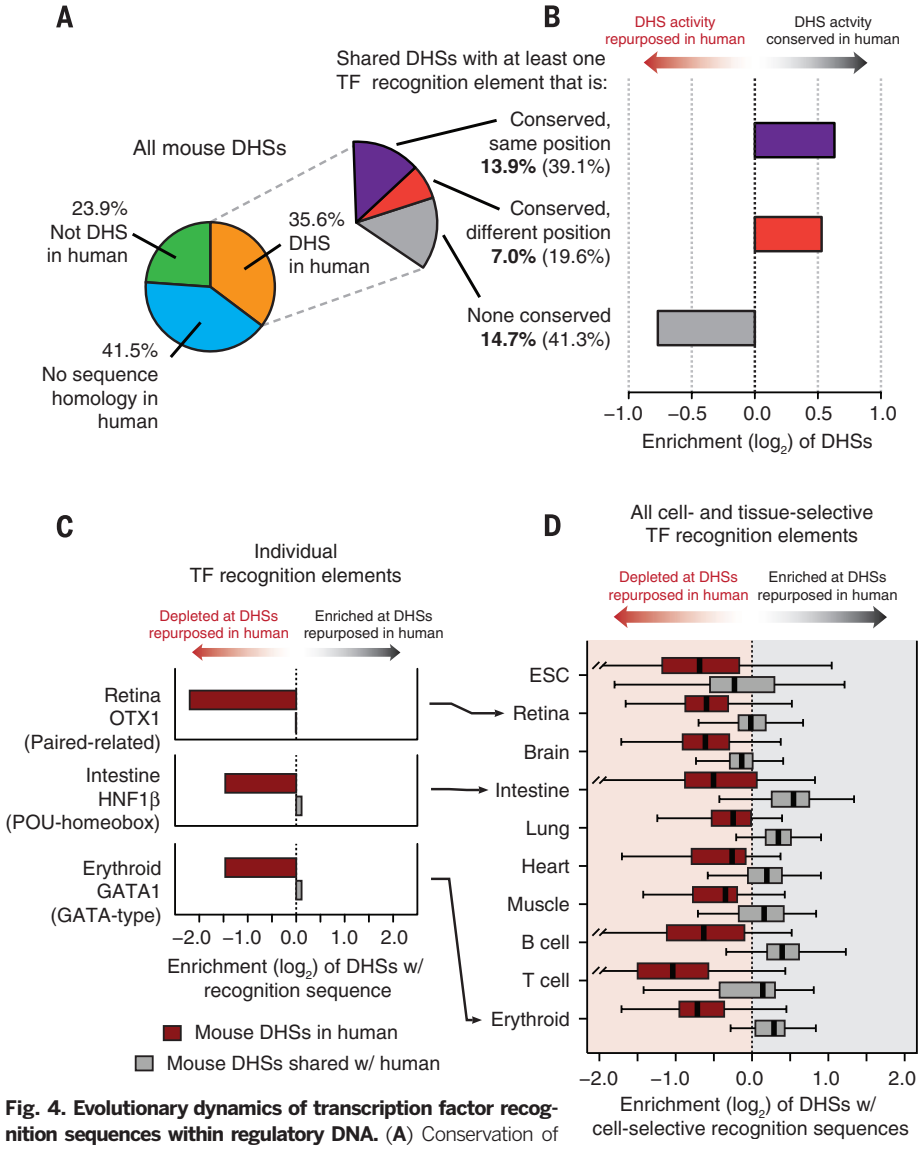


Fig. 4. Evolutionary dynamics of transcription factor recognition sequences within regulatory DNA. (**A**) Conservation of TF recognition sequences within shared DHSs. (**B**) Conserved TF recognition sequences (both positional and operational conservation) are enriched within DHSs that have conserved tissue activity patterns. (**C**) Recognition sequences for cell-selective TFs are preferentially lost at mouse DHSs that are repurposed in human but are maintained or gained in human. Representative examples of individual TF regulators in retina, intestine, and erythroid tissues are shown. (**D**) Same as (C) for recognition sequences of all cell-selective TF regulators (identified in Fig. 2C) within mouse DHSs repurposed in human.

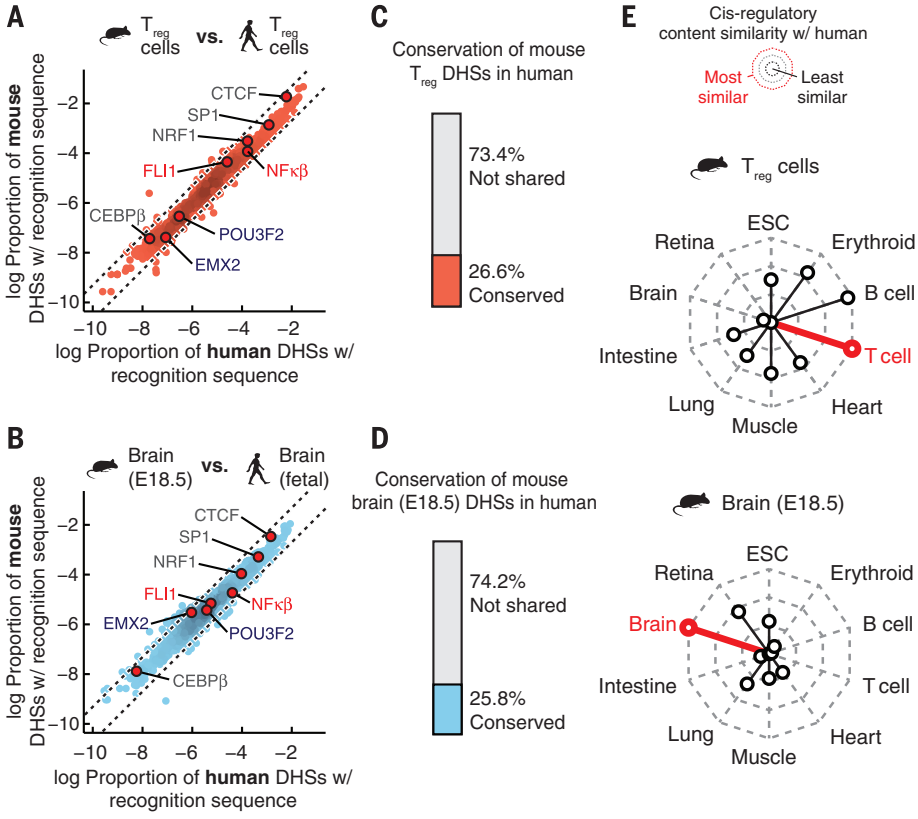


Fig. 5. Conservation of global cis-regulatory content predominates that of individual regulatory elements. (**A**) Density of individual TF recognition sequences in human (*x* axis) and mouse (*y* axis) regulatory T cells. Dotted black lines demarcate a factor of 2 difference in density between mouse and human. (**B**) Same as (A) for human and mouse brain. (**C** and **D**) Proportion of mouse DHSs that are conserved in a matched human tissue. Top, mouse regulatory T cell DHSs that are conserved in human regulatory T cells; bottom, mouse embryonic brain DHSs that are conserved in human fetal brain. (**E**) Radar plots showing the median similarity (Euclidean distance between the distributions of TF recognition sequence densities) of the cis-regulatory content between mouse and human tissues.

Taken together, our results have important implications for understanding the major mechanisms and forces governing the evolution of mammalian regulatory DNA. Performing genomic footprinting on 25 of the cell and tissue samples analyzed herein reveals that the effective in vivo recognition repertoires of human and mouse TFs are highly similar, and that the high turnover of individual TF occupancy sites within regulatory DNA is accompanied by striking evolutionary stability at the level of regulatory networks (*26*). As such, the combination of a highly conserved trans-regulatory environment with a large genome (under weakened selection) may function to potentiate both the de novo creation and the cis-migration of operational TF binding elements. We speculate that high cis-regulatory plasticity may be a key facilitator of mammalian evolution by increasing the potential for innovation of novel functions in the context of an evolutionarily inflexible trans-regulatory environment.

REFERENCES AND NOTES

1. S. N. Hardouin, A. Nagy, *Clin. Genet.* **57**, 237–244 (2000).
2. A. T. Chinwalla *et al.*, *Nature* **420**, 520–562 (2002).
3. E. S. Lander *et al.*, *Nature* **409**, 860–921 (2001).
4. J. L. Guénet, *Genome Res.* **15**, 1729–1740 (2005).
5. K. R. Peterson *et al.*, *Proc. Natl. Acad. Sci. U.S.A.* **90**, 11207–11211 (1993).
6. E. T. Dermitzakis, A. G. Clark, *Mol. Biol. Evol.* **19**, 1114–1121 (2002).
7. D. Schmidt *et al.*, *Science* **328**, 1036–1040 (2010).
8. R. E. Thurman *et al.*, *Nature* **489**, 75–82 (2012).
9. Mouse ENCODE Project Consortium, An integrated and comparative encyclopedia of DNA elements in the mouse genome. *Nature* 10.1038/nature13992 (2014).
10. B. E. Bernstein *et al.*, *Nat. Biotechnol.* **28**, 1045–1048 (2010).
11. L. A. Lettice *et al.*, *Hum. Mol. Genet.* **12**, 1725–1735 (2003).
12. G. Bourque *et al.*, *Genome Res.* **18**, 1752–1762 (2008).
13. D. Schmidt *et al.*, *Cell* **148**, 335–348 (2012).
14. D. Laperriere, T.-T. Wang, J. H. White, S. Mader, *BMC Genomics* **8**, 23 (2007).
15. A. B. Stergachis *et al.*, *Cell* **154**, 888–903 (2013).
16. J. M. Shields, R. J. Christy, V. W. Yang, *J. Biol. Chem.* **271**, 20009–20017 (1996).
17. Q. Xiong *et al.*, *BMC Genomics* **14**, 587 (2013).
18. S. Garel, F. Marín, R. Grosschedl, P. Charnay, *Development* **126**, 5285–5294 (1999).
19. D. G. Edmondson, G. E. Lyons, J. F. Martin, E. N. Olson, *Development* **120**, 1251–1263 (1994).
20. W. Schachterle, A. Rojas, S.-M. Xu, B. L. Black, *Dev. Biol.* **361**, 439–449 (2012).
21. M. K. Anderson, G. Hernandez-Hoyos, R. A. Diamond, E. V. Rothenberg, *Development* **126**, 3131–3148 (1999).
22. M. Merika, S. H. Orkin, *Mol. Cell. Biol.* **13**, 3999–4010 (1993).
23. J. L. Payne, A. Wagner, *Science* **343**, 875–877 (2014).
24. B. Prud'homme *et al.*, *Nature* **440**, 1050–1053 (2006).
25. S. Lin, A. D. Riggs, *Cell* **4**, 107–111 (1975).
26. A. B. Stergachis *et al.*, *Nature* 10.1038/nature13972 (2014).

ACKNOWLEDGMENTS

Supported by NIH grants U54HG007010 (J.A.S.), 1RC2HG005654 (J.A.S. and M.G.), R37DK44746 (M.G. and M.A.B.), and 2R01HD04399709 (L.S.) and by NSF Graduate Research Fellowship DGE-071824 (J.V.). E.E.E. is on the scientific advisory boards for Pacific Biosciences Inc., SynapDx Corp., and DNAnexus Inc. J.V. and J.A.S. designed the experiments and analysis; E.R., R.S., and R.E.T. aided in data analysis and management; all other authors participated in data generation and sample collection; and J.V. and J.A.S. wrote the manuscript with help from E.R. We thank H. Wang and E. K. Salinas for help with figures. All sequence data generated in this study can be accessed with GEO accession numbers found within tables S1 and S2.

SUPPLEMENTARY MATERIALS

www.sciencemag.org/content/346/6212/1007/suppl/DC1
Materials and Methods
Figs. S1 to S19
Tables S1 to S4
References (*27*–*52*)

25 September 2013; accepted 27 October 2014
10.1126/science.1246426



BUT NOTHING COUNTS LIKE THE COUNTESS® II FL AUTOMATED CELL COUNTER

You see the potential in every sample, in every cell. In your work, simplicity, affordability, and flexibility mean more time for discovery.

Count cells in a whole new light with the quantifiably brilliant Countess® II FL Automated Cell Counter.



Everything counts at **lifetechnologies.com/countessII**

life technologies

A Thermo Fisher Scientific Brand

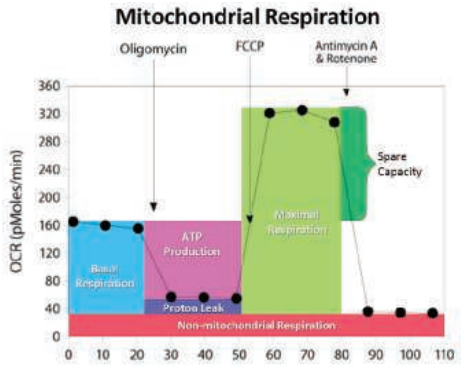
For Research Use Only. Not for use in diagnostic procedures. © 2014 Thermo Fisher Scientific Inc. All rights reserved. All trademarks are the property of Thermo Fisher Scientific and its subsidiaries unless otherwise specified. **CO011895 1014**

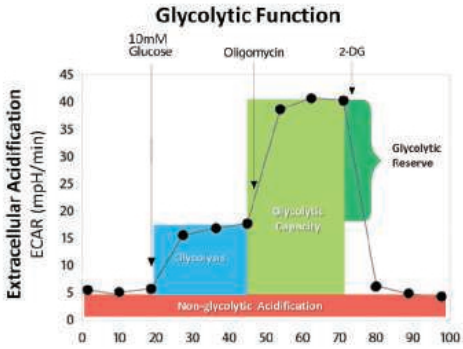
A NEW PERSPECTIVE TO

cancer metabolism research

XF technology provides the easiest and most comprehensive assessment of cancer cell metabolism, measuring glucose and glutamine metabolism, and fatty acid oxidation of cancer cells in a microplate, in real time!

— Kacey Caradonna, Ph.D.,
Application Scientist,
Seahorse Bioscience







The NEW XFp Extracellular Flux Analyzer

With the XFp Analyzer, it is easier than ever to perform functional metabolic measurements in live cells in your own lab. The XFp is designed to perform standard metabolic assays reliably and consistently on your precious samples. The compact format of the XFp Analyzer and XF stress tests make this new platform ideal for pairwise comparisons to validate your genomic or proteomic data.

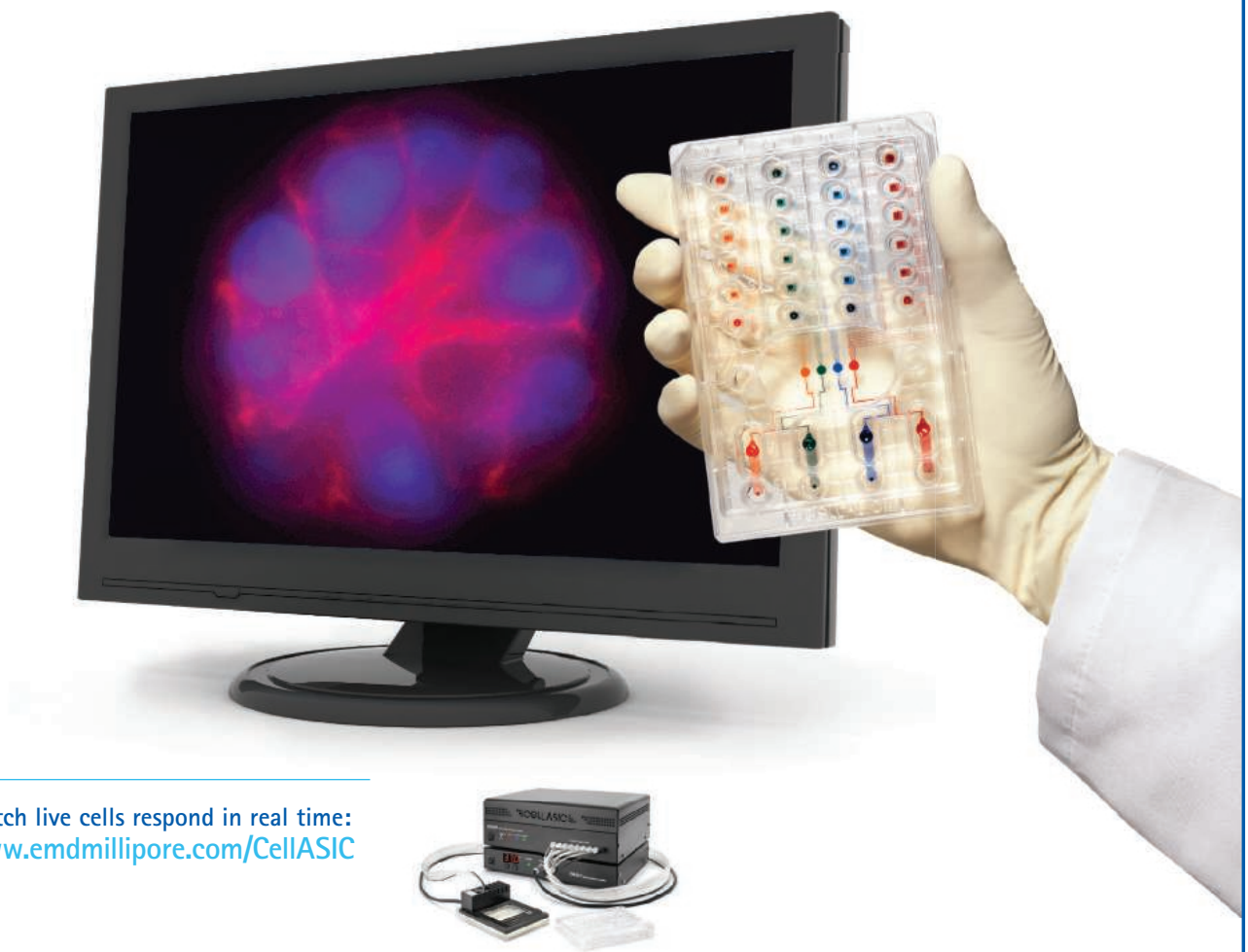
See what's possible.

Scan this QR code to view videos and see what the XF^e Analyzer can achieve.
Visit **www.seahorsebio.com/science** for more information!

Seahorse Bioscience

Take Control
with dynamic cell culture.

Biology is so much more than DMEM/FBS, 37 °C, 5% CO_2.
It's easy to program automated changes to culture media, gas and temperature, while tracking cell responses, with the flexible, intuitive CellASIC® ONIX Microfluidic Platform. By taking control of this truly *in vivo*-like environment, you'll be able to perform dynamic, time-lapse experiments never before possible.



Watch live cells respond in real time:
www.emdmillipore.com/CellASIC

EMD Millipore is a division of Merck KGaA, Darmstadt, Germany

EMD Millipore and the M logo are trademarks and CellASIC is a registered trademark of Merck KGaA, Darmstadt, Germany.
© 2014 EMD Millipore Corporation, Billerica, MA, USA. All rights reserved. BS GEN-14-09917 03/2014

150



BIO-RAD'S DROPLET DIGITAL™ PCR SYSTEMS

Over 150 Peer-Reviewed Droplet Digital PCR (ddPCR™) Publications*

From detection of rare mutations and cancer biomarkers to quantification of gene expression and miniscule viral loads, the QX100™ and QX200™ Droplet Digital PCR Systems have been used to redefine the limits of absolute nucleic acid quantification. With over 150 peer-reviewed publications, ddPCR platforms have outperformed other digital PCR systems by several orders of magnitude. The third generation QX200™ AutoDG™ System now brings automation and scalability to digital PCR.

Visit **bio-rad.com/info/150list** for a full publication list and to learn more.

BIO-RAD

*Based on PubMed data, September 2014.



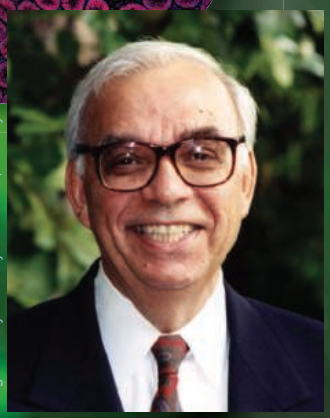


Image courtesy University of California, Berkeley.

Nicholas R. Cozzarelli,
former PNAS Editor-in-Chief.

Call for 2014 Cozzarelli Prize Nominations

The PNAS Editorial Board is now accepting nominations through January 9, 2015 for the 2014 Cozzarelli Prize. This award recognizes scientific excellence and will be given to six papers published in PNAS during 2014.

Nominations should be sent to pnas@nas.edu and should include a citation and brief explanation of the merits of the work. The award recipients will be recognized during the PNAS Editorial Board Meeting and the NAS Annual Meeting Awards Ceremony on April 26, 2015 in Washington, DC.

PNAS
www.pnas.org

For more information and a list of previous winners visit www.pnas.org/site/misc/cozzarelliprize.xhtml.

This person is made up of 20,000 unique proteins.

Want to take a closer look?

For the first time a comprehensive database of 13,000,000 annotated images, mapping the human proteins in all major organs and tissues, all in one place. The Human Protein Atlas (HPA) is a fully searchable database that has taken a team of scientists and IT engineers over 1,000 man years to compile. 20,000 protein coding-genes analyzed with transcriptomics and antibody-based profiling down to the single cell level.

A truly unique resource that is completely free with unrestricted access.

Want to take a closer look yourself?
Then why not search for your favourite protein.
Visit **www.proteinatlas.org**.



THE HUMAN PROTEIN ATLAS

The Keystone Symposia 2015 Meeting Series



Precision Genome Engineering & Synthetic Biology (A1)
Organizers: Philip D. Gregory, Jennifer A. Doudna & Ron Weiss
Jan 11–16, 2015 | Big Sky Resort | Big Sky, Montana | USA

Viral Immunity (A2)
Organizers: Jonathan W. Yewdell, Donna L. Farber, Nicole Baumgarth & Jack R. Bennink
Jan 11–16, 2015 | Beaver Run Resort | Breckenridge, CO | USA

The Biological Code of Signaling – A Tribute to Tony Pawson (F1)
Organizers: Tony Hunter & Rune Linding
Jan 11–16, 2015 | Sheraton Steamboat Resort | Steamboat Springs, CO | USA

Integrating Metabolism & Tumor Biology (J1)
Organizers: Ralph J. DeBerardinis, Robert T. Abraham & Eyal Gottlieb
joint with **PI 3-Kinase Signaling Pathways in Disease (J2)**
Organizers: Lori Friedman, David A. Fruman & Phillip T. Hawkins
Jan 13–18, 2015 | Fairmont Hotel Vancouver | Vancouver, BC | Canada

Immunity to Veterinary Pathogens: Informing Vaccine Development (A3)
Organizers: William T. Golde, Wendy C. Brown & Ivan Morrison
Jan 20–25, 2015 | Keystone Resort | Keystone, CO | USA

Host Response in Tuberculosis (J3)
Organizers: JoAnne L. Flynn & Willem A. Hanekom
joint with **Granulomas in Infectious & Non-Infectious Diseases (J4)**
Organizers: Thomas A. Wynn, Paul Kaye & Vishva M. Dixit
Jan 22–27, 2015 | Santa Fe Community Convention Center | Santa Fe, NM | USA

Epigenetics & Cancer (A4)
Organizers: Tony Kouzarides & Kristian Helin
Jan 25–30, 2015 | Keystone Resort | Keystone, CO | USA

Neuroinflammation in Diseases of the Central Nervous System (A5)
Organizers: Richard M. Ransohoff, Christopher K. Glass & V. Hugh Perry
Jan 25–30, 2015 | Sagebrush Inn & Suites | Taos, NM | USA

Mitochondria, Metabolism & Heart Failure (J5)
Organizers: Richard N. Kitsis, Gerald W. Dorn II & Rong Tian
joint with **Diabetes & Metabolic Dysfunction (J6)**
Organizers: Jeffrey E. Pessin, Alan R. Saltiel & Deborah M. Muoio
Jan 27–Feb 1, 2015 | Santa Fe Community Convention Center | Santa Fe, NM | USA

Autoimmunity & Tolerance (B1)
Organizers: Jane L. Grogan, Joanne L. Viney & Gerald T. Nepom
Feb 3–8, 2015 | Keystone Resort | Keystone, CO | USA

Endoderm Lineages in Development & Disease (B2)
Organizers: Lori Sussel, Hans-Willem E. Snoeck, James M. Wells & Aaron M. Zorn
Feb 8–13, 2015 | Keystone Resort | Keystone, CO | USA

Tumor Immunology: Multidisciplinary Science Driving Combination Therapy (J7)
Organizers: Elizabeth M. Jaffee & Axel Hoos
joint with
Antibodies as Drugs: Immunological Scaffolds as Therapeutics (J8)
Organizers: Pablo Umaña, Mark X. Sliwkowski & Martin J. Glennie
Feb 8–13, 2015 | Fairmont Banff Springs | Banff, AB | Canada

Plant Receptor Kinases: From Molecules to Environment (B3)
Organizers: Cyril Zipfel & Steven C. Huber
Feb 8–13, 2015 | Sagebrush Inn & Suites | Taos, NM | USA

Systems Biology of Lipid Metabolism (B4)
Organizers: Matej Orešič, Antonio J. Vidal-Puig & Ana Maria Cuervo
Feb 9–13, 2015 | Beaver Run Resort | Breckenridge, CO | USA
Deadlines: Discounted Registration – Dec 10

RNA Silencing in Plants (G1)
Organizers: Robert Martienssen & Craig S. Pikaard
Feb 17–22, 2015 | Keystone Resort | Keystone, CO | USA
Deadlines: Discounted Registration – Dec 17

Neuroepigenetics (B5)
Organizers: Hongjun Song & Li-Huei Tsai
Feb 22–26, 2015 | Eldorado Hotel & Spa | Santa Fe, NM | USA
Deadlines: Discounted Registration – Dec 18

Hematopoiesis (B6)
Organizers: Timm Schroeder, Hanna K.A. Mikkola & Patricia Ernst
Feb 22–27, 2015 | Keystone Resort | Keystone, CO | USA
Deadlines: Discounted Registration – Dec 18

Gut Microbiota Modulation of Host Physiology: The Search for Mechanism (C1)
Organizers: Fredrik Bäckhed, Ruth E. Ley & Yasmine Belkaid
Mar 1–6, 2015 | Keystone Resort | Keystone, CO | USA
Deadlines: Abstract – Dec 2 ; Discounted Registration – Jan 5

Heart Disease & Regeneration: Insights from Development (X1)
Organizers: Vincent M. Christoffels, James F. Martin & Deborah L. Yelon
joint with
Cell Biology of the Heart: Beyond the Myocyte-Centric View (X2)
Organizers: Peter Kohl, Robert G. Gourdie & Stefanie Dimmeler
Mar 1–6, 2015 | Copper Mountain Resort | Copper Mountain, CO | USA
Deadlines: Abstract – Dec 3; Discounted Registration – Jan 6

DNA Replication & Recombination (X3)
Organizers: Simon J. Boulton, Karlene A. Cimprich & Stephen D. Bell
joint with **Genomic Instability & DNA Repair (X4)**
Organizers: Daniel Durocher, Jiri Lukas & Agata Smogorzewska
Mar 1–6, 2015 | Whistler Conference Centre | Whistler, BC | Canada
Deadlines: Abstract – Dec 4; Discounted Registration – Jan 7

Hybrid Methods in Structural Biology (C2)
Organizers: Jens Meiler, Patrick Cramer & Ron A. Milligan
Mar 4–8, 2015 | Granlibakken Resort | Tahoe City, CA | USA
Deadlines: Abstract – Dec 9; Discounted Registration – Jan 8

Biology of Sirtuins (C3)
Organizers: Raul Mostoslavsky, Shin-ichiro Imai, Marcia C. Haigis & Eric M. Verdin
Mar 8–12, 2015 | Hilton Santa Fe Historic Plaza Hotel | Santa Fe, NM | USA
Deadlines: Abstract – Dec 9; Discounted Registration – Jan 8

Dendritic Cells & Macrophages Reunited (C4)
Organizers: Jacques F. Banchereau & Siamon Gordon
Mar 8–13, 2015 | Fairmont The Queen Elizabeth | Montreal, QC | Canada
Deadlines: Abstract – Dec 10; Discounted Registration – Jan 9





KEYSTONE SYMPOSIA™
on Molecular and Cellular Biology
Accelerating Life Science Discovery

www.keystonesymposia.org/meetings

PO Box 1630 | Silverthorne, CO 80498 | 1.800.253.0685 | 1.970.262.1230

Optogenetics (C5)
Organizers: Edward S. Boyden, Klaus M. Hahn & Chandra Tucker
Mar 12–16, 2015 | Westin Downtown Denver | Denver, CO | USA
Deadlines: Abstract – Dec 11; Discounted Registration – Jan 13

Co-Infection: A Global Challenge for Disease Control (C6)
Organizers: Rodrigo Corrêa-Oliveira, David Dunne & Andrea Graham
Mar 15–20, 2015 | Centro de Artes e Convenções (UFOP) | Ouro Preto, MG, Brazil
Deadlines: Abstract – Dec 16; Discounted Registration – Jan 14

Long Noncoding RNAs: From Evolution to Function (C7)
Organizers: Leonard Lipovich, Jeannie T. Lee, John L. Rinn & James (Ben) Brown
Mar 15–20, 2015 | Keystone Resort | Keystone, CO | USA
Deadlines: Abstract – Dec 16; Discounted Registration – Jan 15

Pathways of Neurodevelopmental Disorders (C8)
Organizers: Randi J. Hagerman, Mustafa Sahin & Paul J. Hagerman
Mar 16–20, 2015 | Granlibakken Resort | Tahoe City, CA | USA
Deadlines: Abstract – Dec 16; Discounted Registration – Jan 15

HIV Vaccines (X5)
Organizers: Giuseppe Pantaleo, Rafick P. Sekaly & Leonidas Stamatatos
joint with **The Golden Anniversary of B Cell Discovery (X6)**
Organizers: Patrick C. Wilson, Michael P. Cancro & Anne Durandy
Mar 22–27, 2015 | Fairmont Banff Springs | Banff, AB | Canada
Deadlines: Abstract – Dec 17; Discounted Registration – Jan 20

Obesity & the Metabolic Syndrome: Mitochondria & Energy Expenditure (X7)
Organizers: Johan Auwerx, Eleftheria Maratos-Flier & Thomas Langer
joint with
Liver Metabolism & Nonalcoholic Fatty Liver Disease (NAFLD)(X8)
Organizers: Jay D. Horton, Douglas G. Mashek & Brian N. Finck
Mar 22–27, 2015 | Fairmont Chateau Whistler | Whistler, BC | Canada
Deadlines: Abstract – Dec 18; Discounted Registration – Jan 21

Transcriptional & Epigenetic Influences on Stem Cell States (C9)
Organizers: Thomas P. Zwaka, Rudolf Jaenisch & Joanna Wysocka
Mar 23–28, 2015 | Sheraton Steamboat Resort | Steamboat Springs, CO | USA
Deadlines: Abstract – Dec 19; Discounted Registration – Jan 22

Gram-Negative Resistance (D1)
Organizers: Robert E.W. Hancock & Eric D. Brown
Mar 29–Apr 2, 2015 | Granlibakken Resort | Tahoe City, CA | USA
Deadlines: Scholarship/Discounted Abstract – Dec 1; Abstract – Jan 6; Discounted Registration – Jan 27

Viruses & Human Cancer (D2)
Organizers: Charles R.M. Bangham, Thomas F. Schulz & Paul M. Lieberman
Mar 29–Apr 3, 2015 | Big Sky Resort | Big Sky, MT | USA
Deadlines: Scholarship/Discounted Abstract – Dec 2; Abstract – Jan 6; Discounted Registration – Jan 27

T Cells: Regulation & Effector Function (D3)
Organizers: Alexander Y. Rudensky, Dan R. Littman & Kristin A. Hogquist
Mar 29–Apr 3, 2015 | Snowbird Resort | Snowbird, UT | USA
Deadlines: Scholarship/Discounted Abstract – Dec 2; Abstract – Jan 7; Discounted Registration – Jan 28

DNA Methylation (Z1)
Organizers: Alexander Meissner & Dirk Schübeler
joint with **Epigenomics (Z2)**
Organizers: Bing Ren & Daniel Zilberman
Mar 29–Apr 3, 2015 | Keystone Resort | Keystone, CO | USA
Deadlines: Scholarship/Discounted Abstract – Dec 3; Abstract – Jan 8; Discounted Registration – Jan 29

Neural Control of Metabolic Physiology & Diseases (D4)
Organizers: Dongsheng Cai & Martin G. Myers, Jr.
Apr 12–17, 2015 | Snowbird Resort | Snowbird, UT | USA
Deadlines: Scholarship/Discounted Abstract – Dec 4; Abstract – Jan 13; Discounted Registration – Feb 12

Beige & Brown Fat: Basic Biology & Novel Therapeutics (D5)
Organizers: Bruce M. Spiegelman & Sven Enerbäck
Apr 17–22, 2015 | Snowbird Resort | Snowbird, UT | USA
Deadlines: Scholarship/Discounted Abstract – Dec 16; Abstract – Jan 15; Discounted Registration – Feb 18

The Crossroads of Lipid Metabolism & Diabetes (D6)
Organizers: Russell A. DeBose-Boyd, Sudha Biddinger & Alan D. Attie
Apr 19–24, 2015 | Tivoli Hotel & Congress Center | Copenhagen | Denmark
Deadlines: Scholarship/Discounted Abstract – Dec 17; Abstract – Jan 20; Discounted Registration – Feb 18

Innate Immunity & Determinants of Microbial Pathogenesis (Z3)
Organizers: Robert L. Modlin, Jenny P.Y. Ting & Foo Y. Liew
joint with **Mechanisms of Pro-Inflammatory Diseases (Z4)**
Organizers: Virginia Pascual, Mark S. Anderson & Daniel Kastner
Apr 19–24, 2015 | Resort at Squaw Creek | Olympic Valley, CA | USA
Deadlines: Scholarship/Discounted Abstract – Dec 18; Abstract – Jan 21; Discounted Registration – Feb 19

The Human Proteome (D7)
Organizers: Matthias Mann, Mathias Uhlén, Catherine E. Costello & Albert J.R. Heck
Apr 24–29, 2015 | Clarion Hotel Sign | Stockholm | Sweden
Deadlines: Scholarship/Discounted Abstract – Dec 22; Abstract – Jan 27; Discounted Registration – Feb 24

Mechanisms of HIV Persistence: Implications for a Cure (E1)
Organizers: Olivier Lambotte, Steven G. Deeks & Guido Silvestri
Apr 26–May 1, 2015 | Boston Park Plaza | Boston, MA | USA
Deadlines: Global Health Travel Award – Nov 25; Scholarship/Discounted Abstract – Dec 22; Abstract – Jan 28; Discounted Registration – Feb 26

The Arthropod Vector: The Controller of Transmission (E2)
Organizers: Serap Aksoy, Stephen K. Wikel & David S. Schneider
May 12–17, 2015 | Sagebrush Inn & Suites | Taos, NM | USA
Deadlines: Scholarship/Discounted Abstract – Jan 13; Abstract – Feb 11; Discounted Registration – Mar 11

Hypoxia: From Basic Mechanisms to Therapeutics (E3)
Organizers: Cormac T. Taylor, M. Celeste Simon, Sean P. Colgan & Roland H. Wenger
May 12–17, 2015 | Royal Dublin Society | Dublin | Ireland
Deadlines: Scholarship/Discounted Abstract – Jan 13; Abstract – Feb 12; Discounted Registration – Mar 12

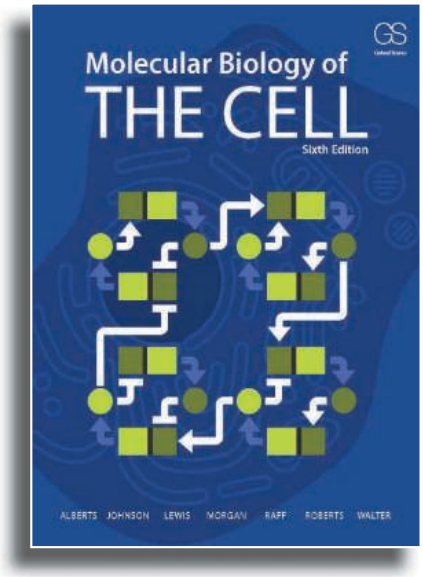
Hippo Pathway: Signaling, Development & Disease (E4)
Organizers: Fernando D. Camargo, Kun-Liang Guan & Helen McNeill
May 17–21, 2015 | Sagebrush Inn & Suites | Taos, NM | USA
Deadlines: Scholarship/Discounted Abstract – Jan 20; Abstract – Feb 19; Discounted Registration – Mar 17

MicroRNAs & Noncoding RNAs in Cancer (E5)
Organizers: Frank J. Slack, Manel Esteller & Lin He
Jun 7–12, 2015 | Keystone Resort | Keystone, CO | USA
Deadlines: Scholarship/Discounted Abstract – Feb 5; Abstract – Mar 5; Discounted Registration – Apr 7

Autophagy (E6)
Organizers: Eric H. Baehrecke & Jayanta Debnath
Jun 19–24, 2015 | Beaver Run Resort | Breckenridge, CO | USA
Deadlines: Scholarship/Discounted Abstract – Feb 17; Abstract – Mar 17; Discounted Registration – Apr 21

Abstracts submitted by the abstract deadline will be considered for short talks. Scholarships are for students/postdoctoral fellows. Scholarship application and discounted abstract deadlines precede meetings by four months, abstract deadlines by three months and discounted registration deadlines by two months. View full, up-to-date meeting programs at **www.keystonesymposia.org** and then **/** and the **program code** (e.g., **www.keystonesymposia/15A1**).

NEW
SIXTH EDITION



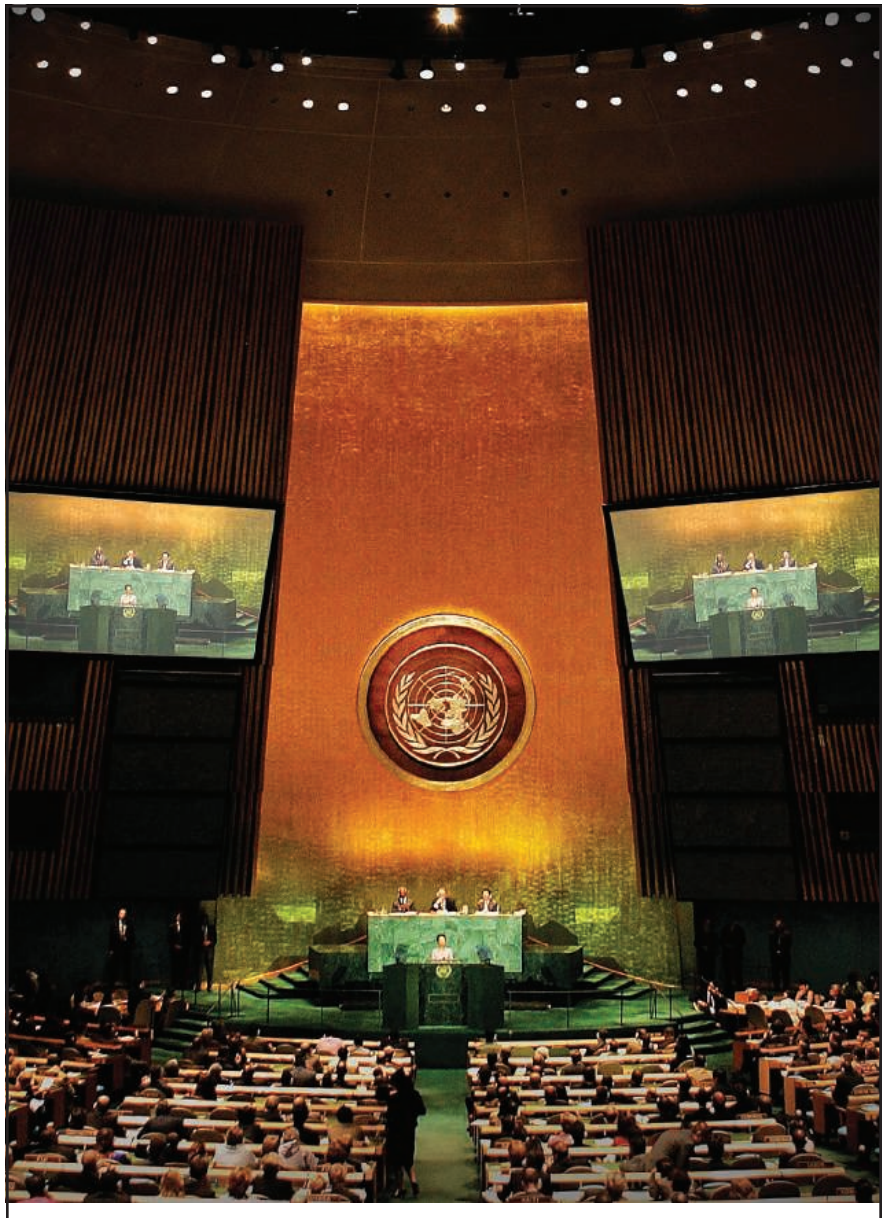
ALBERTS • JOHNSON
LEWIS • MORGAN • RAFF
ROBERTS • WALTER

December 2014
1,464 pp • 1,492 illus
Hardback • 978-0-8153-4432-2

As the amount of information in biology expands dramatically, it becomes increasingly important for textbooks to distill the vast amount of scientific knowledge into concise principles and enduring concepts. As with previous editions, ***Molecular Biology of the Cell*, Sixth Edition** accomplishes this goal with clear writing and beautiful illustrations. The Sixth Edition has been extensively revised and updated with the latest research in the field of cell biology, and it provides an exceptional framework for teaching and learning.

garlandscience.com/mboc6

GS Garland Science
Taylor & Francis Group



AAAS is here – Science Funding, Climate Regulation, Human Rights.

Around the world, governments turn to AAAS as an objective, multidisciplinary scientific authority to educate public officials and judicial figures on today's most pressing issues. And this is just one of the ways that AAAS is committed to advancing science to support a healthy and prosperous world. Join us. Together we can make a difference.

To learn more, visit
aaas.org/plusyou/policy

AAAS + U = Δ



I'm a purist. My work is all about precision, and my samples are precious. There is simply no room for error and no place for substitutes. That's why I choose the most cited and the most trusted brand of reverse transcriptase.

Go super at **lifetechnologies.com/superscript**

life technologies

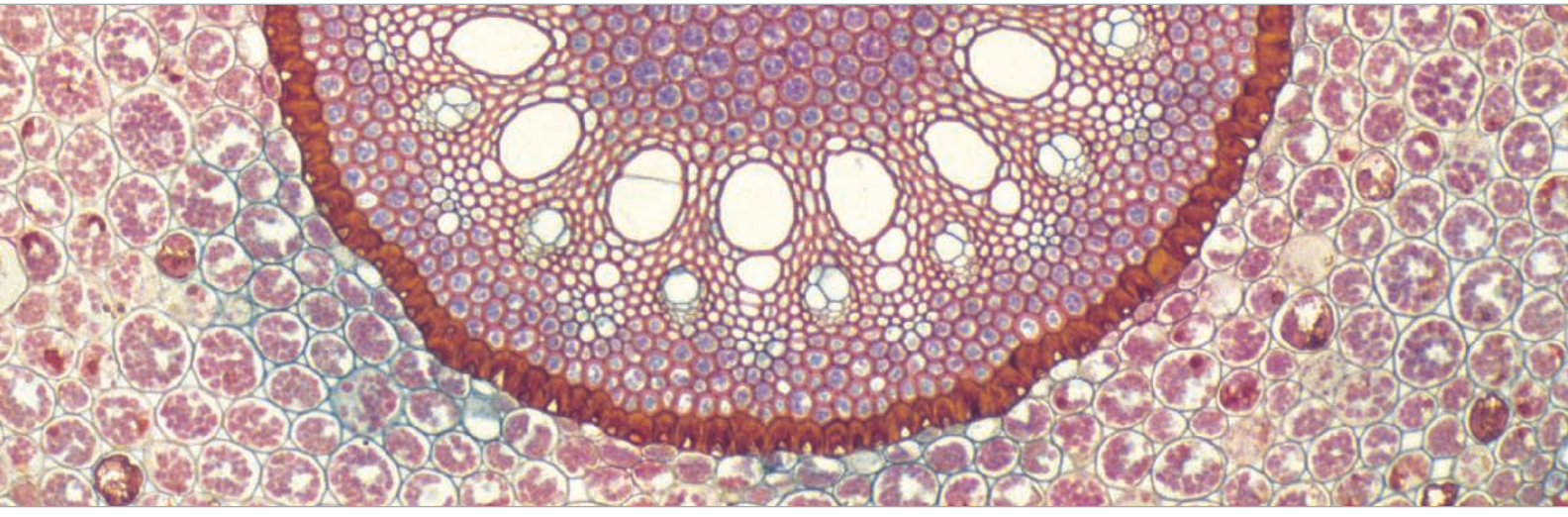
A Thermo Fisher Scientific Brand

© 2014 Thermo Fisher Scientific Inc. All rights reserved.
All trademarks are the property of Thermo Fisher Scientific and its subsidiaries unless otherwise specified. **CO012089 1014**

AAAS

ADVANCING SCIENCE, SERVING SOCIETY

The American Association for the Advancement of Science gratefully acknowledges individuals who have made substantial contributions to sustain our most timely and important activities.



Cross-section of a Corn root stele *(Zea mays)*, a monocot.
Dr. James Richardson/Visuals Unlimited, Inc.

KENNETH A. COWIN

GREGORY S. FERRISS

STEPHEN AND JANELLE FODOR

RICHARD M. FORESTER

GOLDEN FAMILY

BENJAMIN C. HAMMETT

FRED KAVLI

PAULINE P. LEE
IN MEMORY OF BERNARD S. LEE

ALAN I. & AGNES F. LESHNER

LAWRENCE H. LINDEN

GILBERT S. OMENN & MARTHA A. DARLING

CLAIRE E. PERRY

ELLEN SCHERL HARBUS, MD

XIMENA & DANIEL SESSLER
IN MEMORY OF ANDREW M. SESSLER

RUTH BERNSTEIN & JONATHAN SESSLER
IN MEMORY OF ANDREW M. SESSLER

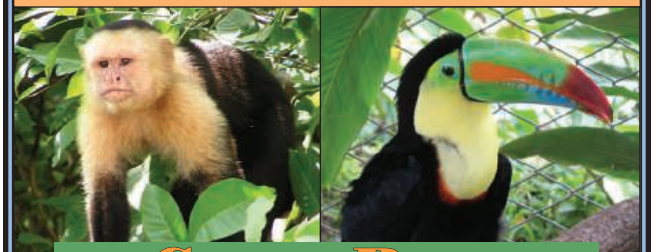
PHILLIP A. SHARP

DAVID EVANS SHAW

WILLIAM F. WARD

THESE DONORS' PLEDGES AND CONTRIBUTIONS WERE RECEIVED BETWEEN NOVEMBER 19, 2013 AND OCTOBER 20, 2014.

AAAS *Travels*



COSTA RICA

Discover Tropical Wildlife and Parks!
February 6-15, 2015

Visit Volcan Poas, with an excellent introduction to the fiery history of an active volcano near San Jose; the Monteverde Cloudforest, a world-renowned mountain reserve cloaked in mists; Carara Biological Reserve, beautifully situated on the Pacific Coast; Braulio Carillo, a montane rainforest park with an aerial tram to view the spectacular rainforest canopy; and charming San Jose, the capital city near the mountainous backbone of Costa Rica. $2,995 pp + air

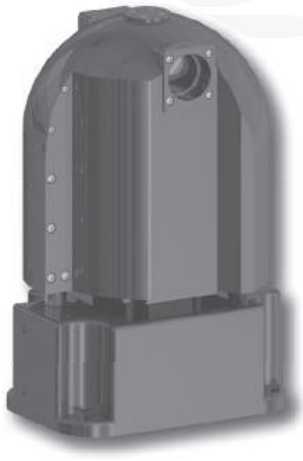
For a detailed brochure, call (800) 252-4910
All prices are per person twin share + air

BETCHART EXPEDITIONS Inc.
17050 Montebello Rd, Cupertino, CA 95014
Email: AAASInfo@betchartexpeditions.com
www.betchartexpeditions.com

LAMBDA VF-5
Tunable filter changer

NEW!

Introducing the world's first filter changer to use tunable thin-film optical filters. The Sutter **LAMBDA VF-5** allows you to quickly access any center bandpass from 330 to 800nm in nanometer increments. Building on the VersaChrome® filters from Semrock®, the **LAMBDA VF-5** maintains transmission over the tuning range of each filter.



Easy Wavelength Selection
- Wavelength range as wide as 330-800nm
- Keypad or computer interface (USB or serial)

Flexible
- Suitable for excitation or emission
- Easily switch between fluorophore combinations
- Optional liquid light guide offers absolute vibration isolation
- Images pass through filters

Thin filter advantage
- High transmission
- Steep spectral edges
- High out-of-band blocking
- Polarization independence (s and p nearly identical)

SUTTER INSTRUMENT

PHONE: 415.883.0128 | FAX: 415.883.0572
EMAIL: INFO@SUTTER.COM | WWW.SUTTER.COM

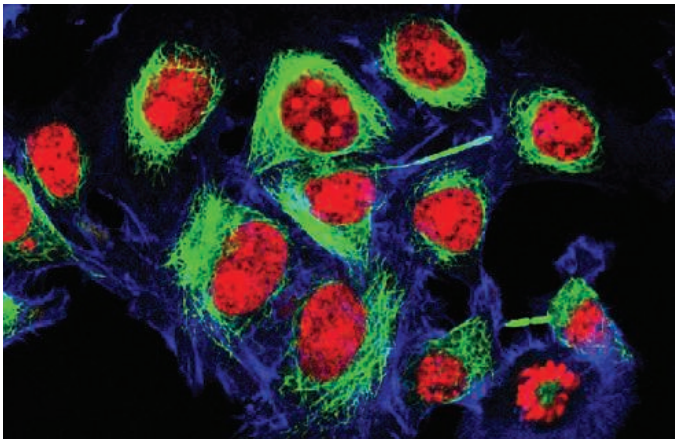
Join the Conversation!

Twitter is a great way to connect with AAAS members and staff about the issues that matter to you most. Be a part of the discussion while staying up-to-date on the latest news and information about your personal member benefits.

Follow us @AAASmember and join the conversation with #AAAS

AAAS MEMBERCENTRAL

MemberCentral.aaas.org



The Art of Culture: Developing Cell Lines

Immortalized cell lines are critical for biomedical research, but establishing new lines can be tricky and frustrating. Researchers who've succeeded at it recommend a combination of old and new tools and techniques. **By Alan Dove**

On February 8, 1951, George Gey of Johns Hopkins University isolated some cells from a cervical cancer biopsy and placed them into a petri dish with some medium. Unlike all of the other cells Gey and his colleagues had tested, these—from a patient named Henrietta Lacks—adapted to their new environment beautifully. Lacks died of her cancer eight months later, but her cells, dubbed HeLa, became the first immortalized cell line, capable of renewing itself in artificial culture indefinitely. In the decades since their isolation, scientists have grown an estimated twenty tons of them.

Meanwhile, researchers have identified numerous ways to transform primary tissues from humans and animals into immortalized cell lines, and now laboratory supply vendors and nonprofit repositories carry hundreds of lines specifically adapted for everything from protein production to virus propagation. Embryonic and induced pluripotent stem cells may get more media attention, but ordinary somatic cell lines still form the backbone of biomedical research.

The selection extends across a zoo of species. "Within [our] general collection, we actually have more than sixty different species, and some are exotic," says Fang Tian, lead scientist and head of the cell biology group at the **American Type Culture Collection** (ATCC) in Manassas, Virginia. ATCC currently holds more than three thousand lines. The **Coriell Institute for Medical Research** in Camden, New Jersey maintains several thousand more, with an emphasis on human lines representing specific diseases.

A problem of scales

Even with thousands of cell lines just a click or phone call away, though, scientists may still find the selection inadequate. That's what happened to Mark Stenglein, a postdoctoral scholar at the **University of California, San Francisco School of Medicine** (UCSF), when he tried to study inclusion body disease (IBD) in snakes.

The project began when a snake enthusiast contacted Joseph DeRisi, Howard Hughes Medical Institute (HHMI) Investigator and professor of biochemistry and biophysics at UCSF and Stenglein's boss. The serpent fan explained that IBD triggers behavioral changes, followed by wasting, secondary infections, and death, and is a major problem in the pet snake trade. Veterinarians had no idea what caused it. Intrigued, DeRisi and Stenglein decided to see if a virus might be responsible.

Working with snake owners and veterinarians, the team performed metagenomic sequencing and uncovered evidence of arenavirus infections in snakes with IBD. The trouble started when Stenglein tried to grow the new viruses. Common arenavirus-friendly mammalian cells didn't work. "There were four reptile cell lines total available at the ATCC, so we ordered all of them," says Stenglein, but the viruses didn't replicate in any of those lines, either.

Through their new veterinary contacts, Stenglein and DeRisi collected tissues from a boa constrictor named Juliet, which had died of lymphoma. Stenglein then tried numerous isolation techniques to immortalize Juliet's cells. "It's sort of one of those multiplication problems, you can start changing conditions and it can get out of control fast," says Stenglein, adding that he had between fifty and a hundred different plates of cells in the incubator at one time. To keep the problem manageable, he minimized as many variables as he could.

For example, he used only one recipe for the cell culture media: minimal essential medium (MEM)—a liquid solution, originally invented by Harry Eagle, which meets the basic requirements for many cells. These days a wide array of other media have been developed to help cater to specific needs, including sensitive and difficult-to-culture cells and lines from different species.

Stenglein also incubated all of the plates at the same temperature, varying only the cell isolation method. The protocol that finally worked involved simply slicing tissues into pieces with scalpels, then immersing them in trypsin overnight. That eventually yielded two new cell lines, one from Juliet's kidneys and one from her spleen.

The new lines have now propagated through continued>

PHOTO: VSHIVKOVA/SHUTTERSTOCK.COM

multiple passages. Using these, the researchers developed a test for the new arenaviruses and used it on snakes with and without IBD. The work showed a strong correlation between arenavirus infection and IBD, suggesting that the viruses may cause the disease.

Stenglein now sees developing new cell lines as simply another laboratory technique that he could use in the future—though he has no immediate plans to do so. "I would only do it if ... I needed it for a project," he says. However, he urges others to consider creating new lines, especially if they work on a species that isn't well represented in the big repositories. "It's not as hard as you might think, it's worth a try if you are in a situation where your research question would benefit from having a [new] cell line."

For those studying reptiles, DeRisi's lab now distributes Juliet's cells to anyone interested in studying or using them. They did offer them to a repository, but were declined.

Repositories of culture

Indeed, researchers who create other lines from "exotic" species may receive similar responses from repositories, chiefly because of funding. "Previously ATCC did have government funding support, so we took whatever researchers requested ... did cell banking, did cell authentication to make sure the line is what it's supposed to be, and expanded them and distributed them worldwide," says Tian. Government funding for the repository ended 20 years ago, though, forcing ATCC to become more selective. Now, the nonprofit organization only adds new lines for which they anticipate high demand and widespread scientific interest.

The Coriell Institute still receives substantial federal funding, but focuses on human and nonhuman primate cells. The institute maintains a trove of several thousand samples that range from umbilical cord blood to clinical isolates from patients with rare genetic diseases.

Besides banking established cell lines, repositories are also at the forefront of creating new ones.

The simplest way to create a new cell line is to modify an existing one, a common strategy when an established line already comes close to meeting the requirements. Cells optimized to grow particular viruses or maximize recombinant protein production often come from such modifications. Establishing an entirely novel cell line can require more exotic techniques. While traditional cut-and-try methods such as those used by Stenglein may work, professional cell line developers constantly look for ways to accelerate the process. Partly as a result of studying lines such as Gey's HeLas, researchers now know that one of the quickest routes to immortalization is through viral infection. For example, the large T antigen from SV40 virus, or the E6 and E7 oncogenes from human papilloma virus, can quickly turn a primary cell culture into an immortalized line.

Because viral oncogenes essentially turn cells into a tumor, they tend to change the cells' characteristics. The available oncogenes also have somewhat restricted ranges, and don't work on all cell types. That's why many cell culture experts are now using a gene called human telomerase reverse transcriptase (hTERT) instead of or in addition to viral oncogenes. Originally developed in 1999, the hTERT technique can yield cells that behave like primary cultures but propagate like immortalized lines.

Tumor samples often need little help becoming immortalized, having already acquired the ability to replicate indefinitely. For lymphoblasts, the easiest method is often infecting the cells with Epstein-Barr virus, which naturally transforms the cells but allows them to maintain much of their normal physiology.

Tian advises researchers who think they need a new cell line to start by reviewing the literature and repository databases. A similar line can often be modified to serve the scientist's needs, which is faster and easier than creating a new line from scratch. If no existing lines seem to come close, the next step is to decide on a general strategy for immortalizing primary cells. "If you want to establish a tumor [line], then a spontaneously established cell line is a big possibility, but if you want to get a non-cancer type normal cell line established, then hTERT ... and viral infection are common tools to use," says Tian.

Companies such as **Applied Biological Materials** in Richmond, British Columbia offer complete kits for immortalizing cells with hTERT, with or without additional oncogenes. BioCat GmbH in Heidelberg, Germany also sells established cell lines and reagents for cell immortalization. Alternatively, researchers can send their primary cells directly to BioCat and let the company develop the cell lines.

Regardless of the specific techniques used to create a new line, the usual problems of any type of cell culture can arise, such as microbial contamination. Mycoplasmas are particularly hard to handle, as they can grow unnoticed in a culture and quietly ruin experiments. Testing kits from ATCC,

Featured Participants

American Type Culture Collection
www.atcc.org

Applied Biological Materials
www.abmgood.com

Coriell Institute for Medical Research
www.coriell.org

Food and Drug Administration
www.fda.gov

Institute of Virology, University of Bonn Medical Center
www.virology-bonn.de

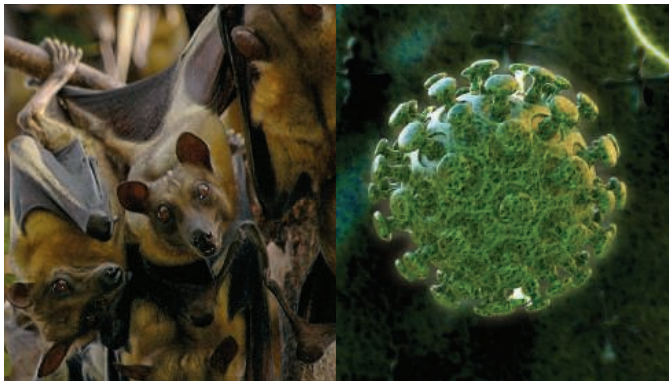
InvivoGen
www.invivogen.com

Lonza
www.lonza.com

Save Lucy Campaign
savelucythebat.org

University of Maryland School of Medicine
medschool.umaryland.edu

University of California, San Francisco
www.ucsf.edu



"Bats are major hosts of maybe the most important virus families regarding airborne transmission, like paramyxoviruses or coronaviruses."

Lonza, and InvivoGen can identify these cryptic invaders. Preventing contamination is even better, and incubator manufacturers have attempted to facilitate this through improved designs with features such as easier to clean surfaces, automatic decontamination cycles, and integrated air filters.

Going to bat

Though clever techniques can sometimes speed the process, each cell line derivation problem will be unique, as Eric Donaldson discovered a few years ago. As a postdoctoral fellow with Matthew Frieman, assistant professor of microbiology and immunology at the **University of Maryland School of Medicine** in Baltimore, Maryland, Donaldson was looking for new coronaviruses. Coronaviruses, the family that includes the causes of severe acute respiratory syndrome (SARS) and Middle East respiratory syndrome (MERS), were thought to be common in bats. Unfortunately, these viruses have been hard to isolate from their natural reservoirs.

Donaldson thought a new bat-derived cell line might help. He quickly discovered that bat biologists are more reserved than the snake enthusiasts that Stenglein worked with. "Bat ecologists are very, very protective of bats, so it took a long time to get my foot in the door," says Donaldson, who is now a virology reviewer for the **U.S. Food and Drug Administration** in Silver Spring, Maryland. He adds that he had to prove to bat biologists that he was interested in helping the animals rather than destroying them.

Eventually, Donaldson and Frieman established a relationship with the **Save Lucy Campaign**, a bat conservation program based in Annandale, Virginia. Whenever a bat was struck by a car or otherwise injured beyond saving, Save Lucy volunteers would contact Donaldson, who would then drive to the campaign's center to harvest tissues from the animal immediately after it died.

Because bats can harbor serious human pathogens, including rabies viruses, the researchers worked with the tissues in a biosafety level (BSL)-2 plus facility with containment cabinets and restricted access. Donaldson used a cell sorter to separate the cells of each tissue, and introduced hTERT and a mouse oncogene called BMI-1 into the cells to try to immortalize them. Most of the experiments, involving multiple tissues from 10 different bats representing four species, failed.

"But when it worked, boy did it work," says Donaldson. He explains that in one experiment "we seeded primary cells on day one, two to three days later the flask was [full of cells]. We had so many cells by the end of four passages we didn't know what to do with them." The team eventually produced three cell lines from three different bat species, and were able to culture novel coronaviruses in the new lines.

Creating new cell lines from three species is impressive, but bats are the most evolutionarily diverse order of mammals, and epidemiologists increasingly suspect that they may be major reservoirs for numerous emerging pathogens. That's why Isabella Eckerle, staff scientist at the **Institute of Virology in the University of Bonn Medical Center** in Bonn, Germany, is trying to establish many more bat cell lines.

Initially, Eckerle encountered the same barrier as Donaldson: bat tissue is hard to get. While working on that problem, she began practicing her tissue culture techniques on pig cells, establishing protocols to turn various primary tissues into immortalized cell lines. She also developed a technique for rapidly freezing cells in the field. "That is something I'm really happy about, so we don't have to go outside and sacrifice bats, but we can connect to already ongoing projects," says Eckerle.

When she finally got some bat tissue, Eckerle and her colleagues created novel lines from the airway epithelia of two bat species representing the two major suborders, Yangochiroptera and Yinpterochiroptera. "Bats are major hosts of maybe the most important virus families regarding airborne transmission, like paramyxoviruses or coronaviruses, or for example influenza viruses have been found in bats recently," says Eckerle. After carefully dissecting the tiny tracheae and establishing primary cultures, she used SV40 T antigen to immortalize them. She and her colleagues are now establishing additional cell lines from other bat tissues and species.

Like others in the field, Eckerle agrees that establishing new cell lines can be frustrating, but she argues that the payoff makes it worthwhile: "Because these models are quite new, there are a lot of things you can do with them."

Alan Dove is a science writer and editor based in Massachusetts.

DOI: 10.1126/science.opms.p1400090

PHOTOS: (FROM LEFT) F. GLOZA-RAUSCH; XRENDOR/SHUTTERSTOCK.COM

Cell Culture Consumables

New Cell Culture Consumables offer a new dimension of safe, reproducible, and reliable cell culture work. Scientists and technical personnel in the field of cell culture have a strong need for easy, safe, and reliable products with improved handling that help prevent contamination. The latest products from Eppendorf deliver exceptional levels of product purity and security, as well as improved, ergonomic and safe handling of cell cultures and advanced protection against contamination. The new, easy resealable packaging concept complements the products' unique features and performance. Eppendorf Cell Culture Consumables are made from ultraclear virgin polystyrene, which complies with USP class VI for highest purity. Cell Culture Consumables have a ISO class /GMP class C clean room production standard and a sterility assurance level (SAL) of 10^{-6} as well as batch specific third-party quality testing ensuring exceptional product and sample safety. Innovative technologies in Eppendorf Cell Culture Consumables deliver ultimate ease of use.

Eppendorf
For info: 800-645-3050
www.eppendorf.com/ccc

Spheroid Culture Microplates

BrandTech Scientific announces the availability of inertGrade microplates for the cultivation of nonadherent cell lines, spheroids, and stem cells in a 96-well plate format. These polystyrene plates are manufactured in one of the largest, most modern cleanroom facilities for laboratory disposable items in the world. Rather than the more common treatments to enhance the natural hydrophobic characteristics of polystyrene, these new microplates are treated with a proprietary hydrogel. This creates a hydrophobic interface between the surface of the plastic and cellular material to inhibit cell and protein attachment. This unique low-binding microplate surface successfully suppresses the adhesion of a wide variety of adherent cell lines, can enhance the formation and maintenance of uniform spheroid cultures, and can inhibit early differentiation of stem cells or neurospheres. InertGrade 96-well microplates are available with round, flat, or curved bottoms in clear, white, black, and colored with transparent bottoms.

BrandTech Scientific
For info: 888-522-2726
www.brandtech.com



Automated Cell Counter

Life science researchers who want to expand their capabilities beyond traditional cell counting instruments can now do so with the Countess II FL, a next generation, benchtop assay instrument with a modular design that broadens the number of applications on a single platform. While most cell counters on the market have been limited to green and red fluorescent protein (GFP/RFP) channels, the new Countess II FL Automated Cell Counter is a three-channel (brightfield and two optional fluorescence channels) system that uses state-of-the-art optics and image analysis to perform assays for cells in suspension, including cell counting, fluorescent protein expression, apoptosis, cell viability, and cell cycle assays. Designed with flexibility in mind, the Countess II FL can also be configured to use a full range of EVOS light cubes that provide more than 13 fluorescence color options. The instrument can operate with a reusable glass chamber slide to reduce the cost of consumables.

Thermo Fisher Scientific
For info: 800-678-5599
www.thermofisher.com

Protein Detection System

The SNAP i.d. 2.0 Protein Detection System for Immunohistochemistry (IHC) represents a much-needed advancement in the IHC workflow. The power of IHC lies in its capacity to localize antigens within tissue samples, thereby identifying the cell types and subcellular compartments in which antigens are located. Traditional immunohistochemistry methods may be subject to process variability; for example, the process typically requires a lot of manual slide handling, as well as the use of pap pens and pipettes. The SNAP i.d. 2.0 Protein Detection System addresses these challenges by systemizing the handling of multiple slides. It decreases slide handling time and enables parallel processing of up to 24 slides at once, reducing slide-to-slide process variation without incurring the costs of automation. In addition, the system speeds wash steps and allows antibodies to be recovered and reused, saving researchers valuable time and resources. The system produces robust and consistent staining, without causing tissue degradation or blotchy artifacts.

EMD Millipore
For info: 800-645-5476
www.emdmillipore.com/snap

Imaging Software

Assisting researchers in gaining a deeper understanding of dynamic biological processes, the new cellSens imaging software (version 1.12) ensures the most efficient use of valuable time-lapse experiments and the latest microscopy hardware. Building on the capabilities introduced by Olympus with its unique Graphical Experiment Manager (GEM) interface, cellSens 1.12 allows the user to truly get in touch with their sample. Enabling effortless setup of complex acquisition sequences and protocols, the GEM presents an intuitive method to seamlessly control motorized hardware, delivering outstanding ease and efficiency for advanced live cell imaging applications. In cellSens 1.12, the GEM has further evolved to maximize the efficiency of multicolor *z*-stacking experiments. Prioritizing the use of fast devices such as piezometric *z*-axis modules reaches a new level of imaging speed, with the freedom to choose the sequence of motorization movements. Enhancing the efficiency of time-lapse applications, the improved GEM also enables investigations into short-term dynamics and long-term sample evolution side by side.

Olympus
For info: +49-402-3773-5913
www.olympus-europa.com/cellsens

Electronically submit your new product description or product literature information! Go to www.sciencemag.org/products/newproducts.dtl for more information.

Newly offered instrumentation, apparatus, and laboratory materials of interest to researchers in all disciplines in academic, industrial, and governmental organizations are featured in this space. Emphasis is given to purpose, chief characteristics, and availability of products and materials. Endorsement by *Science* or AAAS of any products or materials mentioned is not implied. Additional information may be obtained from the manufacturer or supplier.



This is the start of something big.

Science Advances | AAAS

SIGNIFICANT RESEARCH, GLOBAL IMPACT

Introducing *Science Advances* – the new, online-only, open-access journal from *Science* and AAAS. Find out how you can be among the first authors published at **scienceadvances.org.**

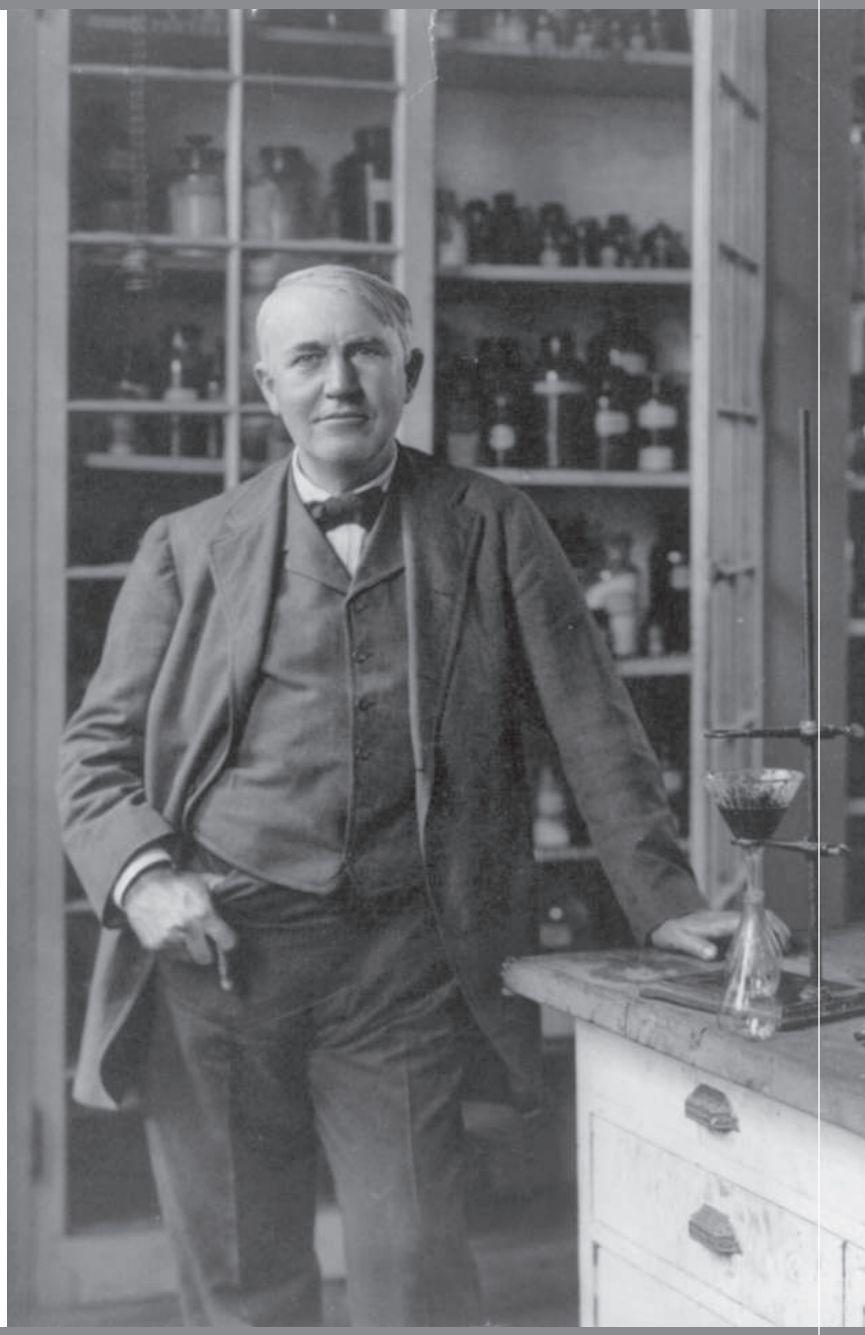
WHAT DO YOU AND THOMAS EDISON HAVE IN COMMON?

AAAS.

By investing in AAAS you join Thomas Edison and the many distinguished individuals whose vision led to the creation of AAAS and our world-renowned journal, *Science,* more than 150 years ago.

Like Edison, you can create a legacy that will last well into the future through planned giving to AAAS. By making AAAS a beneficiary of your will, trust, retirement plan, or life insurance policy, you make a strong investment in our ability to advance science in the service of society for years to come.

To discuss your legacy planning, contact Juli Staiano, Director of Development, at (202) 326-6636, or jstaiano@aaas.org, or visit www.aaas.org/1848 for more information.



1848 SOCIETY
AAAS

"I feel great knowing that I will leave behind a legacy that will be channeled through the AAAS. It also means a lot to me to be able to honor my late parents, too."

–PETER ECKEL
Member, 1848 Society and AAAS Member since 1988



www.cellsignal.com/science125

CST Guide: Pathways and Protocols. From the inception of the antibody as a research tool in the 1890s, to the most up-to-date research, applications, and tools, this is your complete resource for cellular research.

14PADCORPNONE0235END_00

For Research Use Only. Not For Use In Diagnostic Procedures.
© 2014 Cell Signaling Technology, Inc. Cell Signaling Technology® and CST™ are trademarks of Cell Signaling Technology, Inc.

Cell Signaling TECHNOLOGY®

Cell Culture Consumables

New Cell Culture Consumables offer a new dimension of safe, reproducible, and reliable cell culture work. Scientists and technical personnel in the field of cell culture have a strong need for easy, safe, and reliable products with improved handling that help prevent contamination. The latest products from Eppendorf deliver exceptional levels of product purity and security, as well as improved, ergonomic and safe handling of cell cultures and advanced protection against contamination. The new, easy resealable packaging concept complements the products' unique features and performance. Eppendorf Cell Culture Consumables are made from ultraclear virgin polystyrene, which complies with USP class VI for highest purity. Cell Culture Consumables have a ISO class /GMP class C clean room production standard and a sterility assurance level (SAL) of 10^{-6} as well as batch specific third-party quality testing ensuring exceptional product and sample safety. Innovative technologies in Eppendorf Cell Culture Consumables deliver ultimate ease of use.

Eppendorf
For info: 800-645-3050
www.eppendorf.com/ccc

Spheroid Culture Microplates

BrandTech Scientific announces the availability of inertGrade microplates for the cultivation of nonadherent cell lines, spheroids, and stem cells in a 96-well plate format. These polystyrene plates are manufactured in one of the largest, most modern cleanroom facilities for laboratory disposable items in the world. Rather than the more common treatments to enhance the natural hydrophobic characteristics of polystyrene, these new microplates are treated with a proprietary hydrogel. This creates a hydrophobic interface between the surface of the plastic and cellular material to inhibit cell and protein attachment. This unique low-binding microplate surface successfully suppresses the adhesion of a wide variety of adherent cell lines, can enhance the formation and maintenance of uniform spheroid cultures, and can inhibit early differentiation of stem cells or neurospheres. InertGrade 96-well microplates are available with round, flat, or curved bottoms in clear, white, black, and colored with transparent bottoms.

BrandTech Scientific
For info: 888-522-2726
www.brandtech.com



Automated Cell Counter

Life science researchers who want to expand their capabilities beyond traditional cell counting instruments can now do so with the Countess II FL, a next generation, benchtop assay instrument with a modular design that broadens the number of applications on a single platform. While most cell counters on the market have been limited to green and red fluorescent protein (GFP/RFP) channels, the new Countess II FL Automated Cell Counter is a three-channel (brightfield and two optional fluorescence channels) system that uses state-of-the-art optics and image analysis to perform assays for cells in suspension, including cell counting, fluorescent protein expression, apoptosis, cell viability, and cell cycle assays. Designed with flexibility in mind, the Countess II FL can also be configured to use a full range of EVOS light cubes that provide more than 13 fluorescence color options. The instrument can operate with a reusable glass chamber slide to reduce the cost of consumables.

Thermo Fisher Scientific
For info: 800-678-5599
www.thermofisher.com

Protein Detection System

The SNAP i.d. 2.0 Protein Detection System for Immunohistochemistry (IHC) represents a much-needed advancement in the IHC workflow. The power of IHC lies in its capacity to localize antigens within tissue samples, thereby identifying the cell types and subcellular compartments in which antigens are located. Traditional immunohistochemistry methods may be subject to process variability; for example, the process typically requires a lot of manual slide handling, as well as the use of pap pens and pipettes. The SNAP i.d. 2.0 Protein Detection System addresses these challenges by systemizing the handling of multiple slides. It decreases slide handling time and enables parallel processing of up to 24 slides at once, reducing slide-to-slide process variation without incurring the costs of automation. In addition, the system speeds wash steps and allows antibodies to be recovered and reused, saving researchers valuable time and resources. The system produces robust and consistent staining, without causing tissue degradation or blotchy artifacts.

EMD Millipore
For info: 800-645-5476
www.emdmillipore.com/snap

Imaging Software

Assisting researchers in gaining a deeper understanding of dynamic biological processes, the new cellSens imaging software (version 1.12) ensures the most efficient use of valuable time-lapse experiments and the latest microscopy hardware. Building on the capabilities introduced by Olympus with its unique Graphical Experiment Manager (GEM) interface, cellSens 1.12 allows the user to truly get in touch with their sample. Enabling effortless setup of complex acquisition sequences and protocols, the GEM presents an intuitive method to seamlessly control motorized hardware, delivering outstanding ease and efficiency for advanced live cell imaging applications. In cellSens 1.12, the GEM has further evolved to maximize the efficiency of multicolor *z*-stacking experiments. Prioritizing the use of fast devices such as piezometric *z*-axis modules reaches a new level of imaging speed, with the freedom to choose the sequence of motorization movements. Enhancing the efficiency of time-lapse applications, the improved GEM also enables investigations into short-term dynamics and long-term sample evolution side by side.

Olympus
For info: +49-402-3773-5913
www.olympus-europa.com/cellsens

Electronically submit your new product description or product literature information! Go to www.sciencemag.org/products/newproducts.dtl for more information.

Newly offered instrumentation, apparatus, and laboratory materials of interest to researchers in all disciplines in academic, industrial, and governmental organizations are featured in this space. Emphasis is given to purpose, chief characteristics, and availability of products and materials. Endorsement by *Science* or AAAS of any products or materials mentioned is not implied. Additional information may be obtained from the manufacturer or supplier.

Downloaded from www.sciencemag.org on November 22, 2014



Science Careers Advertising

For full advertising details, go to ScienceCareers.org and click For Employers, or call one of our representatives.

Tracy Holmes
Worldwide Associate Director
Science Careers
Phone: +44 (0) 1223 326525

THE AMERICAS

E-mail: advertise@sciencecareers.org
Fax: 202 289 6742

Tina Burks
Phone: 202 326 6577

Nancy Toema
Phone: 202 326 6578

Marci Gallun
Sales Administrator
Phone: 202 326 6582

Online Job Posting Questions
Phone: 202 312 6375

EUROPE / INDIA / AUSTRALIA / NEW ZEALAND / REST OF WORLD

E-mail: ads@science-int.co.uk
Fax: +44 (0) 1223 326532

Axel Gesatzki
Phone: +44 (0) 1223 326529

Sarah Lelarge
Phone: +44 (0) 1223 326527

Kelly Grace
Phone: +44 (0) 1223 326528

JAPAN

Katsuyoshi Fukamizu (Tokyo)
E-mail: kfukamizu@aaas.org
Phone: +81 3 3219 5777

Hiroyuki Mashiki (Kyoto)
E-mail: hmashiki@aaas.org
Phone: +81 75 823 1109

CHINA / KOREA / SINGAPORE / TAIWAN / THAILAND

Ruolei Wu
Phone: +86 186 0082 9345
E-mail: rwu@aaas.org

All ads submitted for publication must comply with applicable U.S. and non-U.S. laws. *Science* reserves the right to refuse any advertisement at its sole discretion for any reason, including without limitation for offensive language or inappropriate content, and all advertising is subject to publisher approval. *Science* encourages our readers to alert us to any ads that they feel may be discriminatory or offensive.

ScienceCareers
FROM THE JOURNAL SCIENCE AAAS

ScienceCareers.org

ASU SCHOOL OF Life Sciences ARIZONA STATE UNIVERSITY

ASU BIODESIGN INSTITUTE ARIZONA STATE UNIVERSITY

Multiple Faculty Positions on Microbiomes at Arizona State University (JOB #11027)

The School of Life Sciences (SOLS) and the Biodesign Institute (BDI) at Arizona State University (ASU) invite applications for up to four tenure-track or tenured positions in the area of microbiome research. Rank and tenure status will be commensurate with experience. Anticipated start date is August 2015.

We seek to establish a strong group of scientists focused on understanding the functional and structural basis of complex systems of microbes, and their relevance for human, animal and plant biology, the environment, and man-made systems. We envision this group as working together to advance the discipline by developing novel techniques (omics or other types) and an integrated systems understanding of microbiomes, so as to establish general functional principles that are not only explanatory, but also predictive of the behavior of communities of microorganisms.

Successful candidates will be expected to develop or maintain an innovative, independent, extramurally funded research program, provide excellent classroom instruction as assigned, mentor students and postdoctoral fellows and interact with a very multidisciplinary group of faculty within SOLS and the Biodesign Institute. Competitive start-up packages will be provided. Group candidacies—either established or proposed—will be considered and are desired. All candidates must have a doctoral degree by the time of appointment in biology, microbiology, genetics, biochemistry, bioengineering, ecology or environmental engineering, biomedical engineering, medicine or a related field with a strong background and proven track record of novel research in microbiome biology. Desired qualifications include a record of publication in refereed journals, demonstrated excellence in teaching and/or mentoring, experience working in a multi-disciplinary environment, and at least two years of postdoctoral experience. Candidates for Associate or Full Professor rank must have a demonstrated record of significant extramural funding.

To apply, please send a cover letter that identifies the rank for which you seek consideration and if you wish to be considered as part of a group and/or as an individual candidate. Group candidates should identify all members who are applying. Additional application materials include a curriculum vitae, three representative publications, statement of research vision and plans, teaching statement, and contact information (name, email, and phone number) for three references. References will only be contacted for finalists at a later stage of the search and only with a candidate's approval. Application materials should be addressed to Raymond N. DuBois, Search Committee Chair, and sent electronically as pdf files to **solsfacultysearch@asu.edu**. Only electronic applications will be considered. The initial closing date for receipt of applications is **December 31, 2014**; if not filled, review will continue every week thereafter until the search is closed. A background check is required for employment.

Arizona State University is a VEVRAA Federal Contractor and an Equal Opportunity/Affirmative Action Employer. All qualified applicants will be considered without regard to race, color, sex, religion, national origin, disability, protected veteran status, or any other basis protected by law. https://www.asu.edu/aad/manuals/acd/acd401.html • https://www.asu.edu/titleIX/

NYU School of Medicine
NYU LANGONE MEDICAL CENTER

The Skirball Institute of Biomolecular Medicine and the Department of Cell Biology

FACULTY POSITIONS

The Skirball Institute of Biomolecular Medicine and the Department of Cell Biology at the New York University Langone Medical Center invite applications for tenure-track positions at the Assistant and Associate Professor level. We seek applicants with exceptional records of achievement to join our highly interdisciplinary faculty (www.skirball.med.nyu.edu). We are looking for interactive and creative candidates whose research interests synergize with the Institute's research interests in genome integrity and interpretation, metabolic signaling, and cellular dynamics within the context of developmental biology, stem cell biology, regeneration, molecular and cellular immunology, microbiology, biophysics and cellular and molecular neurobiology.

NYU Langone Medical Center will support new faculty with generous start-up packages, excellent research laboratory space, and state-of-the-art core facilities. Successful candidates are expected to initiate and maintain vigorous, independent, and highly innovative research programs that synergize with the highly collaborative environment at the Skirball Institute and throughout the NYU research community. New faculty members will hold a primary academic appointment in the Department of Cell Biology and will participate in the NYU School of Medicine graduate programs.

Please format an application as a single PDF document using the following page order: 1) Cover Letter; 2) Curriculum Vitae; 3) Research Statement; and 4) One recent publication. This is an electronic application process only.

Email the application packet to **Skirballsearch@med.nyu.edu**. Applications packages will be reviewed on a rolling basis until the search is closed on January 15, 2015. Three letters of reference should be sent independently to **Skirballsearch@med.nyu.edu**.

NYU School of Medicine was founded in 1841 and is an equal opportunity affirmative action employer. Women and minority candidates are encouraged to apply.

GROUP LEADER POSITIONS at IMBA, Vienna

We invite applications for two fully funded group leader positions at the Institute of Molecular Biotechnology of the Austrian Academy of Sciences (IMBA). We will consider applications in all areas of molecular and cell biology but are particularly interested in strengthening our program in stem cell biology and molecular medicine.

IMBA is one of the world's leading basic biomedical research institutes. Together with the IMP and the MFPL we are located at the thriving and interdisciplinary Vienna Biocenter (VBC). We aim to recruit candidates with a strong and innovative research program particularly in the areas of stem cell biology and molecular medicine. Positions include internationally competitive salaries and generous funds for student, postdoc and technician positions, investments and running costs.

Research groups enjoy free access to our scientific core services including Mass Spectrometry, Peptide Synthesis, Microscopy, Bioinformatics, Flow Cytometry, ES Cell core, a Drosophila facility and a 2000m^2 mouse house. IMBA participates in the VBC international PhD program and the VBC summer school, which are amongst the most competitive graduate and undergraduate research programs in Europe.

Applications should include a CV, a summary of research achievements and future research plans, and the contact details for 3 referees. In your publication list please explain in a few sentences the relevance of your most important work.
Applications should be submitted electronically to Sandra Prassel (***sandra.prassel@imba.oeaw.ac.at***) by ***January 2nd, 2015***.

The Institute of Molecular Biotechnology is home to 170 scientists from over 35 different nationalities. Vienna offers a multicultural environment, consistently ranking in the top 3 cities worldwide for the quality of living. Child care facilities are available at the VBC. For further information, see our website: ***www.imba.oeaw.ac.at***

ÖAW Austrian Academy of Sciences

IMBA Institute of Molecular Biotechnology of the Austrian Academy of Sciences

Tenure-Track Assistant Professorship in Chemistry and Chemical Biology
Harvard University
Cambridge, Massachusetts

Candidates are invited to apply for an open-field tenure-track assistant professorship in the Department of Chemistry and Chemical Biology at Harvard University. The appointment is expected to begin on July 1, 2015. The tenure-track professor will be responsible for teaching at the undergraduate and graduate levels. We are seeking candidates who have an outstanding research record and a strong commitment to undergraduate and graduate teaching. Doctorate required by expected start date. Candidates should arrange to have three letters of recommendation sent independently and provide a curriculum vitae, statement of teaching philosophy, list of publications, and outline of their future research plans. All applications and supporting materials must be submitted via the ARIeS portal (**http://academicpositions.harvard.edu/postings/5829**) no later than **December 15, 2014**.

Harvard is an Equal Opportunity Employer and all qualified applicants will receive consideration for employment without regard to race, color, religion, sex, national origin, disability status, protected veteran status, or any other characteristic protected by law.

WE MAKE LIVES BETTER
UT HEALTH SCIENCE CENTER™
SAN ANTONIO

ASSISTANT PROFESSOR
Department of Cellular and Structural Biology
School of Medicine

Applications are invited for an ASSISTANT PROFESSOR tenure track academic appointment in the Department of Cellular and Structural Biology (http://uthscsa.edu/CSB/) within the School of Medicine at the University of Texas Health Science Center at San Antonio. We seek an outstanding investigator poised to develop a vibrant research program. An ideal applicant will have expertise in genomic approaches and bioinformatic analyses pertinent to stem cell biology, cancer, neurodegeneration, aging, metabolism, or developmental/reproductive biology. Candidates must hold a Ph.D., M.D., D.D.S. or equivalent degree and have a minimum of three years of productive postdoctoral experience. The selected candidate will be expected to participate in departmental teaching to professional students and graduate students. A competitive startup package is available. The Department of Cellular & Structural Biology enjoys a dynamic research program that offers opportunities for multidisciplinary collaborative investigation. The UT Health Science Center at San Antonio is home to the Nathan Shock Center for Excellence in Biology of Aging, an NCI designated cancer center, an NIH funded Clinical Translational Science Award, the Center for Biomedical Neuroscience, and the Greehey Children's Cancer Research Institute. The UT Health Science Center is designated an Hispanic Serving Institution. The UT Health Science Center at San Antonio is a Tier One research institution in the Northwest region of San Antonio and sits as a gateway to the picturesque Texas Hill Country. The San Antonio Military Medical Center, Texas Biomedical Research Institute, Southwest Research Institute, and the Audie Murphy VA Hospital are area institutions that partner with Health Science Center faculty to catalyze the local biomedical research enterprise. San Antonio is a dynamic and multicultural city with a relatively low cost-of-living, and an outstanding cultural and educational environment.

Electronic submission of a PDF containing a full curriculum vitae, statement of research interests, a list of 4 to 5 references with contact information and up to 3 high impact publications will constitute an application. The complete PDF should be submitted by email to **jrfacsc@uthscsa.edu**; applications will be reviewed as received, starting immediately and continuing until the position is filled.

The University of Texas Health Science Center at San Antonio is an Equal Employment Opportunity/ Affirmative Action Employer including protected veterans and persons with disabilities. All faculty appointments are designated as security sensitive positions.

ScienceCareers online @sciencecareers.org

The University of New Mexico

BIOLOGY OF INFECTIOUS DISEASE
Open Rank-Assistant/Associate Professor
Department of Biology, The University of New Mexico
Center for Evolutionary and Theoretical Immunology

The Department of Biology at the University of New Mexico invites applications for an Open Rank full-time, tenure-track appointment in the area of the **biology of infectious disease** at the Assistant Professor level, beginning in Fall 2015. An appointment at the Associate Professor level (with tenure or leading to tenure) may be considered for more experienced candidates. This position is funded in part by an NIH Center of Biomedical Research Excellence (COBRE) award that supports the Center for Evolutionary and Theoretical Immunology (**http://ceti.unm.edu**).

Applicants must have a Ph. D. in biology or a related discipline and at least two years relevant postdoctoral experience. For complete details or to apply, please visit: **https://unmjobs.unm.edu/** and reference the posting number **0827817**. Best consideration date is **January 16, 2015**. The position will remain open until filled. The successful candidate will demonstrate excellence in research with a significant laboratory or field-based component as evidenced by pre- and post-doctoral work; have a demonstrated publication record in peer-reviewed journals; complement existing research in the department and be committed to establishing an internationally recognized and externally funded research program in the area of the biology of infectious disease. In addition, we seek a colleague who will demonstrate a commitment to excellence in teaching at the undergraduate through graduate level in a minority majority institution and shows enthusiasm for working in a broadly collaborative biology department with diverse research strengths.

To apply, applicants must submit a letter of interest, curriculum vitae, three recent publications, statements of research and teaching interests, and a list of names and contact information of three referees. All materials must be submitted directly to **https://unmjobs.unm.edu/** by the best consideration date. When letters of recommendation are requested, the letters should be e-mailed as PDF attachments to **LSEASST@unm.edu** as soon as possible. Questions can be directed to **Dr. Charles Cunningham** (**ccunnin@unm.edu**).

The University of New Mexico is an Equal Opportunity/Affirmative Action Employer and Educator. Women and underrepresented minorities are encouraged to apply.

utmb Health

Chair
Department of Neuroscience and Cell Biology
The University of Texas Medical Branch
Galveston, Texas

The University of Texas Medical Branch (UTMB Health) is seeking candidates to serve as Chair of the Department of Neuroscience and Cell Biology. Candidates with rank of Professor/Associate Professor with strong research experience will be considered. The successful candidate will have demonstrated leadership skills, be nationally recognized for his/her contributions to the field.

The Department has a long-standing tradition of excellence research and education. The mission of the Department of Neuroscience and Cell Biology is dedicated to pushing the frontiers of basic and translational research in the neurosciences and cell biology and to medical, graduate, residency and postdoctoral education. Currently, there are 17 faculty members in the department. Two graduate programs are affiliated with the department – the Neuroscience and Cell Biology programs.

UTMB Health is a billion-dollar health science center comprised of four schools, three institutes and over 10 exceptional research centers. Interested candidates should send a current curriculum vitae, cover letter and the names and contact information for three references to **Dara Childress** at **301 University Boulevard, Galveston, Texas 77555-0133** or to **dbchildr@utmb.edu**.

UTMB Health strives to provide equal opportunity employment without regard to race, color, national origin, sex, age, religion, disability, sexual orientation, gender identity or expression, genetic information or veteran status. As a VEVRAA Federal Contractor, UTMB Health takes affirmative action to hire and advance women, minorities, protected veterans and individuals with disabilities.

Assistant Professor Positions Available at Princeton University

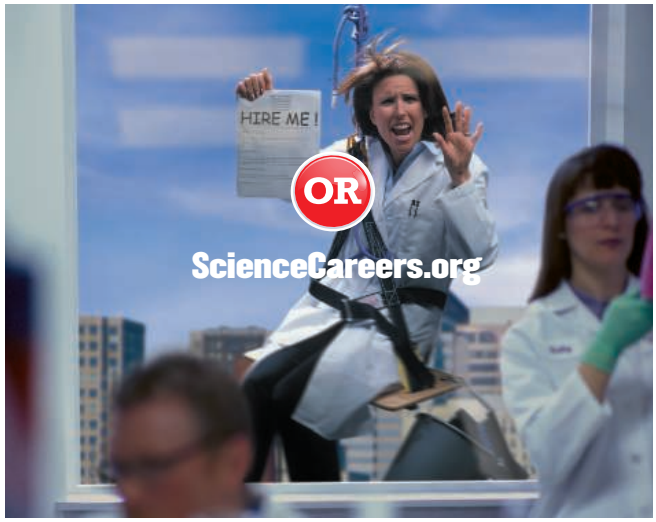
The Lewis-Sigler Institute for Integrative Genomics at Princeton University invites applications for tenure-track faculty positions at the Assistant Professor level. We are seeking outstanding scientists with strong interest and experience in quantitative, systems-level approaches to understanding any area in modern experimental molecular biology, chemistry, or evolutionary biology. Appointments at the Lewis-Sigler Institute are made jointly with an appropriate home department. A strong record of experimental work and quantitative analysis is essential. The successful candidate will have research laboratories at the Institute, and teaching responsibilities (both graduate and undergraduate) will be shared between the Institute and the home department.

The Lewis-Sigler Institute for Integrative Genomics, housed in the Carl Icahn Laboratory at Princeton University, was established to innovate in research and teaching at the interface of modern biology and the more quantitative sciences. The Institute provides significant support to its faculty through heavy investment in state-of-the-art research infrastructure, an NIH-funded graduate training program, and a high level of administrative support as well.

Essential Qualifications: All applicants must have a Ph.D., M.D., or equivalent degree. In addition, applicants must have a very strong record of research productivity, demonstrate the ability to develop a rigorous research program, and be committed to teaching at both the undergraduate and graduate levels.

How to Apply: Applications must be submitted online at: **http://jobs.princeton.edu/applicants/Central?quickFind=65989** and should include a cover letter, curriculum vitae, a two-page research description, as well as contact information for three references. Applications will be reviewed beginning on **January 5, 2015**.

Princeton University is an Equal Opportunity Employer. All qualified applicants will receive consideration for employment without regard to race, color, religion, sex, national origin, disability status, protected veteran status, or any other characteristic protected by law. This position is subject to the University's background check policy.



Don't let your job search leave you washed up.

- Search thousands of job postings
- Create job alerts based on your criteria
- Get career advice from our Career Forum experts
- Download career advice articles and webinars
- Complete an individual development plan at "myIDP"

Target your job search using relevant resources on **ScienceCareers.org**.

ScienceCareers
FROM THE JOURNAL SCIENCE AAAS

北京理工大学
BEIJING INSTITUTE OF TECHNOLOGY

Open Senior Faculty Positions

Beijing Institute of Technology (BIT) is a prestigious national key university in China and enjoys a high reputation in research and education in science, technology and other areas of scholarship. The institute was founded in 1940, which is one of the first Chinese universities to run a graduate school, and one of the national "Project 211" and "Project 985" universities which are given priority for development by the Chinese government.

I. Talent programs

The University is especially interested in candidates who can contribute, through their research, teaching, and/or service, to the diversity and excellence of the academic community, and is actively seeking to hire outstanding faculty members according to the following recruitment programs: the Recruitment Program of Global Experts (Its subprograms include Long-term Program for Innovative Talents, Short-term Program for Innovative Talents, Young Scholars Program, Global Experts Program, and Top Talents and Innovation Team Program.)supported by the Chinese government, the Chang Jiang Scholars Program, the Program supported by the China National Science Foundation for Distinguished Young Scholars, the Program supported by the China National Foundation for Excellent Young Scholars, the New Century Excellent Talents in University Program supported by the Ministry of Education (MOE), and the recruitment programs supported by the University.

II. Major open faculty positions

Equipment Science • • Technology Engineering	Mechanical Engineering	Optical Engineering	Information and Communication Engineering
Mechanics	Control Science and Engineering	Materials Science and Engineering	Management Science and Engineering
Chemical Engineering and Technology	Power Engineering and Engineering Thermo Physics	Electronic Science and Technology	Computer Science and Technology
Software Engineering	Biomedical Engineering	Aeronautic and Astronautic Science and Technology	Mathematics
Physics	Chemistry		

III . Application and Contact us

Applicants can visit http://renshichu.bit.edu.cn/ for more information. Please send a curriculum vitae via email to: sscsr@bit.edu.cn, or shizike@bit.edu.cn. And contacts with Mr. Shi or Mr. He. Tel.: +8610-68918577/68912338

For more faculty positions, please visit our website http://renshichu.bit.edu.cn/ .

Qingdao Technological University Recruits for High-end Talents

Qingdao Technological University is a multiversity includes Science, Engineering, Economics, Management, Literary, Law and Arts. Particularly at Science and Engineering, Civil Construction, Machine Manufacturing, and Environmental Energy.

Enjoys a 60 years history, the university builds a higher education system with undergraduates, masters and doctors. The university now has three campuses: Shibei, Huangdao, and Feixian, which accommodates 19 academic schools, 59 undergraduates programs, 18 level-1 disciplines offering master's degree programs, 1 first-level discipline offering doctoral degree programs, 7 second-level disciplines offering doctoral degree programs, 2 first-level discipline post-doc research stations, and 25 provincial key disciplines, key labs and engineering technical research centers. Now the University has 2215 faculty and staff members, and over thirty thousand students .

In accordance with the university development, now we are recruiting high-end talents globally.

Disciplines

Civil Engineering, Mechanical Engineering, Environmental Science and Engineering, Architecture, Rural and Urban Planning, Landscape Architecture, Design Planning, Communication and Transportation Engineering, Safety Science and Engineering, Computer Science and Technology, Software Engineering, Information and Communication Engineering, Control Science and Engineering, Materials Science and Engineering, Mechanics, Management science, Business Administration, and Applied Economics.

Requirements

Applicants should have doctorate, also hold the position of assistant professor, associate professor, and professor at leading universities or research institutions overseas. Professionals and talented management at well-known enterprise or financing institution would be acceptable as well.

Contact information

For more information, please check on our main site: http://www.qtech.edu.cn
Tel: +86-0532-85071322
E-mail: qdlgrc@163.com

西南交通大学 Southwest Jiaotong University

Southwest Jiaotong University, P.R.China Anticipates Your Working Application

Southwest Jiaotong University (SWJTU), founded in 1896, situates itself in Chengdu, the provincial capital of Sichuan. It is a national key multidisciplinary "211" and "985 Feature" Projects university directly under the jurisdiction of the Ministry of Education, featuring engineering and a comprehensive range of study programs and research disciplines spreading across more than 20 faculties and institutes/centers. Boasting a complete Bachelor-Master-Doctor education system with more than 2,500 members of academic staff, our school also owns 2 first-level national key disciplines, 2 supplementary first-level national key disciplines (in their establishment), 15 first-level doctoral programs, 43 first-level master programs, 75 key undergraduate programs, 10 post-doctoral stations and more than 40 key laboratories at national and provincial levels.

Our university is currently implementing the strategy of "developing and strengthening the university by introducing and cultivating talents". Therefore, we sincerely look forward to your working application.

More information available at http://www.swjtu.edu.cn/

I. Positions and Requirements

A.High-level Leading Talents

It is required that candidates be listed in national top talents programs such as ***Program of Global Experts, Top Talents of National Special Support Program, "Chang Jiang Scholars", China National Funds for Distinguished Young Scientists and National Award for Distinguished Teacher.***

Candidates are supposed to be no more than 50 years old. The limitation could be extended in the most-needed areas of disciplinary development.

Candidates who work in high-level universities/institutes and reach the above requirements are supposed to be no more than 45 years old.

B. Young Leading Scholars

Candidates are supposed to be listed in or qualified to apply for the following programs:

- ***National Thousand Young Talents Program***
- ***The Top Young Talents of National Special Support Program(Program for Supporting Top Young Talents)***
- ***Science Foundation for the Excellent Youth Scholars***

Candidates should have good team spirit and leadership, outstanding academic achievements, broad academic vision and international cooperation experience and have the potential of being a leading academic researcher.

C. Excellent Young Academic Backbones

Candidates under 40 years old are expected to graduate from high-level universities/institutes either in China or other countries. Those who are professors, associate professors and other equal talents from high-level universities/institutes overseas could be employed as professors and associate professors as well.

D. Excellent Doctors and Post Doctoral Fellows

Candidates under 35 years old are supposed to be excellent academic researchers from high-level universities either in China or other countries.

II. Treatments

The candidates will be provided with competitive salaries and welfares that include settling-in allowance, subsidy of rental residence, start-up funds of scientific research, assistance in establishing scientific platform and research group as well as international-level training and promotion . As for outstanding returnees, we can offer further or specific treatments that can be discussed personally.

III . Contact us:

Contacts: Ye ZENG & Yinchuan LI Telephone number: 86-28-66366202 Email: *talent@swjtu.edu.cn*
Address: Human Resources Department of SWJTU, the western park of high-tech zone, Chengdu, Sichuan, P.R.China, 611756

http://www.swjtu.edu.cn/

Faculty Positions available at Hohai University, Nanjing, China

Hohai University invites applications for faculty positions at the assistant, associate, or full professor level in the area of engineering, science, economics, management, liberal arts, and law. Applicants should have a doctoral degree from a prestigious university. For the complete job announcements and directions on how to apply, visit: rsc.hhu.edu.cn or contact the Department of human resource at 86-25-83786205.

Hohai University, founded in 1915, wins its worldwide reputation on the research of Water Science& Civil Engineering&Environment Engineering. It is a National key university of China, and among the universities of the National "*211 Project*" and Innovation Bases of the National "*985 Project*". Hohai University aims to be a research oriented university.

ScienceCareers online @sciencecareers.org
OPPORTUNITIES IN CHINA

Online Career Fairs

December 10, 2014



For careers in science, there's only one **Science**

Meet recruiters without leaving your lab or desk!

Science Careers is excited to bring you an easy, efficient and powerful way to connect with employers from all over... all in one place. This virtual event allows you to queue up to visit with representatives from any companies you are interested in during the event hours.

Features and Benefits of Attending this Event

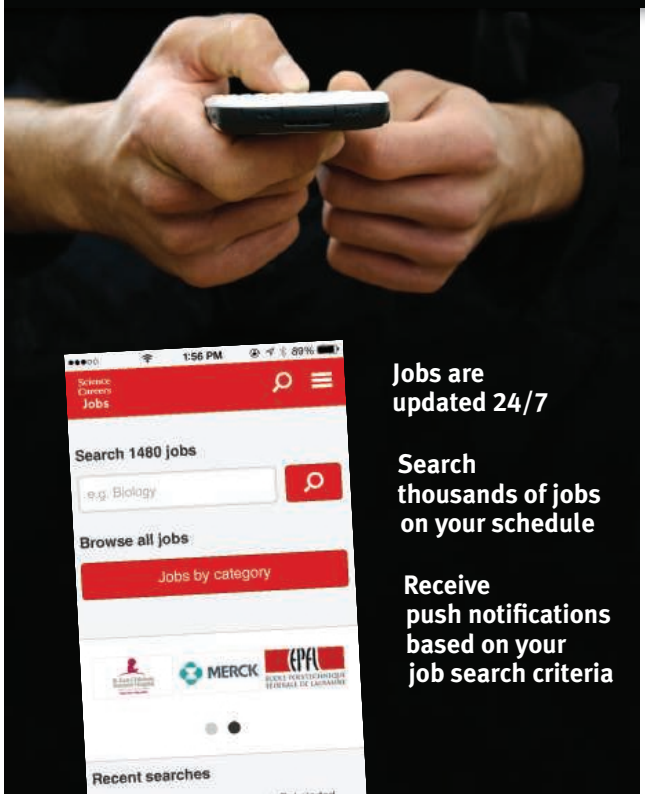
- No travel required—you can login from anywhere
- Queues tell you how many people are in line ahead of you and how long you will be waiting so you can better manage your time
- Login before the event to learn more about participating employers
- Employers can see your resume while you are talking to them



ScienceCareers
FROM THE JOURNAL SCIENCE AAAS

For more information, visit:
ScienceCareers.org/onlinecareerfair

Download the *Science* Careers jobs app from Science



Jobs are updated 24/7

Search thousands of jobs on your schedule

Receive push notifications based on your job search criteria

Get a job on the go.
Search thousands of scientific jobs in academia, industry, and government from around the globe. The seamless application process includes linking you directly to job postings from your customized push notifications.

Scan this code to download app or visit **apps.sciencemag.org** for information.

ScienceCareers
FROM THE JOURNAL SCIENCE AAAS

ScienceCareers.org

ScienceCareers online @sciencecareers.org

Science Careers

Cernet

“《科学》职业” 已经与Cernet/赛尔互联开展合作。中国大陆的高校可以直接联系Cernet/赛尔互联进行国际人才招聘。



请访问 Sciencecareers.org/CER 点得联系信息。

招募学术精英，《科学》是您的不二之选 Science

UNIVERSITY OF SOUTH CAROLINA
Arnold School of Public Health

Department of Exercise Science

The Department of Exercise Science in the Arnold School of Public Health at the University of South Carolina invites applications for a tenure-track position at the Assistant or Associate Professor level to begin in August 2015. Priority will be given to candidates who have or will develop a collaborative, multidisciplinary research program that complements the Department's current strengths in physical activity, cancer, inflammation, nutrition, and rehabilitation. Individuals will be expected to teach and interact with a network of researchers in the Arnold School of Public Health (http://sph.sc.edu) and/or other university networks including the Center for Colon Cancer Research (http://cccr.sc.edu/), the Center on Dietary Supplements and Inflammation (http://cobre.med.sc.edu), and the Center for Targeted Therapeutics (https://www.sccp.sc.edu/). Research approaches can be basic or applied, making use of in vitro, small animal, and/or human models, and can include clinical trials, epidemiology and/or community engagement methodology. For full description of position and application instructions, please visit: **http://sph.sc.edu/exsc/pdf/ExerciseScience_2015position.pdf**.

POSITIONS OPEN

BETCy EFRC

POSTDOCTORAL ASSOCIATE AND RESEARCH ASSOCIATE POSITIONS

The Biological Electron Transfer and Catalysis Energy Frontiers Research Center (BETCy EFRC) has multiple openings at the postdoctoral level for highly qualified applicants. BETCy EFRC is a multi-institution research center investigating the mechanisms and protein structural features controlling electron bifurcation, electron-ion coupling, nucleotide-coupled electron transfer, and redox catalysis in model enzymes. Understanding how these systems control electron flow will contribute to the knowledge base necessary for developing superior biotechnological solutions for the production of biofuels. BETCy-EFRC offers a unique opportunity to participate in the collaborative research environment fostered by the Center's eleven laboratories located at seven participating institutions across the United States. Detailed information for each position is available at **website: http://eu.montana.edu/betcy-efrc/opportunities.htm.**

FACULTY POSITION
Johns Hopkins University
School of Medicine
Institute for Cell Engineering

The Institute for Cell Engineering invites applications from outstanding individuals with creative, rigorous, and integrative research approaches to enhance its cell engineering investigational strengths in immunology, stem cell biology, neurosciences, and vascular biology. For additional information about the institute, visit **website: http://www.hopkinsmedicine.org/institute_cell_engineering/**. Candidates should have an M.D. and/or a Ph.D. degree with appropriate postdoctoral experience and an outstanding publication record. Primary department affiliation will be determined by the applicant's qualifications and by relevance of the applicant's research program to departmental initiatives. The successful candidate will have experience in any aspect of stem cell biology or related field. Special attention will be give to investigators in the areas of vascular biology or organogenesis.

To apply, submit curriculum vitae, three letters of reference, copies of relevant publications and a concise description of research interests and research plans (up to three pages) to **e-mail: icesearch@jhmi.edu** to the attention of **Ted M. Dawson**, Director, Institute for Cell Engineering. Applications will be assessed on an ongoing basis and the deadline for submission is December 15, 2014. The appointment is expected to be made in 2015.

The John Hopkins University School of Medicine is an Affirmative Action/Equal Opportunity Employer that embraces diversity.

ASSISTANT PROFESSOR
University of Connecticut College of Liberal Arts and SciencesDepartment of Physics

The Department of Physics, at the University of Connecticut, invites applications for a full-time tenure-track faculty position at the rank of Assistant Professor.Outstanding, established candidates at the Associate Professor level will be considered as well. The successful candidate will be expected to contribute to research and scholarship through extramural funding in experimental atomic, molecular, and optical or condensed matter physics. In addition to a strong research profile, the successful candidate will share a deep commitment to effective instruction, diversity, service, and outreach.

This is a full-time, nine-month, tenure-track position with an anticipated start date of August 23, 2015. For a detailed list of position qualifications and application requirements, please see our complete job posting at **website: https://academicjobsonline.org/ajo/jobs/5033.** *The University of Connecticut is an Equal Employment Opportunity/Affirmative Action Employer.*

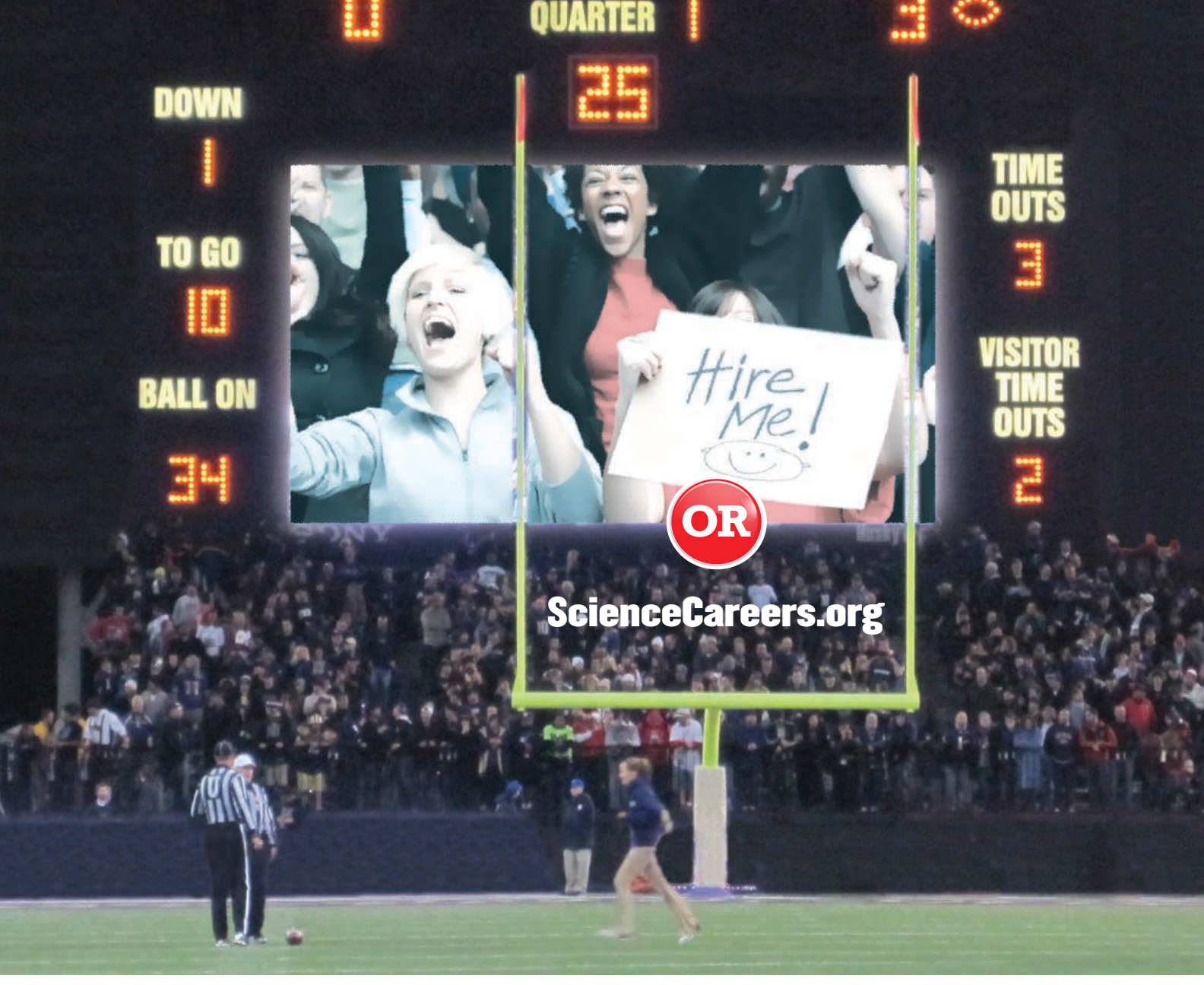
Download your free copy today.

ScienceCareers.org/booklets



From technology specialists to patent attorneys to policy advisers, learn more about the types of careers that scientists can pursue and the skills needed in order to succeed in nonresearch careers.

ScienceCareers
FROM THE JOURNAL SCIENCE AAAS



Learn more and keep your job search out of the cheap seats.

- Search thousands of job postings
- Create job alerts based on your criteria
- Get career advice from our Career Forum experts
- Download career advice articles and webinars
- Complete an individual development plan at "myIDP"

Target your job search using relevant resources on **ScienceCareers.org**.

ScienceCareers
FROM THE JOURNAL SCIENCE AAAS

By **Ranjan Mukherjee**

The winding road

On a bright July day more than 3 decades ago, I turned up at the physics department of the University of Delaware (UD), Newark, hoping to meet my new research adviser. I was met instead with quizzical looks: The professor had died some months before I arrived. No one had told me. ¶ I had come a long way. After finishing a master's degree in physics at the University of Calcutta, I had become interested in biophysics. I had decided to pursue a Ph.D. studying the physical properties of nucleic acids and had won admission to UD, with a teaching assistantship. I packed my bags, got my passport and tickets, and said farewell to family and friends. Half a world from home, I was left scratching my head, contemplating my next step. What would I do? I had student visa requirements and little money. I taught physics labs that summer as I pondered my future.

A month later, I was taking a short cut through the biology department when I came upon an outline of a graduate cell biology course that would be offered in the fall. I liked it. I sought out the professor, told him my story, and proposed doing a biology Ph.D., even though I had never taken a college-level biology course. He looked at me as if to say, "You can't be serious." Still, he agreed, with conditions: I had to get an A in his course, and I had to take the biology Graduate Record Exam (GRE).

The fall semester was busy and tense. I was enrolled in the physics graduate program, taking a full course load, and I was teaching lab courses. I also took the cell biology course. I got an A. I took the GRE and was admitted to the graduate program in biology.



"My career has taken several sudden, unexpected twists and turns."

There were many new things to learn. I took makeup courses, taught lab courses, and did research. It was a wonderful experience. Toward the end of the program, I got married.

I finished my Ph.D., and my wife and I moved to France, where I did a postdoc at the CNRS-LGME in Strasbourg—again the packing of bags, obtaining of visas, fond farewells, the start of a new life on a new continent. I worked hard in Strasbourg but also had fun, traveling around, sampling the local cuisine, and traversing the fabled Route du Vin. Three years later, we returned to the United States, and I began my professional career.

I worked in metabolic disease drug discovery in the pharmaceutical industry for more than 22 years. I worked hard, published papers, presented at national and international conferences, and took fun vacations. Life was good. Last year, the company where I had more than 15 service years ended R&D efforts in diabetes and eliminated several positions, including mine. This was not as shocking as the news of the dead adviser, but it was a major jolt nonetheless. I took the severance package and found myself wondering, "What now?" for the first time in more than 30 years.

A committed traveler and avid reader of travel magazines, I decided to try writing travel articles. I wrote a few articles on Indian wildlife that I had photographed on safaris and a piece on an interesting experience I had when my car broke down on the freeway near Philadelphia. I sent them off to journals and blogs. Three have been accepted, one by a popular U.S. magazine, the second by a major newspaper, and the third by the Indian government for publication on a new government website. It's not a bad start to a writing career.

My career has taken several sudden, unexpected twists and turns. Careers are like that these days. I have accepted the challenges as they've come and done my best to overcome them, with reasonable success. I have always viewed my job as a means to an end, to enjoy life and work. Research offered those rewards—until it didn't. Now I have set off on another kind of exploration. ■

Ranjan Mukherjee is now a freelance writer. For more on life and careers, visit www.sciencecareers.org. Got an interesting career story? Send it to SciCareerEditor@aaas.org.

ILLUSTRATION: ROBERT NEUBECKER

Downloaded from www.sciencemag.org on November 22, 2014

Published by AAAS